Cranfield University
College of Aeronautics

PhD

1995

Howard Smith

A New Method for Predicting the Vortex Induced Aerodynamic Characteristics of a Body of Revolution

Supervisor: P.A.T.Christopher
August 1995

1. SUMMARY

The problem of mathematically modelling the symmetric vortex pair formed on the lee side of a body of revolution at moderate incidence to the freestream direction is addressed with a view to predicting its aerodynamic characteristics. The objective being to develop a model simple enough to enable rapid calculation whilst maintaining acceptable levels of accuracy.

Existing techniques are reviewed and their strengths and weaknesses evaluated.

The physics of the flow are explored with an emphasis on its three dimensional aspects. Experimental results, including surface pressure tapping data and flow visualisation, are used to investigate the nature of the flow. To gain a deeper insight into the flow processes less measurable experimentally, Navier-Stokes solutions are examined in considerable detail.

The mechanisms of vorticity generation and propagation are explored.

A simple mathematical model is presented, based upon an extension to slender body theory, which predicts aerodynamic characteristics that compare well with experiment.

2. ACKNOWLEDGEMENTS

Firstly, I must thank Fred Filby for having enough faith in me to authorise British Aerospaces sponsorship of this PhD. Thanks also go to Toni Hipp and Vic Marshall, chief aerodynamicists, For their supporting my studies.

I would like to thank Tony Sadler and Trevor Birch at DRA for their help and suggestions and for giving me access to data that has greatly supported my thesis. (Thanks Trevor for not once answering your phone with "Not you again!")

Thanks also to Paul Herring at the Sowerby Research Centre for his assistance in tracking down some of the experimental data.

Thanks also go to the countless friends and colleagues who, over the years, have played a part in the completion of this thesis and often made it such a challenge.

I would like to thank Peter Christopher, friend and supervisor, whose unwavering support and encouragement gave me the strength to complete this project. I must also thank Letty for lending me Peter during their well earned retirement.

Thankyou to my parents for ..... everything. Yes, I think that's enough studying for now.

I am indebted to my wife, Mahnaz, who has not only helped in the production of this document, has given me every encouragement over the endless years, but has had to endure the absence of a husband over the countless holidays, weekends and evenings that went into this thesis. Hugs and kisses to my daughter, Stephanie, who has missed so many hugs and kisses. God bless them both.

3. CONTENTS

1	SUMMARY	i
2	ACKNOWLEDGEMENTS	ii
3	CONTENTS	iii
4	NOTATION	v
5	INTRODUCTION	
	5.1 The aerodynamic problem	1
	5.2 Analytical models of slender body aerodynamics	7
	5.3 The vortex cloud method	11
	5.4 Objectives of study	13
6	DISCRETE VORTEX MODELS	
	6.1 Introduction	15
	6.2 Appraisal of current methods	15
7	SURVEY AND ANALYSIS OF EXPERIMENTAL DATA	
	7.1 General experimental data requirement	28
	7.2 Survey and selection of relevant experimental data sources	29
	7.3 The Fage and Johansen test series	30
	7.4 The DFVLR and ONERA test series	45
	7.5 The Tinling and Allen test series	57
8	THREE-DIMENSIONAL INFLUENCES	
	8.1 A comparison of 2 & 3-D separation patterns	59
	8.2 Viscous regions & the significance of transition	66
	8.3 The effect of the boundary layer state on separation	70
	8.4 The effect of separation on the flow field	75
	8.5 Vorticity generation and convection	76
9	SURVEY AND ANALYSIS OF FINITE DIFFERENCE SOLUTIONS	
	9.1 Survey of CFD methods	83
	9.2 Analysis of Navier-Stokes solutions	88
	9.3 Integration of vorticity to obtain circulation in the vortex structure components	92
	9.4 Variation of circulation with axial coordinate	95
	9.5 Rate of generation of circulation	96
	9.6 The sigma factor	102
10	A NEW APPROACH	
	10.1 Theory	104
	10.2 Determination of vortex strength and position	135
	10.3 The linear load	144
	10.4 Integration of the model	145
11	COMPARISON WITH EXPERIMENT	
	11.1 Comparisons	148
	11.2 Experimental data source	149

11.3 Load distribution predictions 151
11.4 Overall aerodynamic characteristics 155
11.5 Vortex path predictions 157
11.6 Additional cases 158
12 DISCUSSION & CONCLUSIONS
12.1 General 160
12.2 Three dimensional effects 160
12.3 A more rational model 164
12.4 Validation 166
12.5 Comparison with requirement 167
12.6 Future work 167
13 REFERENCES 169
14 FIGURES 175
15 TABLES

4. NOTATION

a	body radius
a	longitudinal spacing
$\overline{A_1}$	residue
C_F	coefficient of force
C_M	coefficient of pitching moment
C_N	coefficient of normal force
C_σ	cross section perimeter contour
C_ς	cross section perimeter contour
d	body diameter
e_r, e_θ, e_z	cylindrical polar unit vectors
e	exponential constant
f	frequency of generation of vortices
F_1	complex potential
h	lateral spacing
i	unit vector
j	unit vector
K	rate of increase of circulation
k	unit vector
L	normal force
$\dot{m}$	mass flow rate
M	Mach number
p	pressure
R_e	Reynolds number
R_D, R_{ed}	Reynolds number based upon body diameter
s	one dimensional coordinate of distance
S	body cross sectional area
t	time
U	freestream velocity
u	component of velocity
VCM	Vortex Cloud Method
V	velocity
v	component of velocity
W	complex velocity
w	component of velocity
x	coordinate
X_{cp}	centre of pressure position
y	coordinate
Y	lateral force
z	coordinate
α	angle of incidence
β	angle of side slip
Γ	total circulation
ζ	component of vorticity

ζ	complex coordinate
$\zeta_{(}$	complex coordinate of vortex
η	component of vorticity
θ	separation angle, angular distance
θ	body roll angle relative to incidence plane
λ	vortex circulation
μ	coefficient of viscosity
ν	kinematic viscosity
ξ	component of vorticity
ρ	atmospheric density
σ	vortex strength reduction factor
σ	complex coordinate
σ_i	total body incidence
σ_1	applied vortex strength reduction factor
τ	skin friction
χ	vortex strength
ϕ	angular distance

subscripts

θ, r	polar component, radial component
0	freestream conditions
0, 1	at image vortex, at real vortex
1, 2	outside vortex sheet, inside vortex sheet
Area	over an area
c	cylindrical component
Contour	around a contour
cr	critical
field	accumulated in the flow field
s	at separation point
shed	that has been shed
w	at the wall

5. INTRODUCTION

5.1 THE AERODYNAMIC PROBLEM

5.1.1 The generation of vortices by slender aerospace configurations

When a slender body is raised to a moderate incidence in a freestream flow a set of vortices will be generated that can significantly alter it's aerodynamic characteristics. Before discussing the physics of this problem, albeit initially in a superficial manner, let us first consider how it applies to practical aerospace vehicle configurations.

The prime application is to the determination of the aerodynamic characteristics of missile configurations. Missile configurations tend to consist of slender bodies with slender lifting and control surfaces. This necessitates the ability to operate over a wide range of incidences to enable sufficient lift to be generated to meet the often high lateral acceleration requirements. Clearly during most manoeuvres body vortices will be generated that will effect both the overall aerodynamic forces and moments acting on the airframe as well as the symmetric and asymmetric control powers. Hence a good understanding of the body vortex phenomenon and the ability to predict its effects are vital if a missile concept is to achieve optimum[1] manoeuvrability and controllability.

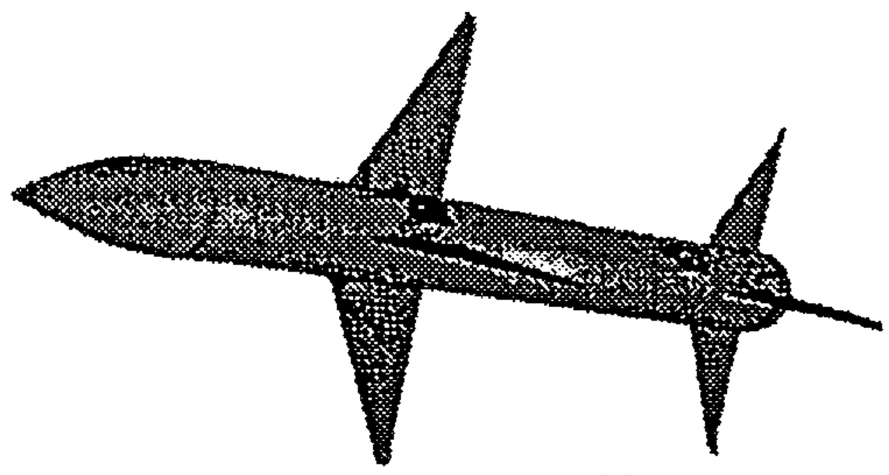

Typical missile configuration

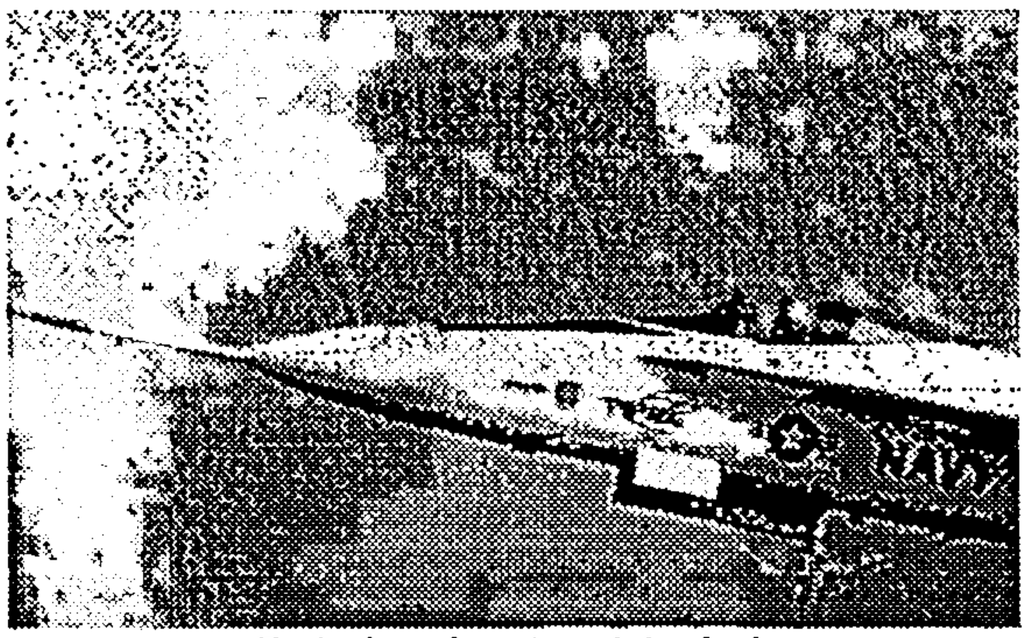

Typical combat aircraft forebody

Another related configuration is that of the combat aircraft. In this case the applicability is more appropriate to the fuselage forebody which although slender may exhibit a wide range of cross-sectional geometry's.

Other vehicles similarly effected include submarines and torpedoes. There are also other situations that may give rise to similar flows such as launcher vehicles operating during their initial phase in a cross wind.

---

[1]Without this ability it may not be possible to achieve any controllability let alone optimal, particularly in roll.

5.1.2 Slender bodies at incidence

Let us consider a slender[3] body enveloped in a subsonic uniform viscous freestream flow raised to some moderate[4] angle of incidence. To the windward side of the body the flow field will exhibit little change from that of the body at zero incidence. To the lee side of the body the near flow field will be unrecognisably different from that of the zero incidence case. Large vortical flow structures will have been created with lateral dimensions of the order of a calibre[5]. These vortices run almost the entire length of the body and persist beyond it's aft-most point. These vortex structures exert considerable influence on the local flow field, inducing velocity components that effect surface pressures and hence body forces and moments.

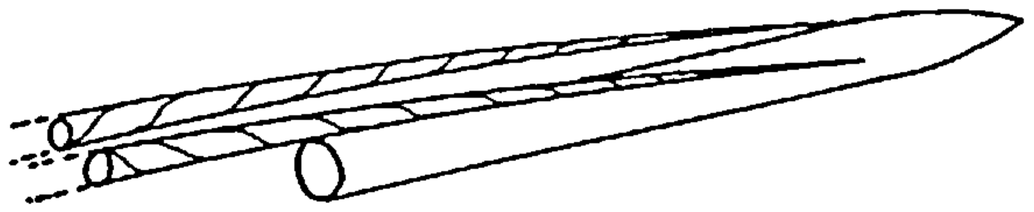

A slender body generating vortices[2]

It might be easy to assume at this point that the prediction of the flow about such a simple body should be straight forward. However, before committing to specific objectives it would be wise to consider, albeit briefly, the magnitude of the problem.

5.1.3 The slender body vortex

Of all the slender configurations that have been investigated over the years it is the slender delta that is the most well known. It is, then, appropriate to look at this geometry before considering the slender body of revolution. Here the flow field structure is simplified in two respects. Firstly, at moderate incidence, the flow will always separate from the leading edge and secondly the flow exhibits strong conical characteristics, the conical origin being the apex of the delta. The form of the resulting vortex pair are the well known conical structures developed about rays slightly inboard of, and above the, leading edges and radiating from the delta apex. We shall now look at the analogous case of the slender body of revolution.

---

[2]As with most aerodynamic flow fields, the vortices are not usually visible. This diagram represents a conceptual model of the vortices only.

[3]We shall discuss the definition of slender later.

[4]Again a more precise definition of moderate incidence will be forthcoming.

[5]1 calibre represents the maximum body diameter.

Let us start by considering the flow about the body at zero incidence. As the freestream is displaced by the volume of the body there will be local velocity perturbations that give rise to pressure changes. Although these effects are significant there is a detail of the flow that will dominate when incidence is applied. This detail, the boundary layer, has, in this context, little effect at low incidence but will prove to be the progenitor of the body vortices.

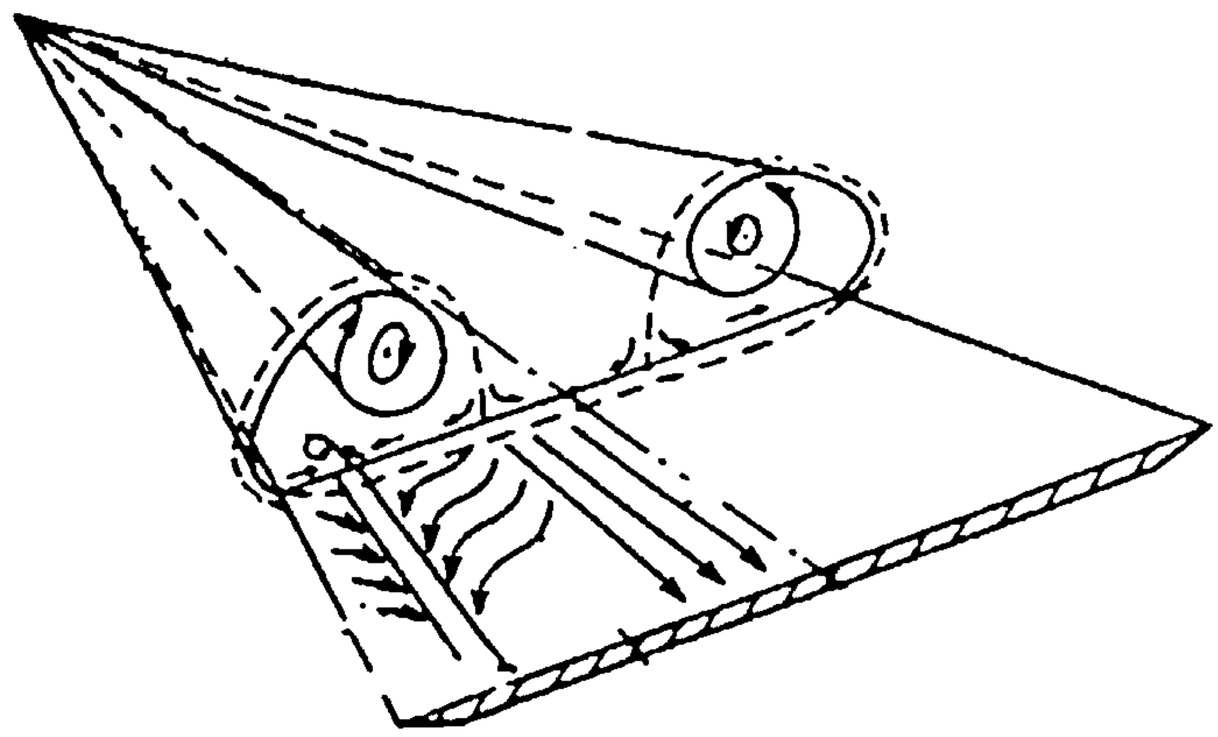

Classical vortex structures generated by a slender delta at incidence

At zero incidence the boundary layer may be considered axisymmetric as indeed is the entire flow field. The flow is retarded at the body surface and the resulting velocity gradients give rise to high levels of vorticity. However, except at the base, the boundary layer remains attached, the regions of high vorticity are limited to the vicinity of the body surface and it's axisymmetric nature essentially retained.

At a moderate angle of incidence the boundary layer is no longer able to remain attached to the body surface. Separation occurs at some line running along the side of the body. The separated boundary layer, or free shear layer, now moves under the influence of the freestream, the body perturbations and the high levels of vorticity in the free shear layer itself. These high levels of vorticity induce the rapidly diffusing shear layer to roll up on itself, thus confining the majority of the flow field circulation within a small region to the lee side of the body. These rolled up vortex structures then propagate along the length of the body in a generally freestream direction under the influence of the freestream flow with the body itself exerting a constraining influence.

Figures 5.1.3.1 (i)-(vi) depict the effect of these processes on the flow in the cross flow plane.

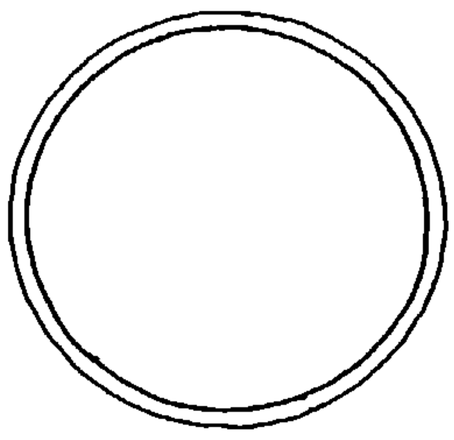

(i)
A cross flow plane section though the boundary layer around a body at zero incidence. The flow is axisymmetric.

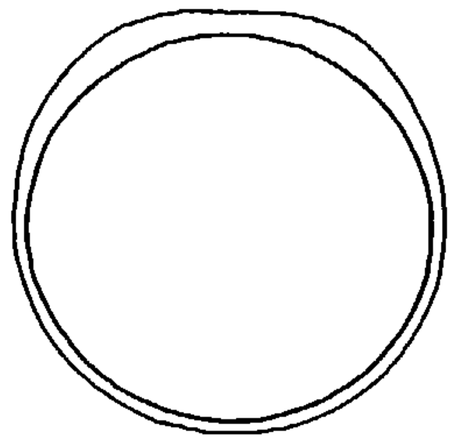

(ii)
At low incidence[6] *(cross flow velocity component upwards) a bulging of the boundary layer on the lee side becomes apparent. Otherwise there is little change in the flow which varies little from the axisymmetric case.*

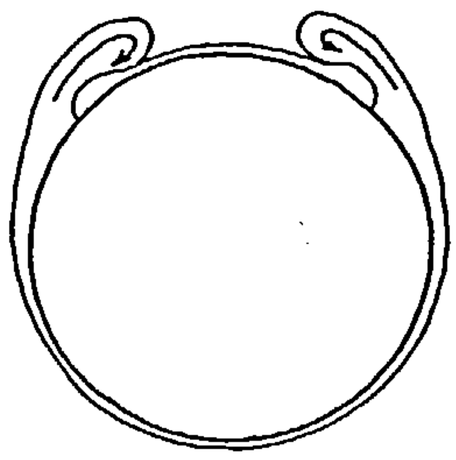

(iii)
With increasing incidence the bulges in the boundary layer begin to form into embryonic vortex structures.

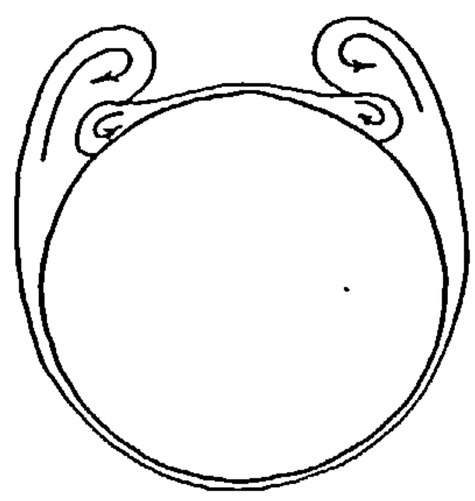

(iv)
As the primary vortices develop a pair of secondary vortices form underneath them. The flow topology now resembles that of the flow about a slender delta.

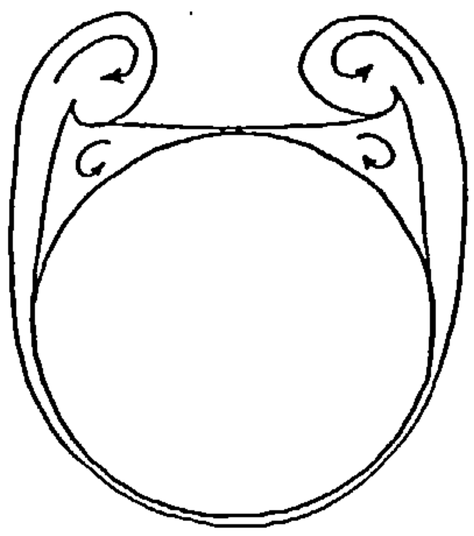

(v)
As the flow develops further the structure formed from the separated boundary layer splits into a distinct vortex and a feeding sheet connecting it to the attached boundary layer

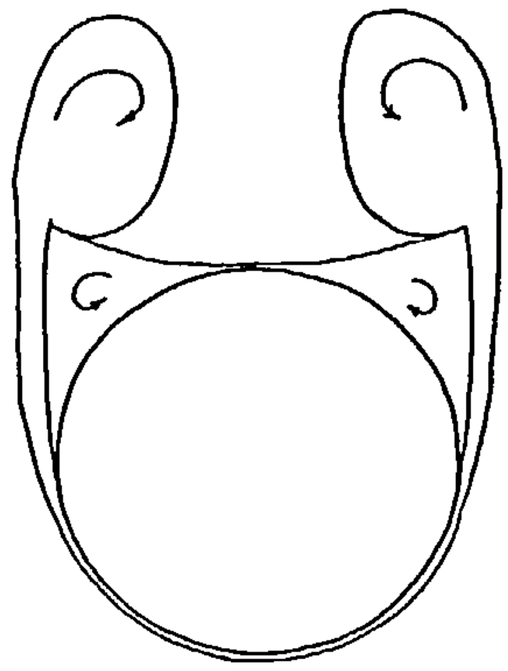

(vi)
Beyond this point the vortices grow in size and strength and move away from the body[7].

Figure 5.1.3.1 Slender body vortex formation

---

[6]It may be noted that there is a similarity between the flow due to varying incidence and varying distance of cross flow plane from the body apex. This will be discussed latter.

[7]Eventually the vortices become asymmetric, again this will be discussed later.

Even at this simple level of understanding it can be seen that the slender body vortex phenomenon is dependent upon;

- Body geometry (including it's roll angle if non-axisymmetric)
- Angle of incidence
- Reynolds number (and any other parameters that may effect the separation position)

In addition to these variables there are also compressibility effects to be considered.

If it were required to predict the formation of slender body vortices and hence their influence upon the aerodynamic characteristics of the body it would be necessary to start from a full understanding of;

- The nature of the boundary layer.
- The circumstances that give rise to boundary layer separation from a smooth surface.
- The generation of vorticity and its convection and dissipation in the flow field.
- The influence of vortices upon the body surface velocity and pressure distributions.

5.1.4 Effect of incidence on vortex field category

It has been indicated that when a slender body is at a modest incidence to the freestream flow a vortex system is generated. From experimental work it can be seen that the form of the vortex system can be divided into discrete classes each of which is associated with an incidence range.

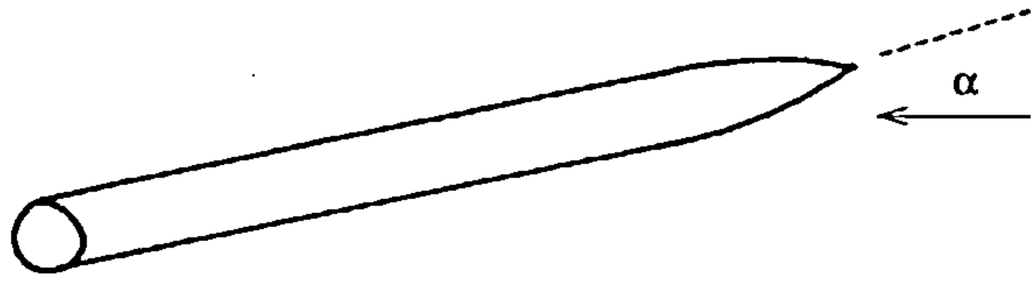

A slender body at low incidence α

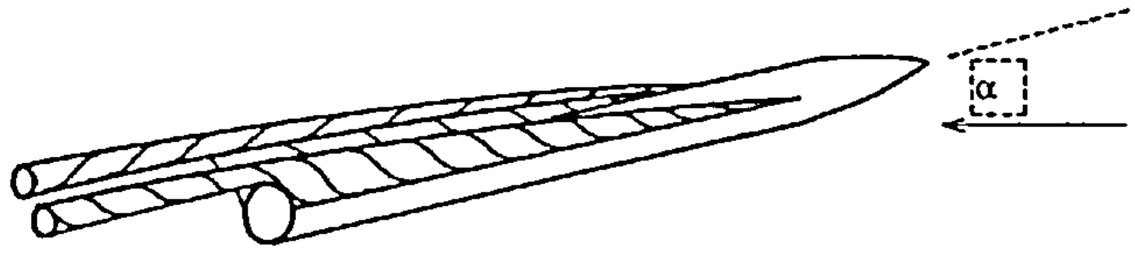

A slender body at moderate incidence (10°-20°)

For a typical slender body separation will not actually occur until 5-6° and hence prior to this incidence there will be no vortex formation[8]. At incidences between 10° and 20° a pair of vortices will form in close proximity to the lee side of the body, exhibiting a high degree

[8]Although the boundary layer may remain attached there may be quite significant local increases in displacement thickness. (See figure 5.1.3.1 (ii))

of symmetry about the incidence plane. If the incidence rises to between 25° and 35° the
symmetry begins to be destroyed. In this case at some position along the body one of the vortices will begin to lift away from its proximity to the body surface. As it does so its counterpart is drawn in underneath it and disrupts the free shear layer that was feeding it. At this point the vortex becomes
free to follow more closely a freestream direction. Subsequently a new vortex begins to form close to the body surface in its place. As the incidence increases still further the asymmetry develops such that free vortices are shed from alternate sides along the length of the body.

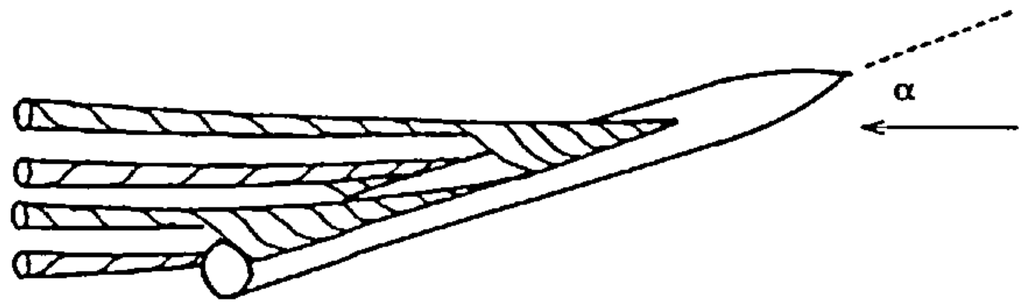

A slender body at high incidence

5.1.5 Influence of vortex flow field upon body forces and moments

It is well known that the presence of a vortex in a flow field will significantly alter the flow topology. Velocities can be induced in the flow at positions quite removed from the immediate vicinity of the vortex. These induced velocities will result in modified surface pressure distributions which will not only change the total lift generated by the body but also shift its point of action. Hence both forces and moments will be affected. Further, the modifications to the surface pressure distribution will itself alter the separation position and hence increase the complexity of the flow. The main parameters that are required to determine the induced velocities are the vortex strengths and positions.

5.1.6 Influence of vortex flow field upon lifting surfaces

In general there will be various lifting and control surfaces associated with the slender body. Vortex induced velocities will affect the pressure distributions on these in the same manner as they affect those on the body itself. However, in addition to changes in lift and pitching moment there will be a tendency for rolling moments to be generated too. Even in the moderate incidence range where the vortex formation is symmetrical about the incidence

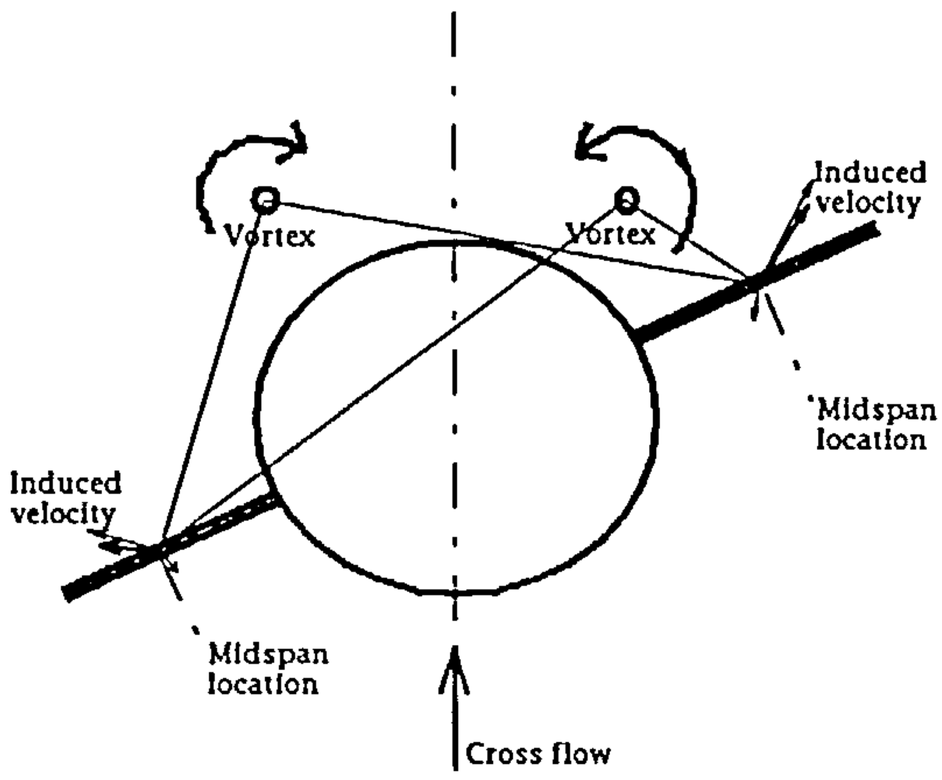

The generation of induced rolling moments through asymmetrically induced velocities: consider, for example, the mid span positions

plane, any asymmetric body roll angle will give rise to an induced rolling moment.

5.2 ANALYTICAL MODELS OF SLENDER BODY AERODYNAMICS

There are many techniques available for the mathematical modelling of the aerodynamics of slender bodies at incidence. Some have been derived to specifically address this problem and others have a very much wider applicability. This section provides a brief introduction to these methods.

5.2.1 Potential theory models

These are the simplest of the analytical solutions and as such are one of the easiest to apply and fastest to produce results. Their derivation, however, is only possible by making a number of sweeping assumptions foremost amongst which is that the flow is inviscid. This enables an axisymmetric body to be modelled as a line of source and sink singularities of strengths appropriate to satisfy the boundary condition at the body surface. At finite angles of incidence a similar approach may be followed by using doublet singularities.

Whilst these methods are elegant in their simplicity their assumption of inviscid flow precludes them from modelling the effect of body vortices since this, as we have seen, is a viscous effect. However, they should not be discarded since their ability to model the potential component of lift is excellent and as mentioned earlier this is the only component at low incidences.

5.2.2 Slender body Theory

In this special case of Potential theory, which again takes no account of viscous effects, an elegant piece of analysis[9] leads to a simple expression for the lift distribution on the body in terms of the rate of change of body cross sectional area. This result can be further integrated analytically to give an expression for the total lift and moment on the body. As with the Potential methods this approach does not include an account of the vortex lift on the body. Furthermore it simplifies the analysis by assuming that the body is slender. In our case this is, of course, acceptable since we are only concerned with slender bodies.

Hence, provided that the body of interest is slender, this approach is even more attractive than the Potential methods described in section 5.2.1 due to its simplicity.

---

[9]This will be explained in some detail later.

5.2.3 Additional viscous terms

The lack of any account of viscosity in the previous approaches can, to some degree, be rectified by the addition of appropriate increments to allow for the effect of the body vortices on normal force and pitching moments. In some methods the, so called, Cross Flow Drag method is used. Here it is assumed that the velocity component normal to the body will locally generate an element of drag comparable to the drag of a two dimensional body of the same local cross section. Thus a viscous component of normal force distribution can be determined.

Since the cross flow drag can only be determined experimentally, this is an empirical modification.

5.2.4 Empiricisms

The technique of applying empirical corrections has now been honed to a fine art. For the class of bodies most often used in missile design, that is the forebody-cylinder, a large experimental database has been assembled from which the Cross Flow Drag terms have been derived over a wide range of Reynolds numbers and Mach numbers. From this it is possible to construct tools[10] to enable forces and moments to be predicted with considerable speed and accuracy. These methods are, however, limited by the bounds of the experimental database and more significantly cannot be used to determine vortex interference on lifting surfaces since the vortex strength and positions are not output.

5.2.5 The Vortex Cloud Method

This useful technique is described more fully in the next section. Briefly, it is possible to model the convection of the vorticity contained in the separated boundary layer shed from the leeside of a bluff two dimensional body by using an array of point vortex singularities[11]. The two dimensional body itself being modelled by another singularity, a doublet in a freestream represents a cylinder for instance.

This technique can be used along with the Impulsive Flow Analogy to relate the unsteady two dimensional Vortex Cloud solution to the steady three dimensional solution of the flow about a three dimensional body. In effect the Impulsive Flow Analogy relates the developing flow field around the impulsively started two dimensional body at some moment in time, t, to the steady flow field

---

[10]Computer programs, data sheets etc.

[11]Hence the name Vortex Cloud.

around the three dimensional body of same cross-section at some length along the body, l.

This method will not only predict aerodynamic forces and moments acting on the body but also the vortex strengths and positions required to determine interference on lifting surfaces.

5.2.6 Panel methods and vortex sheets

The panel method is an extension of the Potential methods mentioned earlier. Here the surface of the body is enveloped within a quadrilateral or triangular panel distribution. Each panel being a planar distribution of singularities such as sources or doublets. The unknown singularity strengths are solved to satisfy the usual boundary conditions thus giving a Potential solution for a truly three dimensional body. As with the earlier Potential methods, no account is taken of viscous effects. One method to allow for this is to use a vortex sheet constructed from quadrilateral vortex rings to model the separated boundary layer.

5.2.7 Finite difference solutions to the Navier-Stokes equations

The state of the art technique for modelling the flow about any three dimensional body is to divide the flow field into a large number of cells and to simultaneously solve the Navier-Stokes equations at each, subject to the relevant boundary conditions at the body surface and at the outer edge of the solution domain.

Although there is still much work to be done in the field of turbulence modelling, this technique may give excellent modelling of the entire flow field including all viscous effects and hence take full account of all body vortex interference.

5.2.8 Finite difference solutions to the Euler equations

The Navier-Stokes equations may be greatly simplified by neglecting the viscous terms. This not only makes the equations easier to solve but also, by implication, relaxes the requirement for higher cell resolution within the boundary layer, which will not exist in this model. The result being that a solution may be reached more rapidly. Although this method lacks the elements essential to the creation of vorticity, if vorticity can be introduced into the field it will be convected correctly. It is possible to introduce vorticity into the flow field by careful modification of the boundary conditions such that a flow separation occurs in the appropriate location.

5.2.9 Application of these techniques in the project environment

In any aerospace organisation there will be a great many activities in progress at any given time. These activities are often categorised by skill area e.g. structures, aerodynamics, control systems. Within any of these skill areas we can, in broad terms, subdivide the activities into those concerned with the acquisition of new knowledge, the application of that knowledge to engineering technology and the use of that technology in creating new products. The two former activities being pure and applied research and the latter being project engineering. The project activities could be further divided into future product research and existing product development. The project engineers are required to work within fairly confining set of constraints in terms of time, money, and other resources and these constraints are referred to as "the project environment".

If the methods[12] mentioned in sections 5.2.1 to 5.2.8 are to be of practical use in the project environment they must satisfy three important criteria:

- The basis of the methods should be reasonably well understood such that its range of applicability can be assessed.
- It should be possible to rapidly pose the problem in terms appropriate to the method.
- The solution should be rapidly forthcoming.
- The accuracy of the solution should be appropriate to its intended use.

Starting with the Potential models and Slender Body theory, these methods are not suitable for modelling body vortex effects due to their lack of the viscous elements. However, their simplicity makes them a suitable base to which viscous terms could be added. In particular Slender Body theory provided that its restrictions do not limit its accuracy.

The pure empiricisms are not applicable if vortex interference is important since the vortex strength and positions are not generated. However, if the requirement is for body forces and moments only and the body geometry is applicable then this would be an excellent option.

The Vortex Cloud Method provides a good compromise between simplicity of model and rationality. It should, then, provide fast but reasonably accurate results. This method certainly bears further investigation.

---

[12]It is assumed that , by this stage, the methods have been embedded in some reasonably 'user-friendly' computer package or expressed in the form of data sheets.

The panel method in isolation will not predict viscous effects but again would make a suitable starting block to which a viscous model could be added. One such model, the vortex sheet, although simple in principle, would be complex to set up and, due to its unsteady nature, computer intensive.

The numerical field solution methods hold excellent promise. When computing power and numerical techniques progress, the Navier-Stokes method may be capable of producing highly accurate flow field solutions from which any level of detail may be extracted. Currently, however, the length of time required to generate a grid and produce a single solution makes its use prohibitive in a project environment.

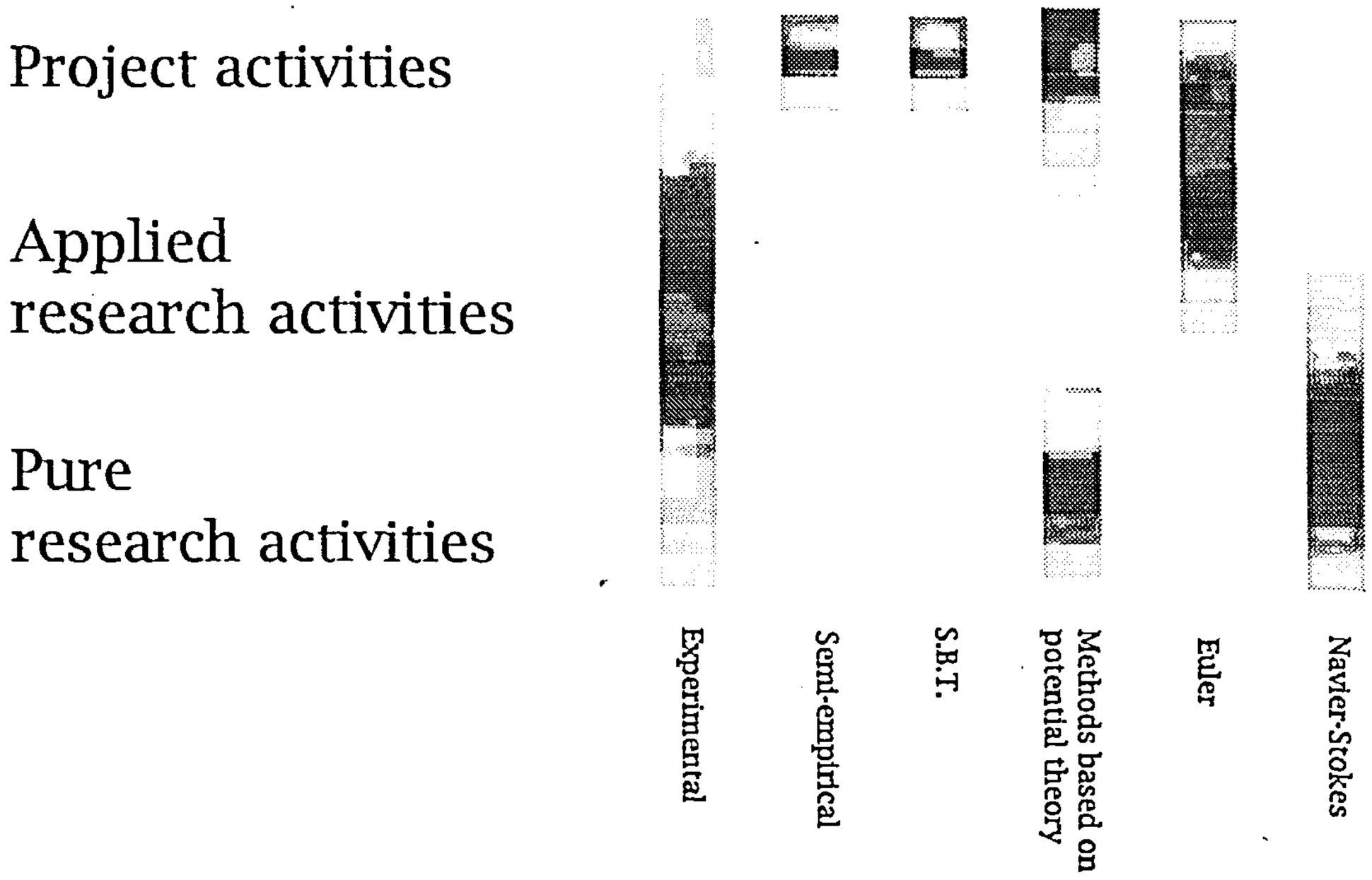

Current utilisation of missile characteristic prediction methods to various business activities

5.3 THE VORTEX CLOUD METHOD

5.3.1 The Vortex Cloud Method in two dimensions

The Vortex Cloud Method (VCM) was initially developed to tackle the problem of modelling separated flow from bluff bodies using simple Potential theory.

Let us consider the simple case of a circular cylinder in a uniform freestream flow. Here the inviscid solution may be modelled using a doublet suitably oriented in a freestream. This approach

neglects the effect of the displacement thickness of the boundary layer although this is likely to be small. It is well known, however, that the flow will not remain attached about the full length of the cylinder circumference. At some point in the vicinity of the cylinder shoulder the boundary layer will separate to form a free shear layer.
In the VCM the free shear layer is segmented into a finite number of elements. The circulation about each element, by virtue of its vorticity, is represented by a vortex singularity of equal circulation strength. With each increment in time a new length of shear layer is generated and hence a new point vortex is introduced. These discrete vortices are allowed to convect under their own influence and that of the doublet and freestream. As time progresses a 'cloud' of vortices develops, representing the vortices that form on the lee side of a circular cylinder.

Simple Potential theory allows the velocity and hence pressure to be determined anywhere in the flow field including on the body surface.

5.3.2 The Impulsive Flow Analogy

The VCM solution for the flow about a circular cylinder commences at time zero with the unseparated solution. As time progresses the separated flow develops into a pair of near symmetric vortices which then become asymmetric, break away and develop into a vortex street. This solution obviously relates to the unsteady flow about a cylinder instantaneously started from rest and is referred to as an impulsive flow.

If we now consider a forebody-cylinder body at incidence to the freestream and examine the flow at successive planes cut through the flow field normal to the body axis along its length there will be a striking similarity to the unsteady two dimensional flow about a circular cylinder. The relationship between the flow after a length of time in the two dimensional case and after a length of body in the three dimensional case is more formally expressed in the Impulsive Flow Analogy[13].

The Impulsive Flow Analogy is used to relate the unsteady two dimensional solution to the steady three dimensional solution that we are concerned with.

5.3.3 Comparison with experiment

Unfortunately the VCM over-predicts the vortex induced interference load on the body. This has traditionally been accounted for by arguing that, amongst other reasons, the simple method used to determine the strength of the discrete vortices produces an over

---

[13]Detailed later in the thesis.

estimate. To correct for this an empirical factor of about 0.6 is applied to the discrete vortex strengths.

5.3.4 Practical aspects of the method

The VCM presents itself as a good compromise between the computationally intensive flow field solution methods and the simple Potential or empirical methods. It is simple to use and will produce a reasonably accurate solution fairly quickly. Its modelling appears to be rational which gives the confidence required to apply the method to a variety of configurations.

The one element of the model that still remains a little vague is the question of the vortex strength factor. A sound explanation as to why this is required would remove much of the empirical 'feel' to this method. Furthermore, one consequence of the Impulsive Flow Analogy is that the higher the value of incidence the more discrete vortices are required. Since each vortex must be individually tracked and its influence on all the other vortices must be calculated computer run times, at even moderate angles of attack, can be excessive[14] in the context of the project environment.

Nevertheless, this useful method is used by industry to predict the aerodynamic characteristics of wing-body-tail configurations.

5.4 OBJECTIVES OF STUDY

5.4.1 Research the development of the Vortex Cloud Method to date

This activity is primarily a literature survey covering the entire history of the development of this and related methods finishing at the current state of the art and how it is applied in industry.

5.4.2 Develop a better understanding of the flow physics

Clearly, if any improvements are to be made in the modelling of body vortex flows then a deeper understanding of the flow is required. Special emphasis will be placed upon three dimensional effects. Even if the eventual model does not reflect every detail of the real flow it must account for the dominant features.

5.4.3 Develop a new method, better matched to the project environment which may, if appropriate, be based upon the VCM.

---

[14]Although VCM run times are still 2-3 orders of magnitude shorter than that of a Navier-Stokes code.

Whilst this may entail the addition of new elements to the model, it may also imply the removal of elements that are not considered to substantially increase its accuracy. Elements of the model that depend upon empiricism will also need to be reviewed. If possible, a new method should posses the following features:

- Simple to apply
- Fast to obtain solution
- Reasonable accuracy
- Based upon a more rational model

6. DISCRETE VORTEX MODELS

6.1 INTRODUCTION

The rapid design and analysis of modern, high performance, conventional and unconventional missiles requires the use of swift and accurate procedures for determining their aerodynamic stability, control and drag characteristics over a wide Mach number and angle of attack range. Despite advances in computational fluid dynamics, the only methods which are currently capable of meeting these requirements in a project environment are the semi-empirical methods.

Semi-empirical methods are usually based upon approximate theoretical methods such as slender body theory and linearised potential theory, along with an extensive compilation of experimental and theoretical results. Once the methodology and database have been finalised, the procedures are usually written in the form of a computer programme, or code, with a user friendly 'front end' to facilitate a rapid input of the geometry and flow conditions and a post processor to present the output in a useful format.

The capabilities of the semi-empirical methods are limited by the databases upon which they depend. This restricts most of the currently used semi-empirical codes [1] to configurations with forebodies with single diameter cylindrical afterbodies and two sets of cruciform wing surfaces. There are only a small number of codes that can cope with geometries that consist of a forebody followed by two or more cylindrical afterbody sections of different diameters joined together by frustum sections also with two or more sets of cruciform wings.

There is a need for methods to be developed that are computationally efficient, such as those used in the 'semi-empirical building block' approach of the existing aerodynamic prediction methods, and yet are not dependent upon (and hence limited by) an aerodynamic database.

This section investigates some of the attempts that have been made to achieve this for the body alone configuration.

6.2 APPRAISAL OF CURRENT METHODS

The normal force generated by a slender body at incidence to the freestream can be expressed [2] as the sum of a potential, often linear, component and a viscous non-linear component. This non-linear component is the result of vortex sheets formed by the boundary-layer fluid leaving the body surface at the separation lines

along the body sides and rolling up into a symmetrical vortex pair. This flow pattern becomes asymmetric at higher angles of attack. Most methods tackle the problem by addressing these two components almost independently. The non-linear component, being the more difficult element, has attracted the most attention. One method that has been applied to the modelling of body vortices is the so called 'Vortex Cloud Method'.

6.2.1 Vortex Cloud Methods

The basic notion of the vortex cloud theory is to model the distributed vorticity fields exhibited by the flow about a slender body at incidence by clouds of discrete potential vortices that are free to move under their mutually induced velocities. (The Kelvin-Helmholtz theorem dictates that vorticity be transported with the local velocity.)

To understand the strengths and weaknesses of this method it is useful to investigate its origin from attempts to model the two dimensional flow about a circular cylinder.

Work by Föppl [2a], which assumed 2-D potential flow past a cylinder with a pair of symmetrical vortices on its lee side, showed that there is a locus of vortex centres (with associated vortex strengths) where the vortices are stationary in the presence of the cylinder i.e., the velocity at the location of either of the two vortices, which is induced by the other vortex, the two vortex images and the cylinder, is zero. This concept showed the possibility of modelling the flow in this way (in 2-D at least). However, since the vortices were of constant strength no account could be taken of the feeding sheets. A feeding sheet can only be present if the vortices are growing in strength as a function of time.

- Bryson [3] improves upon this by calculating the vortex paths and strengths such that the separation point is a stagnation point of the flow and that no net force acts upon the external vortex and its feeding sheet. This leads to a solution for the flow about an impulsively started cylinder.

- The Impulsively Started Cylinder:

When a circular cylinder is suddenly accelerated from rest to a speed V in a fluid it is observed that soon after starting the boundary layer separates at the rearward stagnation point and two separation points propagate symmetrically away from this point around the sides of the cylinder. When these boundary-layer separation points reach a certain angular distance from the rearward point, two regimes of vorticity break away from the boundary layer and move down stream beginning the formation of a wake.

This description applies for Reynolds numbers, R_e=Ud/v, greater than about 5. At lower R_e no wake is formed as the flow is governed primarily by viscous forces (Stokes flow) whilst for $50 < R_e < 100$ an antisymmetry builds up quickly and regular eddy shedding (Karman vortex street) begins. For $R_e > 10^5$, the alternate eddy shedding begins but is quickly superseded by a completely turbulent flow in the wake.

- Bryson's 2-D Method [3]

In terms of the 2-D unsteady problem, the regions of vorticity that separate from the boundary layer and move downstream are quite thin, justifying a description of them as vortex sheets. Furthermore these sheets roll up, concentrating most of the vorticity towards the downstream end of the sheet. If the sheet is approximated by a single concentrated line vortex at the centre of 'gravity' of the vorticity by maintaining, conceptually, a connecting sheet of vanishingly small vorticity to the body, we can formulate a relation for motion of this vortex that gives no net force on the vortex and its connecting sheet.

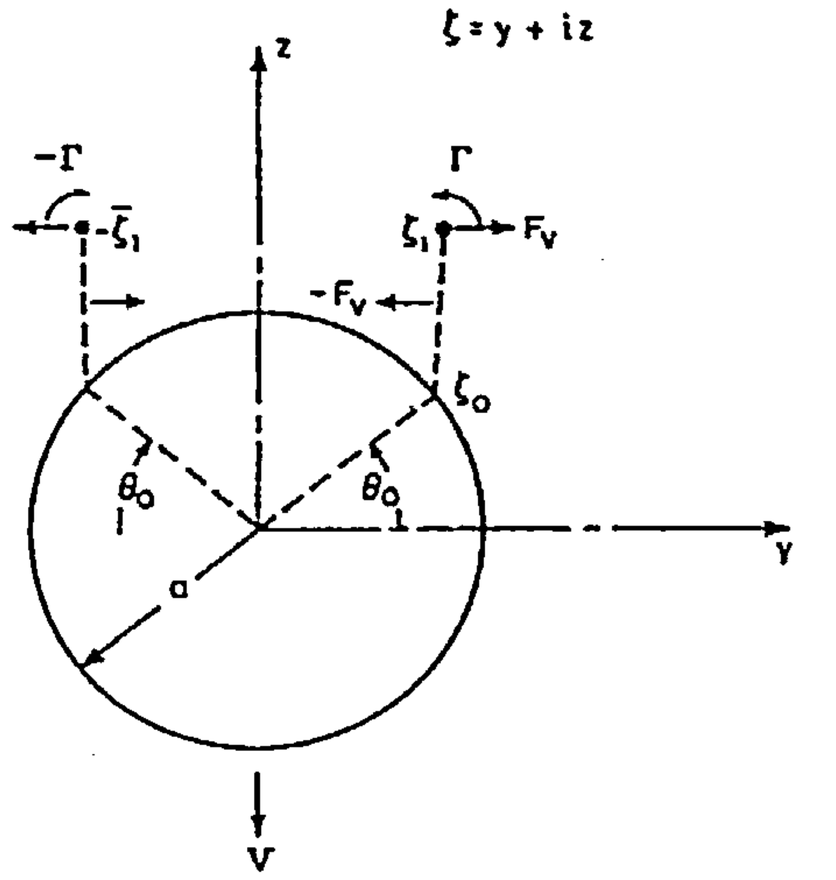

Simplified theoretical model of vortex separation on a circular cylinder [3]

$$\dot{\varsigma}_1 + (\varsigma_1 - \varsigma_0)\frac{\dot{\lambda}}{\lambda} = W_1$$

ς_1 = coord of vortex

ς_0 = coord of separation point

λ = vortex circulation

W_1 = complex velocity at ς_1 excluding that due to point vortex at ς_1

The assumption is made that:
"The feeding points are stagnation points; that is the fluid velocity relative to the cylinder vanishes at these points."
This leads to an expression for the strength of a point vortex depending upon its position and the position of the separation points.

Using these equations, the vortices are marched through time, starting from the separation points, out towards their equilibrium points on the Föppl curve (Figure 10.2.1.2 indicates the shape of the Föpple curve).

Now although the net force on the vortex and its connecting sheet is zero, a moment acts on the combination (since the two forces are not coincident). The model also implies a discontinuous drop in pressure on the body going across the "feeding point" of amount $\Delta p = \rho \quad \Gamma$. These first two comments simply imply a likely limitation on the accuracy of the method, the effect of which can only really be assessed by validation against experimental results. The method does not include a procedure for the determination of the separation points (feeding points) which must be specified. This facility could be added either empirically or by way of an interactive methodology capable of predicting where separation will occur. However, any interactive (viscous/inviscid) method for determining the separation points will give poor results due to the poor modelling of the feeding sheet. This is an important element since the feeding sheet itself will have a considerable influence on where separation occurs.

For a given separation point the method gives a fair prediction of the transient build up of C_D about a circular cylinder. Hence, despite the simplicity of the model, it is capable of producing a reasonable representation of the flow field. The computational simplicity of this method makes it a very attractive possibility although a separation model would be required.

- 3-D Steady Flow Past Slender Bodies Of Revolution At Moderate Angles Of Attack.

Symmetric vortex separation can be observed on the leeward side of slender bodies of revolution at moderate angles of incidence in the subsonic to moderately supersonic range.

If we define a fixed plane in the fluid, perpendicular to the axis of the body, then as the body pierces this plane its trace moves laterally in this plane with velocity $U\sin\alpha$ and time is related to distance x along the body by $t=x/(U\cos\alpha)$ figure 6.2.1.1. If we approximate the flow in this plane as two-dimensional[1], then the flow structure is almost identical to the 2-D flow about a circular cylinder if V is replaced by $U\sin\alpha$. The main difference is the "expanding circle" as the body nose first pierces the fixed plane.

- Bryson's Method 3-D [3]

Brysons [3] method is not directly applicable to the computation of the flow about a general axisymmetric body. However, it can be used in the special case of a cone by assuming that the flow field is

[1] Hence the concept of the quasi two-dimensional representation of three dimensional flows.

conical; i.e., velocity components and pressure are assumed constant along rays passing through the apex. At each axial station then the crossflow picture is the same, only increased in scale. It follows that the circulation strength of the separated vortexes must increase linearly with x.

With these modifications to his original method Bryson continues to produce a solution that compares reasonably well with experimental results in terms of overall lift coefficient. See figure 6.2.1.2.

This method lends itself well to computational solution. It uses a crude model of the vortices and feeding sheets but still appears to give a reasonable prediction of the normal force coefficient. The method also appears to pick up the point at which the non-linear loads begin to become significant (see $\tan\alpha/\tan\delta \approx 2$ on figure 6.2.1.2). Although this formulation of the analysis is not directly applicable to non-conical flow fields it holds great promise due to its accuracy and simplicity. Furthermore, although the flow about a slender body of revolution at incidence is not conical it does exhibit conical like features.

- Angelucci [4]

Angelucci [4] uses a multivortex representation of the feeding sheet. By considering the boundary layer at the point of separation he has been able to unify the modelling of the feeding sheet and the rolled up vortices by evaluating the discrete vortex strengths as they are shed from the separation point and are allowed to move under their mutual influence.

Before going into the detail of Angeluccis [4] work (figure 6.2.1.3) a summary of the methods that had been used to attempt to model the separated flow from slender delta wings would be useful. Edwards [5] and Brown and Michael [6] used a model consisting of two symmetrical concentrated vortices connected to the separation point by two feeding sheets of vanishing strength at the delta wing surface. This model neglects the contribution of the feeding sheet to the separation condition and, except for the case of the cylinder, takes advantage of the conical nature of the flowfield; the condition that no net force is sustained by the concentrated vortex and its feeding sheet is also assumed.

- A more realistic model was used by Mangler and Smith [7] which accounted for finite vorticity in the feeding sheets. Here the two vortex spirals consisted of an inner part which was an isolated potential vortex and an outer vortex sheet lying along an analytical curve, which is defined in a convenient transformation plane by imposing the continuity of pressure and zero normal velocity conditions. The flow is assumed to be conical and lengthy computations and personal judgement are required to solve the governing equations. figure 6.2.1. 4.

• Smith [8] replaced the outer vortex sheet of the previous model with a large number of small concentrated vortices at arbitrarily chosen points along its path. This allows the solution of the equations of Mangler and Smith [7] by using finite difference techniques, the accuracy of the model being a function of the number of vortices used.
• Sacks, Lundberg and Hanson [9] have taken this one step further and represent the vortex sheets by a finite number of vortex sheet segments. These segments are then replaced by concentrated vortices whose subsequent positions are computed step by step from the local induced velocities at each vortex position.

This model allows the vortex sheets to roll up freely without the restrictions of concentrated vortex cores and does not rely upon the assumptions of conical flow.
• Returning to Angelucci [4], here a similar method to [3] is used to determine the flow about an axisymmetric body, though, the separation line must be specified from experiment or semi-empirical theory.

The basic model is as follows:

The actual leeward vortex sheets of a slender body at an angle of attack are approximated by a finite number of discrete elementary vortex sheets. In particular, each elementary vortex sheet pair represents the vorticity shed by the body surface during a time interval _Δt. If the time interval, Δt, is replaced by $x/V \cos\alpha$, each pair of elementary vortex sheets is shed at each of a finite number of corresponding axial positions. The vortex sheet is then replaced by a pair of equivalent concentrated vortices. These vortices are treated as free vortices of constant strength and their subsequent positions are computed step-by-step from the total velocity induced at the vortices. The associated normal force distribution along the body is then computed from the strength and position of the discrete vortices at each axial station. The solution of the problem requires first the determination of a Kutta type separation condition at the feeding point. As with Brysons method it is assumed that the local fluid velocity relative to the body is zero at these points. i.e. that they are stagnation points.

In this method the vortex sheet strength is set by applying the boundary condition that the pressure difference across the sheet should be zero.

The actual vortex sheets are more realistically represented by a finite number of discrete free vortices. The computing time is not a function of the body configuration but of the number of vortices used to represent the vortex sheets. The method is applicable to any slender axisymmetric body and the governing equations are solved in closed form at each axial position without the use of iterative procedures. This method appears to give a more representative model of the flow. It is computationally very simple but, due to the

need to calculate the mutually induced velocities at each vortex, the CPU time increases approximately with the square of the number of vortices.

- Gerrard [10]

To model the flow about an impulsively started 2-D circular cylinder Gerrard [10] uses a large number of discrete free vortices which are shed from the separation points. To set the strength of the vortices as they are shed he uses a method suggested by Fage and Johansen [11] in 1926 for the approximation of the rate at which vorticity is shed from a point of separation[2]. The result simplifies to $\dot{\Gamma} = \frac{U_s^2}{2}$ where U_s is the tangential velocity component at the point of separation.

See section 7.3.3

This very computationally simple method for computing the flow, gives an unsteady solution, the oscillating quantities of which, compare reasonably well with experiment.

The method overpredicts the shed vortex strength and so a factor of between 0.5 and 0.75 must be applied to the vortex strength at the moment of shedding. The shed vortex strength (and hence the solution) is very sensitive to the position of separation due to its effect upon U_S. The surface tangential velocity in the region of separation is most strongly effected by the vortices that have been most recently shed and their strengths and positions in the flow. Again computationally the method is simple to implement, appears rational and appears to model the flow well both qualitatively and quantitatively. However, the method is computationally intensive and a number of weaknesses are beginning to become apparent.

- Wardlaw [12]

Wardlaw computes the 2-D flow field in the same way as Gerrard but by using the impulsive cross flow analogy he applies it to the flow about an axisymmetric body. He obtains solutions up to high incidences and hence predicts in the asymmetric regime. Some of the problems with the VCM start being addressed. The factor applied to the shed vortices is justified by arguing that it is an allowance for the vorticity destroyed by secondary separation.

Wardlaw notes that difficulties were encountered in choosing the position at which new vortices were placed into the flow but does not accept Angeluccis vortex filament method since it introduces two new variables, these being vorticity distribution and length.

Theory compares well with experiment up to about 25 degrees of incidence in terms of C_N and X_{cp}. figure.6.2.1.5. No pressure

---

[2] This will be discussed in both the experimental and numerical analysis sections.

distributions are presented. Computer time requirements will increase rapidly with the number of vortices used in the modelling. Axial position of first separation and cross flow plane separation angle are both defined by simple empirical formulae. Unfortunately the factor applied to the strength of the shed vortices is not justified by arguing that it is an allowance for the vorticity destroyed by secondary separation as will be seen shortly. Marshall and Deffenbaugh [17] model secondary separation but the shed vortices still require factoring

- Deffenbaugh and Marshall [13]

Here the 2-D circular cylinder model has been made more sophisticated by calculating the position at which the point vortices are shed from the cylinder. This position is obtained from a solution to the unsteady incompressible laminar boundary-layer equations.

Also a rear shear-layer model is included to account for backflow induced vorticity. Figure 6.2.1.6. depicts a predicted pressure distribution.

Although the oscillatory flow features are well predicted the cylinder drag does not compare well with experiment. figure 6.2.1.7. The method used to predict the location at which separation occurs should have been developed to, itself, give good comparison with experiment (which it does not) before applying it to this model. The point at which separation occurs has a significant effect on the strength of shed vortices and ultimately the cylinder drag.

- Deffenbaugh and Koerner [14]

Here the 2-D method of Deffenbaugh and Marshall [13] is applied to axisymmetric bodies using the cross flow analogy. The method used to determine the point of separation has been replaced with Stratfords [15] criteria which, although empirical, does allow some degree of coupling between the viscous and the inviscid parts of the solution.

Although experimental pressure distributions are given, no comparison with theory is made. Comparison of side force figure 6.2.1.8. is made, however, which shows that trends (including those of separation position figure 6.2.1.9.) are well predicted even if absolute values are not good.

- Schindel [16]

Here Schindel, and similarly Wardlaw [9], uses Brysons 2-D model with the cross flow analogy to model bodies of elliptic cross section. In the case of the zero thickness ellipse, the body collapses into a flat plate. The analysis of the non-linear lift on a delta wing by Brown and Michael is thus a special case of Schindels method.

Whilst this method apparently shows a simple approach to the problem, yet still gives good results, it does leave one or two questions unanswered .

The normal force coefficient is predicted with reasonable accuracy but some discrepancy is reported in the prediction of the centre of pressure position. This in itself gives reason for some concern since it indicates that whilst the total load on the body is correct, it results from the integration of an incorrect load distribution.

Since the method only predicts the total normal force coefficient and not the load distribution one can only speculate at possible causes. The normal force can be considered to consist of a linear component and a non-linear, vortex induced, component. Firstly the linear component is predicted using Slender Body Theory. For a body of revolution with a 3 calibre nose SBT will tend to slightly overpredict[3] the forebody load[4]. Over the cylindrical section of the body SBT will predict zero load. Although this is correct over the majority of the body there should be some carry-over load at the nose-body junction.

The non-linear component of the normal force coefficient is more difficult to predict. However, if we assume it is correct then the total force should be inaccurate due to the linear term inaccuracy. Thus it is likely that the non-linear term is in error by a compensating amount. The non-linear load is caused primarily by the presence of the lee side vortices. This term is dependent upon strength and position of the vortices. One of the strongest influences on the strength of the vortices is the separation position. Hence the separation position will effect the normal force coefficient. In this method the location of the turbulent separation position is found from a comparison of predicted and measured non-linear normal force on circular cones.

This is, of course, a sweeping empiricism since it is capable of masking any inaccuracies in its path. In applying this method to a more general body contour a further empiricism is applied to adjust to any change in body slope by exponentially approaching its equilibrium value in accordance with a function premultiplied by a factor K of which it is said "a good value for K is 1.4".

Despite the complexity (or rather, sophistication) of the separation model the difference between measured and predicted separation angles exceeded 30°. An additional empiricism is applied in the calculation of the vortex strengths. The starting strength of the vortices is set using parameters which are a function of the body cross sectional shape. The derivation of these "recommended" relations is not given.

---

[3] See figure 10.1.1.2

[4] In fact the test cases are for elliptical section forebodies which could imply even greater inaccuracies.

It might, perhaps, be concluded that some fundamental element of the model is missing. The method is, however, simple and efficient but does lack the ability to predict load distributions.

- Marshall and Deffenbaugh [17]

This method is similar to Deffenbaugh and Koerner but with the separation position obtained from the numerical integration of the unsteady 2-D laminar boundary layer equations. A rear shear-layer is modelled. Point vortices include a viscous core model to reduce induced velocities in close proximity. A diffusion model makes induced velocities a function of vortex age. Coalescence combines close vortices into single vortices to reduce computing time. A vorticity flux factor is required to reduce vortex strength (approximately 0.6 for an ogive-cylinder body).

A very sophisticated model, but still requires a factor on vortex strength. Comparisons of normal force figure 6.2.1.10. and load distributions figure 6.2.1.11. with experiment are very good in most cases although the vortex strength factor has been used to 'tune' the results over the cylinder section figure 6.2.1.12. and the nose region is largely linear anyway. Pressure distributions figure 6.2.1.13. are also presented.

- Nielsen and Mendenhall [18]

This method is based largely upon the work of Marshall and Deffenbaugh but uses Stratfords separation criteria for laminar and turbulent boundary layers.

Comparisons with experiment are made in terms of induced velocities at measured flow traverse locations in the cross flow plane figure 6.2.1.14. These appear to be fairly good comparisons but do not readily give an indication of accuracy in predicting surface pressures, loads and forces or the loss in accuracy (if any) in using the separation criteria.

- Barger [19]

Barger deviates from the usual method of modelling the wake with discrete vortices and opts for short straight-line segments having distributed vorticity.

The method exhibits a greater degree of numerical stability. However, since this does not appear to be a great problem with other methods, this advantage probably does not justify the increase in computing time. The rolled up wake from a wing-body combination qualitatively compares well with flow visualisation experimental data figure 6.2.1.15. No loads, forces or pressures are presented.

- Mendenhall, Spangler and Perkins [20]

Based largely upon the work of Nielsen and Mendenhall this method now extends the theory to noncircular cross section bodies by way of conformal transformation.

Pressure and load distributions for circular bodies are compared with experiment. The comparisons are quite good but no information is given about computing times. The results for noncircular bodies are fairly good as regards the cross flow velocity distributions, although the side forces are not so good.

- Mendenhall [21]

Here Mendenhall uses a supersonic panel method to represent the body and discrete vortices to model the leeside vortex wake.

Predictions show a slight improvement over the previous paper figure 6.2.1.16 & 17. Comparisons of vortex strength as a function of distance downstream are good and highlight the linearity of this parameter figure 6.2.1.18 & 19.

- Mendenhall and Perkins [23]

Comparisons are made between an Euler solver (SWINT) and a vortex cloud method (NOZVTX). Results indicate that the vortex cloud method produces better predictions than those of the Euler solver figure 6.2.1.20, 21 & 22. Conclusions are drawn that the more complicated and time consuming Euler solutions are useful in understanding the physics of the flow field, but they may not be necessary in the preliminary design stage.

As with all Euler solvers, SWINT must force the flow to separate by, for example, modifying local boundary conditions. The SWINT results are particularly poor at Mach 2. This is not unexpected since the program is on its operating limits at this low speed.

- Mendenhall, Perkins and Lesieutre [24]

An example of where a vortex cloud method has been coupled to a six-degree-of-freedom trajectory simulation to predict the forces and moments on a missile undergoing steady and unsteady manoeuvres. Results are presented and show a good comparison between theoretical and experimental C_p distributions for an ellipsoid body in a steady turning manoeuvre.

- Mendenhall and Perkins [25]

This paper gives a good review of the vortex cloud method, used by Nielsen Engineering and Research, Inc. It presents many sets of results including comparisons of predictions with wind tunnel data.

6.2.2 Some General Comments on Vortex Cloud Methods

These "Vortex Cloud" methods have been developed to include sophisticated CPU intensive boundary layer models to compute the position of separation. In addition numerous other features have been added such as

- Vortex coalescence to try to alleviate the exponential growth in CPU requirements as the number of shed vortices increases.
- Vortex core models to prevent high induced velocities.
- Secondary separation models.
- Redistribution of vorticity along feeding sheets and beyond. See Fink and Soh [27]
- Various attempts to model viscous dissipation.

However the method still tends to predict an excess of circulation in the flowfield by comparison with experiment. The result of which is that all of this fine detailed modelling is subjected to a 0.6 (approx.) shed vorticity factor. Being derived from 2-D theory the method assumes that all the vorticity shed is in the crossflow plane. i.e. the axial velocity component plays no part. The method does, however, allow considerable flexibility in body geometry.

6.2.3 Vortex Lattice Methods

Whilst these methods do not come under the heading of Vortex Cloud Methods they are commented upon here since they are applied to similar problems.

- Almosnino [22]

This method uses a vortex lattice method (along with sources to give zero incidence thickness) to model the flow around the body.

Although comparisons with experimental C_N, C_m and C_p are very good figure 6.2.3.1, 2 & 3 separation positions have been input from experimental data. The vortex lattice geometry depends upon the separation position, which must be known a priori. Information on computing time is not given. Since the method uses an iterative technique akin to time marching to a steady state, account is taken of up and downstream influence.

- Costis and Telionis [26]

Costis and Telionis [26] describe the modelling of the flow about a prolate spheroid using the 3-D vortex lattice method.

The body is represented by a straight line segment vortex lattice, the strengths of which are determined by satisfying the

boundary conditions at the panel centroids (though not necessarily in the plane of the panel but on the body surface).

The separated flows are calculated by approximating the separated vortex sheets by vortex lattices. After the first time step a strip of vortex panels is placed parallel to the body a distance 0.2 radii above its surface at the region of separation. After the second time step this strip is convected and then joined by a second strip placed again along the region of separation. Thus as time progresses a free vortex sheet is generated. The rate at which vorticity is shed is given by $\Delta\Gamma = \frac{1}{2}V^2\Delta t$ as in the 2-D vortex cloud methods.

This method estimates the shed vorticity rate at the separation line in 2 dimensions instead of in 1 as in the 2-D case.

In the Costis and Telionis paper pressures on the leeward side of the body caused problems. This appears to be due to large locally induced velocities on the body surface where the vortex sheet approaches it.

It may be possible to overcome the pressure distribution problem by using smaller time steps and hence more shed vortex panels but of weaker strength. Also a viscous core model could be applied to induced velocity calculations. Computing time would be on a par with the Vortex Cloud methods. However, the 2-D vorticity model may possibly be capable of showing where some of the 40% of circulation goes to in the vortex cloud method.

6.2.4 Some General Comments on Vortex Lattice Methods

This approach gives flexibility in body geometry and has the ability to model the vortex sheet with vorticity shed in two planes. These methods may well be more CPU intensive than the vortex cloud methods.

7. SURVEY AND ANALYSIS OF EXPERIMENTAL DATA

7.1 GENERAL EXPERIMENTAL DATA REQUIREMENT

7.1.1 Flow about circular cylinders and other bluff bodies

Many of the methods currently in use to predict the aerodynamic characteristics of slender bodies at incidence are based upon the premise that in some way the steady 3-D flow about the body can be related back to an unsteady 2-D flow about a particular 2-D body.

Hence it is important to have a good understanding of the 2-D flow physics before this can be applied to a 3-D flow problem.

It has already been noted that this type of approach is limited by the fact that the 2-D unsteady flow field can never be made to fully relate to a 3-D steady flow field due to certain fundamental features of the 3-D flow being lacking in the 2-D flow. Again, to fully appreciate the difference a good understanding of the 2-D flow must be obtained before considering the 3-D scenario.

The data required for this purpose must obviously include a reasonably detailed flow field survey to enable the main flow features to be resolved and analysed. The data should, of course, relate to reasonably representative Reynolds number or range of Reynolds numbers. Similarly the Mach number should be appropriate.

7.1.2 Flow about slender bodies at incidence.

The need for experimental data relating to the 3-D flow about slender bodies at incidence is driven primarily by three requirements. Firstly, to enable an understanding to be developed of the physics involved in flow fields of this type. Secondly, to enable the dominant features of the flow to be determined. This is important as it will enable any model development work to focus on the critical features and approximate the remainder. Finally, having developed a model, experimental data will be required for its validation.

This data should ideally contain as detailed a range of tests as possible. Force and moment data will be required in addition to pressure distributions. Flow visualisation, particularly of the surface flow would be useful, as would sufficient flow field survey data to enable the vortices to be located. It is unlikely that 3-D flow field survey data could be found with sufficient resolution to examine the smaller scale features of the flow such as the boundary layer and the feeding sheet.

7.2 SURVEY AND SELECTION OF RELEVANT EXPERIMENTAL DATA SOURCES.

7.2.1 Flow separation from 2-D bluff bodies

For the purpose of investigating the nature of the generation and convection of vorticity from a 2-D bluff body the classic series of tests on this subject were selected. The work was published by Fage and Johansen [28], [29] & [11].

Despite the fact that the tests were performed some 67 years ago the quality of the data is extremely high.

7.2.2 Flow about slender bodies at incidence.

The initial phase of this search indicated that there was a vast array of experimental results relating to the aerodynamic characteristics of slender bodies at incidence. The data covered a wide range of Reynolds numbers and Mach numbers with configurations as varied as early airships to non-circular section air-to-air missiles and some as complex as the Saturn V rocket.

In order that the data base could be brought down to a manageable size and that the data be appropriate to our requirements the range of geometries was limited to slender bodies of revolution. Multidiameter bodies were discarded as were winged bodies.

At this stage the references were examined in more detail to determine the scope of the tests. Many of these were simple force and moment balance tests which would not contain sufficient detail to enable insights to be gained into the nature of the flow. This data was not completely discarded, however, as some elements might prove of use in the validation work.

As regards the Mach number range an attempt was made to obtain low speed data although most of the tests were primarily concerned with transonic and supersonic conditions. In fact the largest test series encountered concentrated almost exclusively on Mach 1.98. Most of the high speed data was discarded as being outside the range of interest.

Of the remaining test series these were examined for scope of data. In addition to force and moment data, load distribution data was also required, implying that the wind tunnel models should be pressure tapped. This also implies that circumferential and longitudinal pressure distributions might also be available. In addition any flow field survey data would be useful in gaining insight into the vortex structures. This would also enable the vortex

strengths and positions to be determined. These two requirements rapidly reduced the number of viable tests series available. Further, it would also be useful to have access to flow visualisation investigations corresponding to the tests. In particular, good quality surface flow visualisations.

Unfortunately, many of the test series that promised to contain much of the required data could not be accessed due to security restrictions (in the case of much of the American data) or company confidentiality restrictions.

The test series that still showed promise at this stage are listed in Table 7.2.2.1. Note that many of the test series were run over a period of several years and the results reported in many separate references[1]. For brevity, only the main reference to each test series is given. The table gives an indication of the scope of each test series.
The test series that stood out as meeting most of the requirements in the most comprehensive manner is that by Hartmann [30] of DFVLR. A similar test series performed by Champigny [31] of ONERA was also selected as it provided a similarly comprehensive, independent and complimenting data source. Thus no single test series would be depended upon.

Unfortunately neither of these test series contained flow survey data. Difficulty was encountered in obtaining data of this type in the public domain. Fortunately Tinling and Allen's [32] 'classic' reference provides some data of this nature and was selected as a third main source.

These sources will be detailed in the remainder of this section.

7.3 THE FAGE AND JOHANSEN TEST SERIES

7.3.1 The nature of vorticity generated by the flow separation from a normal flat plate

The description of this test will be limited to the elements concerned with the results of interest.

The experimental set up consisted of a 7 foot long by 5.95 inches wide steel flat plate with sharp edges as shown in figure 7.3.1.1. Also shown are the locations of 19 pressure tappings. The model was mounted vertically with small clearances between its ends and the floor and roof of one of the 7-

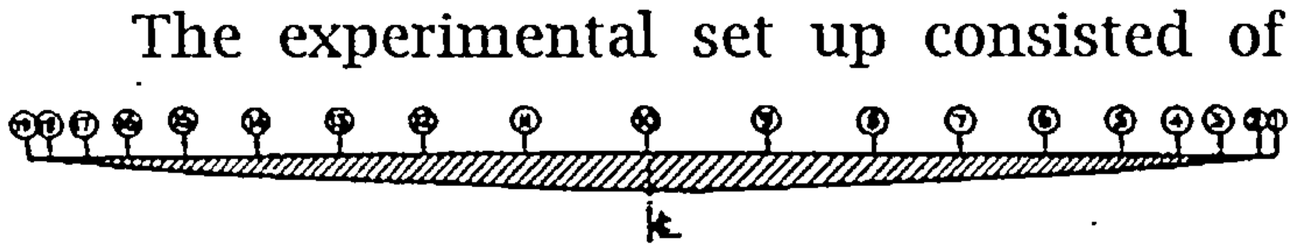

Figure 7.3.1.1

[1] sometimes by various authors

foot wind-tunnels at the N.P.L. The observations, both pressure and field velocity measurements were confined to the plane of symmetry, midway between the floor and the roof, where for all practical purposes the flow is two-dimensional.

In addition to the pressure measurements a hot wire anemometer, figure 7.3.1.2 was used to measure the flow field velocity in various regions including the area in proximity to the edge of the plate. This experimental set up is particularly useful for investigating the nature of the shear layer generated from a flow separation. Firstly, the geometry is very simple thus aiding the conceptual aspects of the experiment. Secondly, the point at which separation occurs is fixed by the geometry and occurs at the sharp edges of the plate.

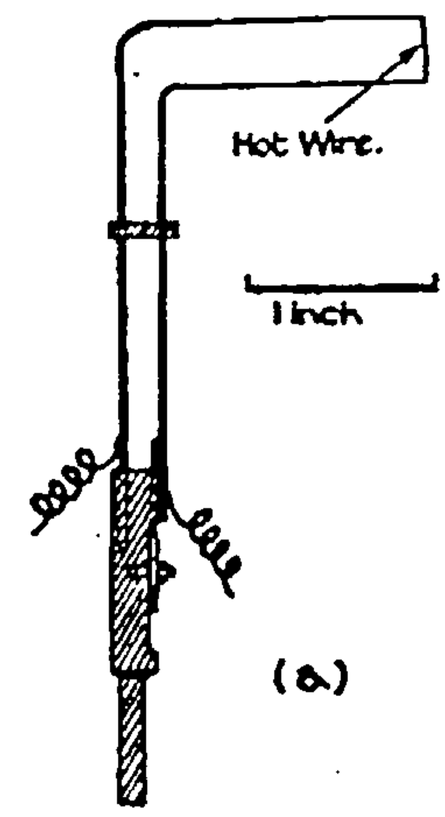

Figure 7.3.1.2

As the flow separates from the sharp edges of the plate a shear layer forms at each edge and propagates back tending to the freestream direction. This shear layer consists of a small region in the flow of very intense vorticity bounded by high vorticity gradients. As the shear layer propagates downstream it becomes wider, the vorticity gradients reduce and the intensity of the vorticity also reduces. Whilst the outer boundary of shear layer region is fairly steady in nature the inner boundary is less so. As the shear layer continues downstream this unsteadiness greatly increases until the vorticity field breaks up and reorders itself into large discrete vortex structures. These vortices form alternately from one edge after the other and propagate, downstream forming the classic 'Vortex Street', figure 7.3.1.3.

This form of flow field can be observed from most types of bluff body, however as previously mentioned, the flat plate gives a good point from which to start.

7.3.2 Quantifying the generation of vorticity

By considering the expression for vorticity in a 2-dimensional flow field:

$$\zeta \doteq \frac{\partial v}{\partial x} - \frac{\partial u}{\partial y}$$

It can be seen that a considerable number of flow field measurements would be required to accurately determine these velocity gradients and hence obtain the vorticity and then repeat this over a region to determine the total circulation over that region.

This is particularly demanding task due to the small scale of the region of interest.

7.3.3 Approximations for the rate of vorticity generation

Having accepted that the direct evaluation of vorticity, and hence rate of generation of circulation, would be too demanding a task given limited experimental capabilities available, a simple approach was sought.

The method used is highly significant since it has been accepted and applied in the Vortex Cloud Method. Hence, any insights gained or observations held concerning this approach will be of great relevance to the development or improvement of the Vortex Cloud Method or any alternative to it.

The assumption is made that the width of the vortex band is infinitesimally small. The velocities on opposite sides of the band are V_1 on the outer side and V_2 on the inner. A length of the vortex sheet, δs, is considered by enclosing it within a rectangle whose sides are parallel and normal to the sheet as shown in figure 7.3.3.1. The circulation around this rectangle can now be integrated thus;

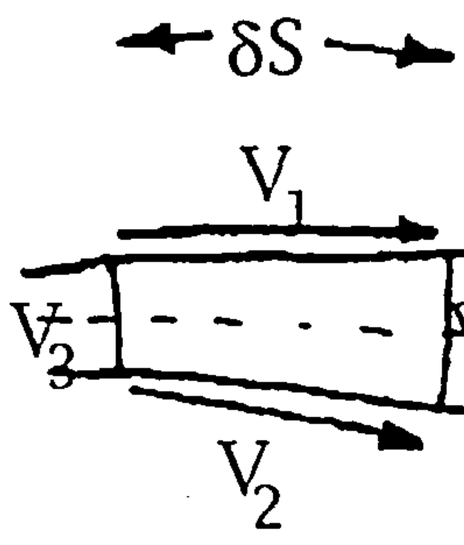

Figure 7.3.3.1

$$\Gamma = \oint V ds$$
$$= V_1 \delta s - V_4 \delta w - V_2 \delta s + V_3 \delta w$$

But since $V_3 \approx V_4 \approx 0$

$$= V_1 \delta s - V_2 \delta s$$
$$= (V_1 - V_2)\delta s$$

Now if δs is the length of the vortex sheet that is generated per unit time then:

$$\dot{\Gamma} = (V_1 - V_2)\frac{\delta s}{\delta t}$$

The mean speed along the axis of the sheet in direction s is

$$V_m = \frac{(V_1 + V_2)}{2}$$

but

$$V_m = \frac{\delta s}{\delta t}$$

hence

$$\dot{\Gamma} = (V_1 - V_2)\frac{(V_1 + V_2)}{2}$$

$$= \frac{(V_1^2 - V_2^2)}{2}$$

Or in non-dimensional form:

$$\dot{\Gamma} = \frac{(V_1^2 - V_2^2)}{2V_0^2}$$

This obviously presents us with an extremely simple method for determining the rate at which vorticity is shed in terms of circulation, where the only experimental information that is required is the magnitude of the inner and outer velocities.

The velocities were measured during traverses across the vortex sheet. This not only enabled the inner and outer velocities to be determined but also the boundaries and hence the shape of the sheet. Table 7.3.3.2. gives this information along with the corresponding values of $\dot{\Gamma}$ at each of 4 x-wise (x being downstream & y the lateral coordinates) stations.

The values of $\dot{\Gamma}$ can be seen to reduce by about 10% across the distance over which measurements were made. This reduction is claimed[2] to be due to the rapid widening of the vortex sheet shortly after its creation at the plate edges, which can be seen in figure 7.3.3.3. This rapid widening may invalidate some of the assumptions

---

[2] by Fage & Johansen

made in the derivation of the expression for $\dot{\Gamma}$. Nevertheless the initial value of 1.10 should be a good estimate.

x/b	y/b at V_1	y/b at V_2	δw/b	V_1/V_0	V_2/V_0	$\frac{V_1^2 - V_2^2}{2V_0^2}$
0	0.505	-	-	1.5	-	1.11
0.033	0.570	0.535	0.035	1.49	0.14	1.10
0.084	0.630	0.570	0.060	1.47	0.17	1.07
0.168	0.695	0.613	0.082	1.42	0.18	0.99

Table 7.3.3.2

It is interesting to note that Fage and Johansen fail to entertain the idea that there may be a physical mechanism present that might actually reduce or appear to reduce the value of $\dot{\Gamma}$ as the vortex sheet progresses in the 's' direction.

These are fundamental issues that will need to be addressed if modelling of these processes is to be improved or, indeed, if the processes are to be fully understood.

7.3.4 The 'far-field' vorticity distribution.

The investigation, so far, has been limited to the flow field region in the immediate vicinity of the plate edges. The furthest downstream station being x=17% of the width of the plate.

As already mentioned, the unsteadiness of the flow, which initially is only evident along the inner edge of the vortex sheet, increases in the downstream direction until the regions of vorticity break up and metamorphose into discrete vortices that propagate downstream.

This unsteady nature means that the method previously used to determine the rate at which circulation passes any given station is no longer appropriate. Whilst, in the near field a steady velocity profile can be measured by traversing the vortex sheet at any given x-direction, in the far field a similar traverse would result in a velocity profile defined by minimum and maximum bounds on the unsteady local velocity. Figure 7.3.4.1 indicates the degree of unsteadiness present in the flow at 5,10 and 20 plate widths downstream.

The fluctuations in velocity at any given point in the flow field are not of random nature, however. They are, of course, a direct result of the discrete vortices passing across the point of interest and inducing velocity measurements appropriate to the strength and size of the vortex and its distance from the point.

It can be shown [32a, b, c & d] that the velocity amplitude at a point situated outside and at a distance y from the centre of a vortex street is given by

$$V_{\max} - V_{\min} = \frac{\chi}{a}\left[\frac{1}{\sinh\frac{2\pi\left(y-\frac{h}{2}\right)}{a}} + \frac{1}{\sinh\frac{2\pi\left(y+\frac{h}{2}\right)}{a}}\right]$$

where χ is the strength of each vortex
a is their longitudinal spacing
h is their lateral spacing

By experimentally measuring the velocity distribution across the flow field and the accompanying frequencies it is possible to deduce all the variables in this equation except for χ which can now be solved for.

The non-dimensional strength of each individual vortex is given by

$$\frac{\chi}{V\,b}$$

The rate at which vorticity is carried downstream in the form of well defined vortices is given by

$$\chi\ f$$

where f is the frequency of the generation of vortices.
Fage and Johansen use this approach to calculate $\dot{\Gamma}$ from their experimental data as, non-dimensionally, $\frac{\chi\ f}{V_0^2}$.
These results are tabulated in table 7.3.4.2.

In Kármán's stability relation [32a & b], which assumes a vortex street of infinite length, it is shown that h=0.281a. This expression can be used to determine values of h from the experimental values of a. It should be noted, however, that experimental evidence indicates that the vortices do not travel in parallel lines but that their trajectories open out downstream. Hence some error may be anticipated here. Nevertheless these results are also given in table 7.3.4.2. for x/b=10.

x/b=10		Kármán theory		wind tunnel		Far field	$\frac{\chi f}{k}$	$\frac{\chi f}{k}$
y/b	$\frac{V_{max}-V_{min}}{V_0}$	h/b	$\frac{\chi f}{V_0^2}$	h/b	$\frac{\chi f}{V_0^2}$	$\frac{k}{V_0^2}$	Kármán	wind tunnel
3.0	0.151	1.475	0.74	2.0	0.57	1.1	0.65	0.51
3.8	0.055	1.475	0.70	2.0	0.55	1.1	0.65	0.51

Table 7.3.4.2

7.3.5 Vorticity conservation

On a simplistic level it might be expected that once generated, the vorticity in the field, or at least the rate at which circulation passes through any station, should be constant.

The data derived so far is ideally suited to investigating this idea. The rate at which circulation is generated at the plate edges is given as $\dot{\Gamma}$ (or K) and the rate at which it passes a given station some distance downstream is given as $\frac{\chi f}{V_0^2}$, hence the ratio of these numbers $\frac{\chi f}{K}$ should equal unity for conservation to be met. From table 7.3.3.2 $\frac{K}{V_0^2}$ is of the order of 1.1 hence using a value of $\frac{\chi f}{V_0^2}$ of 0.57 from table 7.3.4.2, 10 plate widths down stream, we get a ratio of 0.51. Fage and Johansen explain this loss of vorticity as being due to various mechanisms. Firstly, that part of the vorticity is dissipated immediately behind the plate by a mixture of positive and negative vorticity from the two plate edges. The second mechanism is that not all of the vorticity passes downstream in the form of the Vortex Street, some will be in "unattached" vortices, too small to appreciably affect the measured velocity fluctuations outside the wake.

There are also some possibilities not considered by Fage and Johansen. Firstly, that the near field expression for determining the rate at which vorticity is shed is incorrect or inaccurate. No method of validating this approach is offered. Obviously any error in this term will directly effect the near-field /far-field ratio. In fact the only term within this expression that is even checked is $\frac{V_1}{V_0}$ which can be derived from the surface pressure tapping measurements. This indicates a value of 1.54 instead of the 1.5 from the hot-wire

anemometer measurements. Although this 2½% difference is small and does give confidence in the experimental set up, this equates to a difference in $\dot{\Gamma}$ of 7% due to the square effect.

Secondly, the idea that vorticity of opposite sign from the opposite edge may cancel some of the shed vorticity immediately behind the plate is not convincing due to the fact that the vorticity is highly concentrated in the well defined vortex band regions emanating from the plate edges. The vorticity drops to near zero away from these edge regions.

However, this is not to say that there are no mechanisms for the reduction of vorticity levels in the near-field region. Viscous dissipation could be responsible for some loss, although this is likely to be small over such a short distance or short time span. Nevertheless a small reduction in $\dot{\Gamma}$ is recorded in the near-field experiment albeit with some doubts about the validity of the expression used.

The experimental set up attempts to ensure that the flow is as near 2-D as is possible, hence the instrumentation is configured only to record data in two dimensions, However, it is possible that some 3-D phenomena are at play here but can not be observed fully due to the 2-D data gathering.

It is the physics of the near-field that is of greatest significance to the Vortex Cloud Method application. In VCM terms the far-field flow would only be relevant in the case of a very high angle of attack case and then only near the base of the body. However, it is considered important to study this area of the Fage and Johansen data since it gives us our only other reference point in the flow to examine the reduction in the propagation of vorticity. Unfortunately, the method used to determine $\dot{\Gamma}$ in the far-field is probably less reliable than that used in the near field and again no evidence supporting its ability is put forward. A drop in vorticity of 50% is unlikely to be wholly due to an inaccuracy in this method since the experimental evidence indicates that this model appears fairly rational. It is unfortunate, however, that Fage and Johansen do not present data at $\frac{x}{b} = 5$ and 20 as well as 10 so that a drop in $\dot{\Gamma}$ might be detected by this method alone. The explanation offered by them for the reduction in vorticity in this region is that some vorticity is carried by the flow outside the vortices that make up the vortex street. It is claimed that these are so small that they do not effect any of the velocity measurements. However, to produce a loss in vorticity of some 50% without effecting the velocity measurements is difficult to believe.

It is thought more likely that annihilation of vorticity by negative vorticity would occur in this region rather than in the near-field as suggested by Fage and Johansen. But again not on the scale

required to match experiment. An accumulation of vorticity somewhere in the flow field is ruled out due to the long term steadiness of the flow.

In summary, there is strong evidence to suggest that a significant quantity of vorticity is being lost or becoming undetectable in a 2-D experiment. There is evidence to suggest that this loss may occur in the near-field and certainly occurs in the far field. There are a number of possible causes for this loss; however, it is likely that a full understanding of the physics has not yet been attained and hence additional mechanisms may exist.

The magnitude of the loss in vorticity is such that a factor[3] will need to be applied to the simple expression for $\dot{\Gamma}$ if it is to be used in any flow model.

7.3.6 Separation from the circular cylinder

From earlier sections it is evident that it is the modelling of the flow about a 2-D circular cylinder that is of greatest relevance. However, the previous section concentrates on the flow about a 2-D flat plate. This is because the flow contains all the separation features of the circular cylinder with the exception of actual location from which separation occurs. This enabled us to concentrate on the issue of vorticity propagation without the added complexity of Reynolds number and geometry dependant phenomena.

In moving onto the flow about a circular cylinder the problem becomes more complex due to the lack of an obvious point from which separation will occur. As discussed in earlier sections the process of separation is now not only a function of the state of the boundary layer due to the Reynolds number and surface roughness but also the pressure field by virtue of the body curvature. Furthermore there will be an interaction between the separation process and the distribution of vorticity in the flow field. This is the nature of separation from smooth surfaces.

Fage [29] describes another wind tunnel test aimed at investigating the flow about a 2-D circular cylinder and, in particular, the nature of the boundary layer in the vicinity of separation in the complex critical Reynolds number region.

The experimental set-up consisted of an 8.9in diameter circular cylinder mounted between the floor and roof of a 4-ft wind tunnel. Observations were made in the plane passing through the median section of the cylinder where the flow was assumed two-dimensional. The tunnel was run at speeds from 22.0 to 71.4 ft/sec which spans the critical flow region for this cylinder.

---

[3] or more complex model

A total head tube, shown in figure 7.3.6.1, was used to measure values of total head in the flow around the cylinder and, in particular, in the boundary layer. Because of the high resolution required to examine the small scale structures such as the boundary layer the tube, which was made from a hypodermic needle pressed to an external rectangular section 0.0074" by 0.021" and internally 0.0017" by 0.0053", was moved radially by means of a micrometer screw mounted externally on the opposite side of the cylinder.

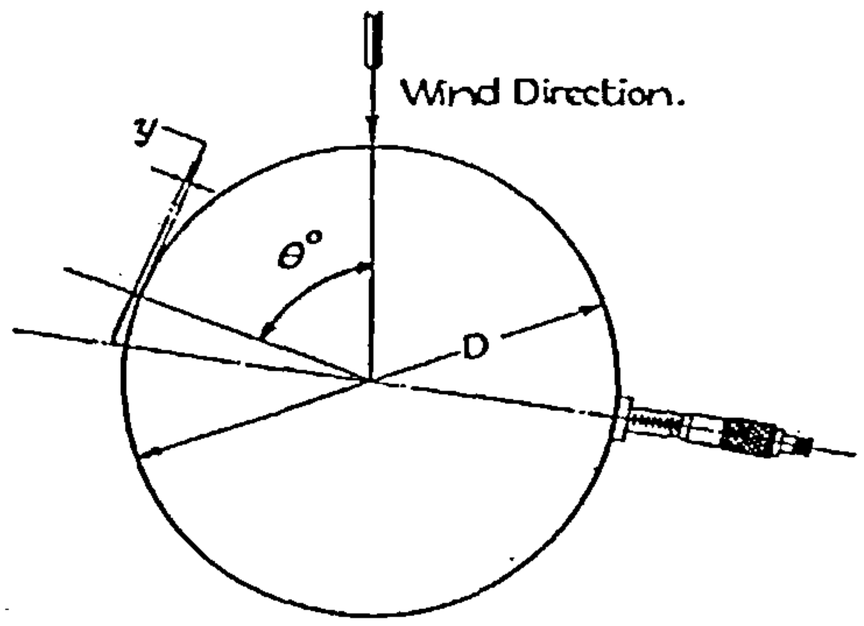

figure 7.3.6.1

The first part of this test conserves the measurement of the pressure distribution about the cylinder. The results of which are depicted in figure 7.3.6.2 taken from Fage [29].

The first point of note is the marked difference in pressure distributions about the cylinder at different freestream velocities. In general terms there is a significant variation in the magnitude of the minimum pressure point, a small variation in the location of the minimum pressure point, a variation in the magnitude of the lee side pressure distribution (which is fairly constant between θ=120° and 180°) and location from which constant lee side pressure begins.
Despite these differences the pressure distributions are all of the same form of a short plateau or slope discontinuity between the minimum pressure location and the point of separation, these regions being between the points B and C in figure 7.3.6.2.

Fage suggests that the plateau region immediately to the lee side of B is due to the effect of boundary layer transition and terminates with total flow separation at point C. His conclusions were drawn by experimentally measuring total head profiles normal to the cylinder surface across the boundary layer. Although he indicates that there are some inconsistencies in some of the data he does not take these any further.

However, by further processing[4] the data from Fage[29] it has been possible to derive velocity profiles normal to the cylinder surface for two free stream velocity cases 22.0 ft/sec and 71.4 ft/sec. Figure 7.3.6.3 depicts velocity profiles close to the body surface at 7 angles around from the windward direction (nominally 60°, 65°, 70°, 75°, 80°, 85° & 95°). To more clearly illustrate the development of the boundary layer velocity profile figure 7.3.6.4 depicts the same velocity profiles with the zero axes displaced proportionally to the appropriate values of θ. Here we can see the classic velocity profile

---

[4] by this author

development as it approaches separation from θ= 59.6° to 79.6° where near zero velocity gradient is achieved. At θ=84.6° a reverse flow region is clearly evident. However, by θ=94.6° the flow appears to have reattached, since the reverse flow region has vanished, but is on the point of separating due to the zero velocity gradient.

By comparison Fage suggests that the flow is fully separated at θ=85° which the velocities confirm. However the velocities also indicate that separation may be occurring as early as θ=79.6° which Fage does not. The zero gradient velocity profile at θ=94.6° does not fit into Fage's concept either.

Figure 7.3.6.5 shows a similar set of velocity profiles at a freestream velocity of 71.4 ft/sec. These profiles were measured over a wider range of θ from about 50° to 130°. Again from θ=49.8° to 89.8° the profile development indicates a boundary layer approaching separation. From θ=89.8° to about 97° (interpolating between the θ=94.8° and θ=99.8° curves) the velocity gradient tends to zero indicating separation is occurring at this point. By θ=99.8° there is evidence of a region of strong flow reversal. By $\theta \approx 107°$ (interpolating between the θ=99.8° and θ=109.8° curves) the velocity gradient has returned to zero indicating a possible reattachment of the flow. After this point the velocity profile develops again although without as severe a velocity gradient as was evident in the earlier region of attached flow. By θ=129.8° the flow appears to be reaching a second point of separation.

This interpretation differs slightly from Fage's which claims only transition occurs between points B and C on figure 7.3.6.2, followed by complete separation at C. The velocity profiles indicate that separation occurs at B followed by a region of flow reversal ending in reattachment at C. The boundary layer then develops further beyond C until reseparation occurs some 20° later. These apparently differing viewpoints will be reconciled later.

Having derived the velocity profiles, it is now possible to examine the vorticity distribution within the boundary layer. Figure 7.3.6.6 shows the vorticity profile at V=22 ft/sec. Over the attached flow phase the vorticity is concentrated within the lower levels of the boundary layer as expected. As separation is approached the vorticity distribution changes with much lower levels at the surface. After separation the surface vorticity is negative due to reverse flow. At the point where the velocity profile indicates that reattachment may follow, the vorticity profile is still markedly different from that of the attached flow however.

Figure 7.3.6.7 depicts the vorticity distributions at V=71.4 ft/sec. As with the velocity profiles the data for V=71.4 ft/sec is considerably clearer than the V=22 ft/sec data. The vorticity distribution is clearly concentrated in the boundary layer near the body surface whilst the flow is attached. As separation is approached and passed the vorticity becomes negative at the surface due to the reverse flow and the

positive peak occurs some short distance above the surface as would be expected in a separated shear layer following separation (see θ=99.8° curve). As the flow approaches reattachment the vorticity collects towards the surface again and eventually takes on a form similar to the attached flow. Finally a second separation occurs resulting in the vorticity peak moving away from the surface again.
Again this appears to conflict with Fage's interpretation of events. However, it is possible to postulate an alternative series of processes that, perhaps, fit the observations more readily and does not contradict all of Fage's ideas:

The flow remains attached on the windward side of the body and, at these Reynolds numbers, the boundary layer remains laminar. Shortly after the minimum pressure peak, labelled A on figure 7.3.6.2, the flow separates at point B. This is confirmed by the velocity gradient at B and the reverse flow region between B and C. Fage claims that transition occurs between B and C and this is correct, the disturbances induced in the process of separation will cause transition to occur in the separated shear layer. As the shear layer becomes turbulent it entrains air from outside and becomes considerably thicker. This thickening process is so rapid that the inner boundary of the shear layer is able to reattach itself to the body surface somewhere in the vicinity of point C. Beyond point C the velocity is not as 'thin' as it was prior to point B and the vorticity is not so concentrated towards the body surface. This is characteristic of a turbulent boundary layer. The boundary layer continues to thicken and appears, for the higher speed case, to remain attached until θ=120-130°, where full separation occurs. This results in the 'dead-air' region on the lee side of the body that gives rise to a near constant pressure distribution. Whether the flow is truly attached between point C and the point of full separation or whether, due to the rapid expansion of the shear layer, the flow merely conforms to the body surface, is perhaps debatable. However, it does allow a greater degree of pressure recovery, it moves the trajectory of the separated shear layer rearward, and will reduce the cross-flow drag, all features of attached flow.

These tests were limited to the Reynolds number region known as 'Critical', where the flow is considerably more complex. At lower values the laminar boundary layer would separate and not reattach and at higher Reynolds numbers the flow would become turbulent without separation, followed by turbulent separation.
It is clear that these complex flows are likely to become more complicated when considered in the 3-D scenarios of a cylinder, or complete body of revolution, at incidence.
These Reynolds number effects are clearly an important feature of 2-D and later 3-D flows and hence any model will need to address them.

7.3.7 Vorticity generation from the circular cylinder and other bluff bodies

Having looked at the vorticity shed from a normal flat plate and the detail of the flow leading up to a separation from a circular cylinder it is now appropriate to consider the nature of vorticity shed from a circular cylinder.

The third source of data drawn upon is another paper by Fage and Johansen [11]. This paper goes on to examine a range of bluff body shapes including both the flat plate and the cylinder.
The models extended between the floor and the roof of a 7ft wind tunnel with measurements being taken in the median plane where the flow would be near two-dimensional, the cylinder diameter being 0.281ft

Two probes were used (see figure 7.3.7.1), the first was a hot wire anemometer for velocity (magnitude) measurements and the other was a total head tube combined with a hot wire flow direction sensor to enable the tube to be aligned with the flow.

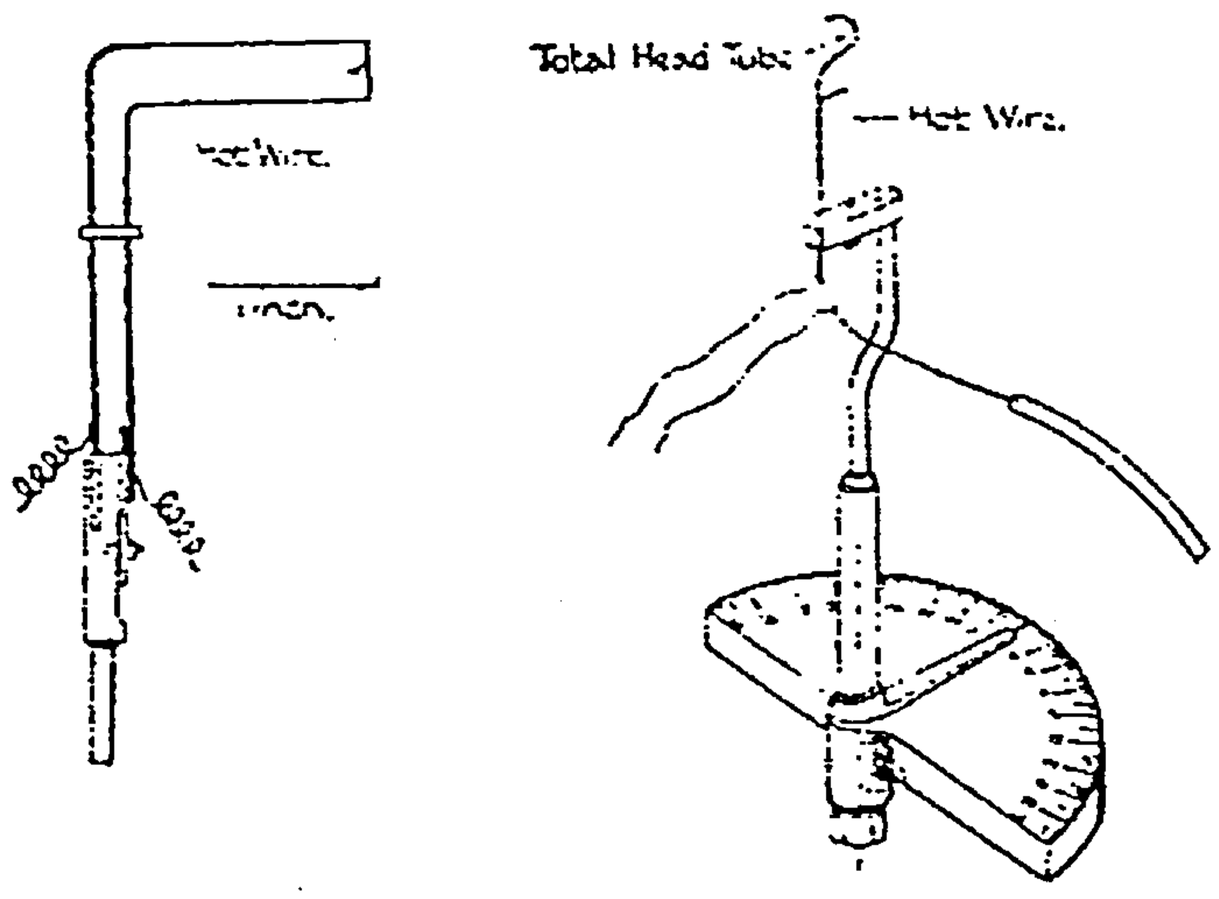

figure 7.3.7.1

The experimental set-up enabled quite accurate velocity profiles to be measured across the plane of the shed vorticity regions. From these velocity profiles it was possible to calculate the vorticity distribution across the vortex sheets. Figure 7.3.7.2 taken from Fage and Johansen [11] clearly shows the vorticity distribution through the vorticity sheet and how it develops as it progresses downstream. The vorticity is seen to be very concentrated over a small width immediately after being shed and gradually becomes less concentrated but spread over a greater width as it progresses. Nonetheless it can be seen that all the vorticity remains in a very confined region of the flow field.

With the availability of relatively accurate velocity data it is possible to determine the variation of $\dot{\Gamma}$ at a number of stations downstream of the point of separation.

Firstly, the circulation in region can be found by integrating the vorticity over the area thus:

$$\Gamma_{Area} = \frac{1}{V_0 b} \iint \left(\frac{\partial v}{\partial x} - \frac{\partial u}{\partial y} \right) dx dy$$

The flow field was divided into 4 regions as shown in figure 7.3.7.3. Γ_{Area} is determined by measuring V and θ in the flow field in the vortex sheet region. From this u and v are determined as a function of x and y. $\frac{\partial v}{\partial x}$ and $\frac{\partial u}{\partial y}$ are found graphically and hence the integral can be evaluated over the regions I, II, III and IV.

Knowing the value of Γ_{Area} for each region and the length of each region it is possible to estimate values of $\dot{\Gamma}$ since

$$\dot{\Gamma} = \Gamma \frac{\left(\frac{V_1}{V_0} + \frac{V_2}{V_0} \right)}{2} \frac{1}{s}$$

The results of which are given in table 7.3.7.4.

The second approach entails finding the total vorticity enclosed by a contour.

$$\Gamma_{contour} = \frac{1}{V_0 b} \int (u dx + v dy)$$

Here Γ is found by obtaining u and v as in the first method and then evaluating the integral around the contour. Once again the result is the total circulation in regions I, II, III and IV. Table 7.3.7.5 contains the results.

It is also possible to determine the value of $\dot{\Gamma}$ directly without first finding Γ:

$$\dot{\Gamma} = -\frac{1}{V_0^2} \int_{y_2}^{y_1} \left(\frac{\partial v}{\partial x} - \frac{\partial u}{\partial y} \right) u . dy$$

= shed vorticity per unit tim

Here the flow velocity and the direction is measured across the vortex sheet at a number of stations. From measured values of v and θ it is possible to calculate u and v. $\frac{\partial v}{\partial x}$ and $\frac{\partial u}{\partial y}$ are obtained graphically. Hence the integral can be evaluated across each station.
Table 7.3.7.5b contains the results.
The approximate method from Fage and Johansen [11] can also be used i.e.:

$$K = \dot{\Gamma} = \frac{V_1^2 - V_2^2}{2V_0^2}$$

The results of which are tabulated in Table 7.3.7.6.

The same reference also describes a method for estimating a value of $\dot{\Gamma}$ in the far field downstream. By making measurements to determine the geometry of the vortex street and by measuring the amplitude of the flow velocity fluctuations at a point in the flow the strength of the shed discrete vortices can be estimated. By measuring the frequency of the shed vortices the rate at which the vorticity is convected downstream can be determined.
The results are given in Table 7.3.7.7.

All of the values $\dot{\Gamma}$ are summarised in Table 7.3.7.8 and plotted in figure 7.3.7.9. It can be seen that the area and contour integral methods give excellent agreement except for the first point which is predicted high using the contour method. The direct integration method of $\dot{\Gamma}$ gives slightly higher results but follows the same trend. The approximation appears to underestimate the values of $\dot{\Gamma}$. Figure 7.3.7.10 shows the same data referenced to the maximum value at the point of separation. Least squares lines have been generated to indicate the trends. It is clearly evident that all the methods, except that by contour integration, show almost identical trends with $\dot{\Gamma}$ and diminish at the same rate downstream. The values of $\dot{\Gamma}$ by contour integration appear poor due to the spurious initial point shown on figure 7.3.7.9. If this first point[5] is adjusted the trend becomes almost identical to the remaining three..

Another, simpler, indication of the propagation of vorticity is the vortex sheet strength. This is simply the velocity difference between the inner and outer bounds of the sheet. i.e. $V_1 - V_2$
Figure 7.3.7.11-15 illustrate the shape of the vortex sheet as it develops downstream. Also shown is the magnitude of $\dot{\Gamma}$ as a function of x/b and the sheet strength. All body shapes indicate the

---

[5] which all other points are referenced to

reduction in vorticity with x. In the case of the circular cylinder $\dot{\Gamma}$ reduces by 30% and the sheet strength by 35%.

Fage and Johansen do not attach any significance to this reduction. Their interest was simply in comparing near-field values with far-field values. In their analysis the near-field values are averaged.

In summary, there appears to be considerable evidence that a significant amount of the vorticity first present in the flow at the point of separation is not present, or at least not readily visible, at some distance downstream.

This is an important feature of the flow that will need to be incorporated into any model for predicting 2 or 3 dimensional aerodynamic characteristics of these types of flow problems. Furthermore, a greater understanding of this phenomenon would obviously assist in its modelling.

7.4 THE DFVLR. AND ONERA TEST SERIES

7.4.1 DFVLR. experimental set-up and scope of test

The wind tunnel used here was the 3m tunnel at DFVLR/AVA which has a 3m square working section with a continuously adjustable wind speed from 0 to 65 m/sec giving a Reynolds number of 4×10^6 per metre. Figure 7.4.1.1 taken from Hartmann [30] show a cross-section through the tunnel. The data in the original reference included information about measured turbulence levels in the working section.

The model comprises a 3-calibre tangent ogive nose on an 11 calibre circular cylinder after-body. A 200mm calibre achieved as high a Reynolds number as possible in consideration of the test section size. Figure 7.4.1.2 depicts the model dimensions including the pressure tapping locations. Note that the nose profile is not a true circular arc tangent ogive but is defined by the following polynomial:

$$\frac{r(x)}{D} = 0.309840\left(\frac{x}{D}\right) - 0.039867\left(\frac{x}{D}\right)^2 - 0.002615\left(\frac{x}{D}\right)^3$$

This shape has its origins at RAE, Farnborough through collaboration between RAE and DFVLR.

The aluminium alloy model contained 360 pressure tappings arranged in rings of 24 at 15° intervals at 15 stations along the body. The 0.5mm diameter pressure tappings were connected to transducers through scani valves. Accelerometers were also mounted in the model to monitor the vibrational behaviour of the model-support system. Figure 7.4.1.3 indicates the type of model support used for the low incidence test runs.

The test programme can be split into two sections. Firstly a detailed survey at 3 Reynolds numbers covering incidences from 0° to 90° in 5° increments. All these were performed with the model at an arbitrarily chosen zero roll position. The second part of the test was limited to two Reynolds numbers and incidences of 20°, 30°, 40°, 50°, 60° and 70° with roll angles from 0° to 360° in 30° increments. The data of particular interest is the low incidence data from the first section of the programme. The reference test numbers are listed in table 7.4.1.5.

The highest Reynolds number was set by the model diameter and tunnel speed. The lowest was set by the tunnel speed giving the lowest acceptable pressure differential at the pressure transducers.

A limited set of flow visualisation tests were performed using smoke to examine the vortex structures. Additionally a series of water tank tests were also performed to obtain similar visualisations using hydrogen bubble techniques.

7.4.2 ONERA experimental set-up and scope of tests

These tests were performed in the pressurised subsonic 4.5m x 3.5m wind tunnel at ONERA Le Fauga-Mavzac Centre. The Mach number was variable between 0.1 and 0.35 with a Reynolds number range of 0.28×10^6 to 2.0×10^6 based on the model diameter.

The model consists of a 3 calibre tangent ogive nose with a 12 calibre circular cylinder after body. Two versions of the model were used. A smooth, unpainted and untapped version for visualisation work and a pressure tapped version, which was painted black, used for pressure distribution measurements. A 'bent' sting support with an internal balance was used which allowed a continuous range of angle of incidence from 0° to 80°.

The second of the two models, figure 7.4.2.1, was designed with 354 pressure tappings over 22 stations each connected to one of eight scani valves. In addition to the 6-component balance the model also incorporated 4 accelerometers to monitor vibrational effects.

The test programme details are listed in table 7.4.2.2. In addition to the range of Reynolds number and incidences a limited number of Mach number variations were explored as well as a small number of roll angles. The overall scope of the tests was less extensive than DFVLR tests and consequently only three of the angles of incidence tested are of use in the present work. These are α= 0°,10° and 20°. However the programme includes some excellent surface flow visualisation tests that can be interpreted to give great insight into the flow.

7.4.3 An overview of the data

From this point onwards it is felt to be more appropriate to discuss the two test series in parallel.
Tables 7.4.3.1 and 7.4.3.2 show a summary of the test numbers for the cases of most interest.

Figure 7.4.3.3 to 7.4.3.7 show the local normal force distributions for DFVLR body at the three Reynolds numbers. Figure 7.4.3.3 relates to the 5° incidence case and shows very little basic difference between the three Reynolds numbers except between about 6 radii (the nose-cylinder junction) and 12 radii. In this zone the local distribution falls to zero at the lower Reynolds numbers, where as at the higher Reynolds number the local distribution is near constant over the whole length of the cylinder. At 10° of incidence, figure 7.4.3.4, a trend starts to appear whereby the lower Reynolds number load is noticeably lower than the other two. By an angle of incidence of 15° this trend is quite marked, the two lower Reynolds number cases indicate a load distribution on the cylinder some 30% lower than the higher Reynolds number case. The 20° incidence cases have been split between figures 7.4.3.6 and 7.4.3.7 the former showing Reynolds number 0.25 million and 0.38 million and the latter showing 0.74 million. These two plots clearly show these three Reynolds number cases giving different magnitudes of load distribution along the length of the cylinder. The highest load occurs at the lowest Reynolds number. As the Reynolds number is increased the load drops by up to 50% but as the Reynolds number is increased still further the load increases again to almost, but not quite, as high as in the low Reynolds number case. The 0.25 million and 0.74 million Reynolds number cases were repeated for a large number of roll angles. At 0.25 million some variation in load is apparent between 6 radii and 12 radii but aft of this region repeatability is very good. For the 0.74 million case repeatability is excellent except for a single[6] point at 10 radii.

In all the above cases it is clear that the load over the nose region is almost Reynolds number independent.

The main area of interest for both DFVLR and ONERA was that of high angle of attack aerodynamics. A particular feature of this is the large out-of-plane forces and moments. These terms are relatively small at moderate incidences being considered here. Figures 7.4.3.8 and 7.4.3.10 confirm this to be the case with magnitudes only starting to build up towards the base of the body at the higher angles of attack.

Figures 7.4.3.11 and 7.4.3.12 similarly summarise the ONERA data in this case at 20° of incidence. The Reynolds number range here does not start as low as the DFVLR data and so does not see the

---

[6] Spurious?

initial reduction in load with Reynolds number. It does, however, clearly show the increase in load as Reynolds number increases. The 0.53 million case appears to be critical with a range of load distributions apparently due to a change in roll angle alone. Similarly the local side force distributions are relatively small except for one case at 2.0 million.

Cases 209,224 and 164, shown on figure 7.4.3.11, are identical configurations and Reynolds numbers but have Mach numbers varying from 0.1 to 0.35 and can be seen to give closely similar load distributions. Hence the results can be assumed to be Mach number independent at low speeds.

As already mentioned, although the main area of interest is the data at moderate incidences, both data sets include high incidence data. Some of the ONERA data is presented in figures 7.4.3.13 to 7.4.3.16 to put the moderate incidence data into context. Figure 7.4.3.13 shows the variation in normal force coefficient with incidence. The curve can be seen to exhibit highly non-linear features around 30°, between 40° and 50° and between 70° and 80°. These forces were measured using the six-component balance. Also shown on the figure are normal force coefficient points derived from pressure integrations. The correlation is clearly very good. Figure 7.4.3.14 contains similar data for the side force coefficient, C_y, verses incidence. This term varies considerable with Reynolds number but in general is very small below 20°.

Figure 7.4.3.15 shows the variation of pitching moment coefficient with incidence. Again, some striking non-linearity are apparent above 40°. Using the C_N and C_M data it is possible to deduce the centre of pressure position. This is shown in figure 7.4.3.16 and again has many non-linear features before tending to the 50% body length position at 90°.

It was noted earlier that whilst the ONERA model had a circular arc tangent ogive nose profile the DFVLR model had a polynomial ogive nose profile. These shapes are very similar and a comparison is shown in figure 7.4.3.17. The polynomial nose profile can be seen to slightly more slender. Also shown on the same figure is the effect on the local normal force distribution as predicted by Slender Body Theory. The difference, characterised by a rearward shift in the point of maximum local normal force, is greater than one might expect considering the slight difference in geometry.

Both test series included some flow visualisation work. Smoke was used to visualise the flow field in planes normal to the body. DFVLR also performed some water tank visualisation work as shown in figure 7.4.3.18. Here the lee side vortex structures are clearly evident at an incidence of 30°. However, the most useful data was the surface flow visualisation performed by ONERA which enabled much insight to be gleaned into the nature of these flows. Figure 7.4.3.19

shows one such visualisation at 50° of incidence. This will be discussed in some detail in the next section.

7.4.4 Flow visualisation - an indicator of separation type

In this section we examine, in some detail, the results of the ONERA surface flow visualisations obtained using the oil[7] method. This method is extremely useful in that a 'frozen' record is made of the air flow at the body surface under the conditions of interest[8]. The results do depend upon some degree of interpretation, nevertheless the main features appear quite clear and relatively unambiguous.

All separation-like features appear as a coalescence of surface streak lines in a rearward direction onto a single line.

From examination of the flow about a two-dimensional circular cylinder we know that three forms of separation are possible; laminar or sub-critical separation, transitional or trans-critical separation and turbulent or super-critical separation. The second of these consists of laminar separation followed by transition occurring in the separated shear layer followed by turbulent reattachment of the rapidly expanding shear layer and ending in turbulent separation.

These features occur in the two dimensional flow about a circular cylinder. However, there is no reason why they should appear in the, considerably more complex, case of the three dimensional flow about a body of revolution at incidence. In fact one might envisage more complex modes of separation. In practice, or at least from the evidence of the flow visualisation tests, three forms of separation appear to prevail, all closely, if not directly, related to the corresponding two-dimensional forms.

Figure 7.4.4.1, although at a higher angle of incidence than of current interest, is useful as it depicts very clearly[9] all three forms of separation. Towards the apex of the nose the flow undergoes laminar separation quite early, just after the 90° mark. Further back along the nose the shear layer, after laminar separation, undergoes transition early enough for reattachment to occur. The now turbulent boundary layer is able to remain attached for another 15° or so before undergoing turbulent separation. Further back along the nose the boundary layer becomes turbulent long before any danger of laminar separation and hence remains attached well beyond the θ=90° mark before turbulent separation occurs. Although in this last case separation is delayed by the turbulent boundary layer it is not delayed as long as in the transitional case.

---

[7] The oil mixture consisted of paraffin oil mixed with oleic-acid

[8] We shall, in fact, see that the presence of the oil does, to some extent, modify the flow.

[9] Not all photographs of visualisations are clear.

We shall now examine in detail some of the flow visualisation data to determine the effect of both Reynolds number and incidence on the mode of separation. The emphasis in this section is on the experimental evidence. Detailed explanations as to the underlying causes will be attempted in section 8.

Clearly the Reynolds number would be expected to have a significant role in determining the mode of separation. Figure 7.4.4.2 illustrates the separation features observed in the flow visualisation tests over a range of Reynolds numbers from 0.28 million to 2.1 million. All four cases correspond to the same incidence of 35° to enable the Reynolds number effect to be isolated. The first case at a Reynolds number of 0.28 million shows that the exhibits laminar separation along the entire length of the body. As the Reynolds number is increased to 0.54 million a dramatic change occurs. The shear layer that underwent laminar separation is able to reattach along the latter part of the nose. After the nose the flow now exhibits turbulent separation along the remaining length of the body. The change in flow as the Reynolds number is increase to 0.92 million is more subtle and can be seen as a forward movement of the transitional separation region and the start of the turbulent separation region. By the time the Reynolds number has reached 2.1 million the flow separation is entirely of the turbulent form. Figure 7.4.4.3 shows a schematic of the three forms of flow separation being exhibited.

Figure 7.4.4.4 shows a similar set of visualisations this time at 50° incidence. As at 35° the 0.28 million case exhibits purely laminar separation. The behaviour at 0.54 million differs from 35° case in that it shows transitional separation along the entire length. By the time a Reynolds number of 0.92 million has been reached most of rear of the cylindrical after body exhibits turbulent separation with transitional separation limited to around the nose section. Increasing the Reynolds number to 2.1 million pushes the transitional separation region further forward onto the nose.

These figures clearly show the direct relationship between Reynolds number and separation type irrespective of the angle of incidence. They also show that, in general, the more rearward along the length of the body one goes the more turbulent will be the nature of the boundary layer. Both of theses conclusions are as would be expected. It is also evident that there is some phenomenon occurring in the flow in the region of the nose-body junction that accelerates the transition to turbulent separation. This will be discussed in section 8. As regards incidence, it appears to push the flow back towards the transitional and laminar forms of separation. This is illustrated in the final picture in figure 7.4.4.3 which retains the Reynolds number at 2.1 million but reduces the incidence by 5°. This is sufficient to produce turbulent separation over the entire length of the body.

Turning our attention now to the effect of incidence figure 7.4.4.5 shows the separation type at a Reynolds number of 0.54 million over a range of incidences. Starting at 20° the short length of laminar separation rapidly changes to turbulent with only a short, if any, length of transitional separation. At 35° the transitional band lengthens until by 48° it stretches from halfway along the nose to the base of the body. Increasing the incidence still further to 60° lengthens the laminar separation region to just beyond the nose-body junction.

Figure 7.4.4.6 shows a range of incidences at a Reynolds number of 2.1 million. Starting at 20° the flow exhibits turbulent separation along its length. An increase of incidence to 35° results in a small region of transitional separation on the nose. This grows in length through 45° until at 60° it extends almost the full length of the nose followed by turbulent separation from there to the base.
It is clearly evident that an increase in incidence has the reverse effect of an increase in Reynolds number. A more detailed treatise on these effects can be found in section 8.

7.4.5 Circumferential pressure distributions

The total normal force data was obtained by two methods. Firstly, in the case of the ONERA data, with an internal six component balance and secondly, in the case of both the ONERA and the DFVLR data, by integration of the local normal force distribution along the length of the body. The normal force distributions were in turn derived by the integration of the circumferential pressure distributions measured via the surface pressure tappings.

Figure 7.4.5.1 shows an example of a surface pressure distribution at an incidence of 20°. As would be expected from the shape of the local normal force distribution there is considerable variation in the circumferential distribution with x-wise position. Towards the front of the body the distribution appears near-potential as would be expected. At about the nose body junction separation effects modify the distribution and two rearward-running suction peaks spring from the underneath where the lee side vortices would be.

This form of 3-D pressure distribution plot is useful in obtaining an overview of the shape of the distribution, but is not well suited to making a detailed study of the pressures. From here on pressures will be examined on a plane by plane basis.

Another useful method for depicting the circumferential pressure distribution is by using the polar representation. This enables the distribution to be directly related to angular positions on the body. Figure 7.4.5.2 shows the pressure distribution at 20° of incidence for a particular x station at Reynolds numbers from 0.25 million to 0.74 million. The plot clearly shows the degree to which

the lee side (θ=0) pressure recovery is dependent upon Reynolds number. Unfortunately, the polar representation makes the interpretation of the details in the separation region difficult to decipher. These details become more clearly evident when the pressure is plotted on a Cartesian C_p vs theta plot.

Figures 7.4.5.3 to 7.4.5.6 show the effect of x-wise position on the pressure distribution at a given Reynolds number.

Let us first examine these distributions with a view to extracting a general feel for the effect of x-wise position and Reynolds number. Figure 7.4.5.3 relates to a Reynolds number of 0.25 million. At this Reynolds number we would expect to see predominantly laminar separation along most of the length of the body. Over the front of the nose the minimum pressure peak occurs well after the 90° point at about 75°. The pressure peak itself is also fairly low. As we move rearward the pressure peak deepens and moves back to about 90°. Laminar separation occurs in this region giving rise to poor pressure recovery. Moving further back along the body the pressure recovery improves a little but no more than to C_p=-0.5 to -0.1. Considering the final station at x=9.42 it is apparent that at 20° of incidence the first signs of asymmetry are beginning to manifest themselves. There is a slight asymmetry between the levels of pressure recovery between ±60°. Of course upon integration this will not effect the normal force coefficient and the side force coefficient will not be significant due to it being a small difference in the upper quadrant which when resolved will be very small.

Increasing the Reynolds number to 0.28 million ought to move us into the transitional separation regime. The effect on the pressure distribution is quite striking as can be seen in figure 7.4.5.4. After a short region of laminar separation over the front of the nose, there is a very rapid jump to transitional separation characterised by the significant increase in lee side pressure recovery. This pressure now reaches between C_p=-0.1 and 0.3. The distribution shape is more clearly defined and there appears to be little if any flow asymmetry even at the rear of the body.

At 0.53 million, figure 7.4.5.5, there appears to be little change from the 0.28 million case, the pressure recovery being slightly less perhaps. There does appear to be a new feature between x=5.67 and 6.29 where the pressure appears to drop over the range θ=±15°. It is thought that this is due to a detail feature that is always present but can only be seen when it occurs exactly over a pressure tapping. Notice that, despite the curves joining the symbols, the feature is measured at a single pressure tapping only. We shall return to this in a moment. Again there is little evidence of asymmetry in the flow.

Increasing the Reynolds number into the turbulent separation region at 2 million, figure 7.4.5.6, it is clear that, as expected, the pressure recovery is not as good as in the transitional regime. A quite striking difference between this and the previous Reynolds number is

the clearly visible asymmetry over the last 3 calibres of the body. As mentioned before this asymmetry will be less marked than might be expected when integrated into a side force coefficient due its location on the upper quadrant of the body.

Returning to the feature mentioned in figure 7.4.5.5, it was stated that the feature was small. The term small is meant in relation to the pressure tapping resolution of 15°. In one of the test cases the model was tested at roll angles of 0°,10°,-10° and 165°. By comparing these cases it should be possible to detect small features in the pressure distribution which will show up as differences. Figures 7.4.5.7 to 7.4.5.9 show comparisons of these four roll angles at 20° of incidence for a Reynolds number of 0.53 million at three stations along the body. In figure 7.4.5.7 there is very little difference between the three plots as expected since this is further forward than the first appearance of the feature. Figure 7.4.5.8 indicates considerable scatter over the region ±30° although it is not clear why from this plot. This is an x-wise station where the feature was previously apparent. Moving further along the body, figure 7.4.5.9, the differences have reduced but are still significant. The true nature of the feature becomes obvious when the four roll angles are superimposed and a single mean curve plotted through them, as shown in figure 7.4.5.10. With the addition of these extra roll angles the effective resolution now reduces to 5°. This enables two clearly defined suction peaks to be resolved on the lee side of the body at about $\theta=\pm 20°$. The most likely cause of these are the locally high induced velocities due to proximity of the surface to the body vortices. In between the two suction peaks is a very rapid region of pressure recovery. It is clear that, since all the pressure integrations performed to derive local normal force distributions and total normal force coefficients are based upon 15° resolution data, there will be some degree of inaccuracy introduced. However, since the suction peaks and the recovery region are in opposite senses they will to some extent cancel. Furthermore, the peaks only appear over a small region of the body length and so should only have a limited effect on the total forces and load distribution.

It would be useful if the pressure distributions could be used to determine the type and location of flow separation. Referring to the pressure distributions about the two dimensional circular cylinder, it was in this case possible to make these types of interpretations and so, in principle, it should be possible to do the same in three dimensional cases. Obviously it is vital to remember that the three dimensional flow and separation are considerably more complex than the 2-D counterpart.

It was found the features that best categorise the separation phenomenon become more clearly visible by considering the variation in pressure distribution at a given x-wise station, as the Reynolds number varies. Figures 7.4.5.11 to 7.4.5.13 are plots at 3 x-

wise stations to illustrate this. It is useful to plot as many Reynolds number cases as possible and in this case 7 are used from 0.25 million to 2 million. Figure 7.4.5.11 clearly indicates the variation in the level of pressure recovery in the laminar separation regime. As the Reynolds number increases it moves into the transitional separation regime with an accompanying improvement in pressure recovery and finally the pressure recovery reduces again as turbulent separation is achieved. Knowing which pressure distributions correspond to which types of separation it is then possible to identify pressure distribution features that tell us more about the flow. Figures 7.4.5.12 and 7.4.5.13 show that careful study is required to locate these features. It should also be remembered that, fortunately, these features are located outside the $\theta=\pm 20^{o}$ 'uncertainty area'.

Figure 7.4.5.14 shows a schematic of the pressure distribution features that can be used to identify the type of separation and the location of them. Firstly, laminar separation; although this easy to identify by its lack of features, its poor pressure recovery and its late and low suction peak, its lack of features makes it extremely difficult to locate the actual point of separation other than at some point in the vicinity of the suction peak. Transitional separation is relatively simple to identify due to its very good pressure recovery and 'pressure plateau' to the lee side of the suction peak, indicating the points of laminar separation and turbulent reattachment[10]. The point of final separation is not terribly clear but can be estimated knowing the location of the 'dead air' region and taking the 15° resolution limit into consideration. Pure turbulent separation exhibits a level of pressure recovery somewhere in between laminar and transitional separation. The separation position is easier to locate due to the abrupt change from pressure recovery to the 'dead air' region. Figure 7.4.5.14 also shows a potential theory pressure distribution for comparison.

7.4.6 Location of separation lines

Considering the body at a fixed incidence of 20° the pressure distribution was examined in detail to determine the separation type and location as a function of Reynolds number and x-wise position. Figures 7.4.6.1 to 7.4.6.10 show the circumferential pressure distribution at 10 x-wise stations along the length of the body. At each station there are seven distributions covering a range of Reynolds number from 0.25 million to 2 million. On some figures are shown a series of schematics indicating the features used to determine the type and position of separation at each Reynolds number.

---

[10] As discussed in section 7.3.6.

Having located these features it is interesting to examine their variation with x-wise position. Since the positions were identified independently for each station this would also give an indication of the accuracy of the method if any smooth trends appear. Figures 7.4.6.11 to 7.4.6.17 depicts the location of the features in terms of the x-wise station and the θ position where θ=0 identifies the lee side of the body. Each plot relates to a different Reynolds number. The first, figure 7.4.6.11, shows three lines indicating the positions of laminar separation, followed by turbulent reattachment and then turbulent separation. A definite trend is evident indicating that the method used to determine the feature locations has been applied consistently. The trend is as expected and shows that separation occurs closer to the lee side near the nose and tends towards some constant value over most of the after-body. Figure 7.4.6.12 at 0.28 million shows a similar result. It can also be seen that the angular separation between the flow separation locations and the attachment location are roughly constant. At 0.38 million there are indications that the flow is becoming turbulent. Figure 7.4.6.13 shows that laminar separation and turbulent reattachment could not be detected near the base of the body although turbulent separation was still apparent. Figure 7.4.6.14 indicates that by 0.53 million the flow is exhibiting turbulent separation almost along its entire length. Figures 7.4.6.15 to 7.4.6.17 show that above 0.74 million there is little change in the separation position except for a shift of about 5° in the vicinity of the nose.

Figure 7.4.6.18 contains all of the transitional separation cases and indicates that within this regime the final separation position is almost entirely independent of Reynolds number. Figure 7.4.6.19 shows a similar result for the turbulent separation regime with a slight increase in θ with Reynolds number but only in the nose region.

This is a useful result since it indicates that any model of the flow need not include detailed Reynolds number effect modelling provided that it can differentiate between the main separation regimes.

An attempt was then made to validate these results by comparing them with the flow visualisation results. Two cases were considered, the first at a Reynolds number of 2.1 million which should give rise to turbulent separation and the other at 0.54 million which should be in the transitional separation regime. Figure 7.4.6.20 shows how the separation angles were deduced from dimensions measured from the flow visualisation photographs.

Figure 7.4.6.21 shows the comparison of separation positions as determined from pressure distributions and from flow visualisation. As can be seen the 2.1 million case shows excellent agreement. The 0.54 million flow visualisation case appears to be little different to

the turbulent separation case except for a short region of pure laminar separation on the nose.

It is a fundamental law of nature that it's impossible to make any observation of some event or process without, in some way, interfering and hence altering it. Unfortunately it appears that the very presence of the flow visualisation oil has the effect of "roughening" the body surface sufficiently to reduce the critical Reynolds number. This can be seen in figure 7.4.6.22 from Champigny [31] where the value of C_N at 35° and Reynolds number of 0.54 million is greatly effected by the presence of the oil. Hence, it is concluded that the oil has pushed the 0.54 million case into the turbulent separation regime and thus better comparison with the 2.1 million pressure case.

All the preceding analysis relates to a single value of incidence of 20°. It is important, now, to investigate the effect of incidence on separation position. Figures 7.4.6.23 to 7.4.6.28 show the circumferential pressure distributions at incidences of 25°, 15° and 10° and Reynolds number of 0.38 million and 0.74 million. To enable the separation characteristics to be assessed over a range of incidences.

Figure 7.4.6.29 indicates the variation of transitional separation with x and again shows little change with incidence. Figure 7.4.6.30 does, however, show that there is a distinct, albeit small, variation in turbulent separation angle with incidence over the range of 10° to 25°.

Figure 7.4.6.31 summarises these results and shows the effect of both incidence and Reynolds number on turbulent separation. In general an increase in Reynolds number will move the separation line slightly in the windward direction. An increase in incidence moves the whole separation curve in the nose apex direction. Also shown on figure 7.4.6.31 is the mean transitional separation line which not a strong function of either incidence or Reynolds number.
At the bottom of figure 7.4.6.31 is a near scale drawing of a side view of the body indicating the actual positions of the separation lines. As can be seen the actual variation of the separation line with incidence is relatively small.

It can be concluded that although the position of separation line varies very little any model of the flow could benefit from a separation line model that allows for incidence effects at least in the turbulent separation case.

7.4.7 Force and moment data

In the final analysis it is the overall forces and moments that are all-important. In both the DFVLR and ONERA data sets the pressure distributions have been integrated to give overall characteristics. In addition the ONERA model also contained a six component balance.

Figure 7.4.7.1 shows an example of one of the worst case comparisons of normal force by pressure integration and balance measurement. This indicates a possible combined error of 7%. The reason for this is most likely to be due to the pressure integration of a distribution with insufficient resolution to represent all detailed features as discussed in section 7.4.5. However, as shown in figures 7.4.3.13 and 7.4.3.14 in general the comparisons are good.

7.5 THE TINLING AND ALLEN TEST SERIES

7.5.1 The experimental set-up

In this test series [32] local normal force and vortex wake characteristics of a body of revolution were made at subsonic speeds.

The tests were conducted in the Ames 12 foot wind tunnel at Reynolds numbers of 0.44 million and 3 million and at incidences of 5° to 24°. Mach number cases were at 0.3, 0.8,and 0.95. The model, see figure 7.5.1.1 from [32] a 3 calibre tangent ogive nose on a 7 calibre cylindrical body, was pressure tapped and measurements of the circumferential pressure distribution was obtained by rolling the model through 180° in 10° steps.

Surveys of the flow above the body were made with a survey rake and direction probe, also shown in figure 7.5.1.1. These were used to estimate the vortex positions above the body at stations x/d=4.5, 6.0, 7.5 and 10.0.

7.5.2 Effect of Mach number on the local normal force distribution

One useful aspect of the Tinling and Allen test series is the wide range of subsonic Mach number cases considered. The DFVLR data has already verified that there is no change in the local normal force distribution at Mach numbers from 0.1 to 0.35. The Tinling and Allen data, figure 7.5.2.1, show that although the nose load distribution varies with Mach number the load over the cylindrical section of the body changes little from Mach 0.3 to 0.95.

This means that although, if required, any proposed model of the flow should incorporate compressibility corrections in the nose region, the non-linear load distribution is, to the first order, Mach number independent. Since there are a number of methods available for treating the nose this should mean that considerable savings in modelling complexity could be made by ignoring compressibility effects over the after-body section.

7.5.3 Vortex locations

An important aspect of any flow modelling is that the vortex positions should be correctly predicted. This is of particular importance if the effect of these vortices on any lifting surfaces down stream is also to be predicted.

The Tinling and Allen data is one of the few sources to contain data pertaining to vortex positions. This data is given for three angles of incidence at two Reynolds numbers and at four down stream stations.

This data will be useful in the validation phase of any new flow model.

8. THREE-DIMENSIONAL INFLUENCES

8.1 A COMPARISON OF 2 & 3-D SEPARATION PATTERNS

At low angles of attack we know that the flow about a slender body of revolution is quasi two-dimensional and this is the basis of slender body theory. In the simpler mathematical models this idea is extended to the higher angles of attack where flow separation occurs. As we have seen, this type of model is inadequate and we now examine the three-dimensional case in order to understand why.

In the case of an axisymmetric slender body at zero incidence to the freestream there will be no flow separation prior to the base region. The flow itself will, of course, be axisymmetric.

Above angles of incidence of about 5 degrees the surface flow begins to be subjected to regions of adverse pressure gradient sufficient to cause the flow to separate. A simplistic analogy to describe this flow would be to consider the cross-flow components of the freestream velocity impulsively applied to a two dimensional circular cylinder. Under this 'cross flow plane' analogy, as described more generally earlier, it is easy to see how the adverse pressure gradient on the lee side of the cylinder would give rise to the classical $\left.\frac{\partial u_\theta}{\partial r}\right|_{r=0} = 0$ condition in the boundary layer velocity profile required to induce separation and the reverse flow region that follows.

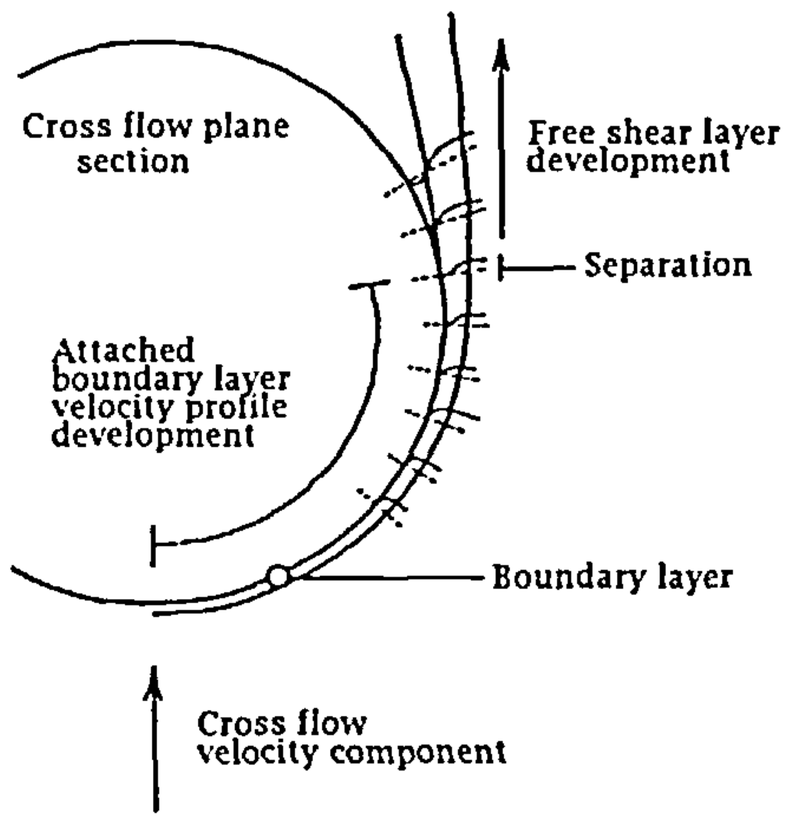

The 2-D cross flow separation concept

It is this explanation that is usually given prior to any discussion on the subject of separation from slender bodies of circular cross-section at incidence. This concept does, however, neglect the longitudinal component of the flow. The consequence of this is that the major velocity component and all of its contribution to the boundary layer and subsequent separation are not present. Further, once this conceptual step has been made, it is too easy to forget that we are dealing with a three dimensional phenomena that may have subtleties that cannot be elucidated from two dimensional considerations.

8.1.1 Three dimensional separation

The flow becomes inordinately more complex when considered in three dimensions. The structures and physical mechanisms of three dimensional separated flows have been considered by a number of authors. See for example LIGHTHILL [33] and MASKELL [34] in considering skin-friction lines on the surface of bodies and TOBAK & PEAKE [35] in extrapolating from surface patterns the flow field away from the surface.

8.1.2 The 'limiting streamline' concept

The most complex region is situated at the most upstream region of separation on the lee side of the body, and a number of plausible flow structures can be postulated for this region.

Before examining these flow structures we shall introduce the concept of the 'limiting streamline'. A streamline some small distance above the body surface will contain velocity components normal as well as tangential to the surface. However, as the height above the surface is reduced so the normal component will vanish far more rapidly than the tangential component. As the streamline becomes parallel to the surface it tends to what is referred to as the 'limiting streamline'. The projections of the limiting streamlines onto the body surface are the same as skin friction lines or surface shear-stress trajectories. See TOBAK & PEAKE [35].

In representing any feature by way of limiting streamlines it is, by definition, being viewed in two dimensions only. The third dimension of the flow field above the surface must be borne in mind for the patterns formed by the limiting streamlines to make any sense. The concept is useful in that limiting streamline patterns can be directly related to the patterns produced experimentally using oil streak flow visualisation techniques.

8.1.3 Elemental surface flow features

In describing the flow on the body surface, it is useful to define a set of surface flow features that occur in the region of singular points, these being points of separation and attachment. Firstly, nodal points of attachment and separation. These features appear in limiting streamline form as two dimensional source and sink flow fields. In one sense this is exactly what they are. In the case of the nodal point of attachment, figure 8.1.3.1 the flow is being 'sourced' from the third dimension. Stream tubes approach the node almost normally from above the surface. As the flow attaches itself it flows

out in all directions across the surface producing a pattern of limiting streamlines radiating from a single point.

The pattern consists of a locally straight streamline that is normal to the 'general direction of the flow' out from which the other stream lines diverge from a single point at which all the lines are tangential. The exception to this is a single streamline that normally bisects the central 'straight' streamline. The orientation of the pattern will depend upon the angle at which the flow approaches the node and the body surface curvature. The significance of the way in which the streamlines become tangential at the singular point will be discussed in detail when the separation line feature is described.

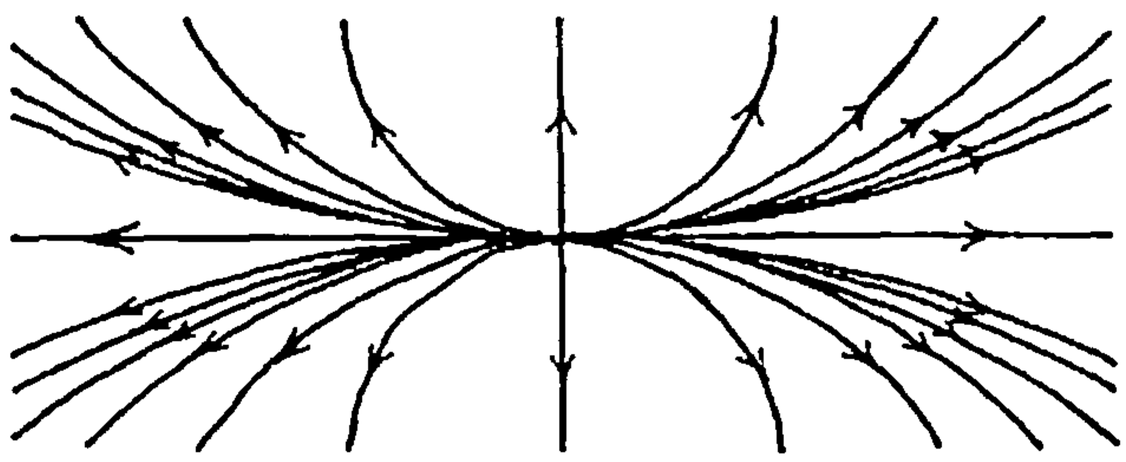

Figure 8.1.3.1 A nodal point of attachment

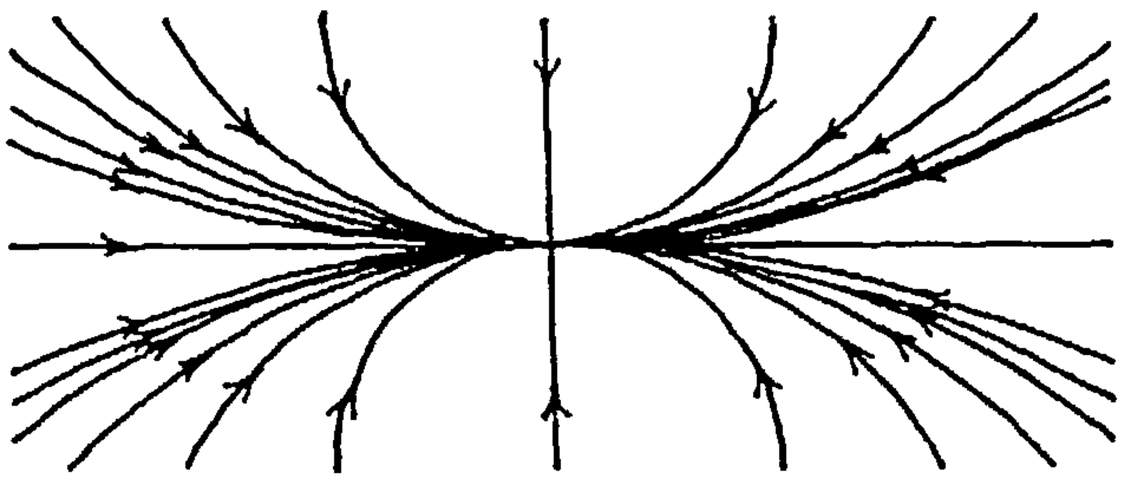

Figure 8.1.3.2 A nodal point of separation

The counterpart to the nodal point of attachment is the nodal point of separation figure 8.1.3.2. The only difference between these two features is that where as, in the case of the attachment node, the limiting streamlines point outwards, in the case of the separation node, they point inwards. The pattern similarly exhibits the general features of a two dimensional sink. In three dimensions the flow is leaving the surface at the singular point.

In certain situations involving rotational flows a type of node can result which has no common tangent line from which the other streamlines emanate. This feature is referred to as a focus, figure 8.1.3.3 & 4, and, as in the case of the nodal point, can be a focus of attachment or separation. The streamline pattern consists of a series of lines radiating from the singular point, each line forming a spiral about the centre. As with the node feature,

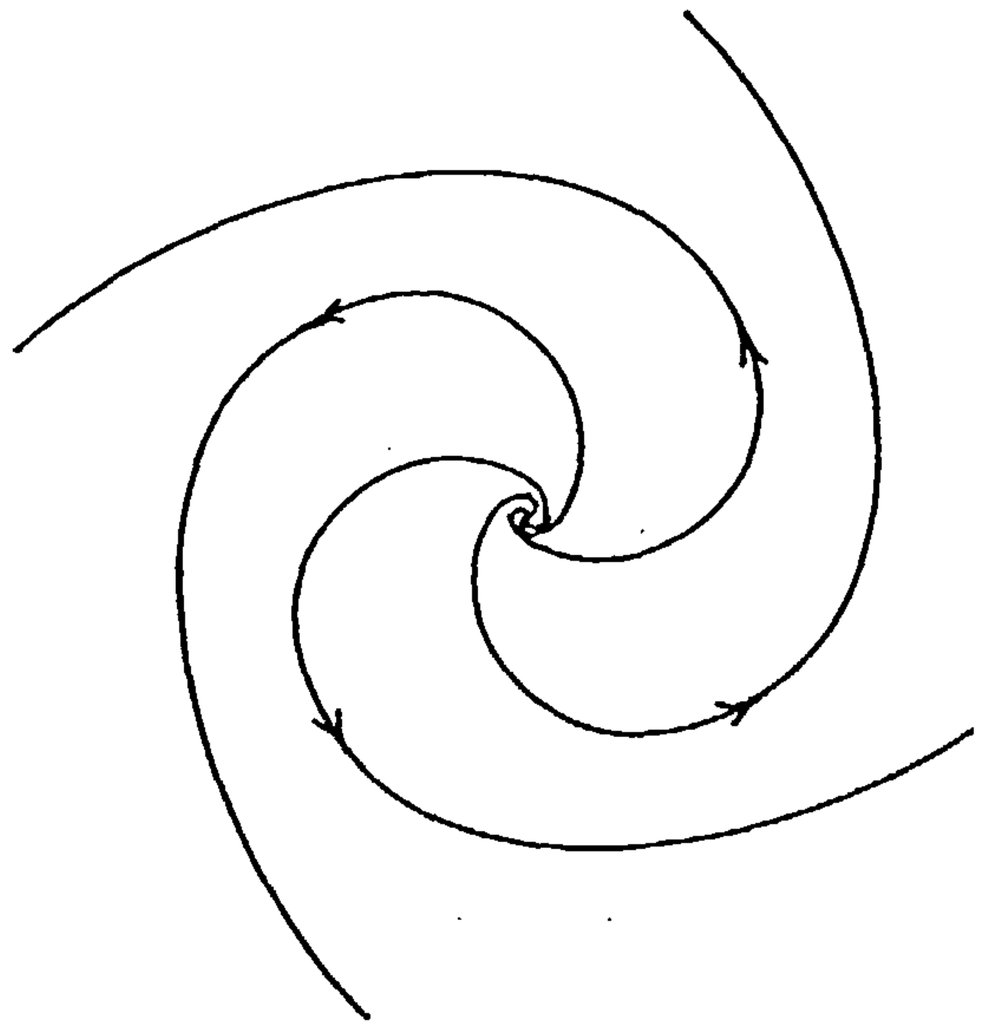

Figure 8.1.3.3 A focus of attachment

the streamlines point inwards in the case of a focus of separation and outwards in the case of a focus of attachment.

The last elemental surface flow feature to be considered occurs at the boundary of, what could be considered as, two opposing flow directions. The flow pattern, known as a saddle point, figure 8.1.3.5, consists of two leading streamlines that oppose from opposite directions and meet at the singular point. Two further streamlines are then emitted from this centre orthogonally to the leading streamlines. The remaining streamlines are then effectively contained within the resulting quadrants and start near parallel to the leading streamlines and finish near parallel to the orthogonal streamlines.

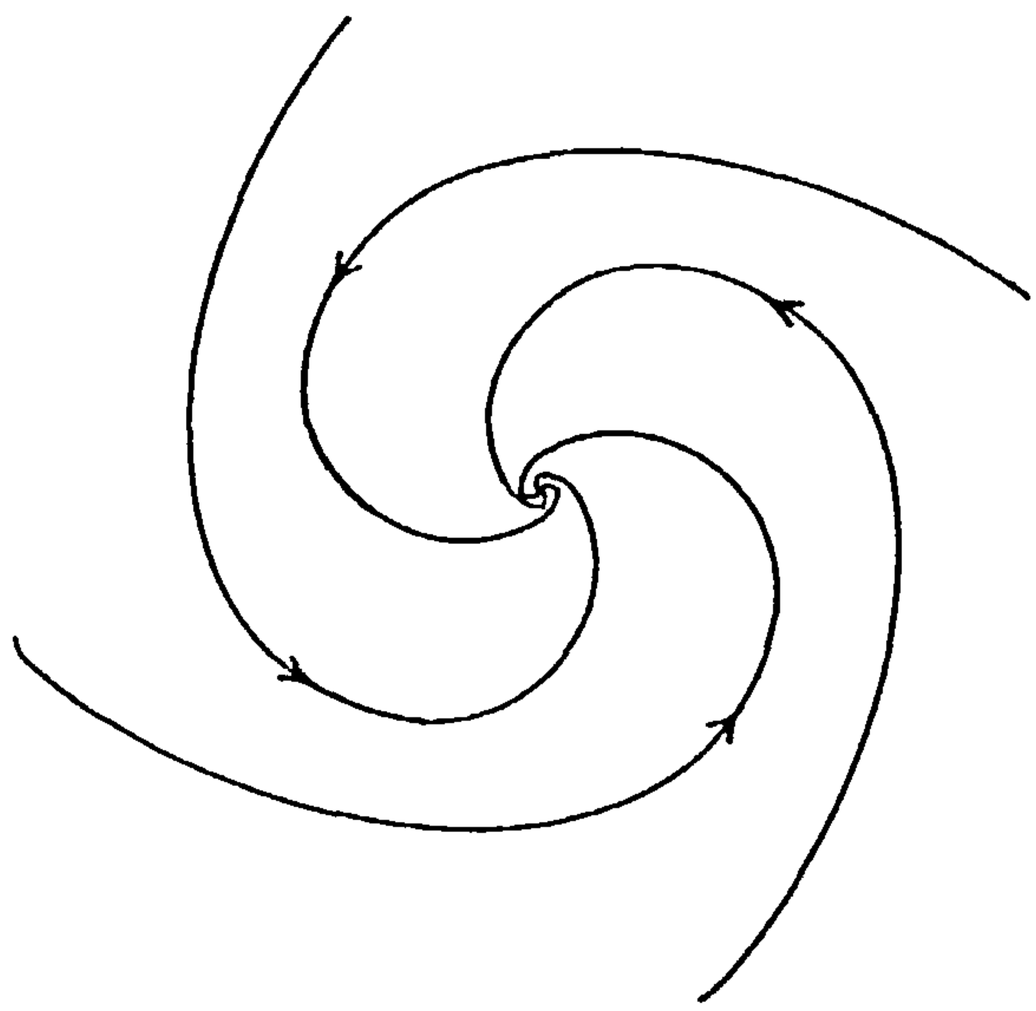

Figure 8.1.3.4 A focus of separation

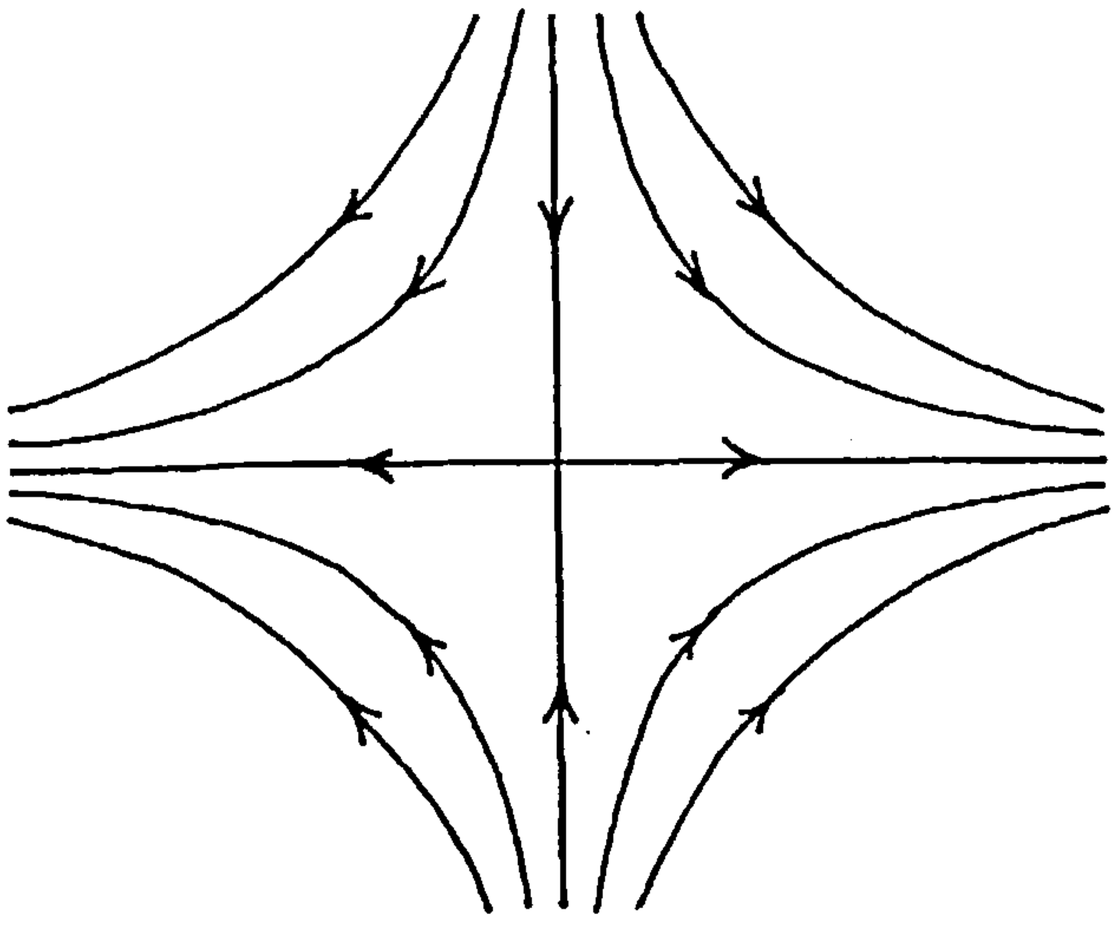

Figure 8.1.3.5 A saddle point

8.1.4 Surface flow features in the separation region

Returning to the problem of the flow in the most forward region of separation we can now examine the various cases that have been proposed.

As the angle of attack increases the first occurrence of separation is likely to involve a saddle point on the lee side surface centre line closely followed by a node of attachment, figure 8.1.4.1. The function of the saddle point being to separate the main flow

from the reverse flow resulting from the attachment node. The orthogonal limiting streamlines emanating from the saddle indicating the position of the separation line[1].

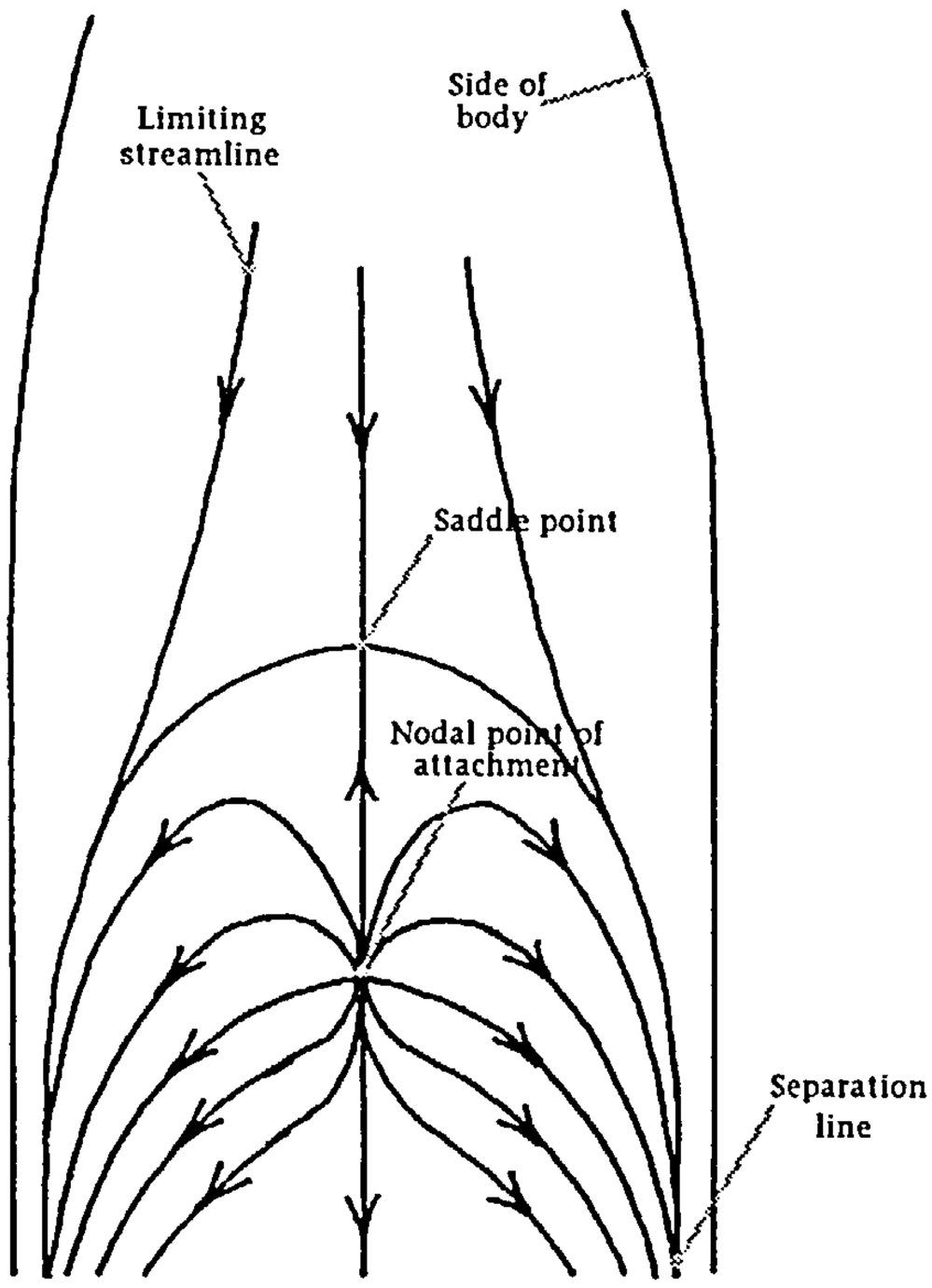

Figure 8.1.4.1 Upstream surface flow features in the separation region involving a saddle point

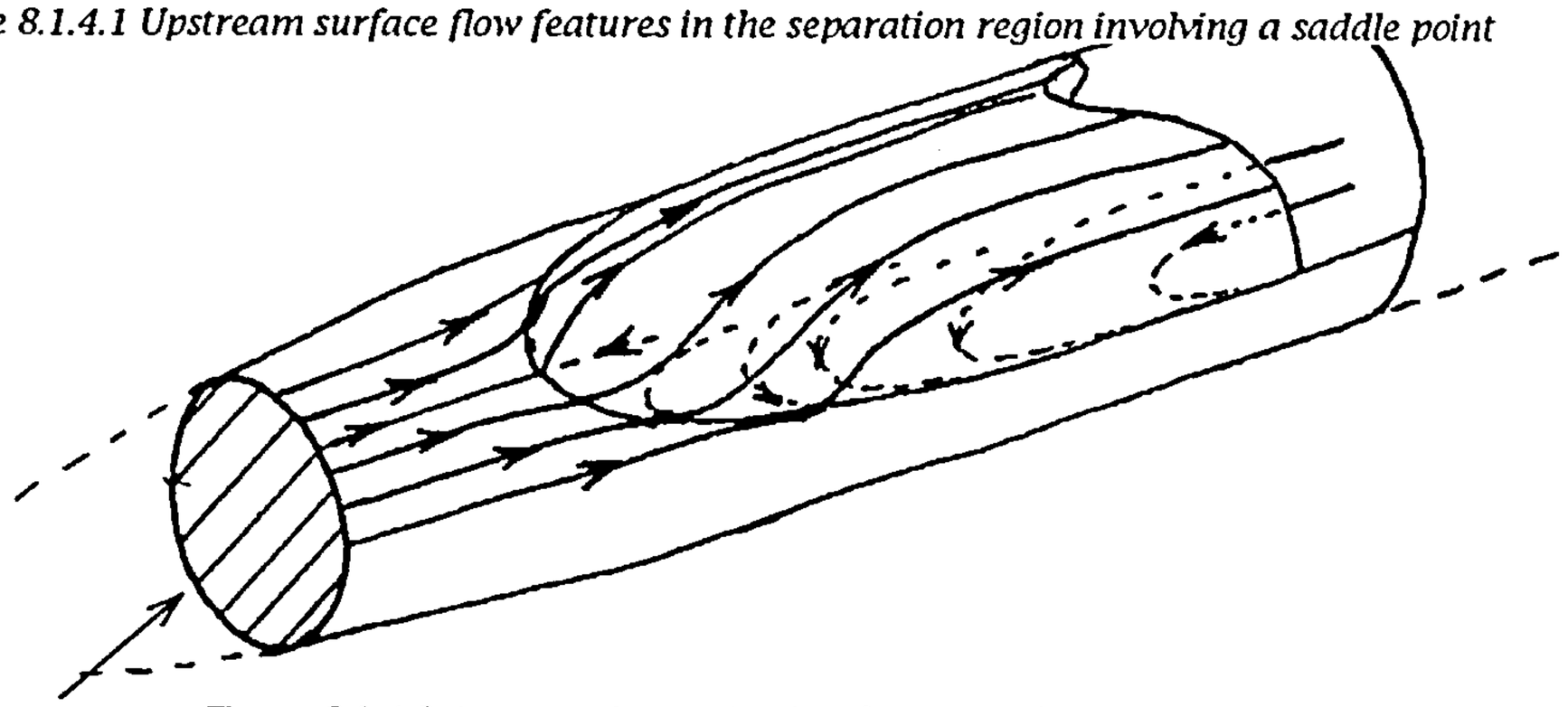

Figure 8.1.4.2 A separation region involving a saddle point

As the flow lifts away from the body surface it starts to form a structure that can be described as a separation bubble. At this point it should be noted that up to now we have been considering the flow in terms of limiting streamlines. Once we start to consider the flow away from the body we must take care not to assign the streamlines all the attributes of limiting streamlines. If the consequence of separation from the surface is a separation line on the body surface, then the consequence of separation into the flow field is a separation surface. In the real flow this separation surface is surrounded by a

[1] The idea of a separation line will be discussed in section 8.1.5.

region that is dominated by viscous characteristics. We shall return to the subjects of separation and the viscous regions later. At this point it is sufficient to say that one effect of this viscous region is to cause the trailing edge of the separation bubble to roll in on itself thus generating the reverse flow region required to produce the node of attachment inside the bubble and also form the embryonic body vortices. This scenario is not the only mechanism possible for dealing with separation.

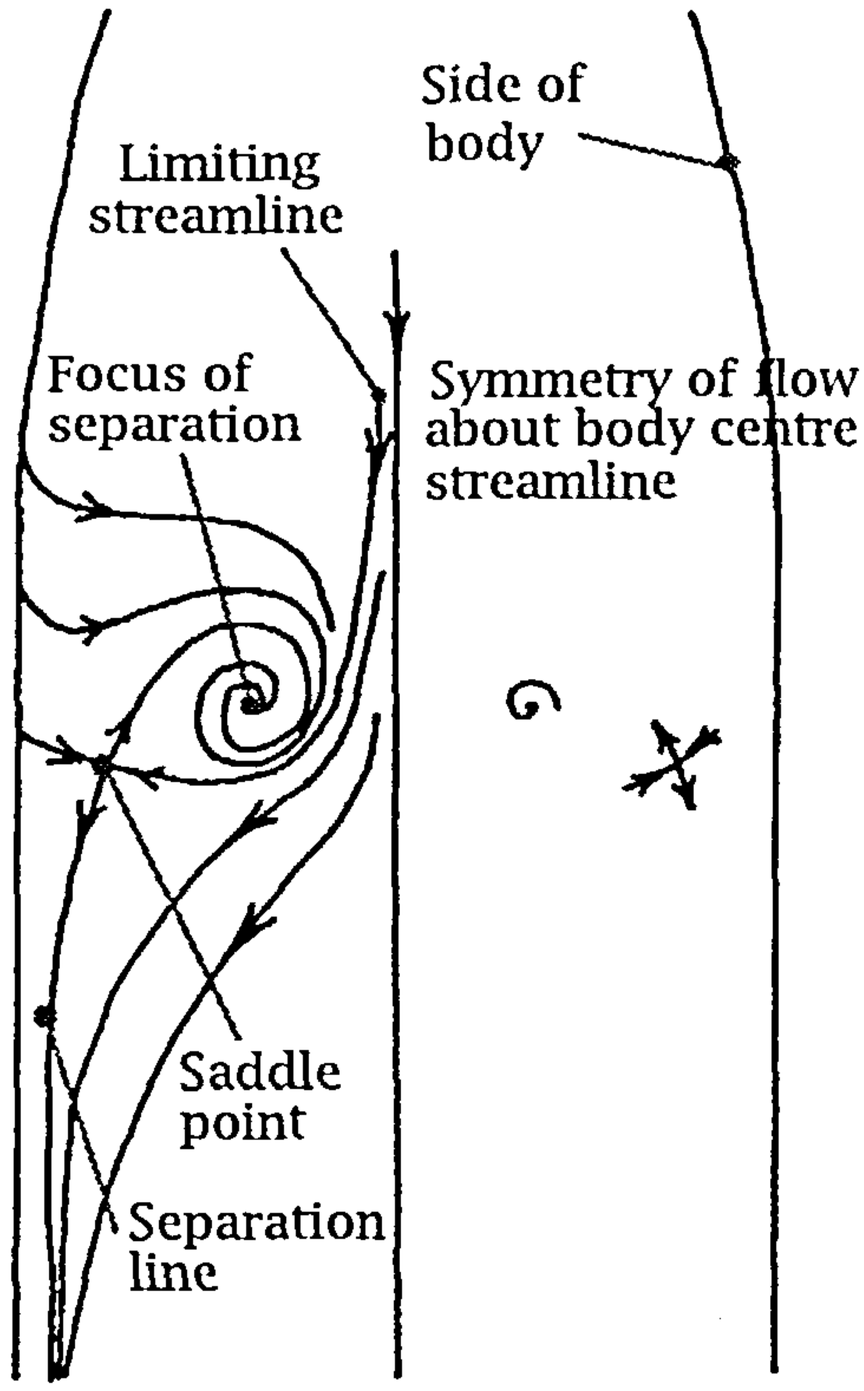

Figure 8.1.4.3 Leeside Surface flow features in the separation region involving a focus point

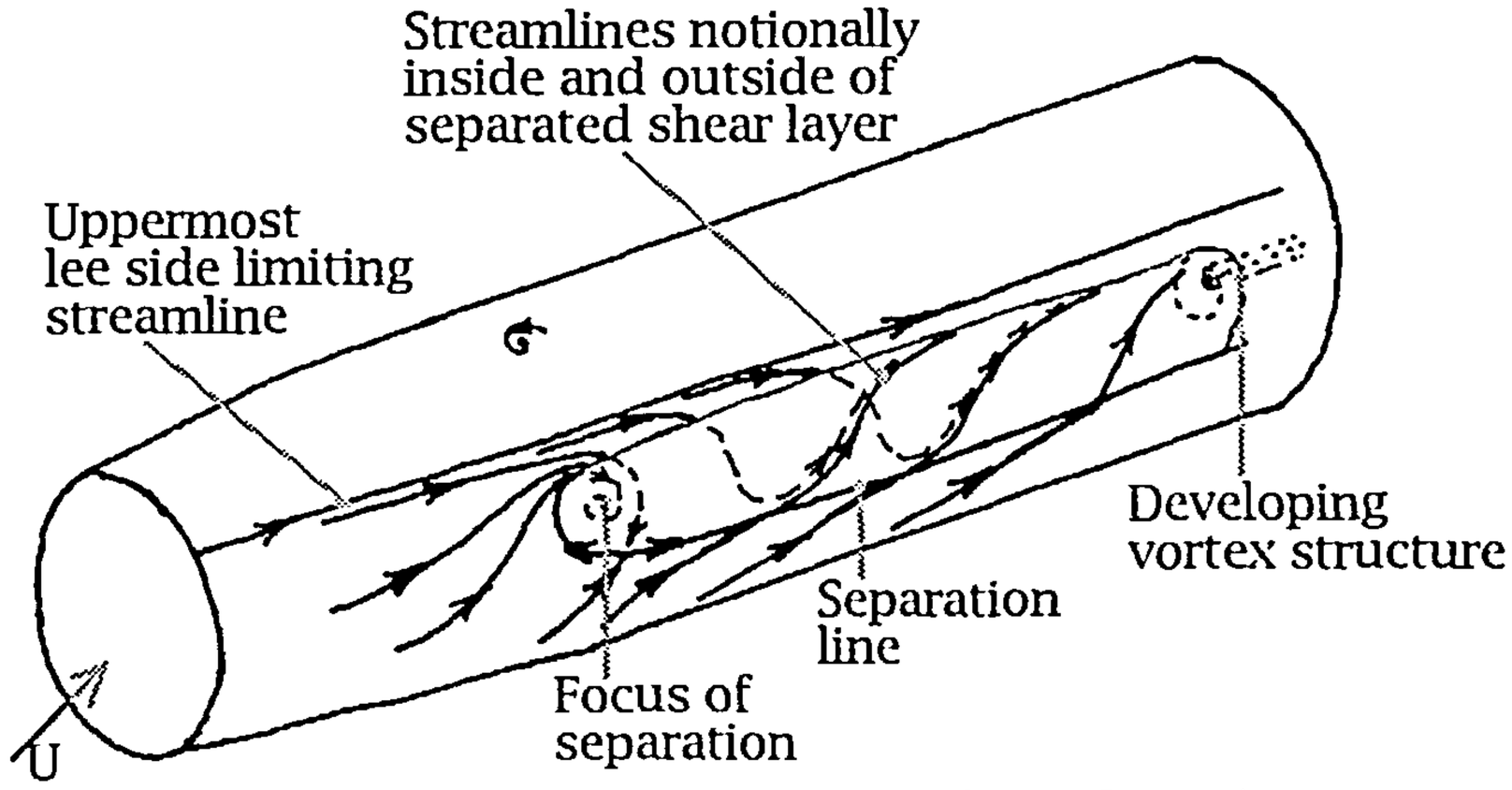

Figure 8.1.4.4 A separation region involving a focus point

In this case the flow spirals into a focus of separation and off of the surface into the flow field. However, part of the surface into the flow orbits the focus but does not enter it. The direction of this part of the flow is rotated through an angle sufficient to cause it to meet the main surface flow 'head on'. Here a saddle point forms with one

orthogonal limiting streamline entering the focus and the other heading downstream as the separation line. The flow separating from the focus is already rotating in the correct body vortex sense as it leaves the body surface. This vortex continues to be fed from the separation line as it progresses down stream.

These types of mechanisms can be extended in complexity to account for secondary separation by, for example, replacing the focus by a pair of counter-foci (rotation in opposite sense) separated by a saddle point. However, we shall not pursue this further since our main concern is the primary separation line itself.

8.1.5 Surface flow features slightly above the separation region

Up to this point we have not investigated the details of the flow feature of separation, or for that matter attachment, and how it relates to the pattern of limiting streamlines. Since all the separation features involve the converging of limiting streamlines let us deal with this first. Consider a stream tube who's section is defined by a width, w, equal to the distance between two adjacent limiting streamlines at some point on the body surface close to the separation line and a height, h, of some arbitrary but small value figure 8.1.5.1. The mass flow rate through this stream tube is given by

$$\dot{m} = \rho \ \bar{v}(wh),$$

where $\bar{v}$ is the mean velocity in the tube.
The skin friction coefficient is

$$\tau_w = \mu\left(\frac{\partial v}{\partial r}\right)_{r=0}$$

or

$$\tau_w = \mu\left(\frac{\bar{v}}{h/2}\right)$$

$$\therefore \bar{v} = \frac{\tau_w h}{2\mu}$$

Putting this into the mass flow equation gives

$$\dot{m} = \frac{h^2 w \tau_w}{2\mu/\rho}$$

$$= \frac{h^2 w \tau_w}{2\upsilon}$$

Rearranging for h gives

$$h = \sqrt{\frac{2\upsilon \ \dot{m}}{w\tau_w}}$$

Now as we approach the separation line w and τ_w tend to zero and hence h becomes large.

In this way it can be seen how the streamlines forming the outer edge of the stream tube are forced away from the body surface as the stream tube approaches the separation line. See figure 8.1.5.1. In the earlier discussion concerning separation mechanisms it was seen how a separation surface projects from the separation line into the flow field. It can now be seen more clearly how the phenomenon of separation influences the flow, not just at the separation line and surface, but in the vicinity of the separation line. Clearly the phenomenon of separation from a slender body is a complex three dimensional process.

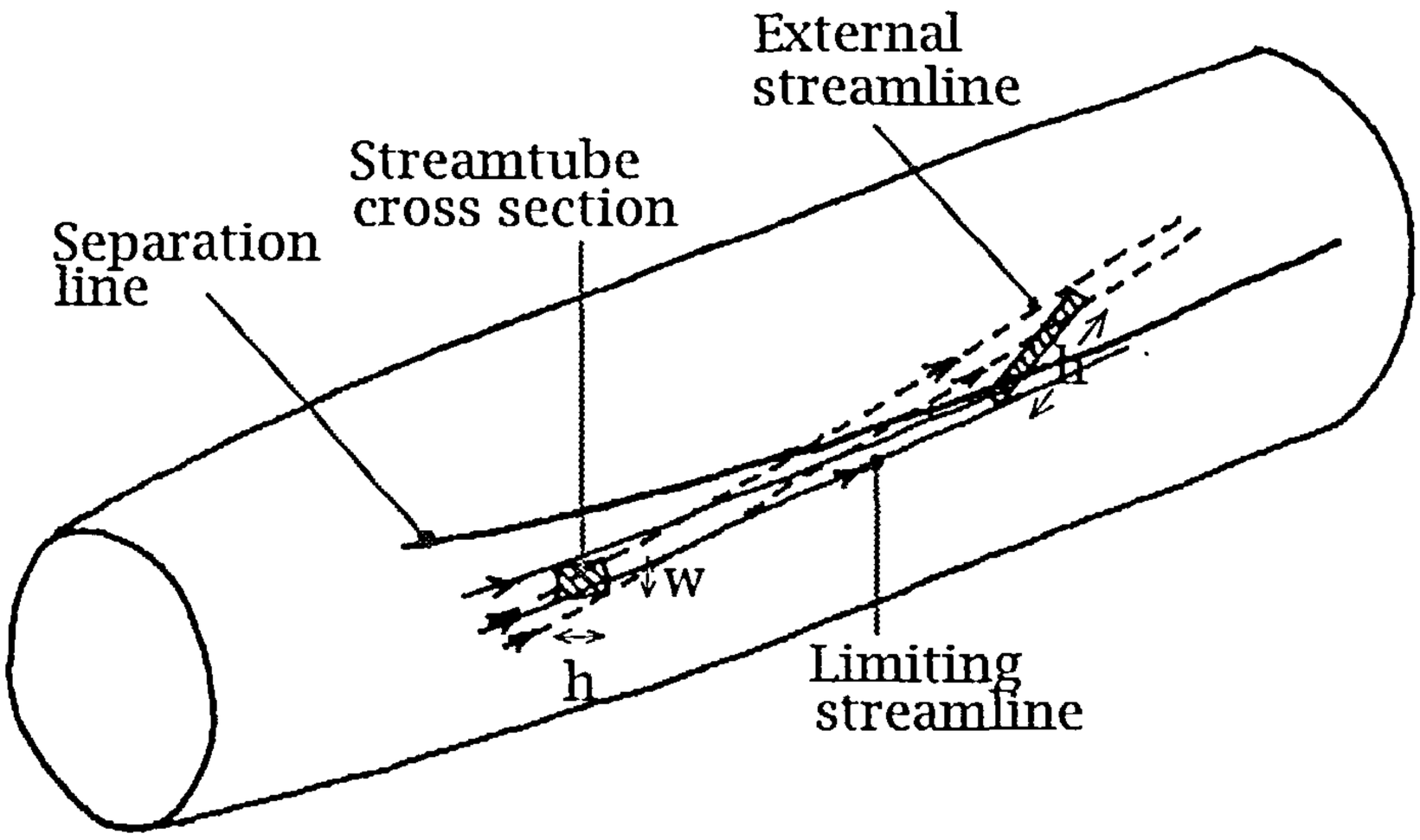

Figure 8.1.5.1 Streamlines forming the outer edge of a stream tube being forced away from the body surface as the stream tube approaches a separation line

The above explanation for the process of separation along a line can also be utilised in the case of a line of attachment. Here, of course, the process is the reverse of that for separation. The stream tube approaches the body surface from the flow field and in so doing causes the limiting streamlines in the proximity of the attachment line to diverge away from the line. Further, attachment and separation from nodes and foci may also be explained in this manner. In the case of the node the limiting streamlines diverge from or converge to a single streamline towards a point. The limiting streamlines of a focus simply converge to or away from a single point in a spiral fashion.

8.2 VISCOUS REGIONS & THE SIGNIFICANCE OF TRANSITION

In the previous section the root cause of separation was attributed to the effect of an adverse pressure gradient on the velocity profile in the boundary layer. In this section we shall look in more detail at the boundary layer and its relevance to the current problem.

It was Prandtl who, in 1904, suggested that the fluid flow about a body could be divided into two regions. The first being the outer region where viscous effects are negligible and the second being the thin 'boundary' region around the body where viscous effects are dominant. To this we shall add two more regions that are important in the problem under consideration. Firstly the viscous shear layer that is generated from the separation line and flows out into the flow field. The second being the 'core' of the vortex that is formed by the subsequent development and convection of the shear layer.

8.2.1 Mechanisms influencing the development of the boundary layer

Let us start by considering the state of the boundary layer. From the investigations of the flow about a two dimensional circular cylinder it is clear that the state of the boundary layer at the moment of separation has a significant effect on the position from which separation occurs, the trajectory of the viscous shear layer and the position in space of the rolled up vortex. The predominant parameters influencing the development of the boundary layer are the Reynolds number, surface roughness and the body shape. In the case of a specific geometry, such as a circular cylinder at 90^{o} to the onset flow, the effect of increasing the Reynolds number is to advance the nature of an instability of the laminar boundary layer (Tollmien-Schlichting) that results in transition to a turbulent boundary layer. As discussed earlier, the significant injection of momentum into the turbulent boundary layer makes it sufficiently energetic to penetrate further into the adverse pressure gradient and thus delays separation beyond the capability of the laminar boundary layer. In the case of separation occurring whilst the boundary layer is still laminar another form of instability will come into effect. Free shear layer instability is due to the amplification of small disturbances in the separated laminar boundary layer which ultimately results in transition to a turbulent shear layer. The turbulent state of the shear layer causes it to entrain a significant amount of the surrounding flow which in turn results in a rapid thickening of the shear layer in much the same way as the surface boundary layer thickens more rapidly after transition to turbulence. Under the influence of a number of factors such as Reynolds number, the point of transition in the shear layer creeps back towards the point of separation and at the same time closer to the body surface. At some point the thickening of the turbulent shear layer occurs sufficiently close to the body surface to enable the flow to 're-attach' itself. The attached shear layer now becomes a turbulent boundary layer and will continue around the surface of the cylinder until it finally succumbs to the adverse pressure gradient and separates. The

angle at which this form of separation occurs is greater than both laminar and turbulent separation.

8.2.2 Three dimensional phenomena influencing transition

This is merely a recapitulation of the flow about a two dimensional circular cylinder and the importance of transition to the subsequent flow development. However, when the cylinder is inclined to the flow the problem loses its two dimensional nature, particularly with reference to the boundary layer. It should be mentioned that three dimensional separation structures can be generated from a high aspect ratio cylinder in a pure cross flow, DALLMANN [36] describes some such structures and presents experimental evidence. Since we are mainly concerned with bodies at low incidences this is of academic interest only. At incidences less than 90^{o} and particularly at low incidences the boundary layer becomes three dimensional and additional phenomena influence transition.

8.2.3 Attachment line instability

Firstly, when at incidence, the flow attaches to the body along a

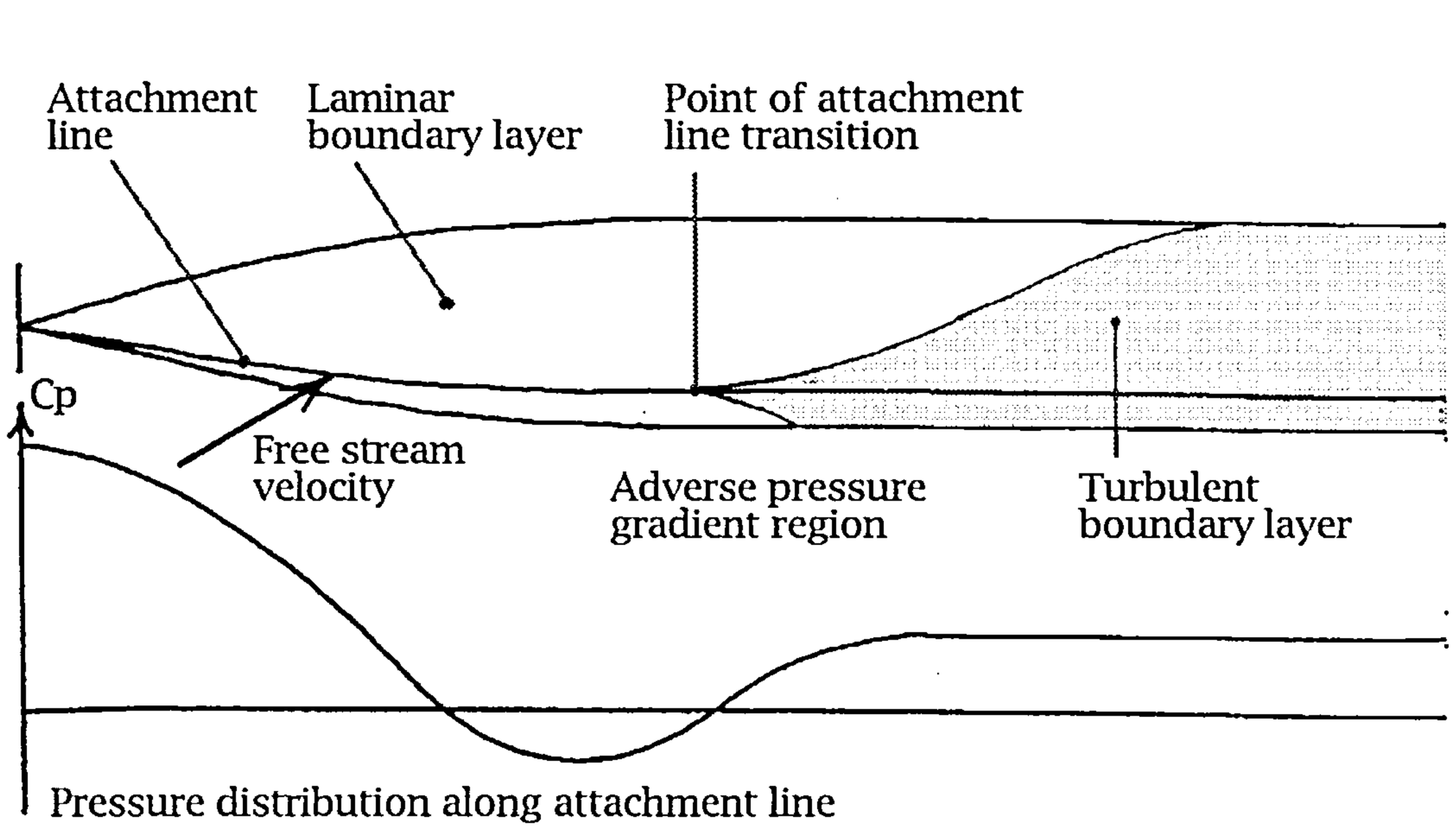

Figure 8.2.3.1 Influence of attachment line instability on the boundary layer state down stream

line that runs the length of the windward side, figure 8.2.3.1. There will, of course, develop a boundary layer along this attachment line that will initially be laminar. The state of the boundary layer in this region will be subjected to the usual influences likely to initiate transition. In the case of an ogive-cylinder body the pressure distribution along the attachment line includes a region of significant

adverse gradient in the vicinity of the nose-body junction. Once transition has occurred it is likely that the entire boundary layer in the region of influence of the turbulent portion of the attachment line will become turbulent. This transition mechanism is referred to as attachment line instability.

8.2.4 Cross flow instability

The second transition mechanism relevant to three dimensional flows is the cross flow instability. This phenomenon is not so simple to visualise. If we consider the streamlines external to the boundary layer it is clear that they follow a curved trajectory. Let us consider a point on one such external streamline, referred to as the external point, figure 8.2.4.1, and drop a perpendicular from it to the surface to define the surface point. If we now consider the velocity component profile in the direction of the flow at the external point, across the boundary layer we see that it takes the form of the usual boundary layer velocity profile and is referred to as the local

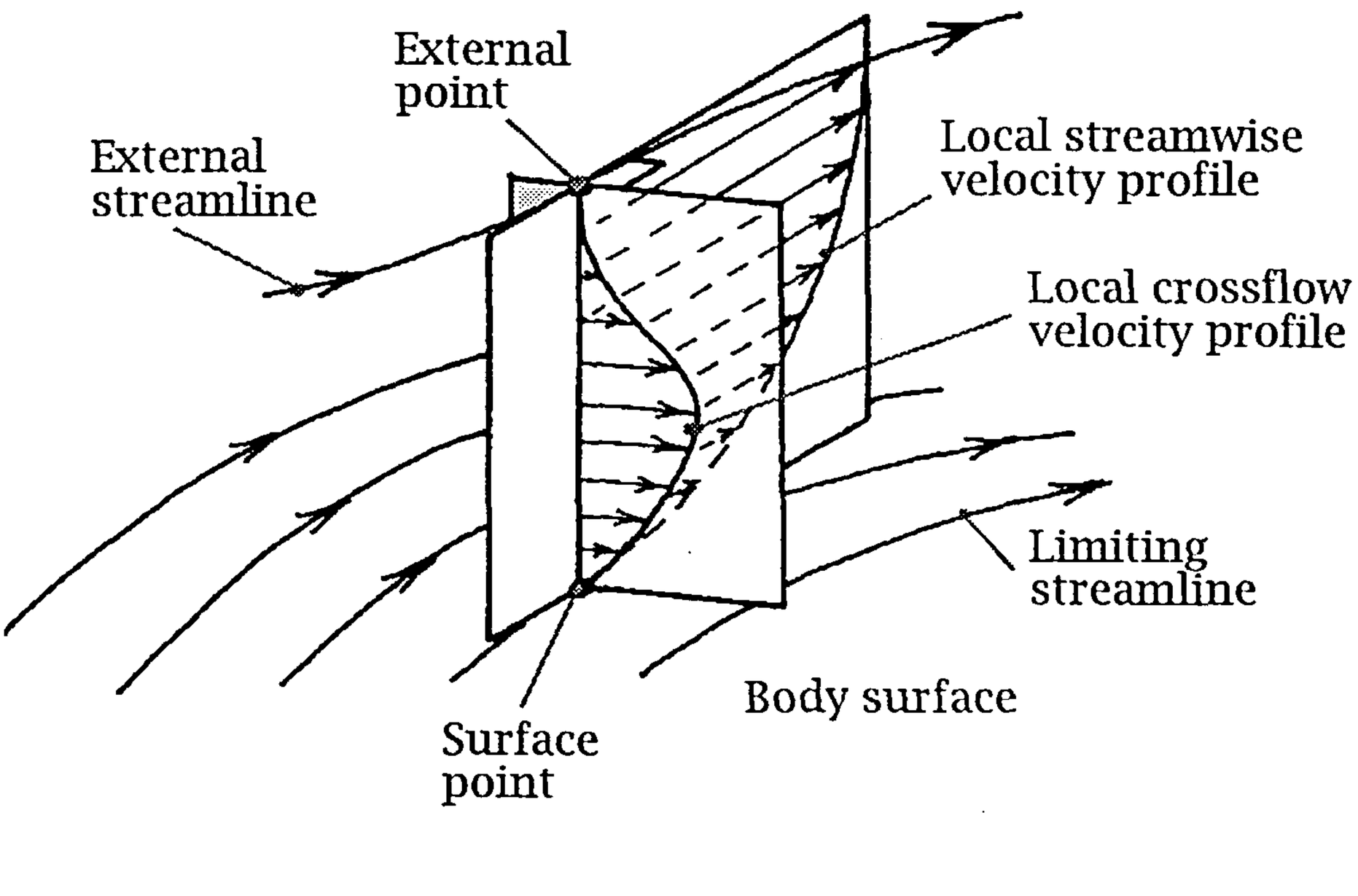

Figure 8.2.4.1 The local cross flow velocity profile

stream wise velocity profile. However, if we consider the component perpendicular to the direction of the flow at the external point, contrary to expectation, a non-zero distribution results. The component is zero at the external point (by definition), zero on the surface point due to the physical effects of viscosity and reaches a maximum somewhere in between. This component is referred to as the local cross flow velocity profile and results from an imbalance

between the pressure forces and the centripetal forces acting on the flow as its curved motion is retarded through the boundary layer towards the body surface.

The important feature of this is that the cross flow velocity profile becomes unstable to disturbances at a Reynolds number considerably lower than that critical to the stream wise velocity profile. A more detailed discussion on this phenomenon can be found in POLL [37]. It is interesting to note here that in a flow that exhibits a local cross flow velocity profile there may be a significant difference between projections of the external streamline pattern on to the body surface and the limiting streamline resulting from the twisting of the external local resultant velocity vector as we descend through the boundary layer through to the surface.

8.3 THE EFFECT OF THE BOUNDARY LAYER STATE ON SEPARATION

With an understanding of the mechanisms influencing transition and separation, it is now possible to relate these to the case of an ogive-cylinder body at incidence.

8.3.1 Classification and characteristics of separation types as a function of R_N and α

If at first we consider the flow about the body at some arbitrary position down stream from the nose, we can examine the processes leading up to separation at that station. Assuming a fixed angle of attack of, say, 15^o then at a low Reynolds number attachment line contamination will not have occurred and hence the boundary layer away from the attachment line will be laminar. At this Reynolds number the cross flow instability condition would not have been reached either and hence the boundary layer will still be laminar at separation. Due to the inability of the laminar boundary layer to remain attached far into the adverse pressure gradient, separation will occur at about 80^o around from the attachment line. This state remains, as the Reynolds number is increased, until the free shear layer reattaches itself to the surface. The boundary layer is now able to continue further into the adverse pressure gradient due to its turbulent nature until it finally re-separates at as much as 140^o around from the attachment line. As we increase the Reynolds number still further the attachment line instability criteria is reached and the boundary layer is then turbulent from the attachment line onwards. This means that laminar separation cannot take place and hence no separation bubble can be generated by the shear layer reattaching itself. This turbulent boundary layer is able to resist the

adverse pressure gradient far better than the laminar boundary layer and separates at about 115^{o} around from the attachment line, but cannot penetrate as far as the laminar bubble structure. We have already seen this process occurring in the experimental data and was discussed in section 7.4.4. Referring to figure 7.4.4.2 we can see that a point located just aft of the nose-body junction would experience the aforementioned separation states over an appropriate range of Reynolds number

It should also be noted that the angle of incidence also plays a strong role in determining the type of separation that occurs i.e. laminar, bubble (or transitional) or turbulent. Consider the case of a fixed Reynolds number (Red) of $0.2x10^{6}$ based on body diameter at a very low incidence. Here the attachment line contamination mechanism will result in a fully turbulent boundary layer resulting in turbulent separation (if any). As the angle of incidence is increased the attachment line becomes laminar again and enables transitional separation to occur. Increasing the angle of attack still further results in the laminar shear layer being unable to reattach itself resulting in pure laminar separation. Again, this can be observed experimentally, see figure 7.4.4.5 and is discussed in section 7.4.4.

Up to this point we have not mentioned the cross-flow instability mechanism. This only comes into play at higher angles of incidence of the order of 25^{o} and above. In these circumstances the cross-flow instability causes transition and subsequent turbulent separation at a lower Reynolds number than that required for eventual turbulent separation resulting from attachment line contamination transition.

8.3.2 Separation type boundaries

Clearly the two important parameters here are Reynolds number and angle of incidence. POLL suggests boundaries for the transition mechanism boundaries as follows:
Free shear layer instability:

$$R_D x10^{-6} = \frac{\tan\alpha}{\cos\alpha\left(1+3.3\tan^2\alpha\right)}$$

Attachment line instability:

$$R_D x10^{-6} = 1.1\tan\alpha\sec\alpha$$

Cross flow instability:

$$R_D x10^{-6} = 0.145\frac{1+3.3\tan^2\alpha}{\sin\alpha}$$

Stream flow instability (Tollmien-Schlichting):

$$R_D x10^{-6} = 4.0$$

These boundaries can be used to determine the separation type likely to occur at any given incidence and Reynolds number and can be as shown in figure 8.3.1.1.

These boundaries were also determined experimentally by LAMONT [39]

Many practical cases would occur to the left of the attachment line instability criteria boundary and hence are likely to exhibit turbulent separation. From one point of view they could be considered to be Reynolds number independent.

As regards the angle of attack, since we are only concerned with moderate angles of attack we need only concern ourselves with the left hand portion of this plot as shown in figure8.3.1.2.

It should not be concluded from this description that if turbulent separation occurs at some point, then all instances of separation from the body at this attitude and Reynolds number will also be turbulent. It is, in fact, conceivable that all three types of separation could co-exist at different situations along the body. For instance the boundary layer over the forward section of the nose could be laminar and may lead to laminar separation. At some short distance aft of the nose apex the laminar shear layer may start to reattach itself forming a laminar bubble and result in transitional separation over the remainder of the body. This would give rise to two forms of separation under one set of conditions. Further, if the incidence and Reynolds number are appropriate the sharp adverse pressure gradient that occurs near the windward side of the nose-body junction can cause the attachment line boundary layer to become turbulent and hence, via the attachment-line contamination mechanism, cause all of the body boundary layer in the zone of influence of the turbulent part of the attachment line to become turbulent. So in this case we would obtain flow that exhibits laminar separation over the forward section of the nose, followed by a region of transitional separation, followed by a large region of turbulent separation, figure 8.3.2.3.

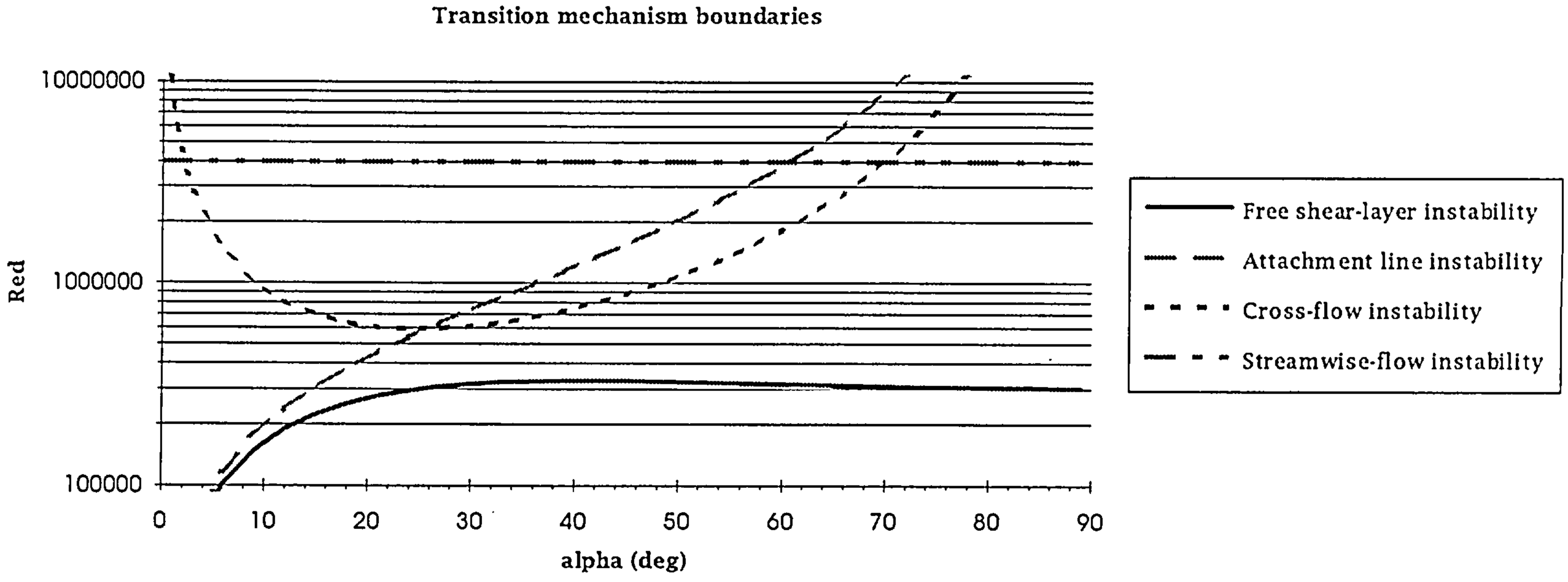
Transition mechanism boundaries
10000000
1000000
100000
Red
0
10
20
30
40
50
60
70
80
90
alpha (deg)
Free shear-layer instability
Attachment line instability
Cross-flow instability
Streamwise-flow instability

Figure 8.3.1.1

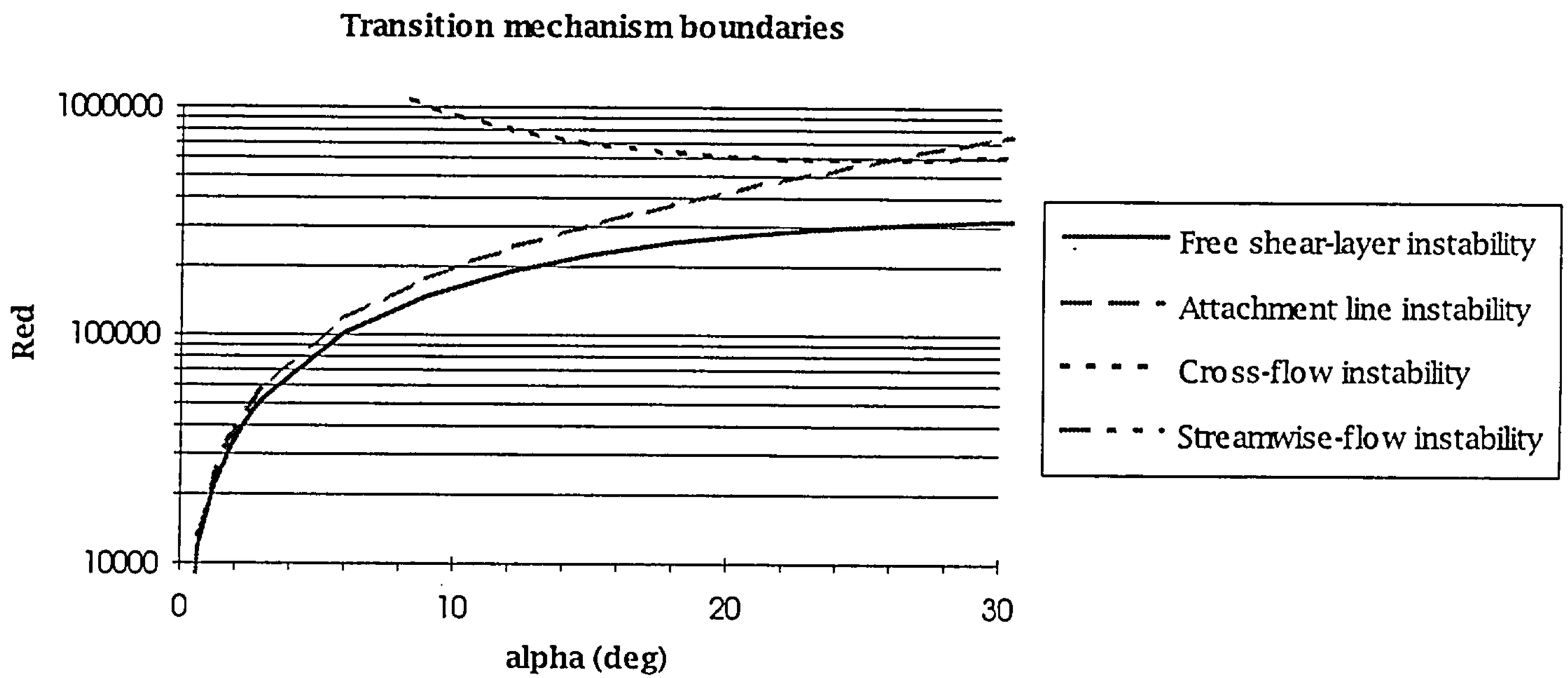
Transition mechanism boundaries
1000000
100000
10000
Red
0
10
20
30
alpha (deg)
Free shear-layer instability
Attachment line instability
Cross-flow instability
Streamwise-flow instability

Figure 8.3.1.2

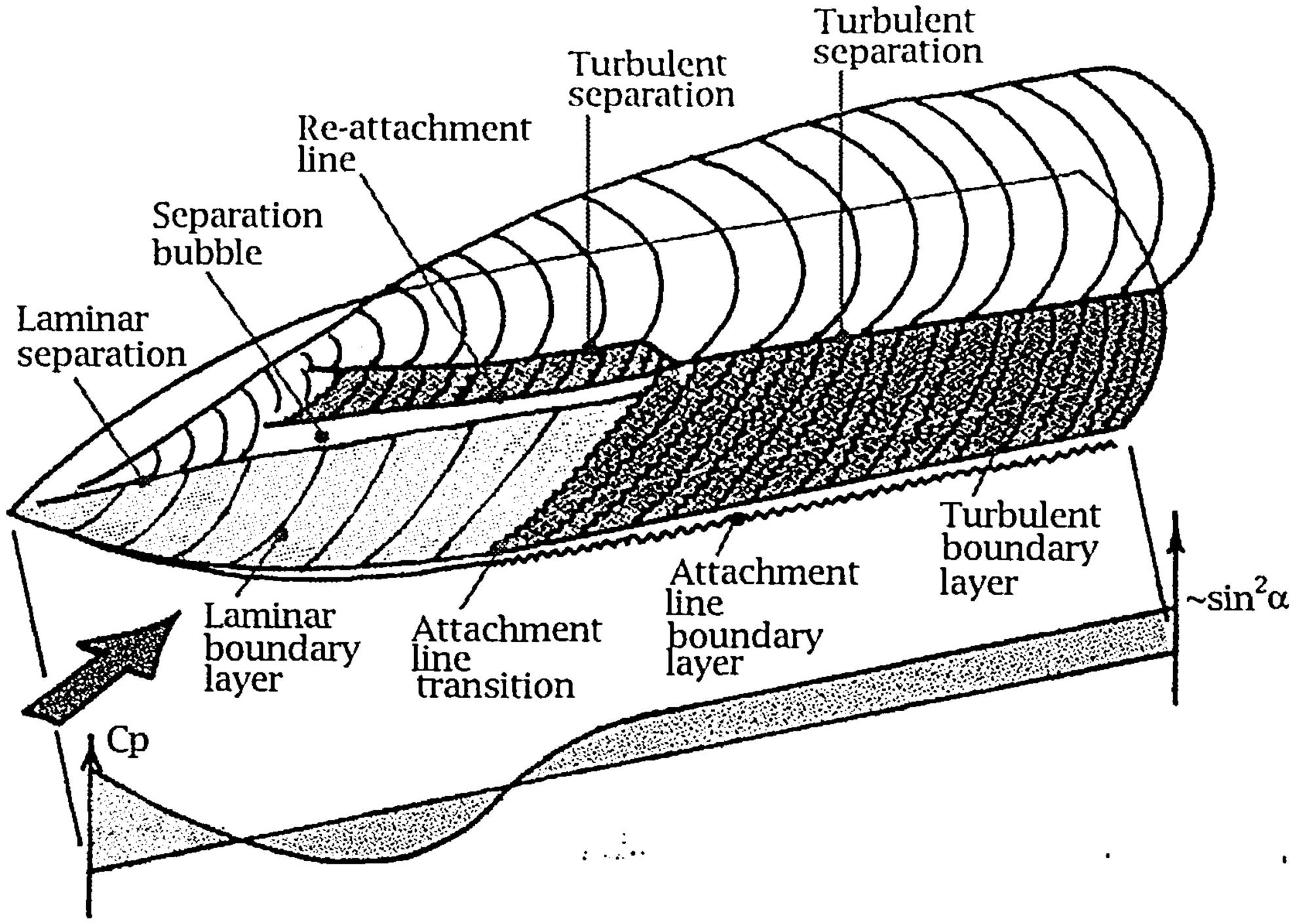

Figure 8.3.2.3 The effect of boundary layer state upon separation from a three dimensional body at incidence

8.4 THE EFFECT OF SEPARATION ON THE FLOW FIELD

Let us now consider how the state of the boundary layer and the various transition mechanisms influence the large scale flow field around the body.

The presence of the boundary layer does not directly effect the pressure distribution on the body surface since the external (to the boundary layer) pressure is transmitted through the boundary layer. The first mechanism of influence is due to the displacement effect of the boundary layer. This will obviously be a function of Reynolds number and geometry (including incidence). The effect of transition here is clearly to cause a rapid increase in displacement thickness due to the thickening rate of the turbulent boundary layer. However, this effect is small when compared to the effect of separation and can usually be ignored in simple flow modelling work.

By far the most significant effect of the boundary layer state and transition is its influence on the position at which separation occurs. From the simple reasoning presented in the description of the vortex cloud model we can see that the rate at which vorticity is shed from the body via the separated shear layer into the flow field is proportional to the square of the local external velocity at the point of separation. Since this local velocity varies significantly as we move from the attachment line via the body shoulder and around to the lee

side of the body, it is clear that the separation position can directly effect the rate of vorticity generation.

We have seen that the three main types of separation occur at different angles around the body and hence the type of separation, resulting in a free shear layer, directly influences the rate at which vorticity is shed.

The shed vorticity 'feeds' the vortex pair, which grow in strength as they continue down stream. The higher the rate at which vorticity is fed into them the faster they grow in strength. As we have already seen these vortices have a very significant effect on the flow field and induce high velocities on the lee side of the body resulting in an increased load distribution. In this way it can be seen that the position at which separation occurs effects the aerodynamic forces and moments acting on the body.

An added complexity, that should also be mentioned, is that the induced velocities due to the vortices will also affect the separation position due to their modification of the pressure distribution. It is important that this effect be considered in any flow modelling. It becomes more clearly apparent at the higher angles of attack where asymmetries appear in the separation positions on opposite sides of the body. In this situation the only asymmetry in the configuration is in the vortex pair themselves.

8.5 VORTICITY GENERATION AND CONVECTION

8.5.1 The definition of the vorticity components

Let us now consider in more detail the way in which vorticity is generated in the three dimensional boundary layer, how it is shed and how it then moves in the flow field.

In this section we shall be discussing the distribution of a vector quantity through a three dimensional domain. It is, thus, now a good point at which to define this vector.

It clearly makes sense to align the three components of vorticity with the x, y and z axes of our body. If the local flow velocity q and vorticity is defined as curl q then the components of vorticity are:

$$\text{curl } q = \begin{vmatrix} i & j & k \\ \frac{\partial}{\partial x} & \frac{\partial}{\partial y} & \frac{\partial}{\partial z} \\ u & v & w \end{vmatrix}$$

$$= i\left(\frac{\partial w}{\partial y} - \frac{\partial v}{\partial z}\right) + j\left(\frac{\partial u}{\partial z} - \frac{\partial w}{\partial x}\right) + k\left(\frac{\partial v}{\partial x} - \frac{\partial u}{\partial y}\right)$$

$$= i\xi + j\eta + k\zeta$$

where *i, j* and *k* are the unit vectors.

In our case the main component of vorticity will be contained within the vortex pair on the lee side of the body. Since this aligns fairly well with the k unit vector direction we would expect to find most of the vorticity in the flow field to be in the ζ term.

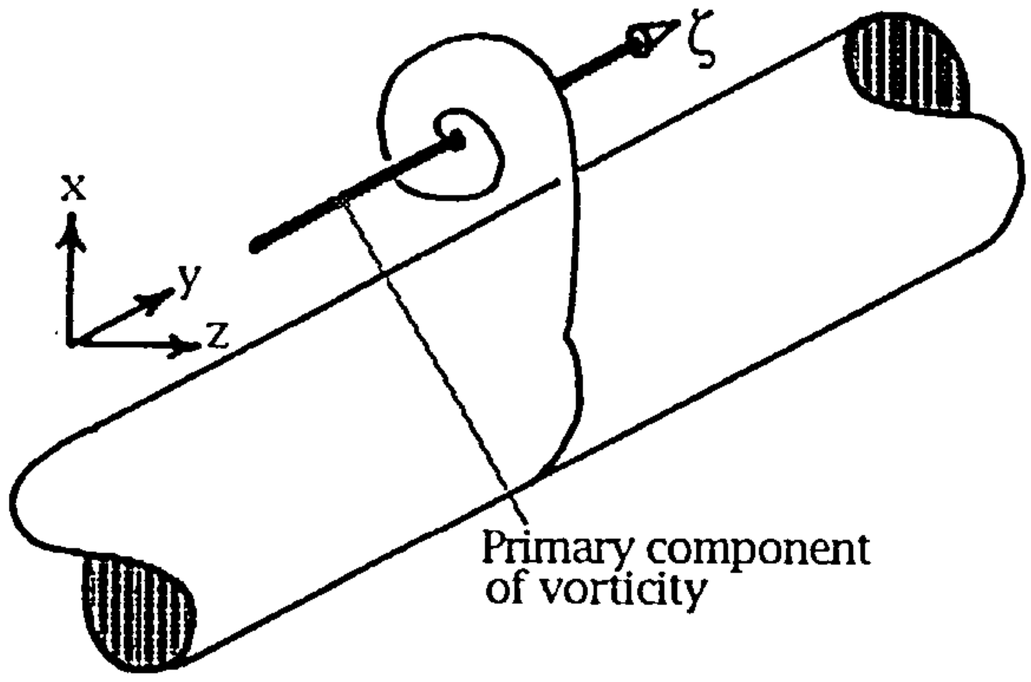

Figure 8.5.1.1 The sense of the main component of vorticity on the lee side of a slender body at incidence

There is another significant source of vorticity in the flow field, that being the vorticity locked in the boundary layer due to the freestream direction of flow. Consider the body at zero angle of incidence. The velocity gradient in the boundary layer due to viscosity will generate high values of vorticity, γ, oriented tangentially to the body circumference. In Cartesian co-ordinates this vorticity will have both ξ and η components. These components will vary according to the angular position, θ. If we were to examine these three components of vorticity in Cartesian co-ordinates, although ζ may make sense, ξ and η will be confusing.

A better approach may be to consider the ζ component as in the Cartesian co-ordinates but define η as being tangential to the body surface. Since our body is circular in cross section this equates to using a cylindrical co-ordinate system.

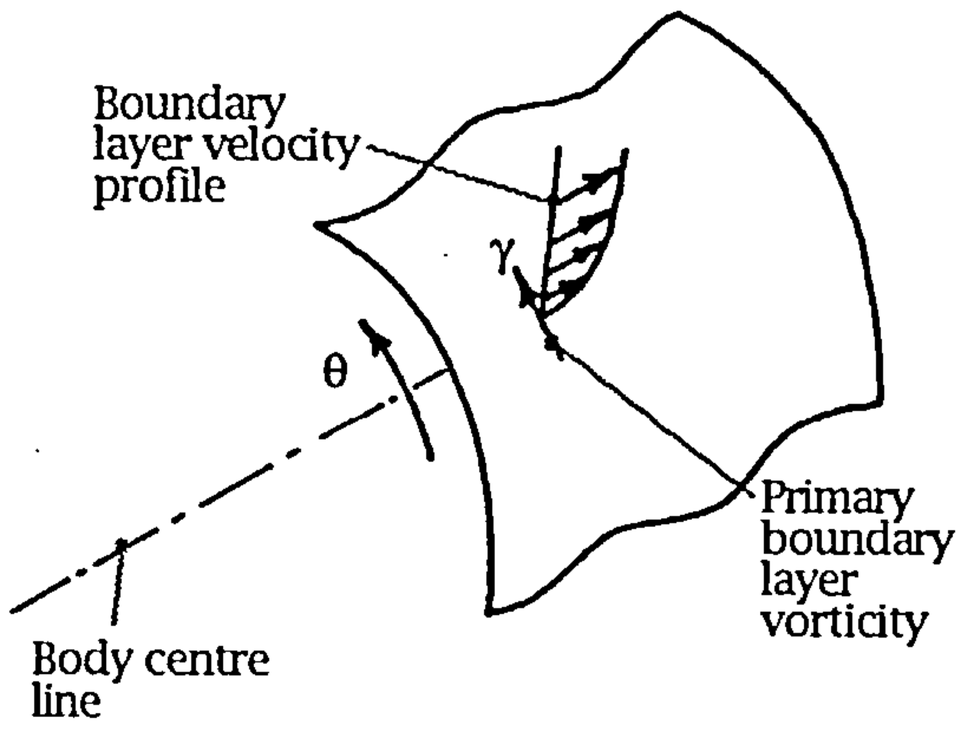

Figure 8.5.1.2 The primary component of vorticity in the boundary layer

Care will still need to be taken in interpreting the three cylindrical components of vorticity, particularly at some distance from the surface, however, interpretation should be easier than in a Cartesian co-ordinate system.

In this case curl *q* is given by:

$$\text{curl}\, q = \begin{vmatrix} e_r & re_\theta & e_z \\ \frac{\partial}{\partial r} & \frac{\partial}{\partial \theta} & \frac{\partial}{\partial z} \\ u_r & ru_\theta & w \end{vmatrix}$$

$$= e_r\left(\frac{1}{r}\frac{\partial w}{\partial \theta} - \frac{\partial u_\theta}{\partial z}\right) + e_\theta\left(\frac{\partial u_r}{\partial z} - \frac{\partial w}{\partial r}\right) + e_r\left(\frac{1}{r}\frac{\partial (ru_\theta)}{\partial r} - \frac{1}{r}\frac{\partial u_r}{\partial \theta}\right)$$

$$= e_r\xi_c + e_\theta\eta_c + e_z\zeta_c$$

where e_r, e_θ and e_z are the cylindrical polar unit vectors.

8.5.2 Vorticity fields in the boundary layer and rear shear layer

Let us consider the three dimensional vorticity field about the body at incidence. This is obviously a highly complex flow field so we will start by considering each component separately and initially consider the flow in a quasi-two dimensional sense to obtain the main sources of vorticity generation. Then the more complex three dimensional effects will be considered.

Perhaps the obvious place to start is with the ζ component. This is the component that is of prime importance since it is usually considered to contain virtually all of the vorticity of the body vortices and their feeding sheets. In fact it is quite usual to ignore the other two components of vorticity when examining an Euler or Navier-Stokes solution and similarly in the case of experimental flow field surveys.

This preconception of the importance of the ζ component, perhaps, comes from consideration of the cross flow plane analogy where all the shed vorticity is generated by the freestream velocity component normal to the body. In this case the vorticity can only be in the ζ sense and is similar in nature to the two dimensional circular cylinder case.

This idea may be further reinforced by the fact that the ζ distribution can be determined from flow field variables contained in a single plane normal to the body since ζ only contains terms in $\frac{\partial}{\partial r}$ and $\frac{\partial}{\partial \theta}$. In the case of experimental data, it is usually only possible to survey individual planes and hence only ζ can be derived. It is more difficult to extract the η and ξ components since they contain $\frac{\partial}{\partial z}$ terms. To determine η and ξ experimentally requires a series of at least 2 or maybe 3 closely separated planes of data. In the case of finite difference solutions to the Euler or Navier- Stokes equations, in particular space marching implementations, it is relatively easy to extract a series of consecutive planes. In the case of time marching solutions some interpolation may be required to do this. In either case further interpolation is required to obtain the data required to determine the $\frac{\partial}{\partial z}$ terms. These can be found by using a central

difference approach, for example. In summary, it may have been easier to reason that the η and ξ terms were small and hence they were neglected. We shall see later that this is not the case.

However, returning to the ζ component of vorticity let us consider the cross flow velocity component in the boundary layer profile development. The boundary layer develops from the windward side attachment line and grows towards the separation line. The boundary layer on the leeward side develops under the influence of the vortex region and so also grows towards the separation line.

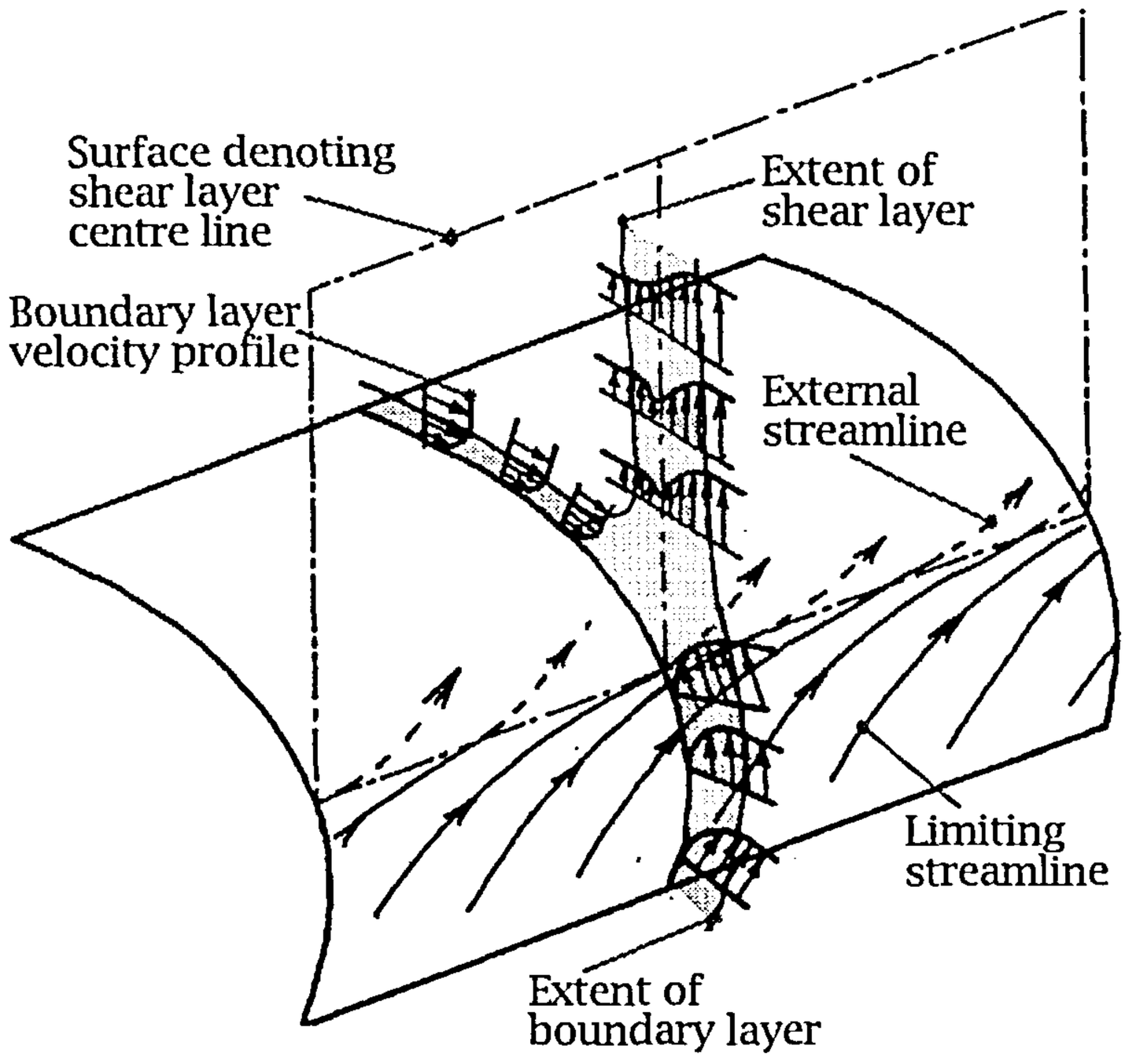

Figure 8.5.1.3 Development of the cross flow boundary layer component resulting in ζ vorticity

At the point of separation these two boundary layers meet and lift away from the surface in a complex three dimensional manner as described in section 8.1. For the present we are considering only the cross flow components. In this case it is fairly simple to visualise how the velocity profile in the boundary layers merge to give the velocity profile through the separated shear layer. The two velocity profiles act in the same direction and a short distance off the surface would develop into a simple velocity gradient between the velocities on the windward and leeward sides. The velocity profile contains components of u_r and u_θ with gradients in the θ and r directions respectively, which are the components of ζ. This vorticity distribution would be expected to diffuse over a wider area as the shear layer extends away from the surface. This would result in lower local values of ζ but it would be spread over a larger area. Finally, the

rotational nature of the flow will tend to roll the vorticity into and about a large vortex structure, that being one of the two lee side body vortices.

In predicting what might be expected of the remaining two components of vorticity let us look again at the basic vorticity equations in cylindrical co-ordinates.
We have:

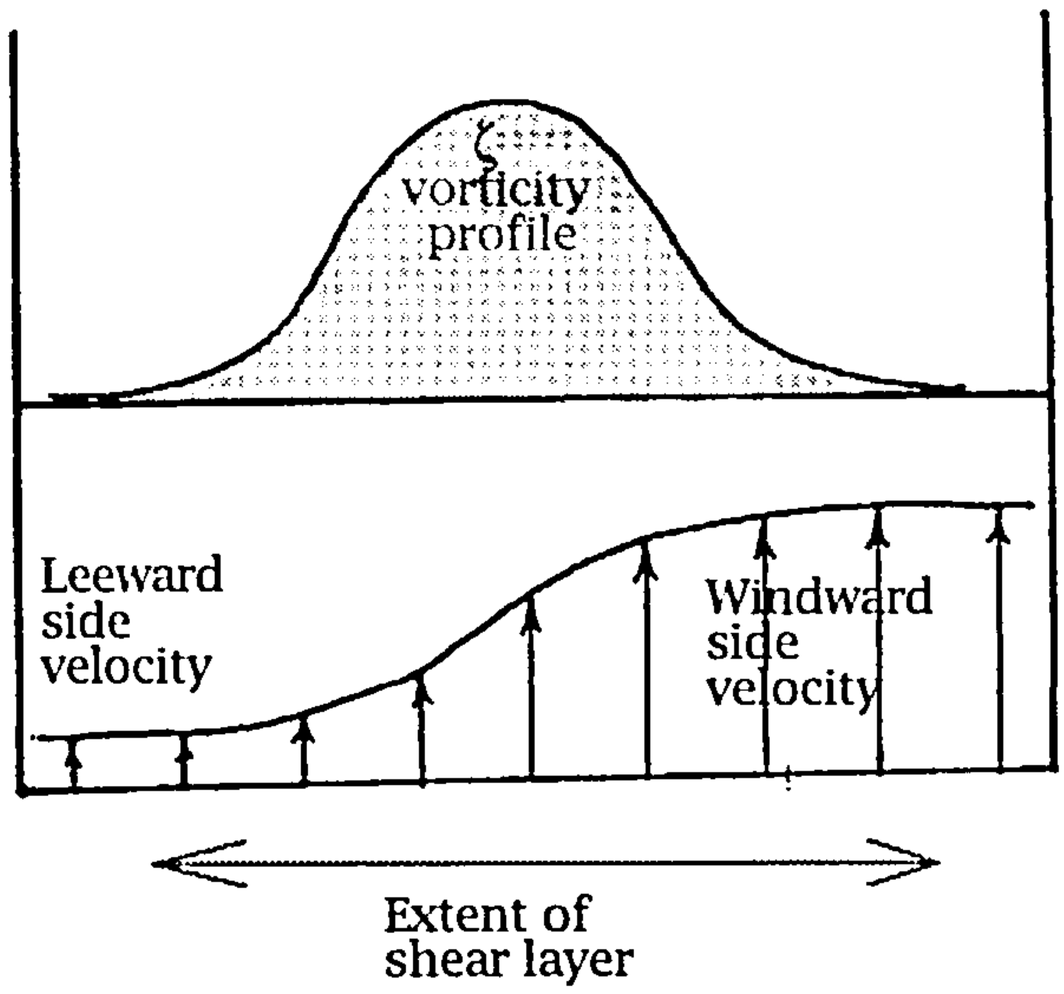

Figure8.5.1.4 The ζ vorticity and velocity profile through the shear layer

$$\xi = \frac{1}{r}\frac{\partial w}{\partial \theta} - \frac{\partial u_\theta}{\partial z}$$
$$\eta = \frac{\partial u_r}{\partial z} - \frac{\partial w}{\partial r}$$

Since our body is slender the terms $\frac{1}{r}\frac{\partial w}{\partial \theta}$ and $\frac{\partial w}{\partial r}$ are likely to be dominant. So, for example, consider a body at zero incidence. At some large distance from the body the value of w tends towards the freestream velocity. As the surface of the body is approached viscosity rapidly reduces w to zero as would be expected from boundary layer theory. Hence close to the body surface there will be a rapid rise in $\frac{\partial w}{\partial r}$. So, as expected, the boundary layer contains a high concentration of η vorticity. Increasing the angle of attack will obviously introduce components of vorticity in the ζ and ξ directions but η will remain dominant close to the body surface.

Once the angle of incidence is sufficient to generate a

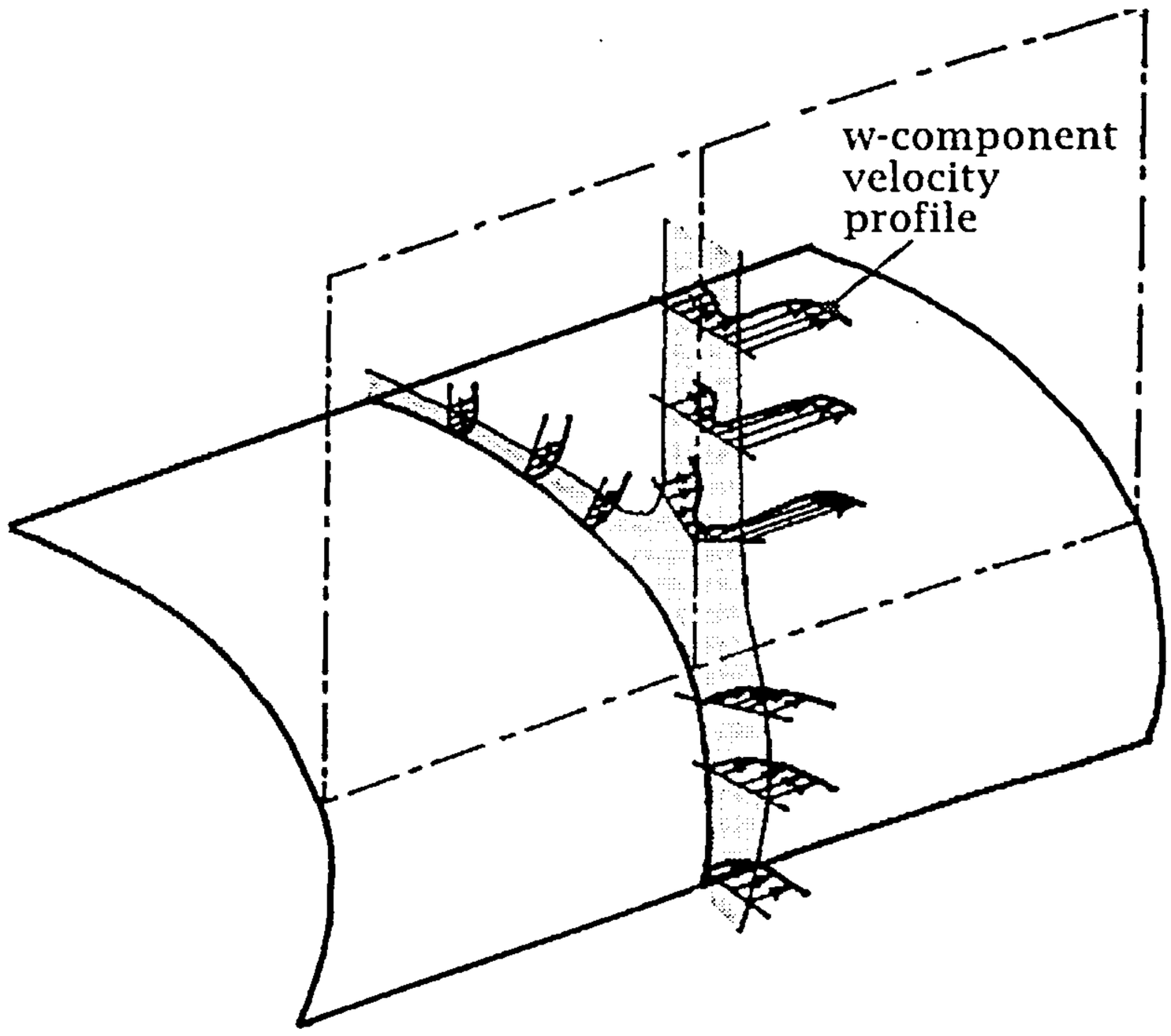

Figure 8.5.1.5 Development of the boundary layer components resulting in η & ξ

symmetric pair of body vortices, one effect of the vortices is to retard the w component of velocity on the leeward side of the body. This will give rise to significant values of $\frac{\partial w}{\partial \theta}$, and hence ξ, in the region of separation.

Let us now consider what happens when the windward and leeward side boundary layers 'peel' away from the surface at the separation line to form the separated shear layer. The w component of velocity across the shear layer differs from the u_θ and u_r components in that there is a distinct dip between the values of w at the shear layer extremities. This gives rise to a different vorticity profile across the shear layer. Dependent upon the angle at which the shear layer leaves the body surface, the w component gradients give rise to $\frac{\partial w}{\partial \theta}$ and $\frac{\partial w}{\partial r}$ terms. In this way vorticity with components in both the η and ξ senses is generated.

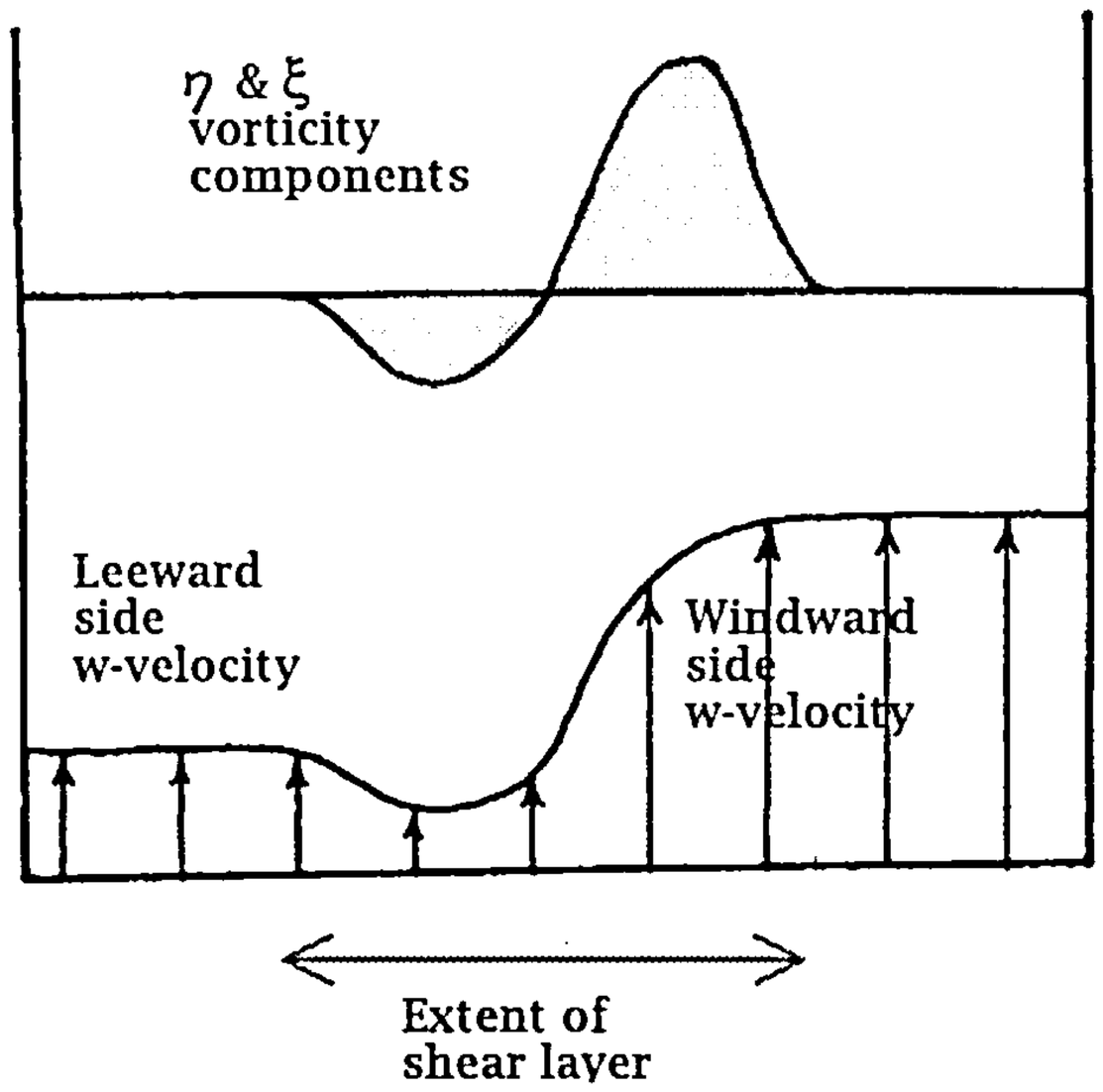

Figure 8.5.1.6 The η & ξ vorticity and velocity profile through the shear layer

This gives rise to a vorticity distribution in the η and ξ directions that is quite contrary to expectation. The implication is that η and ξ do not reach a maximum at the shear layer centre line, as ζ does, but instead they actually equal zero. This phenomenon may prove useful in defining the centre of the shear layer.

8.5.3 Vorticity convection away from the shear layer

The convection of vorticity in close proximity to the body surface is relatively easy to anticipate since it is dominated by the local fluid flow field. Even within the feeding sheet this is still the case. However, moving away from the body surface the manner in which the vorticity is convected is greatly effected by the induced velocity fields generated by the presence of the vorticity itself. Whilst it is possible to envisage the flow resulting from the presence of the ζ component of vorticity, the fully three dimensional effects are harder to anticipate.

One would expect the feeding sheet, or at least the region of flow with a high vorticity content, to induce itself into a rotational

swirl to the lee side of the body. This new structure in the flow field, the primary vortex, differs from the other structures such as the feeding sheet in that a process of accumulation occurs within it and it exhibits characteristics appropriate to this. The size of the vortex grows as it proceeds along the length of the body and hence it affects the position of the feeding sheet. Its strength also increases and hence the induced flow field about it increases its sphere of influence resulting in an alteration of the separation position and the generation of features such as secondary separation.

Beyond this there will be effects due to the η and ξ components of vorticity that, as mentioned earlier, will be present in significant amounts. Of course it must be remembered that the three components of vorticity are really the three projections of a single vorticity vector which may alter its orientation. Thus the three components can in principle exchange vorticity.

It can be concluded from this that it would be of great benefit to be able to examine the three dimensional nature of vorticity in this context. This is one of the objectives of the next chapter.

9. SURVEY AND ANALYSIS OF FINITE DIFFERENCE SOLUTIONS

9.1 SURVEY OF CFD METHODS

9.1.1 CFD in general

The corner stone of aerodynamic science, and indeed all science, is experiment. Through mathematical analysis models have been developed to give insight into the physical world and to enable its behaviour to be predicted.

Over the past 30 years a new technique has been developed that offers possibilities not available through experimental or analytical techniques. Utilising the numerical methods branch of mathematics, combined with the rapidly expanding availability of fast computers, complex sets of equations may now be solved enabling highly detailed mathematical models to be constructed. This approach has now become quite distinct in nature from the classical analytical techniques and hence is now considered as the third branch in the science of aerodynamics.

The way in which these three techniques might best be exploited can be seen by examining their strengths and weaknesses.

The first point to consider is the validity of the equations used in the particular CFD model. That is to say how well do they enable the real flow characteristics to be predicted, assuming their solution can be obtained. Even if we consider the most complete representation of the flow equations, Navier-Stokes, various simplifying assumptions will have been made in their derivation and a few more will need to be made if they are to be solved. These problems will be discussed further in the next section. However, the point made here is that the equations are at best an approximation of the real flow physics. For this reason great care must be used in the interpretation of results whenever CFD techniques are being applied.

In practical terms CFD solutions are expensive to obtain. The generation of grids and solutions requires considerable CPU time. Even on current day super-computers the elapsed time can be considerable. The consequence of this is that the technique is not well suited to use in the design environment where engineers require rapid turn round times and particularly where the application involves parametric analysis.

Once obtained, the solutions are usually represented by large fields of data that are cumbersome to handle and require considerable post processing before useful results can be extracted.

There are, however, many redeeming qualities that make CFD an attractive approach. Firstly, the technique enables solutions to be

found to problems that could only be tackled analytically after considerable simplification. Secondly, the solutions obtained can contain a finely detailed representation of the flow. At first sight the benefit of this second point is not immediately obvious when, obviously, an 'infinitely' detailed solution can easily be produced experimentally in a wind tunnel. The problem with the experimental approach is that although some flow feature of interest will be present in full detail it is difficult to devise the instrumentation required to observe the result with sufficient resolution and to do so at all without interfering with the flow. The numerical solution, on the other hand, can offer a reasonable level of resolution if requested and can be examined at any level without changing the solution in any way. This ability to examine the solution and hence investigate flow features is probably the single most important characteristic of the numerical approach.

In this chapter an attempt will be made to see if any further insights can be obtained by modelling the flow using the numerical approach.

9.1.2 An overview of methods of solving the Navier-Stokes equations

The equations which contain a full description of the flow of a perfect gas, including the dissipative, transport phenomenon of viscosity and thermal conduction, are the Navier-Stokes equations. A good standard text book on this subject is FLETCHER [40].

These fundamental equations are based on the physical principles of the conservation of mass, Newton's second law of motion and the conservation of energy. An assumption, at this point, is that the fluid motion although a ramification of the mean motion of its atoms and molecules can be viewed as a continuous medium.

In order that these equations could be solved the calculation would need to be applied over a very fine grid consisting of a large number of grid points throughout the flow field and would involve minute time scales in order to resolve the turbulence terms. Unfortunately, the requirement for high numbers of grid points and time steps implies that the necessary CPU time would be prohibitive even with the fastest currently available super-computers (~10 Teraflops).

The currently favoured approach to the problem is to incorporate an internal turbulence model. This allows larger time scales and coarser internal grids to be used thus reducing CPU time requirements. Obviously this does not get around the need for high resolution in the vicinity of small scale flow features such as the boundary layer. These equations are then referred to as Reynolds-averaged Navier-Stokes equations. Although their solution is now a

practical proposition it does introduce the added complexity of the turbulence model.

Another approach is to assume that the only significant viscous terms are those associated with velocity gradients normal to a solid surface. This assumption leads to the thin-layer Navier-Stokes equations which, although they still require a high grid resolution normal to the surface, can tolerate a much lower resolution in the direction tangential to the surface. Again this simplifies the problem sufficiently to enable reasonable CPU times to be achieved.

In general, due to their elliptic form[1], the Navier-Stokes equations are dealt with by time marching to a steady state solution[2]. This is still the case for supersonic flow fields, despite the lack of upstream influence, owing to the thin subsonic region in the boundary layer. However, by neglecting this region and the time dependent terms it is possible to parabolise the equations enabling their solution to be obtained through a space-marching technique. This results in a dramatic reduction in CPU time.

9.1.3 An overview of methods of solving the Euler equations

Inviscid flow is one in which viscosity has been assumed to be zero. The governing equations for an unsteady, three-dimensional, compressible inviscid flow are obtained by dropping the viscous terms from the Navier-Stokes equations. The resulting equations are the Euler equations.

This greatly simplifies the equations and removes the requirement for high grid resolution in the boundary layer[3].

For steady subsonic flow fields or steady flow fields with subsonic patches the solutions are generally obtained by time marching to the steady state. As with the parabolised Navier-Stokes equations, space marching is valid for supersonic flow fields.

Owing to their economical use of CPU time, the Euler equations are the most widely used form of the flow equations. Further simplifications can be made that result in the Full Potential equation and the Transonic Small Perturbation equation but these will not be considered here, particularly as they do not support vorticity. These methods are now viewed as being superseded.

Returning to the Euler equations, it is important to consider the implication of dropping the viscous terms from the Navier-Stokes equations. This obviously implies that no viscous phenomena will be present in the solutions. One such phenomenon of particular interest

---

1 Although modifications can be made to parabolise the equations.
2 assuming the required solution is for a steady flow
3 Since the equations are inviscid and the boundary layer is a viscous phenomenon no boundary layer can be supported.

to us is that of flow separation from smooth surfaces[4]. Since this phenomenon results in the primary source of vorticity[5] in the flow field about bodies of revolution at incidence, its absence is significant. Although the mechanism for generating vorticity is absent (other than by shock waves), once present in the flow vorticity will be convected correctly by the Euler equations.

When the case of a body of revolution with slender sharp edged delta wings is modelled using the Euler equations the predicted characteristics are fairly acceptable. This is due to the fact that, depending upon the geometry, the wing can mask inaccuracies in the body aerodynamic terms. However, for bodies with small wings or body alone configurations the lack of separation modelling can lead to poor predictions.

JONES ET AL [41] present some predictions of a range of widely used CFD codes that can be used to illustrate this point. The codes under consideration originated from the Naval Surface Weapons Centre.

The first code is a space marching Euler code for predicting the aerodynamic characteristics of Supersonic Wing, INlet and Tail configurations (SWINT). The Euler equations are integrated step by step downstream using a Mac Cormack predictor-corrector scheme. Stability is assisted by smoothing in the form of a type of artificial viscosity. An attempt was made to force the flow to separate at an experimentally prescribed location by specifying the direction of streamlines near to the required separation line. This method was abandoned in practice for an alternative, but perhaps less rational, approach called 'clipping'. The method limits the local cross flow Mach number by an empirically derived function:

$$M_{cr} = 0.145\sqrt{\alpha}\left(\frac{r}{b}\right)^3$$

This constraint is thus more severe closer to the body than further away. This limits the cross flow velocity, v, without effecting pressure, density, enthalpy or entropy and in effect adds to the total circulation. Figure 9.1.3.1 depicts this function. Figure 9.1.3.2 shows a comparison of the circumferential pressure distribution predicted by SWINT without clipping with experimental results. It can be seen that in the nose region, prior to separation, the prediction is good. However, after separation the lee ward side prediction is poor. Figure 9.1.3.3 shows the improvement with 'clipping' included.

ZEUS is another method based on a Zonal Euler Solver (ZEUS) and uses a secondorder Godunov method. ZEUS offered a method of producing accurate solutions for complicated geometry's using

---

[4] Euler will support flow separation from a sharp edge such as the leading edge of a slender delta wing.

[5] Supersonically vorticity may be generated by shock waves.

efficient grids and without the need for artificial viscosity. Since ZEUS is an Euler solver it, like SWINT, can not model separation effects. Again 'clipping' can be used and figure 9.1.3.4 illustrates the marked improvement in the predicted load distribution.

A further attempt was made to include a more rational separation model[6] into ZEUS by modifying the pressure and density on each side of the empirically derived separation line. The velocity components at these cells are computed from the constraint of total enthalpy and the specification of streamline directions on each side of the separation line. The ensuing vortex sheet is then captured by the numerical scheme. Figure 9.1.3.5 depicts the normal force coefficient Vs incidence for a body of revolution. It can be seen that ZEUS under predicts C_N at 11° by nearly 40% but the inclusion of the separation model gives a great improvement.

These results clearly show the importance of correctly modelling separation.

9.1.4 Selection of numerical approach

In selecting a CFD code it is important to keep in mind the objectives of the study. Ideally it would be useful to be able to examine the development of the vortex pair and their progression downstream. It would be informative to be able to monitor the direction of the vorticity vectors during the development of the vortices and the ability to estimate the rate at which vorticity is being shed may provide further insight. From this information it may be possible to draw some inference on the need to factor down the rate at which vorticity is generated before it is fed into the main vortex structures in most analytical models.

It is clear that whichever method is selected it must be capable of modelling separation from smooth surfaces. This clearly rules out the pure Euler equations solution. As we have seen, however, acceptable overall results can be achieved by forcing separation to occur by the application of appropriate boundary conditions. This approach requires the location of the separation line to be known a priori; which, since the method is not intended as a flexible prediction method in itself, is acceptable. The method also requires a number of other parameters to be specified such as the angles of streamlines leaving the separation line. These parameters are more critical since they may influence the magnitude and direction of the vorticity vector being generated. This makes the Euler solution a less attractive option. Furthermore, since the boundary layer would not

---

[6] referred to as the Salford Separation Model

be modelled in any sense it would not be possible to examine the full development of the lee side vortices from their origin.

This leads us to the Navier-Stokes approach. The limiting factor here is the general availability of these codes. In fact the author was unable to locate a generally accessible (or otherwise) N-S code capable of operating at low Mach numbers. This was disappointing since it meant that solutions could only be obtained supersonically. The Defence Research Agency (DRA), Bedford, were most helpful in this respect in offering solutions from a Reynolds averaged N-S code and a parabolised N-S code. In practice, difficulties were encountered in producing solutions from the former which cast some doubt upon their accuracy. The later produced apparently good results and in any case was a code that had been well validated by the DRA using their extensive experimental data base.

It was felt that this approach would allow all the objectives of the study to be met. The only reservation being the required higher Mach number range for this code might introduce the added complication of shock generated vorticity. This will be addressed later.

9.2 ANALYSIS OF NAVIER-STOKES SOLUTION

9.2.1 Derivation of 3 components of vorticity from N-S solutions.

As discussed in section 8 the vorticity will be examined in a cylindrical coordinate system. The total vorticity is given by

$$e_r\xi_c + e_\theta\eta_c + e_z\zeta_c ,$$

where e_r, e_θ, and e_z are the cylindrical polar unit vectors, whilst

$$\xi_c = \frac{1}{r}\frac{\partial\ w}{\partial\theta} - \frac{\partial\ u_\theta}{\partial\ z}$$

$$\eta_c = \frac{\partial\ u_r}{\partial\ z} - \frac{\partial\ w}{\partial\ r}$$

$$\&\ \zeta_c = \frac{1}{r}\frac{\partial(ru_\theta)}{\partial\ r} - \frac{1}{r}\frac{\partial\ u_r}{\partial\theta}$$

Thus the local vorticity components and indeed the local total vorticity magnitude can be derived from the local velocity components and their space derivatives.

The velocities computed in the numerical solution were in Cartesian co-ordinates and were first converted to cylindrical co-

ordinates. The derivative terms were then calculated using a central difference method. It is appropriate to mention at this point an additional advantage of the numerical technique over an experimental approach. In order that these derivative terms can be evaluated the spatial resolution of the velocity data needs to be relatively fine not just in the cross flow plane direction but also in the axial direction. This would imply a prohibitively large experimental program.

Having derived the local vorticity vectors throughout the flow field it is now possible to consider how best to visualise the data.

9.2.2 Visualisation of vorticity fields.

Whilst the vorticity has been evaluated throughout the entire 3-D flow field it still makes sense to examine it in cross flow planes at a number of stations along the axial length of the body.

There are many ways of visualising vector data in a field or across a plane. One way is to plot the vectors as projections of 3-D arrows where their orientation indicates their direction and their length indicates their magnitudes. The disadvantage of this type of approach is that it lacks clarity particularly in the vicinity of detailed features. Increasing the resolution, by adding more vectors, only serves to further clutter the picture.

The method of visualisation chosen is that of contour plots. These provide very clear images of the distribution of the chosen parameter across the plane and by looking at a number of planes 3-D structures can be deduced. Contour plots are particularly good at depicting regions of high or low parameter values shown as islands and rates of change of parameter values shown by the contour interval spacings. The disadvantage of the method is that it can only represent scalar data. Thus only the magnitude of vector components or the total vector magnitudes can be shown.

Figures 9.2.2.1 to 9.2.2.15 show contour plots of the three components of vorticity at 5 axial stations located at approximately z=4, 5.75, 7.25, 8.5 and 9.75 calibres along a 3 calibre ogive nose-cylinder body at Mach 2.5 and 14° of incidence.

Starting with the figure 9.2.2.1, this shows distribution of the ζ component of vorticity. This is the vector component normal to the paper and is traditionally thought of as the main component of the lee side vortices. The plot is taken at a z-wise station 4 calibres from the nose and covers the right hand side of the plane (symmetry has been assumed about the incidence plane). The domain extends from the semicircle on the left, which represents the body circumference, to the arc on the right, which represents the location of the bow shock wave.

It can be seen that over about 98% of the region plotted the magnitude of the vorticity is near zero. As expected the vorticity is concentrated in close proximity to the body surface.

Although this plane is only 1 calibre behind the nose-cylinder junction, the main elements of the vortex structure are already starting to form. The lower quadrant of the body is enveloped by vorticity generated by the cross-flow component of the boundary layer flow. This region can be seen to thicken as it progresses around the body until it separates, just past the body shoulder, to form a free shear layer. The shear layer can be seen to be starting to 'roll-up' at its upper most extremity, to form a concentrated region of ζ-vorticity. Sitting beneath this primary vortex can be seen a small secondary vortex also starting to develop. This all neatly fits what would be expected. One interesting feature also visible here is a thin region of vorticity of opposite sign that envelopes the boundary layer in the lower quadrant and extends slightly along side the outer edge of the feeding sheet. An explanation for this will be attempted later.

Many models of body vortices only consider the ζ component of vorticity. When deducing vorticity from experimental data consisting of cross flow plane flow surveys there is usually insufficient data to evaluate all three components of vorticity. Even when post processing CFD data the remaining η and ζ components of vorticity are often neglected. These components are now examined in detail to see if light can be shed on the predicted loss of vorticity that the analytical models suggest.

Figure 9.2.2.2 shows the magnitude of the η-component of vorticity. In cylindrical co-ordinates this is the component that would dominate in the boundary layer of a body of revolution in axisymmetric flow. The vector is always in a direction tangential to the body surface (though not necessarily adjacent to it).

As with the ζ-component, the vorticity is concentrated around the body surface. This component of vorticity, within the boundary layer, extends further away from the body surface since it has been developing over a much greater length. It can be seen that a significant amount of this vorticity is swept up by and contained within the feeding sheet. Making sense of this component of vorticity beyond the feeding sheet is difficult since the vector is changing direction and as such becomes conceptually difficult to interpret from a scalar contour plot. An important point to note however is that the magnitude of the η-vorticity although small compared to the ζ vorticity component is nonetheless significant.

Figure 9.2.2.3 shows the magnitude of the third component of vorticity ξ. This is the component acting in the radial direction and again although small, is significant. At this stage the structure in this component is unclear.

It can be seen that any vorticity generated by the bow shock is small. This will be considered further later.

Figures 9.2.2.4 to 9.2.2.6 show the development some 1.75 calibres downstream. The ζ-component of the primary vortex structure is more clearly formed and has lifted away from the body surface. The vortex core is becoming more circular in form. Although still smaller in magnitude the η and ξ components of vorticity are now developing a clear and unanticipated structure. Each component appears to be forming a partial halo of concentrated vorticity around the primary vortex core. Individually these patterns are difficult to interpret but when examined side-by-side one can envisage a rotation of the η and ξ vector components such that their resultant magnitude forms a complete halo. This phenomenon will be examined in this manner later.

Figures 9.2.2.7 to 9.2.2.9 and 9.2.2.10 to 9.2.2.12 show the development of the structure in three vorticity components at stations further down stream. The primary vortex continues to lift away from the body surface and the feeding sheet and the secondary vortex have become more distinct.

Figures 9.2.2.13 to 9.2.2.15 show the development at the last station being considered. It is useful to compare the detailed structure with that anticipated in section 8.5. In this section the distribution of the three components of vorticity through the feeding sheet are considered. Figure 8.5.1.3 shows the cross flow velocity component in the boundary layer and feeding sheet. Figure 8.5.1.4 shows how these velocities give rise to the ζ vorticity component distribution in the feeding sheet. It can be seen that a bell shaped distribution is expected. Figure 9.2.2.13 shows that the distribution is of this form.

Figure 8.5.1.5 shows the axial component of velocity in the boundary layer and feeding sheet and 8.5.1.6 shows the resulting η and ξ velocity component distribution. It can be seen that the distribution consists of two bell shaped curves of opposite sign. Figure 9.2.2.14 and 9.2.2.15 can be seen to follow this pattern. Figure 9.2.2.16 shows an enlargement of figure 9.2.2.14, the ξ component in the feeding sheet. The maximum and minimum ridges can clearly be seen. Note that the periodic island features are caused by the contour plotting software and are not true features of the solution. Figures 9.2.2.17 to 9.2.2.19 are contour plots that only contain regions between -0.025 and +0.025 i.e. they indicate regions of near zero vorticity. The purpose of these plots are twofold. Firstly, they highlight the fact that most of the flow field away from the body and primary vortex contains little or no vorticity. Secondly they show clearly the regions where vorticity changes sign. Figure 9.2.2.17 shows the bounds of the feeding sheet and the region occupied by the secondary vortex. The region of negative ζ-component vorticity outside the feeding sheet is also clearly shown. Figures 9.2.2.18 and 9.2.2.19 show the bifurcation of the feeding sheet in the η and ξ components of vorticity.

Figure 9.2.2.20 shows the resultant magnitude of the η and ξ components. The halo effect can clearly be seen. Comparing with figure 9.2.2.21 it is clear that the halo surrounds the peak in ζ vorticity in the vortex core. In terms of the total vorticity vector these plots indicate that the vector outside the vortex core is aligned roughly in an axial direction. As we move towards the vortex core the vector moves away from axial alignment in a direction conical about the vortex core. As we enter the vortex core the total vorticity vector becomes axial again. Figure 9.2.2.22 shows the magnitude of the total vorticity vector. The core minimum of the η and ξ components can be seen clearly in figure 9.2.2.23 which shows the resultant of the η and ξ terms as a percentage of the total vorticity magnitude.

Figures 9.2.2.24 to 9.2.2.27 show that the same phenomenon can be seen at other z-wise stations.

It is quite apparent from these results that to assume that all the flow field vorticity (other than the attached boundary layer) is aligned with the body axis, i.e. has a ζ component only, is a considerable simplification of the flow physics. Not only is a significant proportion of the vorticity being neglected but interchanges are occurring between the three components[7].

It is now quite easy to imagine that if only the ζ component of vorticity were to be monitored in a real flow one might see vorticity levels reduce or increase without any apparent reason.

It is possible, in this case, that some explanation for the 0.6 factor could be found, at least in part, by investigating this further.

9.3 INTEGRATION OF VORTICITY TO OBTAIN CIRCULATION IN THE VORTEX STRUCTURE COMPONENTS

9.3.1 Method of integration

The manner in which vorticity accumulates in the lee side vortices as they propagate downstream is of great interest. But before we can look at this we must first be able to look at the vorticity in some quantitative way at some arbitrary station. The most logical method for doing this is to derive a value for the circulation in the flow field.

As we have seen the vorticity has three components to its vector. The majority of the vorticity is in the ζ sense, but significant components exist in the η and ξ senses.

Now the circulation, Γ, about a closed curve in the flow field is defined by the contour integral:

---

[7] or the direction of the total vorticity vector is changing

$$\Gamma = \oint \overline{V} . d\overline{\sigma}$$

where $\overline{\sigma}$, here, is the element along the closed curve.

Circulation can also be expressed as the integral of vorticity over an area thus:

$$\Gamma = \int \omega . ds$$

Where the integral is over an area S

Whilst this type of approach works well for one component of vorticity acting normal to the plane over which the integrals are performed i.e. from a two dimensional view point, the full three dimensional problem is more complex.

Of course, the remaining two components of vorticity can be integrated across planes defined as normal to their vectors or surfaces in the case of cylindrical co-ordinates. However, the meaning of these circulation values is less than clear since they do not relate to each other in any way.

Consider, for instance, the circulation over an area on a particular cross flow plane. ζ can be integrated over this area to derive a value of Γ_ζ. How can we now derive corresponding values of Γ_ξ and Γ_η. η and ξ can not be integrated over the same area since this plane is neither normal to η nor ξ. As said above, if the area is redefined to be on another plane then the resulting integral will not relate to Γ_ζ.

To enable some analysis to proceed only the ζ component of vorticity will be integrated and integrated across cross-flow-planes. Whilst this does not permit the whole picture to be analysed in quantitative terms it does give a useful window through which to study the flow particularly since the ζ terms are by far the most dominant. It must, of course, be borne in mind that there are other components of vorticity and that circulation may be exchanged between these components. Furthermore, this approach relates well to the other methods of computing vortex flows about bodies of rotation since they compute flow variables at discrete cross-flow-planes along the body[8].

Since the value of vorticity is known across the plane at a great many points by the nature of numerical solutions, the second form of the circulation integral is the most computationally efficient method of computing circulation. Hence the plane can be divided into small cells of known area and known vorticity from which the circulation

---

[8] Although in the numerical solution the other components are still present.

of that cell can be computed. The sum of these elements results in the total circulation.

9.3.2 Regions of integration

Consideration is now given to the area of integration. Since the numerical solution assumes lateral symmetry, integration of vorticity across an entire cross flow plane would result in zero circulation since any area of positive vorticity on one side of the body has an identical area of negative vorticity on the other side. Furthermore, it may be informative to partition the plane in several regions which relate to specific structures within the flow field.

Hence the flow field will be divided into the primary vortex, the feeding sheet, the boundary layer the secondary vortex and what shall be referred to as the 'outer region'. The outer region is an area just outside the boundary layer primarily on the windward side of negative vorticity that was mentioned in the discussion of the vorticity distribution.

The definition of these regions in terms of actual co-ordinates is less easy to define since the size and location of the features change from plane to plane.

To overcome this ζ contour plots were generated at each plane to be considered and the regions defined by inspection[9]. It was found that the regions could be defined by the location of one control point, x_p, y_p, linear dimension x_s and the separation angle, θ_s.

Figure 9.3.2.1 illustrates the regions defined. The function of the control point is clear from the figure, the dimension x_s serves to split the negative vorticity of the secondary vortex from that of the 'outer region' and the separation angle θ_s differentiates the boundary layer from the feeding sheet.

Mathematically:

. If ($x>x_p$) AND +ve OR ($y<y_p$ AND $\theta>\phi$) AND +ve
then region is either the feeding sheet or the boundary layer.

. If $\theta>\theta_{sep}$ it is the feeding sheet
else it is the boundary layer.

. If $x<x_p$ AND $\theta<\phi$ AND +ve then the region is primary vortex

. If $x<x_s$ AND $y>0$ AND -ve then region is the secondary vortex
else if -ve then it is the 'outer region'

Figure 9.3.2.2 illustrates the selection of the control point for one particular station. To ensure that the control point varies

---

[9] A sensitivity study was performed on this process to ensure human error (or prejudice) did not influence results.

smoothly in the axial, z, direction x_p was plotted against z and a smooth curve fitted as in figure 9.3.2.3.

9.3.3 Distribution of circulation

Upon integrating the vorticity[10] it becomes possible to see where in the flow field the circulation concentrations are. The most prominent concentration of circulation is, as expected in the primary vortex. However, it is surprising to find that the circulation locked up within the feeding sheet is of the same order. A somewhat smaller amount of circulation is contained within the boundary layer. The largest source of negative circulation is contained within the secondary vortex, however, an additional albeit small area of negative circulation is the thin strip just outside the boundary layer/feeding sheet, referred to as the 'outer region'.

9.4 VARIATION OF CIRCULATION WITH AXIAL COORDINATE

Having derived values for the circulation locked within the various structures within the flow field it is now possible to examine their variation along the length of the body. Figure 9.4.1.1 shows these variations. It is clear from this figure that, as expected, the total circulation is increasing. Since the feeding sheet is generating a constant supply of vorticity this comes as no surprise. It can be seen that the increase is due entirely to the increase in circulation within the feeding sheet/primary vortex combination. Looking at these two elements separately it is apparent that the increase in circulation within the feeding sheet is small and the main mechanism for the accumulation of circulation is the primary vortex structure. This concurs with the traditional view on the subject. The apparent accumulation of circulation within the feeding sheet, particularly in the early stages of its development, is probably due to the increase in its length, and hence area, as the primary vortex lifts away from the body surface rather than some inherent mechanism. Figure 9.4.1.2 illustrates clearly the development of the component structures within the flow field including the lengthening of the feeding sheet. Returning to figure 9.4.1.1 it also appears that the boundary layer, although exhibiting a fairly constant level of circulation, does initially reduce. Again this is due to the lengthening of the feeding sheet by virtue of a windward shift in the separation point.

---

[10] Note that, as previously mentioned, this analysis only relates to the ζ component of vorticity.

The two negative regions of circulation are small and almost constant. Although small they are being continuously fed and hence it is possible that their vorticity is changing orientation or more likely being annihilated. The mechanism may be contributing, albeit in a minor way, to the 0.6 sigma factor.

9.5 RATE OF GENERATION OF CIRCULATION

9.5.1 The generation of vorticity

The primary source of vorticity entering the flow field is from the separation of the boundary layer and the formation of the feeding sheet. Refer to section 8 for a more detailed discussion of this mechanism.

We have seen that it is possible to quantify the amount of circulation accumulated in the flow field. If we consider the variation of this accumulation in the axial direction we can deduce the rate at which the circulation is increasing. This rate is due to the generation of vorticity from all sources[11] less any dissipation or annihilation. Furthermore vorticity may, within the framework of this study, be 'lost from sight' by rotation of vorticity vector away from the prime, ζ, direction.

If a figure could be determined for the rate of generation of vorticity from its point of source this could be compared with the rate of accumulation of vorticity within the flow field. Assuming zero losses within the system the two figures would be equal. If there are additional sources of vorticity then the rate of accumulation would be greater than the rate generated by the feeding sheet. This is not thought to be the case but will be discussed later. If there are 'losses' then the rate of accumulation would be less than the rate of generation.

Based upon the empirical results of the analytical models proposed to date one might expect the rate of accumulation to be approximately equal to 0.6 of the rate of generation by the feeding sheet[12].

A detailed investigation of the feeding sheet would be useful.

---

[11] which in general may not solely be from the feeding sheet.
[12] Although one reference suggests that sigma may be some complex function of M and $M_{crossflow}$.

9.5.2 The flow field in the vicinity of the feeding sheet.

Since our primary interest is in the generation of vorticity let us start by examining the distribution of vorticity within the feeding sheet. One way of presenting this information is to take a slice through the feeding sheet on a plane at some axial station along the body. We can define the position of the 'slice' as passing through the centre of the body and extending radially outwards at some angle, θ, from the horizontal. Thus a slice extending in the y-axis direction is given by θ=0.

Figure 9.5.2.1 shows the vorticity distribution through the feeding sheet at a plane at z=7.26 calibres from the nose. The first slice is at θ=-1.1° and shows the bell shaped distribution as anticipated in section 8. Since the distribution is well developed it can be assumed that separation occurred considerably earlier than θ=-1.1°. As the distance from the body centre, R, tends to a high value the vorticity tends to zero. It can be seen that dimensionally the width of the feeding sheet is small, less than 0.05 of the body radius. Another feature, noted earlier, is that there is small region of slightly negative vorticity to the windward side of the feeding sheet.

If we now rotate the position of the slice by increasing θ four characteristics can be observed. Consider the slice at θ=13.8°. It can be seen that the bell shape distribution has moved away from the surface, the peak having moved some 0.04R. The peak itself has reduced in magnitude and width of the sheet has increased to 0.07R. Finally a region of negative vorticity is apparent to the lee ward side of the sheet ie. between 0.5R and 0.53R. This region is due to the θ slice intersecting the secondary vortex.

Figure 9.5.2.2 shows the corresponding velocity profiles through the feeding sheet. Consider the profile at θ=-1.1. It can be seen that the velocity increases rapidly away from the surface and tends to the freestream value at about 0.65R. However, before reaching the freestream value a distinct overshoot can be seen at 0.54R. This is thought to be due to the velocity component referred to as the local cross flow velocity profile which results from an imbalance between the pressure forces and the centripetal forces acting on the flow as its curved motion is retarded through the boundary layer towards the body surface. This phenomenon is discussed in section 8.2.4. Figures 9.5.2.3 to 9.5.2.7 show the velocity profiles for the attached boundary layer region on the wind ward side of the body. It can be seen that this phenomenon also occurs in this region along the entire length of the body.

Tracing the velocity profile away from the surface, on figure 9.5.2.2, we can see that a peak in vorticity might be expected at about 0.52R where $\frac{\partial U_\theta}{\partial R}$ is at a maximum and a zero vorticity just after

0.54R. The velocity overshoot then gives rise to negative value of $\frac{\partial U_\theta}{\partial R}$ reaching its peak at about 0.56R and tending to zero at large R.

At θ=13.8° the profile is similar except that the reverse flow region due to the secondary vortex is now visible and the velocity overshoot is much less pronounced.

Figure 9.5.2.8 shows the distribution across the feeding sheet of the product of vorticity and velocity. This vorticity flux quantity gives an indication of the rate at which vorticity is being transported along the feeding sheet. The distribution shows the same characteristics as the vorticity profile, that is a bell shaped distribution reducing in height but expanding in width along the direction of the feeding sheet.

9.5.3 Vorticity Flux

Having examined the nature of the vorticity contained within the feeding sheet it is now necessary to attempt to quantify the rate at which vorticity is being generated and fed into the flow field.

Let us consider a small element within the feeding sheet of length ds, width δr and velocity $v = \frac{ds}{dt}$. If the vorticity within the element is ζ then we can write

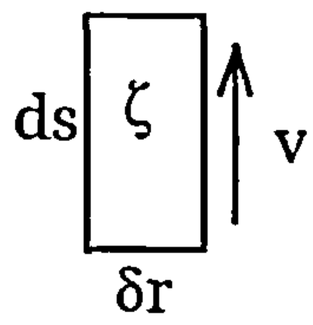

$$d\Gamma = \int_0^r \zeta ds(r).dr$$

$$\dot{\Gamma} = \frac{d\Gamma}{dt} = \int_0^r \zeta \frac{ds(r)}{dt}.dr$$

Thus by integrating across the feeding sheet at any cross section through its length it is possible to quantify the rate at which circulation is being added to the flow field.

This process can be repeated at a number of axial stations along the body. One remaining question is at which point along the length of the feeding sheet should the cross section of integration be chosen? Figure 9.5.3.1 shows the variation of $\dot{\Gamma}$ as a function of cross section location, θ, for a number of z-wise stations. It is clear that once a certain value of θ has been reached the value of $\dot{\Gamma}$ remains fairly constant. This is as expected since the function of the feeding sheet is thought to be to convect vorticity rather than to create or destroy it. It can also be concluded that once the constant value of $\dot{\Gamma}$ has been reached the value of θ is not critical.

It has been mentioned previously that there are regions of negative vorticity near the feeding sheet. Figure 9.5.3.2 depicts the value of $\dot{\Gamma}$ if the negative regions are excluded from the integration process, this is referred to as $\dot{\Gamma}$ maximum. This gives a measure of the significance of the negative regions. Figure 9.5.3.3 compares the two results at a single station. It can be seen that the total $\dot{\Gamma}$ is almost constant whilst the maximum $\dot{\Gamma}$ is still tending down towards the same constant value. It is possible, in the light of this, that a small proportion of the positive vorticity is being annihilated by the negative vorticity. If comparisons are to be made of $\dot{\Gamma}$ then the total $\dot{\Gamma}$ should be used.

Returning to figure 9.5.3.1 and the question of which value of θ to take, a rational approach would be to determine the point of separation. Since it is reasoned that the vorticity is generated in the attached boundary layer there should be no further increase in $\dot{\Gamma}$ after this point has been reached.

The point of separation can best be determined by considering the velocity profile at some small distance[13] above the body surface. Figure 9.5.3.4 shows two components of cross flow velocity, U_r normal to the body surface which is always near zero and U_θ, tangential to the body surface which is positive on the wind ward side of the body but drops to zero as the flow separates. The negative velocity regions on the lee side of the body are induced by the primary and secondary vortices. From this plot it is possible to determine the position of separation fairly accurately. Figure 9.5.3.5 shows the near surface velocity profile at the next station. The profile is similar in shape but indicates that the point of separation has moved towards the windward direction. Figures 9.5.3.6 - 9.5.3.8 show how the separation position varies with axial position.

These separation positions can be superimposed on figure 9.5.3.1 (shown as small triangles, ∇ symbols) to locate a value of $\dot{\Gamma}$ for use in further analysis. It can be seen that as expected the region of constant $\dot{\Gamma}$ follows separation. Prior to separation $\dot{\Gamma}$ increases as vorticity is generated within the attached boundary layer. There can also be seen a short region immediately prior to separation where $\dot{\Gamma}$ reduces slightly. The explanation for this effect is likely to be found by consideration of the complex three dimensional interactions that are occurring in this region.

---

[13] The velocity on the surface will always be zero due to the applied boundary conditions.

9.5.4 An approximation to the generation of vorticity

In many simple analytical models of separated flow, both two and three dimensional, an approximation for the rate of generation of vorticity is used. The result, derived in an earlier section, used is $\frac{U^2}{2}$ where U is the flow velocity just outside the boundary layer at the point of separation. (In practice the method is applied to inviscid models and hence the velocity at the body surface is used.)

This method is very simple, hence its attractiveness, but consequently may be very approximate. In fact, it is not too difficult to suspect that the entire 0.6 factor might derive from this source.

Using the numerical solution it is a simple matter to extract the relevant velocity and use it to derive a value of $\dot{\Gamma}$.

Figure 9.5.4.1 shows a comparison of the integrated shed $\dot{\Gamma}$ with the $\frac{U^2}{2}$ derived $\dot{\Gamma}$ as a function of axial position. It can be seen that the prediction is excellent considering its simplicity.

9.5.5 Rate of accumulation of circulation in the flow field.

The amount of circulation in the flow field at any given station has already been determined by the integration of vorticity over the appropriate area. By considering the circulation over a series of three consecutive planes the rate of change of circulation can be found using a central difference technique. Hence $\dot{\Gamma}$ can be found, in this case, corresponding to the rate of accumulation of circulation in the flow field.

Figure 9.5.4.1 shows the variation of this parameter, labelled $\dot{\Gamma}_{\text{field c-diff}}$, with axial position along the body. Since five planes have been analysed the central difference process results in three values. It can be seen that $\dot{\Gamma}$ appears to reduce with z.

This reduction is, however, also apparent in the values of $\dot{\Gamma}$ derived from integration across the feeding sheet and by the approximation. The slopes of these lines are almost identical which gives some degree of confidence in the method.

9.5.6 Other sources of vorticity

In the current study the primary source of vorticity has been assumed to be in the separation of the boundary layer to form the feeding sheet. For the flow conditions of interest this is a valid

assumption. However, due to the difficulties discussed at the start of this chapter it was necessary to analyse a supersonic numerical solution. Under these conditions it is quite possible that other sources of vorticity exist.

Whilst, for the purpose of this study, it is not essential that these other sources be zero they should be relatively small if they are not to confuse the arguments being applied.

One difference between sub and super sonic flow is the presence, in the case of our geometry, of shock waves. The entire body is enveloped within a shock surface emanating from the body apex. This bow shock is a potential source of vorticity since it is known that curved shock waves generate vorticity. Consider the shock system about the leading edge of a faceted two dimensional body. Across the streamline emanating from the point of intersection of the bow shock with the first expansion wave, there is a finite velocity difference resulting in a shear layer. If we take this idea one step further and turn the flow in a continuous fashion a curved shock wave would result and give rise to a vorticity field in its wake. A relationship can be derived between the flow curvature and the resulting vorticity by considering Crocco's Law which states that the product of the vorticity and the speed is equal to T, the temperature behind the shock, times the magnitude of the entropy gradient. This results in

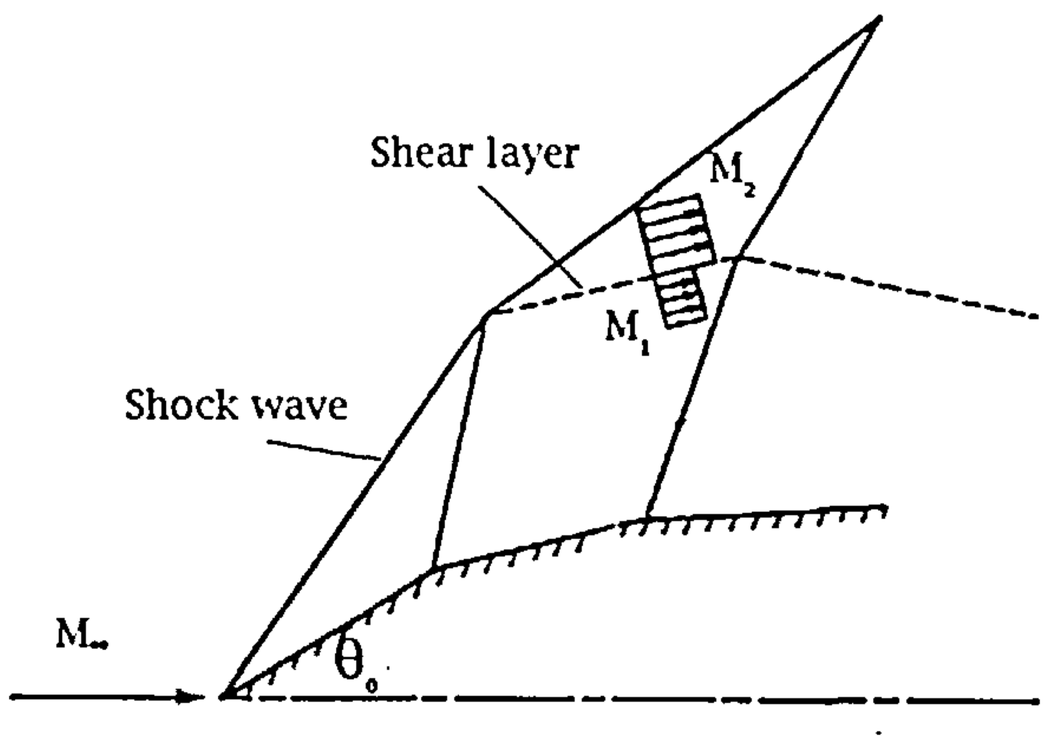

$$\zeta_s = -U\varepsilon^{-1}(1-\varepsilon)^2 \cos\sigma \frac{d\sigma}{dx}$$

where σ is the local shock angle (see [41a] for details).

It has been shown that this relationship holds for axisymmetric flow.

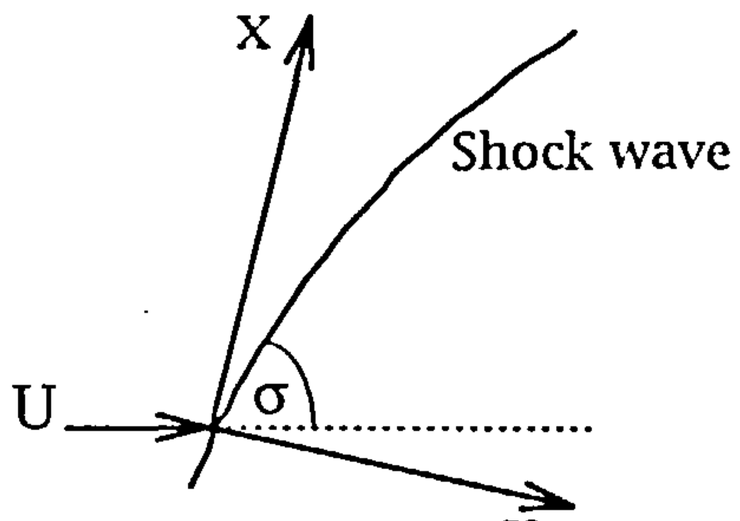

If we now consider the implications for vorticity generation by the bow shock within our configuration we can firstly see that any vorticity generated would be orientated in the η direction. Secondly, since σ will be relatively large, particularly in proximity to the body, cosσ will be small. Similarly the curvature $\frac{d\sigma}{dx}$ will be small, hence

the magnitude of the vorticity will be small. MARCONI [42] mentions in his investigations of shock induced vorticity about slender cones that the bow shock vorticity is some two orders of magnitude lower than any other source in the flow field.

As regards our numerical solution, figure 9.2.2.2 shows that away from the body surface there are no significant regions of vorticity even in the proximity of the bow shock.

Under certain conditions it is also possible for shock waves to form locally within the flow particularly when the cross flow Mach number is high. Shock waves can occur in the cross flow plane to assist in turning the flow to the lee symmetry plane. The shock, which is near normal, is strongest at the body side where the velocity is greatest and approaches zero strength away from the surface where the cross flow velocity is sonic. This variation in strength produces a cross-flow entropy gradient and thus a vorticity field. MARCONI [42] shows that at high Mach numbers and incidences the cross-flow shock waves on slender conical bodies can generate sufficient vorticity to induce separation within an inviscid Euler solution.

However, for the cases considered in this study there is little evidence that these shock waves are occurring. Figures 9.5.6.1 and 9.5.6.2 show Mach number contours and total pressure contours which do not appear to exhibit any of the step changes that characterise shocks. A distrotion in the contours at the 2 O'clock position indicates a possible weak shock smeared by the lower grid resolution away from the body surface. However, and more importantly, figures such as 9.2.2.1 do not indicate regions of vorticity generation in the areas that cross-flow shocks are likely to appear.

It can be concluded that in this case the feeding sheet is the primary source of vorticity in the flow field.

The aim of this study is to investigate the balance between vorticity generated and the accumulation of circulation in the flow field. Since it is believed that the flow field appears to contain less circulation than is generated by the feeding sheet any additional sources of vorticity would in fact serve to highlight[14] the phenomenon rather than mask it.

9.6 THE SIGMA FACTOR

The values thus obtained can be thought of as analogous to the quasi two dimensional analytical approaches. The value of $\dot{\Gamma}$ derived

---

[14] Since the sense of the vorticity generated by crossflow shocks is the same as that by the feeding sheet.

from the integration of vorticity flux across the feeding sheet is equivalent to the rate at which vorticity is generated. In fact the approximate value of this parameter uses the actual approximation used in the Vortex Cloud Method.

The value of $\dot{\Gamma}$ derived from the flow field vorticity integration method is equivalent to the circulation feed into the flow field after applying the sigma factor.

Hence by finding the ratio of $\dot{\Gamma}_{shed}$ to $\dot{\Gamma}_{field}$ one can derive an equivalent value for sigma. Figure 9.5.4.1 shows values of this ratio. The ratio appears to be fairly constant at about a value of 0.7. Whilst this value corresponds numerically with the actual value used for sigma, it should not be taken as confirmation that the empirical value is correct. One reference claims that although a value of 0.6 is apparent to subsonic cases, which are of interest here, it may not always hold true at supersonic speeds.

However, the objective of this study was not to confirm the value of this parameter, rather to provide some insight into why it is required at all.

Although it was not possible to run a subsonic case, as mentioned at the start of this chapter, it was possible to run a second supersonic case. A higher Mach number of 3.5 was available at an incidence of 18°. This case was postprocessed in the same manner as the previous case. The flow field was sectioned at a large number of stations as in figure 9.6.1.1 and the rate of accumulation of circulation was determined as in figure 9.6.1.2.

Figures 9.6.1.3 and 9.6.1.4 show the vorticity flux at sections cut across the feeding sheet. These enable the rate at which vorticity is being generated to be evaluated. Figures 9.6.1.5 to 9.6.1.13 show the near surface velocity profiles from which the separation point locations can be determined as a function of axial position along the body. The locations can be superimposed upon figure 9.6.1.3 to enable $\dot{\Gamma}_{shed}$ to be determined as a function of axial position.

Again a central difference process was applied to the figures for the rate of accumulation of circulation in the flow field to obtain $\dot{\Gamma}_{field\ c\text{-}diff}$. In this case the analysis was performed at a greater level of resolution such that seven values could be obtained.

These results are presented in figure 9.6.1.14 which shows the rate of accumulation of circulation compared to the rate of its generation. As before the ratio of these two parameters gives an equivalent value of sigma.

In this case there is more scatter present and the value varies between just above 0.9 and just below 0.8. So again this result confirms that some circulation is lost or transformed between its generation and its accumulation in the flow field.

10. A NEW APPROACH

10.1 THEORY

10.1.1 Classical slender body theory

Classical slender body theory and its application to missile aerodynamics is discussed in NIELSEN [43]. CHRISTOPHER [44] provides a more lucid derivation of one of its most widely known results:

$$\frac{dC_N}{dx} = \frac{4\pi}{S_R} R \frac{dR}{dx} \sin\alpha \cos\alpha$$

This result offers an extremely simple expression that may be used to estimate the local normal force distribution along a slender body at low incidence. The distribution being a simple function of the rate of change of body cross sectional area. Moreover, simple expressions such as this lend themselves to further analytical derivations. For example the total normal force can now be determined by integration of the local normal force distribution along the length of the body.

We can start by saying

$$C_N = \int_0^{x_N} \frac{dC_N}{dx} dx$$
$$= \frac{4\pi \sin\alpha \cos\alpha}{S_R} \int_0^{x_N} R \frac{dR}{dx} dx,$$

where x_N= nose length.
Changing the variable of integration we get

$$C_N = \frac{4\pi \sin\alpha \cos\alpha}{S_R} \int_{R_0}^{R_{xN}} R dR,$$

where R_0= radius at x=0
R_{xN}= radius at $x=x_N$.

And if R_{xN}=a=1

$$= \frac{4\pi \sin\alpha \cos\alpha}{S_R} \int_0^1 R dR.$$

Evaluating the integral

$$C_N = \frac{4\pi \sin\alpha \cos\alpha}{S_R}\left[\tfrac{1}{2}R^2\right]_0^1$$

$$= \frac{4\pi \sin\alpha \cos\alpha}{S_R}\frac{1}{2}$$

But $S_R = \pi \ a^2 = \pi$

$$= \frac{2\pi \sin\alpha \cos\alpha}{S_R}$$

$$= 2\sin\alpha \cos\alpha$$

So for small α

$$C_N = 2\alpha$$

and hence the lift curve slope

$$\frac{dC_N}{d\alpha} = 2.$$

It is interesting to note that within the bounds of the theory this result is independent of the nose geometry.

Since most slender bodies will start to generate non-linear lift from quite moderate incidences, this linear form of the lift curve will only apply at low incidence.

Returning to the local normal force distribution, a useful result to have is the location of the maximum load. This will obviously occur when

$$\frac{d^2C_N}{dx^2} = 0$$

i.e.

$$\frac{d\left(\frac{dC_N}{dx}\right)}{dx}$$

$$= \frac{d\left(\frac{4\pi}{S_R} R \frac{dR}{dx}\alpha\right)}{dx}$$

$$= \frac{4\pi\alpha}{S_R}\frac{dR\frac{dR}{dx}}{dx}$$

$$= \frac{4\pi\alpha}{S_R}\left(R\frac{d^2R}{dx^2} + \frac{dR}{dx}\frac{dR}{dx}\right)$$

or, since in general, $\alpha \neq 0$,

$$R\frac{d^2R}{dx^2} + \left(\frac{dR}{dx}\right)^2 = 0$$

To take this analysis further the body radius distribution must be known. Let us consider the case of a 3 calibre tangent ogive nose. This shape is defined by

$$R = 2\left[8.75 - \left\{85.5625 - \left(\frac{x}{2} - 3\right)^2\right\}^{\frac{1}{2}}\right]$$

thus

$$\frac{dR}{dx} = 2(x-6)/(1225+48x-4x^2)^{\frac{1}{2}}$$

$$\frac{d^2R}{dx^2} = \frac{2}{\sqrt{1225+48x-4x^2}} + \frac{8x^2-96x+288}{(1225+48x-4x^2)^{\frac{3}{2}}}$$

so

$$\frac{d^2C_N}{dx^2} = \frac{4\pi\alpha}{S_R}\left(\left[\left[2\left(8.75 - \sqrt{85.5625 - \left(\frac{x}{2}-3\right)^2}\right)\right]\right.\right.$$

$$\left.\left.\left[\frac{2}{\sqrt{1225+48x-4x^2}} + \frac{8x^2-96x+288}{\left(1225+48x-4x^2\right)^{\frac{3}{2}}}\right] + \left[\frac{2(x-6)}{\sqrt{1225+48x-4x^2}}\right]^2\right)\right.$$

$$= 0$$

Solving for x we get four solutions:

$$x_1 = 2.47194$$
$$x_2 = 9.52805$$
$$x_3 = 49/2$$
$$x_4 = -25/2$$

Since this body has a 6 radii length nose
$\frac{dC_N}{dx}$ is a maximum at x=2.47194
At this point

$$\frac{dC_N}{dx} = \left[\frac{4\pi}{S_R} R \frac{dR}{dx}\alpha\right]_{2.47194}$$
$$= 4\pi\alpha \quad 0.128311$$
$$= 1.61\frac{\alpha}{S_R}$$

Slender Body Theory implies that the local load distribution is linear and proportional to incidence or sinα cosα to a higher order of

accuracy. Hence if a data set containing the local normal force distribution at a number of incidences is divided through by $\sin\alpha\cos\alpha$ the distributions should collapse onto a single line. Figure 10.1.1.1 shows three such distributions at 10°, 15° and 20° of incidence. It is clear that the data collapses as expected. There is evidence that towards the rear of the ogive the non-linear component is starting to build up causing some dispersion of the points particularly at 20°. Also shown on the figure is the local normal force distribution as predicted by Slender Body Theory which shows reasonable comparison with the experimental data.

By definition Slender Body Theory should only be applied to slender bodies. There is, of course, no specific cut-off point above which the theory should not be applied, rather, a gradual decrease in accuracy with less slender bodies. It is useful, however, to have a feel for the relationship between slenderness and accuracy in practical terms. Figure 10.1.1.2 depicts three bodies each consisting of a tangent ogive nose followed by a circular cylinder body. The lengths of the tangent ogive forebodies are 2 calibres, 3 calibres and 6 calibres thus giving a range of body slenderness. Also shown on the figure are local normal force distributions as predicted by a potential method based on a source singularity panel method. It can be seen that the bluntest configuration, the 2 calibre nose, has a high peak value of local normal force and a considerable degree of load carry-over from the nose section onto the body section. The most slender configuration, the 6 calibre nose, has the lowest peak value of local normal force but, of course, the load is spread over a 6 calibre length. The carry-over load is less significant in this case. The 3 calibre nose configuration is midway between the other two in all respects.

Also shown on figure 10.1.1.2 are the corresponding Slender Body Theory predictions of local normal force distribution. Although the distribution shapes are well predicted, including the location of the load peak, the accuracy of the local magnitude reduces as the nose gets shorter. Since Slender Body Theory does not predict the carry-over load, prediction of this element also becomes worse for the shorter nose configurations. It must also be noted that if the body apex is locally blunted with a higher nose angle then Slender Body Theory will be correspondingly less accurate in this region.

The simplicity and accuracy of Slender Body Theory means that it is used extensively in the prediction of missile aerodynamic characteristics.

10.1.2 Slender body theory in the presence of multiple vortices of varying strength and position

In section 10.1.1 it was shown that it is possible to derive a simple yet accurate expression that can be used to determine the

local normal force distribution along a slender body at low incidence. At moderate incidences the non-linear terms begin to become significant particularly along the length of body aft of the forebody section. If it were possible to introduce some of these non-linear elements into the basic Slender Body Theory this might form the basis of a useful tool for modelling the flow about these configurations.

It is clear from the work contained in the earlier sections that the primary cause of the non-linear load is the pair of vortices on the lee side of the body. An attempt will now be made to include these elements into Slender Body Theory to form a more generally applicable extension.

At this stage no assumptions will be made concerning the number of vortices present nor will the assumption of symmetry be invoked.

So starting in a similar manner to the derivation of classical Slender Body Theory, CHRISTOPHER [44] shows that the axial distribution of normal force on a slender body can be given by:

$$\frac{dC_F}{d(-x)} = \frac{2i\sigma_i}{S_R}\left\{\frac{\partial}{\partial x}\oint \overline{F_1}\,d\overline{\sigma} - ie^{-i\vartheta}\frac{dS}{dx} + \sigma_i e^{-i\vartheta}\oint \frac{dF_1}{d\sigma}d\sigma\right\}$$

where F_1 is the complex potential per unit of cross-flow velocity, S is the cross sectional area, σ is the complex coordinate, σ_i is the body total incidence and θ is the body roll angle relative to the incidence plane.

Let us now consider the three parenthesised terms on the right hand side of this expression.

Firstly,

$$\oint \overline{F_1}\,d\overline{\sigma}$$

Now,

$$\oint_{C_\sigma} \overline{F_1}(\overline{\sigma})\,d\overline{\sigma} = \oint_{C_\zeta} \overline{F_1}(\overline{\zeta})\frac{d\overline{\sigma}}{d\overline{\zeta}}d\overline{\zeta}$$

where C_σ and C_ζ are the cross section perimeter contours in the σ, arbitrary section, plane and the transformed, circular section, plane.

At this stage it is possible to apply a suitable transformation to enable the treatment of non-circular bodies. So for the case of a body of elliptic cross-section we can use:

$$\overline{\sigma}(\overline{\zeta}) = \overline{\zeta} + \frac{b^2 - c^2}{4\overline{\zeta}}$$

which on differentiating with respect to $\overline{\zeta}$ gives us

$$\frac{d\overline{\sigma}}{d\overline{\zeta}} = 1 - \frac{b^2 - c^2}{4\overline{\zeta}^2}$$

For the time being let us limit our attention to the case of a circle, which requires no transformation. However, to facilitate the later incorporation of a specific transformation we shall apply an identity transformation. i.e.,

$$\frac{d\overline{\sigma}}{d\overline{\zeta}} = 1$$

This gives the result

$$\oint_{C\sigma} \overline{F}_1(\overline{\sigma})\, d\overline{\sigma} = \oint_{C_\zeta} \overline{F}_1(\overline{\zeta}) \cdot 1\, d\overline{\zeta} = \oint_{C_\zeta} \overline{F}_1(\overline{\zeta})\, d\overline{\zeta}$$

In order that we may proceed further, we must now consider the complex potential for the case of interest in detail.

The total complex potential shall be assembled from three types of component a uniform potential, a doublet and a series of point vortices. The first of these will be used to represent the onset flow field, the second will generate the flow field due to a circular cylinder in this onset flow and the third to represent a number of body vortices.

Since these complex potentials are solutions to Laplaces equation, which is linear, it is possible to superpose them to form a valid solution of Laplaces equation for a more complex flow field. The only difficulty being that a vortex image must be appropriately positioned for each body vortex if the resulting closed streamline, which represents the body circumference, is to remain circular.

So we will use:

Type	Complex potential	Flow feature
Uniform	$F = -U_\infty \sigma_i \zeta \; e^{-i\vartheta}$	Onset flow
Doublet	$F = \frac{m e^{i\vartheta}}{\zeta}$	Used with above to represent the flow about a circular cylinder
Vortex	$F = -\frac{i}{2\pi}\sum_{k=1}^{m} \Gamma_k \ln(\zeta - \zeta_k) + \frac{i}{2\pi}\sum_{k=1}^{m} \Gamma_k \ln\left(\zeta - \frac{R^2}{\overline{\zeta}_k}\right)$	m point vortices and their images

where σ_i is the total incidence.

Combining the first two elements to represent the flow about a cylinder of radius R produces:

$$F(\zeta) = -U_\infty \sigma_i \zeta \; e^{-i\vartheta} - U_\infty \sigma_i \frac{R^2}{\zeta} e^{i\vartheta}$$

and adding the point vortices and their images to produce the total potential gives us

$$F(\zeta) = -U_\infty \sigma_i \zeta \; e^{-i\vartheta} - U_\infty \sigma_i \frac{R^2}{\zeta} e^{i\vartheta} - \frac{i}{2\pi} \sum_{k=1}^{m} \Gamma_k \ln(\zeta - \zeta_k) + \frac{i}{2\pi} \sum_{k=1}^{m} \Gamma_k \ln\left(\zeta - \frac{R^2}{\overline{\zeta_k}}\right)$$

Now, using the Euler formula, $e^{i\vartheta} = \{\cos\vartheta + i\sin\vartheta\}$

$$F(\zeta) = -U_\infty \sigma_i \zeta \{\cos(-\vartheta) + i\sin(-\vartheta)\} - U_\infty \sigma_i \frac{R^2}{\zeta} \{\cos\vartheta + i\sin\vartheta\} -$$
$$\frac{i}{2\pi} \sum_{k=1}^{m} \Gamma_k \ln(\zeta - \zeta_k) + \frac{i}{2\pi} \sum_{k=1}^{m} \Gamma_k \ln\left(\zeta - \frac{R^2}{\overline{\zeta_k}}\right)$$

Using that $\sin(-\vartheta) = -\sin(\vartheta)$ and $\cos(-\vartheta) = \cos\vartheta$ and rearranging gives:

$$F(\zeta) = \left(-U_\infty \sigma_i \zeta - U_\infty \sigma_i \frac{R^2}{\zeta}\right)\cos\vartheta + i\left(U_\infty \sigma_i \zeta - U_\infty \sigma_i \frac{R^2}{\zeta}\right)\sin\vartheta -$$
$$\frac{i}{2\pi} \sum_{k=1}^{m} \Gamma_k \ln(\zeta - \zeta_k) + \frac{i}{2\pi} \sum_{k=1}^{m} \Gamma_k \ln\left(\zeta - \frac{R^2}{\overline{\zeta_k}}\right)$$

To obtain $F_1(\zeta)$, divide by $-U_\infty \sigma_i$, giving

$$F_1(\zeta) = \left(\zeta + \frac{R^2}{\zeta}\right)\cos\vartheta - i\left(\zeta - \frac{R^2}{\zeta}\right)\sin\vartheta +$$
$$\frac{i}{2\pi \; U_\infty \sigma_i} \sum_{k=1}^{m} \Gamma_k \ln(\zeta - \zeta_k) - \frac{i}{2\pi \; U_\infty \sigma_i} \sum_{k=1}^{m} \Gamma_k \ln\left(\zeta - \frac{R^2}{\overline{\zeta_k}}\right)$$

To obtain $\overline{F_1}(\zeta)$, change the sign of the imaginary terms:

$$\overline{F}_1(\zeta) = \left(\zeta + \frac{R^2}{\zeta}\right)\cos\vartheta + i\left(\zeta - \frac{R^2}{\zeta}\right)\sin\vartheta -$$
$$\frac{i}{2\pi\ U_\infty \sigma_i}\sum_{k=1}^{m}\Gamma_k \ln(\zeta - \zeta_k) + \frac{i}{2\pi\ U_\infty \sigma_i}\sum_{k=1}^{m}\Gamma_k \ln\left(\zeta - \frac{R^2}{\overline{\zeta_k}}\right)$$

To obtain $\overline{F}_1(\overline{\zeta})$, change all ζ to their conjugates, $\overline{\zeta}$:

$$\overline{F}_1(\overline{\zeta}) = \left(\overline{\zeta} + \frac{R^2}{\overline{\zeta}}\right)\cos\vartheta + i\left(\overline{\zeta} - \frac{R^2}{\overline{\zeta}}\right)\sin\vartheta -$$
$$\frac{i}{2\pi\ U_\infty \sigma_i}\sum_{k=1}^{m}\Gamma_k \ln(\overline{\zeta} - \overline{\zeta_k}) + \frac{i}{2\pi\ U_\infty \sigma_i}\sum_{k=1}^{m}\Gamma_k \ln\left(\overline{\zeta} - \frac{R^2}{\zeta_k}\right)$$

Expanding the vortex terms as a Laurent series for large $\overline{\zeta}$:

$$\overline{F}_1(\overline{\zeta}) = \left(\overline{\zeta} + \frac{R^2}{\overline{\zeta}}\right)\cos\vartheta + i\left(\overline{\zeta} - \frac{R^2}{\overline{\zeta}}\right)\sin\vartheta - \frac{i}{2\pi\ U_\infty \sigma_i}\sum_{k=1}^{m}\Gamma_k\left(\ln\overline{\zeta} - \frac{\overline{\zeta_k}}{\overline{\zeta}} - \frac{1}{2}\frac{\overline{\zeta_k}^2}{\overline{\zeta}^2} - \ldots\right) +$$
$$\frac{i}{2\pi\ U_\infty \sigma_i}\sum_{k=1}^{m}\Gamma_k\left(\ln\overline{\zeta} - \frac{R^2}{\overline{\zeta}\ \zeta_k} - \frac{1}{2}\frac{R^4}{\overline{\zeta_k}^2} - \ldots\right)$$

By taking the $\frac{1}{\overline{\zeta}}$ terms only, we obtain the residues as:

$$\overline{A_1} = R^2\cos\vartheta - iR^2\sin\vartheta + \frac{i}{2\pi\ U_\infty \sigma_i}\sum_{k=1}^{m}\Gamma_k\overline{\zeta_k} - \frac{i}{2\pi\ U_\infty \sigma_i}\sum_{k=1}^{m}\Gamma_k\frac{R^2}{\zeta_k}$$
$$= R^2(\cos\vartheta - i\sin\vartheta) + \frac{i}{2\pi\ U_\infty \sigma_i}\sum_{k=1}^{m}\Gamma_k\left(\overline{\zeta_k} - \frac{R^2}{\zeta_k}\right),$$

where $\oint_{C_{\overline{\zeta}}} \overline{F}_1(\overline{\zeta})d\overline{\zeta} = 2\pi\ i\cdot\overline{A}_1$

Now the second term from our original equation is

$$ie^{-i\vartheta}\frac{dS}{dx}$$

Since we are considering the case of a circle, the cross-sectional area is given by

$$S = \pi\ R^2$$

and so we can write

$$\frac{dS}{dx} = \frac{d\left(\pi\ R^2\right)}{dR}\frac{dR}{dx}$$

$$= 2\pi\ R\frac{dR}{dx}$$

so

$$ie^{-i\vartheta}\frac{dS}{dx} = ie^{-i\vartheta}\cdot 2\pi\ R\frac{dR}{dx}$$

$$= 2\pi\ Ri\left[\cos(-\vartheta)+i\sin(-\vartheta)\right]\frac{dR}{dx}$$

$$= 2\pi\ Ri\left[\cos\vartheta - i\sin\vartheta\right]\frac{dR}{dx}$$

$$= 2\pi\ R\left[\sin\vartheta + i\cos\vartheta\right]\frac{dR}{dx}$$

The third term in σ_i^2 is usually considered to be small and thus neglected. We shall now examine the order of terms in σ_i and their significance in the final solution to ensure that this is valid in our case.

Returning to the expression for $\frac{dC_F}{d(-x)}$

we have

$$\frac{dC_F}{d(-x)} = \frac{2i\sigma_i}{S_R}\left\{\frac{\partial}{\partial\ x}\oint \overline{F}_1 d\overline{\sigma} - ie^{-i\vartheta}\frac{dS}{dx} + \sigma_i e^{-i\vartheta}\oint\frac{dF_1}{d\sigma}d\sigma\right\} \qquad \text{-(i)}$$

where $\overline{F}_1(\zeta)$, the complex potential in the first element, is

$$\overline{F}_1(\zeta) = \left(\zeta + \frac{R^2}{\zeta}\right)\cos\vartheta + i\left(\zeta - \frac{R^2}{\zeta}\right)\sin\vartheta -$$

$$\frac{i}{2\pi\ U_\infty\sigma_i}\sum_{k=1}^{m}\Gamma_k\ln(\zeta-\zeta_k) + \frac{i}{2\pi\ U_\infty\sigma_i}\sum_{k=1}^{m}\Gamma_k\ln\left(\zeta - \frac{R^2}{\overline{\zeta}_k}\right) \qquad \text{-(ii)}$$

It can be seen that the first two terms are independent of σ_i and the other two appear to be of order $\frac{1}{\sigma_i}$. However, the vortex strength

term, Γ_k, is of order σ_i^2 and hence these last two terms are actually of order σ_i .

10.1.2.1 The first element of (i)

In expression (i) the complex potential, $\overline{F}_1(\zeta)$, is integrated with respect to the complex coordinate σ (not to be confused with the angle of attack in the incidence plane, σ_i) and differentiated with respect to x. Neither of these processes change the order of the σ_i terms.

The four terms arising from the first element in (i) are pre multiplied by the σ_i outside the bracket in (i) thus this element contributes terms of order σ_i and σ_i^2 to the complete expression. The terms in σ_i being part of the linear (standard SBT) fraction of the solution and the terms in σ_i^2 adding to the non-linear (vortex induced) fraction of the solution.

Summarising the appropriate analysis from earlier work it can be seen that the integration gives us

$$\oint \overline{F}_1 d\overline{\sigma}$$

$$= 2\pi\ iR^2(\cos\vartheta - i\sin\vartheta) + 2\pi\ i\frac{i}{2\pi\ U_\infty \sigma_i}\sum_{k=1}^{m}\Gamma_k\left(\overline{\zeta_k} - \frac{R^2}{\zeta_k}\right)$$

and the differentiation gives us

$$\frac{\partial}{\partial\ x}\oint \overline{F}_1 d\overline{\sigma}$$

$$= \underline{\left\{\left[4\pi\ R(\sin\vartheta + i\cos\vartheta)\frac{dR}{dx}\right.\right.} - \frac{1}{U_\infty \sigma_i}\sum_{k=1}^{m}\left\{\underline{\left(\overline{\zeta_k} - \frac{R^2}{\zeta_k}\right)\frac{d\Gamma_k}{dx} + \right.}$$

$$\left.\left.\underline{\Gamma_k\frac{d\overline{\zeta_k}}{dx} - \frac{2R\Gamma_k}{\zeta_k}\frac{dR}{dx} + \frac{\Gamma_k R^2}{\zeta_k^2}\frac{d\zeta_k}{dx}}\right\}\right]\right\}$$

and finally pre multiplying by the terms outside the bracket in (i) gives

$$\frac{2i\sigma_i}{S_R}\left\{\frac{\partial}{\partial\ x}\oint \overline{F}_1 d\overline{\sigma}\right\}$$

$$= \underline{\frac{8i\sigma_i\pi\ R}{S_R}\left(\sin\vartheta + i\cos\vartheta\right)\frac{dR}{dx}} - \underline{\underline{\frac{2i}{U_\infty S_R}\sum_{k=1}^{m}\left\{\left(\overline{\zeta_k} - \frac{R^2}{\zeta_k}\right)\frac{d\Gamma_k}{dx} + \Gamma_k\frac{d\overline{\zeta_k}}{dx} - \frac{2R\Gamma_k}{\zeta_k}\frac{dR}{dx} + \frac{\Gamma_k R^2}{\zeta_k^2}\frac{d\zeta_k}{dx}\right\}}}$$

The single underlined term is of order σ_i , is linear and contributes to the standard SBT part of the solution. The double underlined part is of order σ_i^2, since Γ_k, is of order σ_i^2, and contributes to the non-linear, vortex induced part of the solution.

10.1.2.2 The second element of (i)

The second term in equation (i) is independent of σ_i and hence ultimately will only contribute to the linear part of the solution.

In summary it can be show that $ie^{-i\vartheta}\frac{dS}{dx}$ is equal to

$$2\pi\ R\left[\sin\vartheta + i\cos\vartheta\right]\frac{dR}{dx}$$

and on pre multiplying by $\frac{2i\sigma_i}{S_R}$ results in

$$\frac{2i\sigma_i}{S_R}\left\{-2\pi\ R\left[\sin\vartheta + i\cos\vartheta\right]\frac{dR}{dx}\right\}$$
$$= \frac{-i4\pi\ R\sigma_i}{S_R}\left[\sin\vartheta + i\cos\vartheta\right]\frac{dR}{dx}$$

This gives us another term in σ_i which contributes to the standard linear SBT result.

10.1.2.3 The third element of (i)

This case is, in principle, similar to the first element of (i) in that it is derived from the derivative and then integral of the complex potential $F_1(\zeta)$,

where

$$F_1(\zeta)=\left(\zeta+\frac{R^2}{\zeta}\right)\cos\vartheta-i\left(\zeta-\frac{R^2}{\zeta}\right)\sin\vartheta+$$
$$\frac{i}{2\pi\ U_\infty\sigma_i}\sum_{k=1}^{m}\Gamma_k\ln(\zeta-\zeta_k)-\frac{i}{2\pi\ U_\infty\sigma_i}\sum_{k=1}^{m}\Gamma_k\ln\left(\zeta-\frac{R^2}{\overline{\zeta}_k}\right)$$

Again it can be seen that the first two terms are independent of σ_i and the other two appear to be of order $\frac{1}{\sigma_i}$. As before, the vortex strength term, Γ_k, is of order σ_i^2 and hence these last two terms are actually of order σ_i .

The order of these terms remains unchanged when incorporated into the integral of the third term of equation (i), $\oint\frac{dF_1}{d\sigma}d\sigma$. However, the integral is pre multiplied by $\sigma_i e^{-i\vartheta}$ which increments the order of each σ_i term and the $\frac{2i\sigma_i}{S_R}$ term outside the bracket increments the order one step further to give terms in σ_i^2 & σ_i^3.

The σ_i^3 term arises from the vortex dependent terms in the complex potential i.e.,

$$\frac{i}{2\pi\ U_\infty\sigma_i}\sum_{k=1}^{m}\Gamma_k\ln(\zeta-\zeta_k)-\frac{i}{2\pi\ U_\infty\sigma_i}\sum_{k=1}^{m}\Gamma_k\ln\left(\zeta-\frac{R^2}{\overline{\zeta}_k}\right)$$

This term results in a small contribution to the non-linear part of the final solution.

The σ_i^2 term results from the remaining terms i.e.,

$$\left(\zeta+\frac{R^2}{\zeta}\right)\cos\vartheta-i\left(\zeta-\frac{R^2}{\zeta}\right)\sin\vartheta$$

This term, although strictly a non-linear term, can be thought of as adding to the standard SBT terms in the final result since it is independent of Γ_k. The accuracy of SBT and its dependence upon σ_i is well established, hence in applications, where SBT is sufficiently accurate or the linear SBT part of the solution is not of interest, the above mentioned σ_i^2 terms need not be included.

10.1.2.4 Detailed expansion of the third element of (i)

Now considering the term $\oint \frac{dF_1}{d\sigma} d\sigma$ in more detail we can firstly substitute ζ for σ since we are only considering the identity transformation. Thus the expression becomes $\oint \frac{dF_1}{d\zeta} d\zeta$. Starting with the complex potential, F_1:

$$F_1(\zeta) = \left(\zeta + \frac{R^2}{\zeta}\right)\cos\vartheta - i\left(\zeta - \frac{R^2}{\zeta}\right)\sin\vartheta +$$
$$\frac{i}{2\pi\ U_\infty \sigma_i}\sum_{k=1}^{m}\Gamma_k \ln(\zeta - \zeta_k) - \frac{i}{2\pi\ U_\infty \sigma_i}\sum_{k=1}^{m}\Gamma_k \ln\left(\zeta - \frac{R^2}{\overline{\zeta_k}}\right)$$

We can find $\frac{dF_1}{d\zeta}$ by differentiating each of the four terms in turn:

$$\frac{d}{d\zeta}\left(\zeta + \frac{R^2}{\zeta}\right)\cos\vartheta = \left(1 - \frac{R^2}{\zeta^2}\right)\cos\vartheta$$

$$-\frac{d}{d\zeta} i\left(\zeta - \frac{R^2}{\zeta}\right)\sin\vartheta = -i\left(1 + \frac{R^2}{\zeta^2}\right)\sin\vartheta$$

$$\frac{d}{d\zeta}\left\{\frac{i}{2\pi\ U_\infty \sigma_i}\sum_{k=1}^{m}\Gamma_k \ln(\zeta - \zeta_k)\right\} = \frac{i}{2\pi\ U_\infty \sigma_i}\sum_{k=1}^{m}\Gamma_k \frac{1}{\zeta - \zeta_k}$$

$$-\frac{d}{d\zeta}\left\{\frac{i}{2\pi\ U_\infty \sigma_i}\sum_{k=1}^{m}\Gamma_k \ln\left(\zeta - \frac{R^2}{\overline{\zeta_k}}\right)\right\} = \frac{-i}{2\pi\ U_\infty \sigma_i}\sum_{k=1}^{m}\Gamma_k \frac{1}{\zeta - \frac{R^2}{\overline{\zeta_k}}}$$

Combining these terms gives us:

$$\frac{dF_1(\zeta)}{d\zeta} = \left(1 - \frac{R^2}{\zeta^2}\right)\cos\vartheta - i\left(1 + \frac{R^2}{\zeta^2}\right)\sin\vartheta$$
$$+\frac{i}{2\pi\ U_\infty \sigma_i}\sum_{k=1}^{m}\Gamma_k \frac{1}{\zeta - \zeta_k} - \frac{i}{2\pi\ U_\infty \sigma_i}\sum_{k=1}^{m}\Gamma_k \frac{1}{\zeta - \frac{R^2}{\overline{\zeta_k}}}$$

The method of residues can now be used to evaluate the integral $\oint \frac{dF_1}{d\zeta} d\zeta$ as follows:

The residues for the vortex terms can be evaluated at their simple poles at ζ_k and $\frac{R^2}{\overline{\zeta_k}^2}$ since $\text{Res}_{\zeta=a} f(\zeta) = \frac{p(a)}{q'(a)}$ where $f(\zeta) = \frac{p(\zeta)}{q(\zeta)}$ and $p(a) \neq 0$ & $q(\zeta)$ is a simple zero at a.

Thus for

$$f(\zeta) = \frac{1}{\zeta - \zeta_k}$$
$$p(\zeta) = 1 \quad \& \quad q(\zeta) = (\zeta - \zeta_k)$$
$$\therefore q'(\zeta) = 1$$

Hence

$$\begin{aligned}\text{Res}_{\zeta=\zeta_k} f(\zeta) &= \frac{p(\zeta_k)}{q'(\zeta_k)} \\ &= \frac{1}{1} \\ &= 1\end{aligned}$$

and similarly for

$$f(\zeta) = \frac{1}{\zeta - \frac{R^2}{\overline{\zeta_k}}}$$
$$p(\zeta) = 1 \qquad \& \qquad q(\zeta) = \zeta - \frac{R^2}{\overline{\zeta_k}}$$
$$\therefore q'(\zeta) = 1$$

So

$$\begin{aligned}\text{Res}_{\zeta=\frac{R^2}{\overline{\zeta_k}}} f(\zeta) &= \frac{p\left(\frac{R^2}{\overline{\zeta_k}}\right)}{q'\left(\frac{R^2}{\overline{\zeta_k}}\right)} \\ &= \frac{1}{1} \\ &= 1\end{aligned}$$

The residues for the first two terms are found by extracting the terms in $\frac{1}{\zeta}$ of which, in this case, there are none.

So the total residues are given by:

$$\begin{aligned}\overline{A_1} &= \frac{i}{2\pi\ U_\infty \sigma_i} \sum_{k=1}^{m} \Gamma_k . 1 - \frac{i}{2\pi\ U_\infty \sigma_i} \sum_{k=1}^{m} \Gamma_k . 1 \\ &= 0\end{aligned}$$

and hence

$$\oint \frac{dF_1}{d\zeta} d\zeta = 2\pi \ i.\overline{A_1}$$
$$= 0$$

The implication of this is that the order of the σ_i terms are irrelevant here since the integral is equal to zero and hence need not be considered.

So returning to the task in hand, assembling the remaining terms gives us

$$\frac{dC_F}{d(-x)} = \frac{2i\sigma_i}{S_R}\left\{\frac{\partial}{\partial x}\oint \overline{F_1} d\overline{\sigma} - ie^{-i\vartheta}\frac{dS}{dx}\right\}$$

$$= \frac{2i\sigma_i}{S_R}\left\{\frac{\partial}{\partial x}\left[2\pi \ iR^2(\cos\vartheta - i\sin\vartheta) + 2\pi \ i\frac{i}{2\pi \ U_\infty \sigma_i}\sum_{k=1}^{m}\Gamma_k\left(\overline{\zeta_k} - \frac{R^2}{\zeta_k}\right)\right] - 2\pi \ R[\sin\vartheta + i\cos\vartheta]\frac{dR}{dx}\right\}$$

$$= \frac{2i\sigma_i}{S_R}\left\{\frac{\partial}{\partial x}\left[2\pi \ iR^2(\sin\vartheta + i\cos\vartheta) - \frac{1}{U_\infty \sigma_i}\sum_{k=1}^{m}\Gamma_k\left(\overline{\zeta_k} - \frac{R^2}{\zeta_k}\right)\right] - 2\pi \ R[\sin\vartheta + i\cos\vartheta]\frac{dR}{dx}\right\}$$

$$= \frac{2i\sigma_i}{S_R}\left\{\frac{\partial}{\partial x}\left[2\pi \ iR^2(\sin\vartheta + i\cos\vartheta) - \frac{1}{U_\infty \sigma_i}\left(\sum_{k=1}^{m}\Gamma_k\overline{\zeta_k} - \sum_{k=1}^{m}\Gamma_k\frac{R^2}{\zeta_k}\right)\right] - 2\pi \ R[\sin\vartheta + i\cos\vartheta]\frac{dR}{dx}\right\}$$

$$= \frac{2i\sigma_i}{S_R}\left\{\frac{\partial}{\partial x}\left[P - \frac{1}{U_\infty \sigma_i}(Q)\right] - 2\pi \ R[\sin\vartheta + i\cos\vartheta]\frac{dR}{dx}\right\}$$

where

$$P = 2\pi \ iR^2(\sin\vartheta + i\cos\vartheta)$$
$$Q = \left(\sum_{k=1}^{m}\Gamma_k\overline{\zeta_k} - \sum_{k=1}^{m}\Gamma_k\frac{R^2}{\zeta_k}\right) \quad .$$

Differentiating the terms in the square bracket with respect to x we have

$$\frac{\partial P}{\partial x} = \frac{\partial\left(2\pi R^2(\sin\vartheta + i\cos\vartheta)\right)}{\partial x}$$
$$= 4\pi R(\sin\vartheta + i\cos\vartheta)\frac{dR}{dx}$$

and

$$\frac{\partial Q}{\partial x} = \frac{\partial\left(\sum_{k=1}^{m}\left(\Gamma_k\overline{\zeta_k} - \Gamma_k\frac{R^2}{\zeta_k}\right)\right)}{\partial x}$$
$$= \sum_{k=1}^{m}\left\{\left(\overline{\zeta_k} - \frac{R^2}{\zeta_k}\right)\frac{d\Gamma_k}{dx} + \Gamma_k\frac{d\overline{\zeta_k}}{dx} - \frac{2R\Gamma_k}{\zeta_k}\frac{dR}{dx} + \frac{\Gamma_k R^2}{\zeta_k^2}\frac{d\zeta_k}{dx}\right\}$$

So assembling all the terms we get

$$\frac{dC_F}{d(-x)} = \frac{2i\sigma_i}{S_R}\left\{\left[4\pi R(\sin\vartheta + i\cos\vartheta)\frac{dR}{dx} - \frac{1}{U_\infty\sigma_i}\sum_{k=1}^{m}\left\{\left(\overline{\zeta_k} - \frac{R^2}{\zeta_k}\right)\frac{d\Gamma_k}{dx} + \right.\right.\right.$$
$$\left.\left.\left.\Gamma_k\frac{d\overline{\zeta_k}}{dx} - \frac{2R\Gamma_k}{\zeta_k}\frac{dR}{dx} + \frac{\Gamma_k R^2}{\zeta_k^2}\frac{d\zeta_k}{dx}\right\}\right] - 2\pi R[\sin\vartheta + i\cos\vartheta]\frac{dR}{dx}\right\},$$

and then putting $\sigma_i\sin\vartheta = \alpha$ and $\sigma_i\cos\vartheta = \beta$ and rearranging the expression produces

$$\frac{dC_F}{d(-x)} = \frac{2}{S_R}\left\{\left[4\pi R(i\alpha - \beta)\frac{dR}{dx} - \frac{i}{U_\infty}\sum_{k=1}^{m}\left\{\left(\overline{\zeta_k} - \frac{R^2}{\zeta_k}\right)\frac{d\Gamma_k}{dx} + \right.\right.\right.$$
$$\left.\left.\left.\Gamma_k\frac{d\overline{\zeta_k}}{dx} - \frac{2R\Gamma_k}{\zeta_k}\frac{dR}{dx} + \frac{\Gamma_k R^2}{\zeta_k^2}\frac{d\zeta_k}{dx}\right\}\right] - 2\pi R[i\alpha - \beta]\frac{dR}{dx}\right\}$$

$$= -\frac{8\pi R}{S_R}\frac{dR}{dx}\beta + \frac{4\pi R}{S_R}\frac{dR}{dx}\beta + i\left\{\frac{8\pi R}{S_R}\frac{dR}{dx}\alpha - \frac{4\pi R}{S_R}\frac{dR}{dx}\alpha - \right.$$
$$\left.\frac{2}{S_R U_\infty}\sum_{k=1}^{m}\left\{\left(\overline{\zeta_k} - \frac{R^2}{\zeta_k}\right)\frac{d\Gamma_k}{dx} + \Gamma_k\frac{d\overline{\zeta_k}}{dx} - \frac{2R\Gamma_k}{\zeta_k}\frac{dR}{dx} + \frac{\Gamma_k R^2}{\zeta_k^2}\frac{d\zeta_k}{dx}\right\}\right\}$$

$$= -\frac{4\pi R}{S_R}\frac{dR}{dx}\beta + i\frac{4\pi R}{S_R}\frac{dR}{dx}\alpha -$$
$$i\frac{2}{S_R U_\infty}\sum_{k=1}^{m}\left\{\left(\overline{\zeta_k} - \frac{R^2}{\zeta_k}\right)\frac{d\Gamma_k}{dx} + \Gamma_k\frac{d\overline{\zeta_k}}{dx} - \frac{2R\Gamma_k}{\zeta_k}\frac{dR}{dx} + \frac{\Gamma_k R^2}{\zeta_k^2}\frac{d\zeta_k}{dx}\right\}$$

The first two terms in this expression are clearly recognisable as the linear terms for the local normal and side force distributions as given by Classical Slender Body Theory.

The third term clearly contains the terms concerning the vortices and their images. As a simple check if the vortices were assumed to be of zero strength both $\Gamma_{k=1\text{ to }m}$ and $\left(\frac{d\Gamma_k}{dx}\right)_{k=1\text{ to }m}$ would be zero and hence the expression reduces to the classical Slender Body Theory result.

Forces acting in the i direction act normal to the body such as the term in α and forces acting in the real direction act laterally such as the term in β. Although the non-linear term is premultiplied by i the presence of other complex terms means in general it will have components in both directions.

Considering the non-linear term in a little more detail we see that it is a function of not just the strengths and positions of the vortices at any point along the body but also the rate of change of both strengths and positions. It is also a function of the local rate of change of body radius.

Although more complicated than Classical Slender Body Theory this result is still relatively simple and, accuracy permitting, will form the basis of this simple model.

10.1.3 The constant position and strength symmetric vortex pair case (Sack's result)

SACKS [45] developed formulae for the forces and moments due to vortex interference on slender wing-body-tail combinations of general cross section in terms of the positions and strengths of the shed vortices.

Sacks considers a slender body-canard combination. The main objective was to find an expression for the normal force induced on the section of the body aft of the canard by the canard vortices. The effect of the body vortices is ignored and the body radius aft of the trailing edge of the canard is assumed constant. Since the vortices cease to be fed once they leave the trailing edge of the canard they can be assumed to be constant.

Figure 10.1.3.1 shows the notation used in Sacks' result. In his notation the body force is given as

$$Y_l - iL_l = -i\rho\ U_0\left[\left(\sum_{k=1}^{m}\Gamma_k\overline{\sigma_{k_r}}\right)_{x=l} - \left(\sum_{k=1}^{m}\Gamma_k\overline{\sigma_{k_r}}\right)_{x=x_{TE}}\right]$$

Sacks summarises this expression thus:

"The lateral force Y_l $+iL_l$ due to each vortex of strength Γ shed from a forward wing of a slender wing-body-trail combination in steady straight flight is equal to the change, from wing trailing edge to base of the airplane, of the quantity $i\rho U_0\Gamma\sigma_r$ where σ_r is the (complex) distance between the vortex and the image in the plane in which the body cross section is mapped onto a circle while leaving the flow field at infinity unchanged."

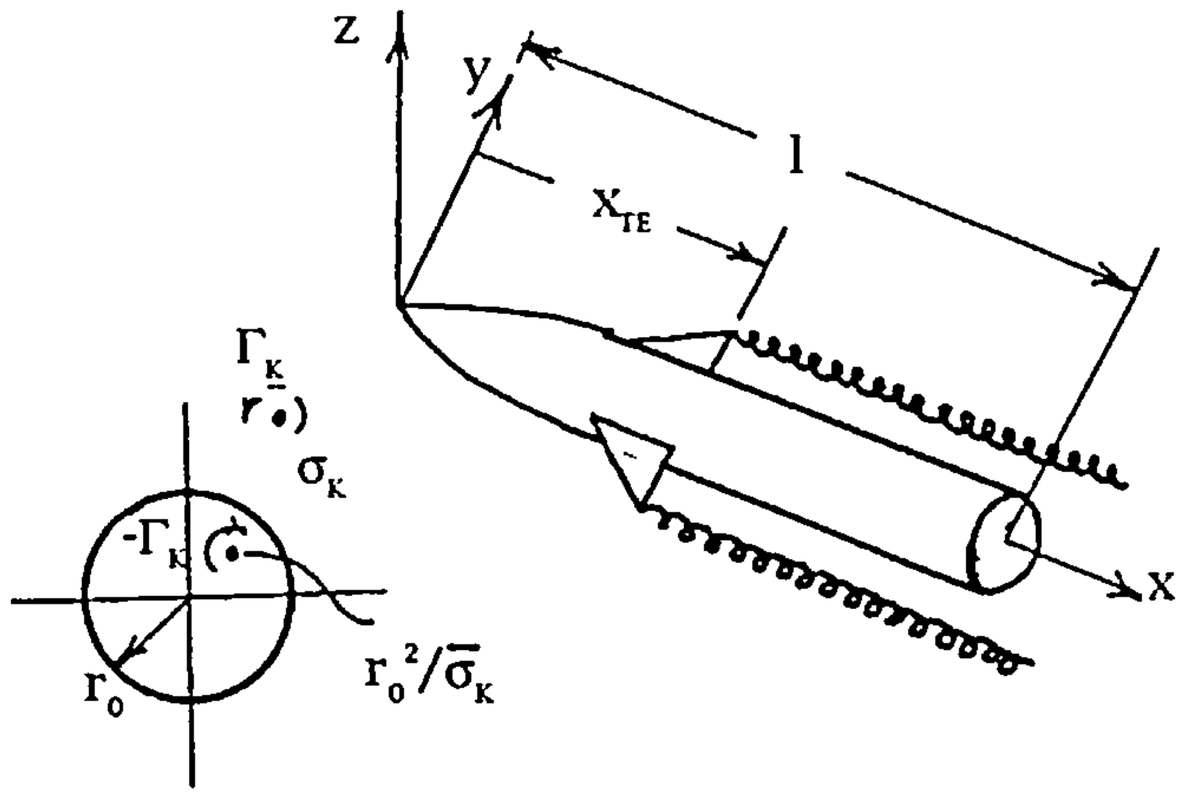

Figure 10.1.3.1

This case ought to be a special case of the more general result derived in 10.1.2 above.

So starting from

$$\frac{dC_F}{d(-x)} = -\frac{4\pi}{S_R}\frac{R}{dx}\frac{dR}{dx}\beta + i\frac{4\pi}{S_R}\frac{R}{dx}\frac{dR}{dx}\alpha$$

$$-i\frac{2}{S_R U_\infty}\sum_{k=1}^{m}\left\{\left(\overline{\zeta_k} - \frac{R^2}{\zeta_k}\right)\frac{d\Gamma_k}{dx} + \Gamma_k\frac{d\overline{\zeta_k}}{dx} - \frac{2R\Gamma_k}{\zeta_k}\frac{dR}{dx} + \frac{\Gamma_k R^2}{\zeta_k^2}\frac{d\zeta_k}{dx}\right\}$$

But in this case R=constant

& Γ_k=constant,

giving

$$\frac{dC_F}{d(-x)} = -i\frac{2}{S_R U_\infty}\sum_{k=1}^{m}\left\{\Gamma_k\frac{d\overline{\zeta_k}}{dx} + \frac{\Gamma_k R^2}{\zeta_k^2}\frac{d\zeta_k}{dx}\right\}.$$

Integrating from the wing trailing edge at x_{TE} to the base of the body:

$$C_F = \int_{x_l}^{x_{TE}} \frac{dC_F}{d(-x)} dx$$

$$= -\frac{i2}{S_R U_\infty} \left\{ \sum_{k=1}^{m} \Gamma_k \int_{x_l}^{x_{TE}} \frac{d\overline{\zeta_k}}{dx} dx + \sum_{k=1}^{m} \Gamma_k R^2 \int_{x_l}^{x_{TE}} \frac{1}{\zeta_k^2} \frac{d\zeta_k}{dx} dx \right\}$$

$$= -\frac{i2}{S_R U_\infty} \left\{ \sum_{k=1}^{m} \Gamma_k \left(\overline{\zeta_{k_{xl}}} - \overline{\zeta_{k_{xTE}}} \right) + \sum_{k=1}^{m} \Gamma_k R^2 \left(-\frac{1}{\zeta_{k_{xl}}} + \frac{1}{\zeta_{k_{xTE}}} \right) \right\}$$

$$= -\frac{i2}{S_R U_\infty} \left\{ \sum_{k=1}^{m} \Gamma_k \left(\overline{\zeta_k} - \frac{R^2}{\overline{\zeta}_k} \right)_{x_l} - \sum_{k=1}^{m} \Gamma_k \left(\overline{\zeta_k} - \frac{R^2}{\zeta_k} \right)_{x_{TE}} \right\}$$

Putting $\overline{\zeta_k} - \frac{R^2}{\zeta_k} = \overline{\zeta_{k_R}}$, the relative distance between a vortex and its image, gives us:

$$C_F = -\frac{i2}{S_R U_\infty} \left\{ \left(\sum_{k=1}^{m} \Gamma_k \overline{\zeta_{k_R}} \right)_{x_l} - \left(\sum_{k=1}^{m} \Gamma_k \overline{\zeta_{k_R}} \right)_{x_{TE}} \right\}.$$

Re-dimensionalising

$$F = -i\rho \; U_\infty \left\{ \left(\sum_{k=1}^{m} \Gamma_k \overline{\zeta_{k_R}} \right)_{x_l} - \left(\sum_{k=1}^{m} \Gamma_k \overline{\zeta_{k_R}} \right)_{x_{TE}} \right\}$$

as in equation (12) of Sacks [45]

Although expressed in the form of a total load, Sack's result has been used to derive a load distribution, thus;

$$\frac{\Delta F}{\Delta x} = -i\rho \; U_\infty \frac{\Delta \sum \Gamma_k \left(\overline{\zeta_k} - \frac{R^2}{\zeta_k} \right)}{\Delta x}$$

$$\frac{\Delta C_R}{\Delta (x)} = -\frac{2}{S_R U_\infty} \frac{\Delta \sum \Gamma_k \left(\overline{\zeta_k} - \frac{R^2}{\zeta_k} \right)}{\Delta x}$$

For 2 vortices

$$\frac{\Delta C_R}{\Delta x} = -\frac{i2}{S_R U_\infty} \left\{ \frac{\Delta \left[\Gamma_1 \left(\overline{\zeta_1} - \frac{R^2}{\zeta_1} \right) + \Gamma_2 \left(\overline{\zeta_2} - \frac{R^2}{\zeta_2} \right) \right]}{\Delta x} \right\}$$

Putting $\zeta_2 = -\overline{\zeta_1}$ & $\Gamma_2 = -\Gamma_1$

$$\frac{\Delta C_R}{\Delta x} = -\frac{i2}{S_R U_\infty}\left\{\frac{\Delta\left[\Gamma_1\left(\overline{\zeta_1} - \frac{R^2}{\zeta_1}\right) - \Gamma_1\left(-\zeta_1 - \frac{R^2}{\overline{\zeta_1}}\right)\right]}{\Delta x}\right\}$$

$$\zeta = \xi + i\eta \quad \& \quad \overline{\zeta} = \xi - i\eta$$

$$\frac{\Delta C_R}{\Delta x} = -\frac{i2\Gamma_1}{S_R U_\infty}\left\{\frac{\Delta\left[\xi_1 - i\eta_1 - \frac{R^2}{(\xi_1 + i\eta_1)}\frac{(\xi_1 - i\eta_1)}{(\xi_1 - i\eta_1)} - (-\xi_1 - i\eta_1) - \frac{R^2}{(\xi - i\eta_1)}\frac{(\xi_1 + i\eta_1)}{(\xi_1 + i\eta_1)}\right]}{\Delta x}\right\}$$

$$= -\frac{i2\Gamma_1}{S_R U_\infty \Delta x}\left\{\Delta\left[2\xi_1 - \frac{R^2(\xi_1 - i\eta_1)}{\xi_1^2 + \eta_1^2} - \frac{R^2(\xi_1 + i\eta_1)}{\xi_1^2 + \eta_1^2}\right]\right\}$$

$$= \frac{-i2\Gamma}{S_R U_\infty}\left\{\frac{\Delta\left[2\xi - \frac{2R^2\xi}{\xi^2 + \eta^2}\right]}{\Delta x}\right\}$$

Since Sacks assumes, in his derivation, that Γ is constant with x, Γ can be taken outside the bracket. Many authors have subsequently used this result with $\Gamma = f(x)$ which violates one of the basic assumptions. Here the expression is:

$$\frac{\Delta C_R}{\Delta x} = -\frac{i2}{S_R U_\infty}\left\{\frac{\Delta\Gamma\left[2\xi - \frac{2R^2\xi}{\xi^2 + \eta^2}\right]}{\Delta x}\right\}$$

Now considering my more general result but assuming Γ and R are constant (as in Sacks analysis) we get:

$$\frac{dC_F}{d(-x)} = -i\frac{2}{S_R U_\infty}\sum_{k=1}^{m}\left\{\Gamma_k\frac{d\overline{\zeta_k}}{dx} + \frac{\Gamma_k R^2}{\zeta_k^2}\frac{d\zeta_k}{dx}\right\}$$

For a pair of vortices:

$$= -i\frac{2}{S_R U_\infty}\left\{\Gamma_1\frac{d\overline{\zeta_1}}{dx} + \frac{\Gamma_1 R^2}{\zeta_1^2}\frac{d\zeta_1}{dx} + \Gamma_2\frac{d\overline{\zeta_2}}{dx} + \frac{\Gamma_2 R^2}{\zeta_2^2}\frac{d\zeta_2}{dx}\right\}$$

Assuming Γ_2=-Γ_1 and $\zeta_2 = -\overline{\zeta_1}$

$$= -i\frac{2}{S_R U_\infty}\left\{\Gamma_1\frac{d\overline{\zeta_1}}{dx}+\frac{\Gamma_1 R^2}{\zeta_1^{\,2}}\frac{d\zeta_1}{dx}+\Gamma_1\frac{d\zeta_1}{dx}+\frac{\Gamma_1 R^2}{\left(-\overline{\zeta}\right)^2}\frac{d\overline{\zeta_1}}{dx}\right\}$$

putting $\zeta = \xi + i\eta$

$$= -i\frac{2\Gamma}{S_R U_\infty}\left\{\frac{d(\xi - i\eta)}{dx}+\frac{R^2}{(\xi+i\eta)^2}\frac{d(\xi+i\eta)_1}{dx}+\frac{d(\xi+i\eta)}{dx}+\frac{R^2}{(\xi-i\eta)^2}\frac{d(\xi-i\eta)_1}{dx}\right\}$$

$$= -i\frac{2\Gamma}{S_R U_\infty}\left\{\frac{d\xi}{dx}-i\frac{d\eta}{dx}+\frac{R^2}{(\xi+i\eta)^2}\left[\frac{d\xi}{dx}+i\frac{d\eta}{dx}\right]+\frac{d\xi}{dx}+i\frac{d\eta}{dx}+\frac{R^2}{(\xi-i\eta)^2}\left[\frac{d\xi}{dx}-i\frac{d\eta}{dx}\right]\right\}$$

$$= -i\frac{2\Gamma}{S_R U_\infty}\left\{2\frac{d\xi}{dx}+\frac{R^2}{(\xi+i\eta)^2}\left[\frac{d\xi}{dx}+i\frac{d\eta}{dx}\right]+\frac{R^2}{(\xi-i\eta)^2}\left[\frac{d\xi}{dx}-i\frac{d\eta}{dx}\right]\right\}$$

$$= -i\frac{2\Gamma}{S_R U_\infty}\left\{2\frac{d\xi}{dx}+\frac{R^2}{(\xi+i\eta)^2}\frac{(\xi-i\eta)^2}{(\xi-i\eta)^2}\left[\frac{d\xi}{dx}+i\frac{d\eta}{dx}\right]+\frac{R^2}{(\xi-i\eta)^2}\frac{(\xi-i\eta)^2}{(\xi-i\eta)^2}\left[\frac{d\xi}{dx}-i\frac{d\eta}{dx}\right]\right\}$$

$$= -i\frac{2\Gamma}{S_R U_\infty}\left\{2\frac{d\xi}{dx}+\frac{R^2(\xi-i\eta)^2}{(\xi^2+\eta^2)^2}\left[\frac{d\xi}{dx}+i\frac{d\eta}{dx}\right]+\frac{R^2(\xi-i\eta)^2}{(\xi^2+\eta^2)^2}\left[\frac{d\xi}{dx}-i\frac{d\eta}{dx}\right]\right\}$$

$$= -i\frac{2\Gamma}{S_R U_\infty}\left\{2\frac{d\xi}{dx}+\frac{R^2}{(\xi^2+\eta^2)^2}(\xi^2-2i\eta\xi\ \ -\eta^2)\left[\frac{d\xi}{dx}+i\frac{d\eta}{dx}\right]\right.$$
$$\left.+\frac{R^2}{(\xi^2+\eta^2)^2}(\xi^2+2i\eta\xi\ \ -\eta^2)\left[\frac{d\xi}{dx}-i\frac{d\eta}{dx}\right]\right\}$$

$$= -\frac{i2\Gamma}{S_R U_\infty}\left\{2\frac{d\xi}{dx}+\frac{R^2}{(\xi^2+\eta^2)^2}\left(\xi^2\frac{d\xi}{dx}+i\xi^2\frac{d\eta}{dx}-2i\eta\xi\ \ \frac{d\xi}{dx}+2\eta\xi\ \ \frac{d\eta}{dx}\right.\right.$$
$$-\eta^2\frac{d\xi}{dx}-\eta^2 i\frac{d\eta}{dx}+\xi^2\frac{d\xi}{dx}+2i\eta\xi\ \ \frac{d\xi}{dx}-\eta^2\frac{d\xi}{dx}$$
$$\left.\left.-i\xi^2\frac{d\eta}{dx}+2\eta\xi\ \ \frac{d\eta}{dx}+\eta^2 i\frac{d\eta}{dx}\right\}\right)$$

$$= -\frac{i2\Gamma}{S_R U_\infty}\left\{2\frac{d\xi}{dx} + \frac{R^2}{(\xi^2+\eta^2)^2}\left(\frac{d\xi}{dx}[\xi^2 - 2i\eta\xi \quad -\eta^2 + \xi^2 + 2i\eta\xi \quad -\eta^2]\right.\right.$$
$$\left.\left. + \frac{d\eta}{dx}[i\xi^2 + 2\eta\xi \quad -\eta^2 i - \xi^2 + 2\eta\xi \quad +\eta^2 i]\right)\right\}$$

$$= -\frac{i4\Gamma}{S_R U_\infty}\left\{\frac{d\xi}{dx} + \frac{R^2}{(\xi^2+\eta^2)^2}\left(\frac{d\xi}{dx}(\xi^2+\eta^2) + \frac{d\eta}{dx}2\eta\xi \quad \right)\right\}$$

This compares with the expansion of the general result with terms in $\frac{d\Gamma}{dx}$ and $\frac{dR}{dx} = 0$.

This result represents the differential expression for Sacks incremental equation. They are equivalent since, as shown earlier, the integration of the general result gives Sacks result.

Note that this result only applies when Γ and R are constant. Hence the result cannot be applied to body vortices which grow in strength with x.

10.1.4 The variable strength and position symmetric pair case

Although we have derived the fully general result for the body load distribution under the influence of m vortices, from the work in earlier sections we know that not only are we only likely to see only 2 body vortices but they will be symmetrically disposed about the incidence plane. It is thus possible to further simplify the result.

Before attempting this simplification it is useful to first expand the general result :

$$\frac{dC_F}{d(-x)} = \underline{-\frac{4\pi}{S_R}\frac{R}{dx}\frac{dR}{dx}\beta + i\frac{4\pi}{S_R}\frac{R}{dx}\frac{dR}{dx}\alpha} \underline{\underline{-i\frac{2}{S_R U_\infty}\sum_{k=1}^{m}\left\{\left(\overline{\zeta_k} - \frac{R^2}{\zeta_k}\right)\frac{d\Gamma_k}{dx} + \Gamma_k\frac{d\overline{\zeta_k}}{dx} - \frac{2R\Gamma_k}{\zeta_k}\frac{dR}{dx} + \frac{\Gamma_k R^2}{\zeta_k^2}\frac{d\zeta_k}{dx}\right\}}}$$

$$= \underline{\text{Linear terms}} + \underline{\underline{\text{Non - linear terms}}}$$

Considering the first of the non-linear terms, i.e.

$$\left(\overline{\zeta_k} - \frac{R^2}{\zeta_k}\right)\frac{d\Gamma_k}{dx}$$

$$= \left(\xi_k - i\eta_k - \frac{R^2}{(\xi_k + i\eta_k)}\right)\frac{d\Gamma_k}{dx}$$

we may separate the real & imaginary parts to obtain

$$= \left\{ \xi_k - i\eta_k - \frac{R^2}{(\xi_k + i\eta_k)} \frac{(\xi_k - i\eta_k)}{(\xi_k - i\eta_k)} \right\} \frac{d\Gamma_k}{dx}$$

$$= \left\{ \xi_k - i\eta_k - \frac{R^2(\xi_k - i\eta_k)}{\xi^2 - i\xi_k\eta_k + i\xi_k\eta_k - i^2\eta_k^2} \right\} \frac{d\Gamma_k}{dx}$$

$$= \left\{ \xi_k - i\eta_k - \frac{R^2(\xi_k - i\eta_k)}{\xi^2 + \eta_k^2} \right\} \frac{d\Gamma_k}{dx}$$

$$= \left\{ \xi_k - \frac{R^2\xi_k}{\xi^2 + \eta_k^2} - i\left(\eta_k - \frac{R^2\eta_k}{\xi^2 + \eta_k^2} \right) \right\} \frac{d\Gamma_k}{dx}$$

The second term is given by $\Gamma_k \frac{d\overline{\zeta_k}}{dx}$

$$= \Gamma_k \frac{d(\xi_k - i\eta)}{dx}$$

$$= \Gamma_k \left(\frac{d\xi_k}{dx} - i\frac{d\eta_k}{dx} \right)$$

The third term is given by $\frac{2R\Gamma_k}{\zeta_k} \frac{dR}{dx}$

$$= \frac{2R\Gamma_k}{\xi_k + i\eta_k} \frac{dR}{dx}$$

$$= \frac{2R\Gamma_k}{(\xi_k + i\eta_k)} \frac{(\xi_k - i\eta_k)}{(\xi_k - i\eta_k)} \frac{dR}{dx}$$

$$= \frac{2R\Gamma_k(\xi_k - i\eta_k)}{\xi_k^2 - i\eta_k\xi_k + i\eta_k\xi_k - i^2\eta_k^2} \frac{dR}{dx}$$

$$= \frac{2R\Gamma_k(\xi_k - i\eta_k)}{\xi_k^2 + \eta_k^2} \frac{dR}{dx}$$

$$= \frac{2R\Gamma_k}{\xi_k^2 + \eta_k^2} (\xi_k - i\eta_k) \frac{dR}{dx}$$

The fourth term is $\frac{\Gamma_k R^2}{\zeta_k^2} \frac{d\zeta_k}{dx}$

$$= \frac{\Gamma_k R^2}{(\xi_k + i\eta_k)^2} \frac{d(\xi_k + i\eta_k)}{dx}$$

$$= \frac{\Gamma_k R^2}{(\xi_k + i\eta_k)^2} \frac{(\xi_k - i\eta_k)^2}{(\xi_k - i\eta_k)^2} \left\{ \frac{d\xi_k}{dx} + i\frac{d\eta_k}{dx} \right\}$$

$$= \frac{\Gamma_k R^2 (\xi_k^2 - i\eta_k\xi_k - i\eta_k\xi_k + i^2\eta_k^2)}{(\xi_k^2 + \eta_k^2)^2} \left\{ \frac{d\xi_k}{dx} + i\frac{d\eta_k}{dx} \right\}$$

$$= \frac{\Gamma_k R^2}{(\xi_k^2 + \eta_k^2)^2} \{(\xi_k^2 - \eta_k^2) - i2\eta_k\xi_k\} \left\{ \frac{d\xi_k}{dx} + i\frac{d\eta_k}{dx} \right\}$$

$$= \frac{\Gamma_k R^2}{(\xi_k^2 + \eta_k^2)^2} \left\{ (\xi_k^2 - \eta_k^2)\frac{d\xi_k}{dx} + i(\xi_k^2 - \eta_k^2)\frac{d\eta_k}{dx} - i2\eta_k\xi_k\frac{d\xi_k}{dx} - i^2 2\eta_k\xi_k\frac{d\eta_k}{dx} \right\}$$

$$= \frac{\Gamma_k R^2}{(\xi_k^2 + \eta_k^2)^2} \left\{ \left[(\xi_k^2 - \eta_k^2)\frac{d\xi_k}{dx} + 2\eta_k\xi_k\frac{d\eta_k}{dx} \right] + i\left[(\xi_k^2 - \eta_k^2)\frac{d\eta_k}{dx} - 2\eta_k\xi_k\frac{d\xi_k}{dx} \right] \right\}$$

Concentrating on the non-linear terms we have:

$$\frac{dC_{F_{NL}}}{d(-x)} = -i\frac{2}{S_R U_\infty} \sum_{k=1}^{m} \left\{ \left[\xi_k - \frac{R^2\xi_k}{\xi_k^2 + \eta_k^2} - i\left(\eta_k - \frac{R^2\eta_k}{\xi_k^2 + \eta_k^2} \right) \right] \frac{d\Gamma_k}{dx} \right.$$
$$+ \Gamma_k \left(\frac{d\xi_k}{dx} - i\frac{d\eta_k}{dx} \right) - \frac{2R\Gamma_k}{\xi_k^2 + \eta_k^2}(\xi_k - i\eta_k)\frac{dR}{dx}$$
$$+ \frac{\Gamma_k R^2}{(\xi_k^2 + \eta_k^2)^2} \left[\left((\xi_k^2 - \eta_k^2)\frac{d\xi_k}{dx} + 2\eta_k\xi_k\frac{d\eta_k}{dx} \right) \right.$$
$$\left. \left. + i\left((\xi_k^2 + \eta_k^2)\frac{d\eta_k}{dx} - 2\eta_k\xi_k\frac{d\xi_k}{dx} \right) \right] \right\}$$

Collecting real and imaginary parts:

$$\frac{dC_{F_{NL}}}{d(-x)} = -\frac{2}{S_R U_\infty} \sum_{k=1}^{m} \left\{ \left(\eta_k - \frac{R^2\eta_k}{\xi_k^2 + \eta_k^2} \right) \frac{d\Gamma_k}{dx} + \Gamma_k \frac{d\eta_k}{dx} - \eta_k \frac{2R\Gamma_k}{\xi_k^2 + \eta_k^2} \frac{dR}{dx} \right.$$
$$- \frac{\Gamma_k R^2}{(\xi_k^2 + \eta_k^2)^2} \left((\xi_k^2 - \eta_k^2)\frac{d\eta_k}{dx} - 2\eta_k\xi_k\frac{d\xi_k}{dx} \right)$$
$$+ i\left[\left(\xi_k - \frac{R^2\xi_k}{\xi_k^2 + \eta_k^2} \right) \frac{d\Gamma_k}{dx} + \Gamma_k \frac{d\xi_k}{dx} - \frac{2R\Gamma_k\xi_k}{\xi_k^2 + \eta_k^2} \frac{dR}{dx} \right.$$
$$\left. \left. + \frac{\Gamma_k R^2}{(\xi_k^2 + \eta_k^2)^2} \left((\xi_k^2 - \eta_k^2)\frac{d\xi_k}{dx} + 2\eta_k\xi_k\frac{d\eta_k}{dx} \right) \right] \right\}$$

Now assume that the system consists of a symmetric pair of vortices, i.e. m=2, $\eta_2=\eta_1$, $\xi_2=-\xi_1$, and $\Gamma_2=\Gamma_1$.

Firstly, consider the real parts,

$$
\begin{aligned}
&= -\frac{2}{S_R U_\infty}\left\{\left(\eta_1 - \frac{R^2\eta_1}{\xi_1^2+\eta_1^2}\right)\frac{d\Gamma_1}{dx} + \Gamma_1\frac{d\eta_1}{dx} - \eta_1\frac{2R\Gamma_1}{\xi_1^2+\eta_1^2}\frac{dR}{dx}\right.\\
&\quad -\frac{\Gamma_1 R^2}{(\xi_1^2+\eta_1^2)^2}\left((\xi_1^2-\eta_1^2)\frac{d\eta_1}{dx} - 2\eta_1\xi_1\frac{d\xi_1}{dx}\right)\\
&\quad -\left(\eta_1 - \frac{R^2\eta_1}{\xi_1^2+\eta_1^2}\right)\frac{d\Gamma_1}{dx} - \Gamma_1\frac{d\eta_1}{dx} + \eta_1\frac{2R\Gamma_1}{\xi_1^2+\eta_1^2}\frac{dR}{dx}\\
&\quad \left.+\left(\eta_1 - \frac{R^2\eta_1}{\xi_1^2+\eta_1^2}\right)\frac{d\Gamma_1}{dx} - \Gamma_1\frac{d\eta_1}{dx} + \eta_1\frac{2R\Gamma_1}{\xi_1^2+\eta_1^2}\frac{dR}{dx}\right\}\\
&= 0
\end{aligned}
$$

Then considering the imaginary parts,

$$
\begin{aligned}
&= -\frac{i2}{S_R U_\infty}\left\{\left(\xi_1 - \frac{R^2\xi_1}{\xi_1^2+\eta_1^2}\right)\frac{d\Gamma_1}{dx} + \Gamma_1\frac{d\xi_1}{dx} - \frac{2R\Gamma_1\xi_1}{\xi_1^2+\eta_1^2}\frac{dR}{dx}\right.\\
&\quad +\frac{\Gamma_1 R^2}{(\xi_1^2+\eta_1^2)^2}\left((\xi_1^2-\eta_1^2)\frac{d\xi_1}{dx} + 2\eta_1\xi_1\frac{d\eta_1}{dx}\right)\\
&\quad +\left(\xi_1 - \frac{R^2\xi_1}{\xi_1^2+\eta_1^2}\right)\frac{d\Gamma_1}{dx} + \Gamma_1\frac{d\xi_1}{dx} - \frac{2R\Gamma_1\xi_1}{\xi_1^2+\eta_1^2}\frac{dR}{dx}\\
&\quad \left.+\frac{\Gamma_1 R^2}{(\xi_1^2+\eta_1^2)^2}\left((\xi_1^2-\eta_1^2)\frac{d\xi_1}{dx} + 2\eta_1\xi_1\frac{d\eta_1}{dx}\right)\right\}\\
&= -\frac{i4}{S_R U_\infty}\left\{\left(\xi_1 - \frac{R^2\xi_1}{\xi_1^2+\eta_1^2}\right)\frac{d\Gamma_1}{dx} + \Gamma_1\frac{d\xi_1}{dx} - \frac{2R\Gamma_1\xi_1}{\xi_1^2+\eta_1^2}\frac{dR}{dx}\right.\\
&\quad \left.+\frac{\Gamma_1 R^2}{(\xi_1^2+\eta_1^2)^2}\left((\xi_1^2-\eta_1^2)\frac{d\xi_1}{dx} + 2\eta_1\xi_1\frac{d\eta_1}{dx}\right)\right\}
\end{aligned}
$$

This is reassuring as it indicates that the side force predicted by these equations for this symmetric case is zero. The symmetry will only occur with β=0, so adding together the real and imaginary parts of the non-linear expression together with the linear term we get;

$$
\begin{aligned}
\frac{dC_F}{d(-x)} = -i\left\{\frac{4\pi}{S_R}R\frac{dR}{dx}\alpha - \frac{i4}{S_R U_\infty}\right.&\left\{\left(\xi_1 - \frac{R^2\xi_1}{\xi_1^2+\eta_1^2}\right)\frac{d\Gamma_1}{dx} + \Gamma_1\frac{d\xi_1}{dx} - \frac{2R\Gamma_1\xi_1}{\xi_1^2+\eta_1^2}\frac{dR}{dx}\right.\\
&\left.\left.+\frac{\Gamma_1 R^2}{(\xi_1^2+\eta_1^2)^2}\left((\xi_1^2-\eta_1^2)\frac{d\xi_1}{dx} + 2\eta_1\xi_1\frac{d\eta_1}{dx}\right)\right\}\right\}
\end{aligned}
$$

This result is now in a form suitable for inclusion in the new model.

10.1.5 The fully simplified result

Here an attempt has been made to reduce the result to its most basic form. The objective is not to produce a useful expression for practical use but to check that the full form of the equation is likely to give results of the right order and will follow the expected trends.

It is interesting to note that, in the case of an ogive-cylinder body, of the various terms that contribute to the non-linear load, one is dominant and the other three are of second order.

The dominant term is $\left(\xi - \frac{R^2\xi}{\xi^2+\eta^2}\right)\frac{d\Gamma}{dx}$ and so a first order load distribution for ogive-cylinder bodies can by given by:

$$\frac{dC_F}{d(-x)} = \frac{4\pi\ R}{S_R}\frac{dR}{dx}\alpha - \frac{4}{S_R U_\infty}\left(\xi - \frac{R^2\xi}{\xi^2+\eta^2}\right)\frac{d\Gamma}{dx}$$

Let us consider the non-linear part of this equation

$$\frac{dC_{FNL}}{d(-x)} = -\frac{4}{S_R U_\infty}\left(\xi - \frac{R^2\xi}{\xi^2+\eta^2}\right)\frac{d\Gamma}{dx} \qquad \text{(i)}$$

From work by Föppl[1] $\sin\theta = \frac{1}{2} - \frac{1}{2r}$

Now $\sin\theta = \frac{\xi}{r}$;so

$$\frac{\xi}{r} = \frac{1}{2} - \frac{1}{2r}$$

Solving for r gives

$$r^2 = 2\xi\sqrt{(\xi^2+1)} + 2\xi^2 + 1 \qquad \text{(ii)}$$

Now since $\xi^2+\eta^2$ in (i) is equal to r we can eliminate η thus:

---

[1] Föppl showed that a pair of vortices behind a cylinder in a freestream flow will remain at rest if this condition is satisfied. Milne-Thompson L.M. [46] P.367 shows analysis that leads to this result.

$$\frac{dC_{FNL}}{d(-x)} \approx -\frac{4}{S_R U_\infty}\left(\xi - \frac{R^2\xi}{2\xi\sqrt{(\xi^2+1)}+2\xi^2+1}\right)\frac{d\Gamma}{dx}$$

If we assume that $\xi \approx 0.4$ & R=1 then

$$\frac{dC_{FNL}}{d(-x)} \approx -\frac{0.867}{S_R U_\infty}\frac{d\Gamma}{dx}$$

Now the vorticity shed by the body due to separation can be crudely approximated by:

$$\frac{d\Gamma}{dt} \approx 0.5U_s^2 ,$$

where U_s is the cross flow velocity at the cylinder shoulder and is of the order $2(U_\infty \sin\alpha)^2$, hence:

$$\begin{aligned}\frac{d\Gamma}{dt} &= 0.5(2U_\infty \sin\alpha)^2 \\ &= 2U_\infty^2 \sin^2\alpha\end{aligned}$$

Now since $\frac{dx}{dt} = U_\infty \cos\alpha$ we get:

$$\begin{aligned}\frac{d\Gamma}{dx} &= \frac{d\Gamma}{dt}\frac{dt}{dx} \\ &= 2U_\infty^2 \sin^2\alpha \frac{1}{U_\infty \cos\alpha} \\ &\approx 2U_\infty\alpha^2\end{aligned}$$

But we know that this will need to be factored by σ with a value of about 0.6. So we get

$$\begin{aligned}\frac{dC_{FNL}}{d(-x)} &\approx -\frac{0.867}{S_R U_\infty}\sigma 2U_\infty\alpha^2 \\ &\approx 1.733\sigma\frac{\alpha^2}{S_R} \\ &\approx 0.331\alpha^2\end{aligned}$$

Hence the magnitudes of the non-linear load component at specific incidences are given below:

Incidence	$\frac{dC_{FNL}}{d(-x)}$
0	0
5	0.003
10	0.01
15	0.023
20	0.04

Comparison with an experimental load distribution such as figure 11.4.3.1 indicates that the magnitudes and the trends are reasonable.

10.1.6 Derivation of result without small angle approximations

The derivations so far have been based upon theory that assumes that small angle approximations are valid. In classical Slender Body Theory this is a reasonable assumption since it is only applied at low incidences. Whilst we shall not be considering high angles of attack, we will be pushing the limits of the small angle assumptions. Hence, we now derive the result without invoking this approximation.

Returning to the result from CHRISTOPHER [44] (2.44) :

$$\frac{dC_F}{d(-x)} = \frac{-2i}{U_\infty^2 S_R}\left\{U\frac{\partial}{\partial x}\oint \overline{F}d\overline{\sigma} + \overline{Q}\oint\frac{dF}{d\sigma}d\sigma - iU\overline{Q}\frac{dS}{d(-x)}\right\}$$

For small angles $\cos\sigma_i \approx 1, \quad \tan\alpha \approx \alpha$

So

$$\begin{aligned} U &= -U_\infty\cos\sigma_1 && \approx -U_\infty \\ V &= -U_\infty\cos\sigma_1\tan\beta && \approx -U_\infty\beta \\ V &= -U_\infty\cos\sigma_1\tan\alpha && \approx -U_\infty\alpha \end{aligned}$$

$$\begin{aligned} \overline{Q} &= V - iW \\ &= -U_\infty\cos\sigma_1(\tan\beta - i\tan\alpha) \end{aligned}$$

Now we also have that

$$\tan\alpha = \frac{W}{U}$$

$$\tan\beta = \frac{V}{U}$$

$$\cos\sigma_1 = \frac{U}{U_R} = \frac{-U}{U_\infty}$$

$$\tan^2\sigma_1 = \tan^2\alpha + \tan^2\beta$$

$$U_R = -U_\infty$$

Consider the first of the 3 terms: $U\frac{d}{dx}\oint \overline{F}d\overline{\sigma}$

Firstly the complex potential, F, must be replaced with the complex potential per unit cross flow velocity F_1.

Now the cross flow velocity $U_c = \sin\sigma_1$ also

$$-\frac{U}{U_\infty} = \cos\sigma_1 \Rightarrow U_\infty = -\frac{U}{\cos\sigma_1} \text{ and } F = -U\tan\sigma_1 F_1$$

$$\text{So } U\frac{\partial\oint \overline{F}d\overline{\sigma}}{\partial\ x} = -U^2\tan\sigma_1\frac{\partial\oint \overline{F}_1 d\overline{\sigma}}{\partial\ x}$$

The second term is $\overline{Q}\oint\frac{dF}{d\sigma}d\sigma$ and as with the first term $\oint\frac{dF}{d\sigma}d\sigma$ becomes

$$-U\tan\sigma_1\oint\frac{dF_1}{d\sigma}d\sigma$$

Now

$$\begin{aligned}\overline{Q} &= V - iW\\ &= -U_\infty\cos\sigma_1\tan\beta + iU_\infty\cos\sigma_1\tan\alpha\\ &= -U_\infty\cos\sigma_1(\tan\beta - i\tan\alpha)\end{aligned}$$

But

$$\begin{aligned}\tan\alpha &= \frac{W}{U}\\ &= -\tan\sigma_1\sin\vartheta\\ \tan\beta &= \frac{V}{W}\\ &= \tan\sigma_1\cos\vartheta\end{aligned}$$

So

$$\begin{aligned}\overline{Q} &= -U_\infty\cos\sigma_1(\tan\sigma_1\cos\vartheta - i\tan\sigma_1\sin\vartheta)\\ &= -U_\infty\cos\sigma_1\tan\sigma_1(\cos\vartheta - i\sin\vartheta)\\ &= -U_\infty\cos\sigma_1\frac{\sin\sigma_1}{\cos\sigma_1}(\cos\vartheta - i\sin\vartheta)\end{aligned}$$

$$\begin{aligned}&= -U_\infty\sin\sigma_1(\cos\vartheta - i\sin\vartheta)\\ &= -\left(-\frac{U}{\cos\sigma_1}\right)\sin\sigma_1(\cos\vartheta - i\sin\vartheta)\\ &= U\tan\sigma_1(\cos\vartheta - i\sin\vartheta)\\ &= U\tan\sigma_1 e^{-i\vartheta}\end{aligned}$$

So

$$\begin{aligned}\overline{Q}\oint\frac{dF}{d\sigma}d\sigma &= U\tan\sigma_1 e^{-i\vartheta}\left(-U\tan\sigma_1\oint\frac{dF_1}{d\sigma}d\sigma\right)\\ &= -U^2\tan^2\sigma_1 e^{-i\vartheta}\oint\frac{dF_1}{d\sigma}d\sigma\end{aligned}$$

The third term is $iU\overline{Q}\frac{dS}{d(-x)}$, and since $U=-U_\infty\cos\sigma_1$

i.e. $U_\infty=-\frac{U}{\cos\sigma_1}$

and from the last term $\overline{Q}=U\tan\sigma_1 e^{-i\vartheta}$

So,

$$iU\overline{Q}\frac{dS}{d(-x)}=iU^2\tan\sigma_1 e^{-i\vartheta}\frac{dS}{d(-x)}$$

Then

$$\frac{dC_F}{d(-x)}=\frac{-2i}{U_\infty^2 S_R}\left\{-U^2\tan\sigma_1\frac{\partial\oint\overline{F}_1 d\overline{\sigma}}{\partial x}-U^2\tan^2\sigma_1 e^{-i\vartheta}\oint\frac{dF_1}{d\sigma}d\sigma-iU^2\tan\sigma_1 e^{-i\vartheta}\frac{dS}{d(-x)}\right\}$$

Neglecting the σ_1^2 term gives

$$\frac{dC_F}{d(-x)}=\frac{-2i}{U_\infty^2 S_R}\left\{-U^2\tan\sigma_1\left(\frac{\partial\oint\overline{F}_1 d\overline{\sigma}}{\partial x}+ie^{-i\vartheta}\frac{dS}{d(-x)}\right)\right\}$$

but $U=-U_\infty\cos\sigma_1$ so

$$\frac{dC_F}{d(-x)}=\frac{-2i}{U_\infty^2 S_R}\left\{-U^2\cos^2\sigma_1\tan\sigma_1\left(\frac{\partial\oint\overline{F}_1 d\overline{\sigma}}{\partial x}+ie^{-i\vartheta}\frac{dS}{d(-x)}\right)\right\}$$

$$=\frac{2i}{S_R}\left\{\cos^2\sigma_1\frac{\sin\sigma_1}{\cos\sigma_1}\left(\frac{\partial\oint\overline{F}_1 d\overline{\sigma}}{\partial x}+ie^{-i\vartheta}\frac{dS}{d(-x)}\right)\right\}$$

$$=\frac{2i}{S_R}\left\{\sin\sigma_1\cos\sigma_1\left(\frac{\partial\oint\overline{F}_1 d\overline{\sigma}}{\partial x}+ie^{-i\vartheta}\frac{dS}{d(-x)}\right)\right\}$$

In the Γ=0 case,

$$\frac{dC_F}{d(-x)}=\frac{2i\sin\sigma_1\cos\sigma_1}{S_R}\left(2\pi R(\sin\vartheta+i\cos\vartheta)\frac{dR}{dx}\right)$$

Now

$$\tan\alpha=-\tan\sigma_1\sin\vartheta$$
$$\tan\beta=\tan\sigma_1\cos\vartheta$$

So

$$\sin\vartheta=-\frac{\tan\alpha}{\tan\sigma_1}$$

and

$$\cos\vartheta=\frac{\tan\beta}{\tan\sigma_1}$$

So,

$$\frac{dC_F}{d(-x)} = \frac{2i\sin\sigma_1\cos\sigma_1}{S_R}\left(2\pi\ R\left(-\frac{\tan\alpha}{\tan\sigma_1}+i\frac{\tan\beta}{\tan\sigma_1}\right)\frac{dR}{dx}\right)$$
$$= \frac{2i\sin\sigma_1\cos\sigma_1}{S_R}\frac{1}{\tan\sigma_1}\left(2\pi\ R(-\tan\alpha+i\tan\beta)\frac{dR}{dx}\right)$$
$$= \frac{2i\sin\sigma_1\cos\sigma_1}{S_R}\frac{\cos\sigma_1}{\sin\sigma_1}\left(2\pi\ R(-\tan\alpha+i\tan\beta)\frac{dR}{dx}\right)$$
$$= \frac{2i\cos^2\sigma_1}{S_R}\left(2\pi\ R(-\tan\alpha+i\tan\beta)\frac{dR}{dx}\right)$$
$$= \frac{2\cos^2\sigma_1}{S_R}\left(2\pi\ R(-i\tan\alpha-\tan\beta)\frac{dR}{dx}\right)$$
$$= -\frac{4\pi\cos^2\sigma_1}{S_R}(\tan\beta+i\tan\alpha)R\frac{dR}{dx}$$

For $\beta=0$, $\sigma_1=\alpha$,

$$\frac{dC_N}{d(-x)} = -i\frac{4\pi\cos^2\alpha}{S_R}\tan\alpha\ \ R\frac{dR}{dx}$$
$$= -i\frac{4\pi\cos^2\alpha}{S_R}\frac{\sin\alpha}{\cos\alpha}R\frac{dR}{dx}$$
$$= -i\frac{4\pi}{S_R}\sin\alpha\cos\alpha\ \ R\frac{dR}{dx}$$

In the SBT version with $\Gamma \neq 0$,

$$\frac{dC_F}{d(-x)} = \frac{2i\sigma_1}{S_R}\left\{2\pi\ R(\sin\vartheta+i\cos\vartheta)\frac{dR}{dx}-\frac{1}{U_\infty\sigma_1}\sum\{\ \}\right\}$$

With full trigonometric terms,

$$= \frac{2i\sin\sigma_1\cos\sigma_1}{S_R}\left\{2\pi\ R\left(-\frac{\tan\alpha}{\tan\sigma_1}+i\frac{\tan\beta}{\tan\sigma_1}\right)\frac{dR}{dx}-\frac{1}{U_\infty\sigma_1}\sum\{\ \}\right\}$$
$$= \frac{2i\sin\sigma_1\cos\sigma_1}{S_R}\frac{1}{\tan\sigma_1}\left\{2\pi\ R(-\tan\alpha+i\tan\beta)\frac{dR}{dx}-\frac{\tan\sigma_1}{U_\infty\sigma_1}\sum\{\ \}\right\}$$
$$= \frac{2i\sin\sigma_1\cos\sigma_1}{S_R}\frac{\cos\sigma_1}{\sin\sigma_1}\left\{2\pi\ R(-\tan\alpha+i\tan\beta)\frac{dR}{dx}-\frac{\tan\sigma_1}{U_\infty\sigma_1}\sum\{\ \}\right\}$$
$$= \frac{2i\cos^2\sigma_1}{S_R}\left\{2\pi\ R(-\tan\alpha+i\tan\beta)\frac{dR}{dx}-\frac{\tan\sigma_1}{U_\infty\sigma_1}\sum\{\ \}\right\}$$
$$= \frac{2\cos^2\sigma_1}{S_R}\left\{2\pi\ R(-i\tan\alpha-\tan\beta)\frac{dR}{dx}-i\frac{\tan\sigma_1}{U_\infty\sigma_1}\sum\{\ \}\right\}$$
$$= \frac{4\pi}{S_R}\cos^2\sigma_1\tan\beta\ \ R\frac{dR}{dx}-i\frac{4\pi}{S_R}\cos^2\sigma_1\tan\alpha\ \ R\frac{dR}{dx}-i\frac{2\cos^2\sigma_1}{S_R}\frac{\tan\sigma_1}{U_\infty\sigma_1}\sum\{\ \}$$

Looking at the last term;

$$i\frac{2\cos^2\sigma_1}{S_RU_\infty\sigma_1}\frac{\sin\sigma}{\cos\sigma}\sum\{\ \} = i\frac{2\sin\sigma_1\cos\sigma_1}{S_RU_\infty\sigma_1}\sum\{\ \}$$

So we have,

$$\frac{dC_F}{d(-x)} = \frac{4\pi}{S_R}\cos^2\sigma_1 \tan\beta \;\; R\frac{dR}{dx} - i\frac{4\pi}{S_R}\cos^2\sigma_1 \tan\alpha \;\; R\frac{dR}{dx} - i\frac{2\sin\sigma_1\cos\sigma_1}{S_R U_\infty \sigma_1}\sum\{\ \}$$

(Note: for $\sigma_1 = \alpha$, $\cos^2\sigma \tan\alpha = \sin\alpha\cos\alpha$)

10.2 DETERMINATION OF VORTEX STRENGTH AND POSITION

The core of our model is now in place. Given that the flow about a slender body at modest incidence gives rise to a pair of symmetric vortices[2], knowing their strengths and positions it is possible to derive the linear and non-linear local normal force distribution along the body.

The next stage is to develop a model that is capable of predicting the strengths and positions of the vortices.

Since the core of the model is capable of producing results very rapidly, it would be appropriate to use a similarly simple and hence rapid method for the vortex modelling.

10.2.1 Bryson's method for a 2-D circular cylinder

BRYSON [3] describes a simple method for the modelling of the flow about an impulsively started two dimensional circular cylinder. The model consists of a potential model of the cylinder in the freestream together with a pair point vortices on the lee side and their images inside the cylinder. The lee side vortices are connected to the cylinder by a notional "feeding sheet". This feeding sheet is a straight line connecting each vortex at ζ_1 to its separation point on the cylinder surface at ζ_0. The feeding sheet is assumed to contain negligible vorticity, all the vorticity in the system is assumed to be contained in the point vortices. Figure 10.2.1.1 from Bryson [3] depicts the elements of the

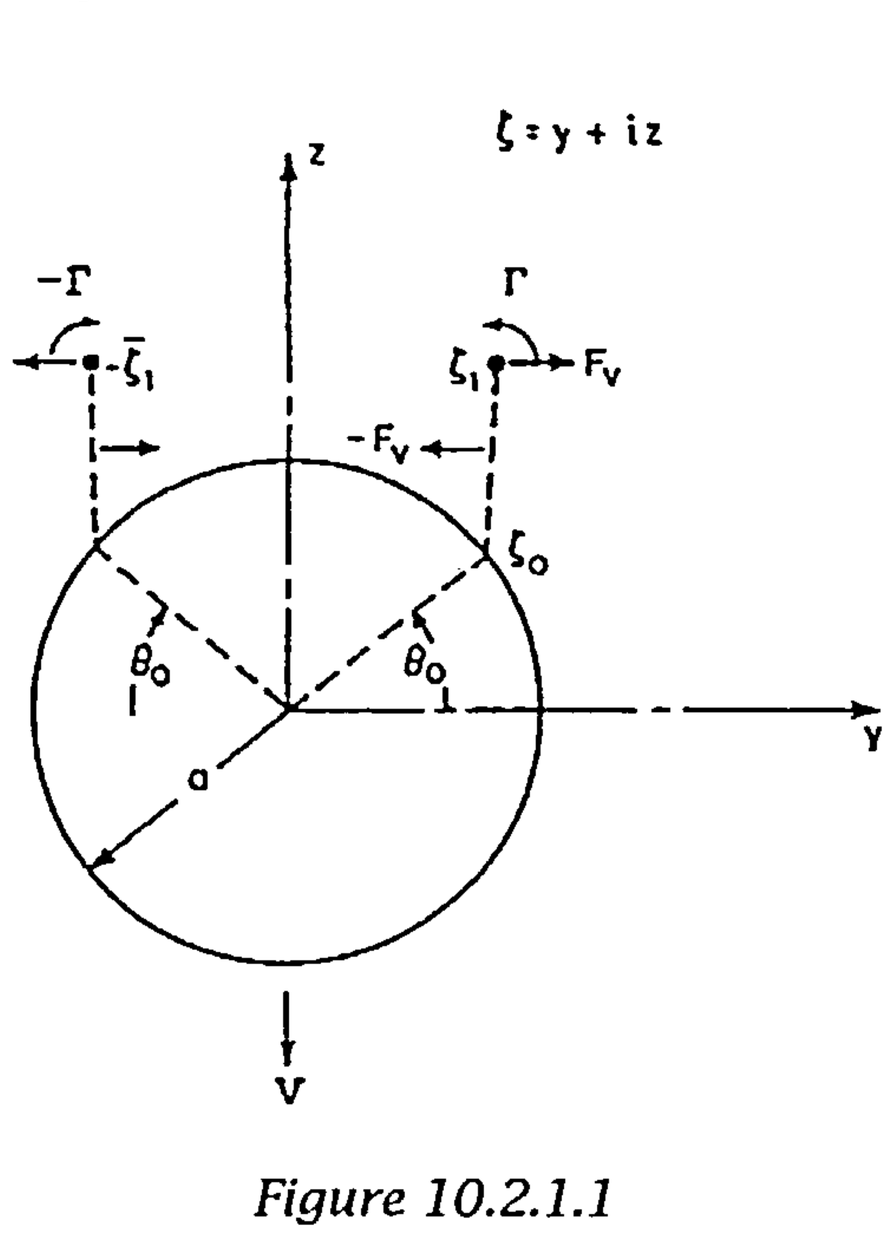

Figure 10.2.1.1

---

[2] In fact if we use the general result we need not restrict ourselves to this.

model and its notation. Bryson formulates a relation for the motion of the point vortices such that there results no net force on the combination of the vortex and its connecting feeding sheet.

Thus

$$\dot{\zeta_1} + (\zeta_1 - \zeta_0)\frac{\dot{\Gamma}}{\Gamma} = W_1 \ ,$$

where $W_1 = v_1 + iw_1$

is the complex velocity vector at ζ_1, leaving out the infinite rotational velocity that would be induced by the vortex at ζ_1 itself.

Once started the vortices will always have some finite strength Γ. However, if the rate at which they are being fed from the separated boundary layer through the feeding sheets, $\dot{\Gamma}$, drops to zero then it can be seen that they will drift with the local fluid velocity.

Hence, by knowing the rate at which the vortices are being fed, $\dot{\Gamma}$, it is possible to determine the instantaneous velocity of the vortices. The position of the vortices can then be determined at any instant by time integration of these velocities.

The next element of the model is the determination of $\dot{\Gamma}$. This is based upon the basic premise that "the feeding points are stagnation points; that is, the fluid velocity relative to the cylinder vanishes at these points".

To express this mathematically we start with the complex velocity potential for the system which consists of a free stream flow, a doublet at the origin to simulate the cylinder, the two point vortices and the reflections, or images, of the vortices inside the cylinder. This can be written as:

$$F = -iV\left(\zeta - \frac{a^2}{\zeta}\right) - \frac{i\Gamma}{2\pi}\log\frac{\zeta - \zeta_1}{\zeta - \frac{a^2}{\zeta_1}}\frac{\zeta + \frac{a^2}{\overline{\zeta_1}}}{\zeta + \overline{\zeta_1}}$$

The complex conjugate velocity vector is then:

$$\overline{W} = \frac{v - iw}{V}$$

$$= -i\left(1 + \frac{a^2}{\zeta^2}\right) - i\lambda\ a\left[\frac{1}{\zeta - \zeta_1} + \frac{1}{\zeta + \frac{a^2}{\zeta_1}} - \frac{1}{\zeta - \frac{a^2}{\overline{\zeta_1}}} - \frac{1}{\zeta + \overline{\zeta_1}}\right] \ ,$$

where $\lambda = \frac{\Gamma}{2\pi\ aV}$

Imposing the boundary condition that v-iw=0 at $\zeta = \zeta_0 = ae^{j\theta_0}$ and rearranging we get:

$$\lambda = \frac{(\zeta_1 - \zeta_0)(\overline{\zeta_1} - \overline{\zeta_0})(\zeta_1 - \overline{\zeta_0})(\overline{\zeta_1} + \zeta_0)}{(\zeta_1\overline{\zeta_1} - a^2)(\zeta_1 + \overline{\zeta_1})}$$

This expression can be used to determine the required strength of a point vortex to set the velocity at the separation point to zero and is a function solely of the location of the point vortex. Figure 10.2.1.2 depicts the λ function.

The expression for the velocity of the vortices can also be written in terms of λ, thus

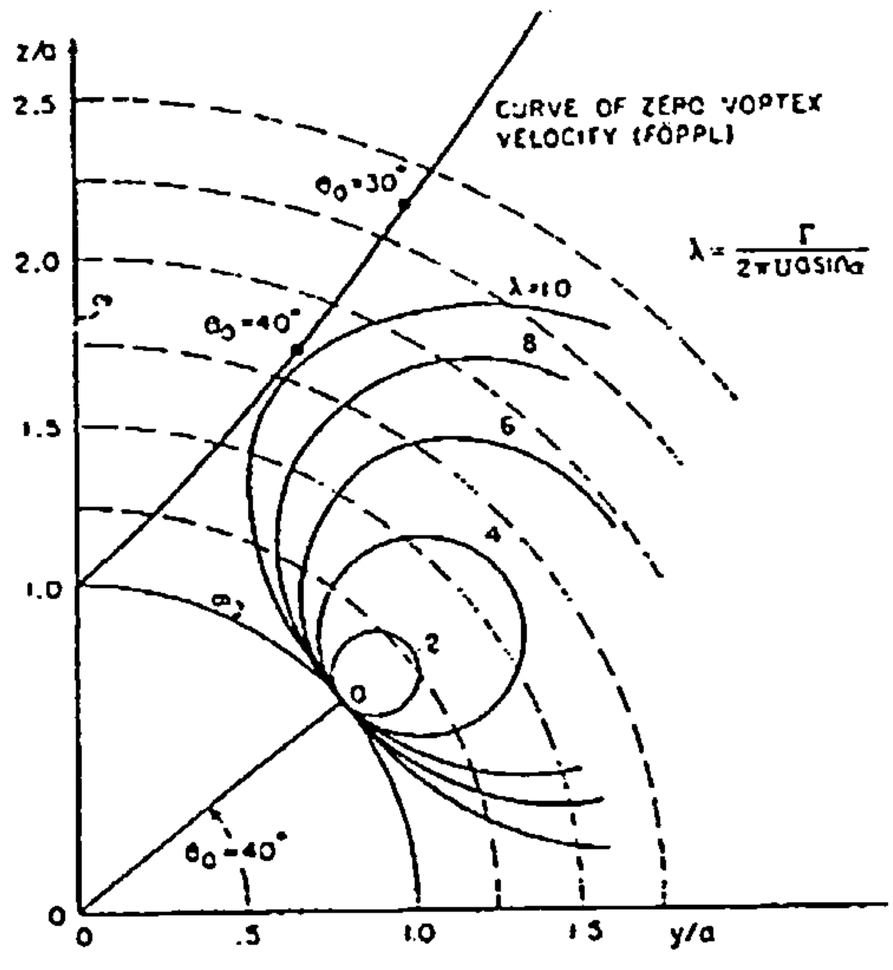

Figure 10.2.1.2

$$\dot{\zeta_1} + (\zeta_1 - \zeta_0)\frac{\dot{\lambda}}{\lambda} = W_1$$

Finally the velocity at vortex 1, W_1 is given by

$$\overline{W_1} = v_1 - iw_1$$

$$= iV\left[1 + \frac{a^2}{\zeta_1^2} + \lambda\ a\left(\frac{1}{\zeta_1 + \frac{a^2}{\zeta_1}} - \frac{1}{\zeta_1 - \frac{a^2}{\overline{\zeta_1}}} - \frac{1}{\zeta_1 + \overline{\zeta_1}}\right)\right]$$

The procedure for solving these equations is to start with the vortex close[3] to the point of separation. It can be seen from figure 10.2.1.2 that its strength, as might be expected, will be near zero. Then by using some initial value of $\dot{\Gamma}$ determined from experience or a value of zero, the vortex velocity $\dot{\zeta_1}$ can then be determined. This can be used to determine how far the vortex will have moved in one time step. With the vortex in its new position a new value of λ can be found. Knowing the initial value of λ and the new value one time step later it is possible to determine $\dot{\lambda}$. This process can now be repeated for as many time steps as required thus giving a complete time history of the vortex strength and position.

There still remains one element of the model that is not specified, that being the separation position θ_0. Figure 10.2.1.3 shows the vortex trajectories over a duration of 200 time steps for four separation positions. The trajectories show an initial unsteadiness in the solutions over the first few time steps in proximity to the separation point. The trajectories then become steady and tend

---

[3] This will be discussed shortly.

towards the Föppl curve[4]. After reaching the Föppl curve the trajectories curve back on themselves again. This can be seen in figure 10.2.1.3 cases θ_0=60° and 45°. The other two cases the vortices have not yet reached the Föppl curve and hence do not curve back on themselves.

Before proceeding to the next phase it is appropriate to note a few shortcomings of this method. Firstly, the simplicity of the feeding sheet model, although computationally efficient, is not entirely consistent. Although the model ensures that there is no net force acting on the vortex and feeding sheet due to their forces being of equal magnitude but opposite in direction, the forces act at different points and as a result give rise to a couple.

Another problem area is the initial instability that occurs at the start of the trajectory. This may, in part, be due to the fact that $\dot{\Gamma}$ is initially unknown, although various methods were used to get around this. The main reason is due to a basic instability in the mathematical problem since the starting points of the vortices are unstable equilibrium points. In fact the vortex trajectories can only start out from these feeding points in one preferred direction[5]; namely, 30 degrees to the downstream tangent to the cylinder. Hence to start the trajectory the vortices are placed on this line at some small distance from the separation point.

So from Bryson ζ_1, moves according to

$$\dot{\zeta_1} = W_1 - (\zeta_1 - \zeta_0)\frac{\dot{\lambda}}{\lambda} = W_1$$

expanding this we get

$$\dot{\xi_1} + i\dot{\eta_1} = v_1 + iw_1 - (\xi_1 + i\eta_1 - \xi_0 - i\eta_0)\frac{\dot{\lambda}}{\lambda}$$

so

$$\dot{\xi_1} = v_1 - (\xi_1 - \xi_0)\frac{\dot{\lambda}}{\lambda}$$

$$\dot{\eta_1} = w_1 - (\eta_1 - \eta_0)\frac{\dot{\lambda}}{\lambda}$$

To locate the starting point we can consider the separation point at θ=0°. The start point will be some small distance, l, from here at 30° to the local tangent as shown in figure 10.2.1.4.

Hence

$$\xi_{s90} = R + l\cos 60$$

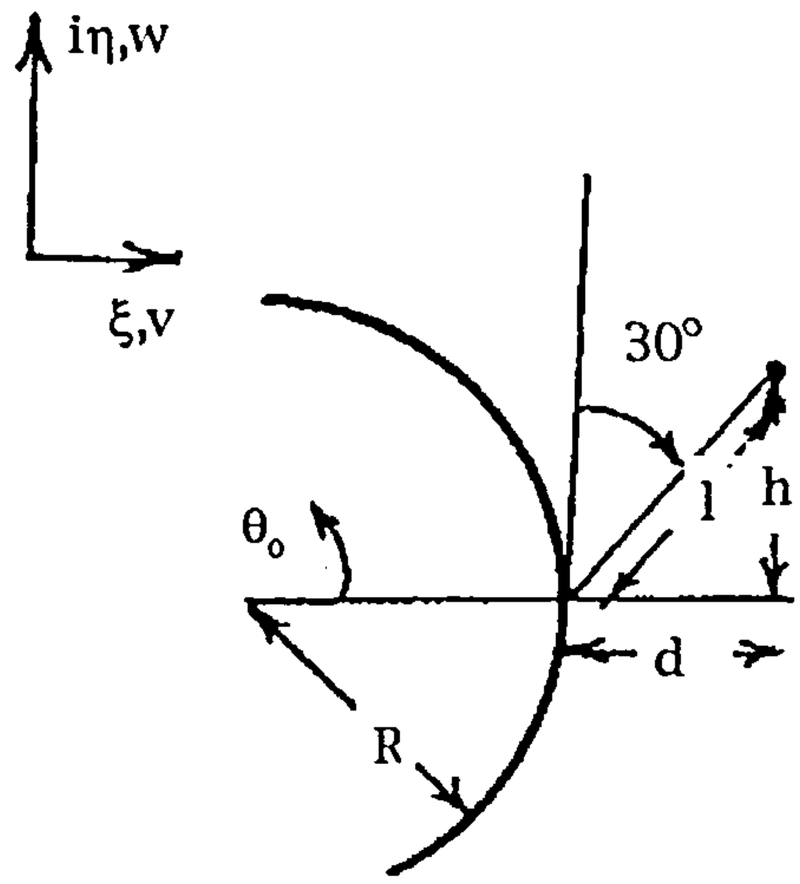

Figure 10.2.1.4

---

[4] The locus of points at which a pair of vortices will remain stationary behind a cylinder in a freestream. See [46]

[5] For detailed discussion see Bryson[3]

$$\eta_{s90} = l\sin 60$$

However, in general the separation point will not be at θ_0=0° hence we need to translate the start point by the appropriate distances shown in figure 10.2.1.5

$$\Delta\xi_T = R - R\cos\theta_0$$

$$\Delta\eta_T = R\sin\theta_0$$

However, the tangent line is now no longer tangent and so we require a final rotation through θ_0.

$$\Delta\xi_R = -b\cos\alpha$$

$$= 2l\sin\left(\frac{\theta_0}{2}\right)\cos\left\{\frac{(180-\theta_0)}{2} - \tan^{-1}\left(\frac{h}{d}\right)\right\}$$

$$\Delta\eta_R = 2l\sin\left(\frac{\theta_0}{2}\right)\sin\left\{\frac{(180-\theta_0)}{2} - \tan^{-1}\left(\frac{h}{d}\right)\right\} \quad ,$$

where $b = 2l\sin\left(\frac{\theta}{2}\right)$

and $\alpha = \frac{(180-\theta_0)}{2} - \phi$,

the notation being given in figure 10.2.1.6.

This method will be used to determine the vortex strengths and positions.

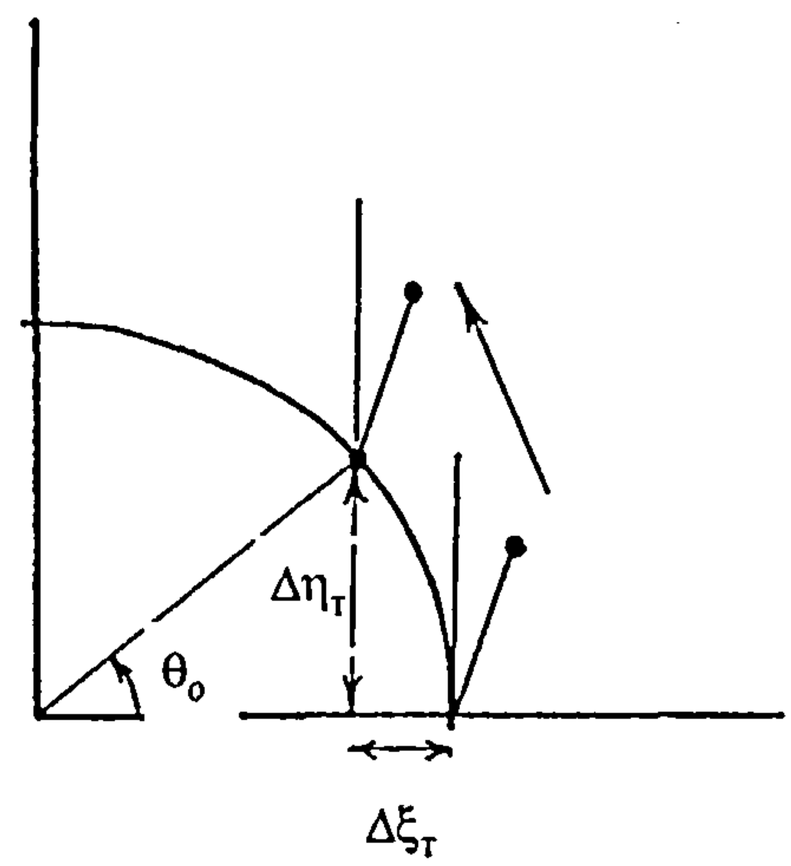

Figure 10.2.1.5

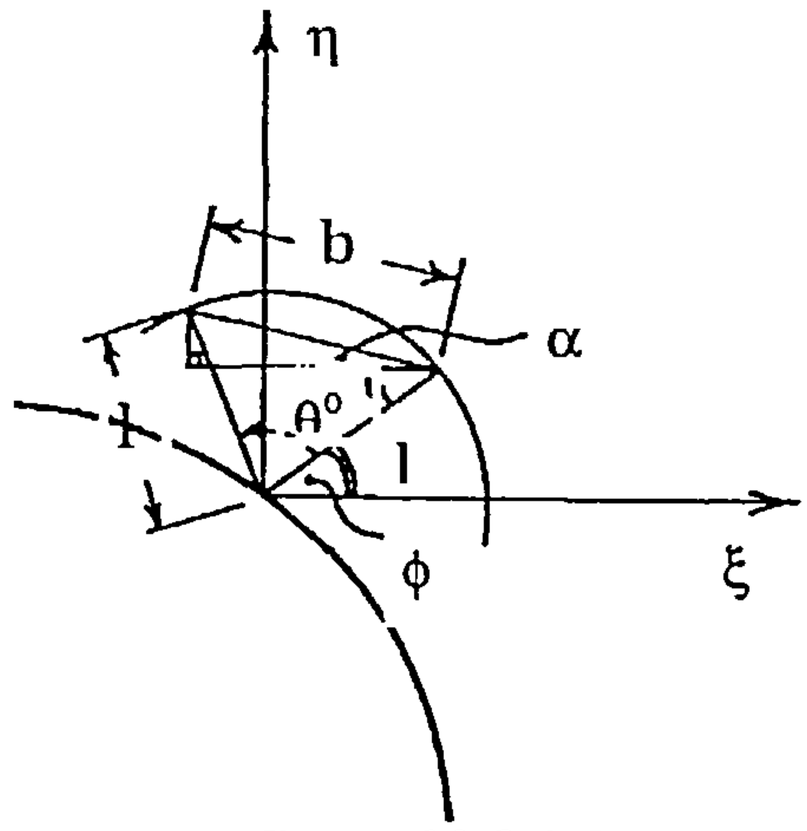

Figure 10.2.1.6

10.2.2 Extension to a slender body at incidence

The method described in the previous section is strictly applicable to two-dimensional flow cases. As has been already discussed the three dimensional flow about a slender body at incidence is considerably more complex than a longitudinal sequence of two dimensional cross-flow planes. However, provided this is borne in mind the impulsive flow analogy would fit in with the concept of keeping the model as simple as possible.

Hence it is possible to relate the unsteady two dimensional solution for the impulsive flow about a circular cylinder to the steady flow solution about a slender body at incidence.

Invoking the impulsive flow analogy we get

$$V_z = U_\infty \sin\alpha$$

Now

$$\Delta t = \frac{\Delta x}{V_x}$$

(see figure 10.2.2.1 for notation)
So

$$\Delta t = \frac{\Delta x}{U_\infty \cos\alpha}$$

Hence

$$\Delta x = \Delta t U_\infty \cos\alpha$$
$$= \Delta t U_\infty \cos\alpha \frac{V_z}{U_\infty \sin\alpha}$$
$$= \frac{\Delta t V_z}{\tan\alpha}$$

Or

$$= \Delta t U_\infty \cos\alpha$$

However, in Bryson's [3] notation

$$1 \text{ time step} = \frac{V}{a}\Delta t$$

So in real time

$$\Delta t = \frac{(\text{time step}) \text{ x } a}{V}$$
$$= \frac{(\text{time step}) \text{x } a}{U_\infty \sin\alpha}$$

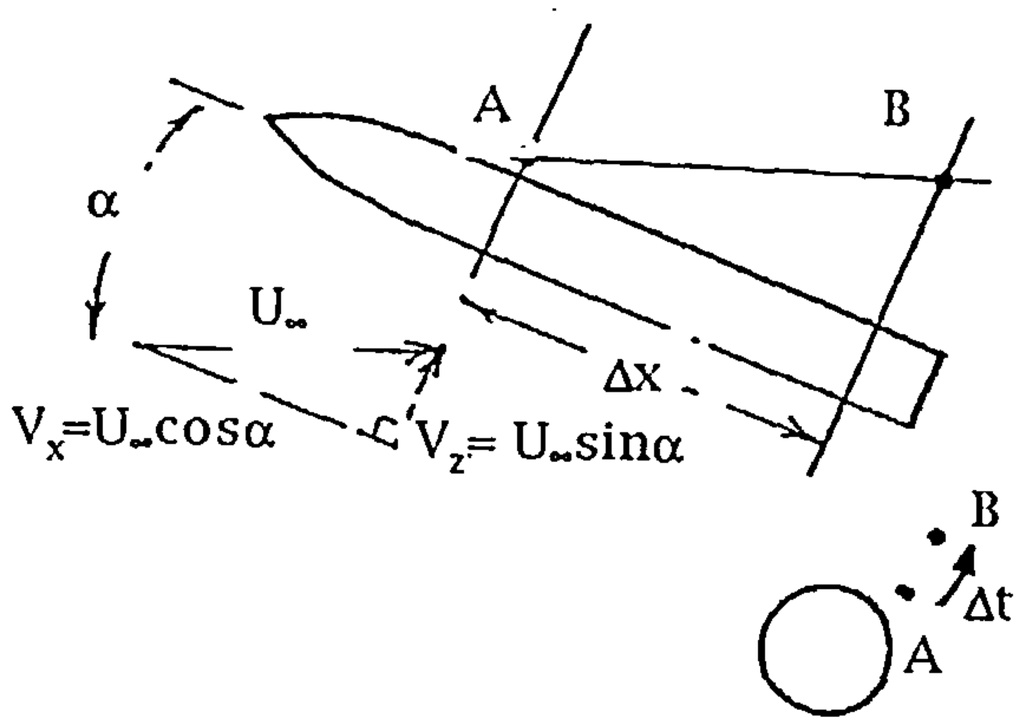

Figure 10.2.2.1

Now $\Delta x = \Delta t U_\infty \cos\alpha$
So

$$\Delta x = \frac{(\text{time step})\ a}{U_\infty \sin\alpha} U_\infty \cos\alpha$$
$$= \frac{(\text{time step})\ a}{\tan\alpha}$$

In this way the strength and position of a vortex in the 2-D solution at a particular moment in time can be related to the strength and position at the appropriate x-wise station along the length of the 3-D slender body.

10.2.3 The effect of the separation point location

We are now in a position to determine the vortex strengths and trajectories as they propagate down stream. Figure 10.2.3.1 shows this information for three widely varying values of separation angle, θ_0=15°,30°,45° and 60°. It can be seen that although the values of ξ are fairly linear the trend for Γ is less so and for η is quite non-linear. This is contrary to the experimental evidence that indicates that Γ, η and ξ should all exhibit a non-linear variation with x.

It is also evident that the value used for θ_0 has a significant effect on the characteristics. It can be seen, for instance, that η

becomes considerably more linear with lower values of θ_0 and the actual co-ordinate varies considerably.

Clearly the determination of θ_0 within the model will need to be given careful consideration.

Figure 10.2.3.2 shows a preliminary comparison between predicted vortex strength and trajectory for θ_0 =45° and 60° and values given by Tinling and Allen [32][6]. If we consider the θ_0 =45° data we can see that the ξ trend is very well predicted and the magnitude is reasonable too. The magnitude of η is predicted a little less accurately but the slope is very good. Similarly although the magnitude is a little on the low side the slope of Γ is well predicted.

10.2.4 The need to factor shed vorticity

Throughout this thesis it has been made clear that not all of the vorticity generated at the separation point finishes up in the lee side vortices, or at least it is not acting in the x-wise sense. It has been argued that one simplistic method for accounting for this effect is to apply a factor to the shed vorticity as it is generated which historically, and empirically derived, has tended to take a value of approximately 0.6.

Let us consider how we might apply such a factor in this mode. If we look at the Vortex Cloud Method approach one could postulate two ways of applying such a factor. Firstly, the method could be used to compute an unfactored solution. This would result in a vorticity distribution along the lee side of the body. At this point each and every discrete vortex could now have its strength factored down by 0.6. Although total vorticity in the flow field will now contain exactly 60% of the vorticity shed no account has been made of how the reduction in vorticity might effect the distribution itself. After all, the way the vorticity propagates during the 3-D solution depends upon the vorticity already in the field at any given station. More specifically the distance through which any discrete vortex moves in any given time step depends upon the strength of every other vortex in the flow field. Furthermore, the quantity of vorticity shed depends upon the induced velocity outside the boundary layer at the point of separation which itself is influences by the instantaneous vorticity distribution in the flow field.

Consequently it makes more sense to apply the factor at each time step as the vorticity is shed. This means that the factor will not just reduce the total quantity of vorticity in the field to 60% but will modify its distribution accordingly as the solution proceeds. The resulting solution should then be self consistent.

---

[6] Note that although ξ and η are measured values, Γ is a semi-empirical result.

With the current method the final vortex strength as a function of x can be factored directly but as with the Vortex Cloud Method would not lead to a self consistent solution for the same reasons[7]. However, it is not quite as straight forward a matter to apply the vorticity factor at source within this model.

Here the factor is applied as the new value of the vortex strength is computed, The vortex then moves some distance appropriate to one time step. However, in moving the value of the vortex strength readjusts itself to ensure that the boundary conditions are met. The consequence of this is that although the strength of the vortex will be factored down and a self consistent final solution will be reached, the ratio of the factored vortex strength at any given point to what its unfactored value would have been will not equal the applied factor. The applied factor, σ_1 in this case, can be thought of as a method of achieving a desired reduction in vorticity, σ. The actual value of this applied factor has little meaning in itself. To relate the achieved vorticity ratio to a VCM type σ it is necessary to compute both a factored and an unfactored solution and calculate the ratio of the two. It appears that to achieve a value of σ of 0.6 requires an applied factor of about 0.2-0.25.

Figure 10.2.4.1 indicates the effect of applying a factor of 0.2 on the strength and position of the vortices. It can be seen that the characteristics are now considerably more linear over the length of the body.

Figures 10.2.4.2 to 10.2.4.4 show the effect of applied factors of 0.22 to 0.25 on the achieved σ factor. It can be seen that σ reduces towards 0.6.

10.2.5 The effect of σ on vortex positions

In this section the effect of σ on the predicted vortex positions will be examined and compared with that of the Vortex Cloud Method.

It was mentioned that due to the interactive nature of the problem that in addition to reducing the achieved vortex strength, the vortex positions would also be effected.

Before looking at the vortex positions, let us first examine the way σ is applied in the Vortex Cloud Method. Here the factor, 0.6, is applied to the shed vorticity i.e. $\dot{\Gamma}$. Figure 10.2.5.1 shows the complex variation of $\dot{\Gamma}$ with x due to the effect of the separation position in the nose region. Aft of the nose $\dot{\Gamma}$ is almost constant except for a step jump caused by the method's separation model jumping from

---

[7] For one thing any change in the value of Γ at this stage would violate the boundary condition of stagnation conditions at the separation point.

laminar to turbulent separation. The effect of σ is clearly a straight reduction in $\dot{\Gamma}$; figure 10.2.5.2 shows the effect on the total vortex strength, that is the sum of the strengths of the discrete vortices. This can be seen to be almost linear, despite the variation in $\dot{\Gamma}$, except for a break point due to transition. The effect on Γ is, again, almost a straight factor of 0.6.

The vortex position predictions will be compared with experimental positions from Tinling and Allen [32], figure 10.2.5.3 illustrates these results. Figure 10.2.5.4 shows the experimental vortex position 60% of the way along a body at 20° of incidence. Due to the diffuse nature of the vortices this should be taken as approximate. Also shown is the discrete vortex 'cloud' of the Vortex Cloud Method. Similarly, an approximate vortex position has been interpreted from these discrete vortices and their velocity vectors by deducing the location of the core about which they are rotating. Despite having applied a factor of unity the method produces a reasonable estimate for the vortex position[8]. The current method estimates the vortex position to be both too low and too far outboard. By applying a σ factor of 0.6 to both methods[9] we get a significant shift in vortex positions. Figure 10.2.5.5 shows that the Vortex Cloud Method now predicts slightly inboard of the experimental position. The current method now estimates slightly outboard of experiment. Both estimates show a similar level of accuracy. Hence the effect of σ is to move the vortices up and towards the incidence plane.

Further towards the base of the body figure 10.2.5.6 shows that the Vortex Cloud Method solution is considerably more developed. Again without the σ factor the interpreted Vortex Cloud centre is a fair way outboard of the experimental position. Similarly the current method estimates the position to be too low and too far outboard. Applying σ in figure 10.2.5.7 brings both the Vortex Cloud Method and the current method very close to the experimental position. In fact these may be within the accuracy with which the experimental position has been determined.

In the previous figures it was necessary to attribute some nominal position to the Vortex Cloud solutions. This was achieved by considering the discrete vortices positions and velocity vectors. A more rigorous approach was considered in figure 10.2.5.8 whereby a vortex centroid was located by virtue of each discrete vortex strength and x & y coordinates analogous to a centre of mass. Variations on this theme were produced by excluding the vortices in the feeding

---

[8] Of course both position and strength will need to be correct to predict the correct local normal force distribution.

[9] In the case of the current method an 'applied' factor of 0.22 was used.

sheet and / or the free vortices[10]. It can be seen that these actually produce a centroid little different from the previous approach, perhaps slightly closer to the prediction of the current method.

10.3 THE LINEAR LOAD

10.3.1 The linear component

The method as so far derived would use Slender Body Theory to predict the linear load over the fore body region. This, as discussed, will provide adequate results. However, it is a simple matter to derive a load distribution using a more accurate method and, due to its linear nature, scale it according to incidence.

10.3.2 A more accurate method

The approach selected for the current method is to predict the linear load distribution using, SPARV [46a], a potential source panel method. The distribution is then scaled according to incidence. Figure 10.3.2.1 indicates although this load is linear with incidence simply dividing the distribution by the incidence, in this case 1° and 20°, does not result in a unique curve. From Slender Body Theory we know that the distribution should be linearly dependent upon $\sin\alpha\cos\alpha$ and figure 10.3.2.2 shows that this does indeed cause the distributions to collapse onto a single line. Also shown is the same result as predicted by SBT which can be seen to be higher and lacks the carry over onto the cylindrical after body section.

10.3.3 Comparison with experiment

It is appropriate, at this stage, to make a brief comparison with some experimental data to confirm that the method meets up to expectations.

Figure 10.3.3.1 shows a comparison with Tinling and Allen [32] data for incidences of 10°,15° and 20° which has been collapsed by dividing each by $\sin\alpha\cos\alpha$. The comparison is extremely good when compared to SBT Although the carry-over appears to be under predicted, it must be remembered that the non-linear load will be starting to accumulate in this region. Similarly a good comparison is shown in figure 10.3.3.2 which compares with ONERA data.

---

10 These vortices have escaped the circulatory influence of the complete vortex structure and will, in time, propagate away in the z-direction.

10.3.4 Other geometries

One disadvantage of this method is that if the panel method is not an integral part of the current method then a separate linear run will be required for each new geometry that is to be predicted. Figure 7.4.3.17 shows the effect of even a small change in geometry, in this case two similar forms of ogive fore body, on the local normal force coefficient distribution as predicted by SBT Figure 10.3.4.2 shows how this can be predicted using the panel method. However, in practice it should not prove too difficult to integrate a simple panel method or even a doublet line method into the current method to provide this element of the model. An added advantage of this approach is that any fore body shape can be considered, even those that, locally at least, would be outside the scope of SBT. Figure 10.3.4.3 illustrates the local normal force distribution prediction for a 2-calibre ogive nose. It can be seen that the prediction is much closer than SBT which is at the limits of its applicability with this body. The experimental data is from Goodwin et al [47] and is at incidences of 4°,8° and 16°.

10.4 INTEGRATION OF THE MODEL

10.4.1 The model elements

Having developed separate models for each of, what from the previous sections are considered to be, the important elements of the flow it is now time to integrate them.

Figure 10.4.1.1 depicts a schematic diagram of the complete model. This shows how the local normal force distribution can be split into a linear and a non-linear component. The linear component is a direct function of the body geometry and the angle of incidence. The derivation of the non-linear load is more complex and starts with the generation of an appropriate unsteady two dimensional flow solution which is dependent upon the separation line model. The impulsive flow analogy is then used in conjunction with the body geometry, the incidence and the rationally argued factor σ, to generate the vortex strengths and trajectories for the three dimensional body at incidence. These strengths and positions are then used to derive the non-linear component of the local normal force distribution by using the new extension to slender body theory. Finally, if required, the load distributions can be integrated to obtain the total normal force coefficient and centre of pressure position.

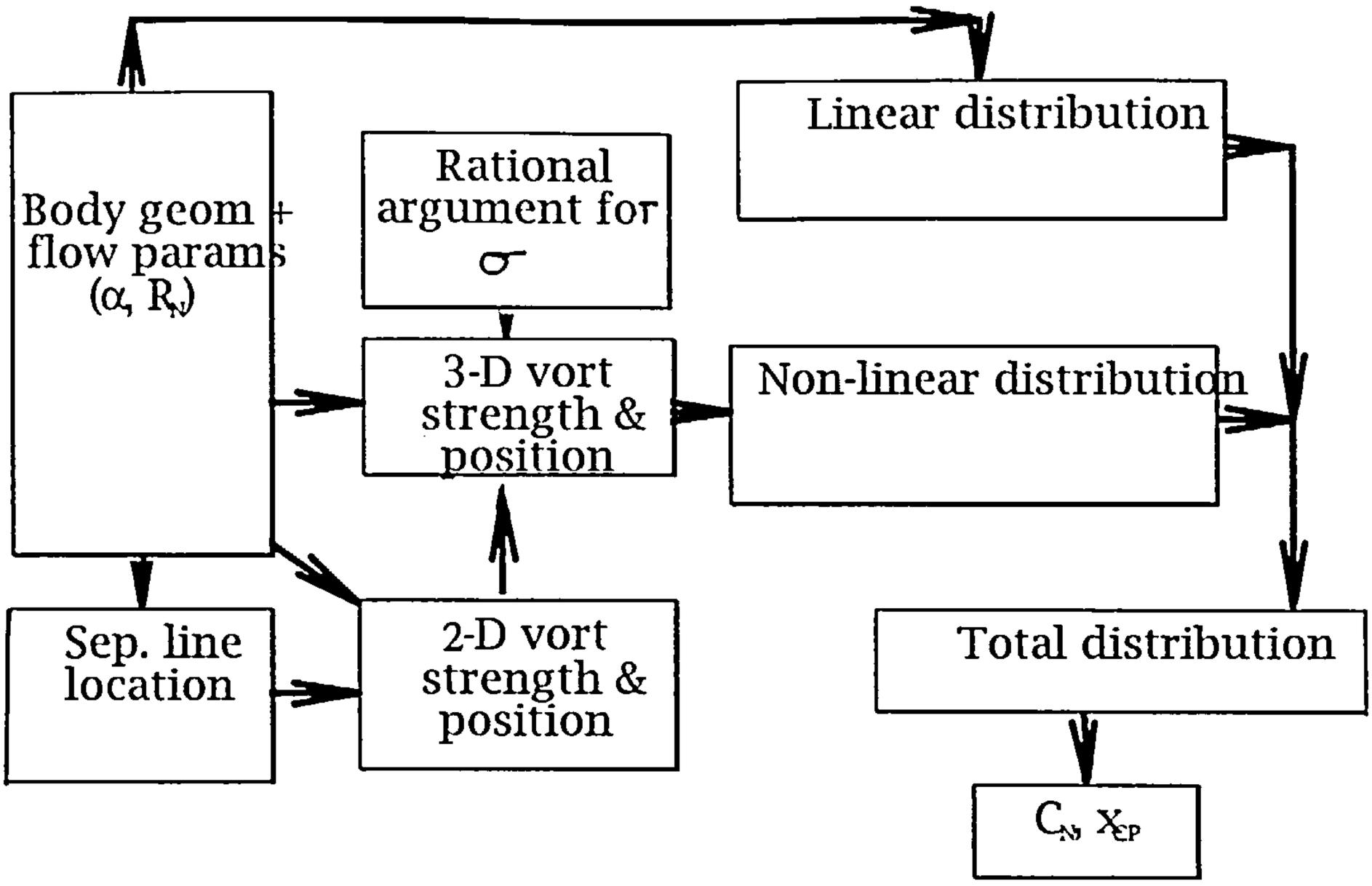

figure 10.4.1.1

10.4.2 Sensitivity to θ_o

Having assembled the complete model it is possible to determine the sensitivity to various parameters. When the model was first run it was found that, due to the derivative terms in the model that derives the load distribution from the vortex strengths and positions, any oscillations in the initial steps of the vortex tracking gave rise to very large spikes in the load distribution. Since the strengths and trajectories were otherwise almost linear, this problem was corrected by using a least squares fit of these parameters.

Having done this the effect of the separation position on the load distribution was investigated. In practice the model used empirical data for this parameter. Figures 10.4.2.1 and 10.4.2.2 show the effect of a $\pm 5^{\circ}$ shift on a nominal separation line position. This can be seen to have a significant effect. Hence the requirement for using a simple empirical data base for this parameter.

By way of comparison figure 10.4.2.3 shows the VCM prediction, the separation angle used by the method and the effect on both of invoking the 'turbulent option in the program. Here a 14° shift in θ_o makes relatively little change in the load distribution. It can be seen that this method predicts turbulent separation poorly (The method is incapable of predicting transitional separation).

10.4.3 Sensitivity to σ

The other parameter that requires sensitivity analysis is σ. This will obviously have an effect on the local normal force distribution.

The effect of increasing this from a nominal σ_1 of 0.2 to 0.22 and 0.25 is shown in figures 10.4.3.1 to 10.4.3.9. Figures 10.4.3.1 and 2 show the effect on predictions of $\frac{dC_N}{dx}$ for incidences of 5°,10°,15° and 20° in turbulent separation. It can be seen that in increasing σ_1 from 0.22 to 0.25 there is, as expected, a small increase in the level of the load distribution. However it is not so great as to move the prediction beyond the bounds of variation in the experimental data. Figure 10.4.3.3 quantifies the increase more readily in terms of C_N. This figure also shows the proportion of linear and non-linear load that make up the total. Figure 10.4.3.4 shows that since the increase in load distribution is fairly constant along the length of the body there is little effect on the centre of pressure distribution. Figures 10.4.3.5 to 10.4.3.8 indicate a similar story for the transitional separation case.

By way of comparison figure 10.4.3.9 shows the effect of varying σ in the case of the Vortex Cloud Method. The nonlinear load distribution varies almost linearly with σ.

11. COMPARISON WITH EXPERIMENT

11.1 COMPARISONS

11.1.1 The nature of Experimental Results

Having developed simple rational models of the elemental processes and mechanisms that go together to describe the aerodynamic flow field around a body of revolution at incidence it is of fundamental interest to compare characteristics predicted by the model with experiment.

Whilst this would be the ideal situation it can not be realised in practice. Although obtaining the predicted data is a simple matter of embedding the model into a computer programme and using it to generate the required results, it is not quite so easy to obtain experimental data. As with any scientific experiment it is not possible to measure any parameter that quantifies some part of a natural system without artificially disturbing the system and hence introducing the possibility of influencing the parameter of interest.

In this case the results are obtained through a series of wind tunnel tests. The tests are set up with all the care and consideration due to any scientific experiment, however, the results still will not correspond to those of nature but an analogue of it. The results will be subject to some degree of experimental error.

It is important that this be born in mind throughout this comparison exercise.

11.1.2 Scope of the Comparisons

The configuration of interest is a simple slender body of revolution and yet the number of parameters that can be varied is considerable. The geometry of the body itself is infinitely variable and even limiting it to the range of forebodies, bodies and afterbodies in general use is still excessively large. The surface finish of the body can effect characteristics as can the Reynolds number, Mach number and, of course, angle of incidence.

It is, thus, apparent that only a subset of those variables can be considered within this thesis.

The objective of this section is to compare the model results with wind tunnel results in sufficient detail to establish whether all the important elements of the flow physics have been considered and with sufficient accuracy to enable reasonable predictions to be obtained. Further, to obtain optimum accuracy for a given level of computer processing time it is important that simplifying assumptions should be in balance with model component accuracy,

since accuracy bought with the CPU time involved in a complex model component can be lost within the accuracy implied by simplifying assumptions made in another component of the model. A feel for this balance should be obtainable.

11.2 EXPERIMENTAL DATA SOURCE

11.2.1 Basic Requirements

If a method for predicting the aerodynamic characteristics of a slender body of revolution is to be of practical use in the design environment it must be capable of rapidly estimating the normal force coefficient and its corresponding centre of pressure at a given angle of incidence. These two parameters are to be of prime importance. However, whilst these results are important to the end user they are not in themselves a particularly good indicator of a correct solution. The reason for this being that there is no unique solution that will give a particular normal force coefficient and accompanying centre of pressure.

Consider, for example, a case that gives a particular value of C_N and with its x_{cp} being half way along the body. Any force distribution along the body that is symmetric about the body centre will result in the required x_{cp}. Subject to this constraint there is still an infinite number of force distributions that would integrate to give C_N. These distributions can, locally, include negative load components. Figure 11.2.1.1 illustrates this principle.

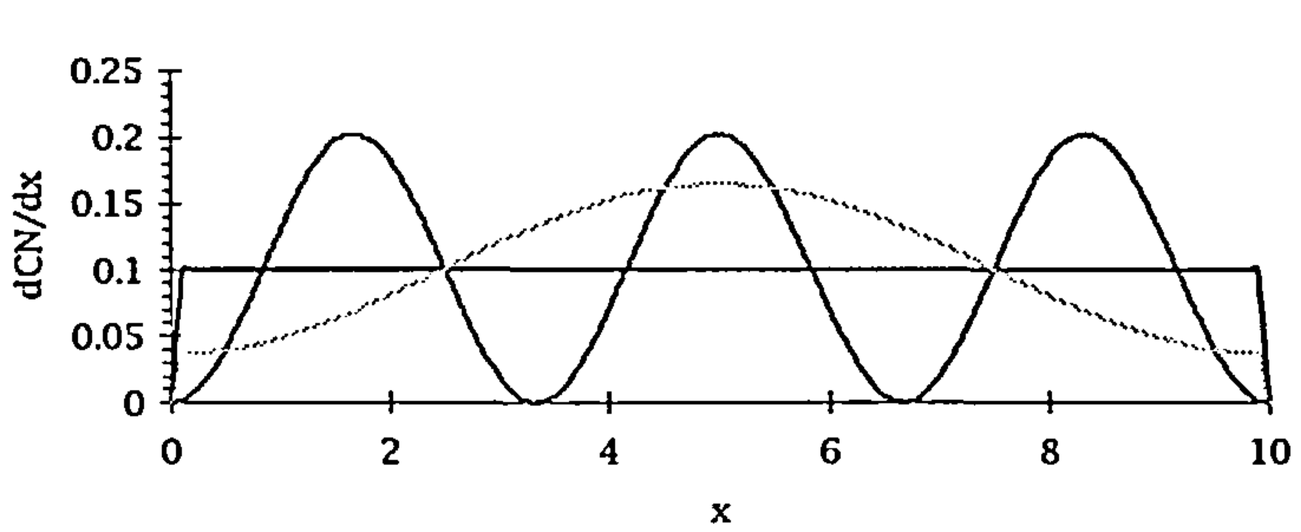

Figure 11.2.1.1 3 load distributions giving equal values of CN and Xcp.

Thus, even though, for a given configuration, a good match is obtained between C_N and x_{cp} this can be purely fortuitous. It is for this reason that the initial emphasis is placed upon the comparison of load distributions.

As discussed in section 7 the following two sets of data were chosen as being good sources of aerodynamic load distributions.

11.2.2 The D.F.V.L.R test series

This test series HARTMANN [30] provides data of the steady pressure measurements which were obtained on the surface of an

ogive- nosed circular body in the incompressible speed range. The tests were performed in the 3m low speed wind tunnel at DFVLR/ AVA in Gottingen (FRG) at angles of attack from 0° to 90° and Reynolds numbers of 2.5x 10^5, 3.7x 10^5 and 7.7x 10^5 (based on body diameter and freestream conditions). The integration of the measured pressures results in the local normal force distributions which can be further integrated to produce total normal force and centre of pressure location.

Of particular interest are the results at incidences of 0°, 5°, 10°, 15° and 20°.

It is important to note at this point that the 3 calibre ogive forebody is described by the following polynomial and is not a true tangent ogive profile:

$$\frac{r(x)}{D} = 0.309840\left(\frac{x}{D}\right) - 0.039867\left(\frac{x}{D}\right)^2 - 0.002615\left(\frac{x}{D}\right)^3$$

The 200 mm diameter model has 24 circumferencially located pressure tappings at each of 15 longitudinal stations along its 2.8 m length.

A more detailed account of this test series is given in section 7.

11.2.3 The ONERA test series

This test series CHAMPIGNY [31], as with the DFVLR series, provides data of the steady pressure measurements which were obtained on the surface of an ogive- nosed circular cylinder body in the incompressible speed range.

The tests were conducted in the pressurised subsonic wind tunnel F1 at ONERA Le Fauga- Mauzac centre. This tunnel has a working section of 4.5m x 3.5m. The freestream Mach number varies from 0.1 to 0.35 and the Reynolds number based on body diameter of between 0.28 to 2.0x 10^6. The use of a special bent sting allowed continuous angles of incidence from 0° to 80°.

Two models were used in the test series. The first was 120mm diameter by 1800mm long including a 3 calibre tangent ogive nose. 354 pressure tappings were distributed across 22 stations. The second model of identical geometry, but with a smooth, untapped surface was used for flow visualisation work.

The main purpose of this test series, and indeed the DFVLR series, was to investigate the aerodynamic characteristics at high angles of attack. Consequently the number of incidence cases is limited. The angles of incidence of interest are 0°, 10° and 20°.

Again, a more detailed account of this test series is given in section 7.

11.2.4 The Tinling and Allen test series

In this test series TINLING & ALLEN [32] the body, an ogival nose 3 calibres long tangent to a cylindrical afterbody 7.7 calibres long was tested at Mach 0.3 at Reynolds numbers of 0.44×10^6 and 3×10^6. The important aspect of these tests is that they include sufficient vortex wake measurements to determine the location of the vortices as they pass down stream.

This data will be used to determine the accuracy with which the vortex paths can be determined.

11.3 LOAD DISTRIBUTION PREDICTIONS

11.3.1 The load components

For the purpose of predicting the longitudinal distribution of local normal force it is convenient to split the load, POLHAMUS [48] fashion, into a linear[1] component and a non- linear component associated with the existence of the vortex structures that so dominate the lee- side flow field.

The linear component, as described in section 10, can easily be derived from slender body theory as a function of the rate of change of body cross- sectional area. Although simple the accuracy of this method is dependent upon the fore body slenderness ratio, furthermore it fails to predict the carry- over load on to any constant diameter body section following the fore- body. For this reason a more accurate potential method based on a source panel method was used for this component.

However the main contribution of this thesis, in addition to the clearer understanding of the flow physics, is the prediction of the non- linear load distribution component.

Although for the purpose of load prediction it makes sense to split the load into its linear and non- linear components this is not so relevant for the purpose of comparison since the experimental data can not be similarly split.

However, since the linear lift acts primaryly on the forebody, this will be considered in detail before comparisons are made for the load over the full length of the body.

11.3.2 Reynolds number regimes

The choice of Reynolds number regimes to be used for comparisons is significant due to its influence over the nature of

---

[1] in this context linear refers to the variation with respect to the angle of incidence.

separation and location from which this occurs. This, subsequently, has an effect on the strengths and locations of the body vortices, which in turn effect the load distributions.

As discussed in section 7 the type of separation occurring on a body at incidence is a function of Reynolds number and incidence and may vary along the length of the body. Clearly specifying a Reynolds number is not necessarily sufficient to define the type of separation likely to occur. Hence the idea of Reynolds number or separation type regimes is used. Here Reynolds numbers are chosen where the separation over a significant length of the body over a reasonable range of incidences is primarily of one particular type. The three separation types being laminar, transitional and turbulent. In practical applications separation would almost always be of the turbulent type. To ensure that the Reynolds number dependence element of the model is reasonably representative the transitional regime will also be examined.

11.3.3 Prediction of forebody load distribution

Before examining the strongly non-linear after body load we shall check the accuracy of the primarily linear forebody load distribution.

The load distribution over the nose section of the body is a strong function of the nose profile. This can clearly be seen by considering the slender body theory expression for the load distribution in this region which depends on the rate of change of cross sectional area along the body length.

The sensitivity of the load to the nose profile is considerable as can be seen in figure 7.4.3.17. Here the tangent - ogive nose profile of the ONERA wind tunnel is compared with that of the polynomial representation of the DFVLR wind tunnel model. As can be seen the two profiles are almost identical, the only difference being that the DFVLR nose is slightly more slender. From section 10.1.1 we see that slender body theory predicts that the point of maximum load occurs at x= 2.47 radii aft of the tangent ogive nose apex but at 2.68 radii aft on the polynomial ogive nose. This represents an aft shift in the load of some 0.2 radii due to a maximum difference in local body radius[2] of only 0.028 radii.

The first comparison is for the DFVLR body in the turbulent separation region and is shown in figure 11.3.3.2. Here we see four lines representing the predictions at 5°, 10°, 15° and 20° of incidence with four corresponding sets of symbols representing the experimental data.

---

[2] this occurs 1.91 radii aft of the nose apex.

The distributions show a slight but consistent over prediction of load. The predictions, being inviscid, do not make any allowance for the slight displacement thickness that will be generated by the boundary layer. This displacement will be a function of both distance from the nose apex and position around the body circumference. However, the effect of the boundary layer on the fore body load will be to induce a more rapid build up of load similar initially to the change in load distribution between the slender polynomial ogive nose profile and the thicker tangent ogive nose profile. Since this difference is not in the same sense as our comparison the discrepancy is not thought to be due to viscous effects of this nature.

Another explanation might be due to inaccuracies in the wind tunnel model nose profile. However, in this case we might expect a shift in the point of maximum local load. This is not apparent, furthermore the discrepancy appears to be more consistent with an overall load scaling of approximately 1½%. This is most probably due to experimental errors from numerous sources such as wind tunnel flow curvatures and tolerances in incidence settings[3]. There will also be errors introduced in the post processing of the wind tunnel data such as the integration of circumferential pressure distributions to find the local normal force component.

Small additional discrepancies in the vicinity of the forebody cylinder junction are due to the non- linear lift terms becoming significant. As expected, these are worse at the highest incidences.

Figure 11.3.3.3 is a similar case but at a Reynolds number consistent with the transitional separation regime. The small over prediction is hardly visible in this case except for the α=20° case at x/a=5.

Figure 11.3.3.4 shows the predicted forebody load distribution for the ONERA wind tunnel model with the tangent- ogive nose profile. In this case the test series was less comprehensive than that of DFVLR and only two incidences were considered, 10° and 20°. This first case, in the turbulent regime, shows the same slight over-prediction apparent in figure 11.3.3.2 but with a slightly greater non-linear discrepancy aft of the linear load peak, particularly at the 4 radii station. This may be due to a rogue pressure tapping , indeed there does seem to be a greater degree of scatter in the data points in this series.

Figure 11.3.3.5, is the ONERA counterpart to figure 11.3.3.3 in the transitional separation regime. This case also indicates a lesser degree of over- prediction compared with the turbulent cases. This may indicate that although the effect is probably not directly due to the boundary layer development it may be Reynolds number related.

---

[3] In this case an incidence setting error of less than 1/3 of one degree would be sufficient.

In conclusion it is evident that the distribution of local normal force over the nose region is good and the small[4] error that is evident[5] will certainly be within the bounds of accuracy of the non-linear predictions and so any more complex a mathematical model in this area would not be justified[6].

11.3.4 Prediction of the total load distribution

Although the load distribution over the nose region represents the major proportion of the total body load, it should be evident, from the earlier sections of this thesis, that it is the load distribution on the after body that is likely to cause the greatest contribution to error due to the complexity involved in predicting its highly non-linear nature, particularly in terms of x_{CP}.

Looking first at the turbulent DFVLR case, figure 11.3.4.1, we can see that the overall form of the load distribution is correct. That is to say, unlike the load over the nose, the load distribution over the afterbody is largely constant, but increases more non-linearly with incidence. This non-linearity appears to be correctly modelled but will be looked at more closely during comparisons of total normal force versus incidence.

Examination at a closer level indicates that the non-linear local load, although relatively constant, does exhibit a small axial variation particularly at the highest incidences. This variation is not reflected by prediction. There is also evidence that a 'dip' in local load occurs in the vicinity of the nose-cylinder junction before the non-linear load builds up. Overall, the prediction is reasonable with, perhaps, a slight tendency to under-predict the distribution.

Figure 11.3.4.2 continues with Reynolds number in the transitional separation regime. As would be expected, the magnitude of the load distribution is less than that in the turbulent separation regime. In this case axial variation of local load is much less marked and hence its prediction is fairly good.

The ONERA turbulent separation case, figure 11.3.4.3, shows a marked under prediction at 20° but a reasonable prediction at 10° of incidence however there is less axial variation of local load and hence this trend is better predicted. The under prediction at high incidence is likely to have an effect on the integrated characteristics which will be discussed in section 11.4.

The corresponding ONERA transitional case fairs much better as shown in figure 11.3.4.4, this prediction compares extremely well.

---

[4] <2%

[5] Assuming that this discrepancy is in the prediction and not due to experimental error (which it may well be).

[6] i.e. CPU time.

11.4 OVERALL AERODYNAMIC CHARACTERISTICS

11.4.1 Integrated results

The most important aerodynamic parameter to be predicted is the normal force coefficient C_N. Having determined the local normal force distribution along the length of the body it is a relatively simple matter to integrate this with respect to x to obtain C_N. Assuming that the load distribution was predicted with reasonable accuracy, it is reasonable to assume that C_N will be obtained to a similar degree of accuracy.

The pitching moment coefficient, C_M, is more sensitive to distribution than the normal force coefficient. Again, this parameter is determined through the integration of the local normal force distribution about the moment reference point[7].

A conceptually, and practically, more useful parameter to accompany the normal force coefficient is the centre of pressure, x_{cp}, the point through which the normal force coefficient is assumed to act. It is particularly useful since its accuracy can be directly related to the length of the body and to the accuracy with which the axial distribution of normal load has been predicted.

Both C_M and x_{cp} will be compared, despite a degree of redundancy, since they can have important consequences for control analysis.

The local normal force distributions contain both linear and non- linear components. Since the normal force and pitching moment coefficients are determined through the integration of the force distributions, they also can be thought of as having linear and non- linear components. These components will also be discussed during the comparisons of theory and experiment.

A value of x_{cp} can be obtained by dividing the linear pitching moment coefficient by the linear normal force coefficient. Although its meaning is less obvious it does indicate the limiting value of x_{cp} as incidence tends to zero where the linear terms dominate.

11.4.2 Normal force and pitching moment coefficients and centre of pressure position

The cases to be compared are the same as the load distribution cases and considered in the same sequence.

Firstly the DFVLR turbulent separation case. Figure 11.4.2.1 depicts the variation of normal force coefficient with incidence. From consideration of the linear component, the growth rate of the non-linear component can readily be deduced. At the higher incidences

---

[7] in this case the nose apex

this term represents approximately half of the total normal force. The accuracy of the prediction appears reasonable (<3%) at 20° although the trend deviates by 8-10% at 15°.

Owing to the fact that the majority of the non- linear load distribution act at a significant distance from the moment reference point the non-linear component of C_M represents approximately 80% of the total at 20°. Due to the heavy dependence on the 'hard to predict' part of the equation the accuracy drops to <8% for this term.

Although the error is predicting C_M may appear significant, figure 11.4.2.2, when viewed in terms of x_{cp} , figure 11.4.2.3, the discrepancy is seen to be quite small. Between 10° and 20° the error is x_{cp} is < 0.3 radii. At incidences of 5° or less the prediction would appear to diverge significantly from the experimental results if x_{cp} were derived by taking the ratio of C_M and C_N. At low incidences this becomes the ratio of two small numbers both of which are tending to zero. The correct method for the determination of x_{cp} as incidence tends to zero is to examine the ratio of the slopes of C_N and C_M with incidence. In the case of predicted centre of pressure this simply tends towards the 'linear x_{cp}' value which is independent of incidence. Using this approach it can be seen that x_{cp} is predicted very well at low incidences also.

Figure 11.4.2.4 shows the effect of reducing the Reynolds number to within the transitional separation regime. In this case less non-linear load is generated, as is expected. However, the theory over predicts by about 6% at 20° reducing to <1% at 10°. As before the experimental results to not give zero C_N at 0° incidence. Similarly the error in C_M, figure 11.4.2.5, at 20° is about 10% and the experimental value at zero incidence is significant. These C_N and C_M predictions combine to give x_{cp} as in figure 11.4.2.6. This reveals that x_{cp} predicted to within 0.2 calibre's at higher incidences. The prediction is slightly off at 5° but improves at low incidences.

Moving on to the ONERA data figure 11.4.2.7 shows the effect of under predicting the local normal force distribution on C_N. At 20° this is almost 10%, however the error at 10° is negligible. Similarly, as would be expected, C_M is also under predicted in figure 11.4.2.8. Nevertheless, since the overall shape of the load distribution is essentially correct, the centre of pressure is fairly well placed (<0.4 calibres) as shown in figure 11.4.2.9.

Dropping down to a transitional Reynolds number the normal force coefficient, figure 11.4.2.10, is predicted to within 3% at 20° and almost exactly at 10°. Figure 11.4.2.11 indicates a similarly good level of accuracy in predicting C_M. Consequently the centre of pressure, figure 11.4.2.12, is almost exactly predicted.

On the whole, the level of accuracy is quite reasonable considering the simplicity and hence speed, of the method. The accuracy of the results is comparable to that of generally used semi-empirical methods.

11.5 VORTEX PATH PREDICTIONS

11.5.1 The significance of vortex locations

As has already been discussed the non-linear component of the normal force distribution along the length of the body is induced by the body vortices. The form and magnitude of this loading is a function of the vortex strengths and positions.

Since the induced load is a function of both strength and position it is conceivable that a given load distribution may be obtained by any number of combinations of strength and corresponding position. It is clear then that is possible that the good results so far obtained for the load distributions and integrated forces could be purely fortuitous[8].

As a precaution the vortex positions should be checked against experimental results.

11.5.2 Comparison with experiment

Although this simple predictive method models the vortices as singular points in the y-z plane that trace a line through space as the plane is swept through the x-co-ordinates, the physical vortices are distinctly finite in size. The region of space occupied by a vortex is usually of the order of a body radius across. The experimental data of TINLING & ALLEN [32] attempts to locate the vortex core and gives this parameter as its 'position'. The vortex core itself occupies a finite region of space and there is always some difficulty in locating it with any great precision, hence the experimental positions should be considered approximate.

It is, of course, difficult to assess the significance of any error in the comparison without some other datum being present. For this reason a third set of data is included which illustrates the accuracy with which the Vortex Cloud Method is able to predict the vortex locations.

Figure 11.5.2.1 depicts y-z plane slice through the flow field at an x station of x/l=0.9385 which is close to the aft end of the body. The body is at an incidence of 20 degrees. The cross symbol indicates the predicted vortex location which is to the lee side of the body. The body is contained within the quarter circle arc about the origin and of radius 1. The experimental vortex location, denoted by the letter E, lies within 0.1 of a radii on the body side of the prediction. Around

---

[8] Improbable considering the scope of the comparisons but one must be rigorous.

these points can be seen the discrete vortex locations generated by Vortex Cloud Method. Each discrete vortex is denoted by a circle symbol and each has a line attached indicating the instantaneous direction and speed of movement. The sheet can clearly be seen on the left of the plot and the main vortex structure towards the centre. The vortex core region is located approximately 0.1 radii in board of the experimental data.

Moving up stream, towards the body apex, figure 11.5.2.2 depicts the flow field in the y-z plane at a station x/l=0.6131. Again the predicted vortex location is within approximately 0.1 radii of the experimental value. In this case the prediction is slightly outboard of the experimental value. The Vortex Cloud Method solution illustrates how the vortex structure is less developed at this station and is more compact and confined to a region closer to the body. The approximate core location by this method is about 0.2 radii inboard of the experimental result.

The third case considered is back at the x/l=0.9386 y-z plane but at an incidence of 15°. Figure 11.5.2.3 shows the predicted vortex location to be approximately 0.2 radii outboard of the experimental value and the Vortex Cloud Method result about 0.25 radii above the experimental value.

The comparisons give a reasonable amount of confidence in the model. In fact some of the results may well be within the accuracy of the experimental data.

11.6 ADDITIONAL CASES

11.6.1 The effect of compressibility

In this section we examine the effect of compressibility on the aerodynamic characteristics of slender bodies.

As in the earlier sections, axial distributions of normal force, DRA [49], will be examined since this is a more sensitive indicator of accuracy than overall forces and moments.

Figure 11.6.1.1 depicts the load distribution over the forebody region at two angles of attack. As might be expected, slender body theory gives a better prediction at Mach 0.7. At the higher Mach numbers of 1.45 and 1.8 ,although the load over the first three radii is predicted well, the following three radii are not so accurate.

Figure 11.6.1.2 depicts the load distribution over the entire length of the body. Whilst it can be seen that the non-linear load is slightly under predicted, it is certainly acceptable in terms of both trend and magnitude.

It can be concluded that the method could certainly be applied at high subsonic Mach numbers, where slender body theory would be used in the nose region. At higher Mach numbers the non-linear load is acceptable but the load from its linear peak to the body junction would need to be re-examined. A supersonic panel method might be appropriate.

12. DISCUSSION & CONCLUSIONS

12.1 GENERAL

The aim of this section is to summarise the work completed in this study, to comment as appropriate on the findings in the wider context and to clarify what has been achieved.

The section starts with some insights gained into the physics of the flow with an emphasis on three dimensional effects. This information is then applied in the construction of a new model. The model is then validated using experimental data.

12.2 THREE DIMENSIONAL EFFECTS

12.2.1 The boundary layer, transition and separation

In many of the quasi-two-dimensional methods, the position at which cross-flow separation occurs has a direct effect upon the estimated rate of vorticity generation since it is a function of the cross flow velocity at the point of separation as described in section 7.3.7 (see approximate method). It is quite likely, then, that the separation line is important in general.

Relating the three dimensional steady flow about a slender body at incidence to the unsteady flow about an impulsively started circular cylinder, (see section 6.2.1) although conceptually enticing, will immediately remove from sight a great many three dimensional processes that may be key to explaining certain phenomena.

A comparison of the 2-D cross flow separation concept of section 8.1 with the 3-D concept, figure 8.1.5.1, illustrates this well. Further more, figure 8.1.5.1 only depicts the processes at the point of separation, whereas figures 8.1.4.1 to 8.1.4.4 depict separation in the wider context.

There can be no doubt that we are dealing , here, with a highly three dimensional process.

As discussed in section 8.3, the state of the boundary layer at the point of separation has a considerable influence upon where separation occurs. Figure 8.3.2.3 illustrates the various features involved. In short, a laminar boundary layer will separate earliest. A turbulent boundary layer will progress further. If the shear layer created by a separated laminar boundary layer becomes turbulent quickly enough, it will re-attach itself and continue as a turbulent boundary layer before separating later than a fully attached turbulent boundary layer.

It is important, then, to know the state of the boundary layer at separation. Sections 8.2.1 to 8.2.4 discuss the various mechanisms that give rise to transition. As can be seen in figures 8.2.3.1 and 8.2.4.1 these are three dimensional phenomenon.

In practical terms, for the geometry of interest, the prime parameters influencing the state of the boundary layer are Reynolds number and incidence. These are discussed in section 8.3. It is clear that the effect of increasing Reynolds number is to increase the extent of the turbulent boundary layer whereas an increase in incidence tends to move the state of the boundary layer towards the laminar end of the spectrum.

These effects can be seen in the experimental data, see figures 7.4.4.2, 7.4.4.4, 7.4.4.5 and 7.4.4.6. Figure 7.4.4.3 shows a sketch of different separation states and figures 7.4.3.19 and 7.4.4.1 show a flow visualisation photograph depicting all three types of separation coexisting on the same configuration.

An additional parameter that can effect transition is the surface roughness of the model. Figure 7.4.6.22 shows how much effect just the flow visualisation oil can have.

12.2.2 Vorticity generation

A sound understanding of the state of, and the mechanisms within, the boundary layer are important since they not only influence the point of separation but it is within the boundary layer that the majority of the vorticity is generated.

It is clear that the boundary layer is highly three dimensional. It follows that the vorticity within it will also exhibit three dimensionality. This is an important concept, one that is over looked in the quasi-two dimensional scenario.

In fact, in the quasi-two-dimensional models the only component of vorticity that can exist is that aligned with the body axis, as in figure 8.5.1.1. However, it is quite clearly evident that the main component of vorticity within the boundary layer of a slender body at low incidence is that tangential to the body circumference, i.e. the sole component that exists at zero incidence.

Section 8.5 discusses the generation of vorticity in more detail and figures 8.5.1.3 and 8.5.1.5 depict the generation of the three components of vorticity.

Whilst it is valid to discuss vorticity in terms of its three components, it should be remembered that these simply describe the orientation of a total vorticity vector. Thus a change in one component represents a change in the total vector that could result in a change in the other two components if the total magnitude were to remain constant, for instance.

Thus it is quite possible to envisage a scenario where the local total vorticity vector changes its orientation and if only one of its components were examined it may appear to reduce (or increase) with no apparent cause. This subject will be returned to later.

It is also interesting to note, particularly since no previous references could be found referring to this phenomenon, that a small region of negative (compared to the sense of the feeding sheet) vorticity is generated outside the boundary layer and to the windward side of the feeding sheet, see figure 9.2.2.13. The mechanism by which this vorticity is generated is described in section 9.5.2 and 9.5.3. Although of little significance in terms of the generation of vorticity, it is associated with a mechanism which can accelerate transition.

Some of the simplified quasi-two-dimensional methods use an approximation for the rate at which vorticity is generated by the separated boundary layer. This approximation has been compared with the actual rate of generation within a Navier-Stokes solution as discussed in section 9.5.4. Figure 9.5.4.1 indicates that the approximation is very good. It appears that this is the first time that this method has been validated in this (very direct) manner and certainly in this context.

12.2.3 Vorticity convection

The manner in which the main component of vorticity, ζ, convects after its generation is best depicted in figure 9.4.1.2. As expected the vorticity is fed through the feeding sheet into the main vortex structure. Figures 9.2.2.11 and 9.2.2.12 show that there is also a significant component of vorticity that is not aligned in the ζ direction.

Figure 9.2.2.20 shows, $\sqrt{\xi^2+\eta^2}$, the magnitude of the vorticity normal to the ζ component direction. This indicates that this vorticity is at its maximum not at the vortex core, as with ζ, but in a halo surrounding it. This curious phenomenon does not appear to have been noted in the literature previous to this study. The most likely reason being that the η and ξ components of vorticity are not so easily extracted, particularly from experimental data sources. Furthermore, previous researchers have tended to examine the ζ component, the total magnitude or helicity, none of which would reveal this effect. Finally, of course, many researchers have been conditioned to think that the ζ component of vorticity is the only term of interest and so have 'blinkered' themselves.

In terms of the total vorticity vector, this would imply that it is aligned with ζ in the vortex core but as one moves out from the core,

in any direction, the vector points slightly inwards in a conical fashion.

12.2.4 Circulation and accumulation of vorticity

One of the key issues to be examined is a comparison of the rate at which vorticity is generated with the rate at which it is accumulated within the body vortices.

The rate at which this accumulation takes place was also calculated for the Navier-Stokes solution. By calculating the circulation about an area containing the body vortex at a particular axial station and then repeating at successive stations it is possible to calculate the rate at which vorticity is being accumulated.

This rate is depicted in figure 9.5.4.1 as a function of axial position along the body. It is interesting to note that the rate appears to reduce with distance but with the same slope as the rate with which the vorticity is generated.

The ratio of the rate of generation to the rate of accumulation is equivalent to the parameter σ. Figure 9.5.4.1 indicates that in this case it is equal to 0.7.

It may not be valid to take this numerical value and compare it with the traditionally accepted value of σ due to the high Mach number of this case, see section 9.5.6. However, it does confirm the disappearance of vorticity between its generation at the point of separation and its accumulation in the body vortices if viewed in two dimensions only.

It is clear that this apparent loss of vorticity is primarily due to the total vector rotating slightly away from the ζ direction.

This, in a sense, now lends credence to the application of the σ factor which was, previous to this study, purely an empiricism. This factor now represents a simple model of an understood phenomenon.

It also confirmed that, to a first order, the rate of increase of accumulated vorticity is linear with distance from the body apex. This fact could be utilised in further work, perhaps exploiting the quasi-conical nature of the flowfield.

To a higher order there is now evidence that the rate of generation of vorticity falls slightly, in a linear fashion, with distance from the body apex

12.3 A MORE RATIONAL MODEL

12.3.1 A return to basics

As has been mentioned earlier, ever increasing complexities have been added to the Vortex Cloud Method in an attempt to remove the need for the σ factor. These attempts were doomed to fail since the model is based upon quasi-two-dimensional theory and, as we now see, the problem is three dimensional.

It then becomes clear that the additional complexities only serve to increase CPU time and as such are best removed.

Accepting that a modification will be required to account for three dimensional effects, it would be best to select the simplest model and model components as possible.

12.3.2 Model components

The mathematical model consists of two main components. One element predicts the strength and position of the body vortices and the other predicts the body axial load distribution induced by, amongst other effects, the vortices themselves.

The first of these is a development of BRYSONs [3] method for predicting the two dimensional flow about one impulsively started circular cylinder and is discussed in section 10.2.1. Here the velocity of the vortices is calculated to satisfy the condition of no net force on the feeding sheet and point vortex. The strength of the vortices is calculated such that the separation points are stagnation points. These two calculations are highly interactive since the vortex position, at any moment in time, depends upon its velocity history, its velocity depends upon its strength and its strength depends upon its position. The time dependent solution of these equations reveals the strength and positions of the vortices on the lee side of an impulsively started cylinder.

The impulsive flow analogy is used to relate Bryson's unsteady two-dimensional solution to the steady three-dimensional solution that we require.

Having derived values for the strengths and positions of the vortices as they progress downstream it would now be possible to determine the vortex induced load distribution along the body. However, the approach relies upon a quasi-two-dimensional step that filters out any true three dimensionality from the solution. As we have seen, this will result in an over estimate of the vortex strengths. Hence, before taking the next step it is necessary to insert a new model to account for these three-dimensional effects. The simplest model is to factor the vorticity by about 0.6. Whilst this may appear

to be as empirical an approach as use in previous methods, it is argued that it is an element of the model that is performing a specific, understood, function and as such is no more[1] empirical than the constants that represent the acceleration due to gravity or the speed of light. It is conceded, however, that it would be impetuous to claim, on the basis of the work so far, that the whole phenomenon is fully understood. Further work may reveal that the constant, σ, is a function of Mach number, for instance.

Section 10.2.4 describes the application of this model. Having calculated the strengths and positions of the vortices it would be a simple matter to apply the factor now. This would result in the strength being reduced by exactly σ. However, this would result in an inconsistent solution since the vortex strengths were originally set by ensuring that they caused the separation points to be stagnation points. This would no longer be the case. Further more, the vortex positions are a function of their strengths and hence their positions would also be inconsistent.

To ensure a constant solution the factor needs to be applied at each time step, whilst the solution is being sought. As mentioned in section 10.2.4 the solution 'adjusts' itself at each step to satisfy the constraints. The consequence of this is that the ratio of the factored strength to the unfactored strength will be different to the applied factor. Thus, the applied factor, σ_1, is necessarily different to the equivalent value of σ, a value of about 0.2 is appropriate.

Having predicted the strengths and positions of the vortices, corrected for three-dimensional effects, the second part of the model can be applied to derive the body axial load distribution. This part of the model is based on a new extension to Slender Body Theory as derived in section 10.1.2. Whilst the method is capable of predicting the linear component of the load a more accurate estimate, subsonically at least, is easily obtained from a panel method and so this approach is used.

The extended Slender Body Theory, although complex in its derivation, is very simple to apply and hence is computationally efficient. A simpler derivation by SACKS [45] produces the result for the total force induced by a symmetric pair of constant strength vortices at a fixed position relative to a constant diameter body. The new, more general, result derived in section 10.1.2 gives the load distribution due to any number of vortices, with arbitrarily varying positions and strengths, along the length of a variable diameter body. If the total force is required, as produced in Sacks method, the load distribution can be integrated.

Section 10.1.3 shows that Sacks result is a special case of the more general result, thus giving confidence in the new derivation.

---

[1] if one can determine different orders of empiricism.

The method, although applied here to a symmetric pair, is capable of dealing with any number of vortices. One application of this ability might be to model the asymmetric vortices as generated by a body at high angles of attack. Whilst a feasible case, this would need to be carefully validated since the fundamental assumptions implicit in Slender Body Theory may be contravened (a worth while exercise nevertheless). A better application would be to model the body vortices in the presence of, say, a pair of vortices generated by an upstream canard control surface.

Having derived the body load distribution it finally remains, if required, to integrate this result to give the total normal force and centre of pressure position.

12.4 VALIDATION

12.4.1 Load distributions

Section 11.3.4 discusses the accuracy of load distribution predictions. Figures 11.3.4.1 to 11.3.4.4 illustrate the ability of the method to predict the distributions over a range of incidences and Reynolds numbers. Considering the simplicity of the method it is clear that the results are very good. The 20° incidence case in figure 11.3.4.3 shows a slight underprediction, also some local variations of the non-linear load are not predicted, however, these are likely to be tolerable particularly if the integrated results are of greater interest.

12.4.2 Forces and centres of pressure

Section 11.4 discusses the overall aerodynamic characteristics and figures 11.4.2.1 to 11.4.2.12 compare the predictions of C_N, C_M and x_{CP} with experimental results. Again these results compare quite reasonably and show that the method should make a useful engineering tool.

12.4.3 Mach number effects

Section 11.6 considers compressibility effects on the accuracy of prediction. Mach numbers of up to 1.8 were considered in this comparison. It is shown that whilst the non-linear component of the load distribution is reasonably predicted the linear load is under predicted. However, reverting back to the purely Slender Body Theory result for the distribution gives a marked improvement. Other simple methods are available for the prediction of the supersonic linear

component and so a further improvement could be obtained if required.

12.5 COMPARISON WITH REQUIREMENT

It is appropriate to review the original objectives of this study, as set out in section 5.4, and compare them with what has been achieved. Objective 5.4.1 has certainly been met in the literature survey.

Objective 5.4.2 has also been achieved through the use of both experimental and numerical data. A better understanding of the three-dimensional generation and convection of vorticity has been obtained, in addition to a previously unnoticed source of negative vorticity. Furthermore, a simple method for the prediction of vorticity generation has been validated against CFD predictions and new insights into the accumulation of vorticity have been gained.

Finally, objective 5.4.3 has been achieved in the development of the new model; a fast, easy to apply, reasonably accurate and rational model of the vortices on the lee side of a body of revolution at incidence. This model was built upon the insights gained into the physics of the flow and a new extension to Slender Body Theory.

12.6 FUTURE WORK

12.6.1 User interface

The implementation of the model within the computer program is still in a development state. With more time devoted purely to programming the program could be made more user friendly.

12.6.2 Extensions to the method

It would be useful to extend the scope of the program to include lifting surfaces. Since the vortex strengths and positions are known it should be possible to obtain better estimates for vortex interference. The method is also capable of modelling vortices that have been generated by lifting surfaces located upstream.

The nature of part of the modelling is such that it should be possible to apply simple mathematical transformations to extend the application to non-circular section bodies. Further work would be necessary to incorporate a non-circular body separation position model.

The case of a transformation to a flat plate section would be a useful start point since the location of separation is known apriori.

12.6.3 Further research

As has been mentioned earlier, it would be interesting to extend the scope of the numerical simulation study to other Mach numbers and incidences. A series of subsonic cases would be interesting as soon as some appropriate solutions become available.

13. REFERENCES

1	Lacau, R.G. Robert, M.	Some trends in missile aerodynamics, AGARD Conference proceedings No493 Missile Aerodynamics, Friedrichshafen, Germany 23-26 April 1990
2	Allen, H.J.	Estimation of forces and moments acting on inclined bodies of revolution of high fineness ratio. NACA RM A9I26 1949
2a	Goldstein, S. (Editor)	Modern developments in fluid dynamics, Volume 1, Oxford: The Clarendon Press 1938 pp.39-40
3	Bryson, A.E.	Symmetric vortex separation on circular cylinders and cones. J.Appl.Mech. Dec 1950 pp.643-646
4	Angelucci, S.B.	A multivortex method for axisymmetric bodies at angle of attack. J,Aircraft Vol.8 No.12 Dec 1971 pp.959-966
5	Edwards, R.H.	Leading-edge separation from delta wings. Jour. Aero.Sci. (readers forum) vol .21 No.2 Feb 1954 pp.134-135
6	Brown, C.E. Michael, W.H.	Effect of leading-edge separation on the lift of a delta wing. J.Aero.Sciences Oct. 1954 pp.690-706
7	Mangler, K.W. Smith, J.H.	A theory of the flow past a slender delta wing with leading edge separation. Proc.Roy.Soc. 1959 Vol.A251, P.200-217
8	Smith, J.H.B.	Improved calculations of leading-edge separation from slender delta wings. RAE TR 66070 March 1966

9 Sacks, A.H.
Lundburg, R.E.
Hanson, C.W.
A theoretical investigation of the aerodynamics of slender wing-body combinations exhibiting leading-edge separation.
NASA CR 719 March 1967

10 Gerrard, J.H.
Numerical computation of the magnitude and frequency of the lift on a circular cylinder.
Phil.Soc. Vol. 261 No.1118
Jan 1967 pp.137-162

11 Fage, A. &
Johansen, F.C.
The structure of the vortex sheet.
Philosophical Magazine. Vol.7
1928 pp.417-436

12 Wardlaw, A.B.
Multivortex model of asymmetric shedding on slender bodies at high angle of attack.
AIAA Paper 75-123 Jan 1975

13 Deffenbaugh, F.D.
Marshall, F.J.
Time development of the flow about an impulsively started cylinder.
AIAA J. Vol.14 No.7
July 1976 pp.908-913

14 Deffenbaugh, F.D.
Koerner, W.G.
Asymmetric Vortex Wake Development on missiles at high angles of attack.
J.Spacecraft Vol.14 No.3
March 1977 pp.155-162

15 Stratford, B.S.
The prediction of separation of the turbulent boundary layer.
J.Fluid Mech. Vol.5
Jan 1959 pp.1-16

16 Schindel, L.H.
Effects of vortex separation on the lift distribution on bodies of elliptic cross section.
J.Aircraft Vol.6 No.6
Nov-Dec 1969 pp.537-543

17 Marshall, F.J.
Deffenbaugh, F.D.
Separated flow over bodies of revolution using an unsteady discrete-vorticity cross wake, Part I - Theory and application.
NASA CR-2414 June 1974

18 Nielsen, J.N.
Mendenhall, M.R.
Symmetric and asymmetric vortices from inclined bodies of revolution - theory and experiment.
Symp. on advanced problems and methods in fluid mechanics, 13th Olszlyn, Poland.
Sept. 5-10 1977 pp.531-551

19 Barger, R.L.
A distributed vortex method for computing the vortex field of a missile.
NASA TP-1183, June 1978

20 Mendenhall, M.R.
Spangler, S.B.
Perkins, S.C.
Vortex shedding from circular and non-circular bodies at high angles of attack.
17th Aerospace sciences meeting, New Orleans, La.
January 15-17, 1979

21 Mendenhall, M.R.
Predicted vortex shedding from non-circular bodies in supersonic flow.
J.Spacecraft Vol.19 No.5
Sept.-Oct. 1981 pp.385-392

22 Almosnino, D.
High angle of attack calculations of the subsonic vortex flow on slender bodies.
AIAA 21st Aerospace Sciences Meeting
Reno, Nevada AIAA 83-0035
January 10-13 1983

23 Mendenhall, M.R.
Perkins, S.C.
Predictions of the vortex wake for non-circular missiles in supersonic flow.
AIAA 22nd Aerospace Sciences Meeting
Reno, Nevada
January 9-12 1984

24 Mendenhall, M.R.
Perkins, S.C.
Lesiutre, D.J.
Prediction of the non-linear aerodynamic characteristics of manoeuvring missiles.
AIAA Paper 85-1776-CP 1985

25 Hemsch, M.J.
Nielsen, J.N.
(Editors)
Tactical Missile Aerodynamics, AIAA Book (Progress in astronautics and aeronautics) New York N.Y. 1986
pp.519-571 "Vortex cloud model for body vortex shedding and tracking."

26	Costis, C.E. Telionis, D.P.	Vortical wakes over a prolate spheroid. AIAA J. Vol.26 No.10 pp.1189-1193 October 1988
27	Fink, P.T. Soh, W.K.	A new approach to roll-up calculations of vortex sheets. Proceedings of Royal Society, London A362 1978 pp.195-209
28	Fage, A. and Johansen, F.C	"on the flow of air behind an inclined flat plate of infinite span.". Aeronautical Research Committee, R&M No 1104 (Ae281) Feb. 1927
29	Fage, A.,	"The airflow around a circular cylinder in the region where the boundary layer separate from the surface", Aeronautical Research Committee, R&M No 1179 (Ae 343), August 1928
30	Hartmann, K.	"Pressure and force distributions on an ogive- nosed circular cylinder at high angles of attack in an incompressible airstream", IB 222-83 A 05, 27-7-1983, Deutsche Forschungs- und Versuchsanstalt Fur Luft- und Raumfahrt /AVA.
31	Champigny.,P.	"pressure and force measurements on a 3D ogive nose and cylindrical body at high angles of attack", Office National D'etudes et de Recherches Aerospatiales, GATEUR Report No 01/AG04 October 1983
32	Tinling.B.E., and Allen, C.Q.,	An investigation of the normal-force and vortex-wake characteristics of an ogive-cylinder body at subsonic speeds, NASA TN-D-1297, 1962
32a	Kármán	'Göttinger Nachr,' 1911 & 1912
32b	Heisenburg	'Phys'. 1922

32c	Goldstein, S. (Editor)	Modern developments in fluid dynamics. Volume 1, Oxford: The Clarendon Press 1938 pp.563-564
32d	Lamb, H.	Hydrodynamics. 6th Edition 1932 Section 156
33	Lighthill M J	Attachment and separation in three dimensional flow, section II 2-6 of "Laminar boundary layers", Ed. Rosenhead L Oxford Univ. Press, 1963 pp 72-82
34	Maskell E C	"Flow separation in three dimensions", RAE Aero rep 2565 Nov 1955
35	Tobak M & Peake D J	Topology of two dimensional and three dimensional separated flows, AIAA paper 79-1480
36	Dallmann, U.	"On topological changes of separating flow structures at transition Reynolds numbers", AIAA-87-1266, AIAA 19th Fluid dynamics, plasma dynamics and Lasers Conference, June 8-10 -1987/Honolulu, Hawaii
37	Poll, D.I.A.	"Some effects of boundary layer transition on slender axi-symmetric bodies at incidence in incompressible flow", CoA Report 8221 Sept. 1982
38	Poll, D.I.A	"On the effects of boundary layer transition on a cylindrical afterbody at incidence in low speed flow". Paper No.1307 Aeronautical J.RAeS. Oct. 1985 pp.315-327
39	Lamont, P.J.	"Pressure measurements on an ogive-cylinder at high angles of attack with laminar, transitional or turbulent separation". AIAA Paper No. 80-1556, Danvers, Massachusetts, 1980.
40	Fletcher C.A.J.	Computational Techniques for fluid dynamics, Vol. I & II, Springer-Verlay 1988

41	Jones D.J, Evans J, Priolo E, Sturek W, Wardlaw A	Application of Euler and Navier-Stokes codes to missile type bodies with high L/D ratios, AGARD CP493 23-26 April 1990
41a	Hayes, W.D. Probstein, R.F.	Hypersonic flow theory. 2nd Edition Volume 1 Academic Press 1966 p.24.
42	Marconi, F.	Supersonic conical separation due to shock vorticity, AIAA Journal Vol. 22 No 8 August 84 pp1048-1055
43	Nielsen J.N.	Missile Aerodynamics, McGraw-Hill book company, Inc. 1960
44	Christopher P.A.T.	An approximate method for estimating the lifting characteristics of thin bodies of non-circular cross-section, Cranfield Institute of Technology, CoA Report 9006, Jan 1990
45	Sacks, A.H.	Vortex interference on slender air planes, NACA TN-3525, 9 Sept. 1955
46	Milne-Thompson L.M.	Theoretical Hydrodynamics, Fourth Edition, MacMillan & Co Ltd, 1960 P.368
46a	Petrie, J.A.H.	User guide for the SPARV panel program, British Aerospace, Brough. Dec 1985
47	Goodwin, F.K., Dillenius, M.F.E. & Nielsen, J.N.	Extension of the method for predicting 6DOF store separation trajectories at speeds up to the critical speed, WP/AFFDL/TR-74/138
48	Polhamus, E.G.	"A concept of the Vortex Lift of sharp edge delta wings based on a leading edge suction analogy", NASA TN-D-3767 1966
49	Defence Research Agency, Bedford	Unpublished data

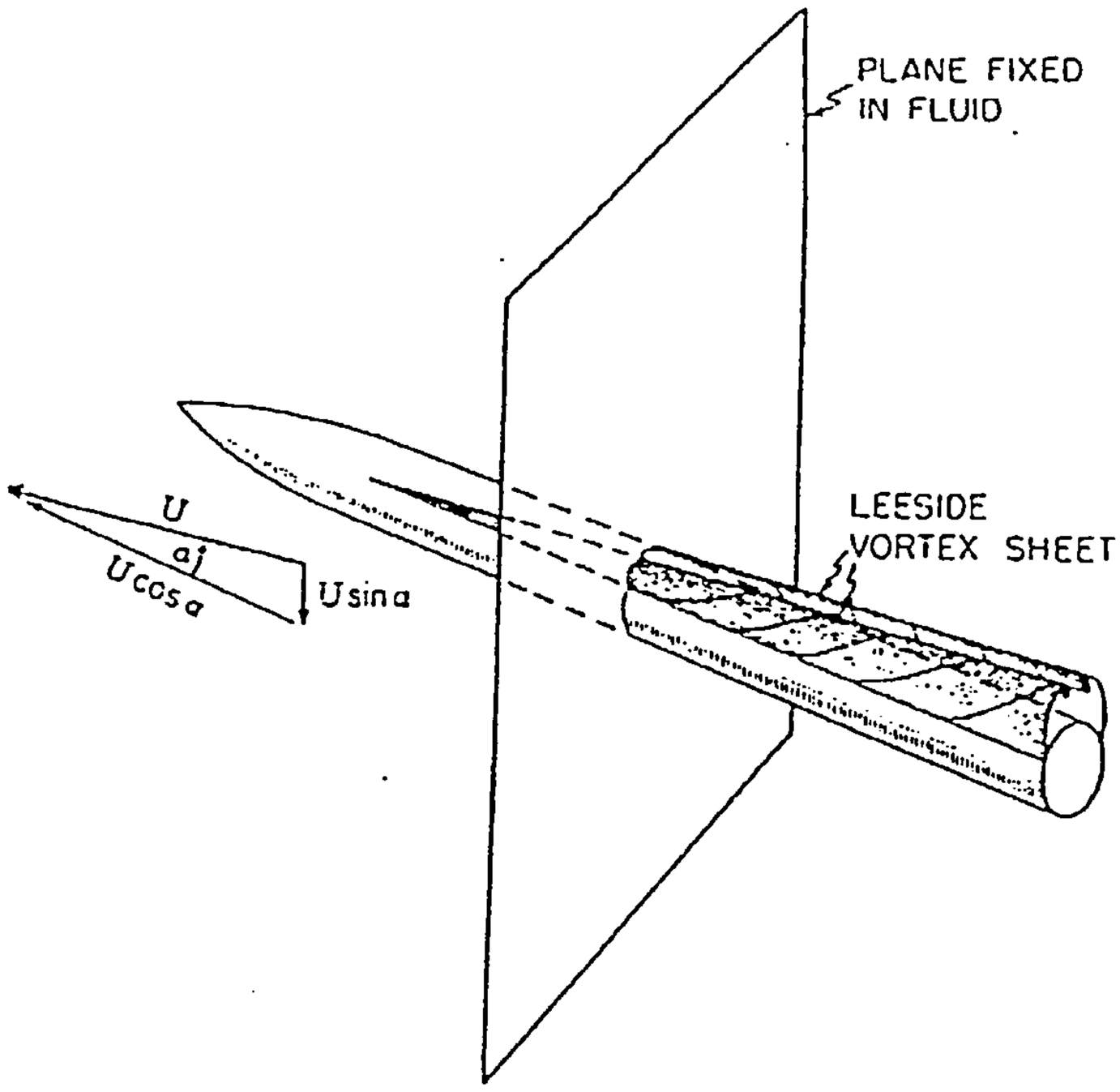

Figure 6.2.1.1 Symmetric vortex separation on a slender body of revolution at high angle of attack

(After Bryson [3])

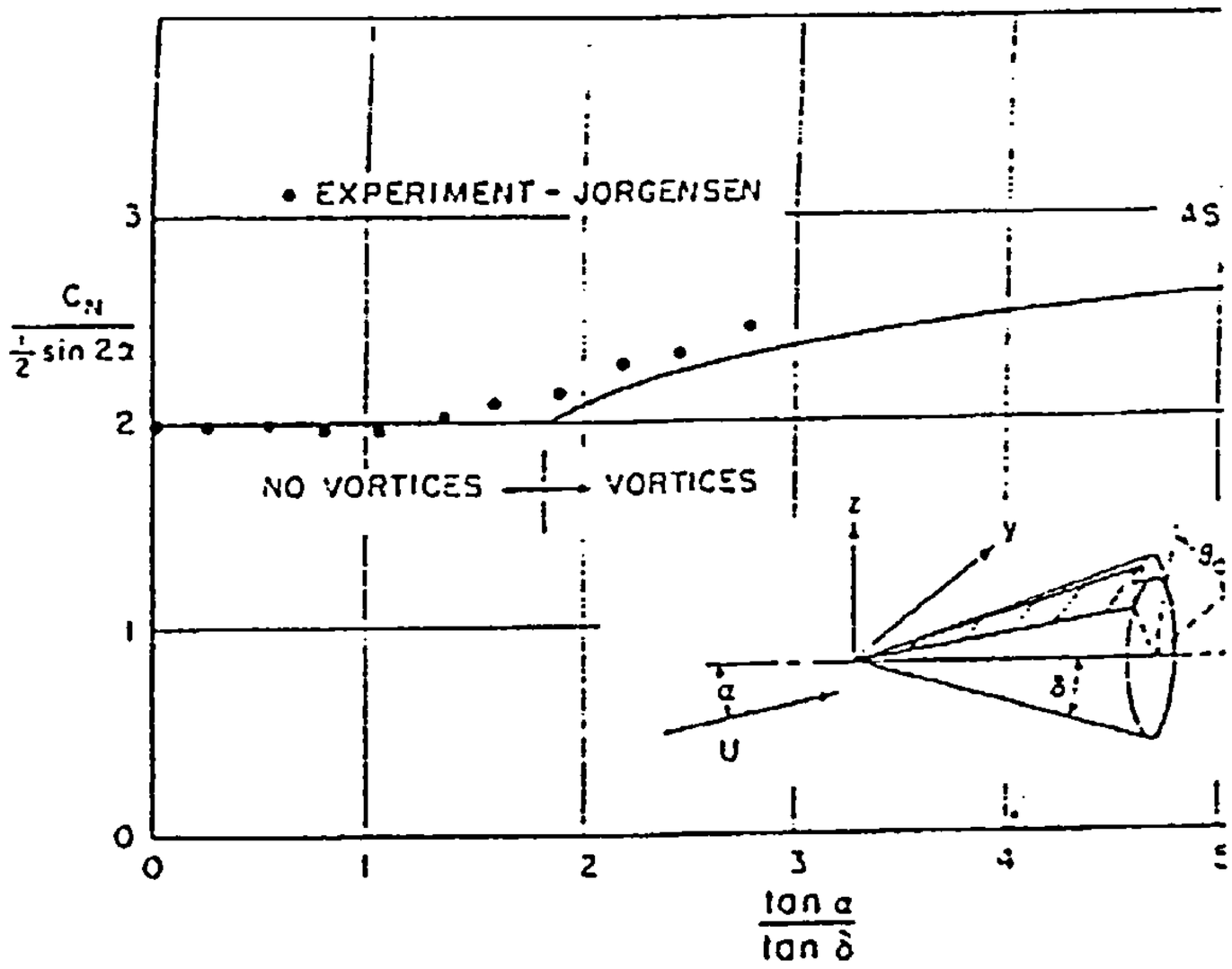

Figure 6.2.1.2 Normal force on a cone with vortex separation as a function of angle of attack

(After Bryson [3])

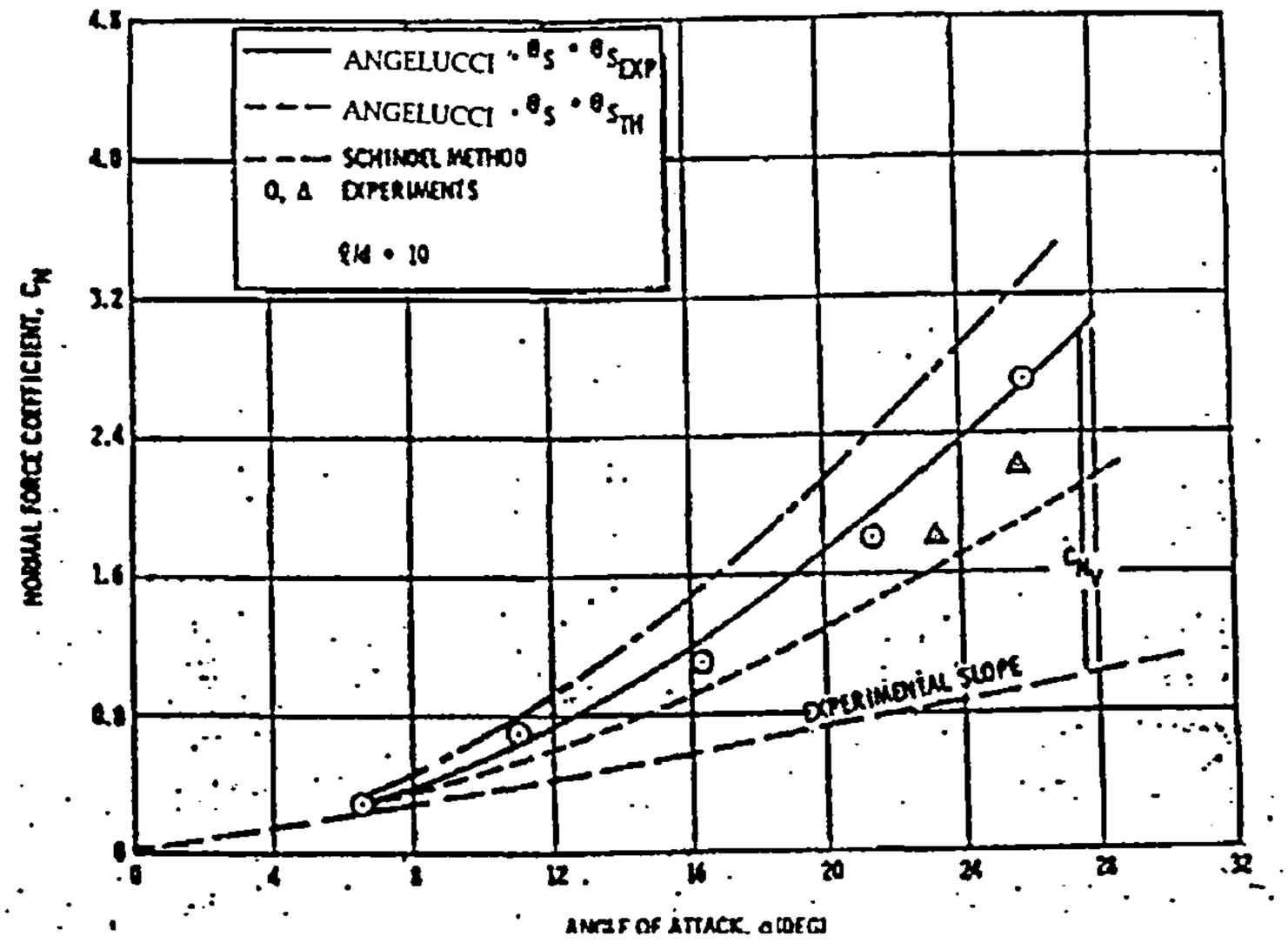

Figure 6.2.1.3 Normal force coefficient of blunted ogive-cylinder configuration
(After Angelucci [4])

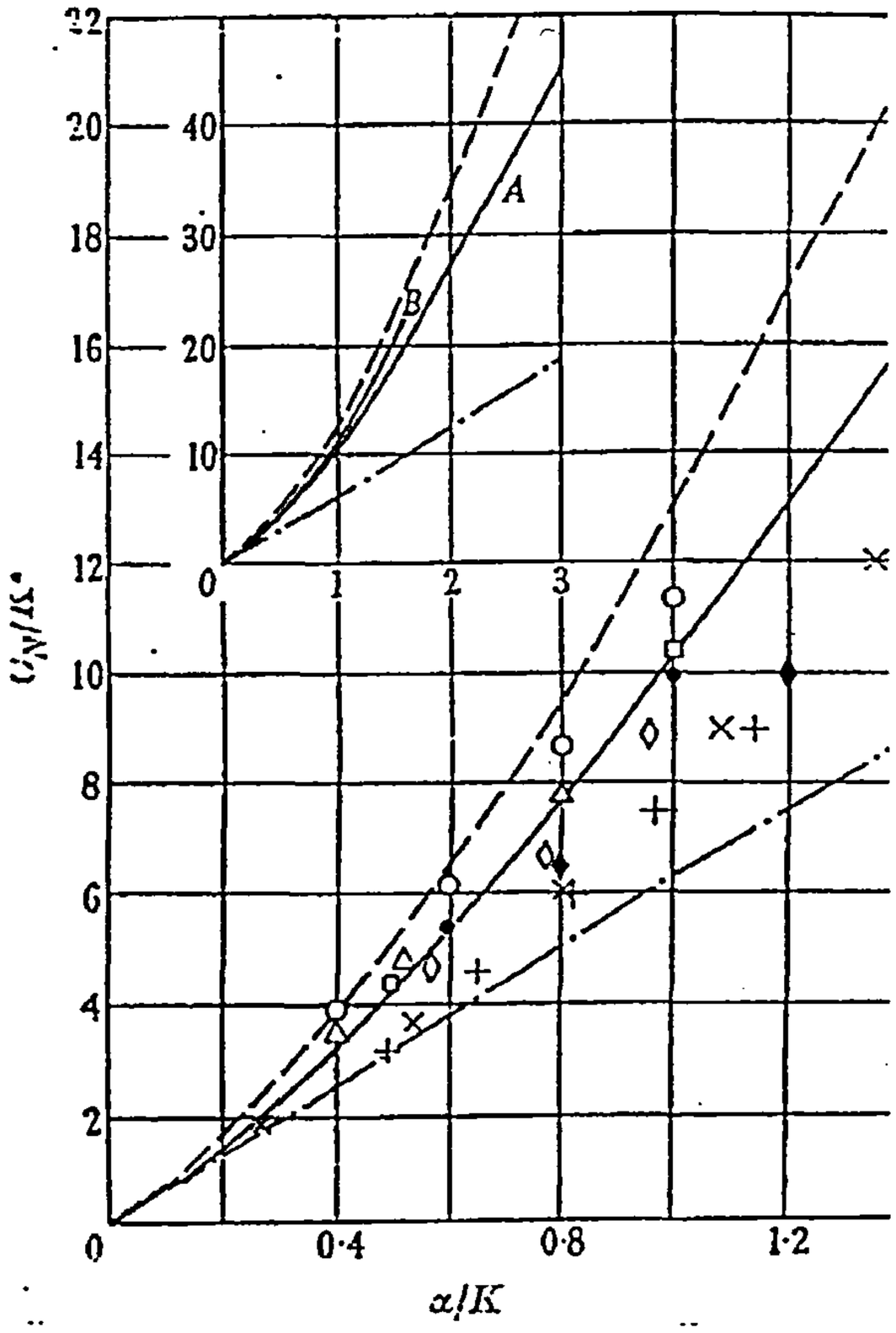

Figure 6.2.1.4 Coefficient of normal force. Theory:___, Brown & Michael paper;_._, Jones. Experiment: O, Michael, balance measurement, γ=5, M=1●; Michael, integral of pressures at 78% chord, λ=5, M=1.9; Δ, Michael, balance measurement, γ=7.5, M=1.9; ◊, Michael, balance measurement, γ=10, M=1.9 ♦, Micheal, integral of pressures at 78% chord, λ =10, M=1.9; ×, Lampert, balance measurement, γ=7.5, M=1.46; +, Lampert, balance measurement, γ=12, M=1.46; , Fink & Taylor, integral of pressures near apex, γ=10, low speed.

(After Mangler and Smith [7])

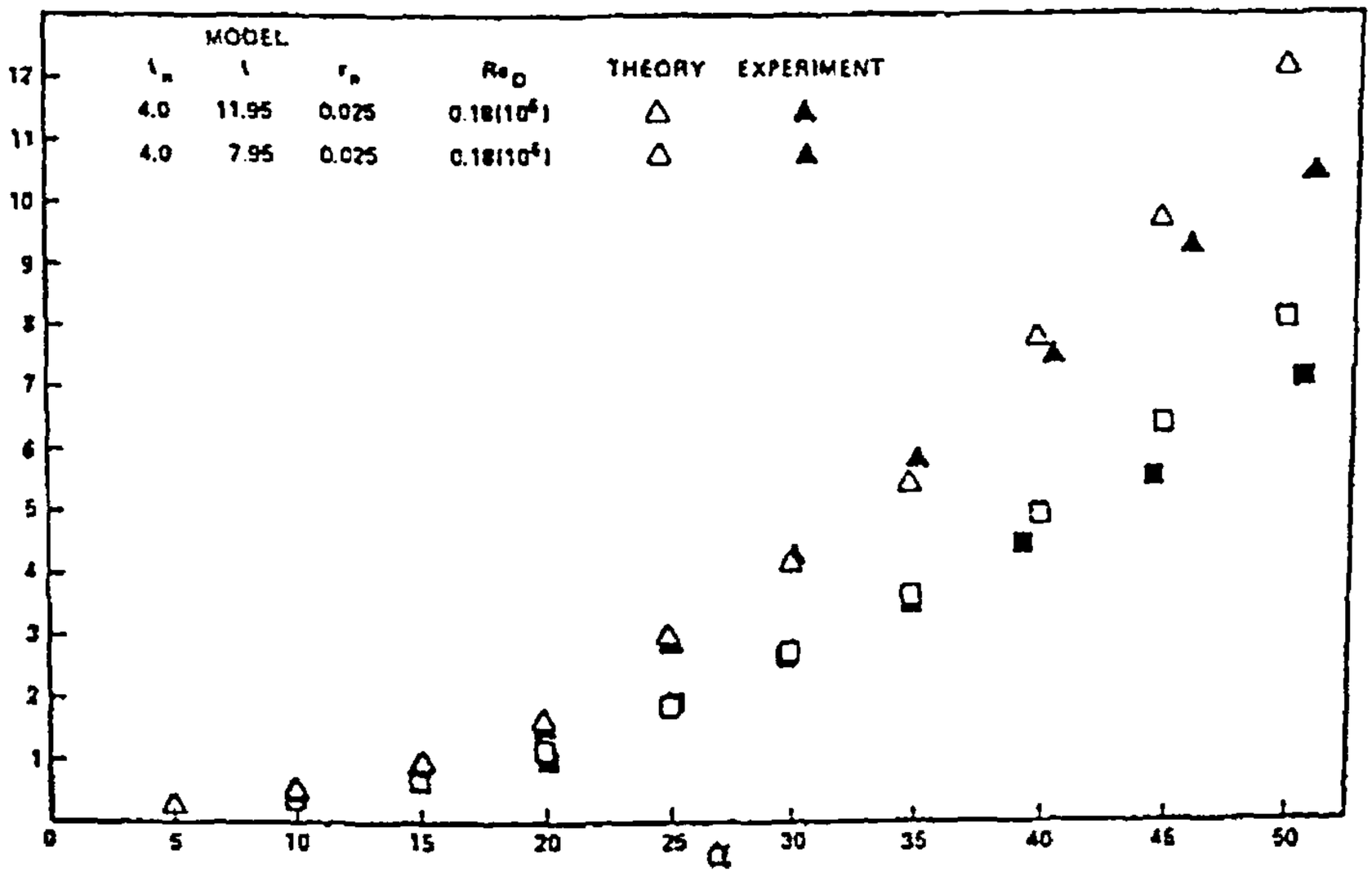

Figure 6.2.1.5 Normal force on pointed bodies at M=0.3

(After Wardlaw [12])

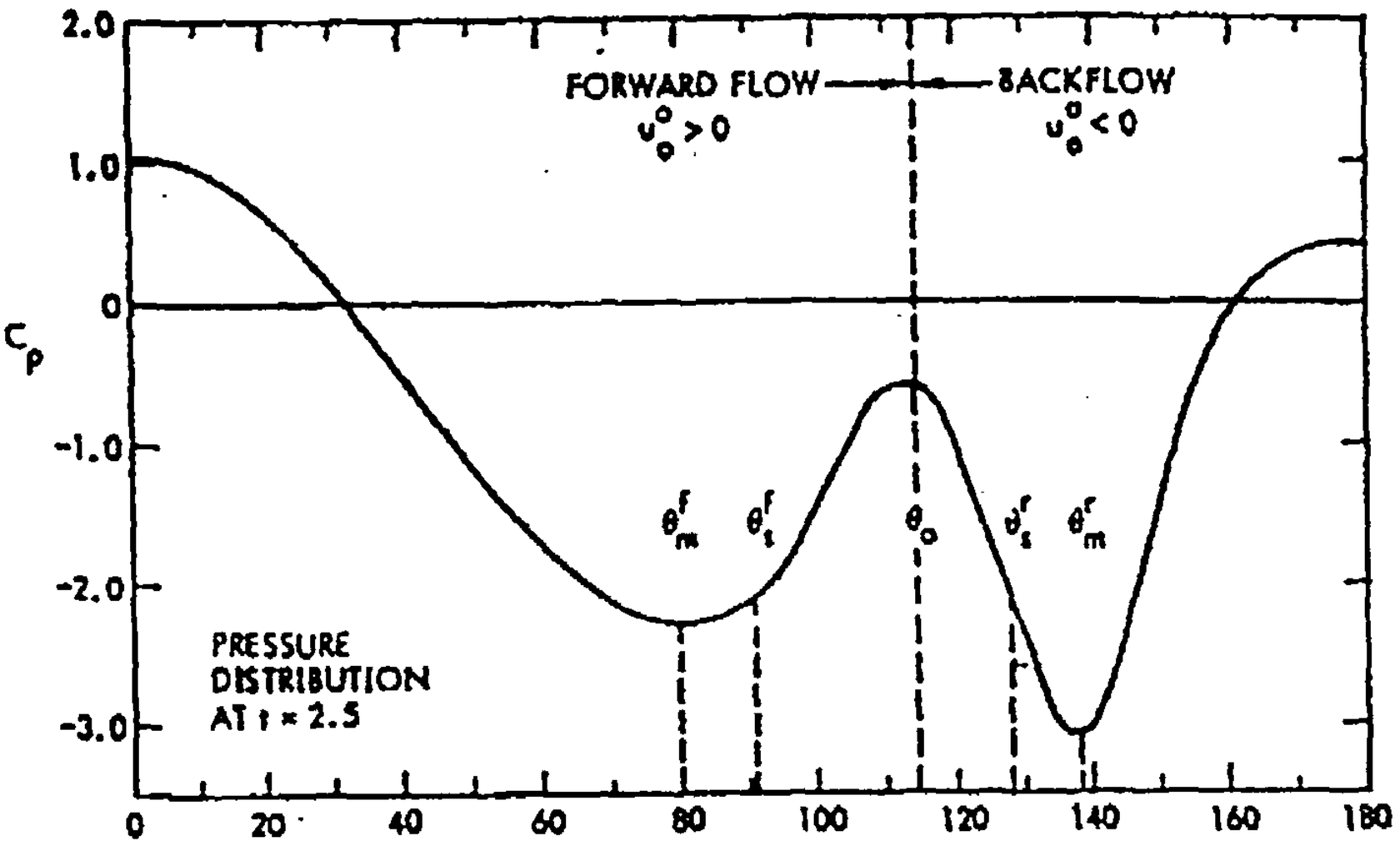

Figure 6.2.1.6 Rear shear layer separation

(After Deffenbaugh and Marshall [13])

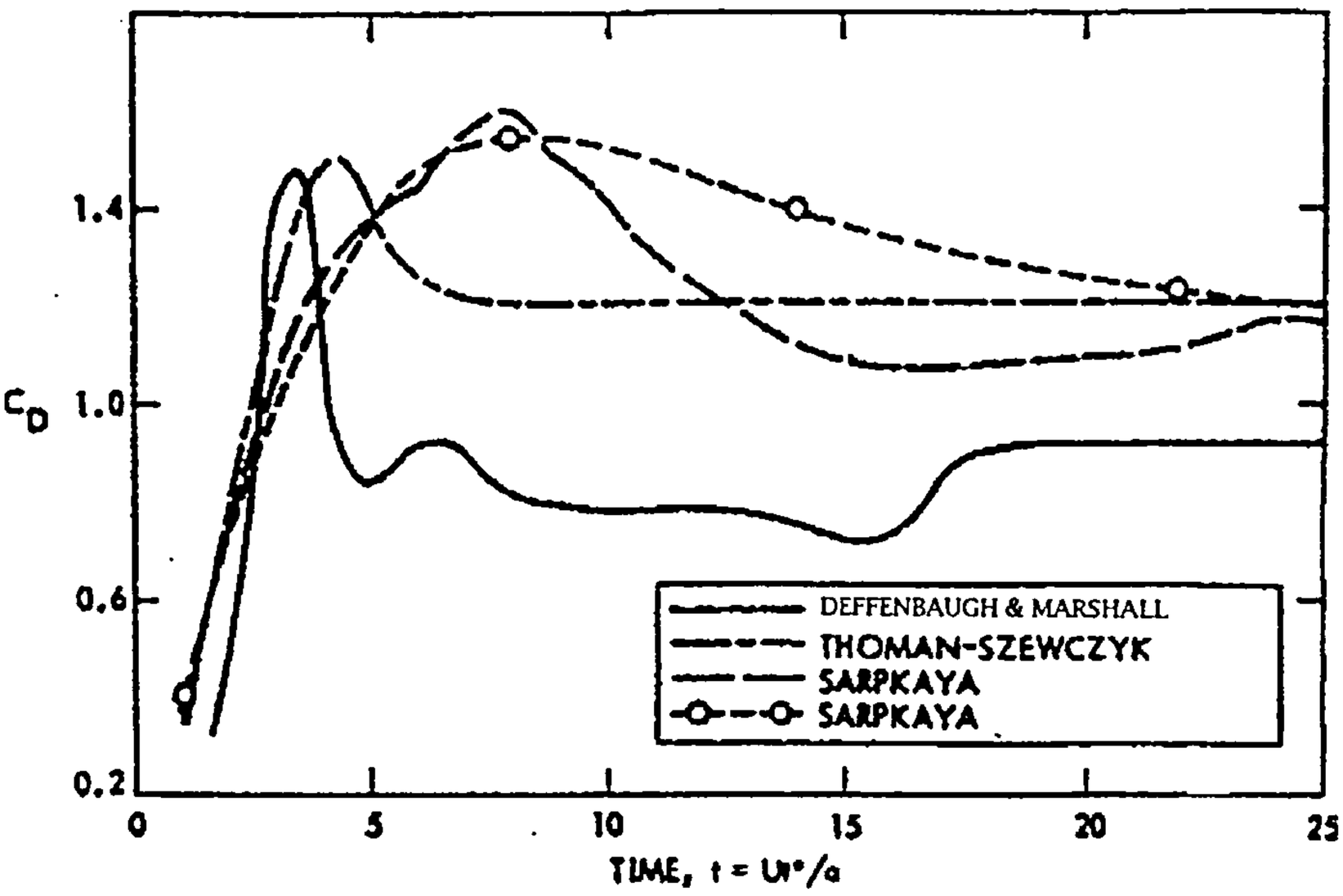

Figure 6.2.1.7 Time dependent drag
(After Deffenbaugh and Marshall [13])

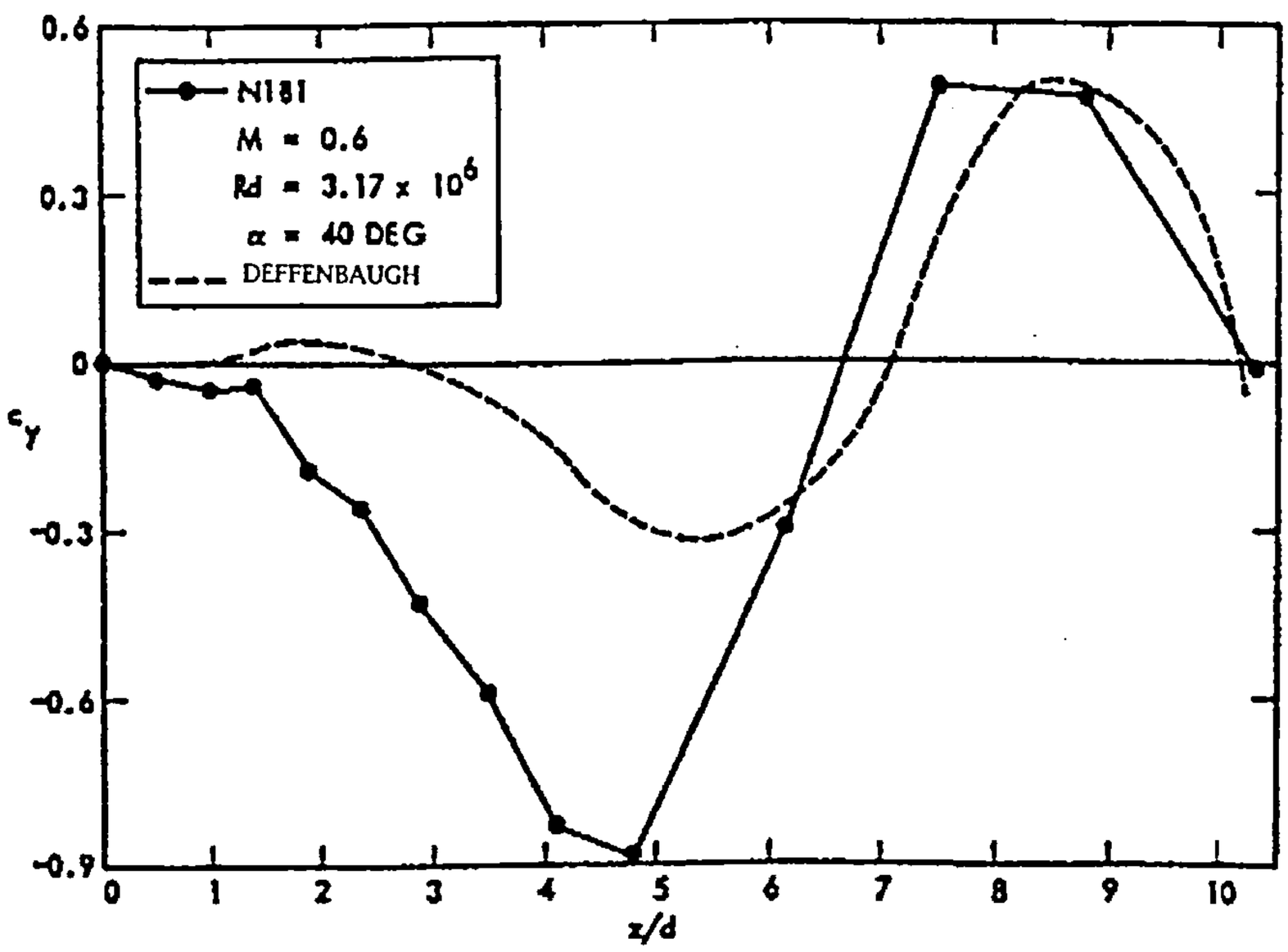

Figure 6.2.1.8 Sectional side-force distribution on N1B1
(After Deffenbaugh and Koerner [14])

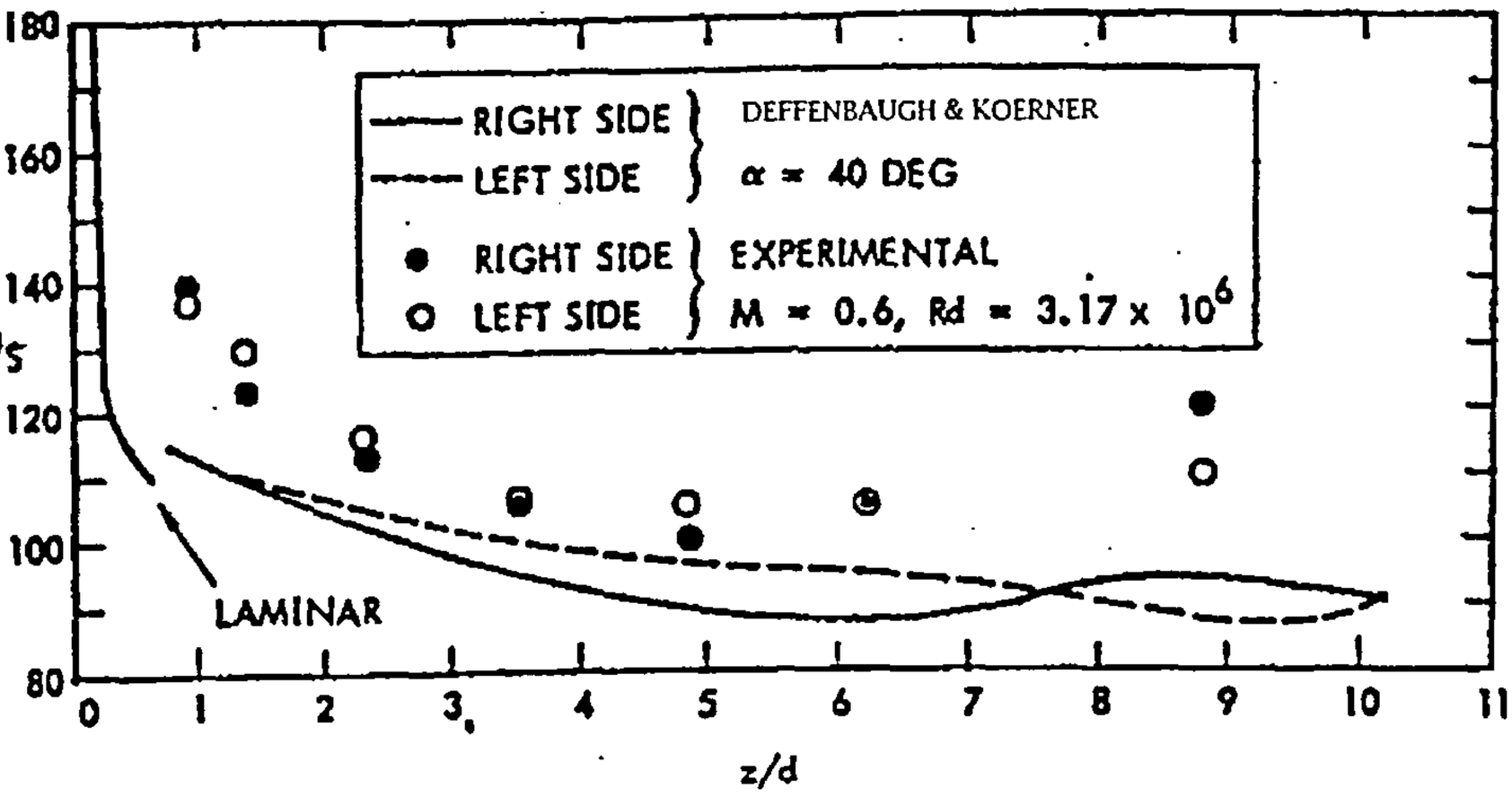

Figure 6.2.1.9 Separation angle looking upstream
(After Deffenbaugh and Koerner [14])

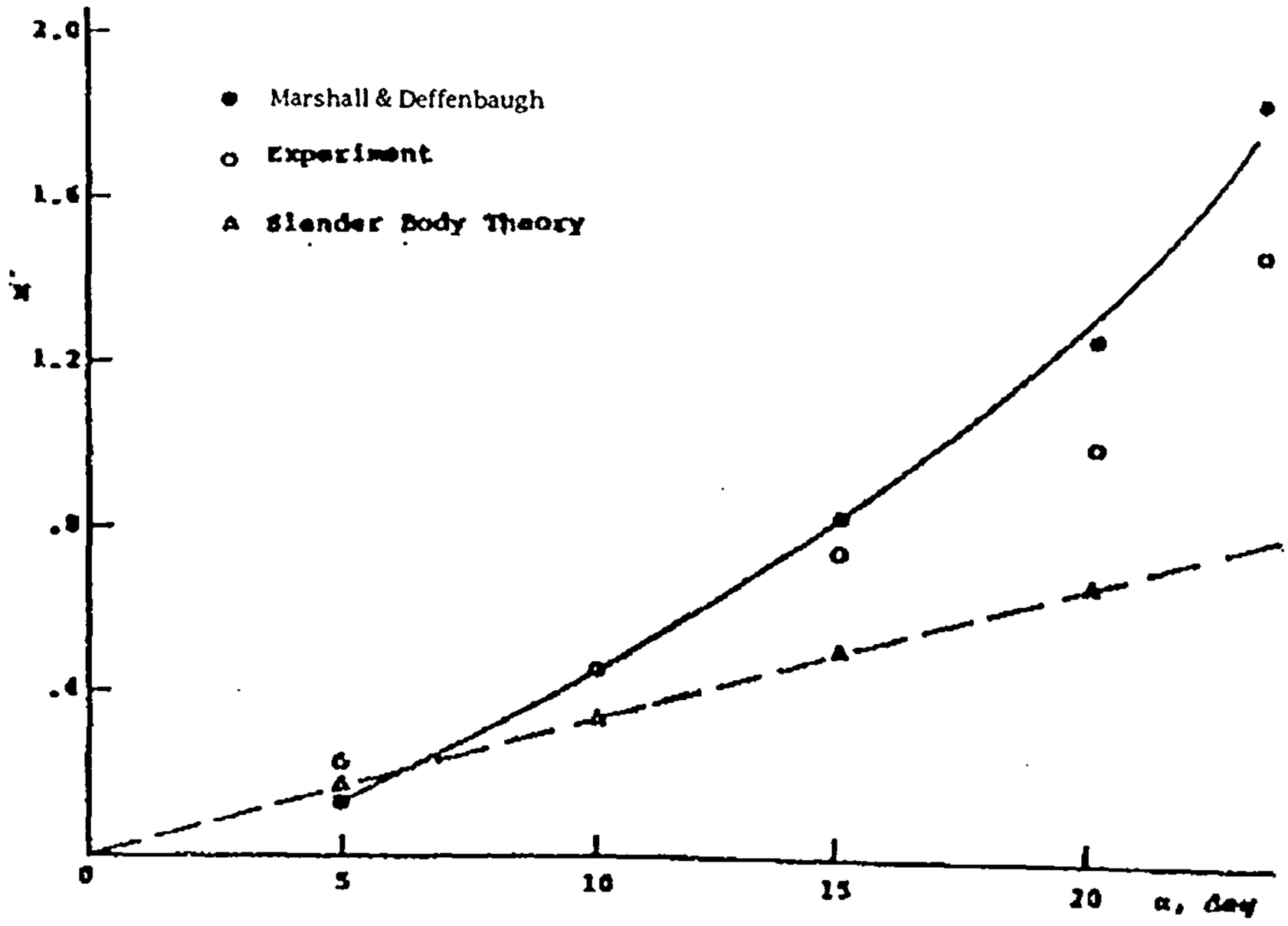

Figure 6.2.1.10 Aerodynamic characteristics of Ogive-cylinder
(After Marshall and Deffenbaugh [17])

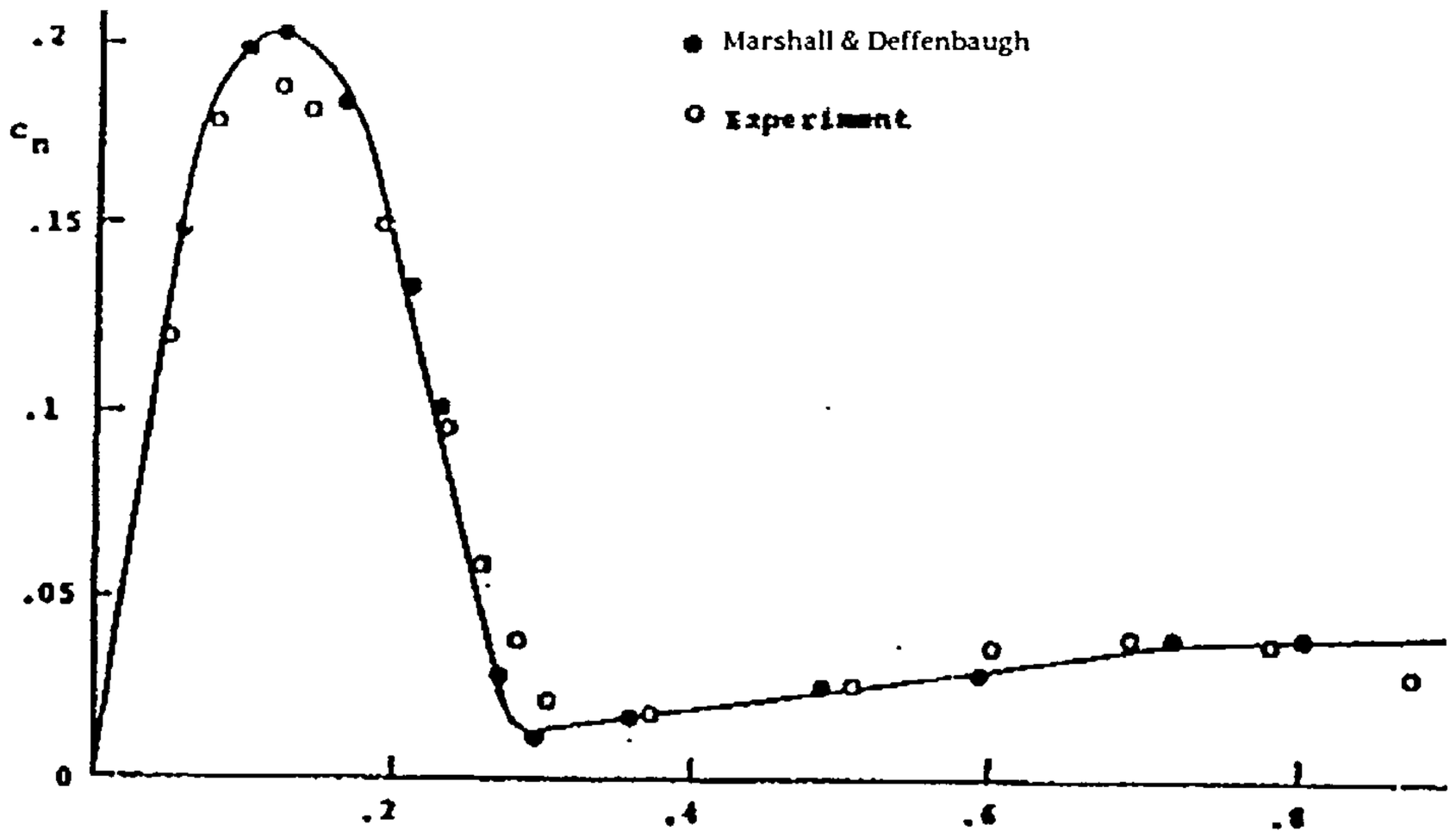

Figure 6.2.1.11 α=15
(After Marshall and Deffenbaugh [17])

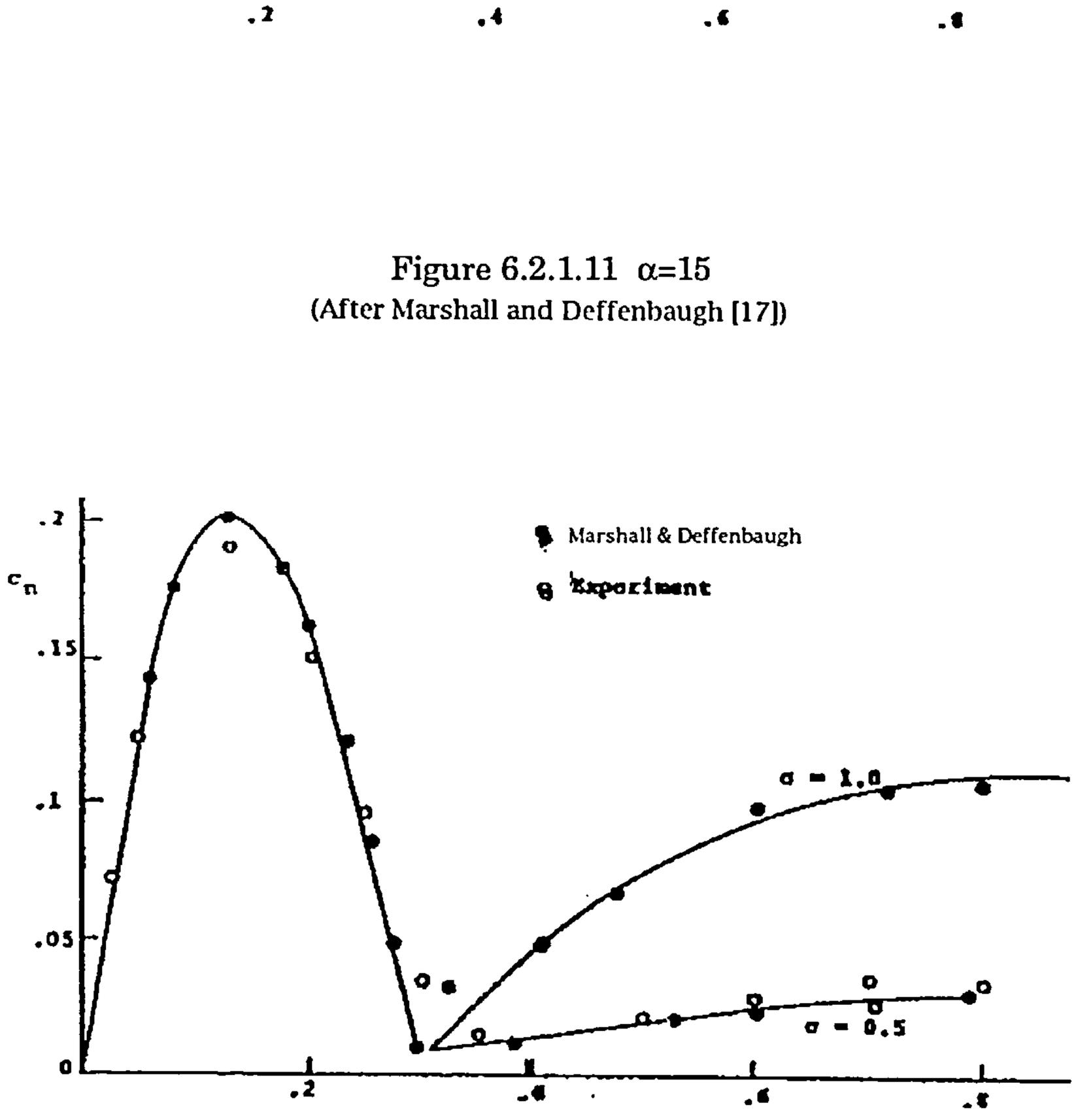

Figure 6.2.1.12 Vortex flux effect on normal force distribution, α=15
(After Marshall and Deffenbaugh [17])

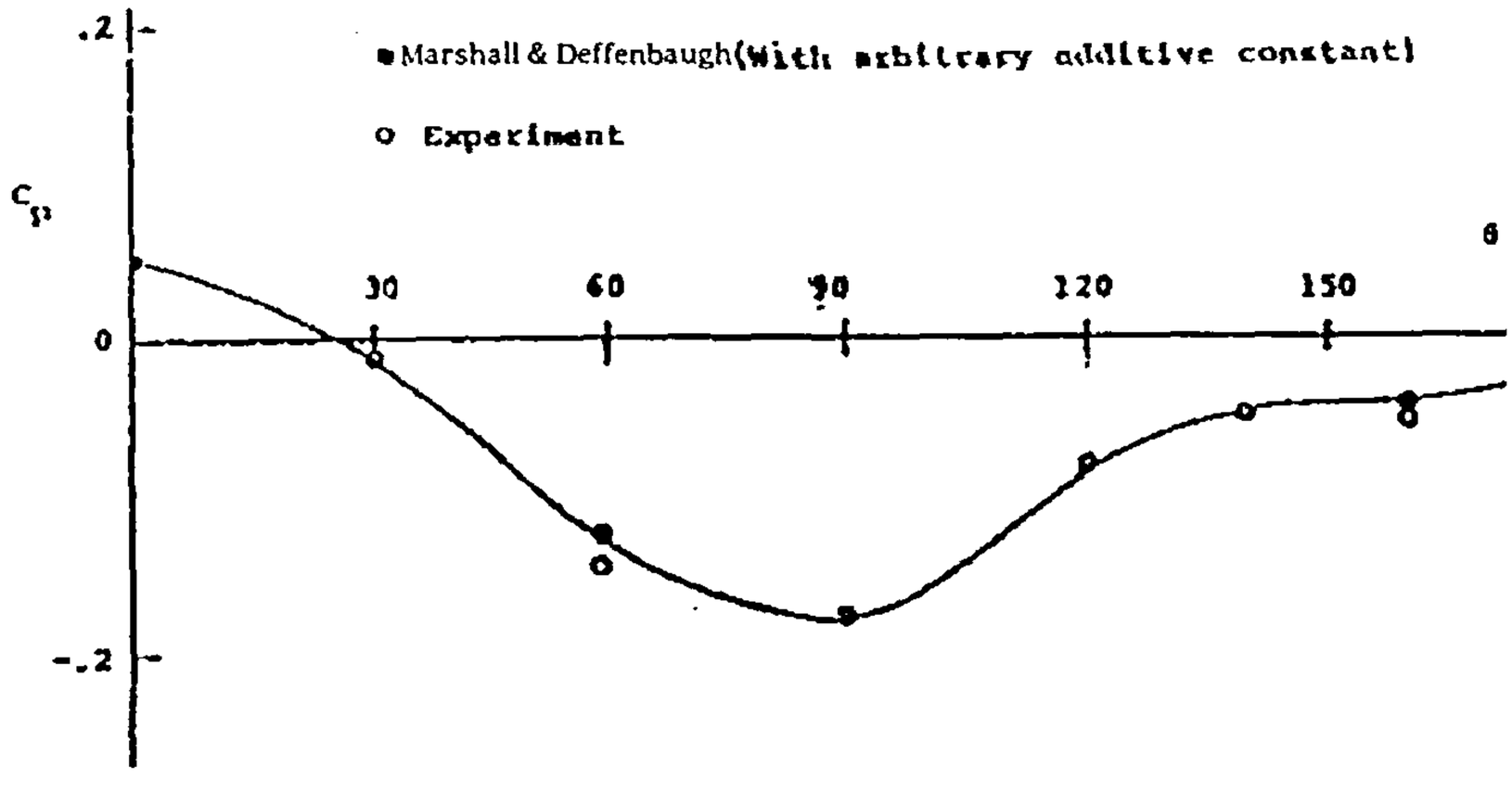

Figure 6.2.1.13 z=.551, α=15
(After Marshall and Deffenbaugh [17])

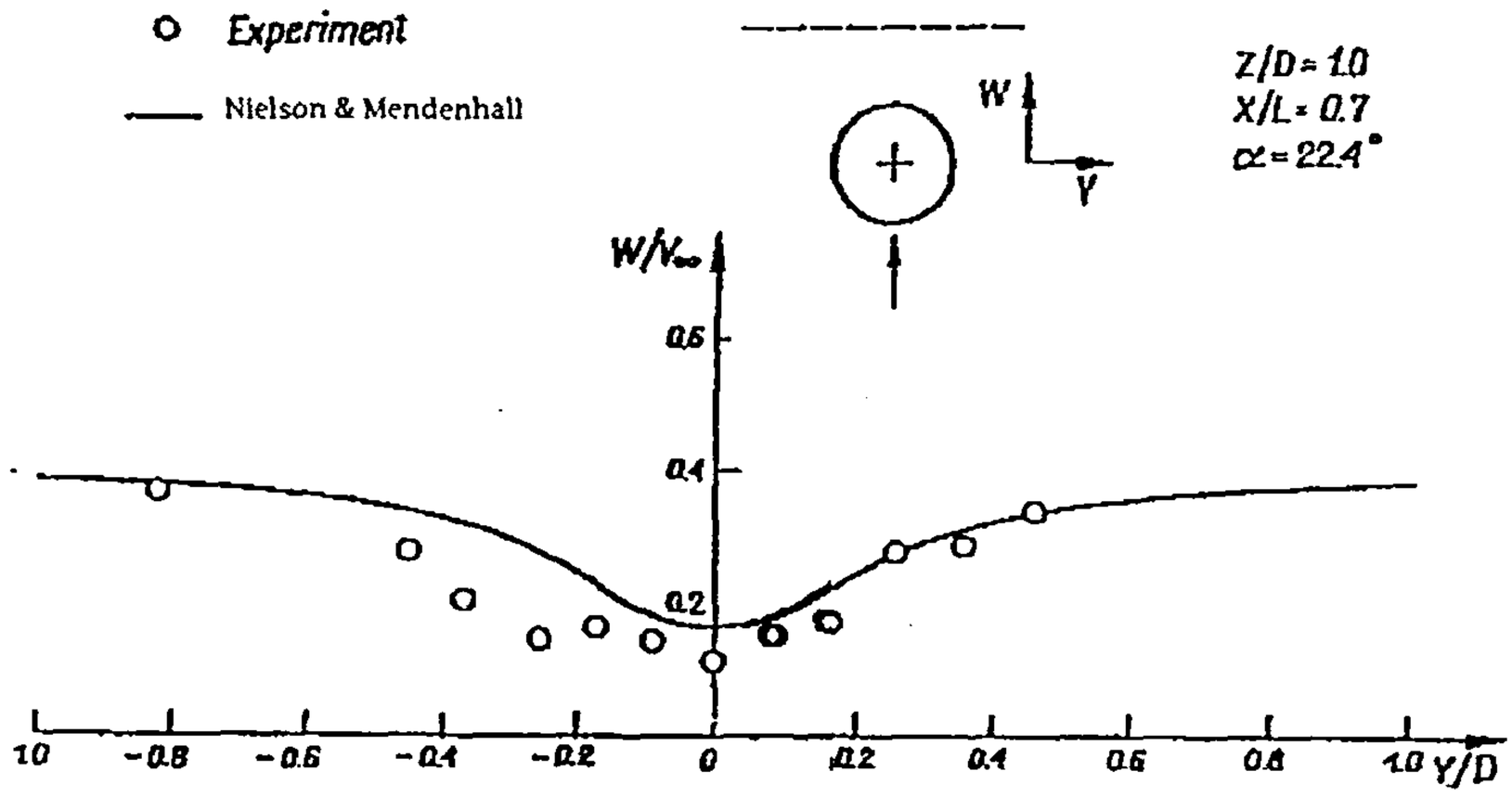

Figure 6.2.1.14 Symmetric vortex flow field, Z/D=1.0 traverse
(After Nielson and Mendenhall [18])

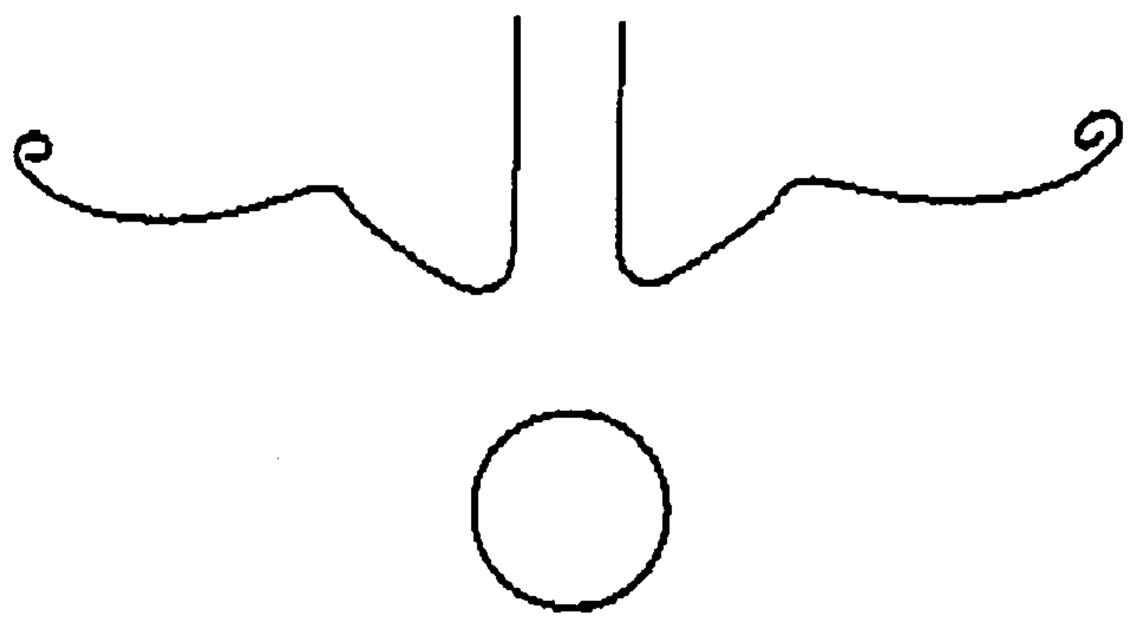

Figure 6.2.1.15a Computed vortex sheet shape 2 body diameters downstream of wing trailing edge.
(After Barger [19])

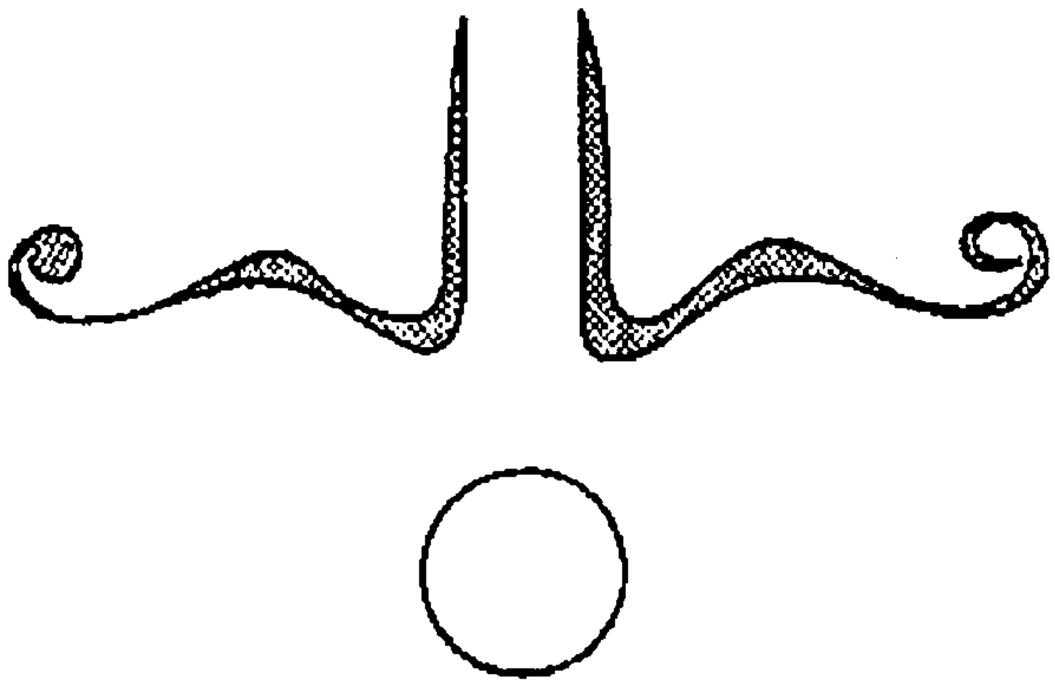

Figure 6.2.1.15b Approximate form of developing vortex sheets 2 body diameters downstream of wing trailing edge as obtained from vapour screen photograph
(After Barger [19])

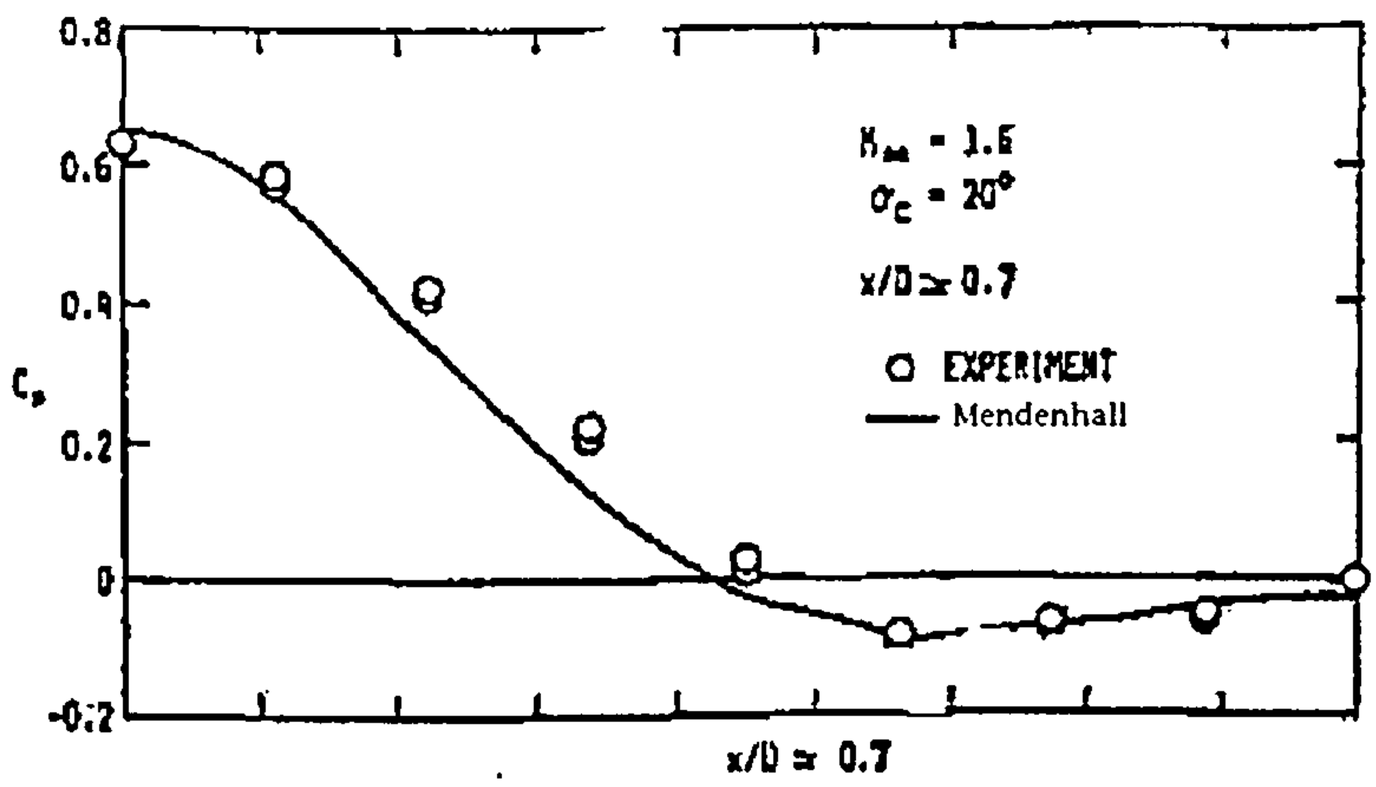

Figure 6.2.1.16 Measured and predicted pressure distribution on an ogive cylinder, α=20

(After Mendenhall [21])

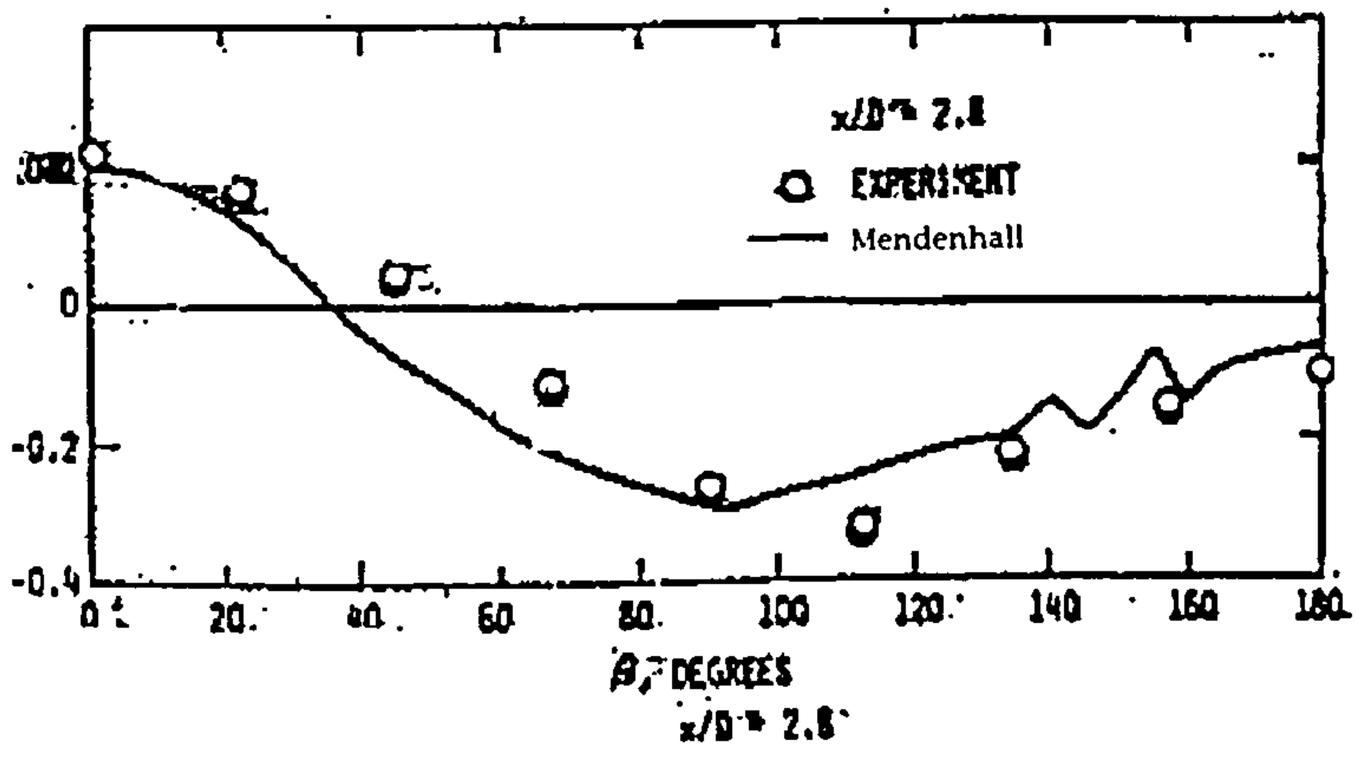

Figure 6.2.1.17 Measured and predicted pressure distribution on an ogive cylinder, α=20

(After Mendenhall [21])

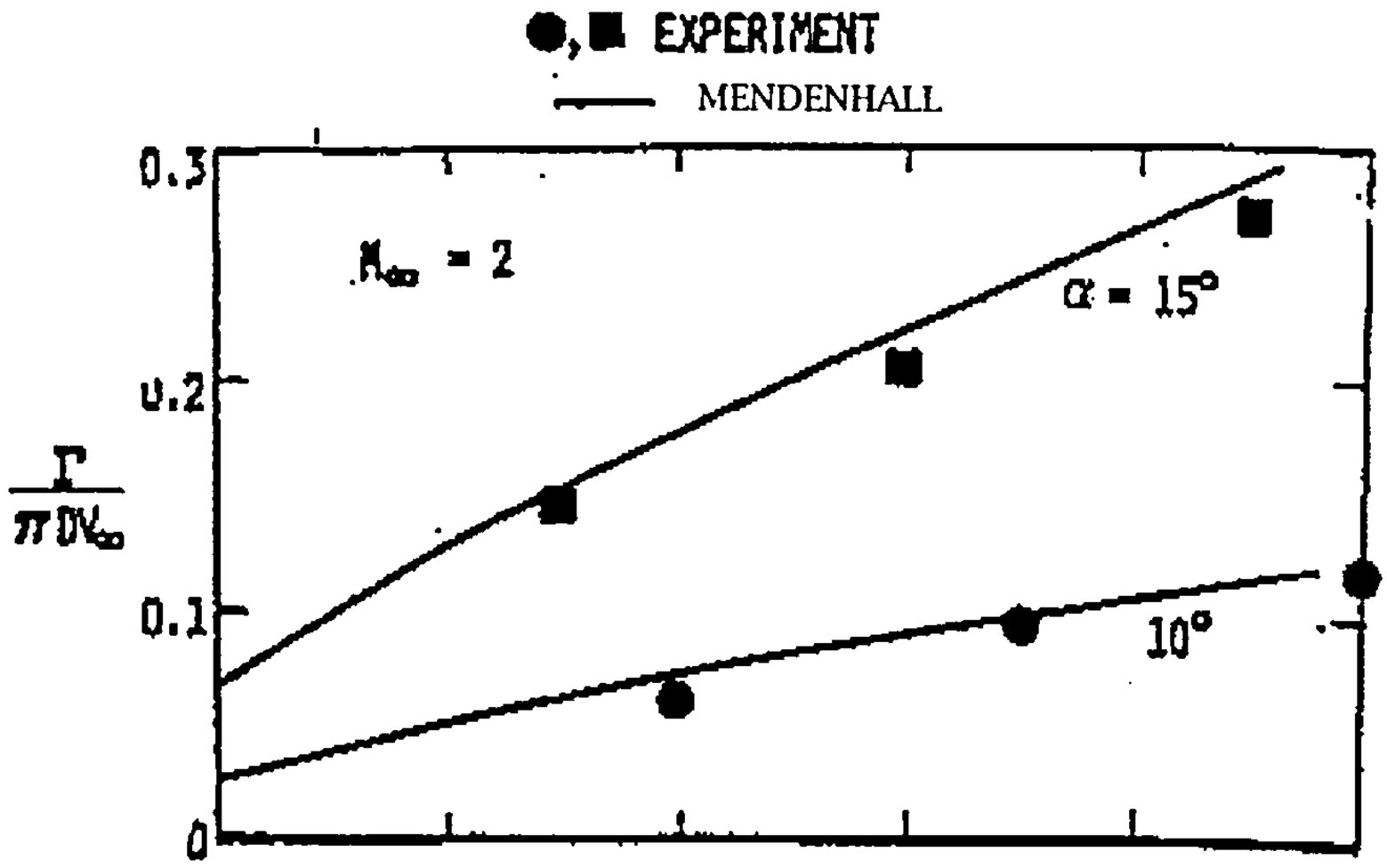

Figure 6.2.1.18 Measured and predicted body vortex strength on the lee side of an ogive cylinder
(After Mendenhall [21])

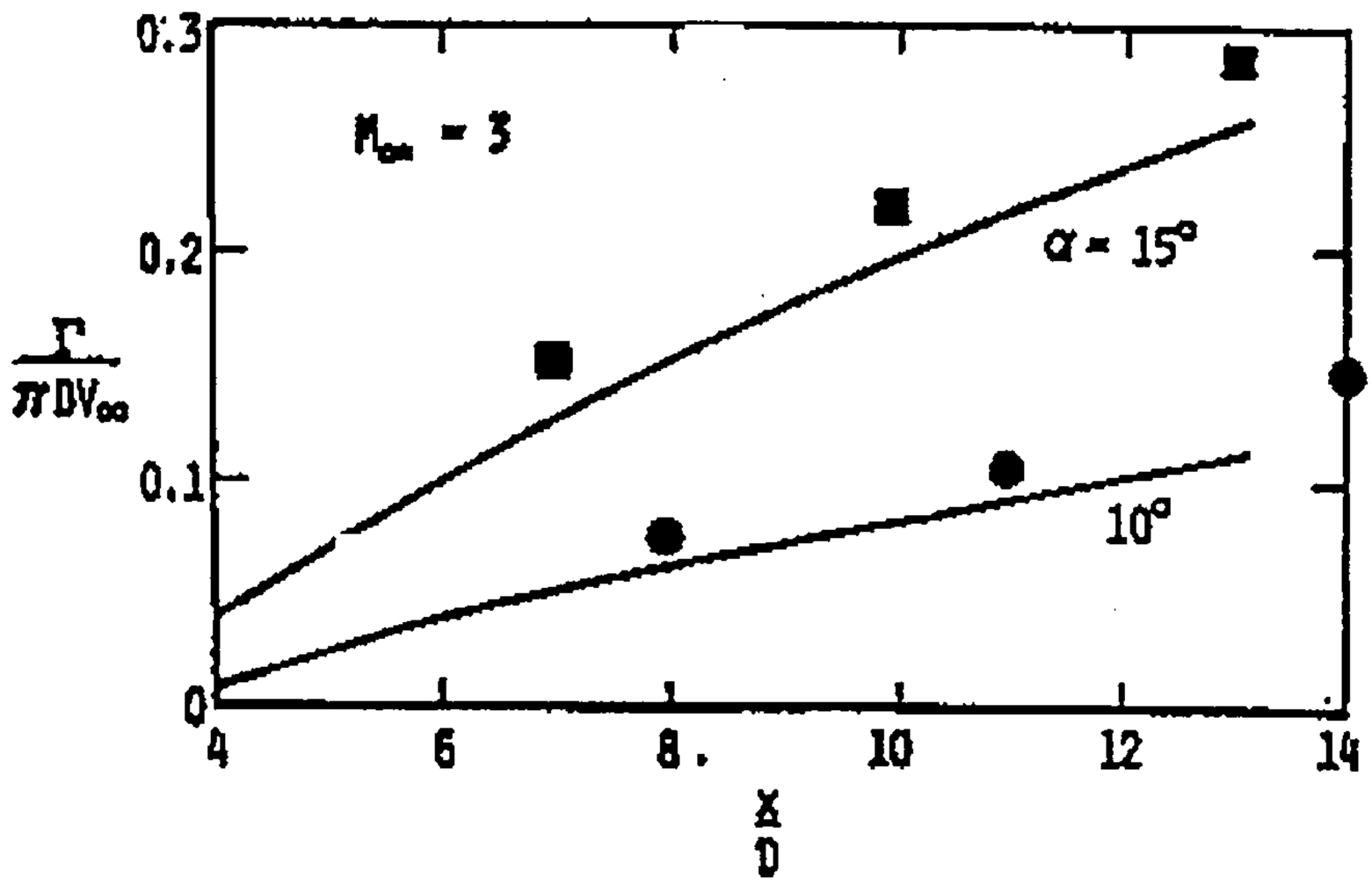

Figure 6.2.1.19 Measured and predicted body vortex strength on the lee side of an ogive cylinder
(After Mendenhall [21])

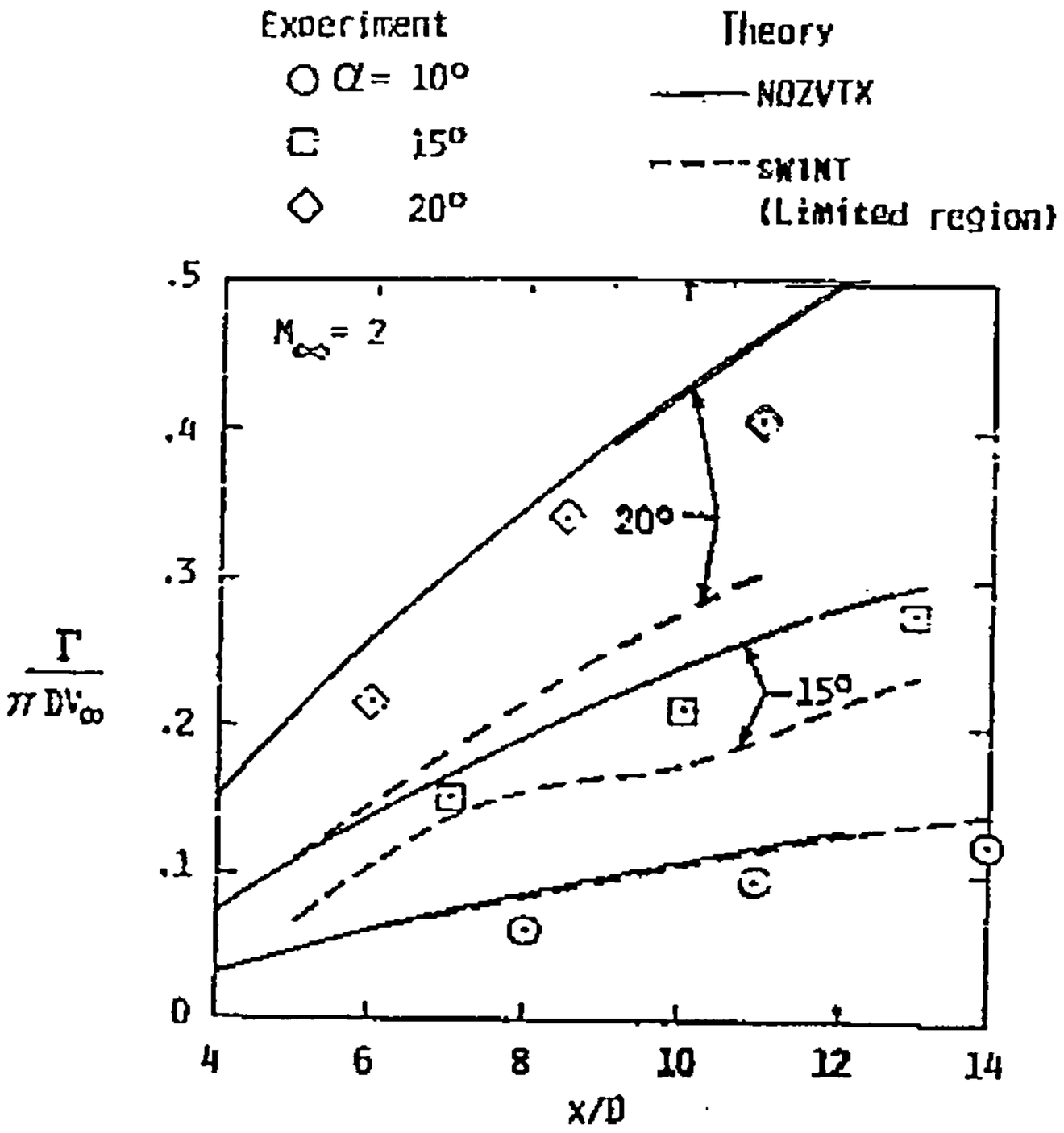

Figure 6.2.1.20 Measured and predicted body vortex strength on an ogive cylinder M=2
(After Mendenhall and Perkins [23])

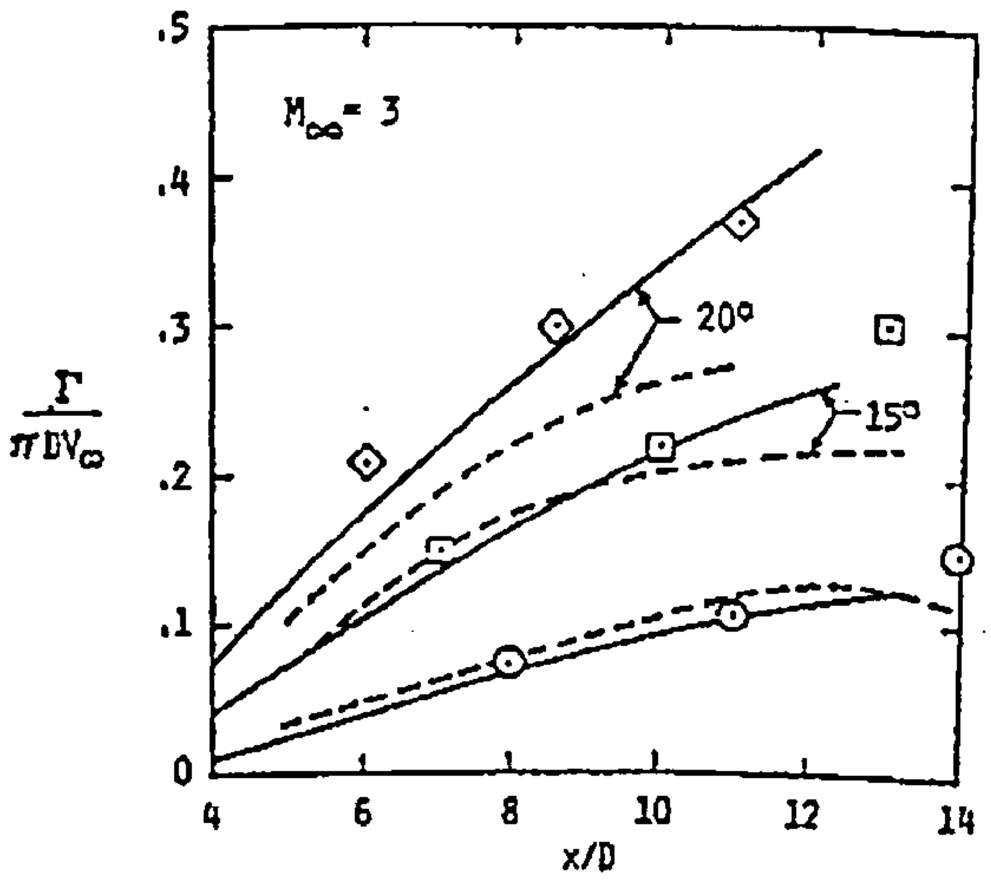

Figure 6.2.1.21 Measured and predicted body vortex strength on an ogive cylinder M=3
(After Mendenhall and Perkins [23])

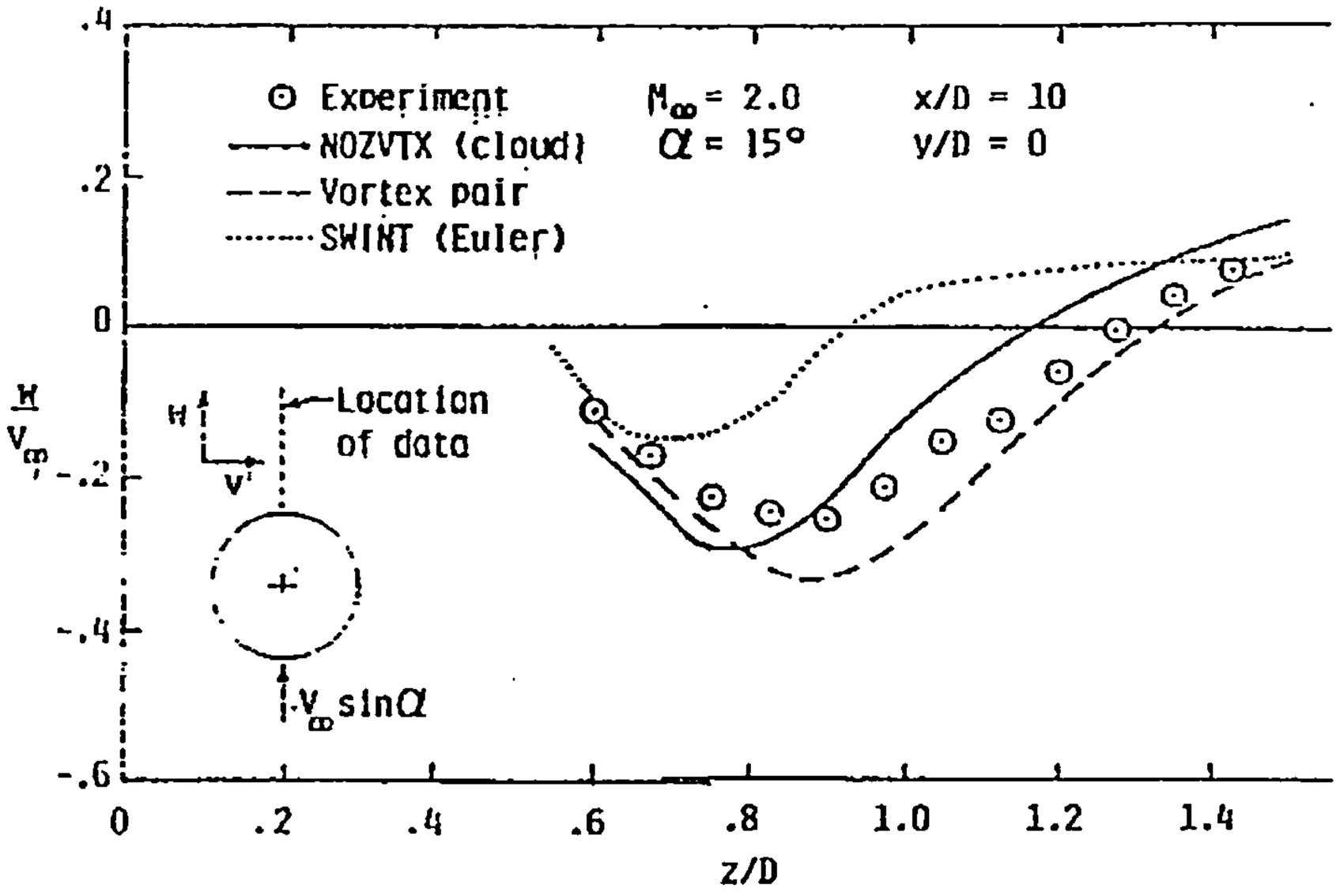

Figure 6.2.1.22 Measured and predicted downwash distribution on the lee side of an ogive cylinder at M=2, α=15

(After Mendenhall and Perkins [23])

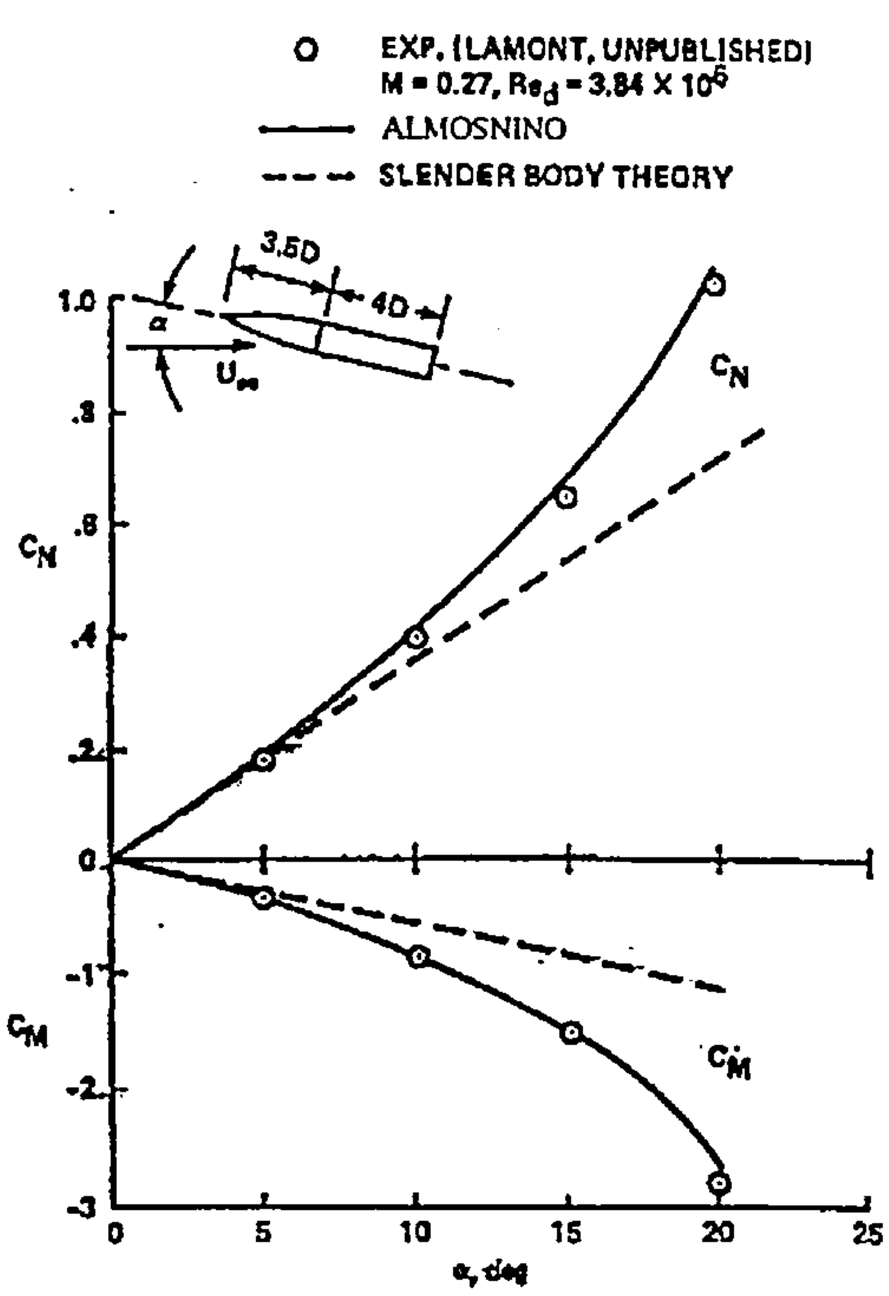

Figure 6.2.3.1 Normal force and pitching moment coefficients on an ogive-cylinder body in subsonic flow

(After Almosnino [22])

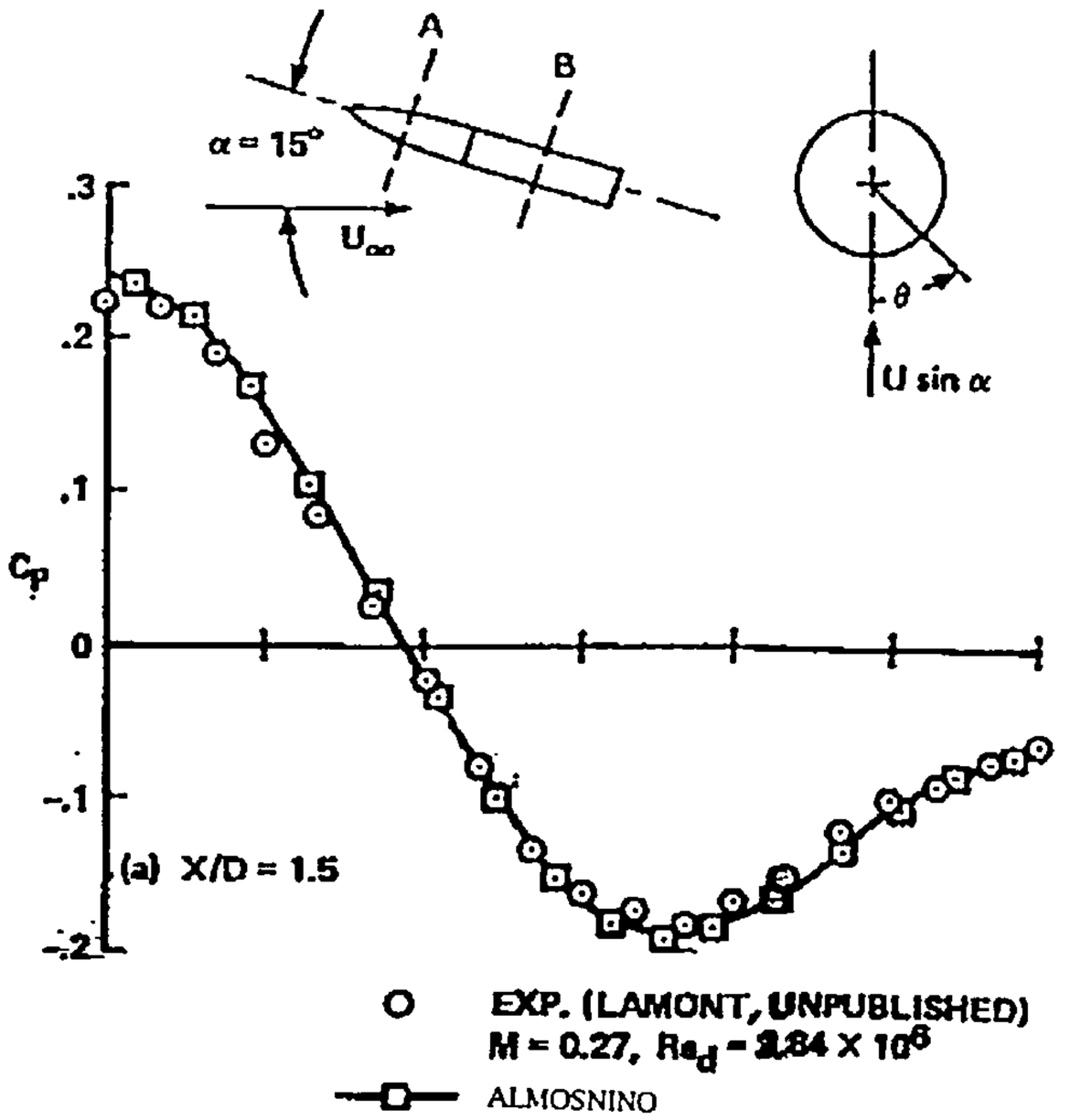

Figure 6.2.3.2 Circumferential surface pressure distributions on an ogive-cylinder body in subsonic flow
(After Almosnino [22])

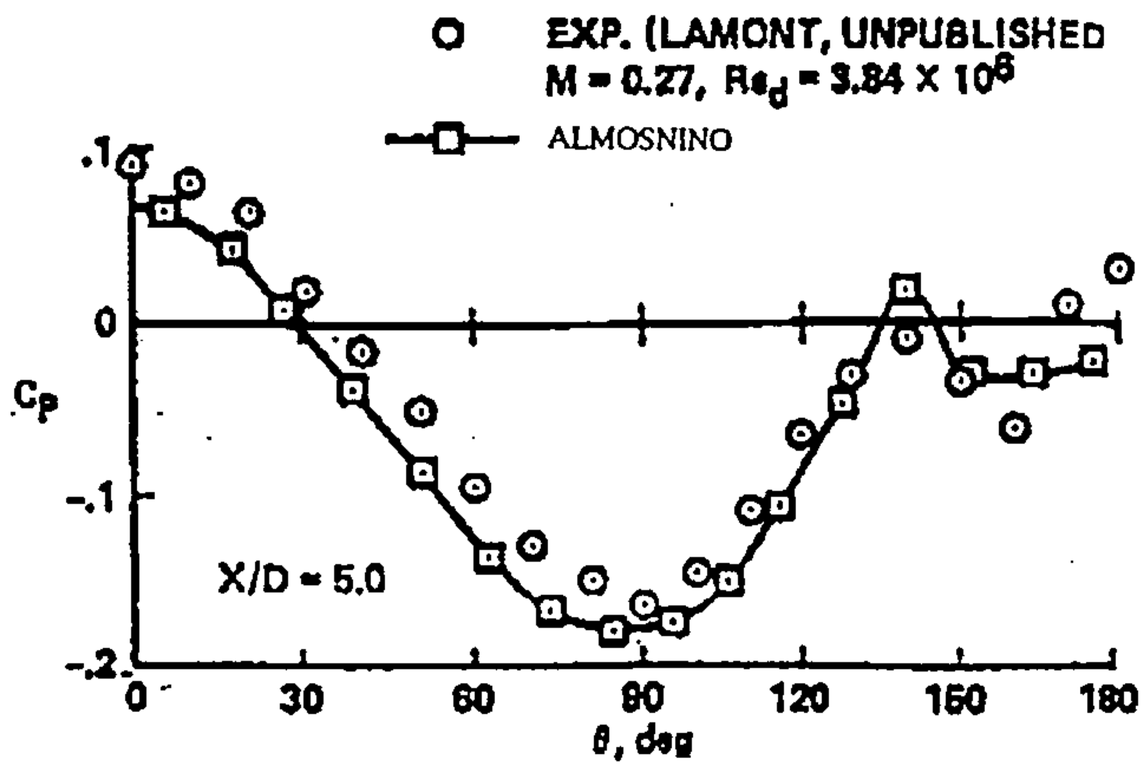

Figure 6.2.3.3 Circumferential surface pressure distributions on an ogive-cylinder body in subsonic flow
(After Almosnino [22])

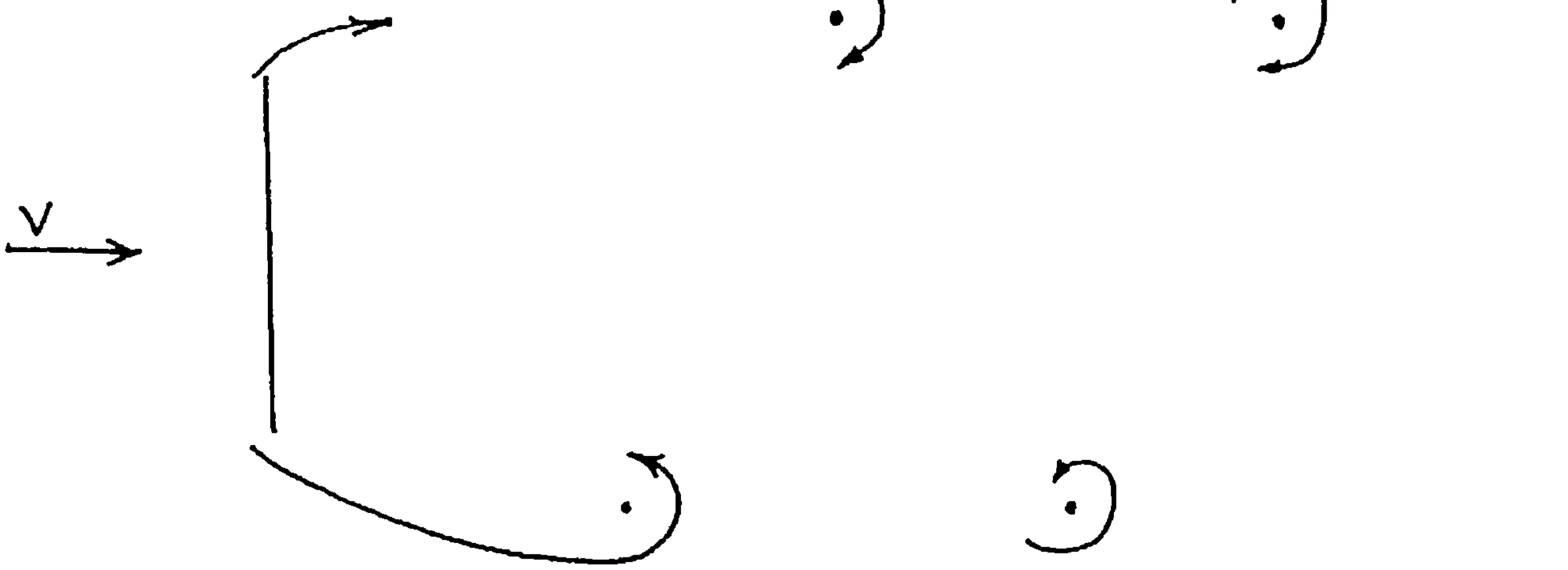

A vortex street behind a flat plate in a free stream

Figure 7.3.1.3

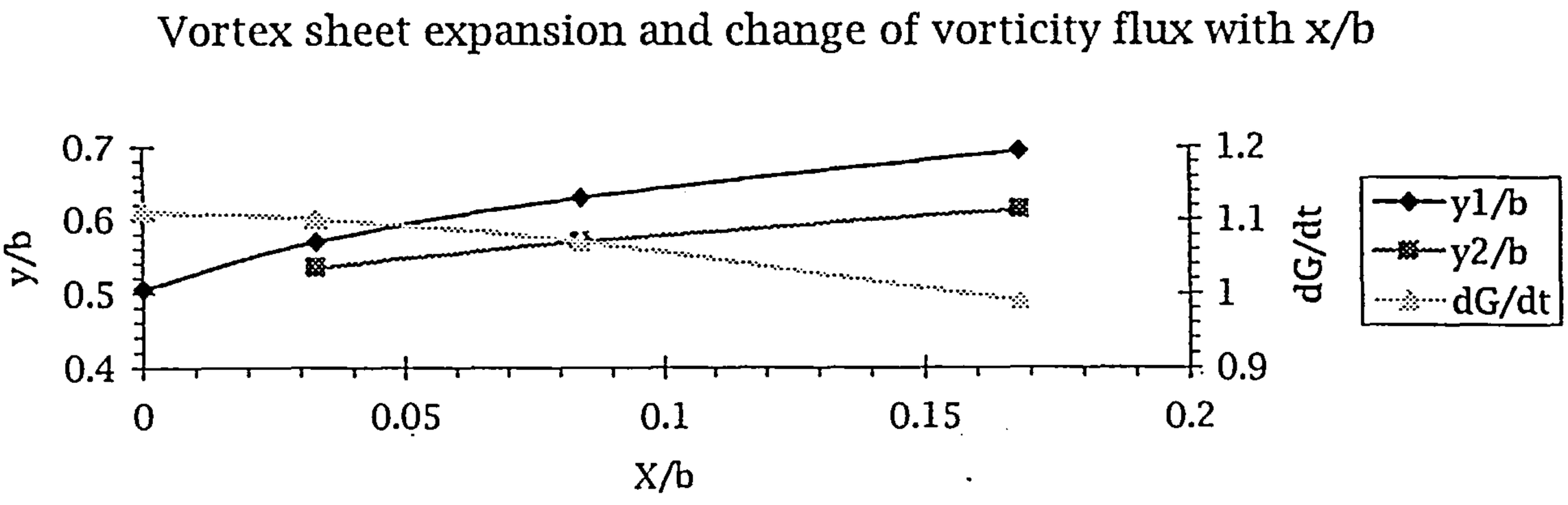

Figure 7.3.3.3

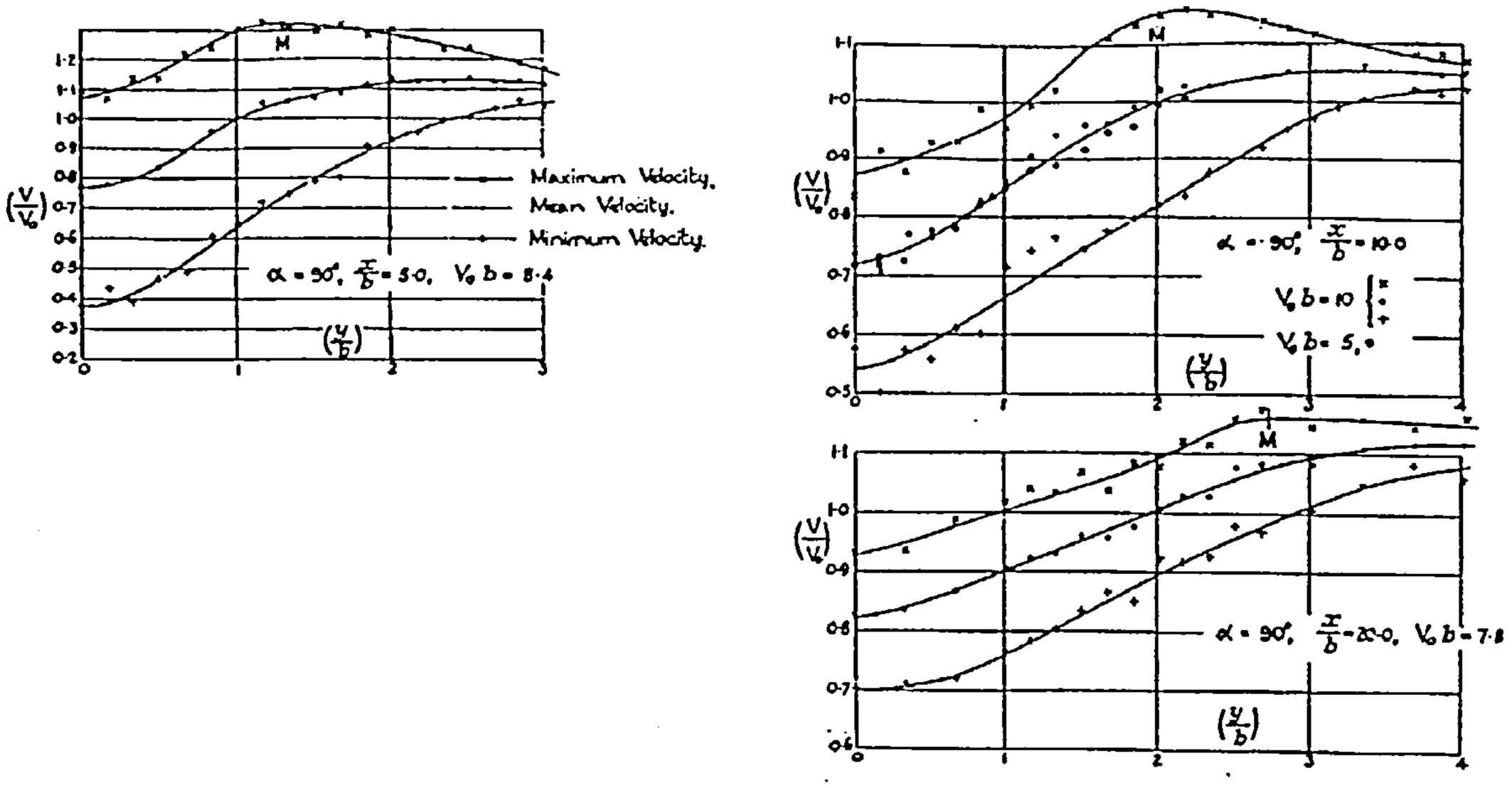

Figure 7.3.4.1
(After Fage and Johansen [11])

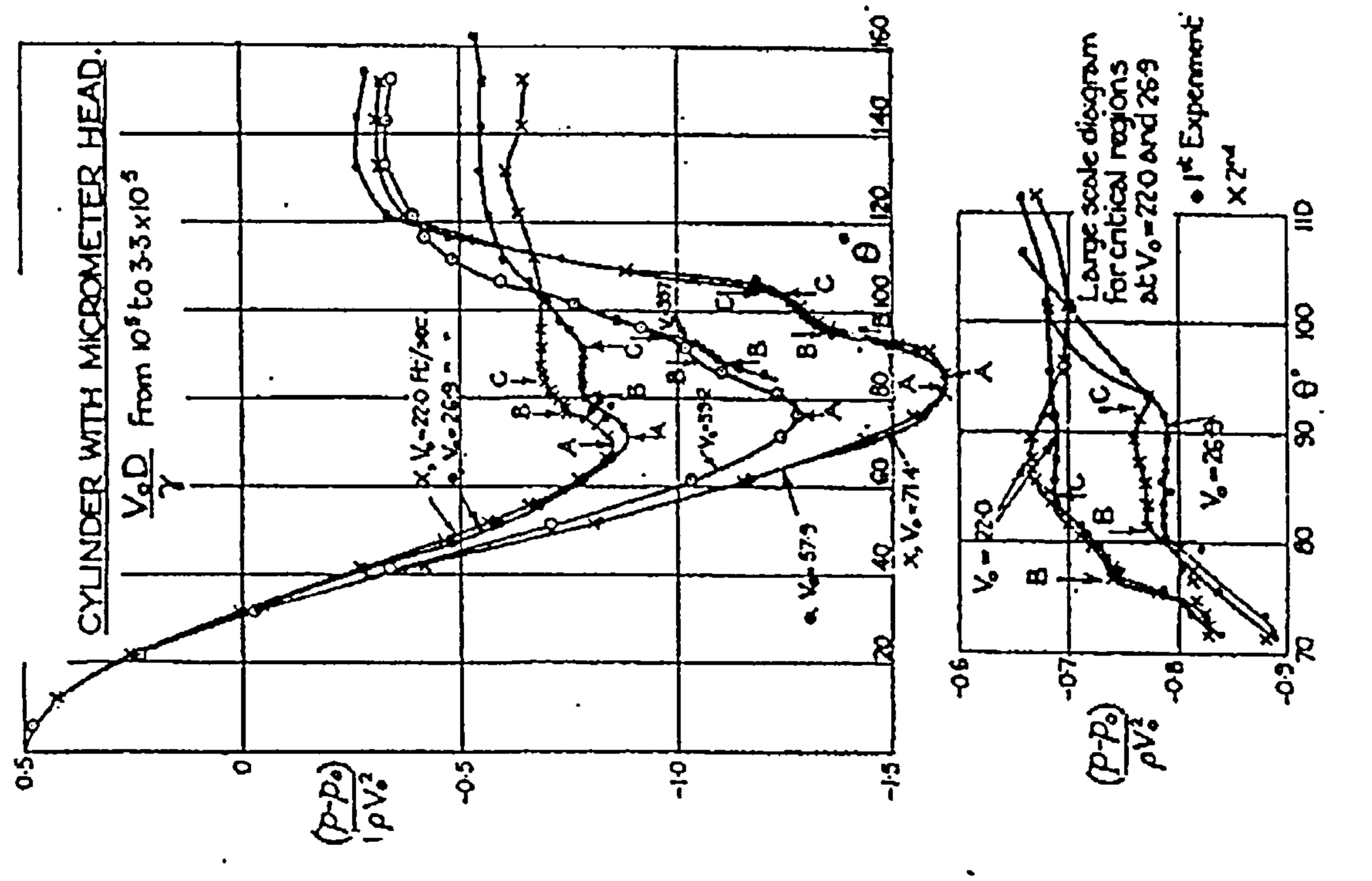

Figure 7.3.6.2
(After Fage [29])

Circular cylinder boundary layer velocity profiles at V=22ft/sec

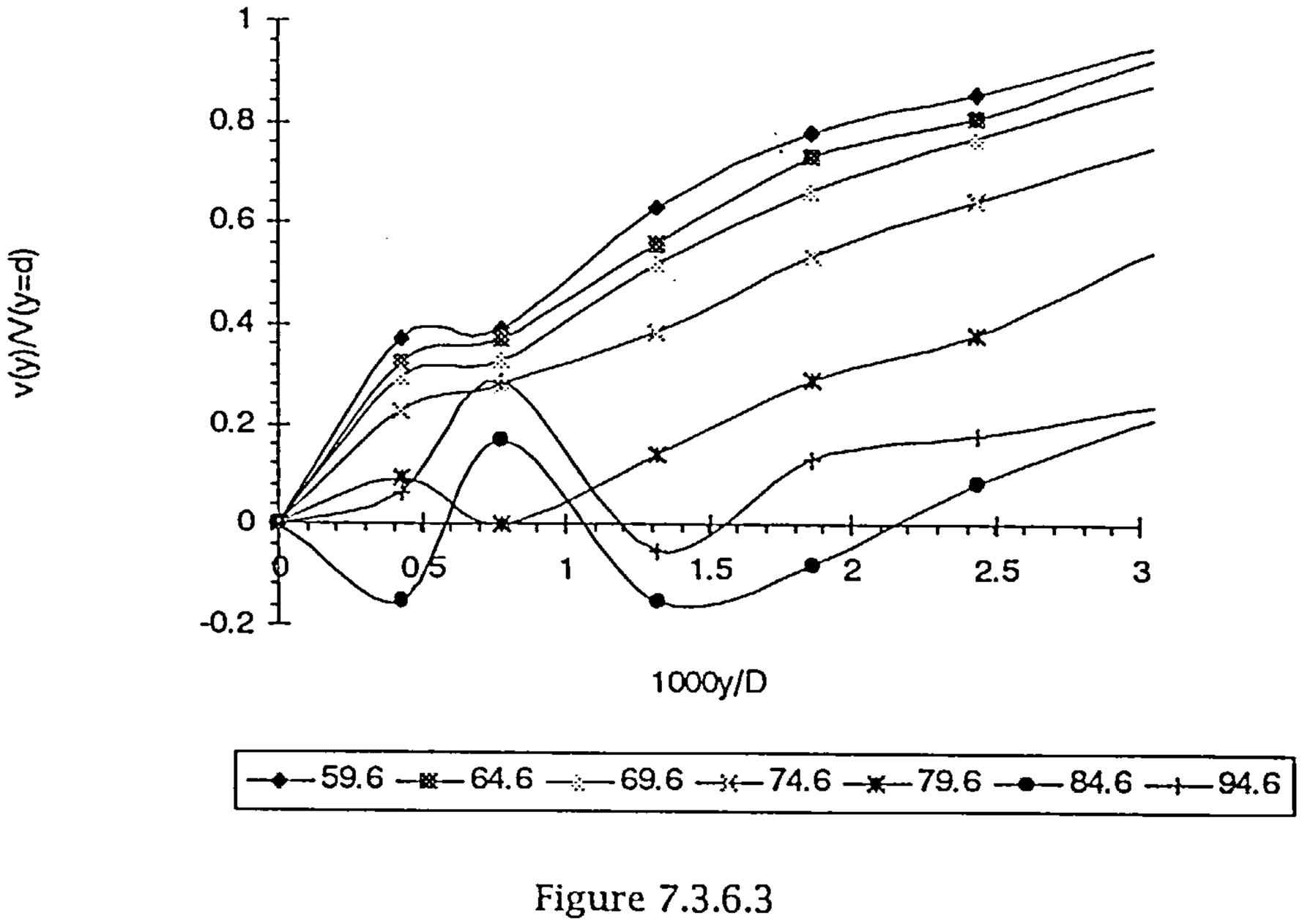

Figure 7.3.6.3

Circular cylinder boundary layer 'Off-set' velocity profiles at V=22ft/sec

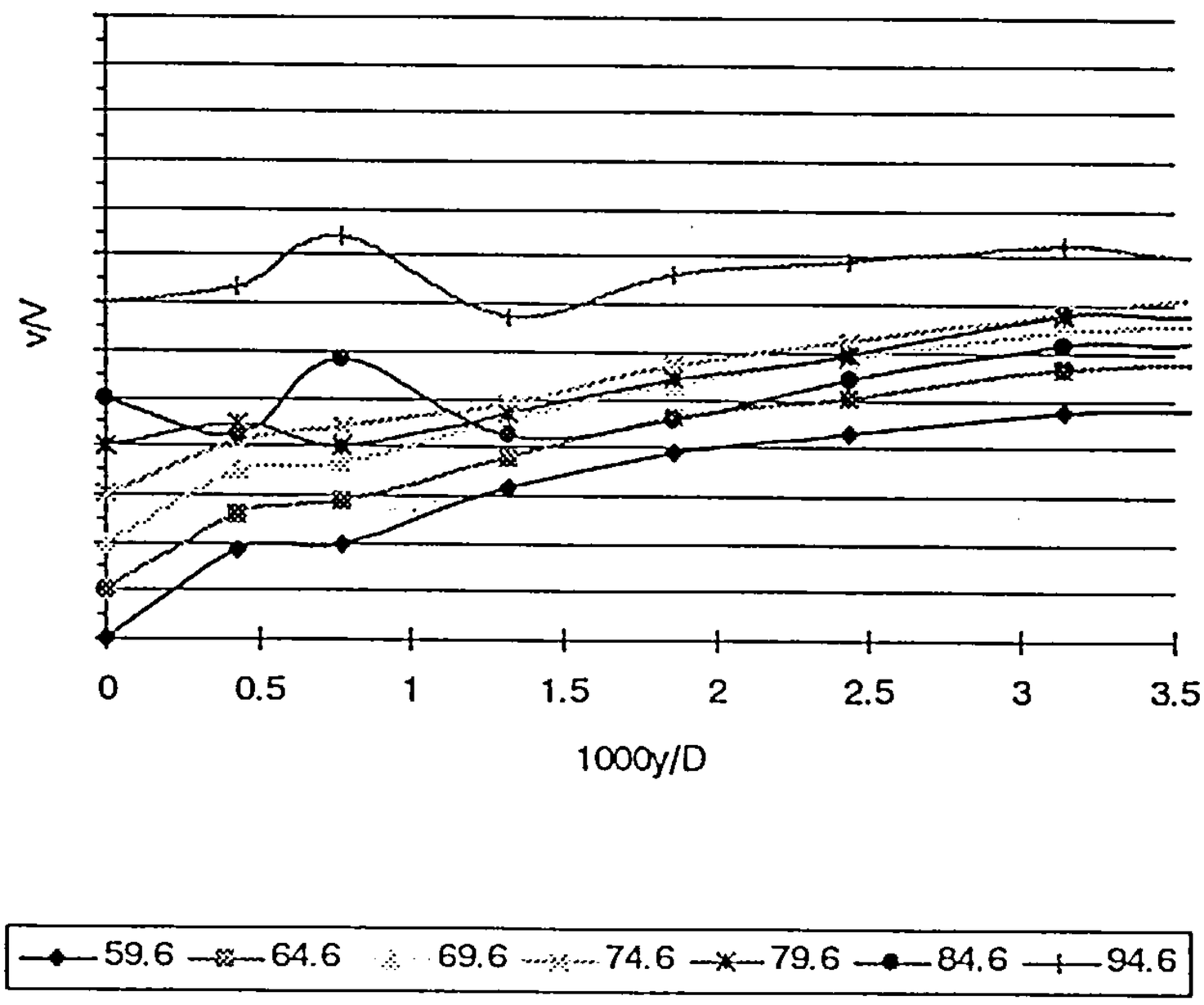

Figure 7.3.6.4

Circular cylinder boundary layer velocity profiles at V=71.4ft/sec

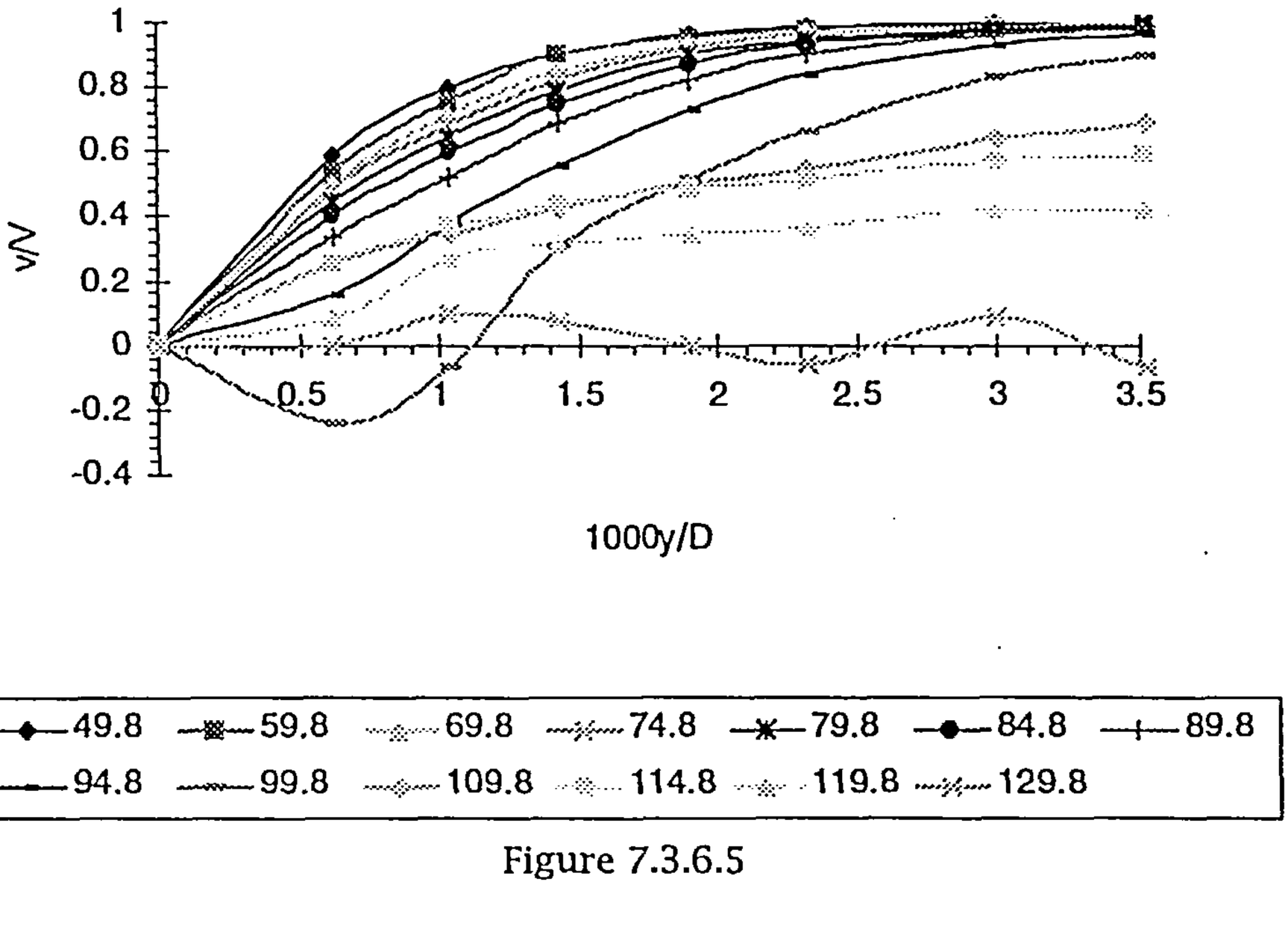

Figure 7.3.6.5

Circular cylinder boundary layer vorticity profiles at V=22.0ft/sec

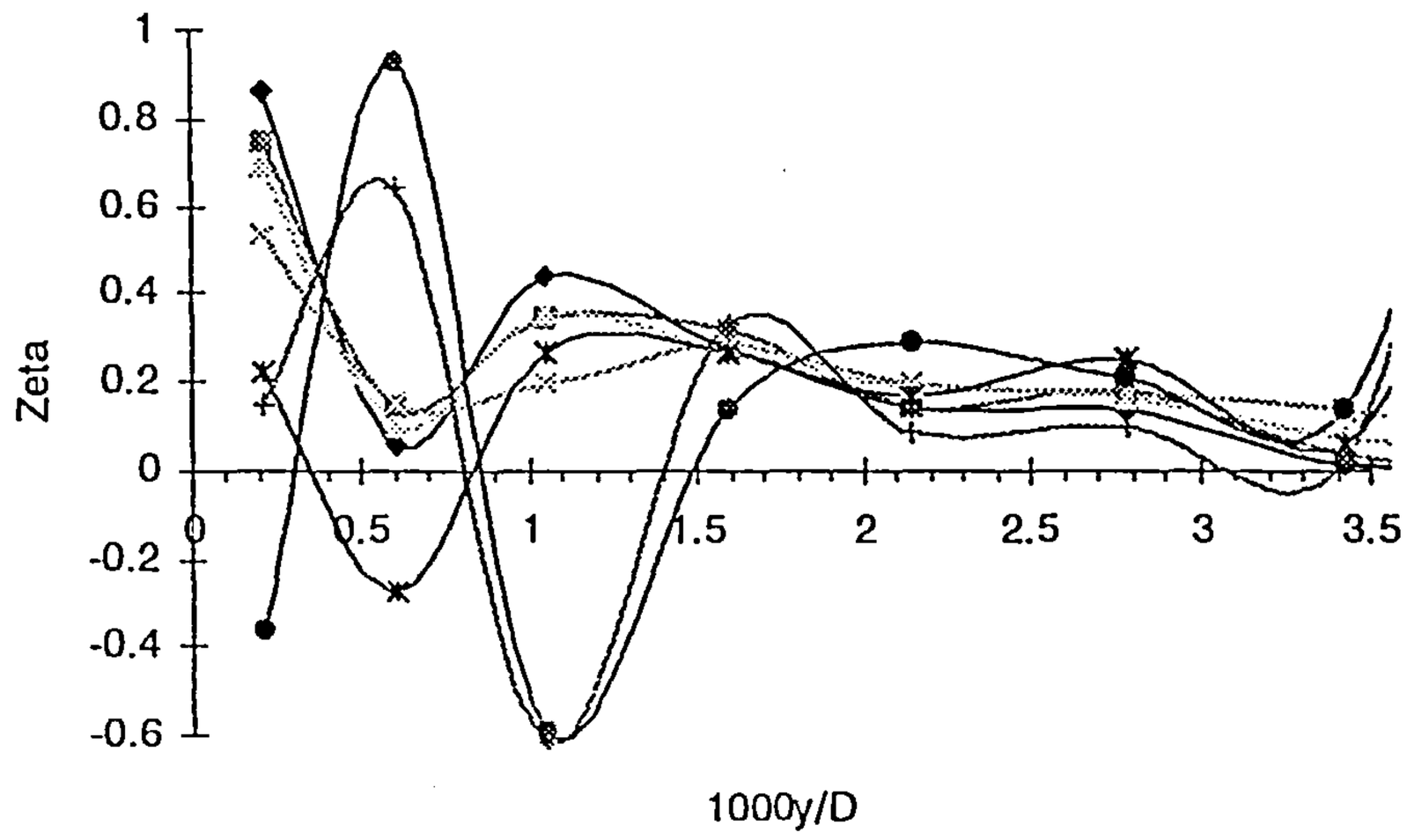

Figure 7.3.6.6

Circular cylinder boundary layer vorticity profiles at V=71.4ft/sec

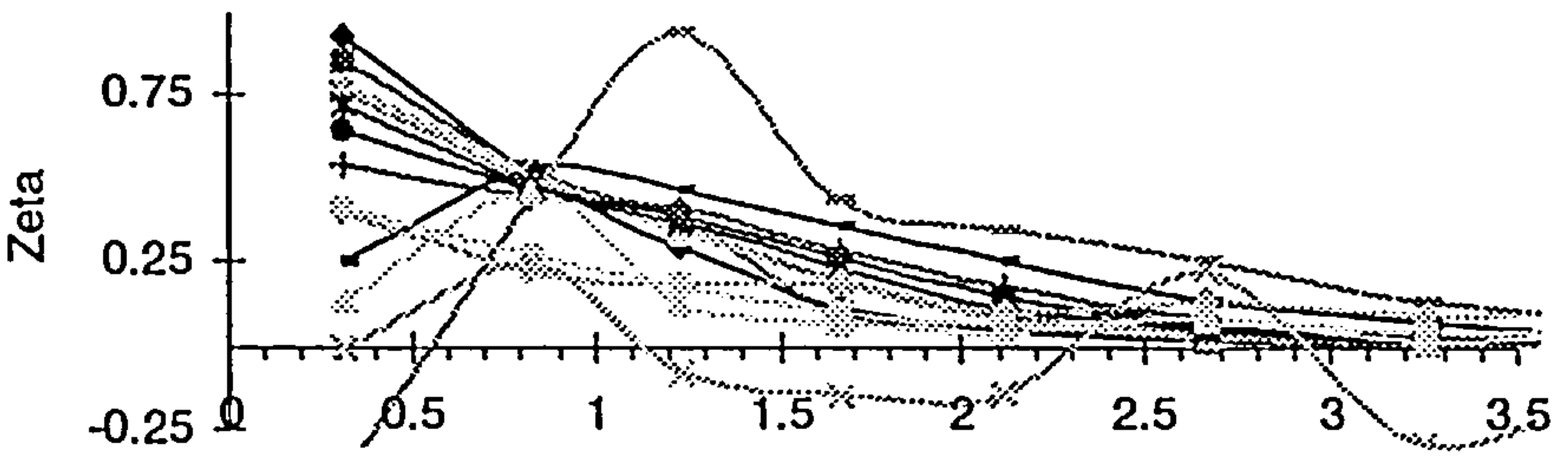

Figure 7.3.6.7

Vorticity Curves.

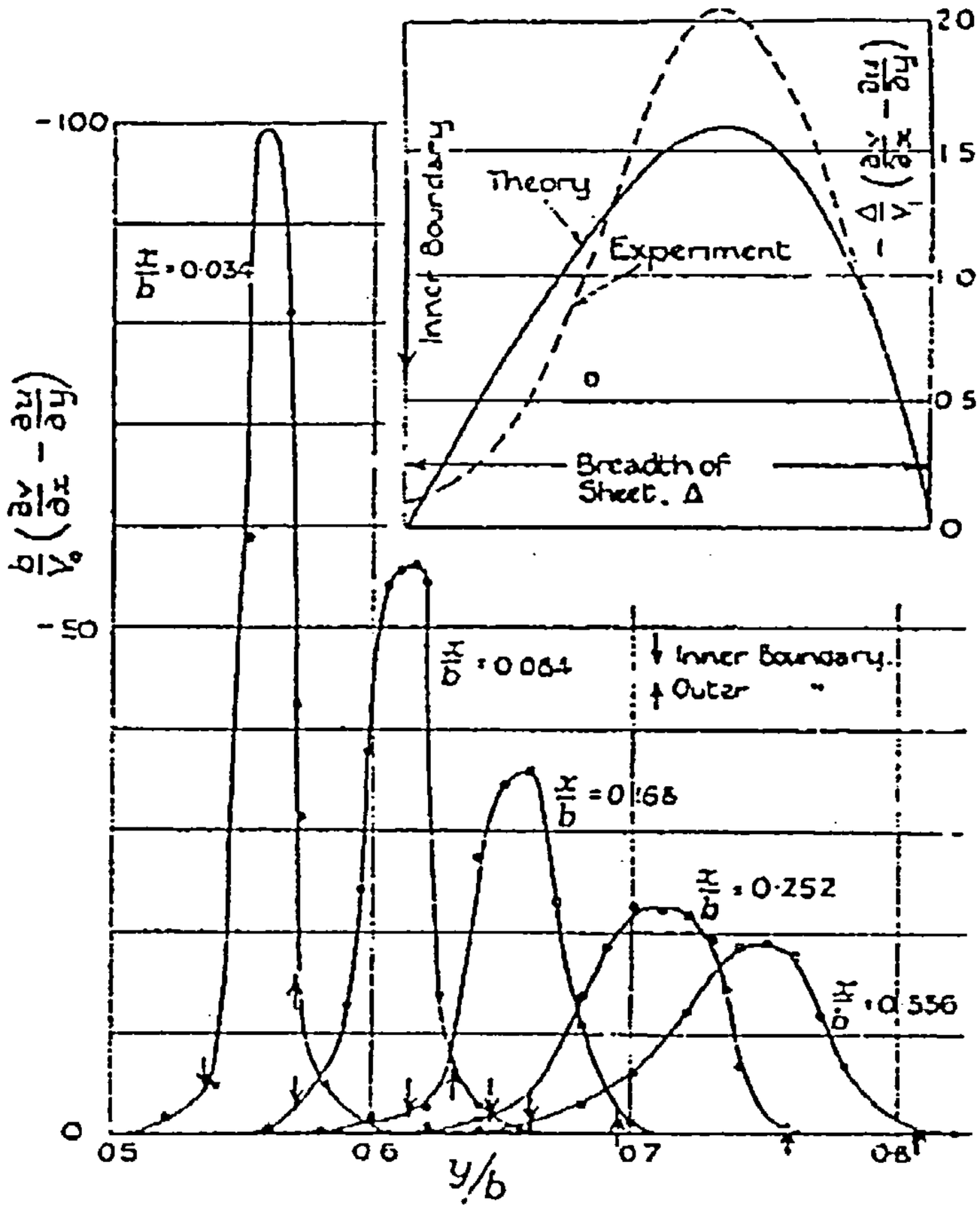

Figure 7.3.7.2

(After Fage and Johansen [11])

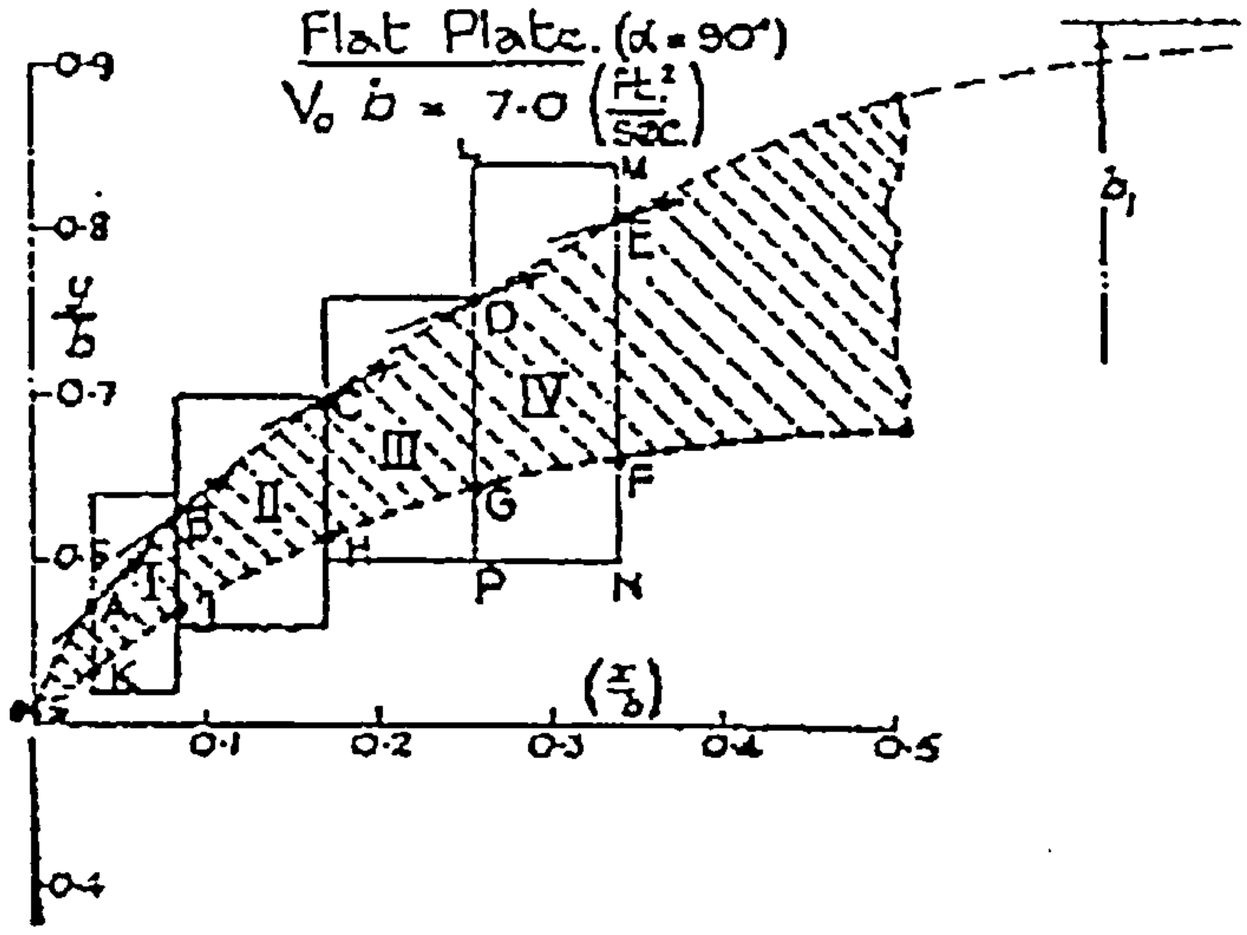

Figure 7.3.7.3
(After Fage and Johansen [11])

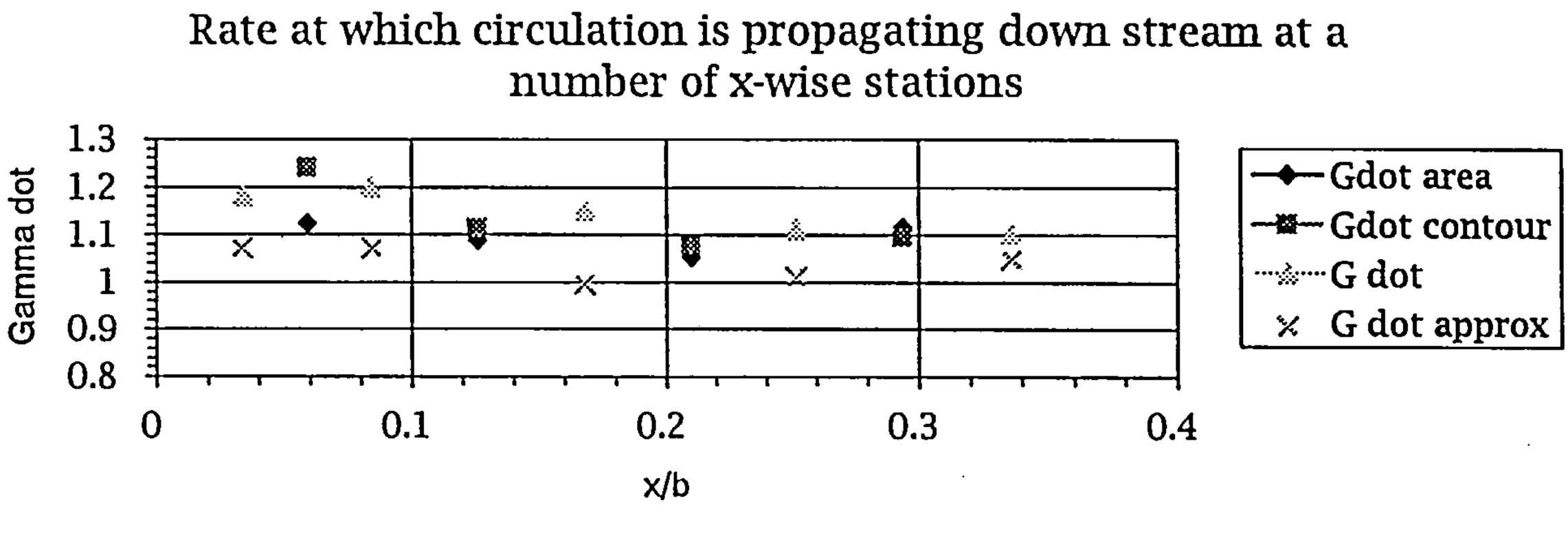

Figure 7.3.7.9

Rate at which circulation is propagating down stream at a number of x-wise stations as a fraction of maximum value

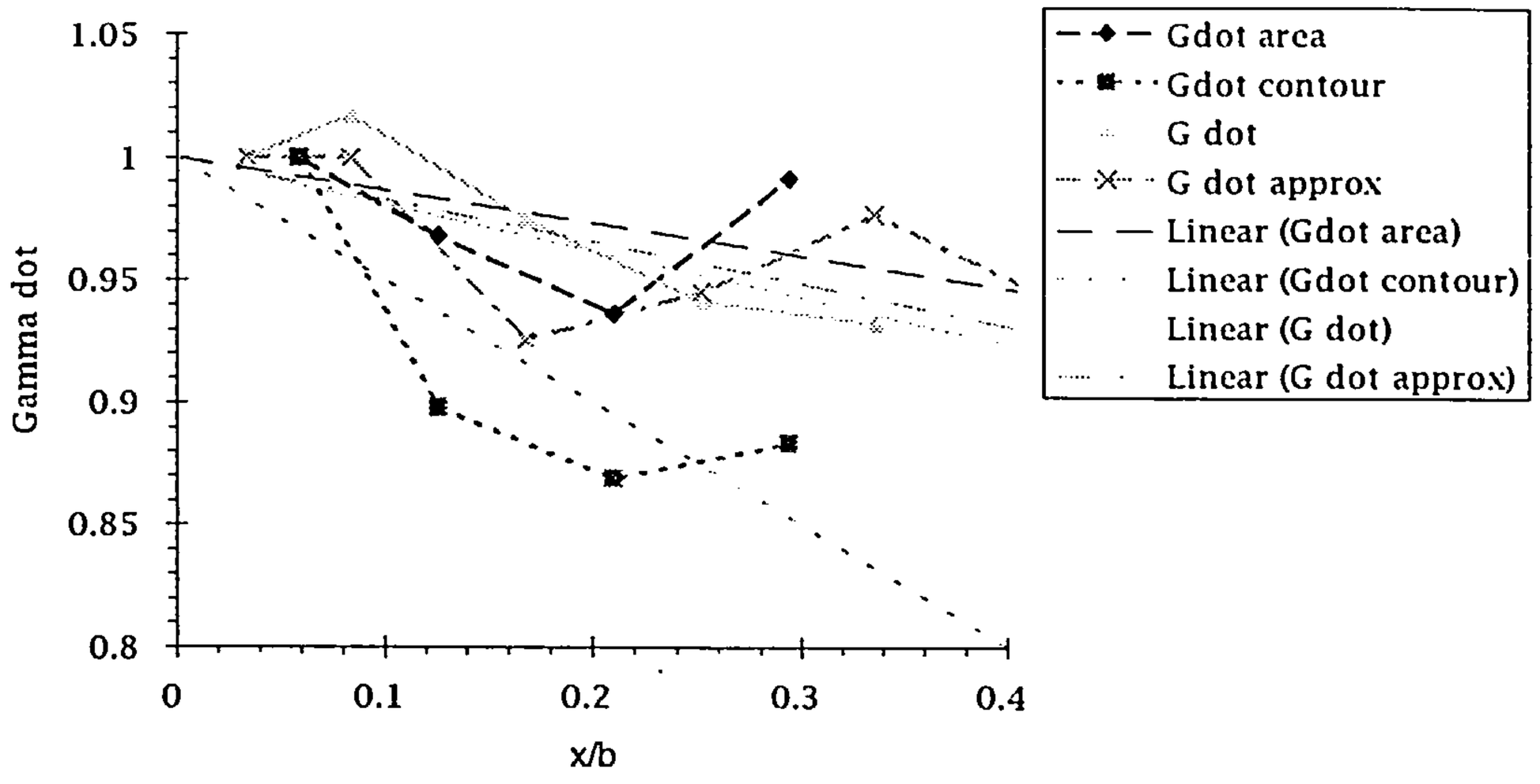

Figure 7.3.7.10

Flat plate vortex sheet geometry, strength and Gamma dot

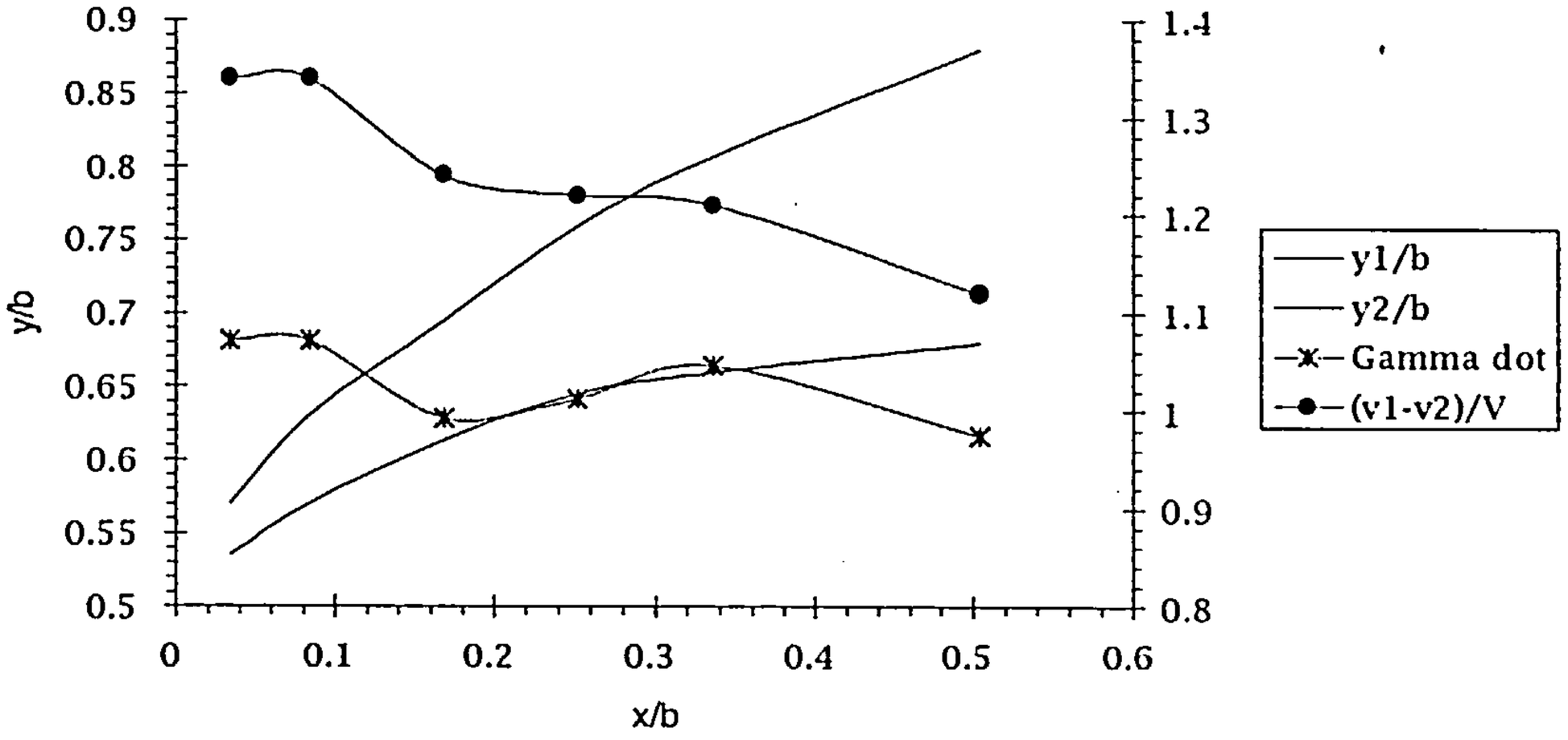

Figure 7.3.7.11

Circular cylinder vortex sheet geometry, strength and Gamma dot

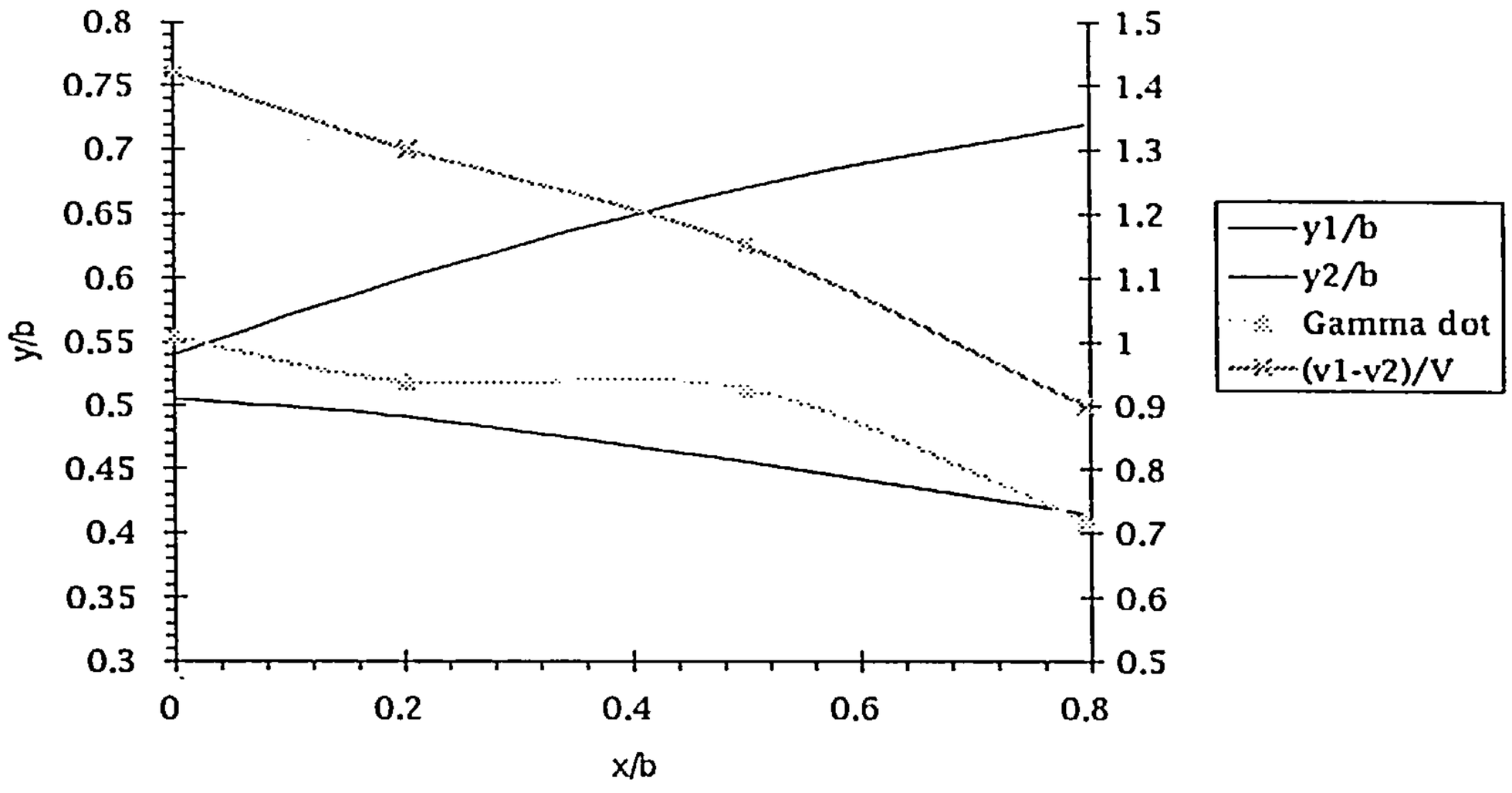

Figure 7.3.7.12

Wedge vortex sheet geometry, strength and Gamma dot

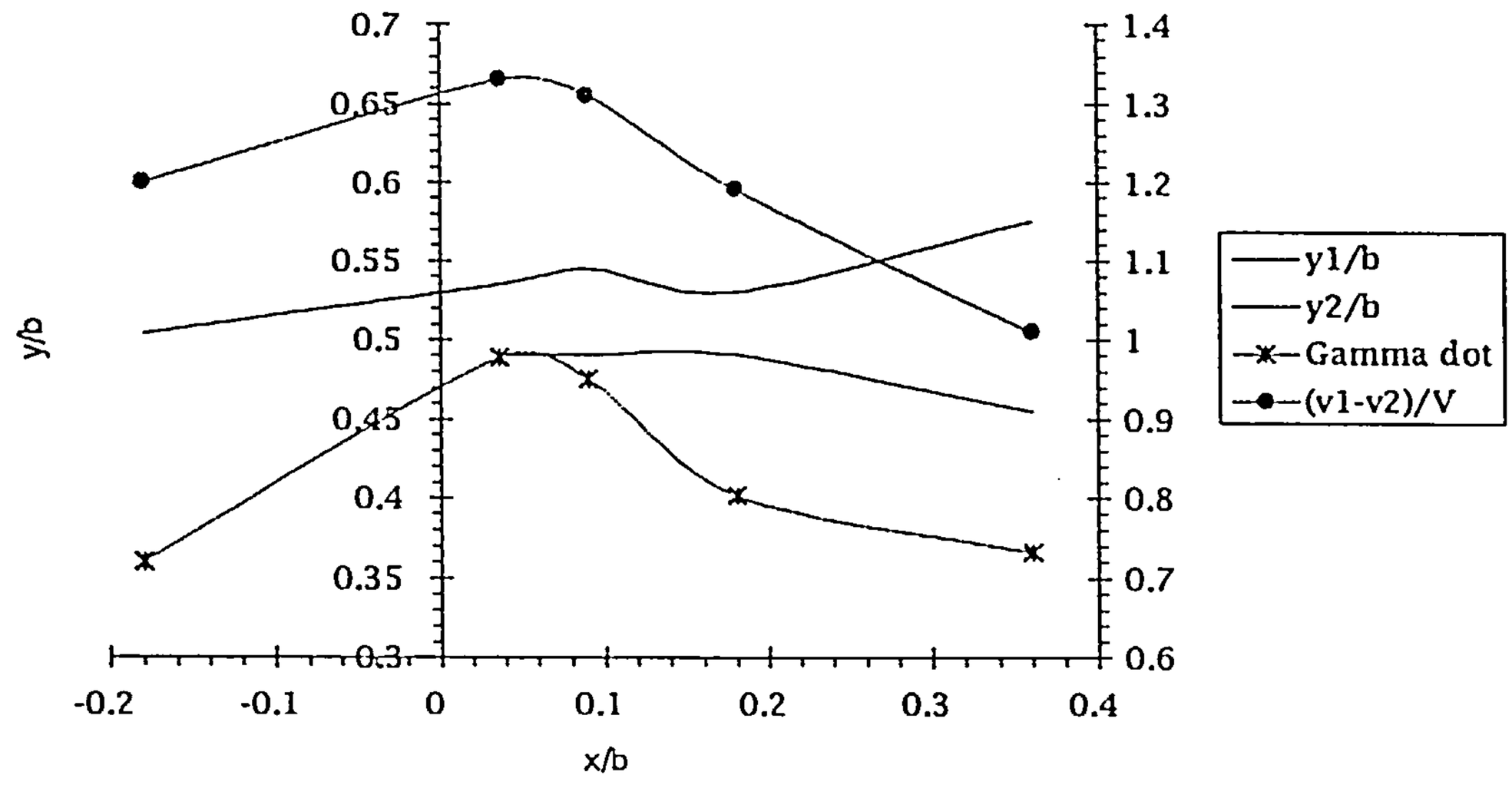

Figure 7.3.7.13

Ogival body vortex sheet geometry, strength and Gamma dot

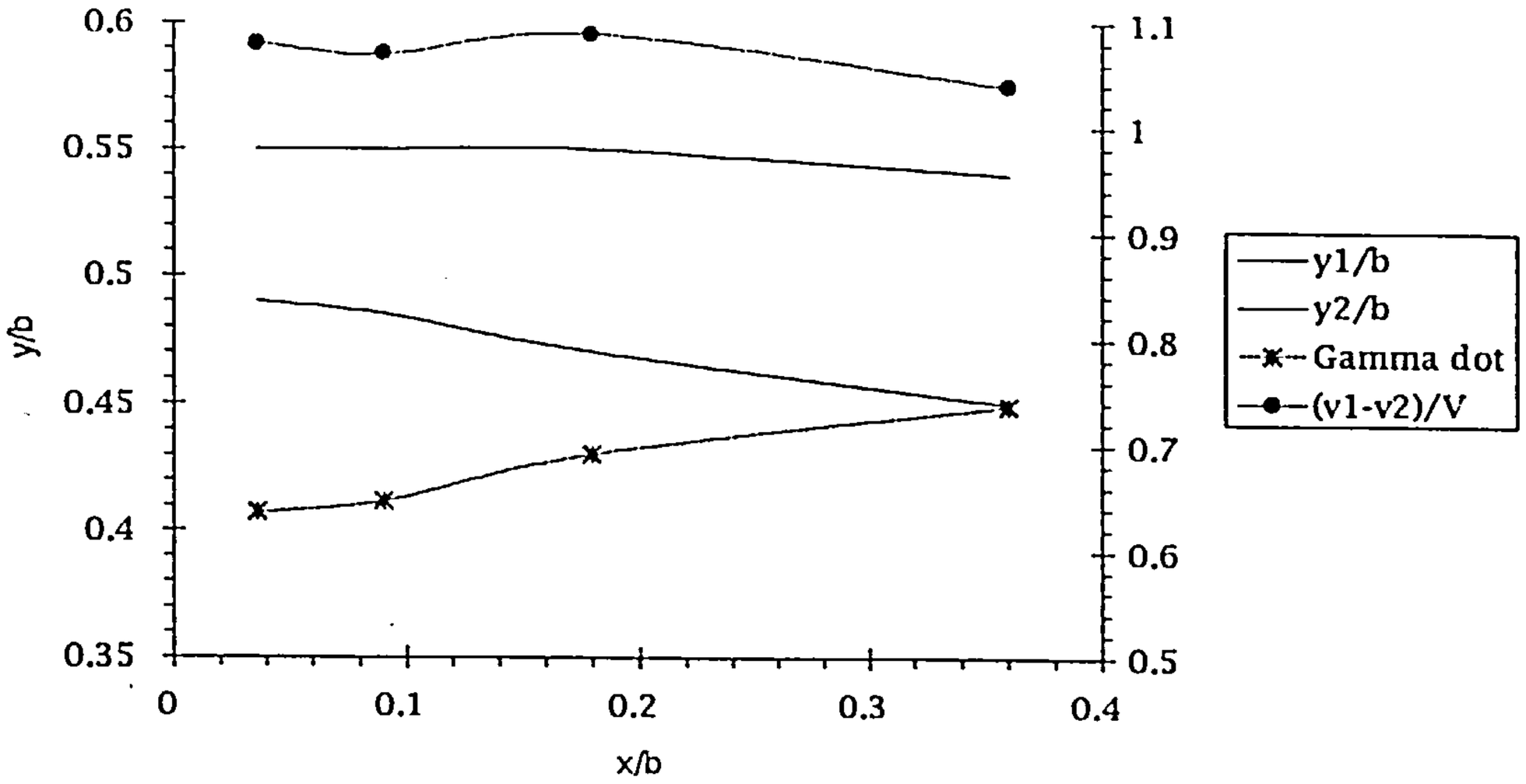

Figure 7.3.7.14

Extended ogival body vortex sheet geometry, strength and Gamma dot

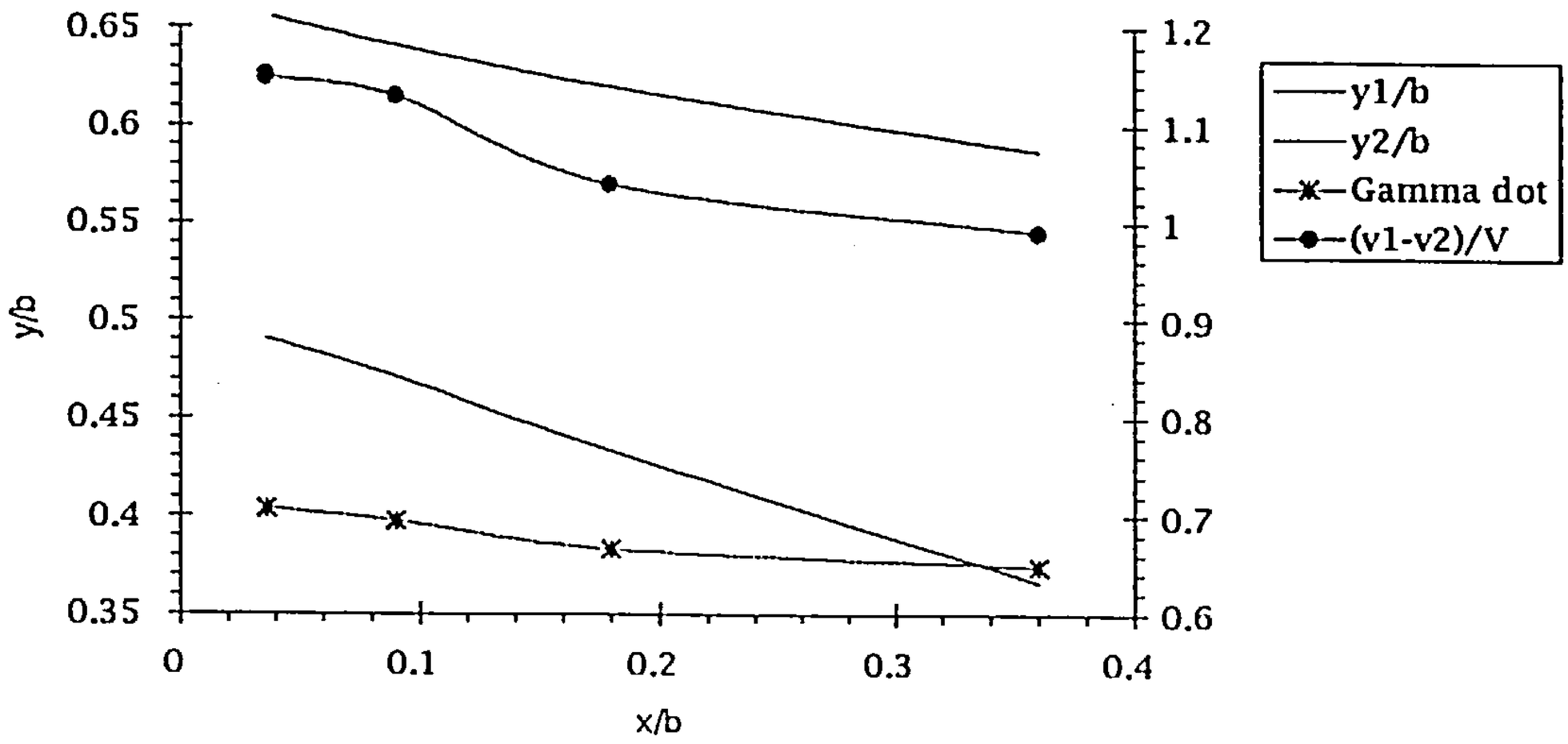

Figure 7.3.7.15

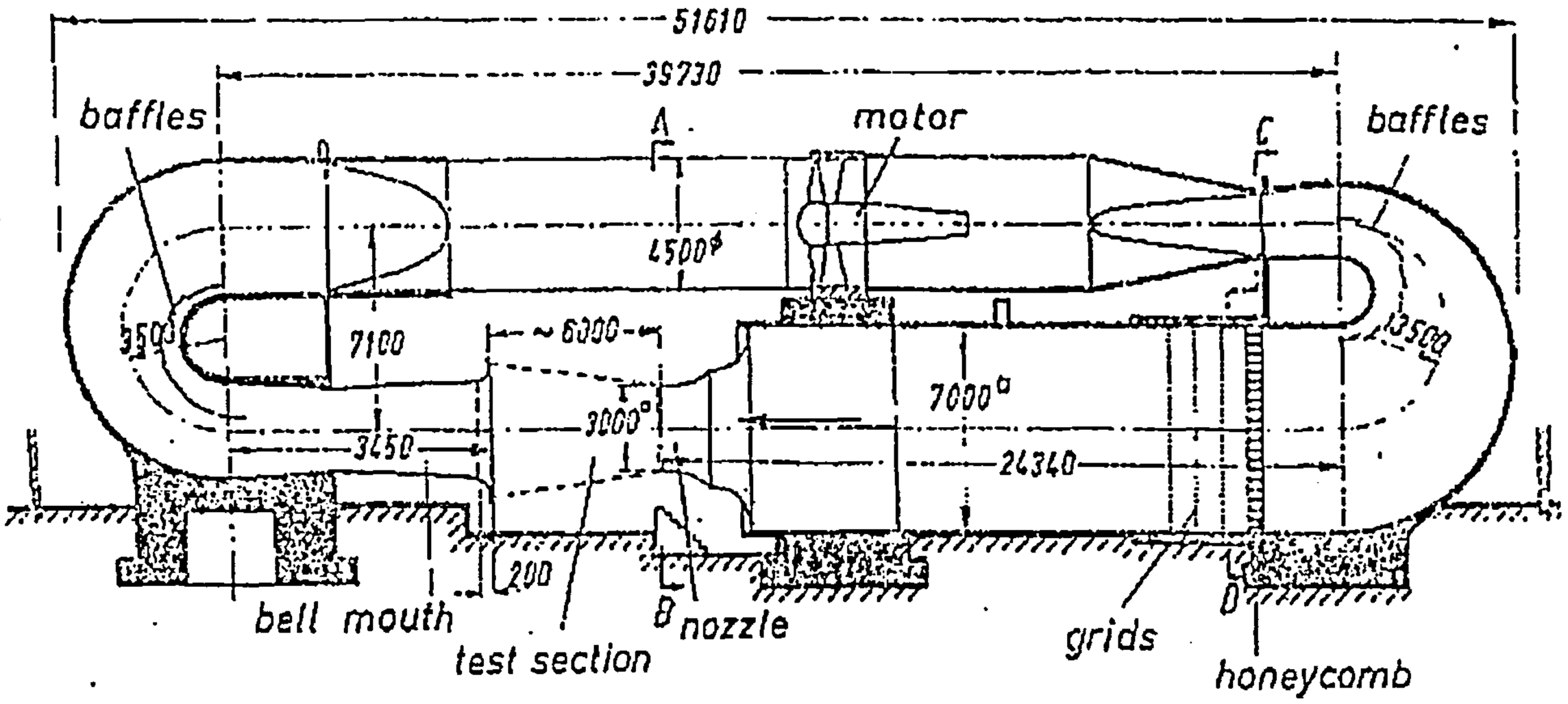

Figure 7.4.1.1
(After Hartmann [30])

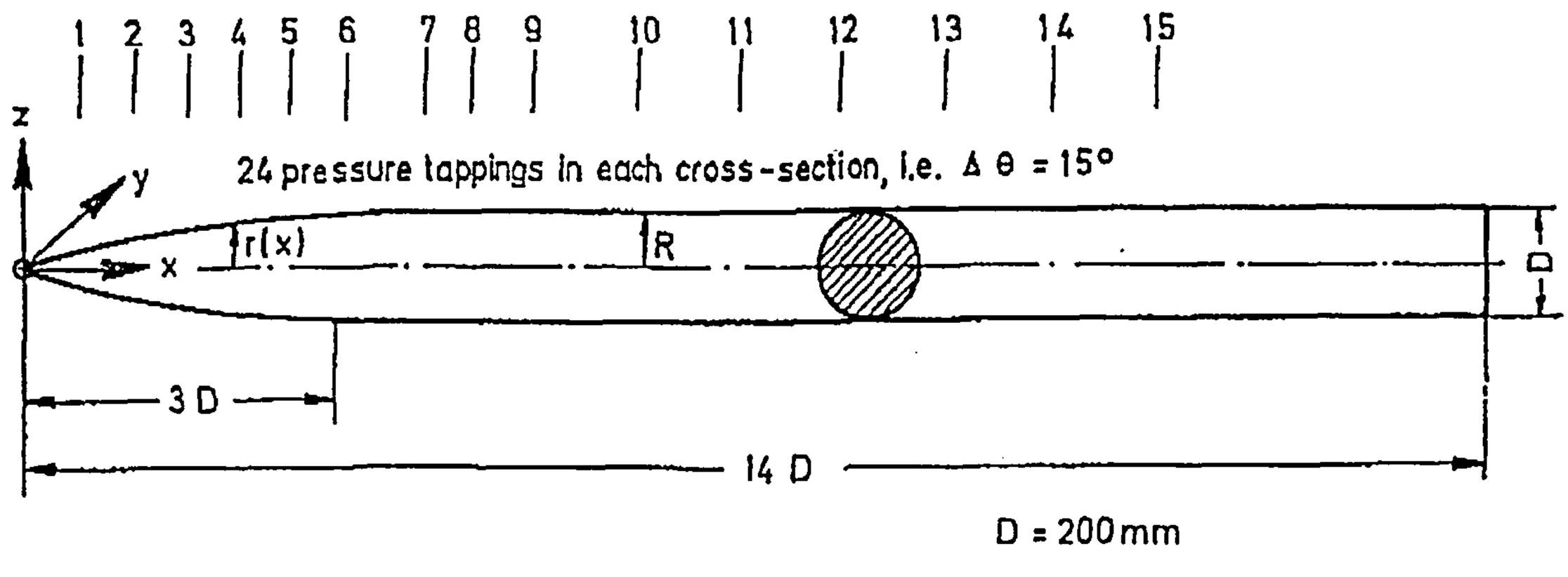

Figure 7.4.1.2
(After Hartmann [30])

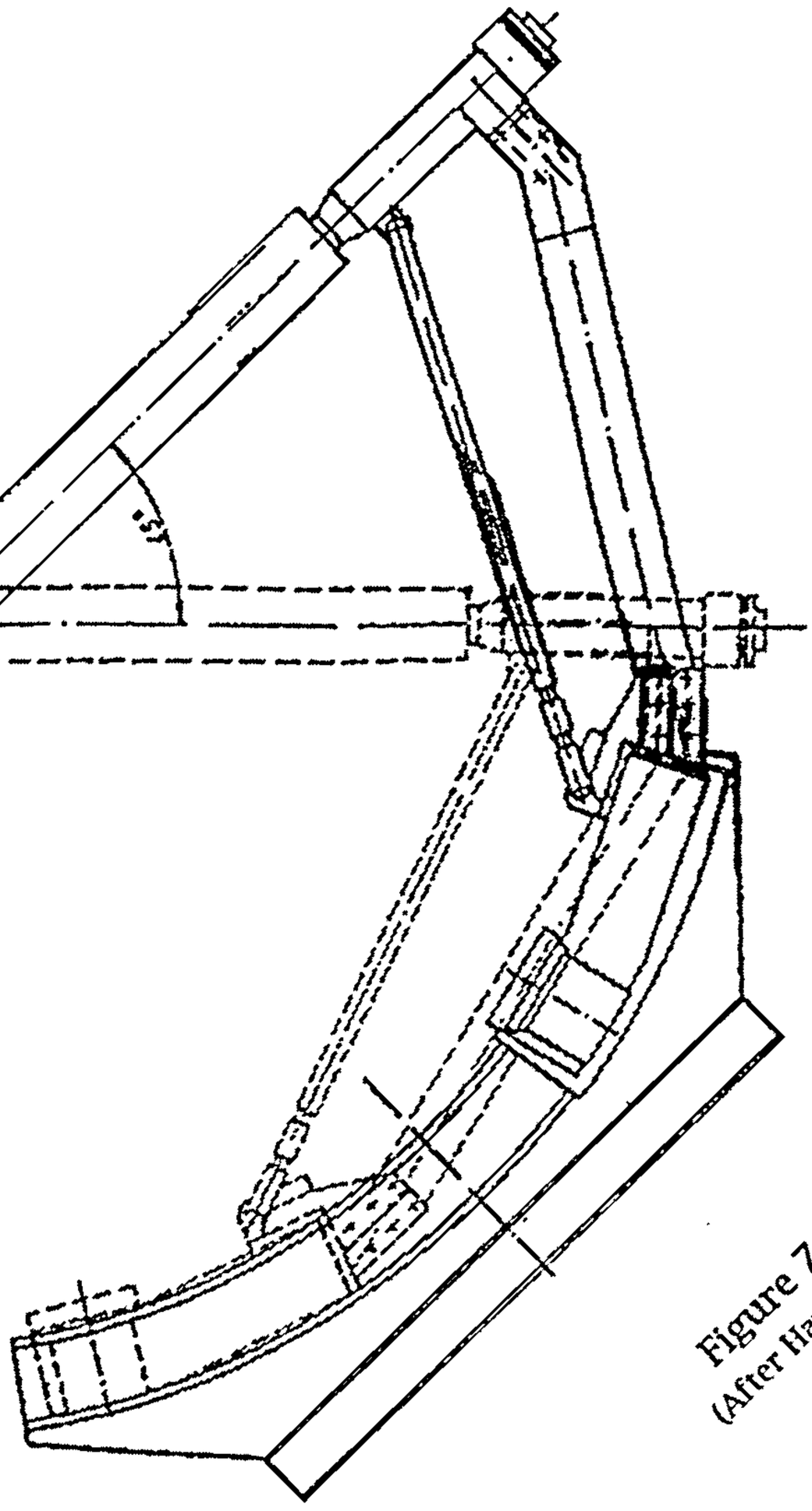

Figure 7.4.1.3
(After Hartmann (30))

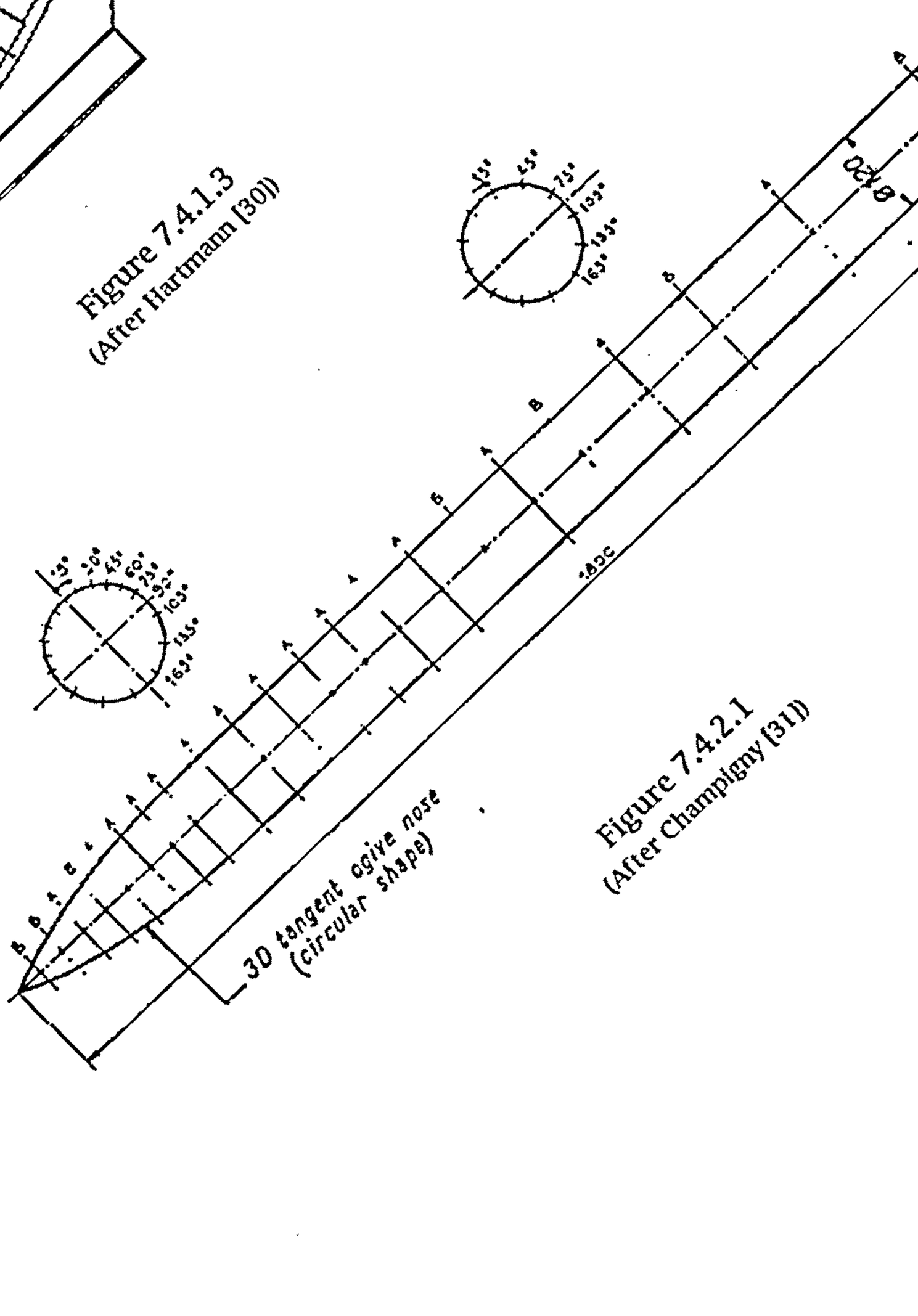

Figure 7.4.2.1
(After Champigny (31))

DFVLR Load distribution on a "near tangent ogive"-cylinder body at alpha=5 ReD=.25 , .38 & .74 million

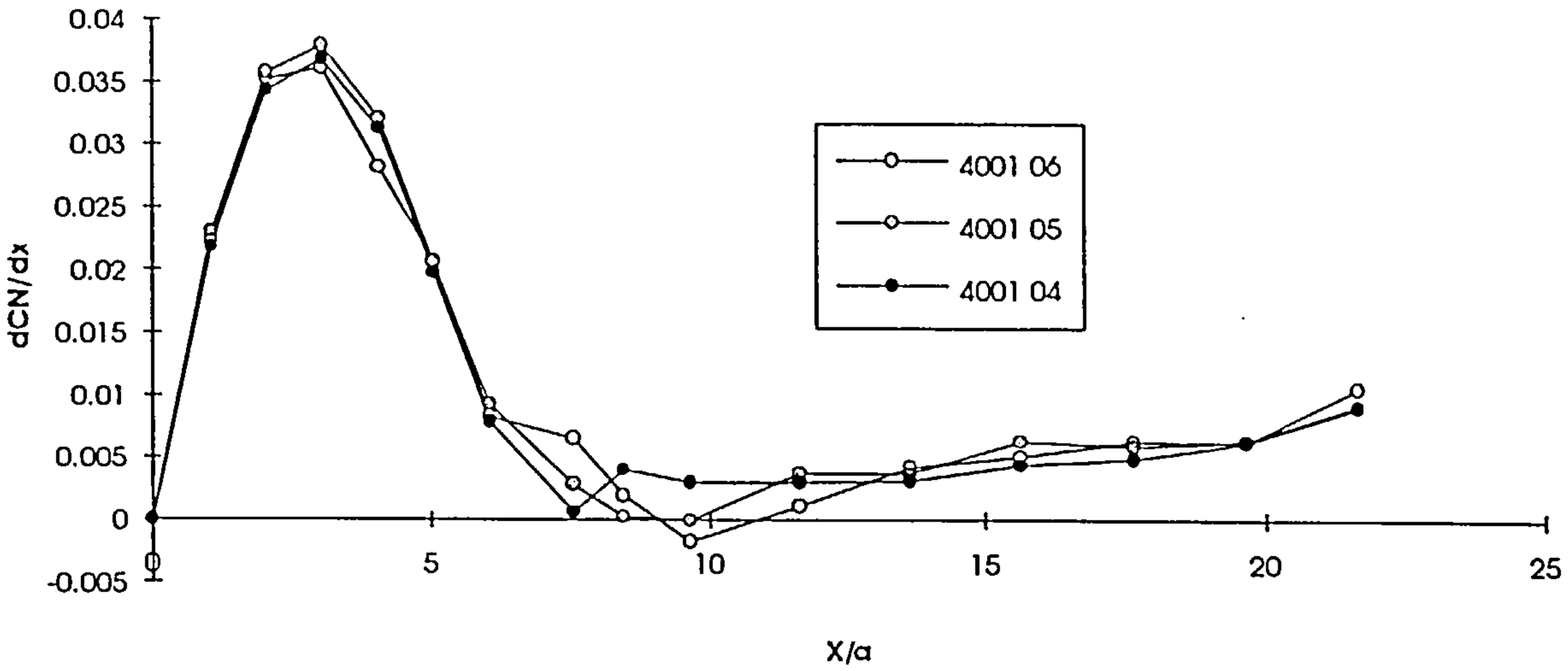

Figure 7.4.3.3

DFVLR Load distribution on a "near tangent ogive"-cylinder body at alpha=10 ReD=.25 , .38 & .74 million

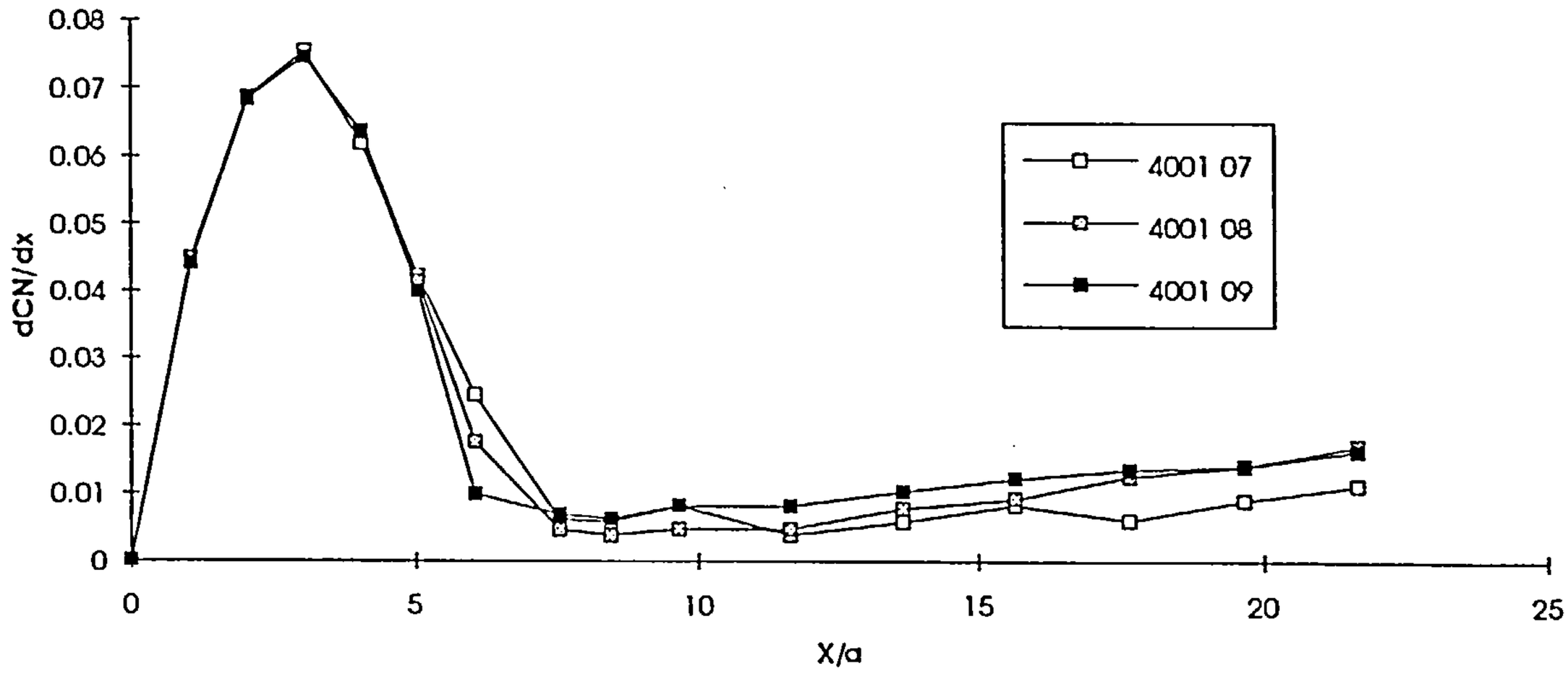

Figure 7.4.3.4

DFVLR Load distribution on a "near tangent ogive"-cylinder body at alpha=15 ReD=.25 , .38 & .74 million

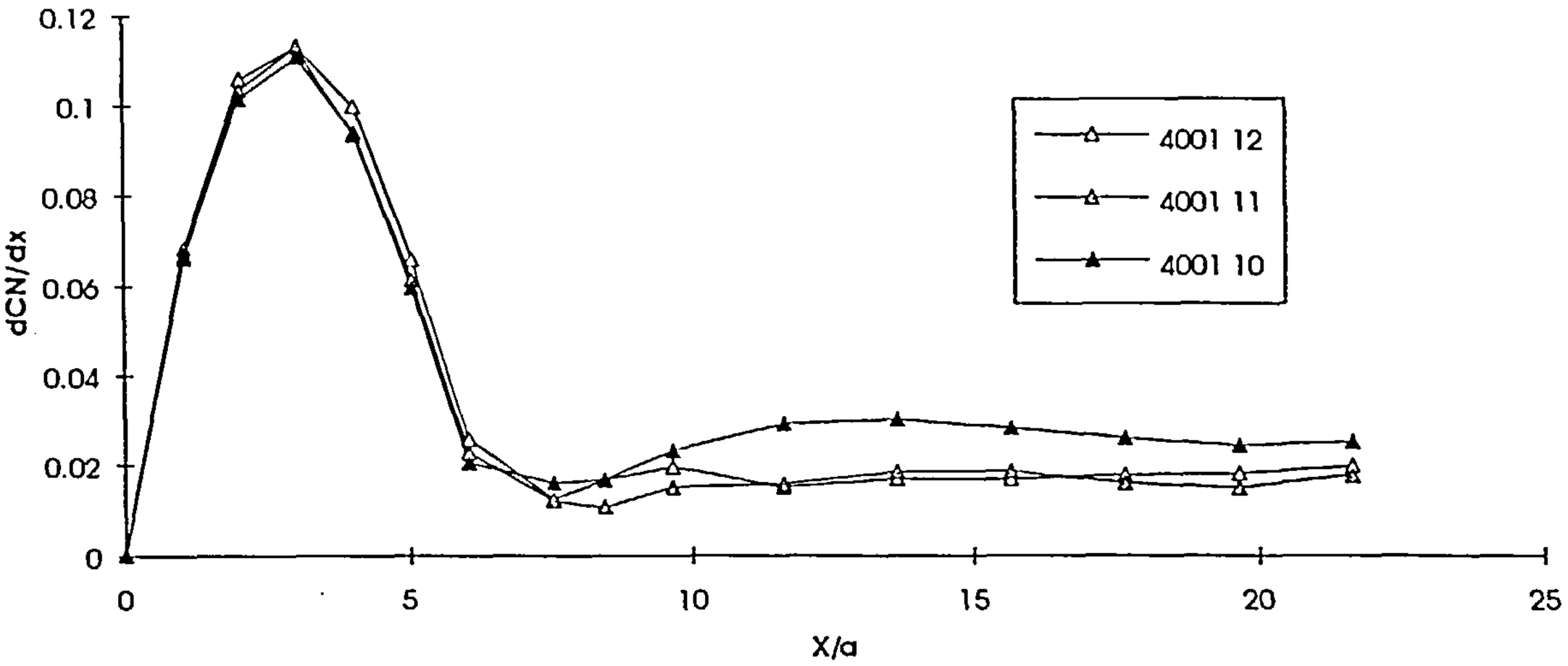

Figure 7.4.3.5

DFVLR Load distribution on a "near tangent ogive"-cylinder body at alpha=20 ReD=.25 & .38 million

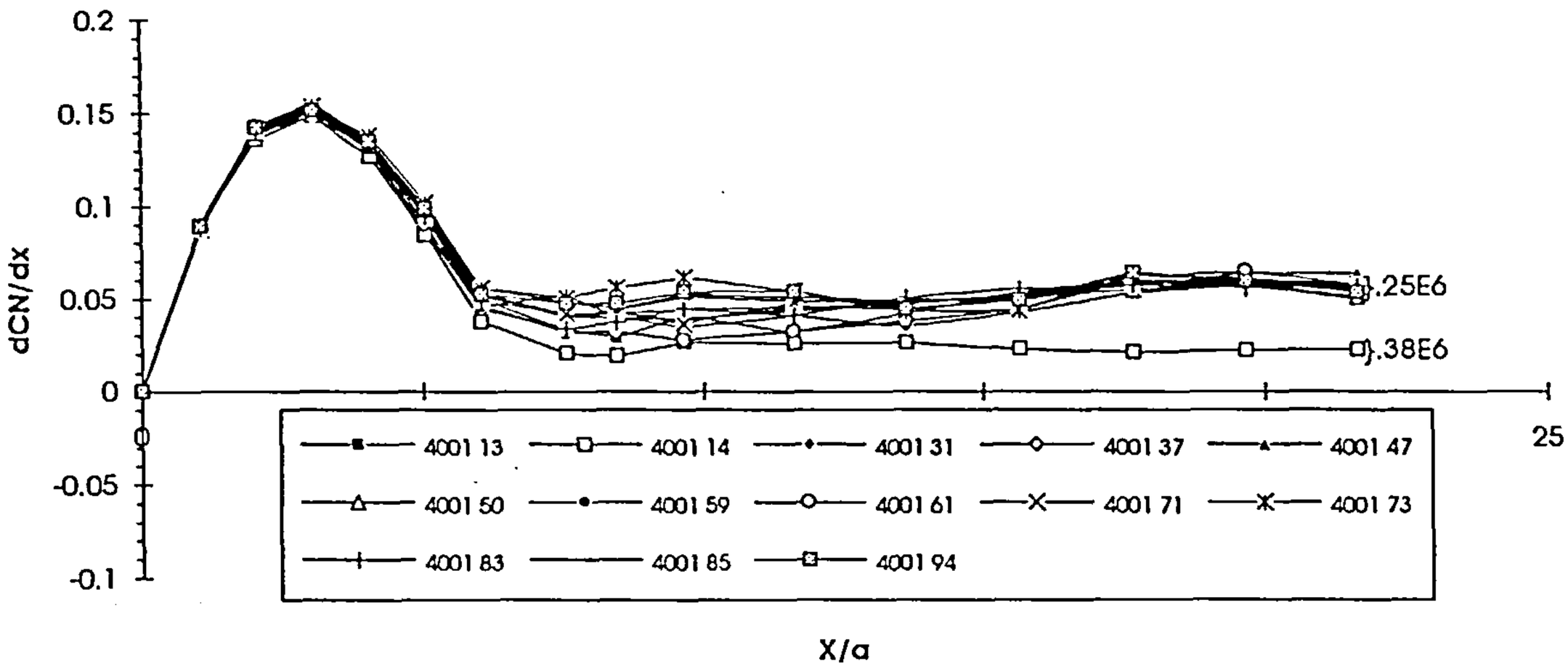

Figure 7.4.3.6

DFVLR Load distribution on a "near tangent ogive"-cylinder body at alpha=20 ReD=.74 million

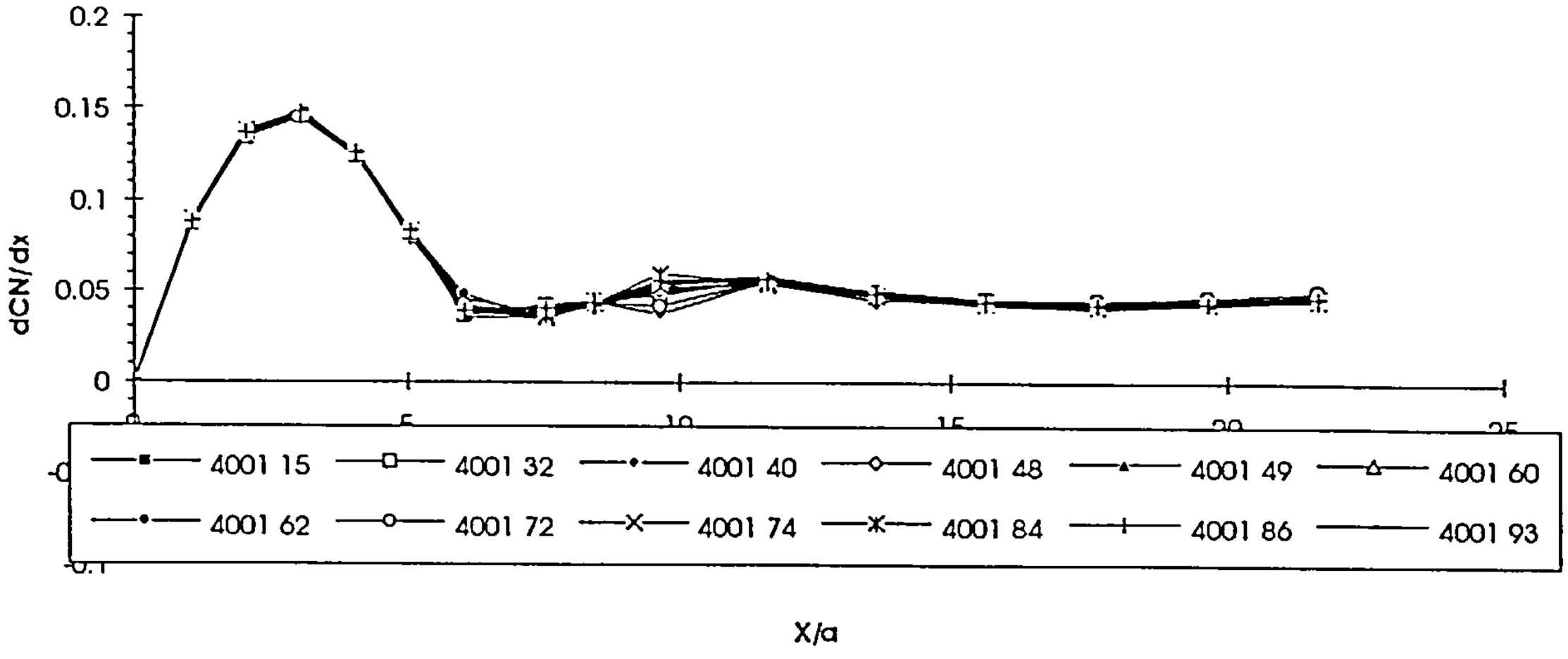

Figure 7.4.3.7

DFVLR Load distribution on a "near tangent ogive"-cylinder body at alpha=5, 10 &15 ReD=.25 , .38 & .74 million

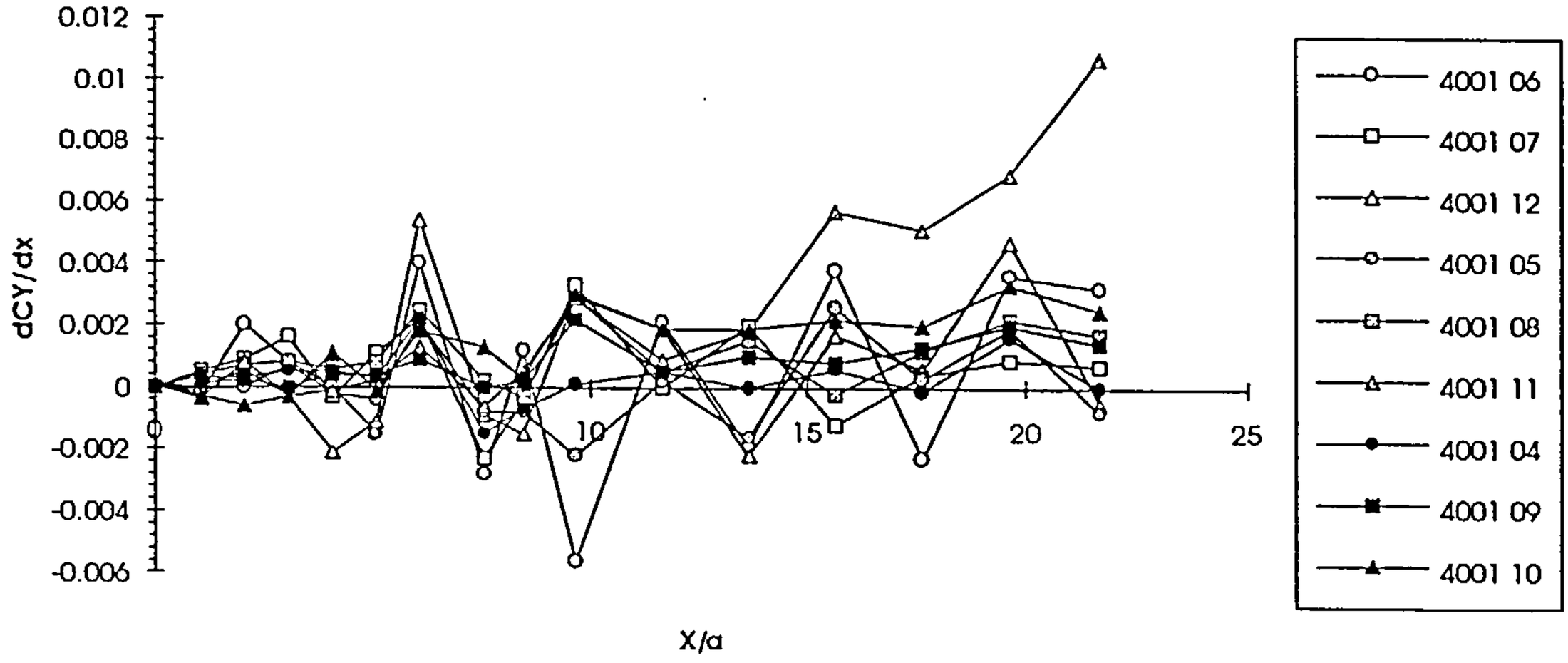

Figure 7.4.3.8

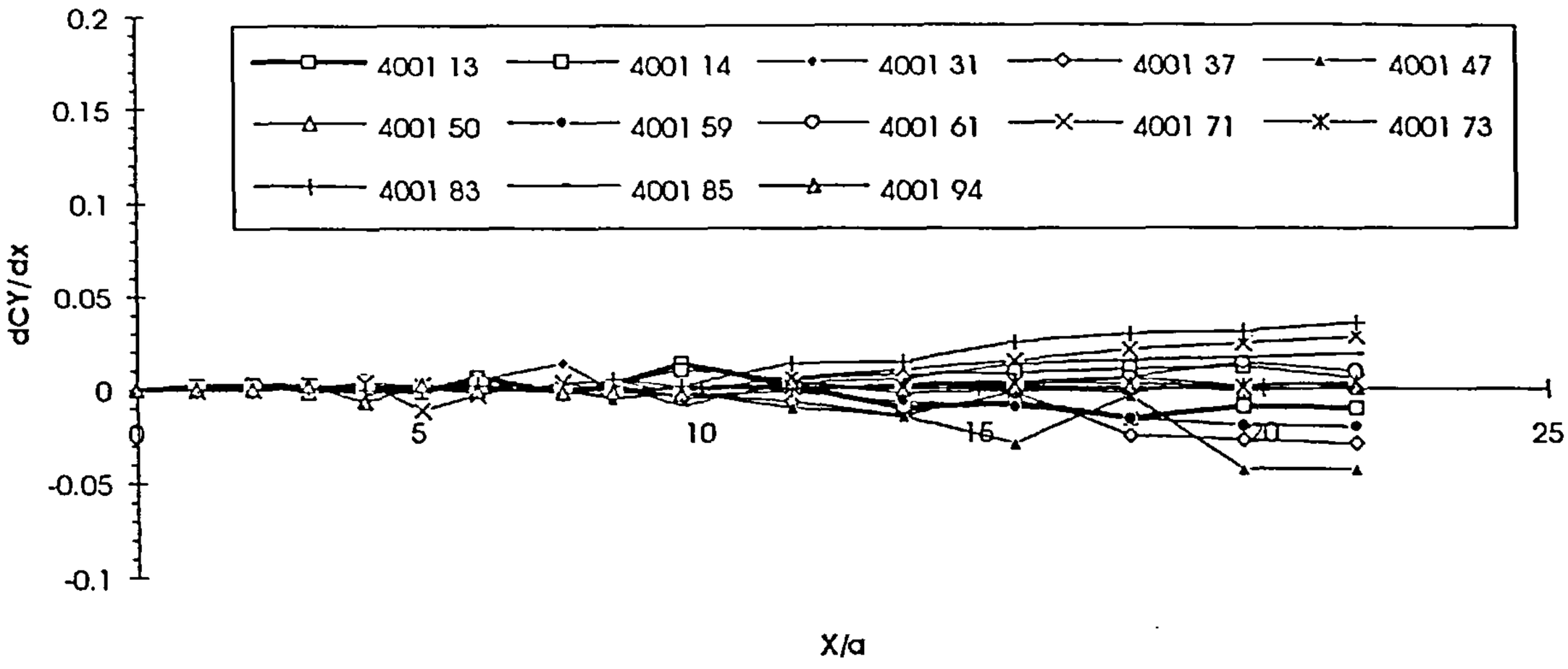

Figure 7.4.3.9

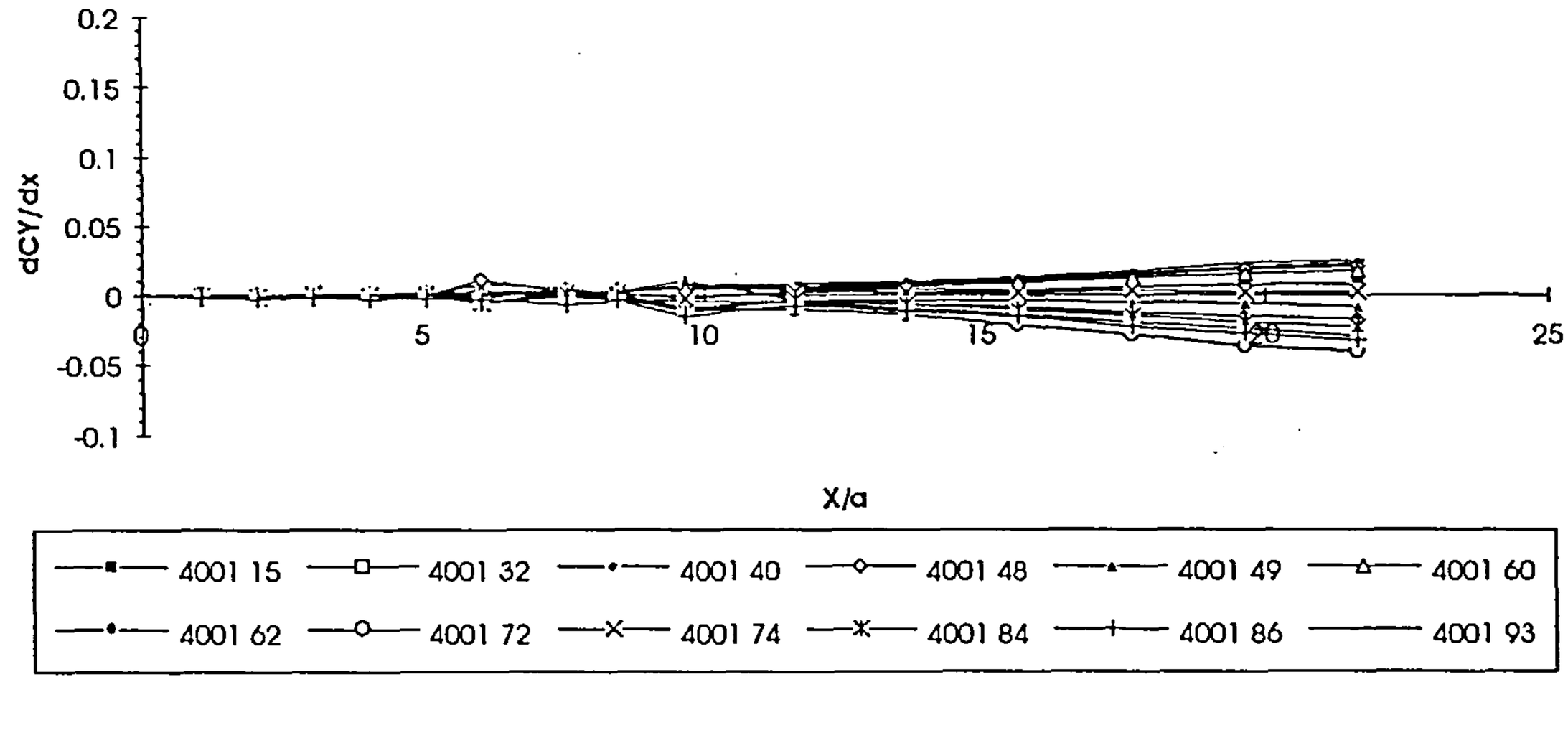

Figure 7.4.3.10

ONERA Load distribution on a tangent-ogive cylinder body at alpha=20

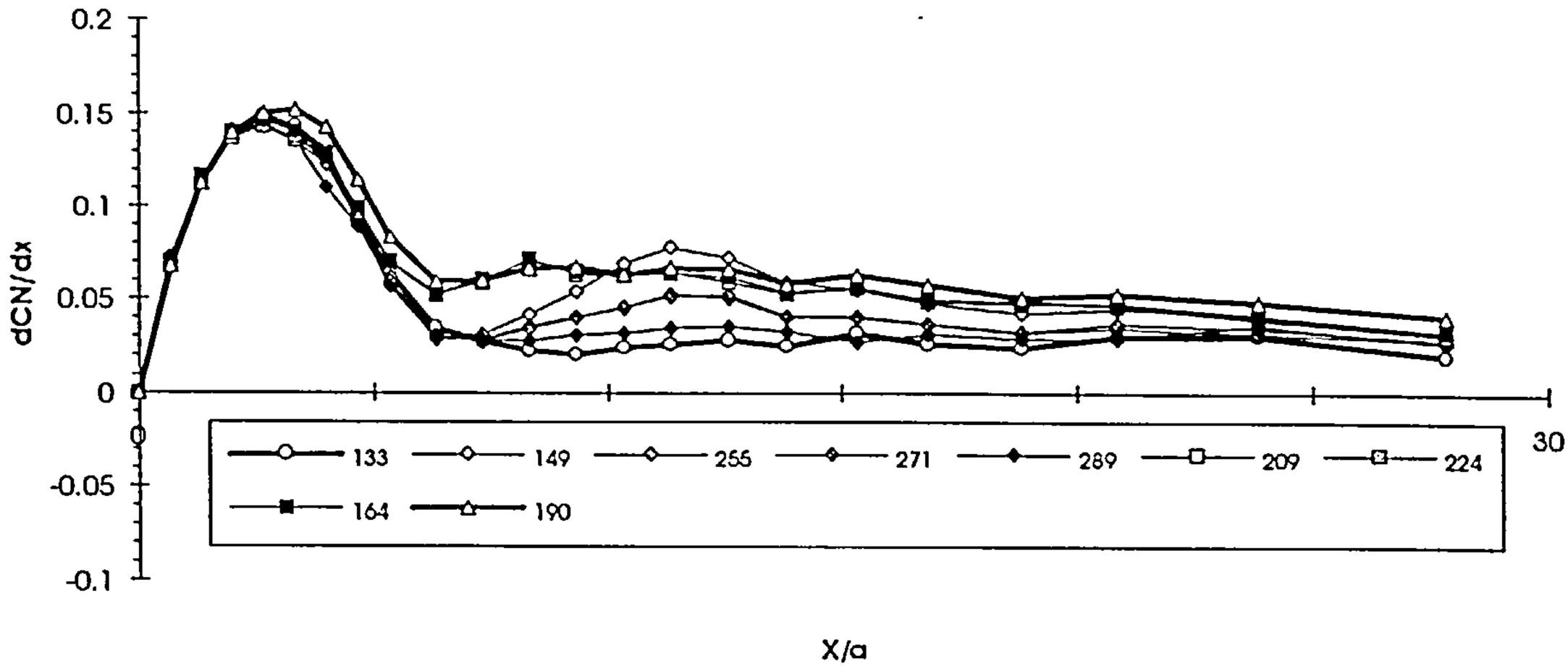

Figure 7.4.3.11

ONERA Load distribution on a tangent-ogive cylinder body at alpha=20

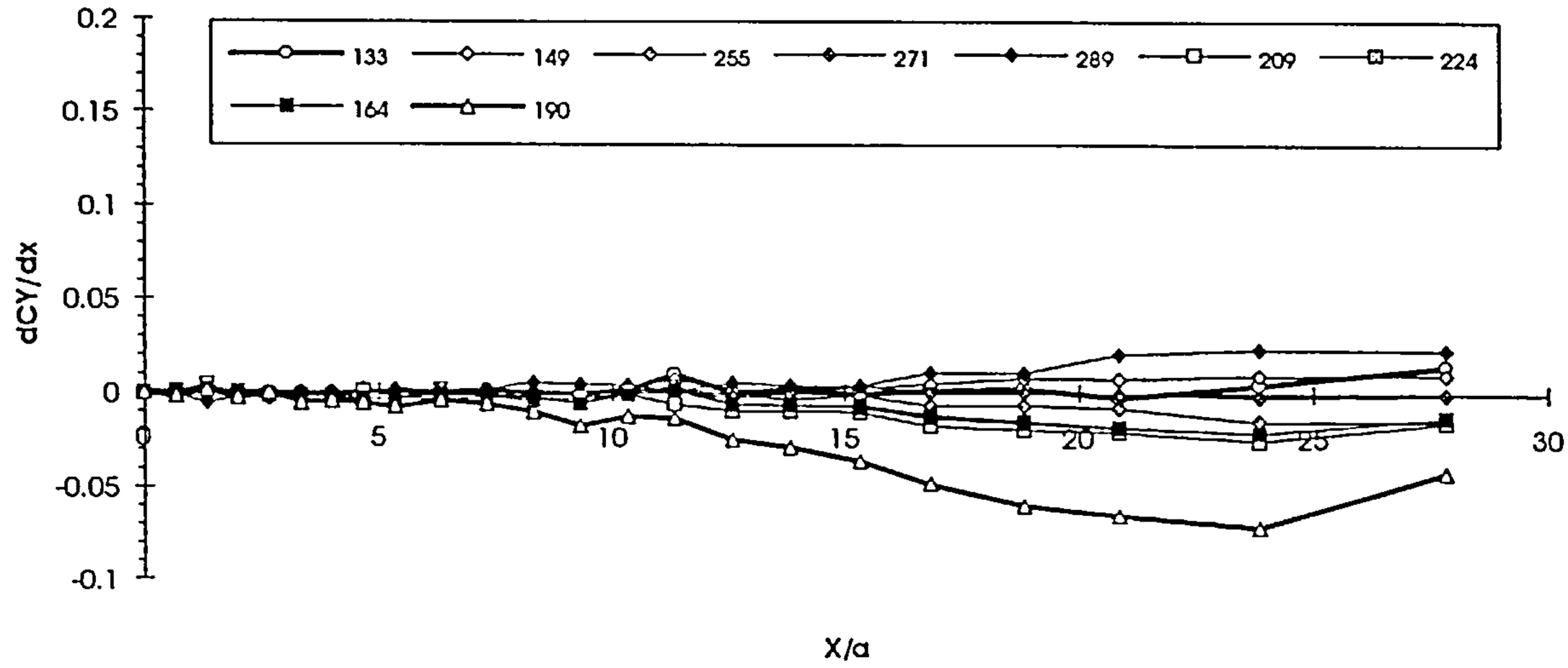

Figure 7.4.3.12

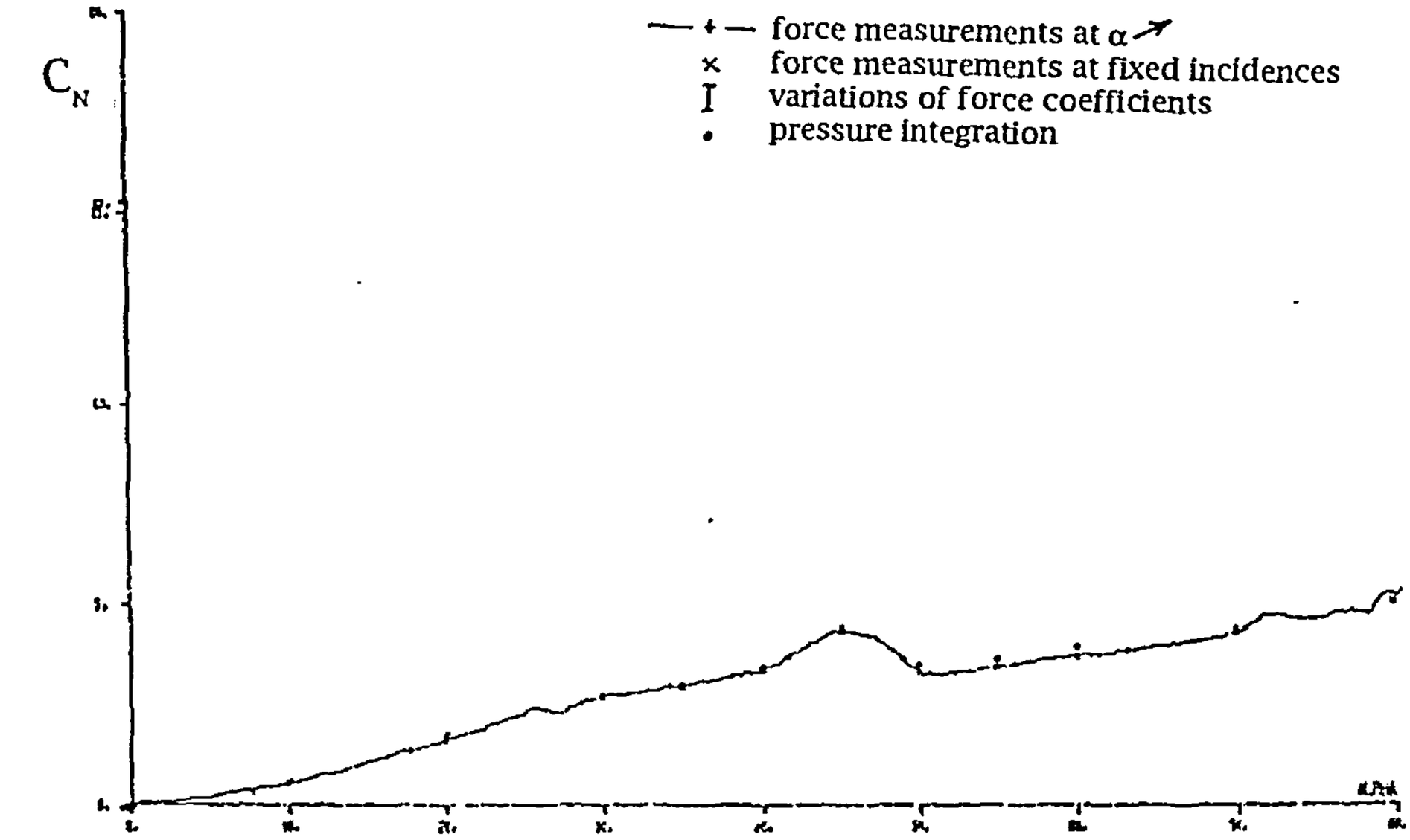

Figure 7.4.3.13
(After Champigny [31])

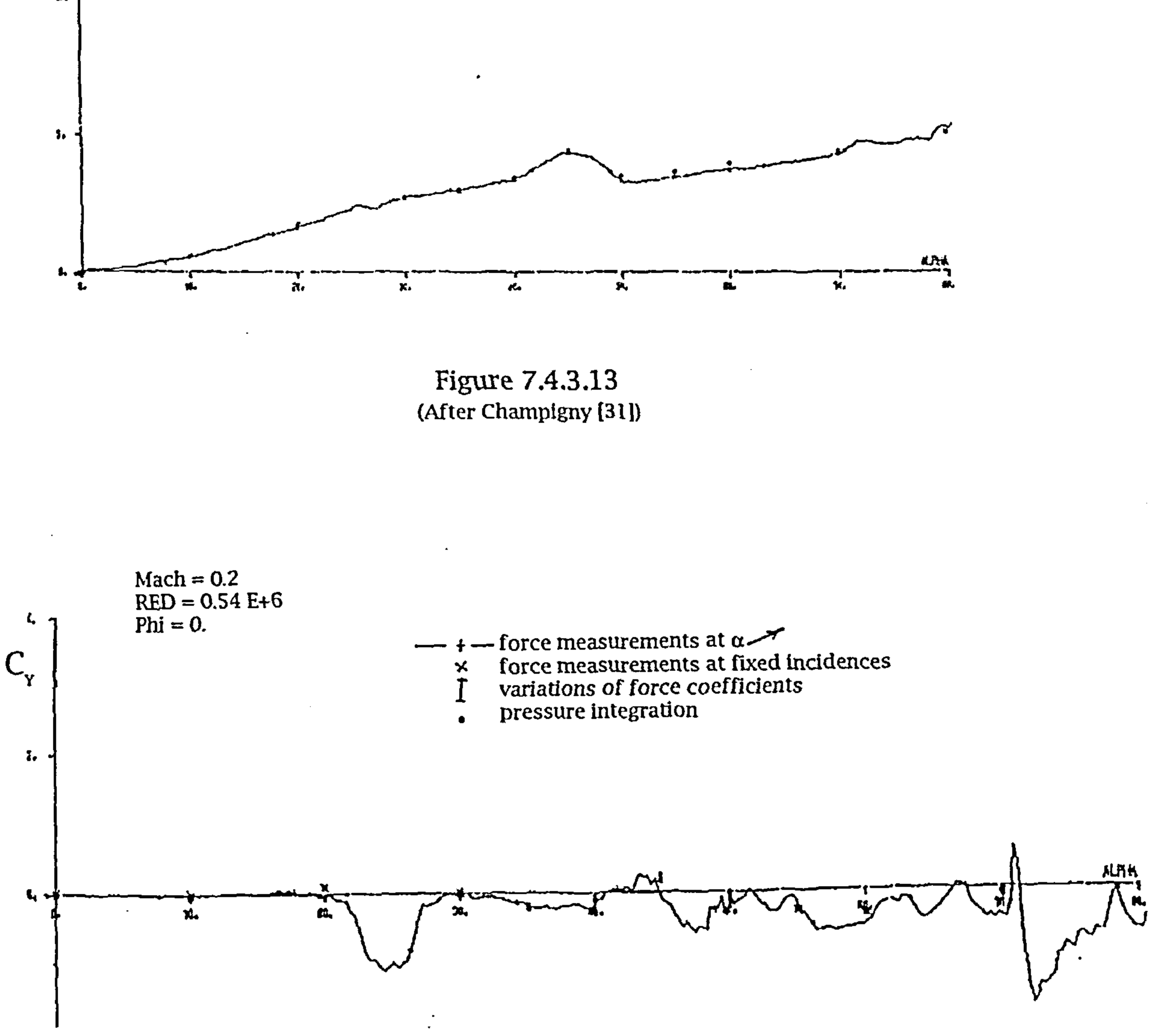

Figure 7.4.3.14
(After Champigny [31])

+ Mach = 0.200 RED = 0.54 E+6 Phi = 0.
□ Mach = 0.200 RED = 0.55 E+6 Phi = -10.
▽ Mach = 0.201 RED = 0.55 E+6 Phi = 10.
• Mach = 0.201 RED = 0.55 E+6 Phi = 165

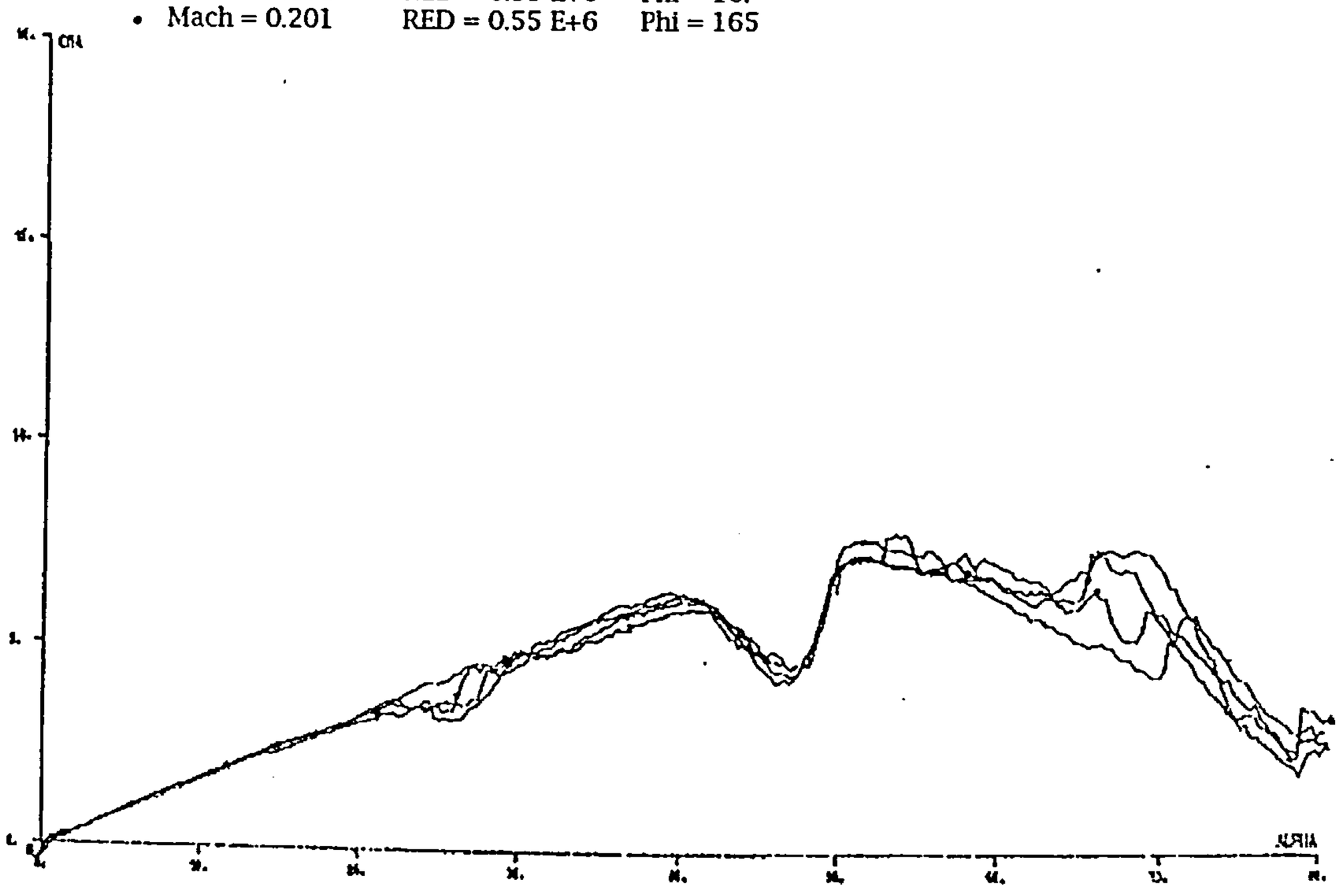

Figure 7.4.3.15
(After Champigny [31])

+ Mach = 0.200 RED = 0.54 E+6 Phi = 0.
□ Mach = 0.200 RED = 0.55 E+6 Phi = -10.
▽ Mach = 0.201 RED = 0.55 E+6 Phi = 10.
• Mach = 0.201 RED = 0.55 E+6 Phi = 165

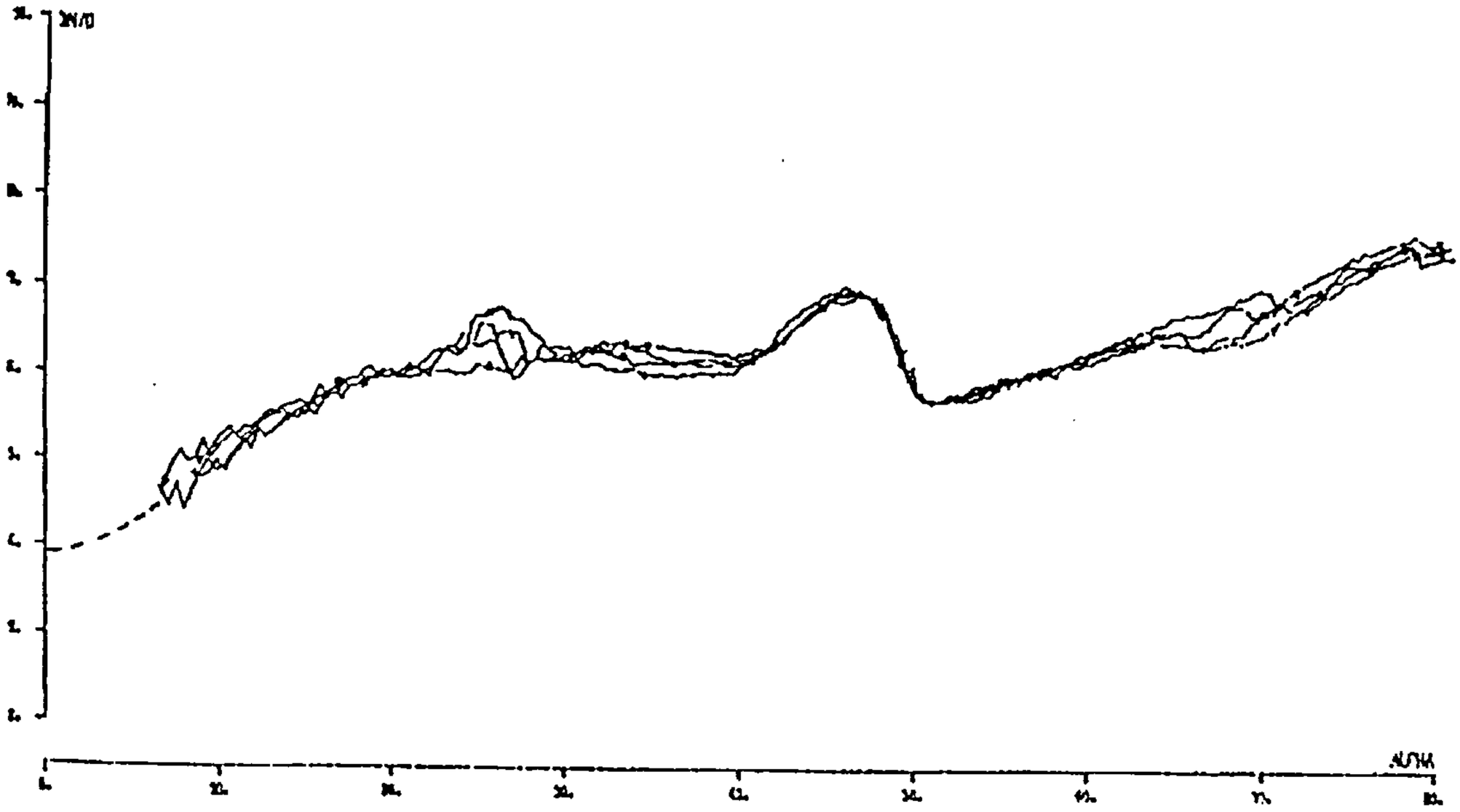

Figure 7.4.3.16
(After Champigny [31])

Comparison of load distribution on an exact tangent-ogive with that on a polynomial approximation

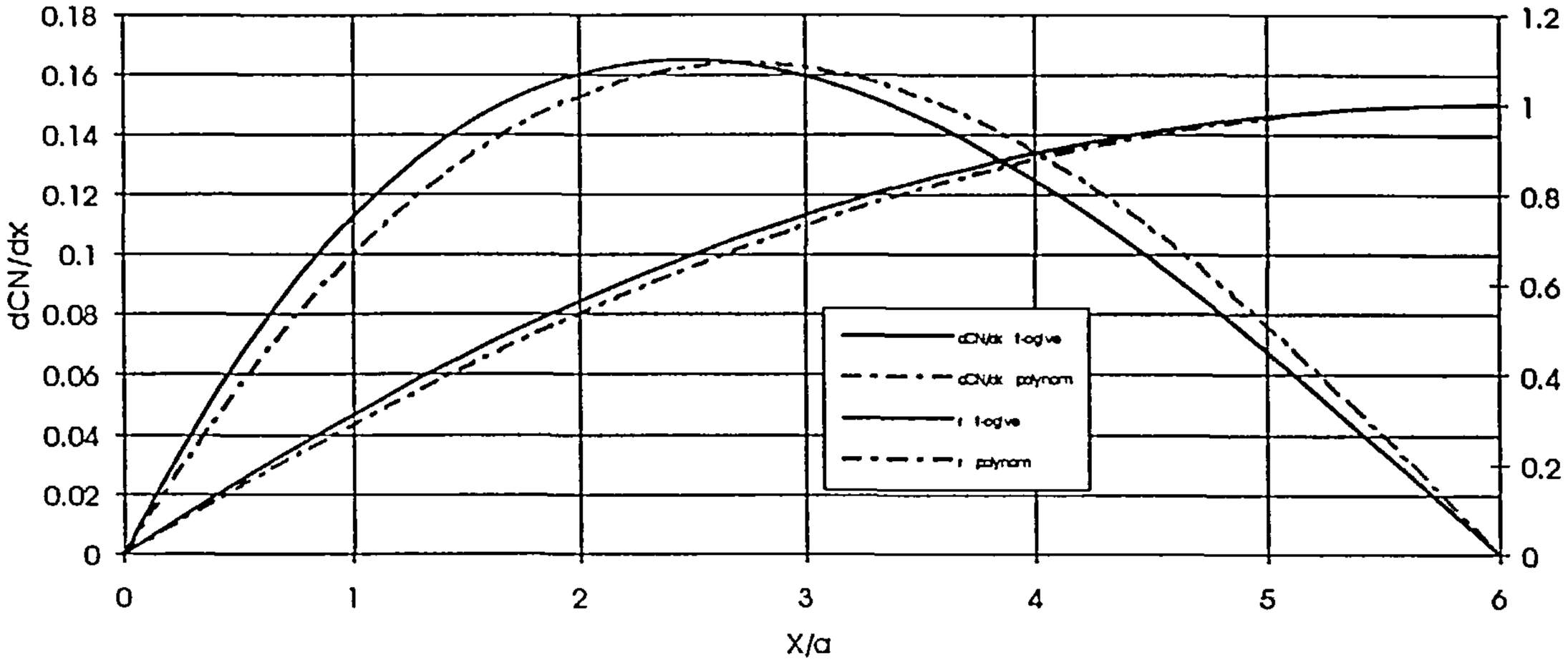

Figure 7.4.3.17

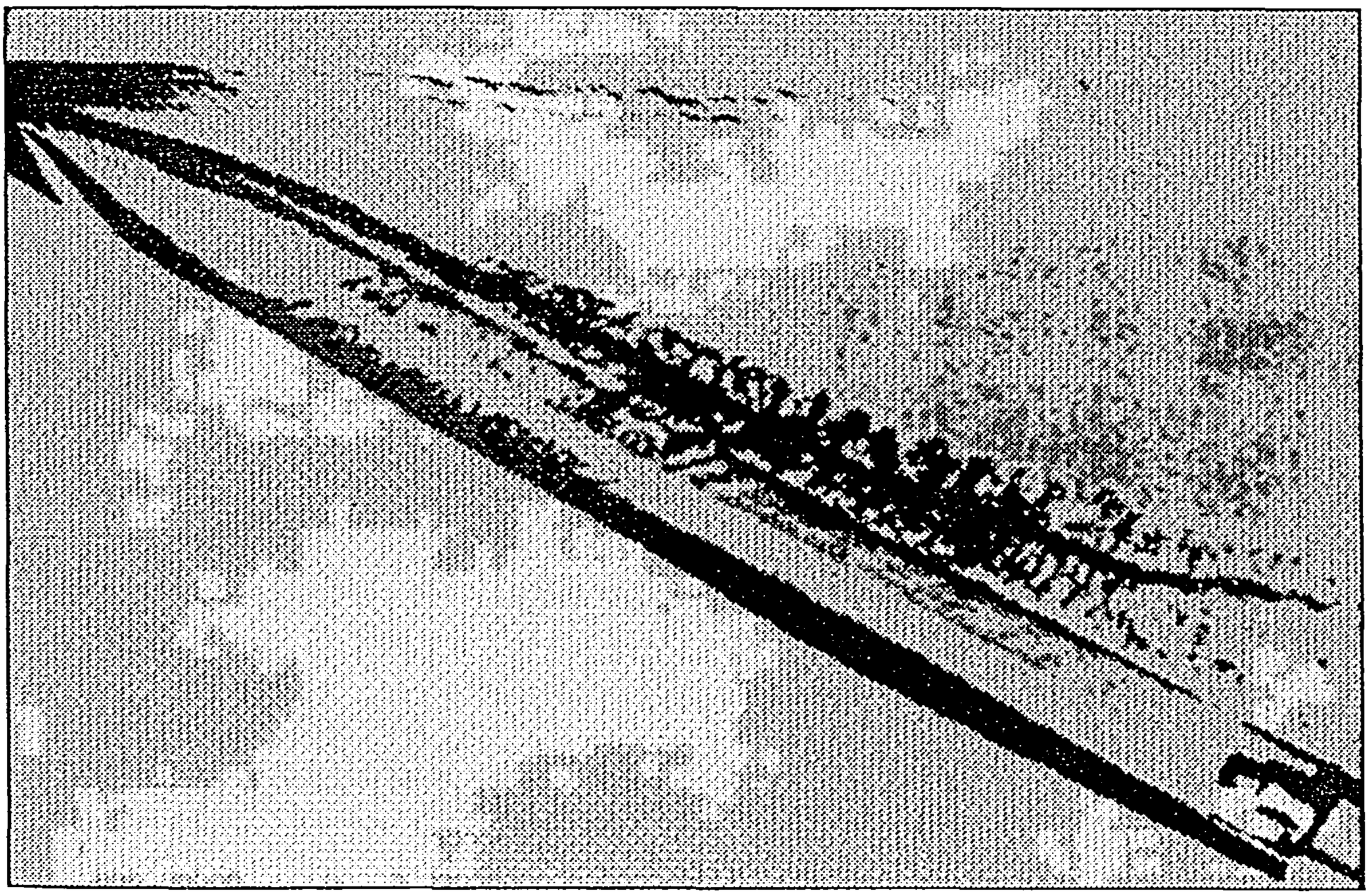

Figure 7.4.3.18
(After Hartmann [30])

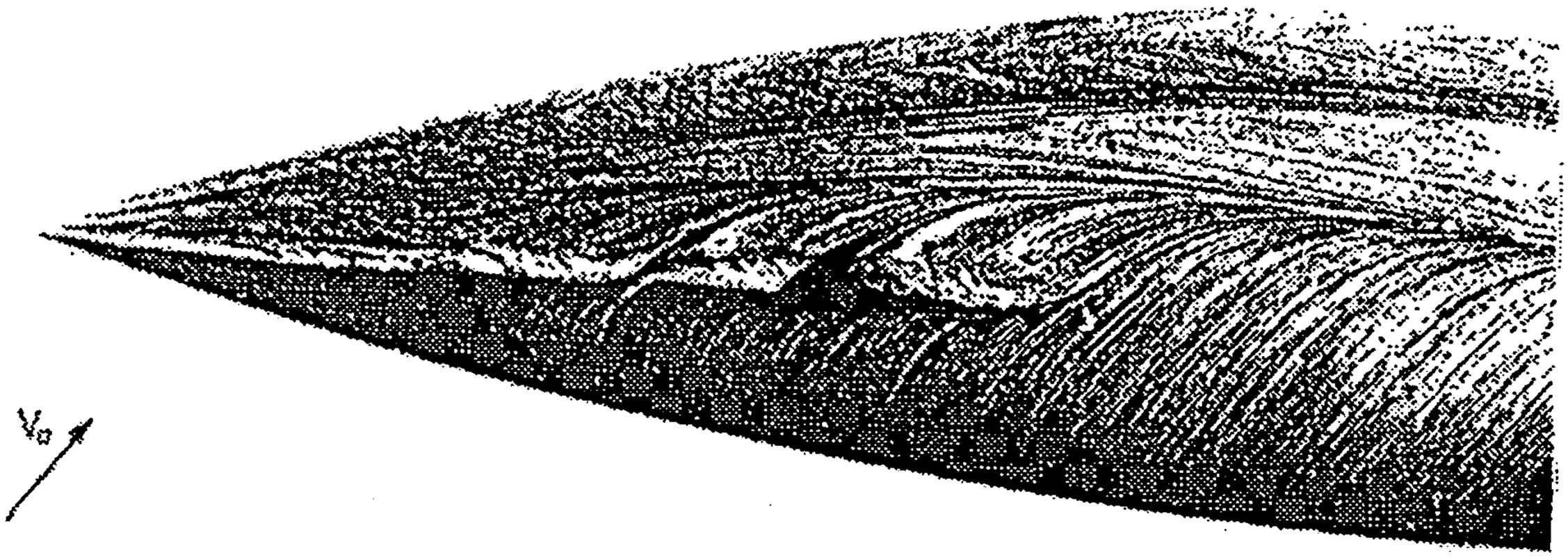

Figure 7.4.3.19
(After Champigny [31])

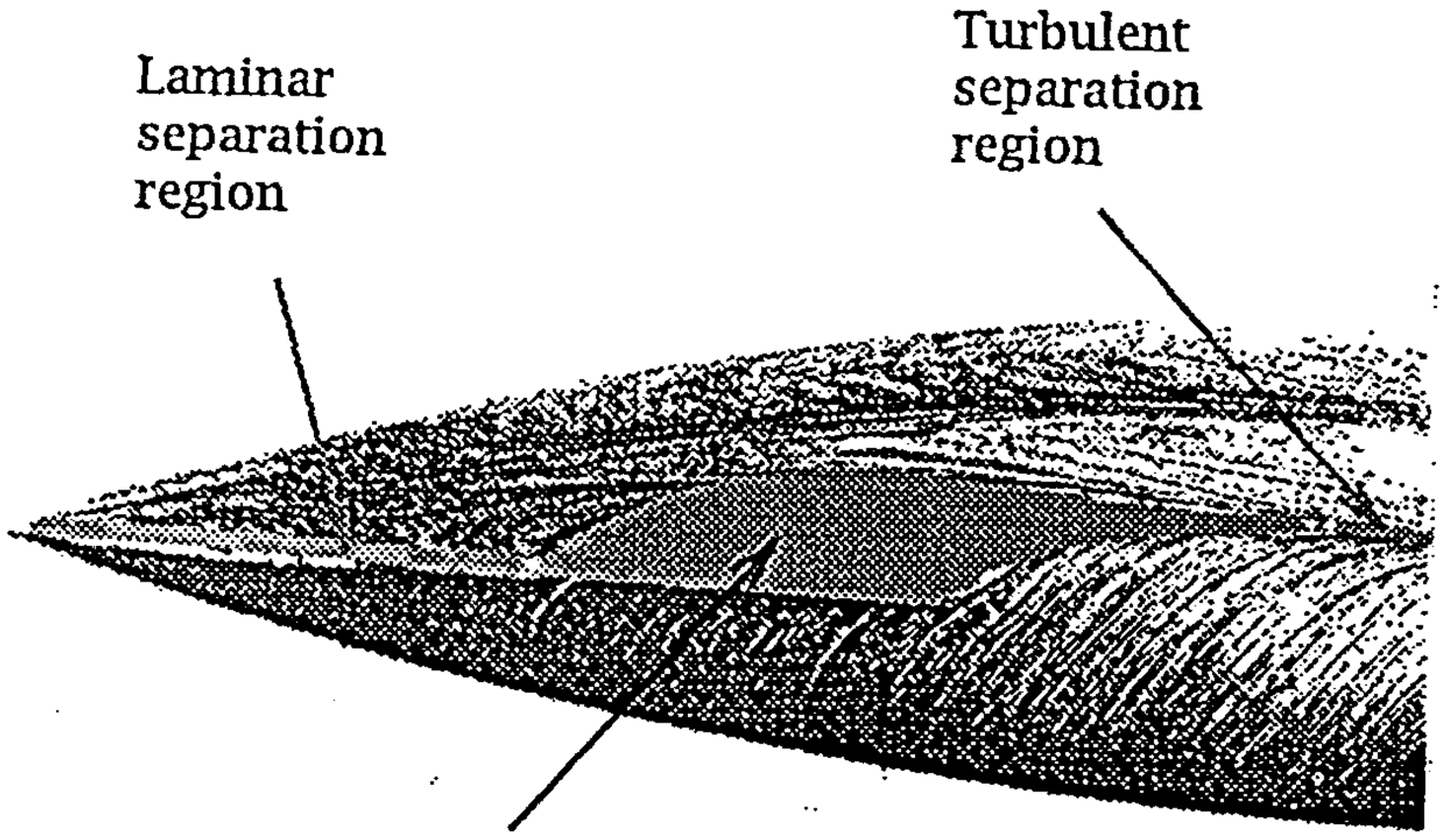

Figure 7.4.4.1

α=35°

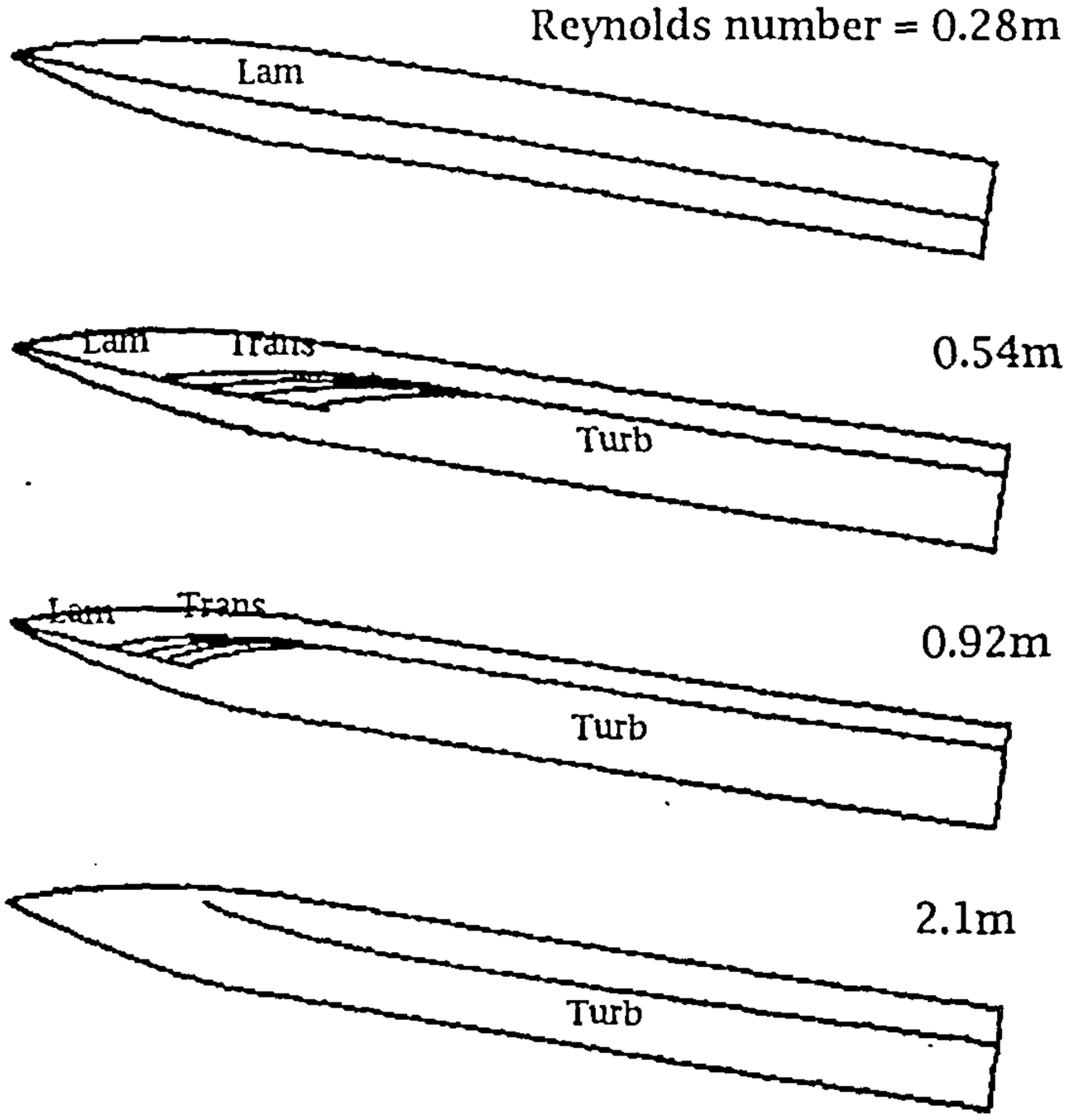

Figure 7.4.4.2

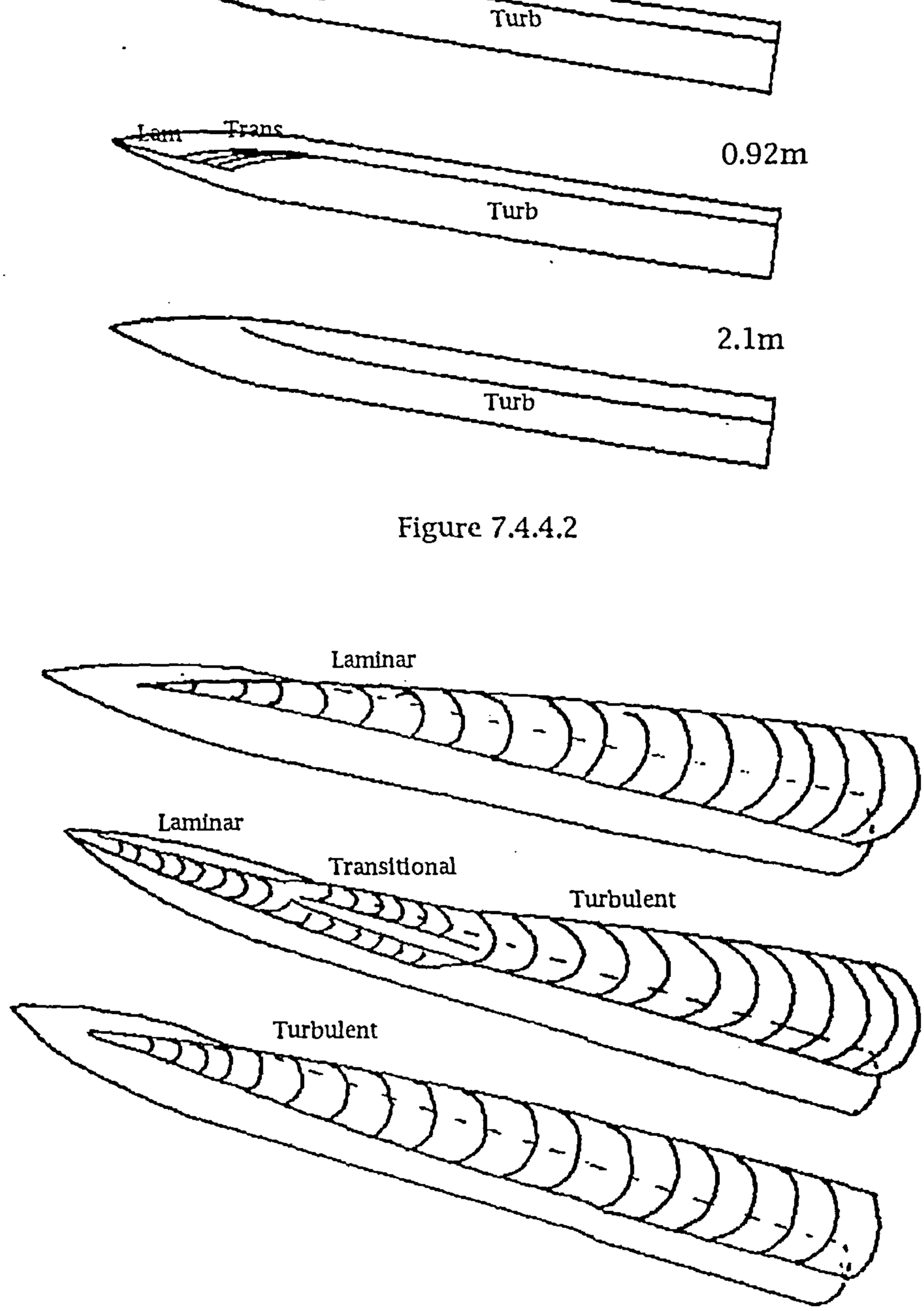

Separation states
Figure 7.4.4.3

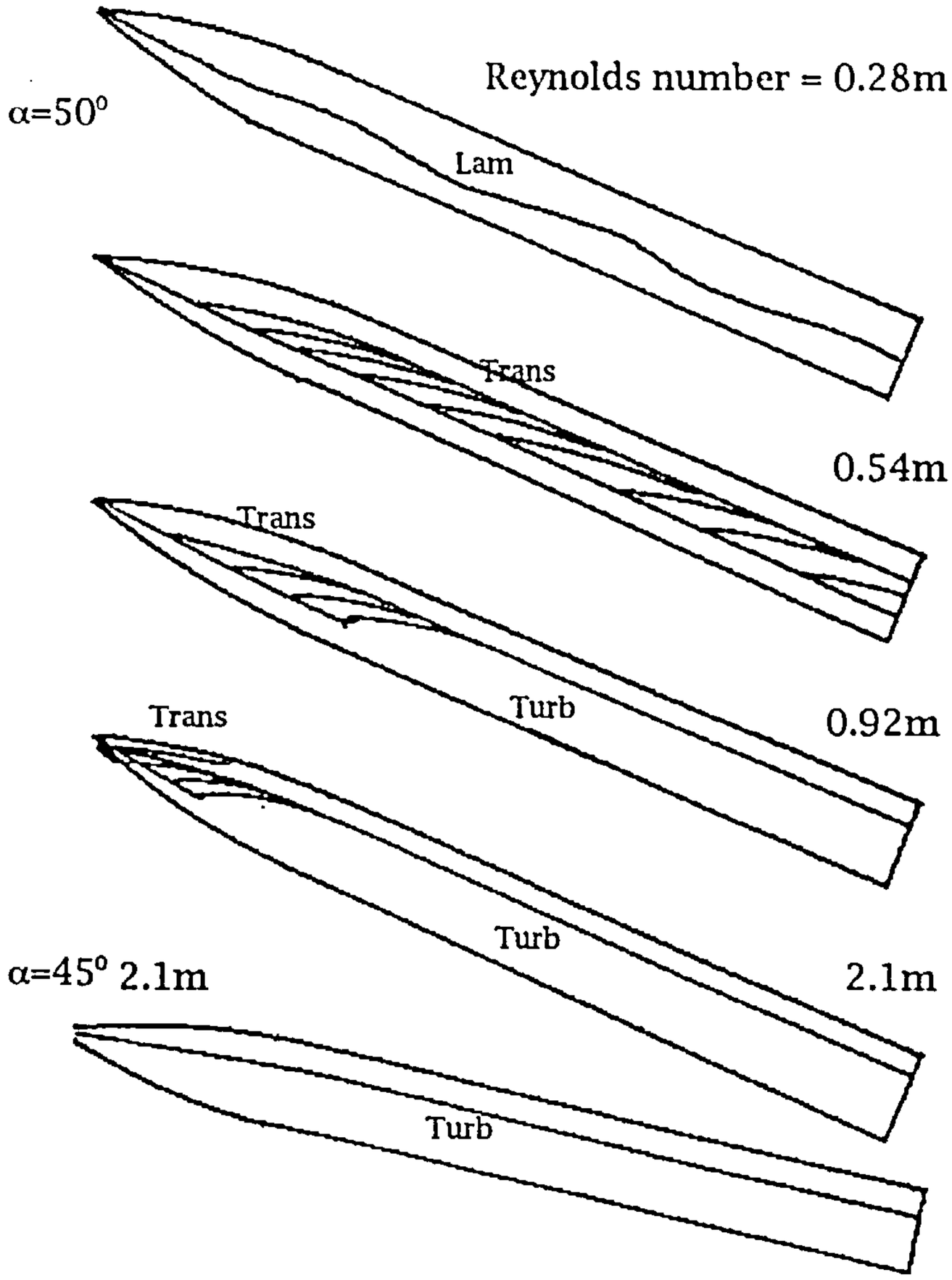

Figure 7.4.4.4

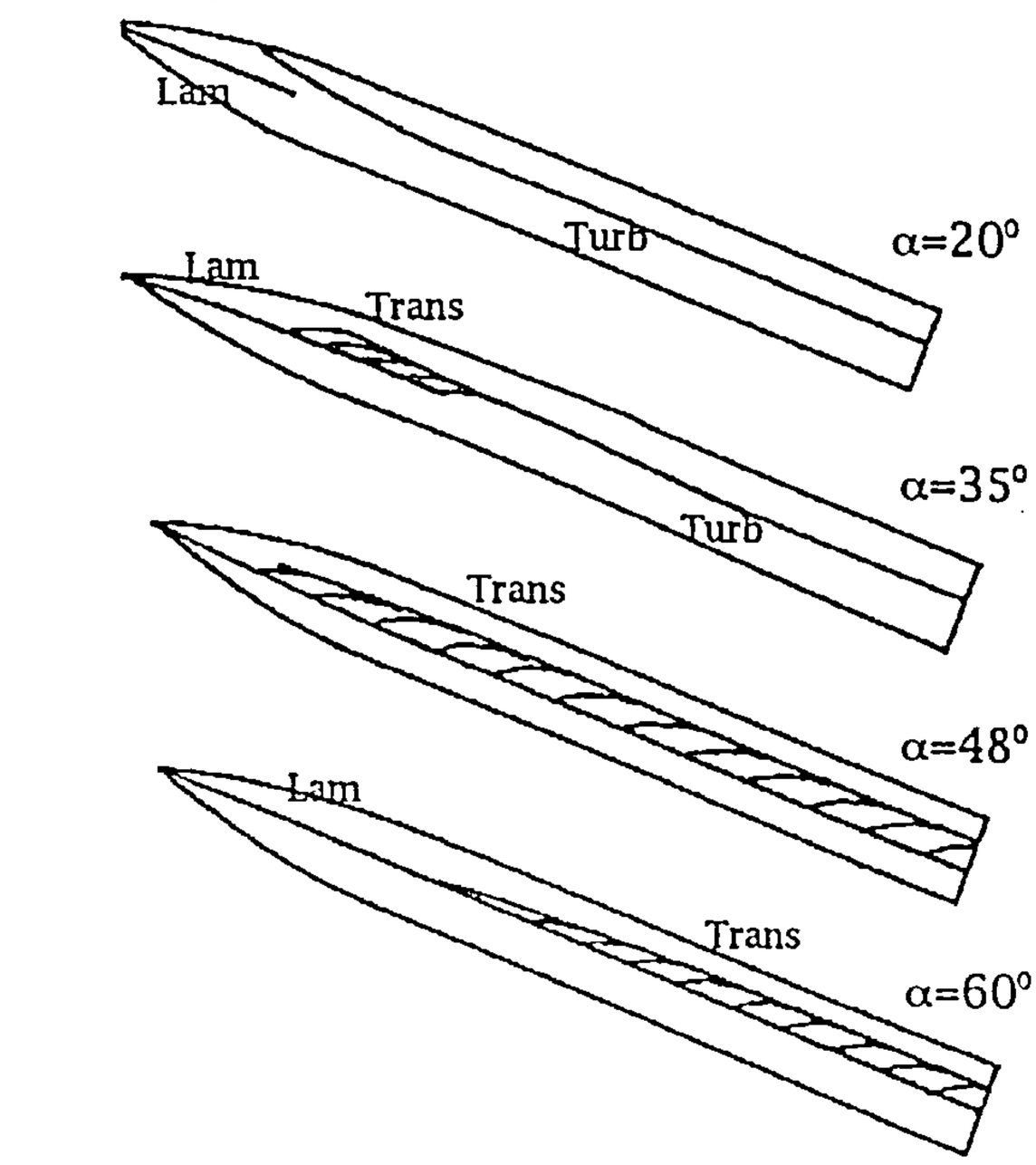

Figure 7.4.4.5

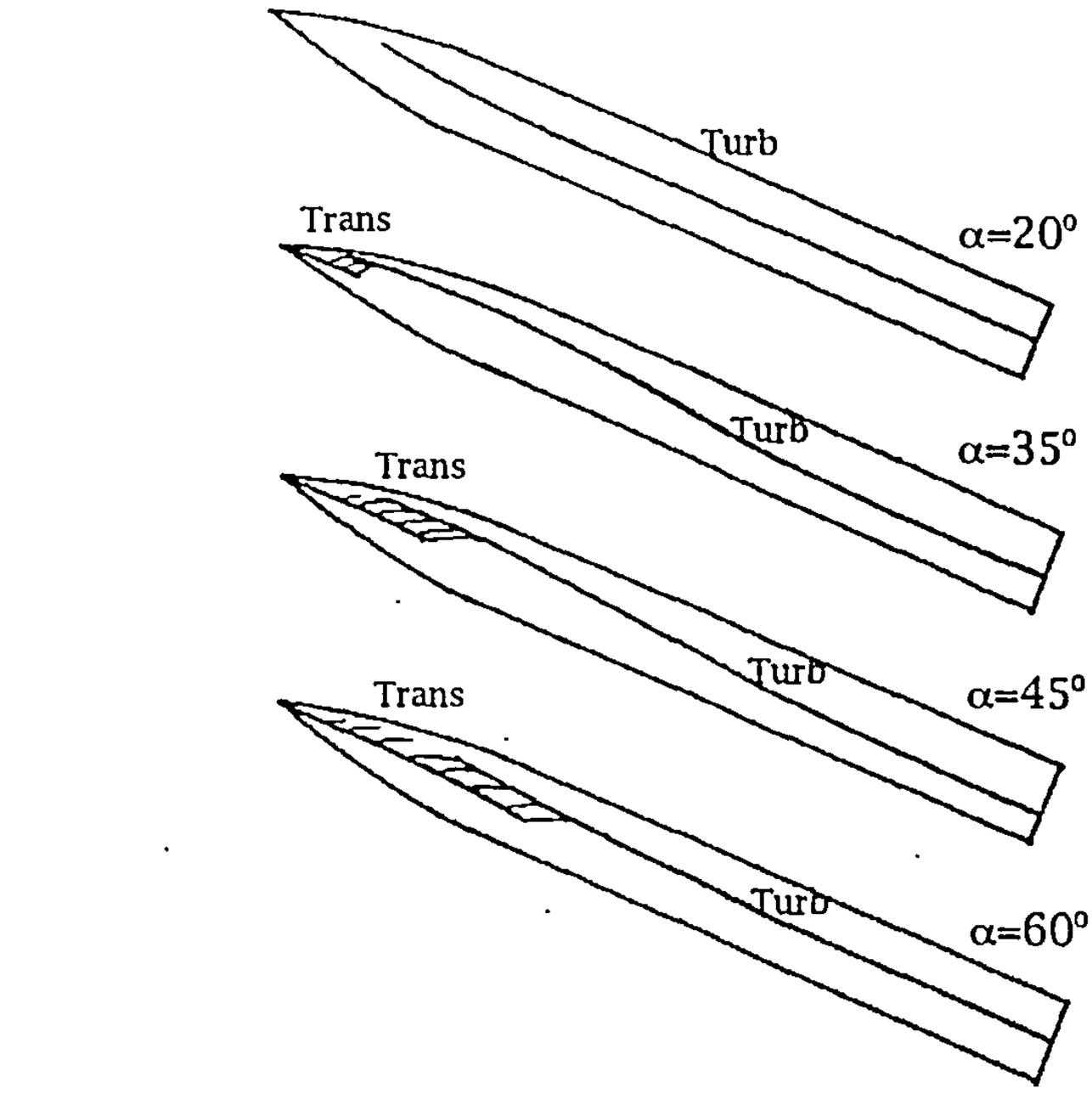

Figure 7.4.4.6

Pressure distribution about a body of revolution at 20 degrees of incidence and a Reynolds number of 0.53 million

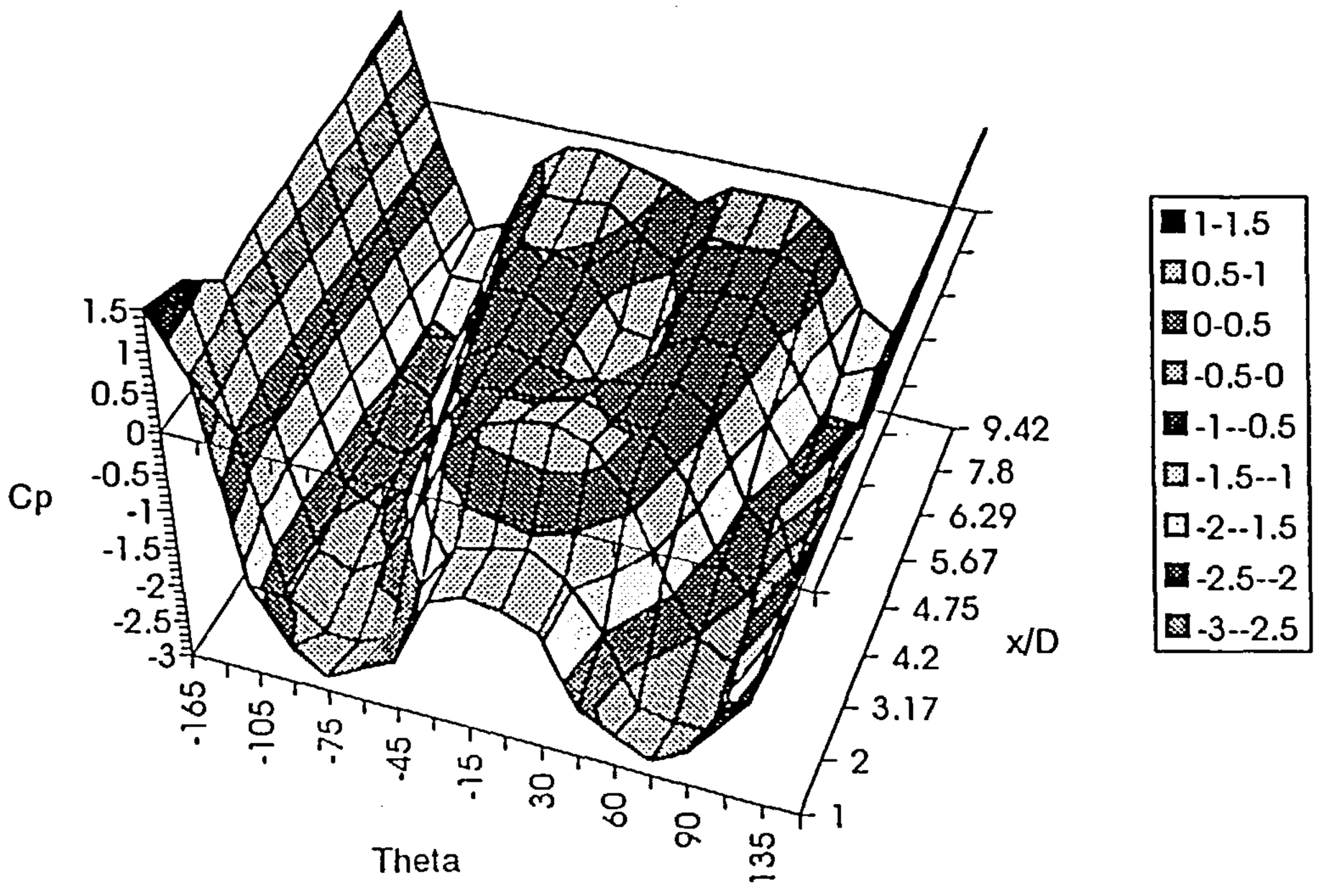

Figure 7.4.5.1

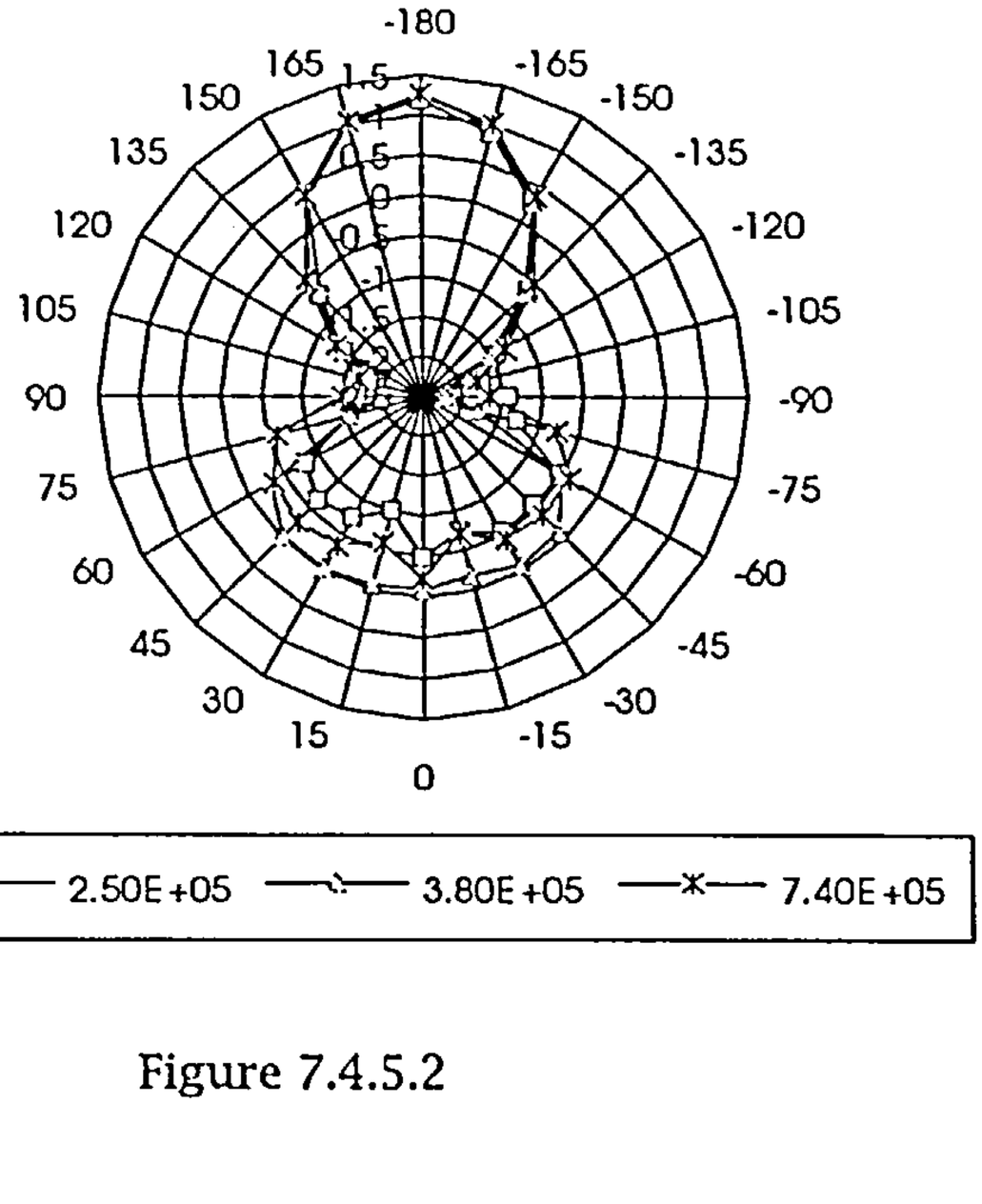

Figure 7.4.5.2

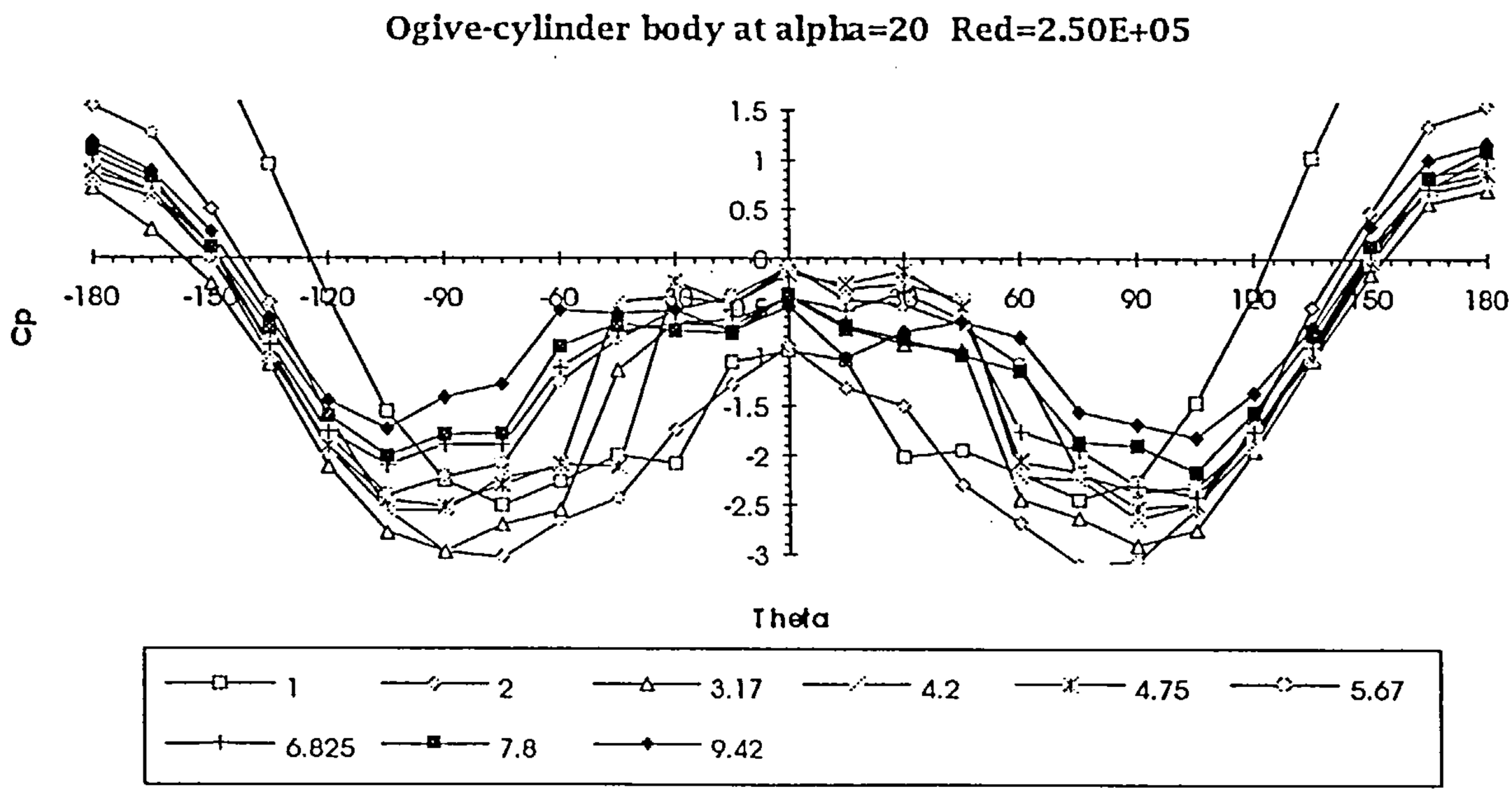

Figure 7.4.5.3

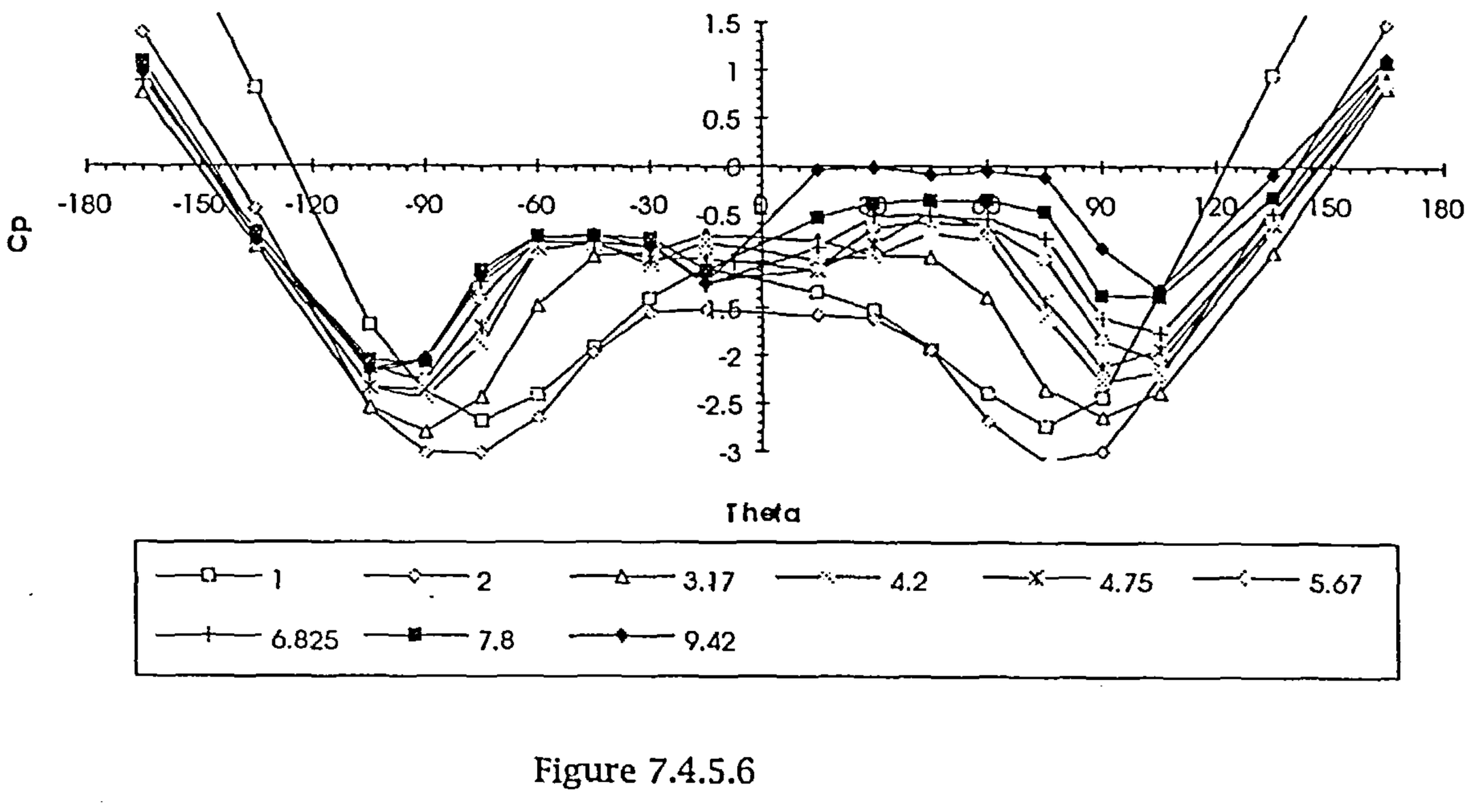

Figure 7.4.5.6

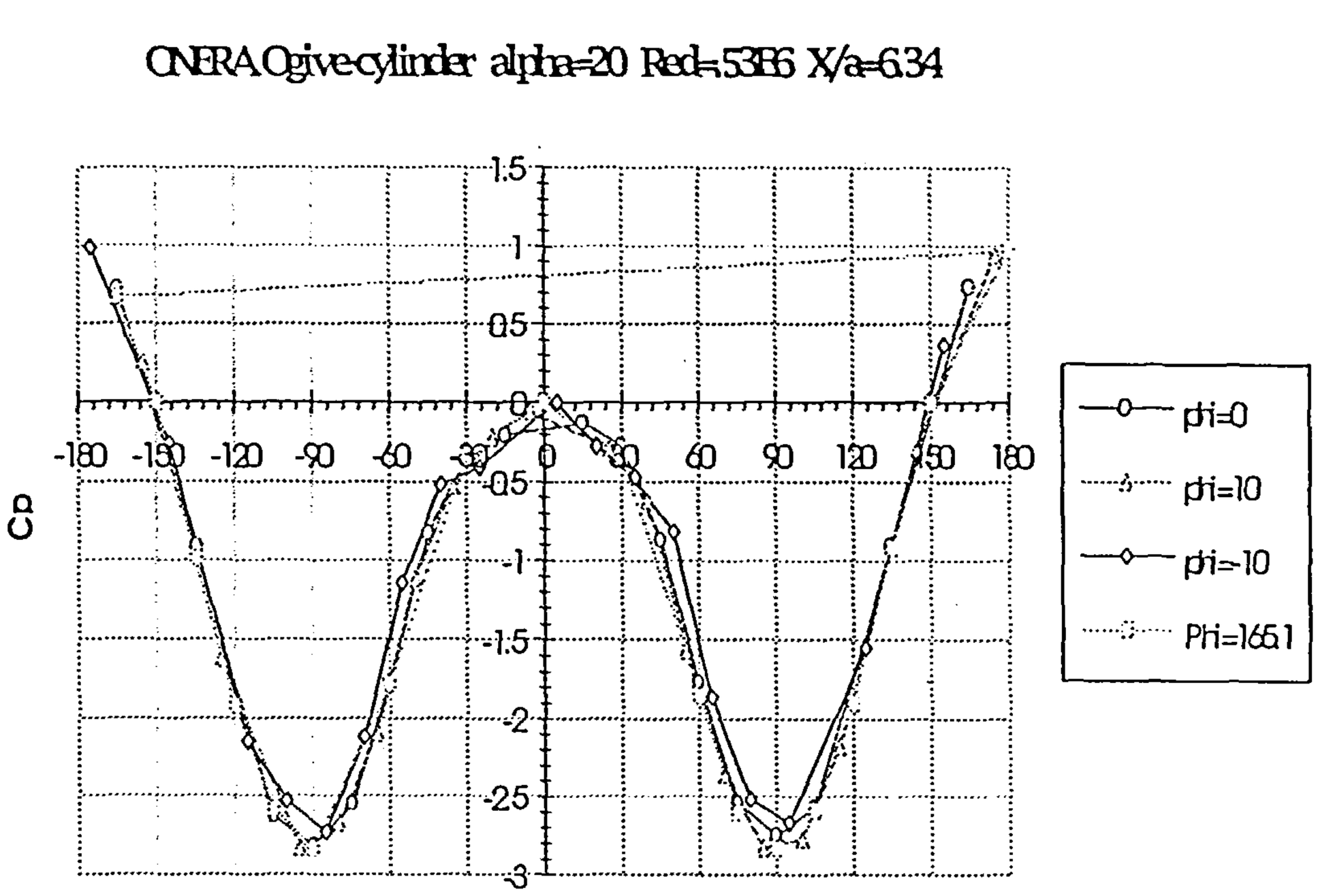

Figure 7.4.5.7

ONERA Ogive-cylinder alpha=20 Red=.53E6 X/a=11.3

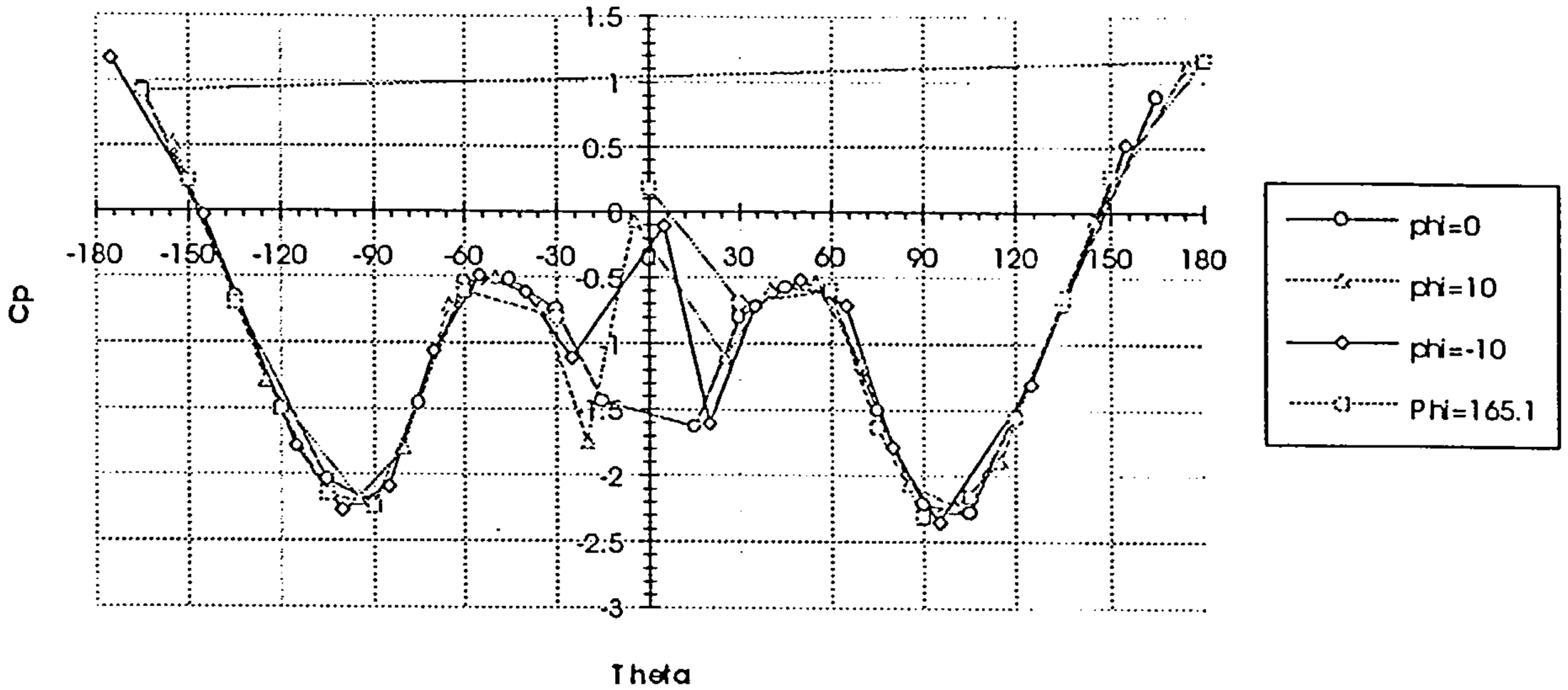

Figure 7.4.5.8

ONERA Ogive-cylinder alpha=20 Red=.53E6 X/a=18.84

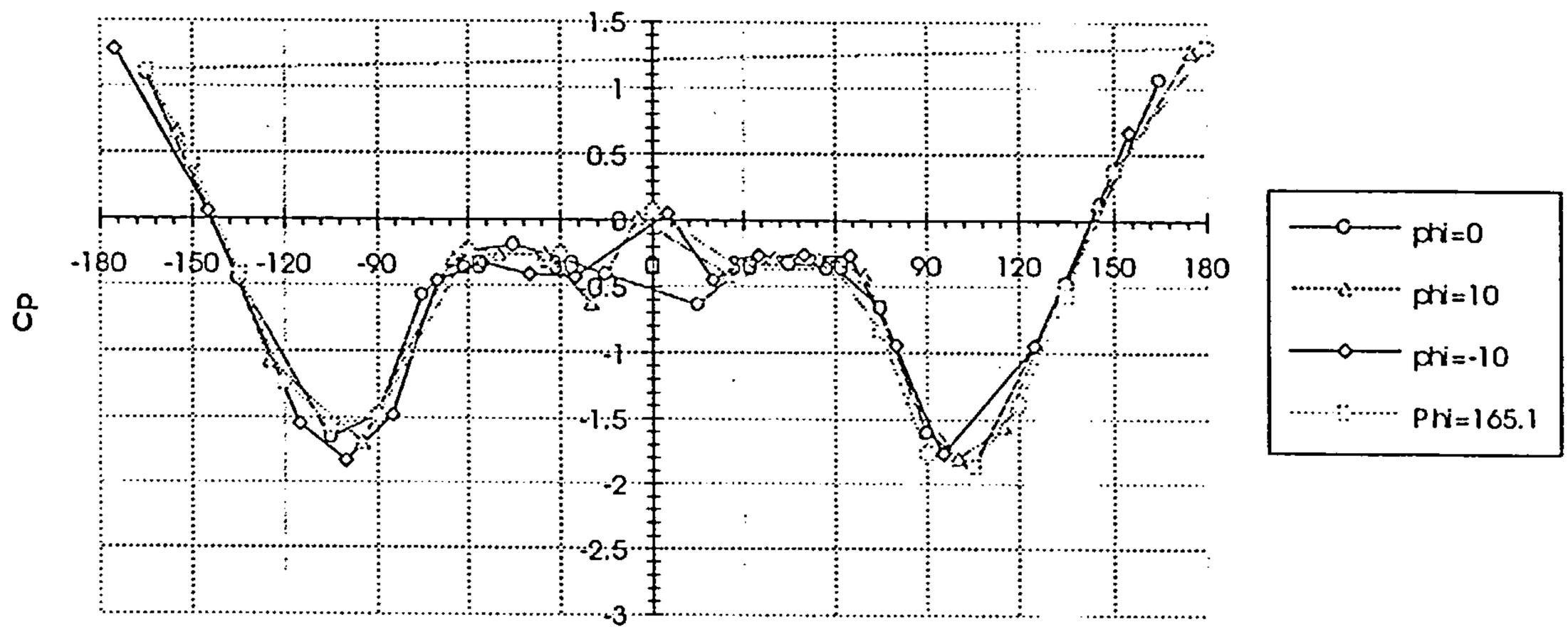

Figure 7.4.5.9

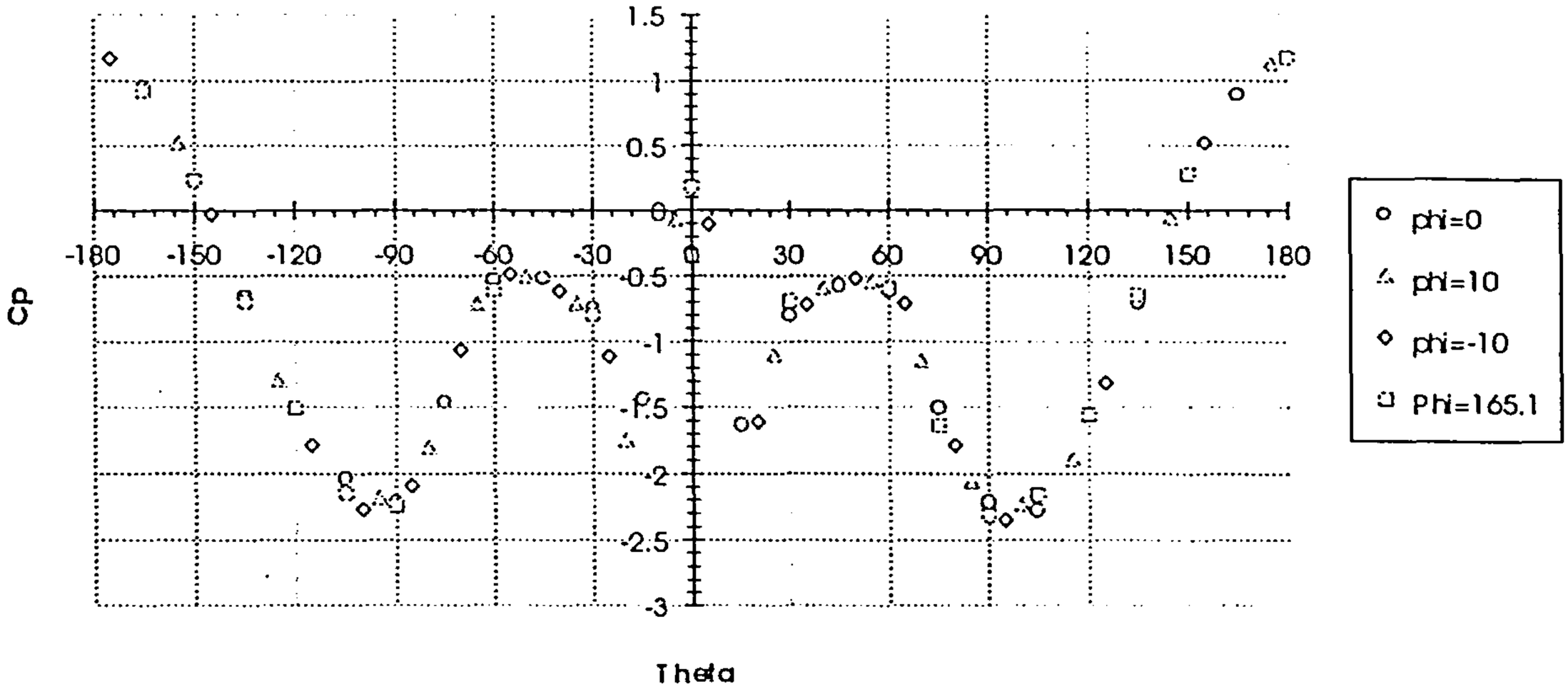

Figure 7.4.5.10

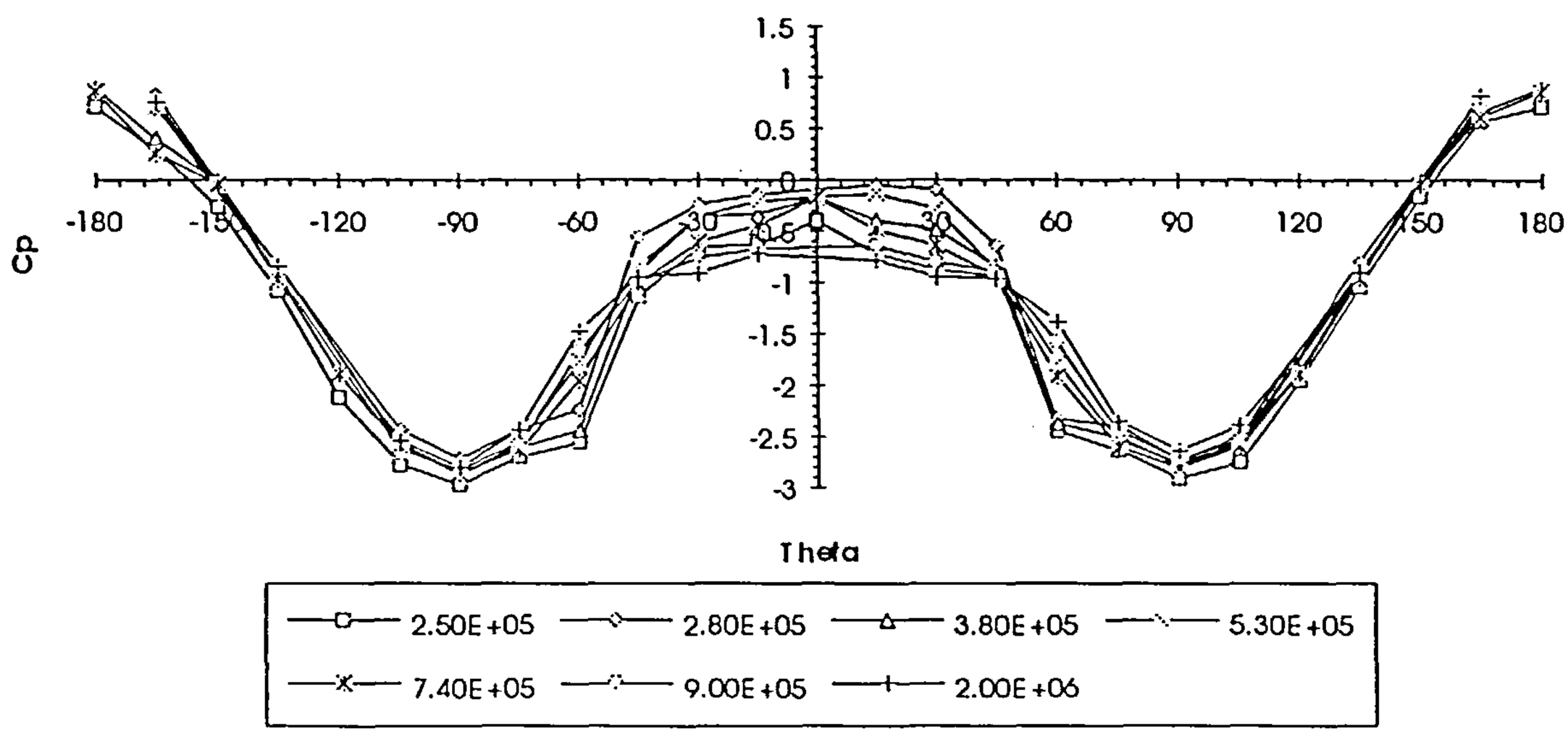

Figure 7.4.5.11

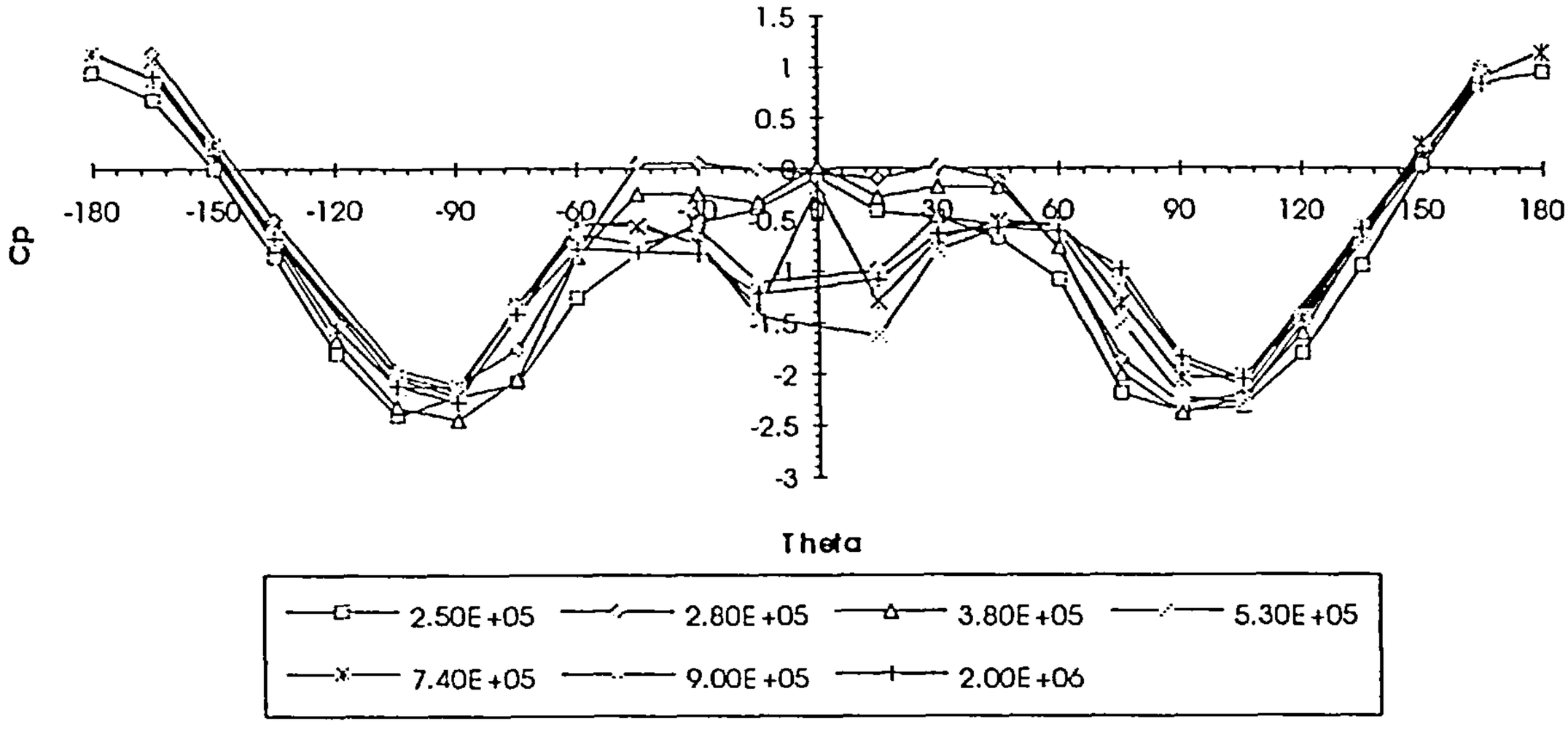

Figure 7.4.5.12

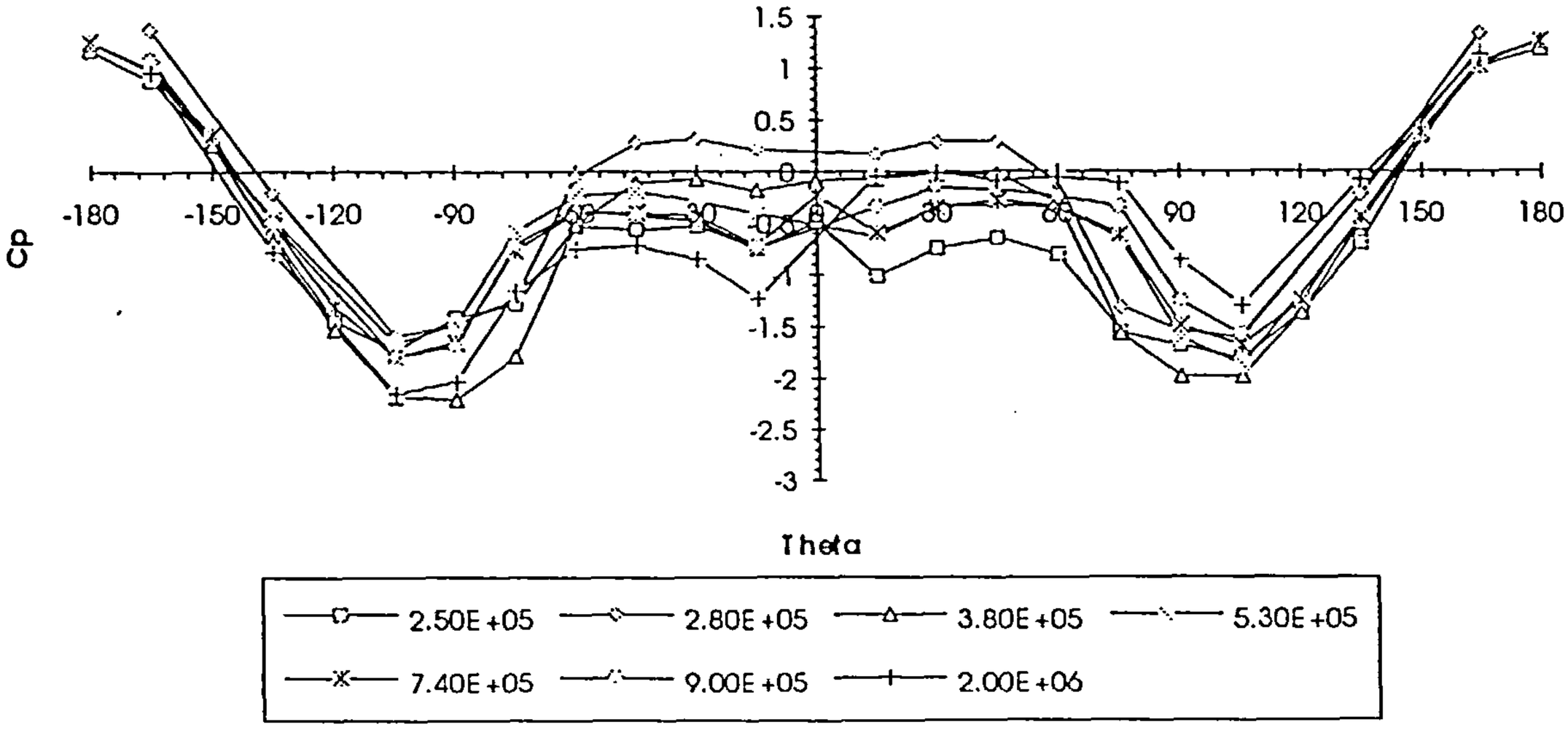

Figure 7.4.5.13

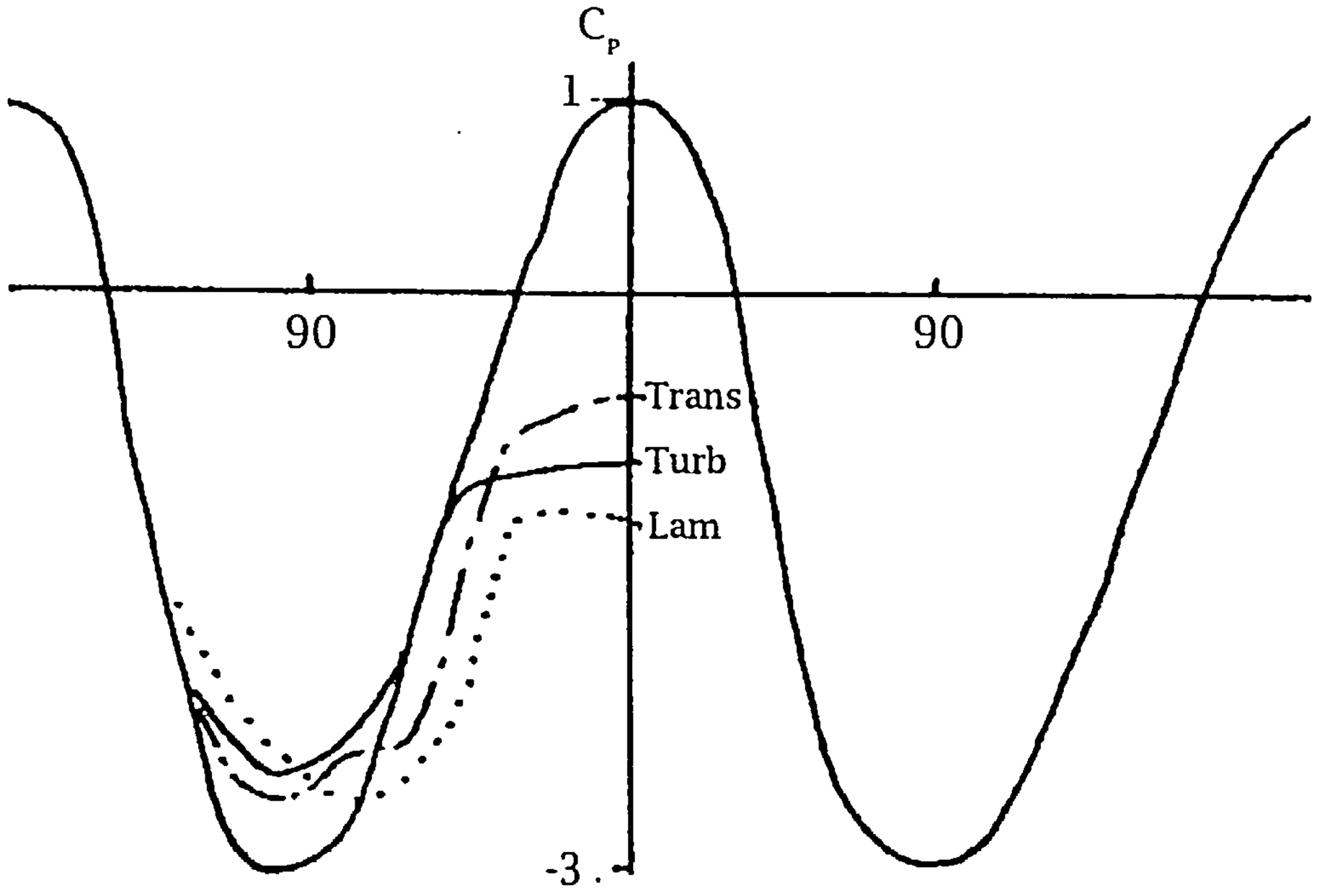

Figure 7.4.5.14

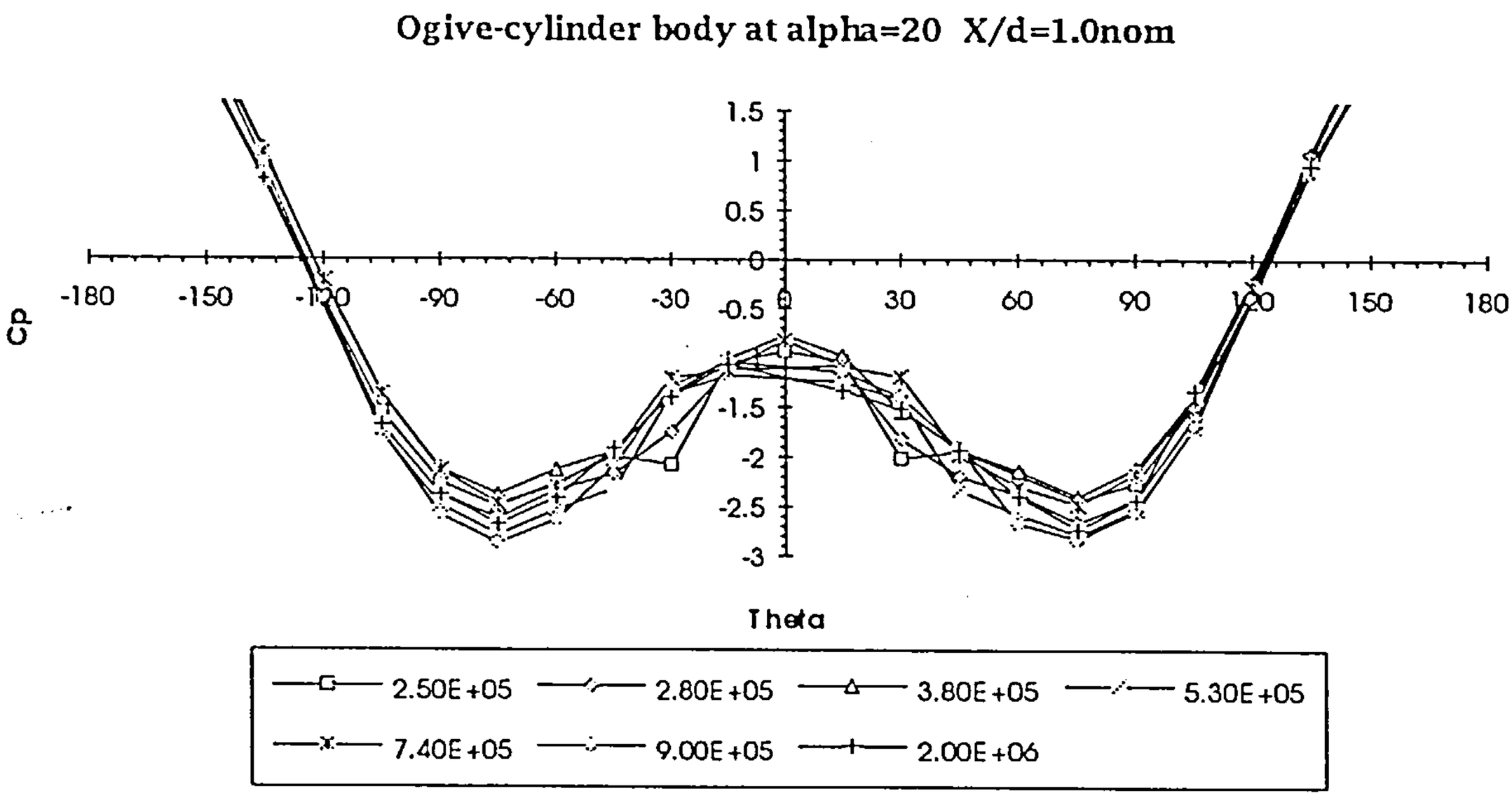

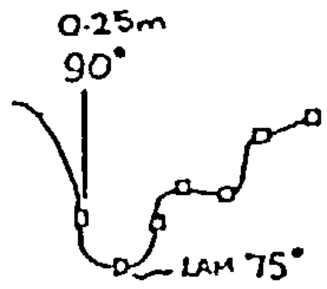

Figure 7.4.6.1

Ogive-cylinder body at alpha=20 X/d=2.0nom

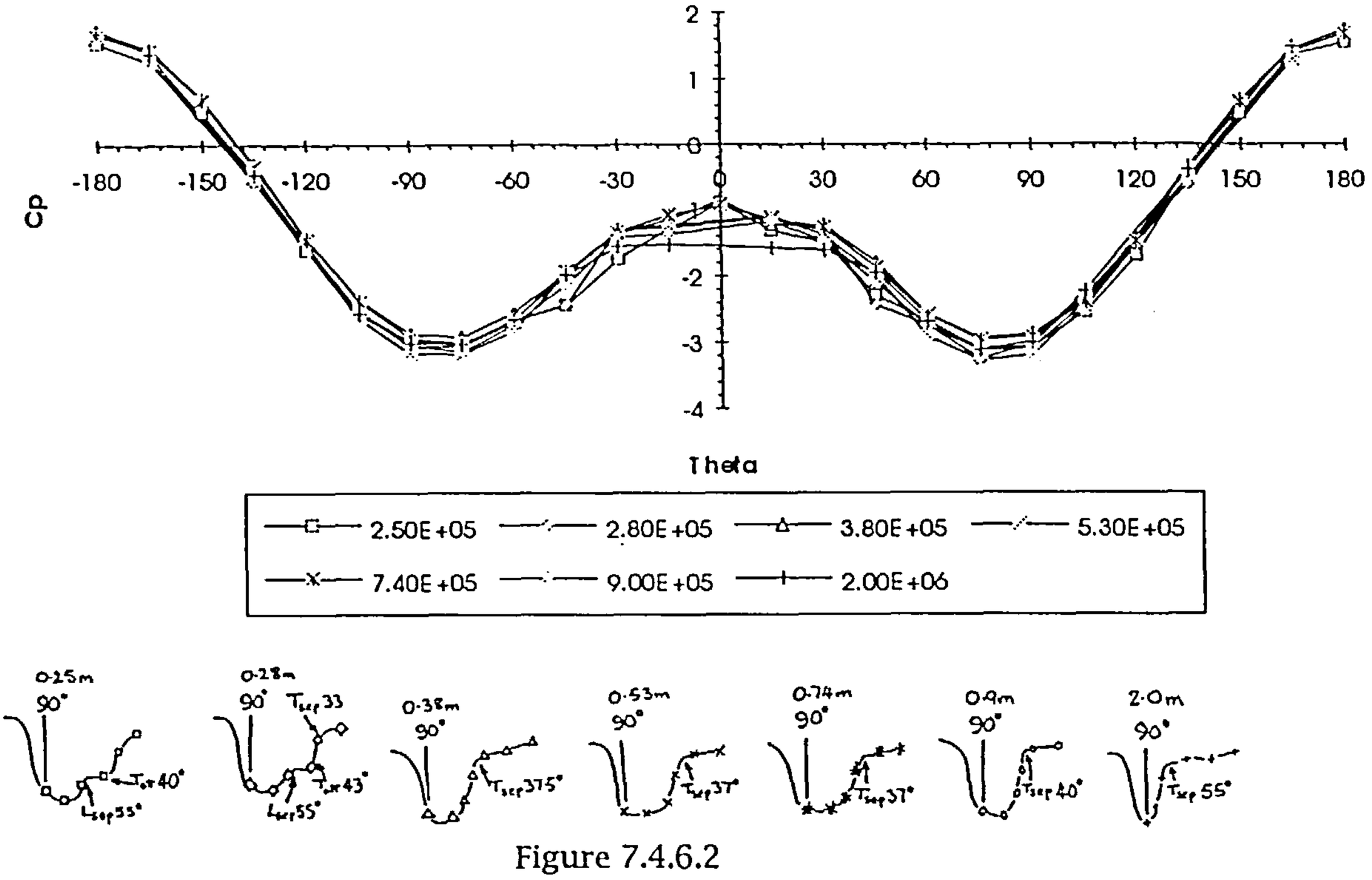

Figure 7.4.6.2

Ogive-cylinder body at alpha=20 X/a=3.17nom

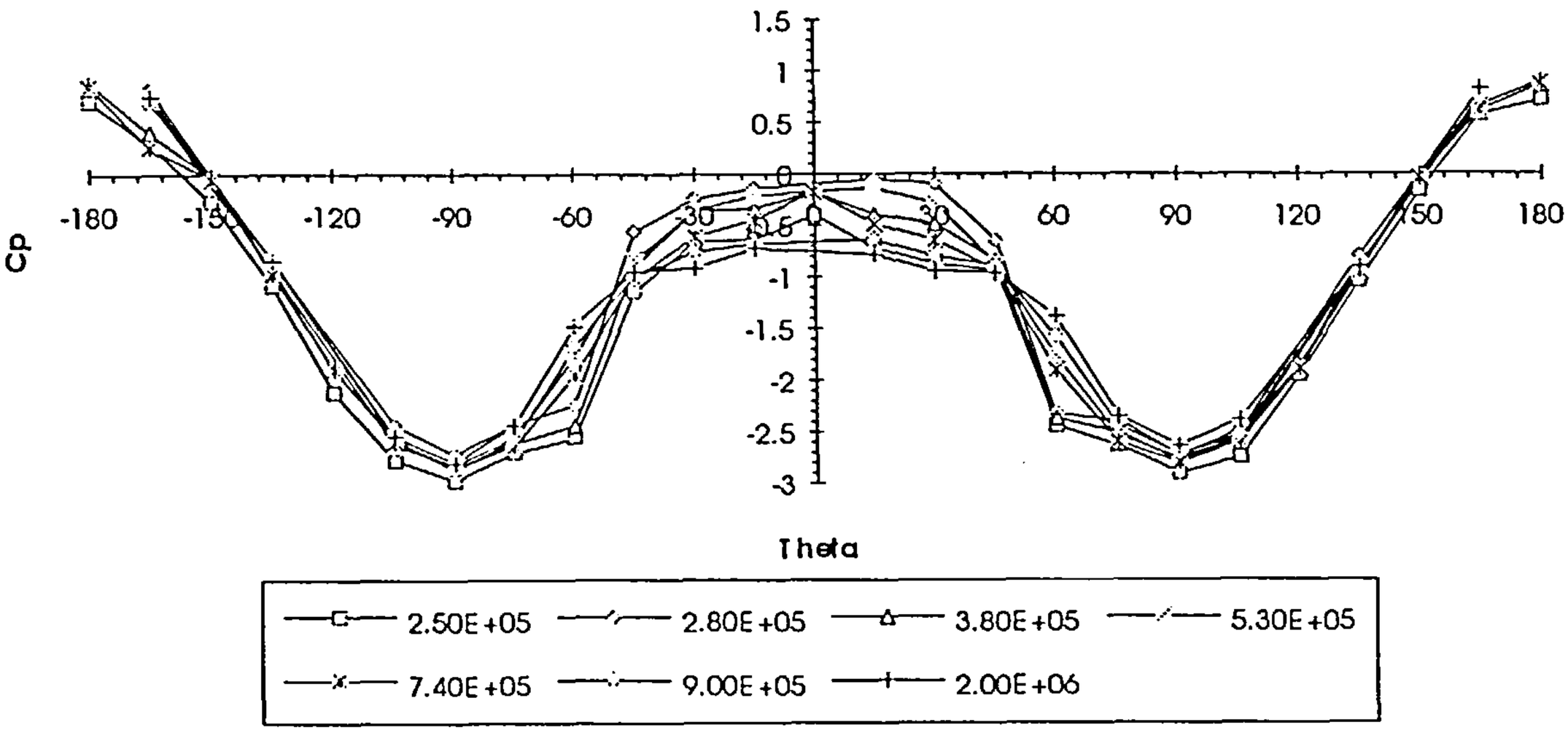

Figure 7.4.6.3

Ogive-cylinder body at alpha=20 X/d=4.2nom

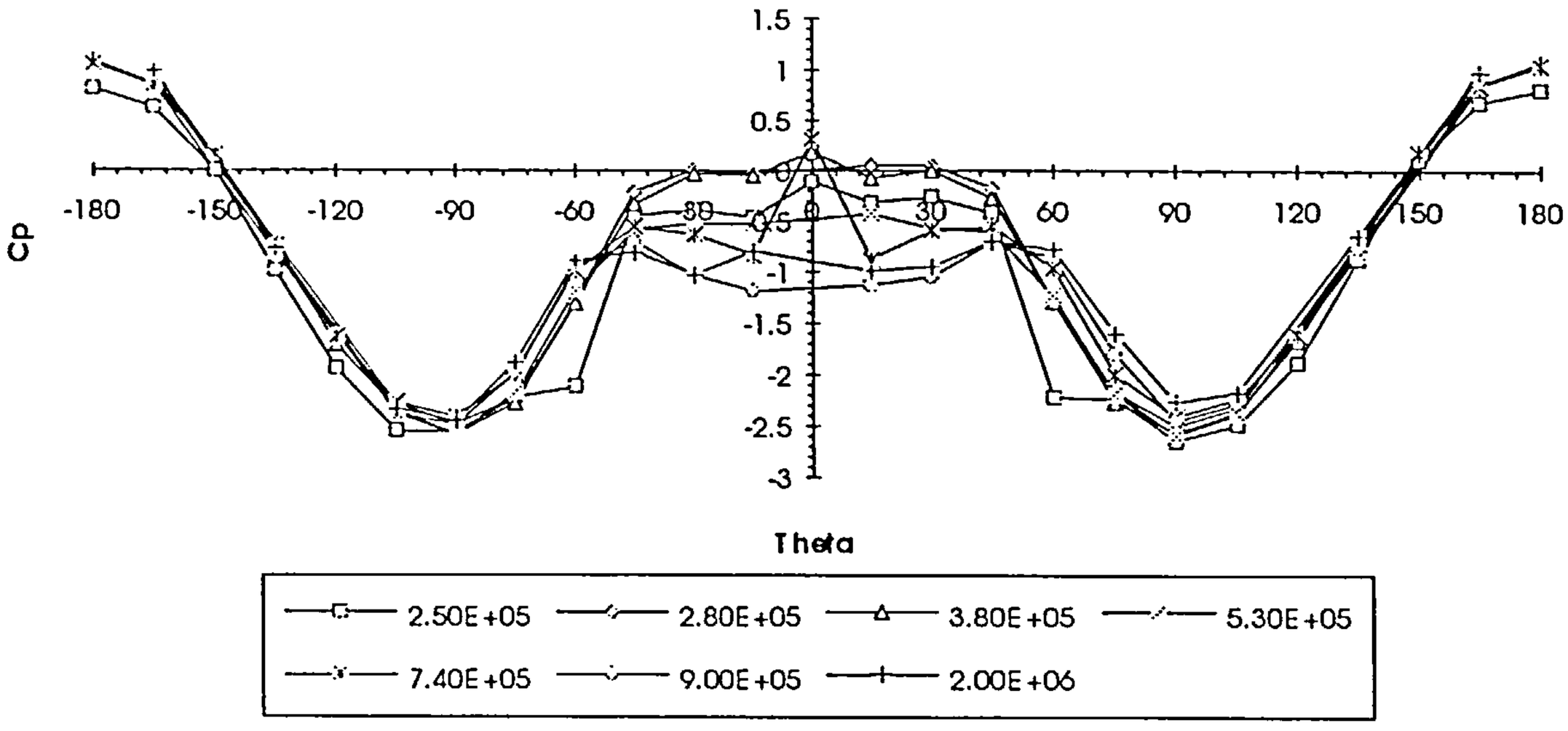

Figure 7.4.6.4

Ogive-cylinder body at alpha=20 X/d=4.75nom

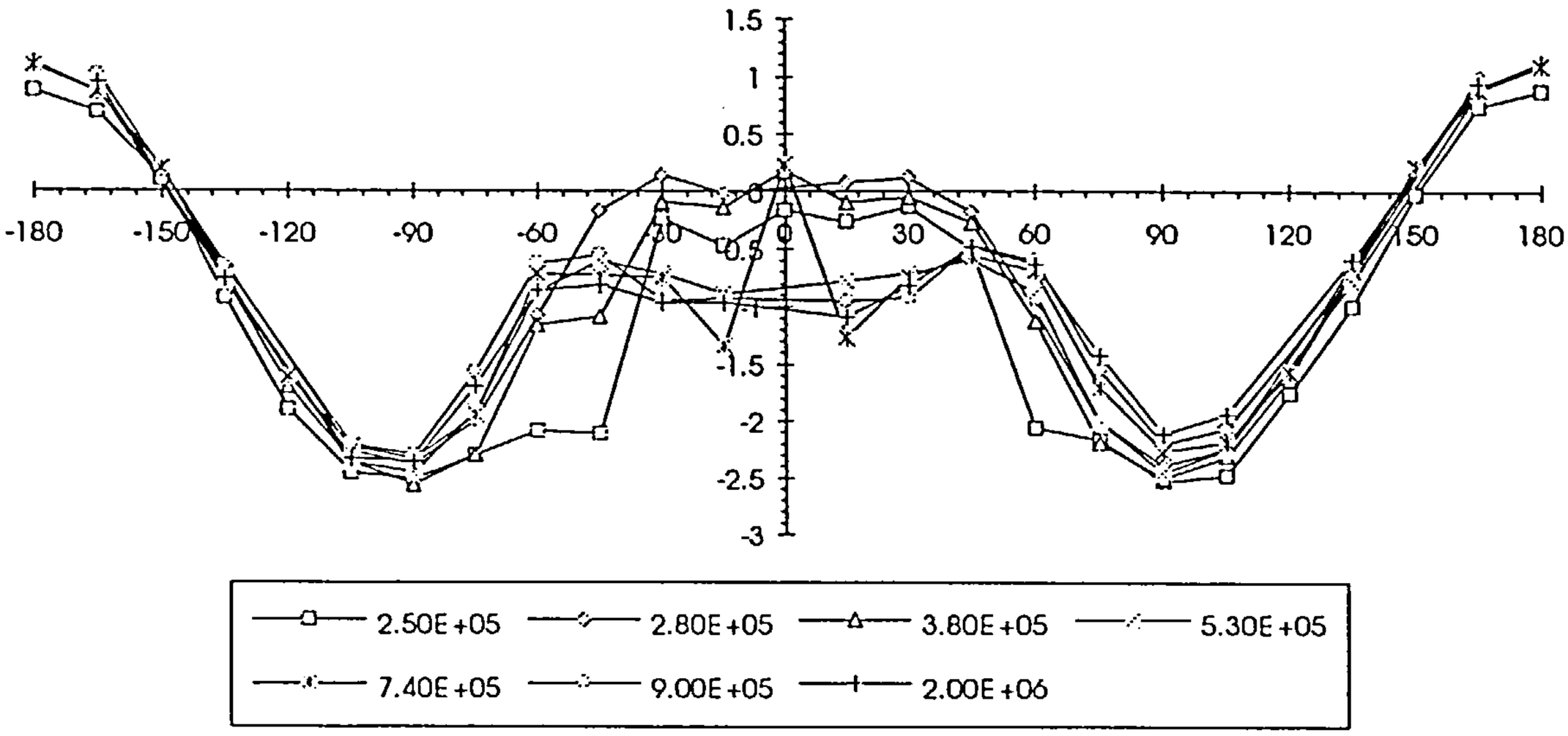

Figure 7.4.6.5

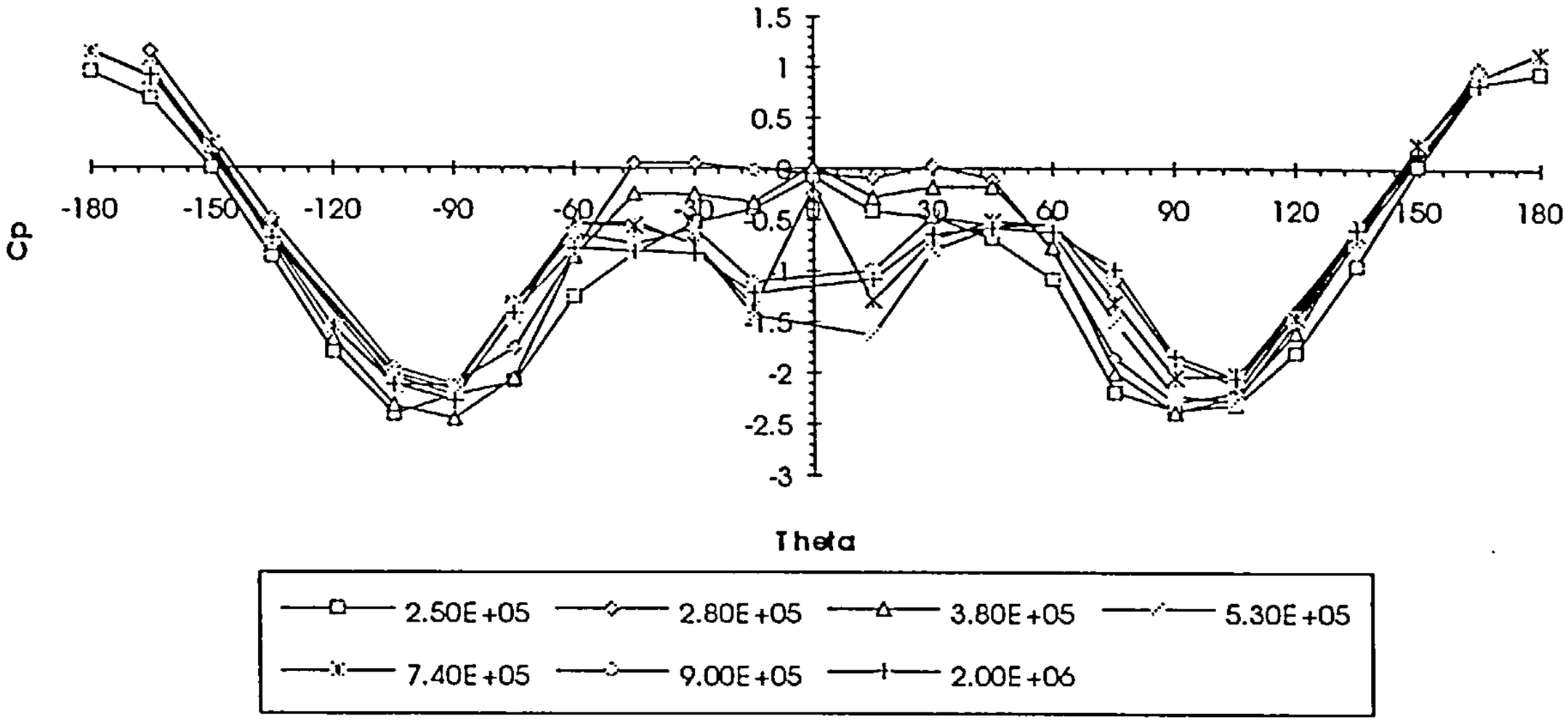

Figure 7.4.6.6

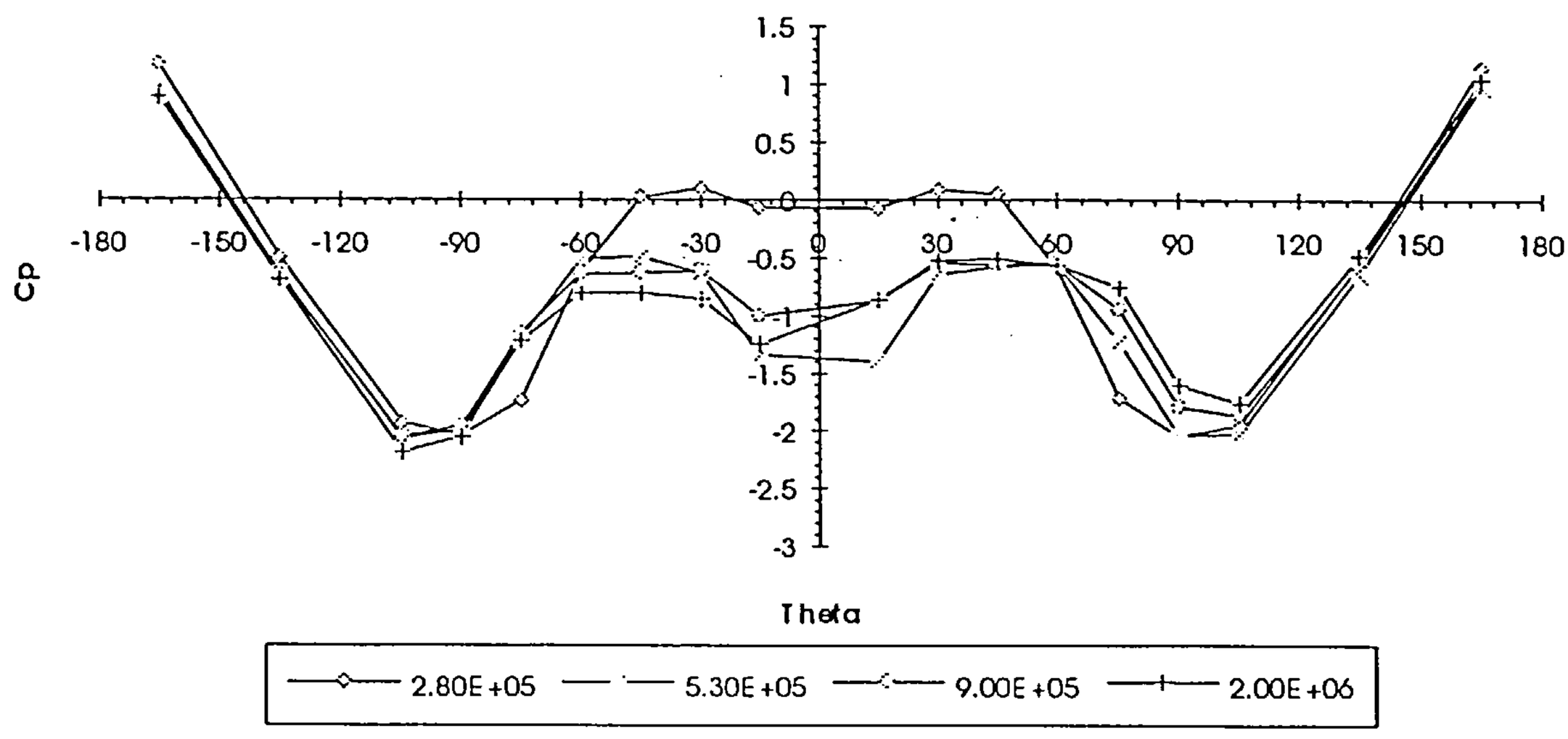

Figure 7.4.6.7

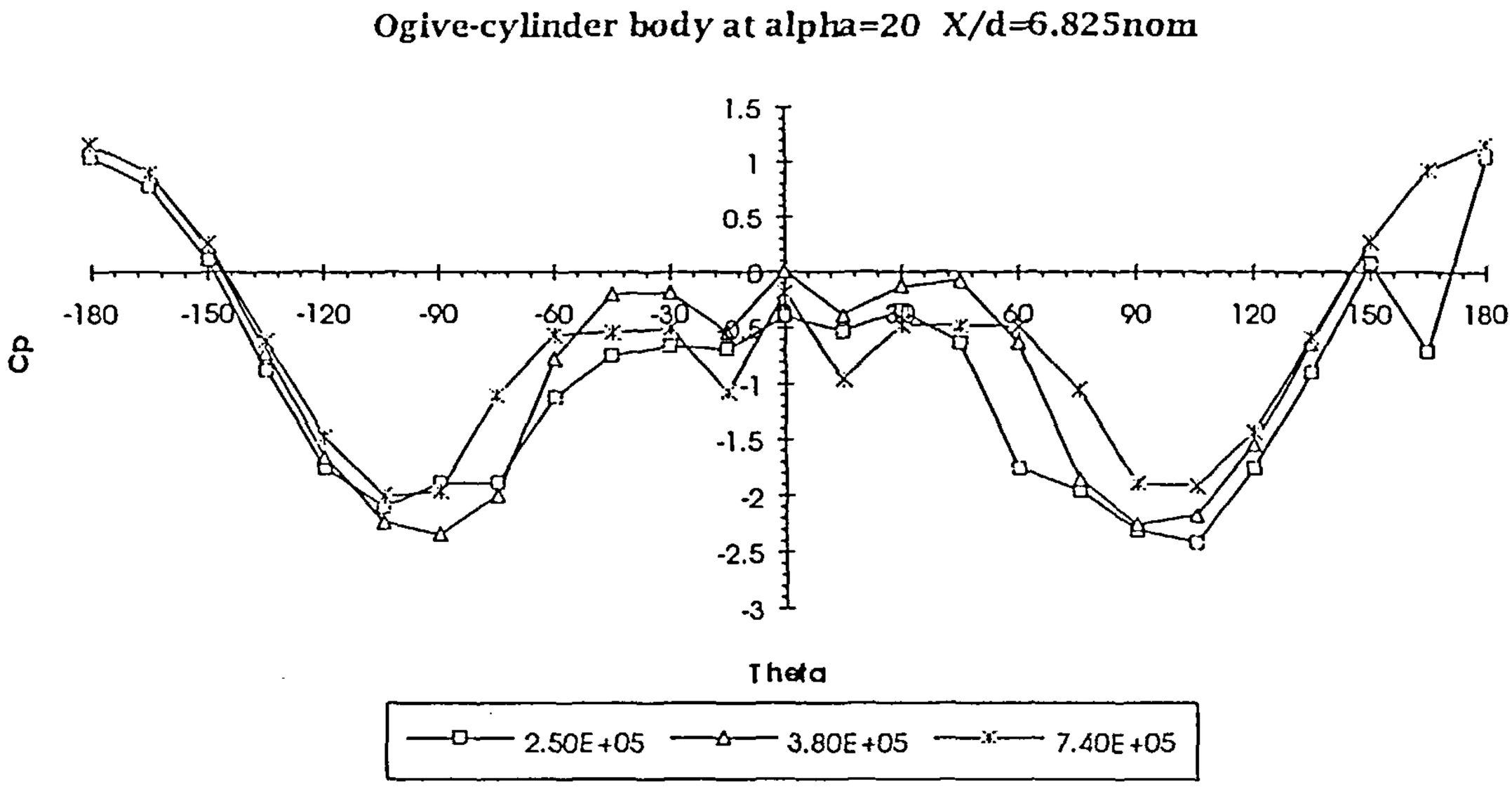

Figure 7.4.6.8

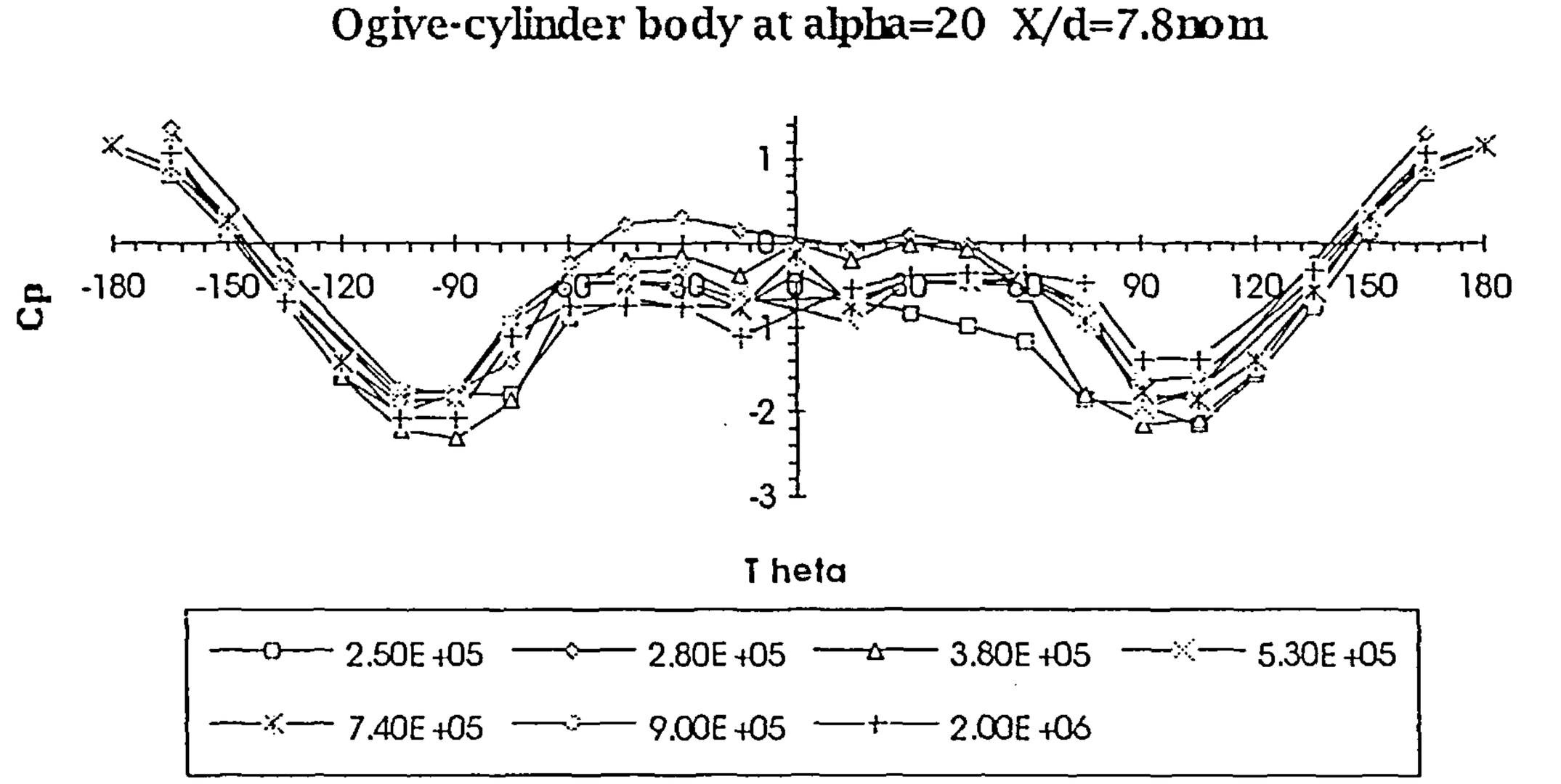

Figure 7.4.6.9

Ogive-cylinder body at alpha=20 X/a=9.42nom

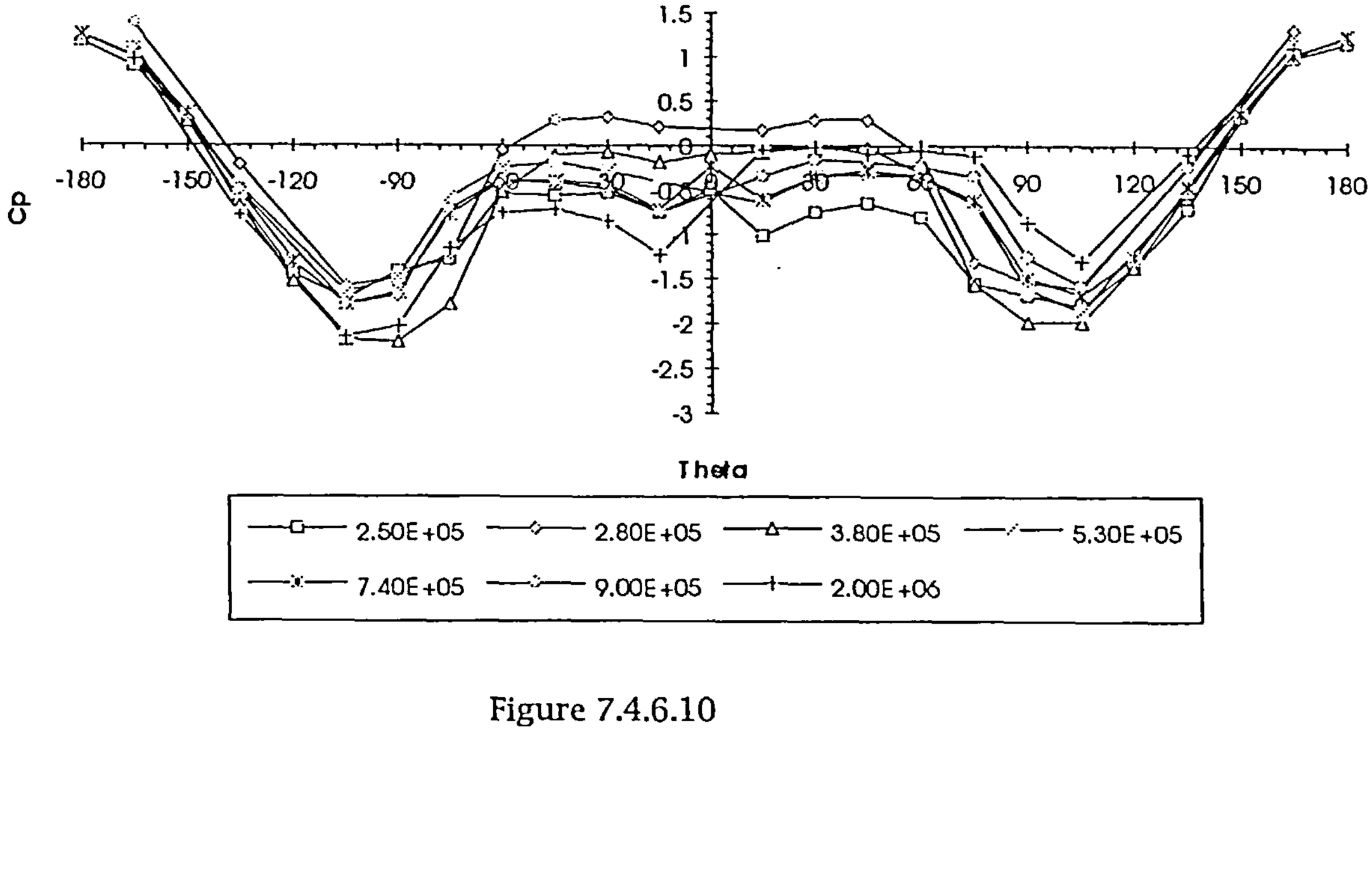

Figure 7.4.6.10

Angular position of separation vs x/d Red=250000

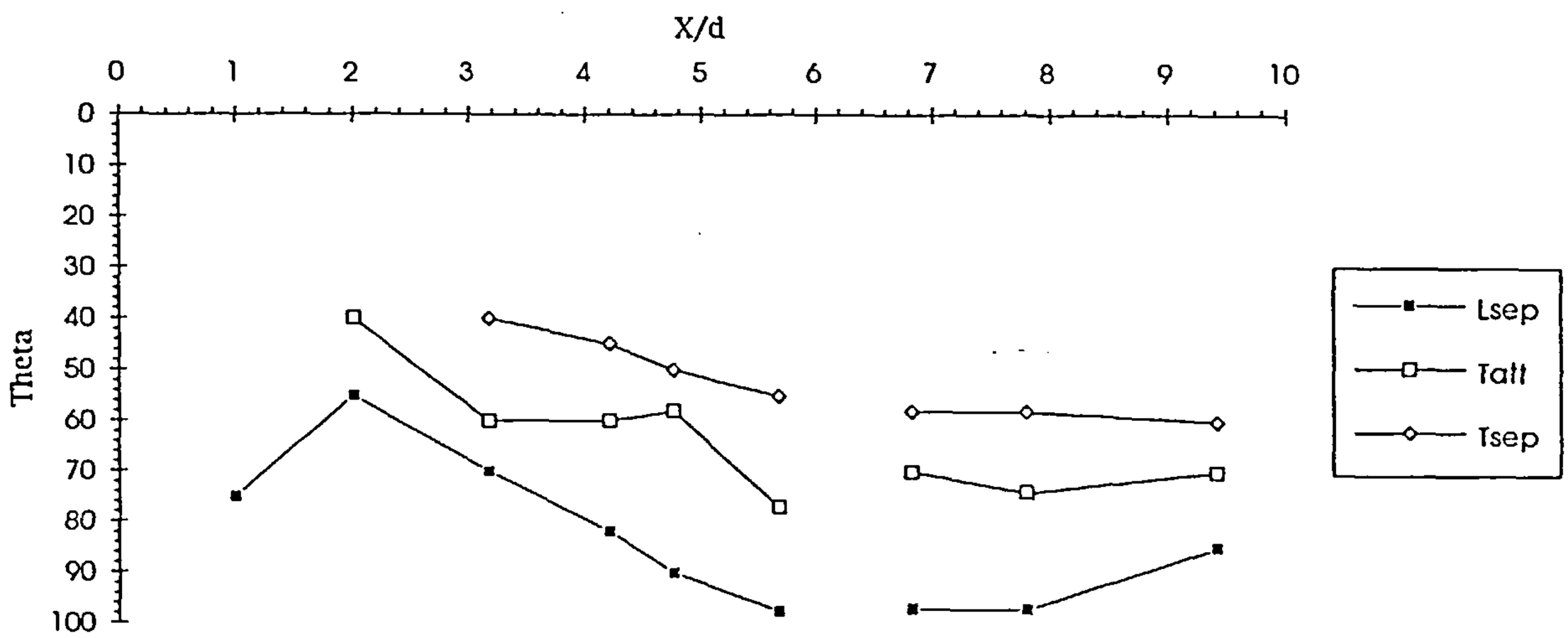

Figure 7.4.6.11

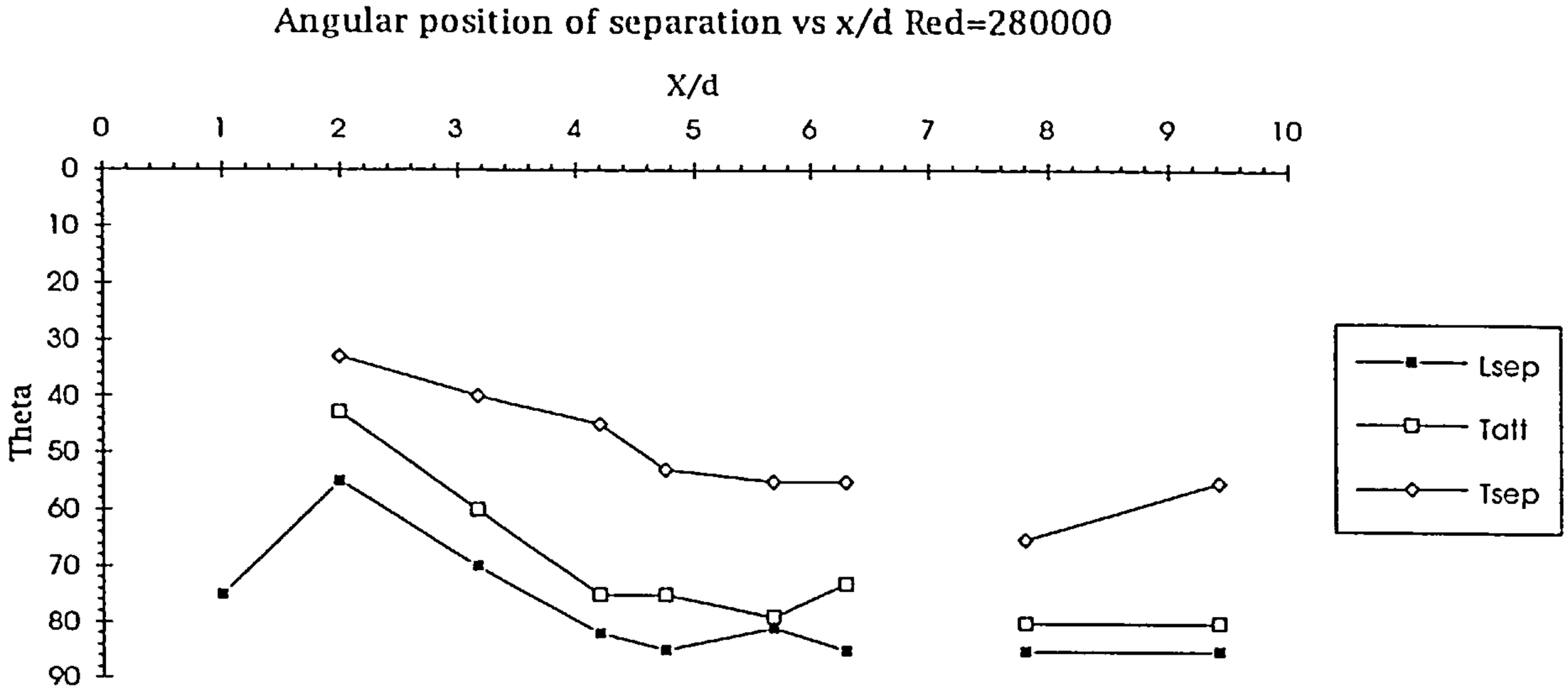

Figure 7.4.6.12

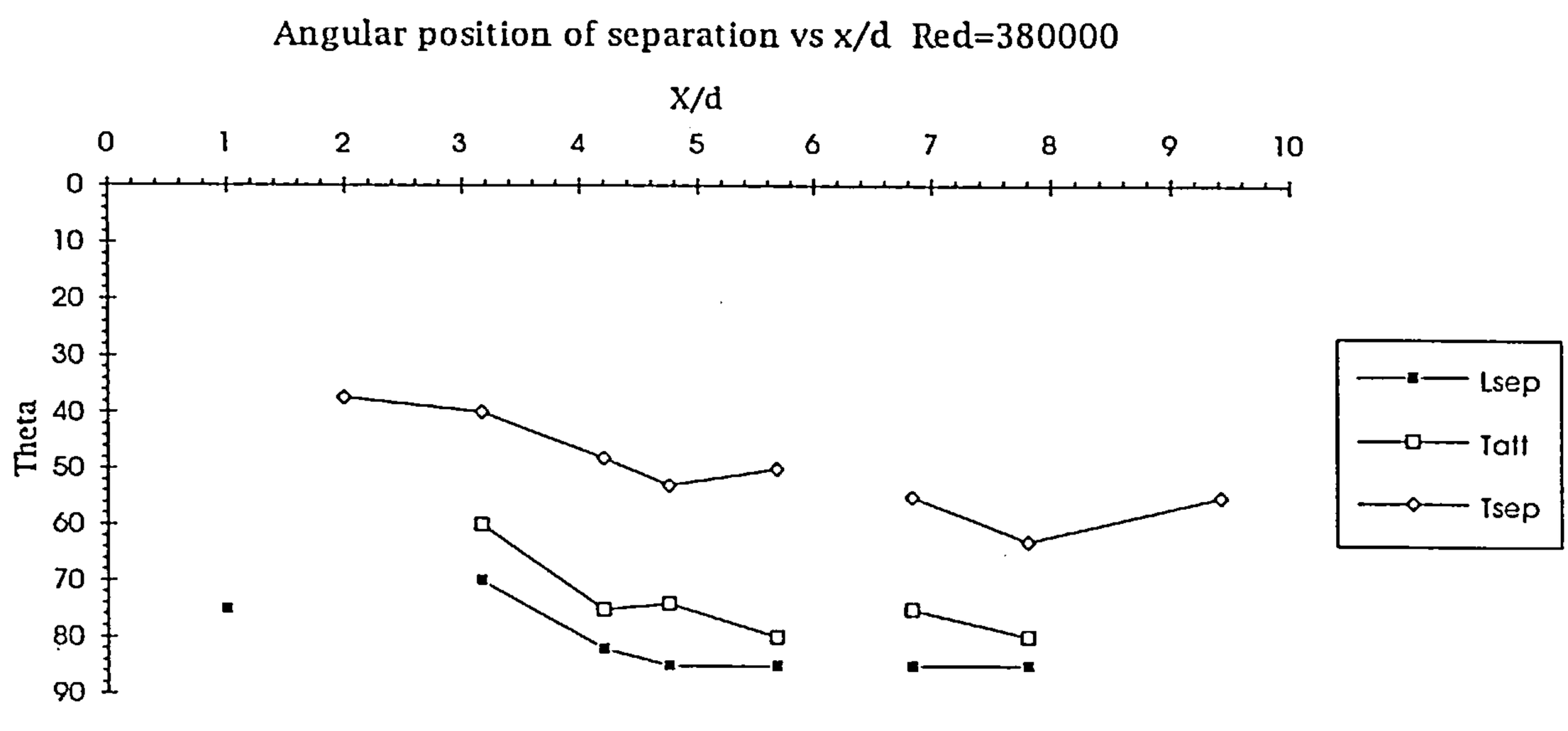

Figure 7.4.6.13

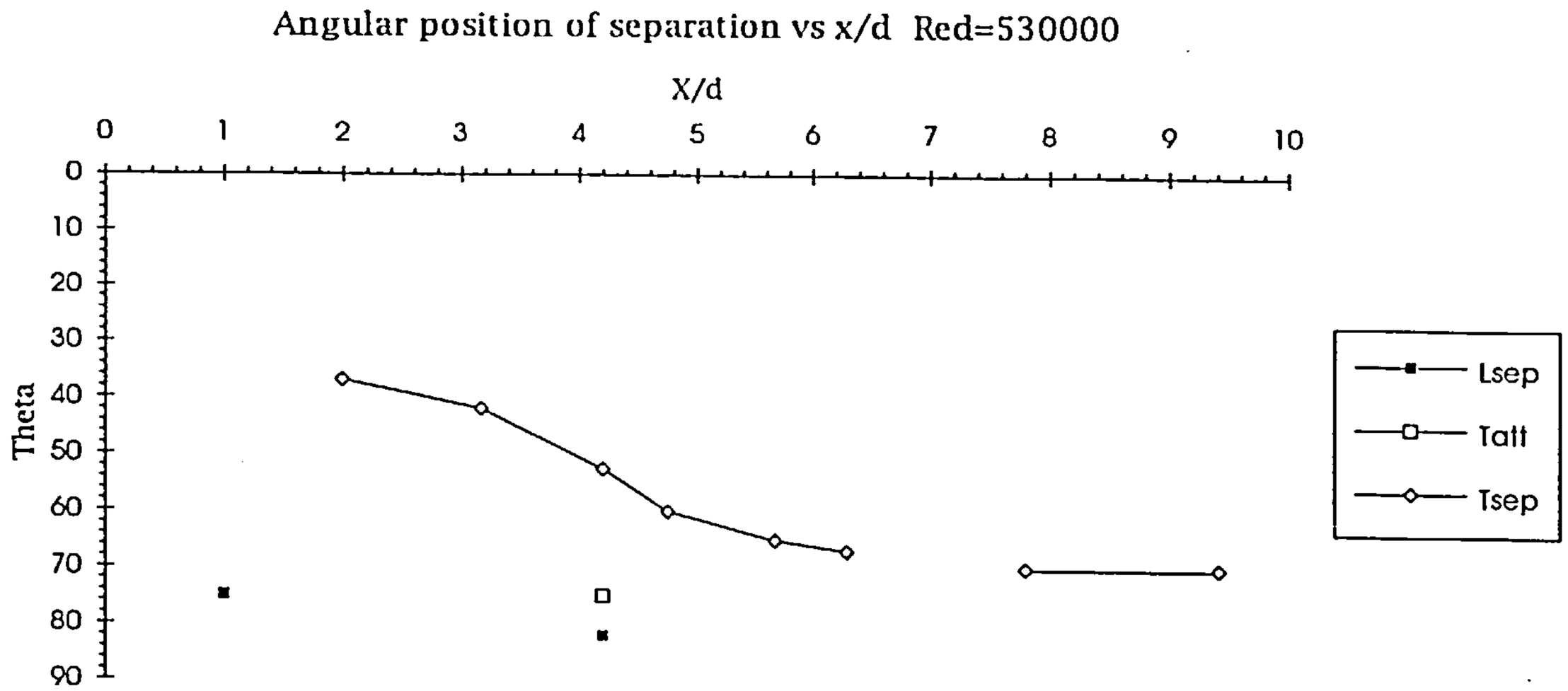

Figure 7.4.6.14

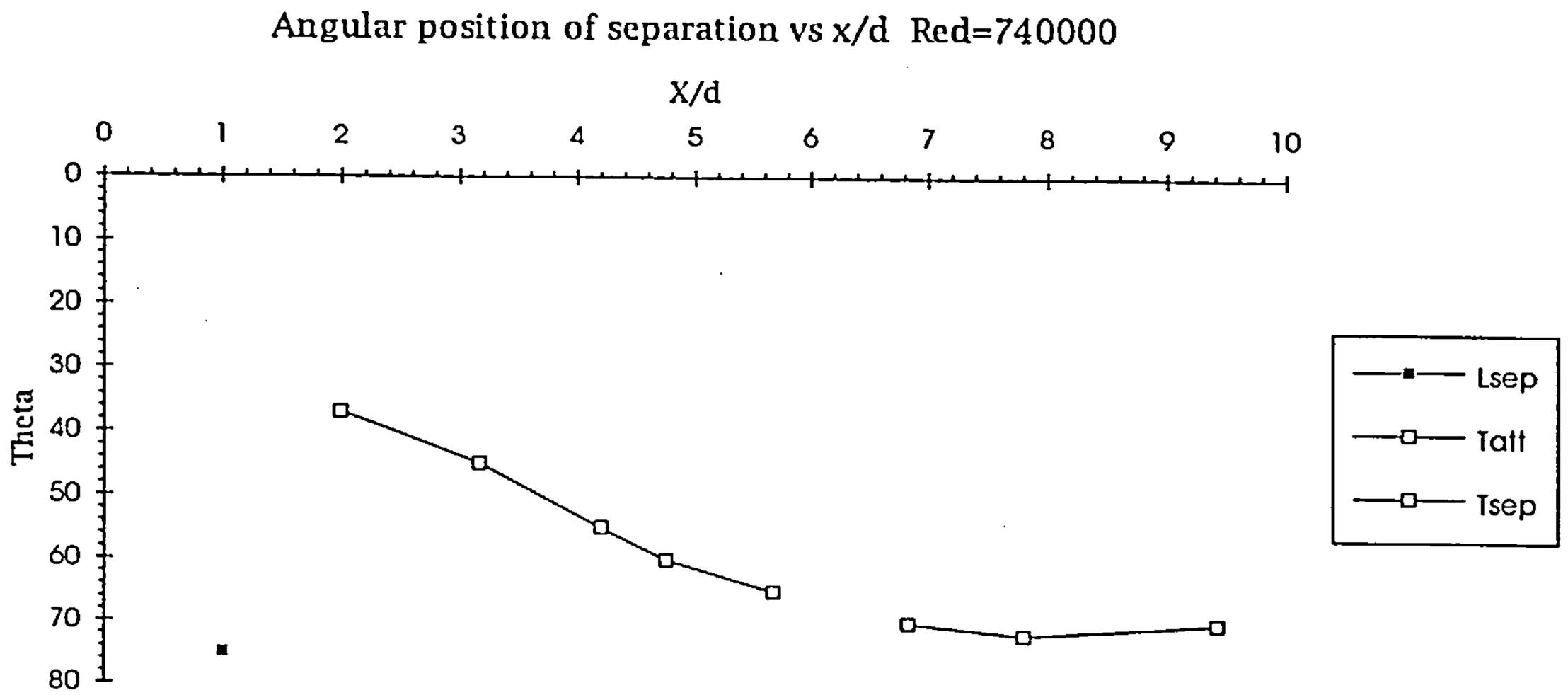

Figure 7.4.6.15

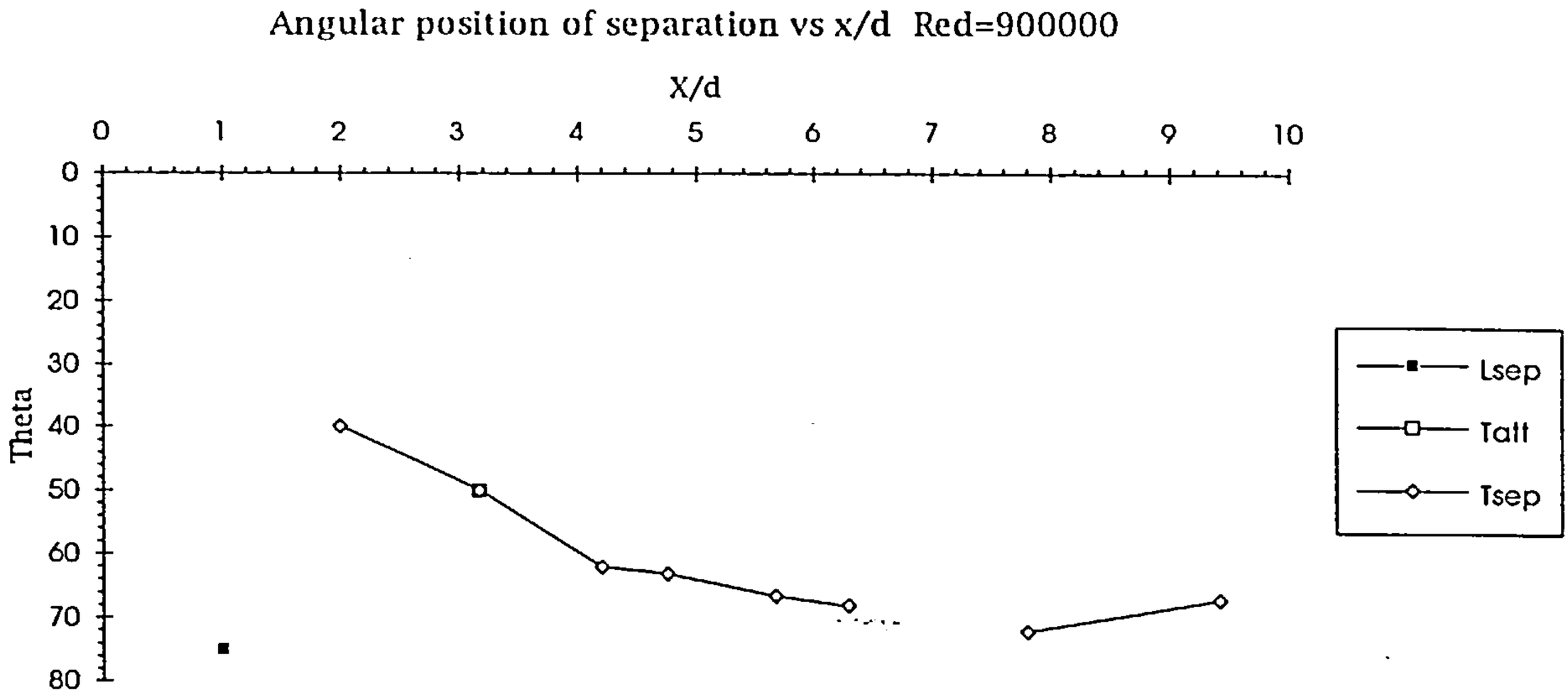

Figure 7.4.6.16

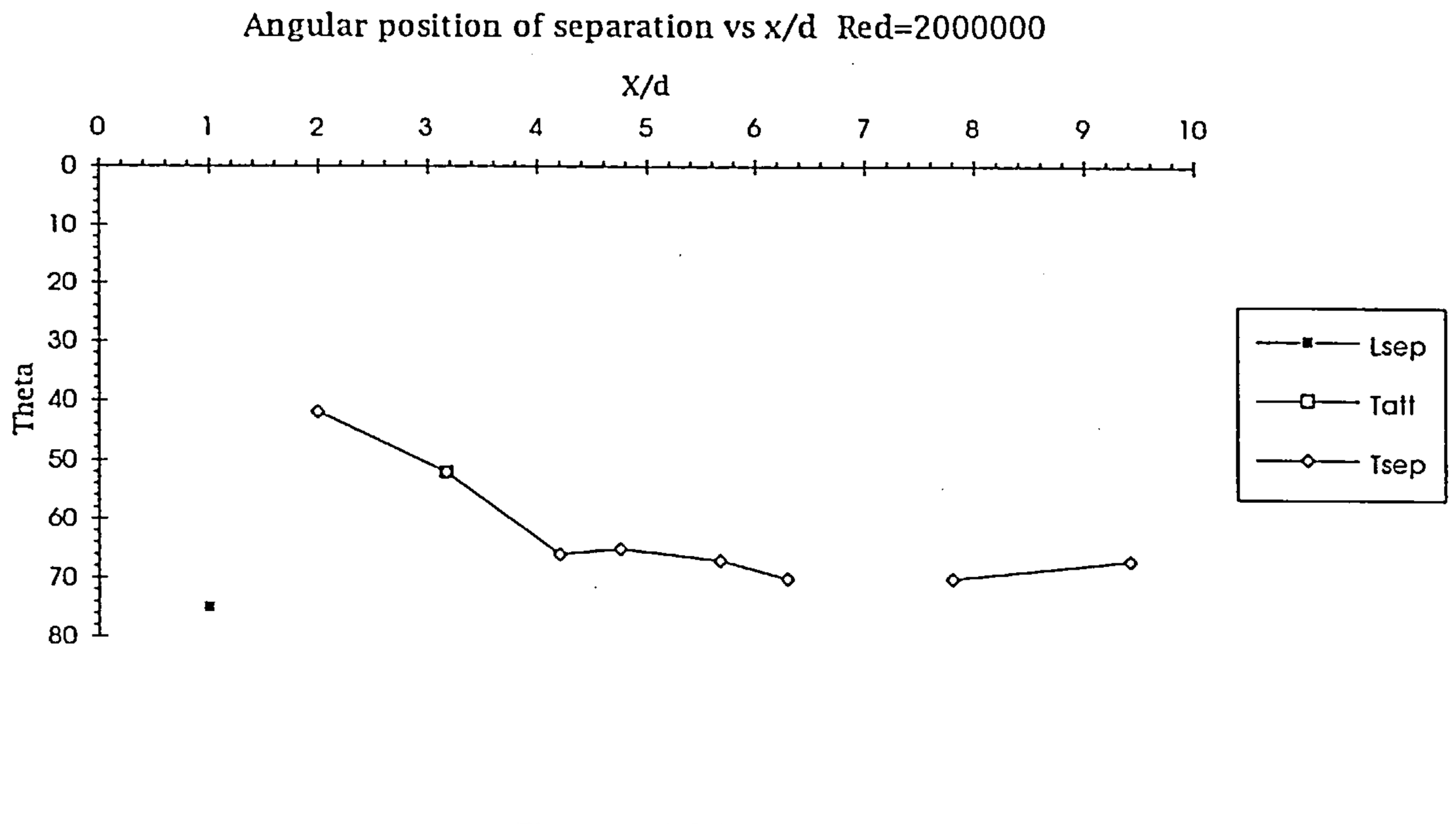

Figure 7.4.6.17

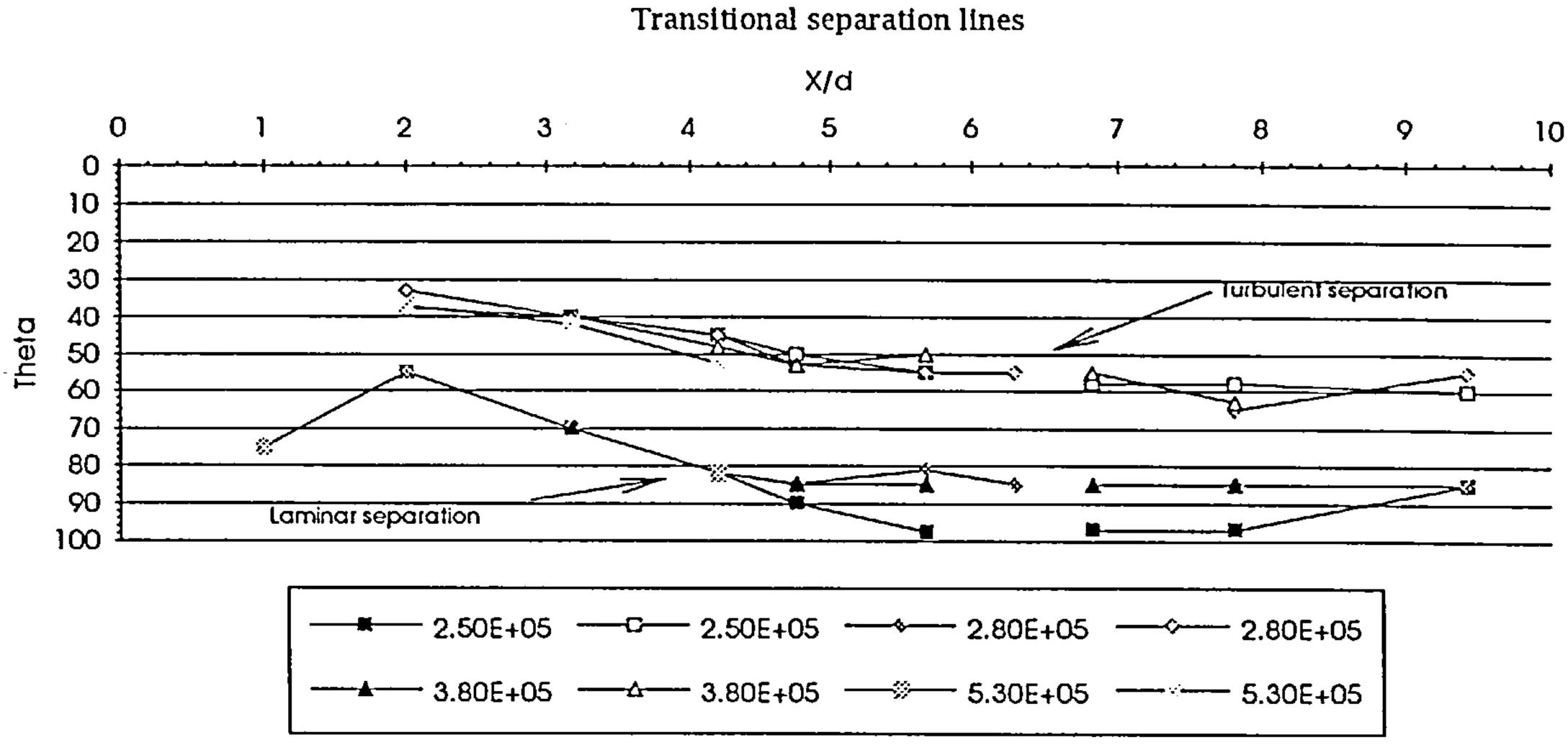

Figure 7.4.6.18

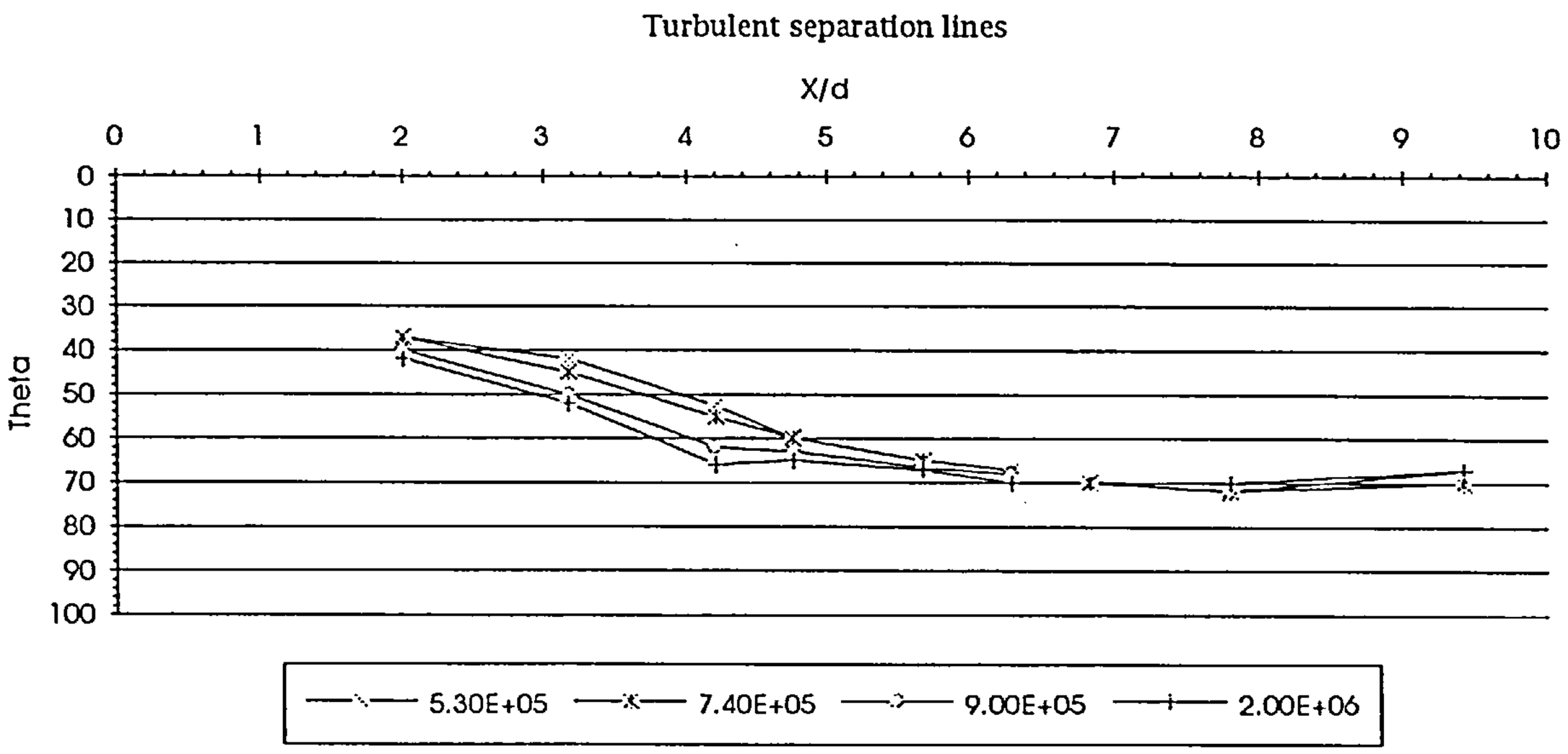

Figure 7.4.6.19

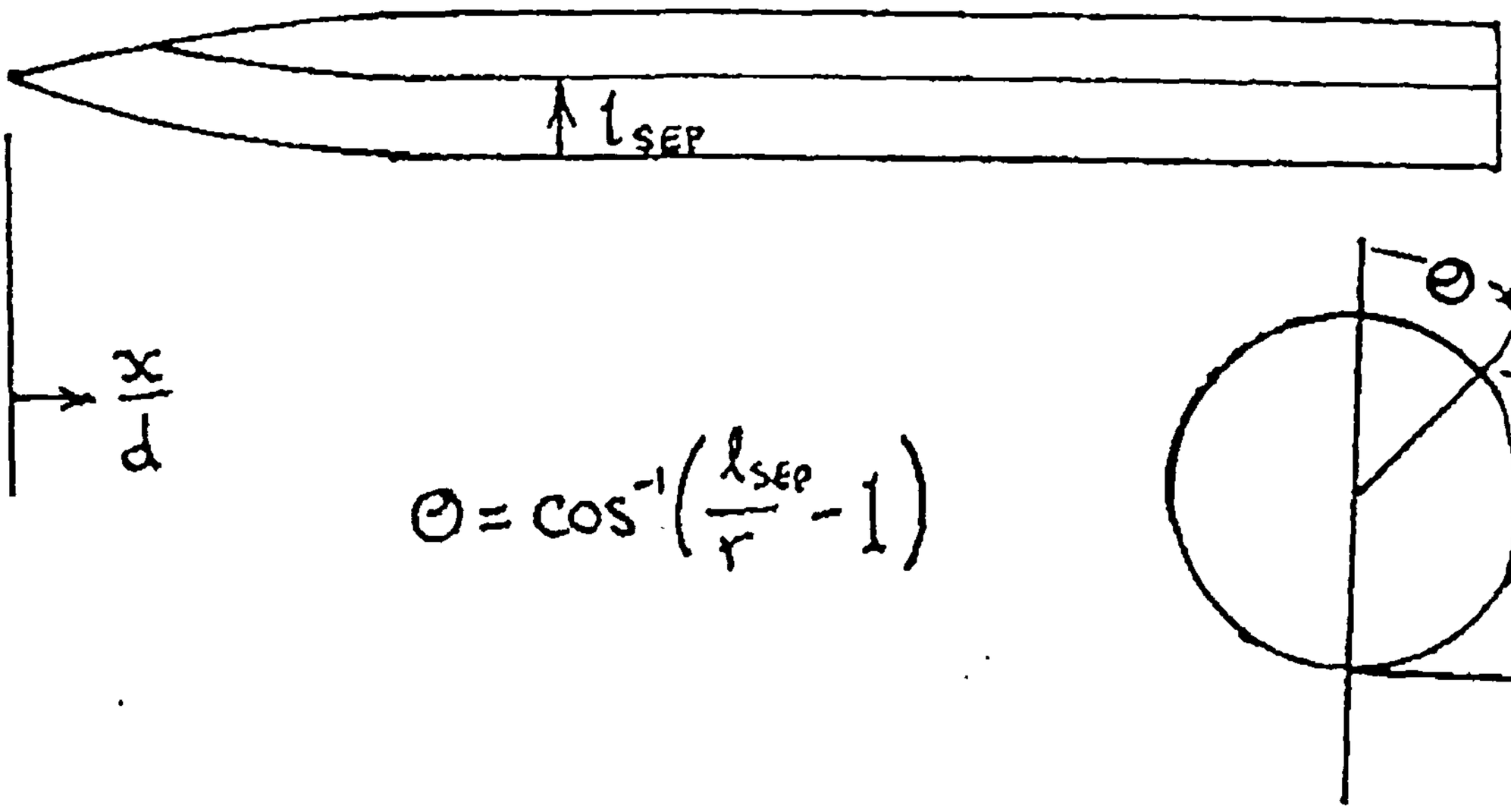

Figure 7.4.6.20

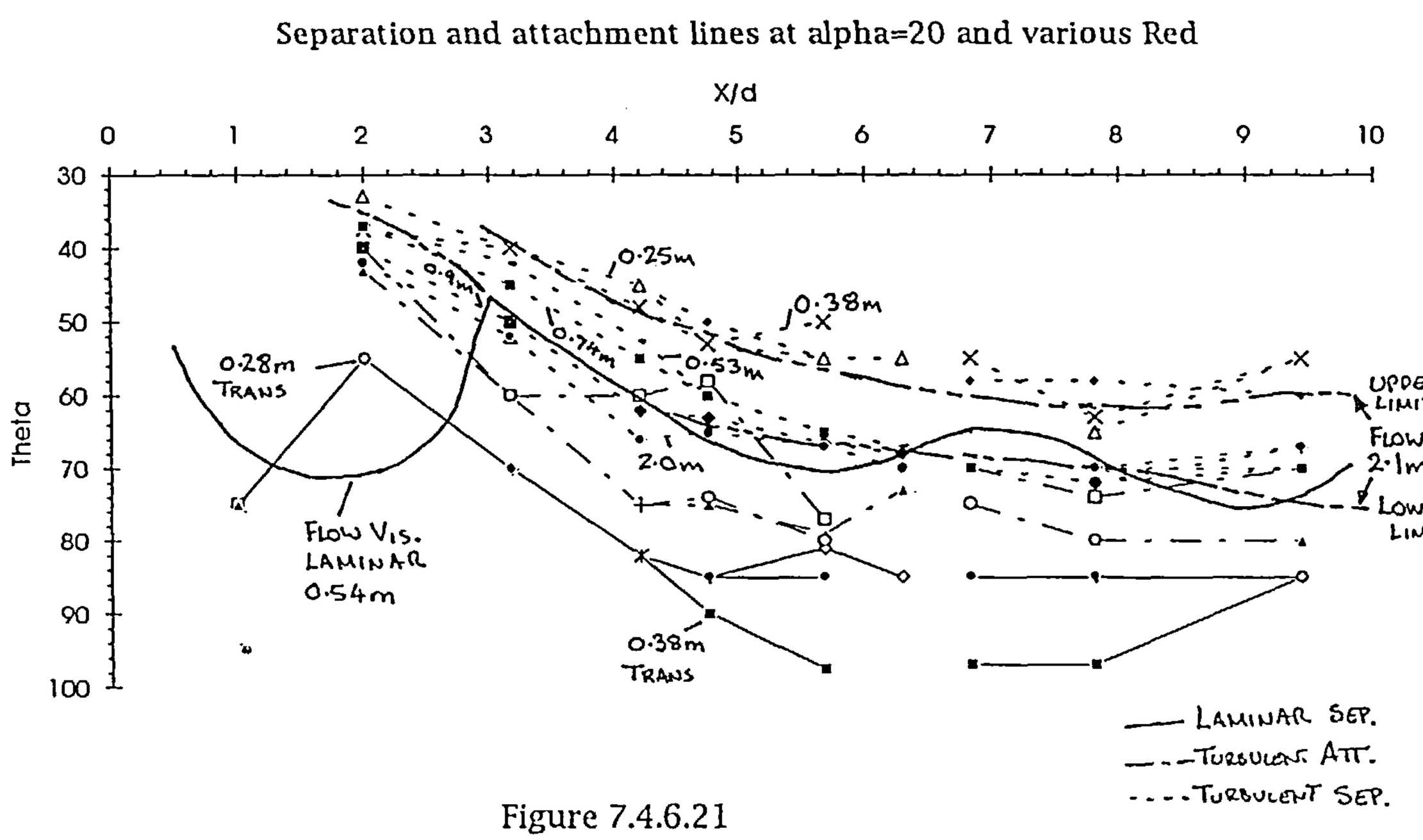

Figure 7.4.6.21

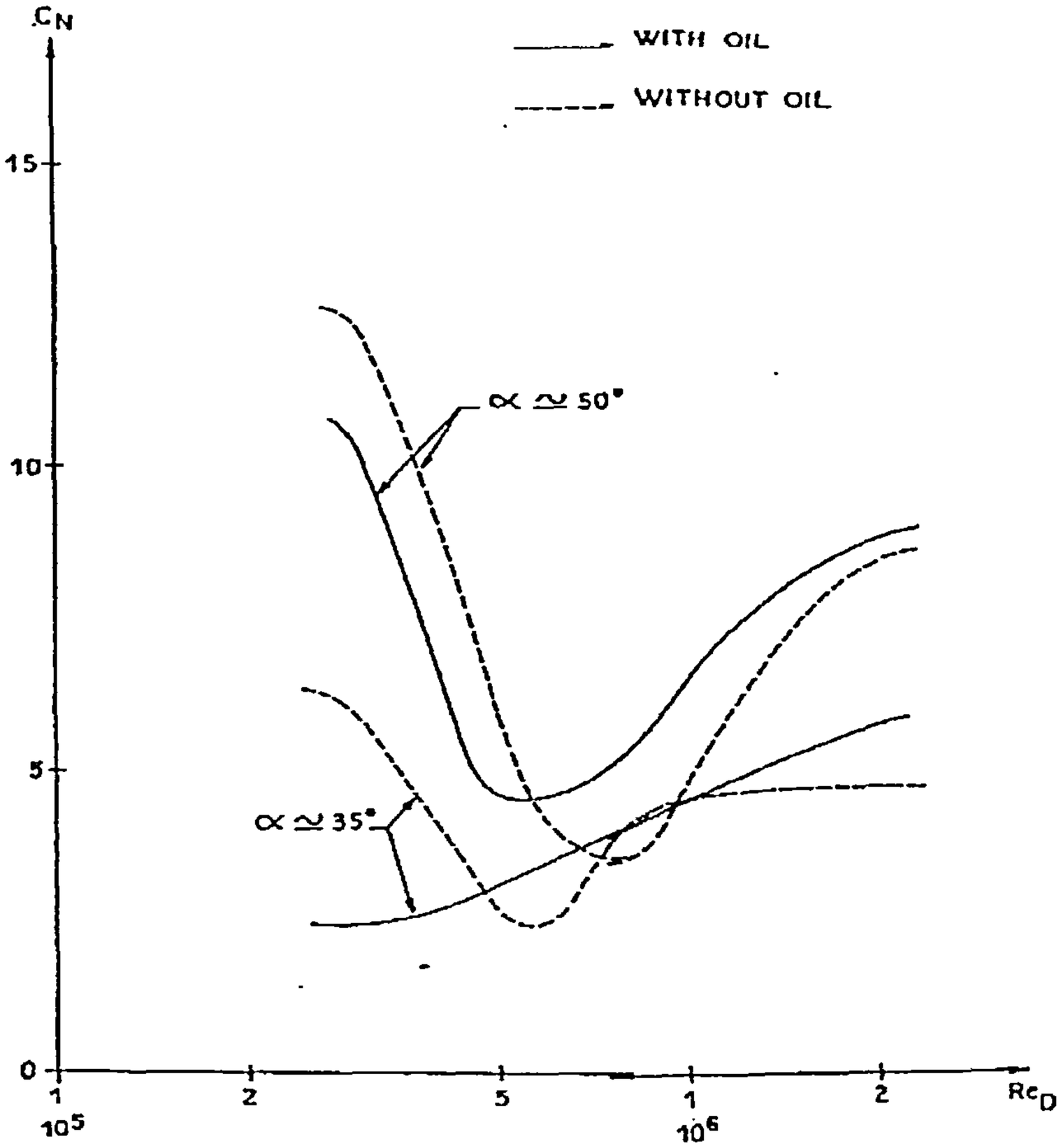

Figure 7.4.6.22
(After Champigny [31])

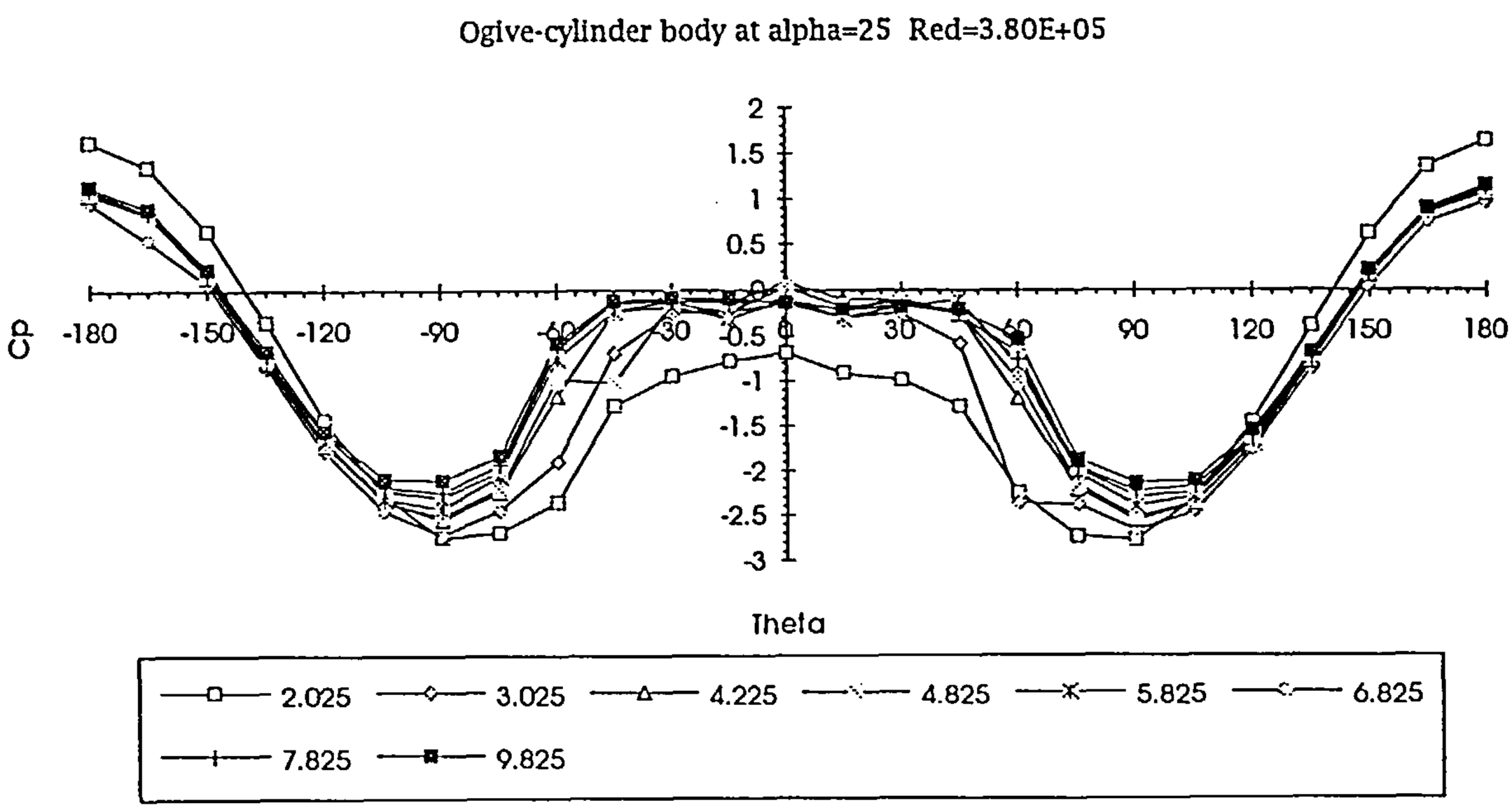

Figure 7.4.6.23

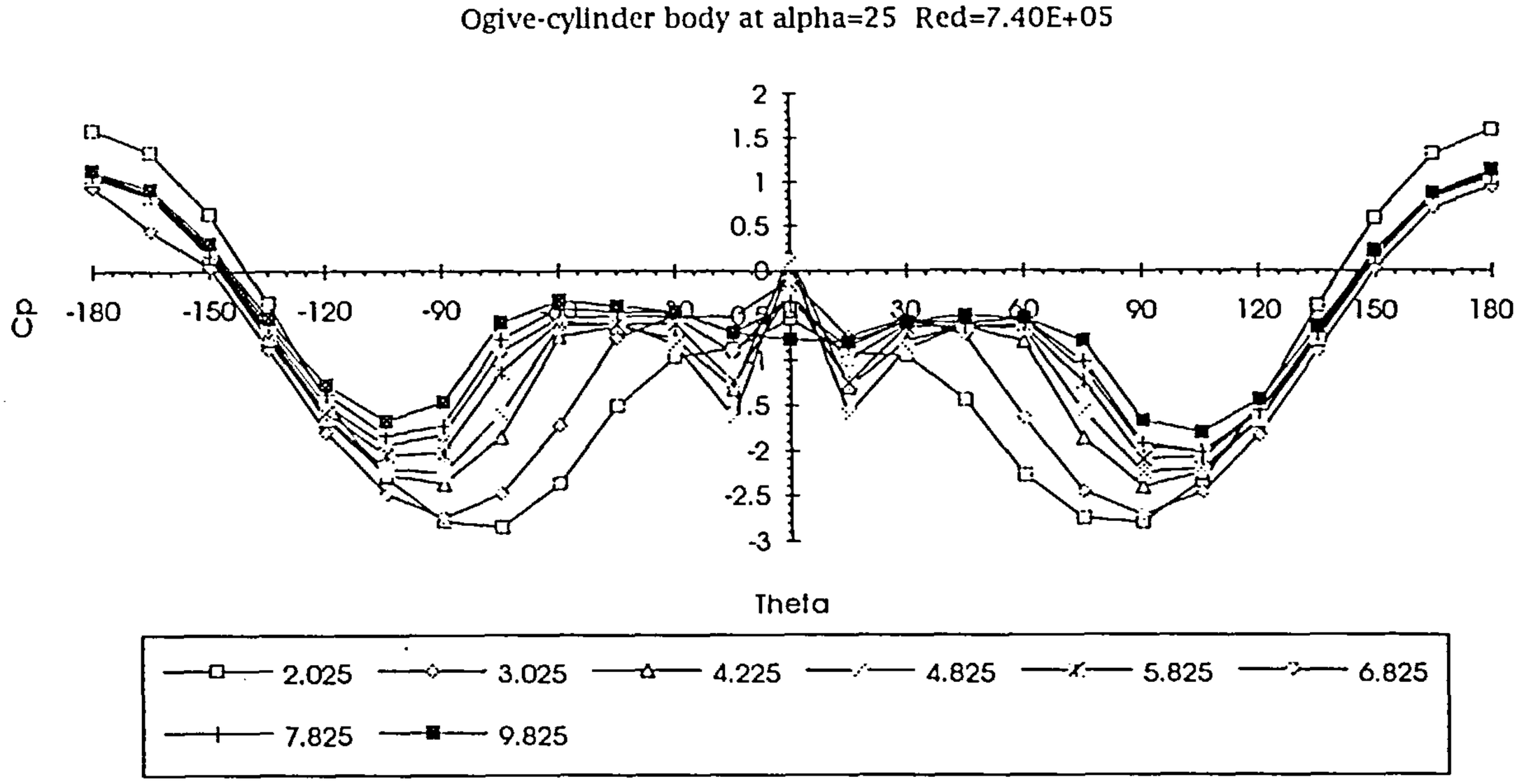

Figure 7.4.6.24

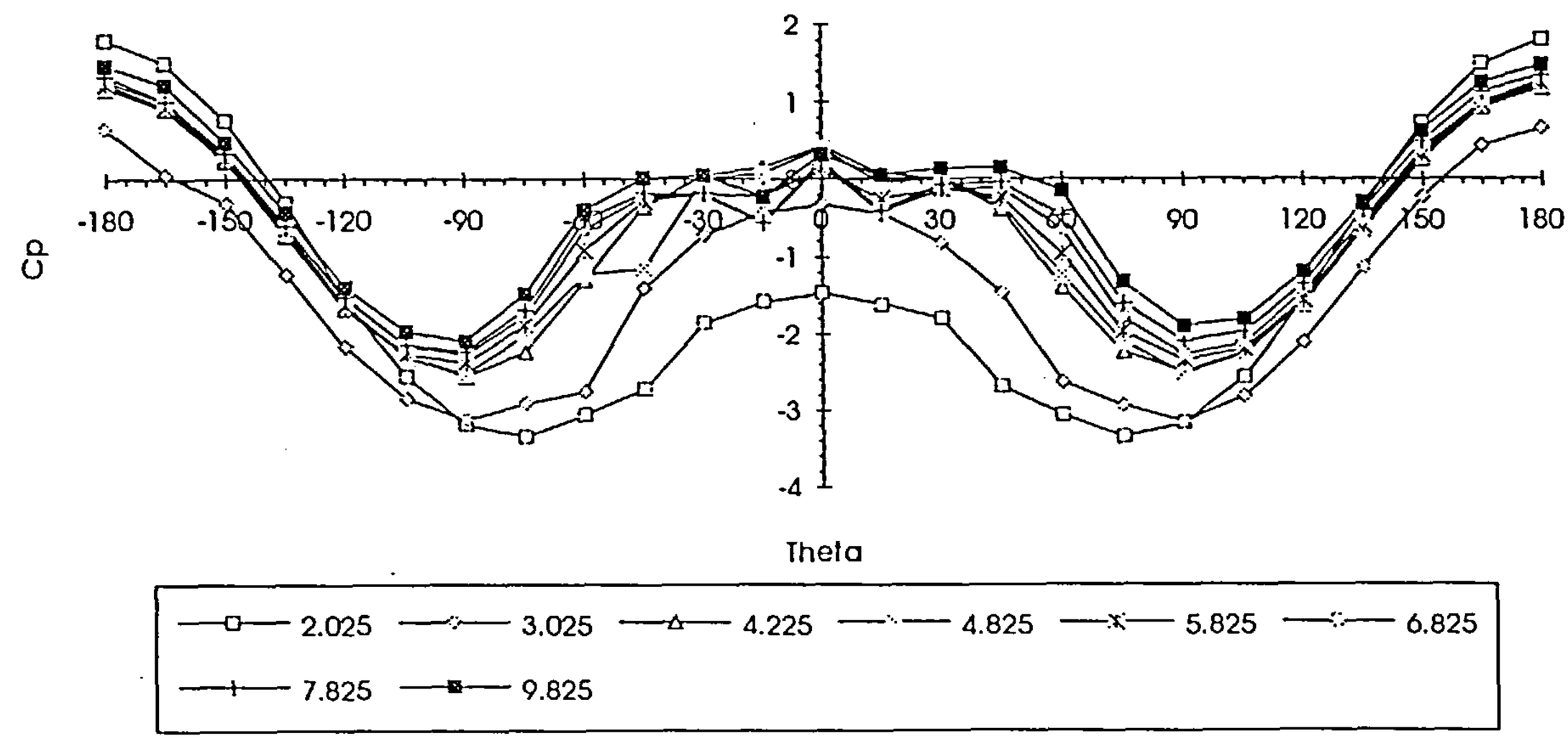

Figure 7.4.6.25

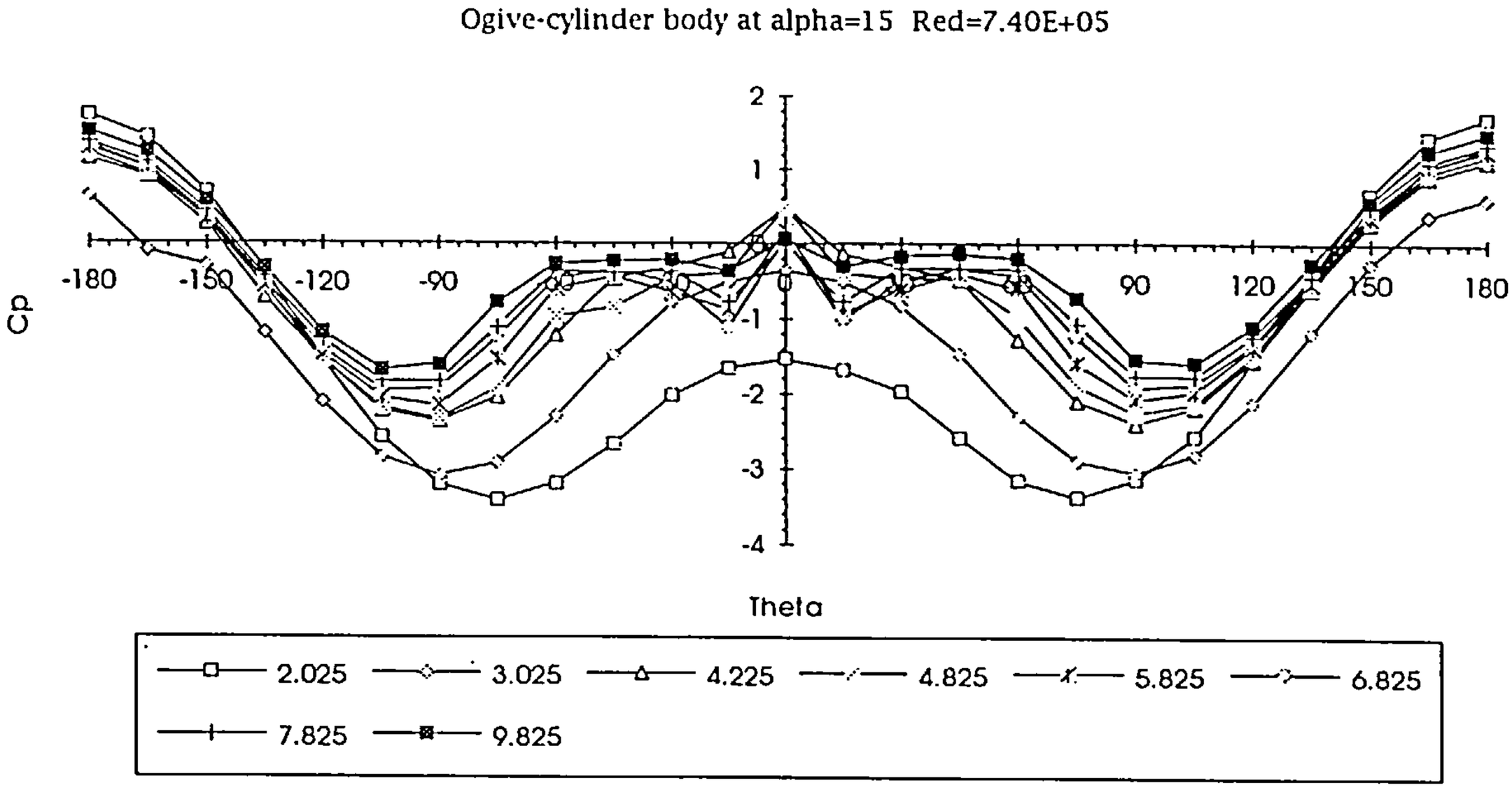

Figure 7.4.6.26

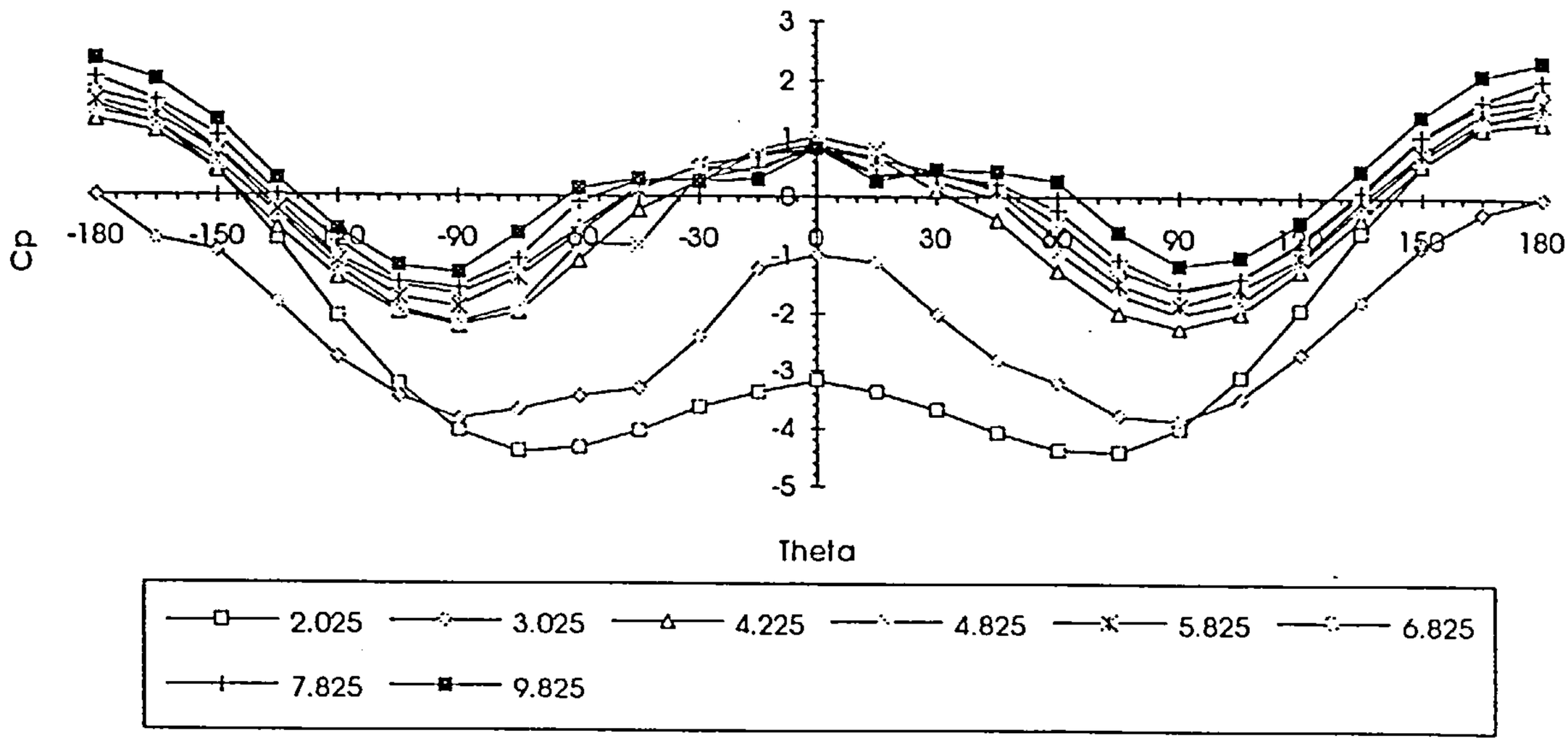

Figure 7.4.6.27

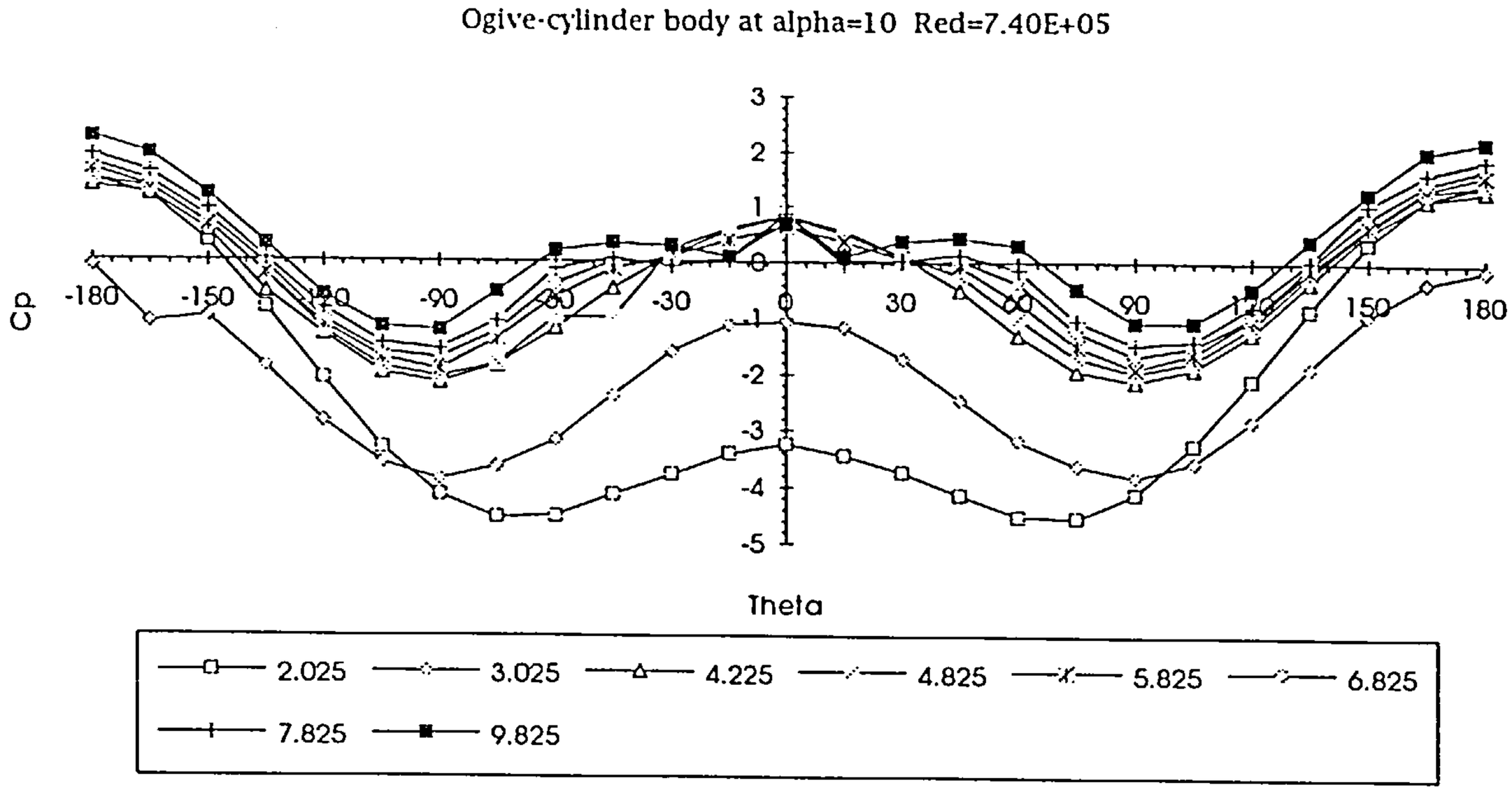

Figure 7.4.6.28

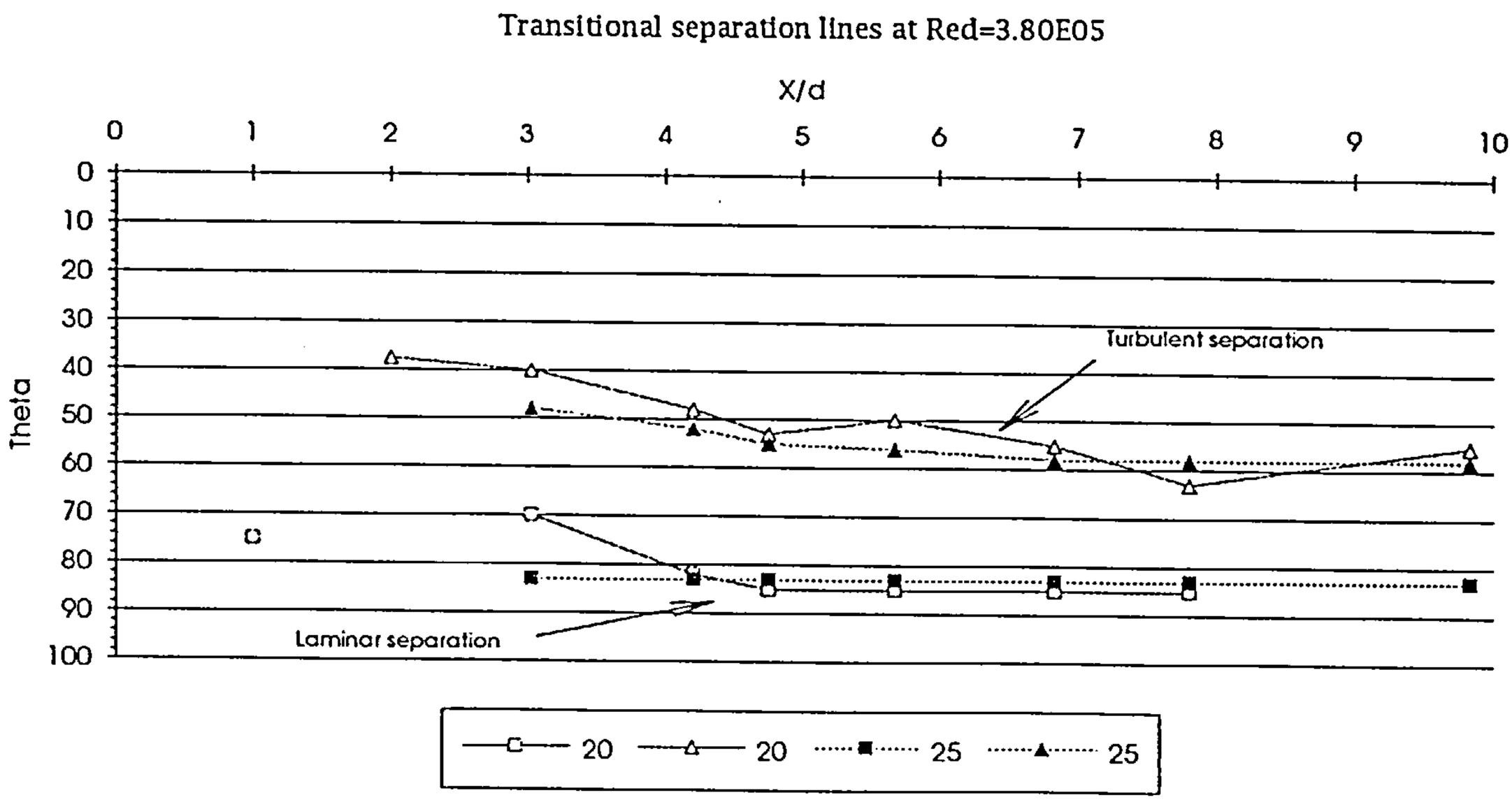

Figure 7.4.6.29

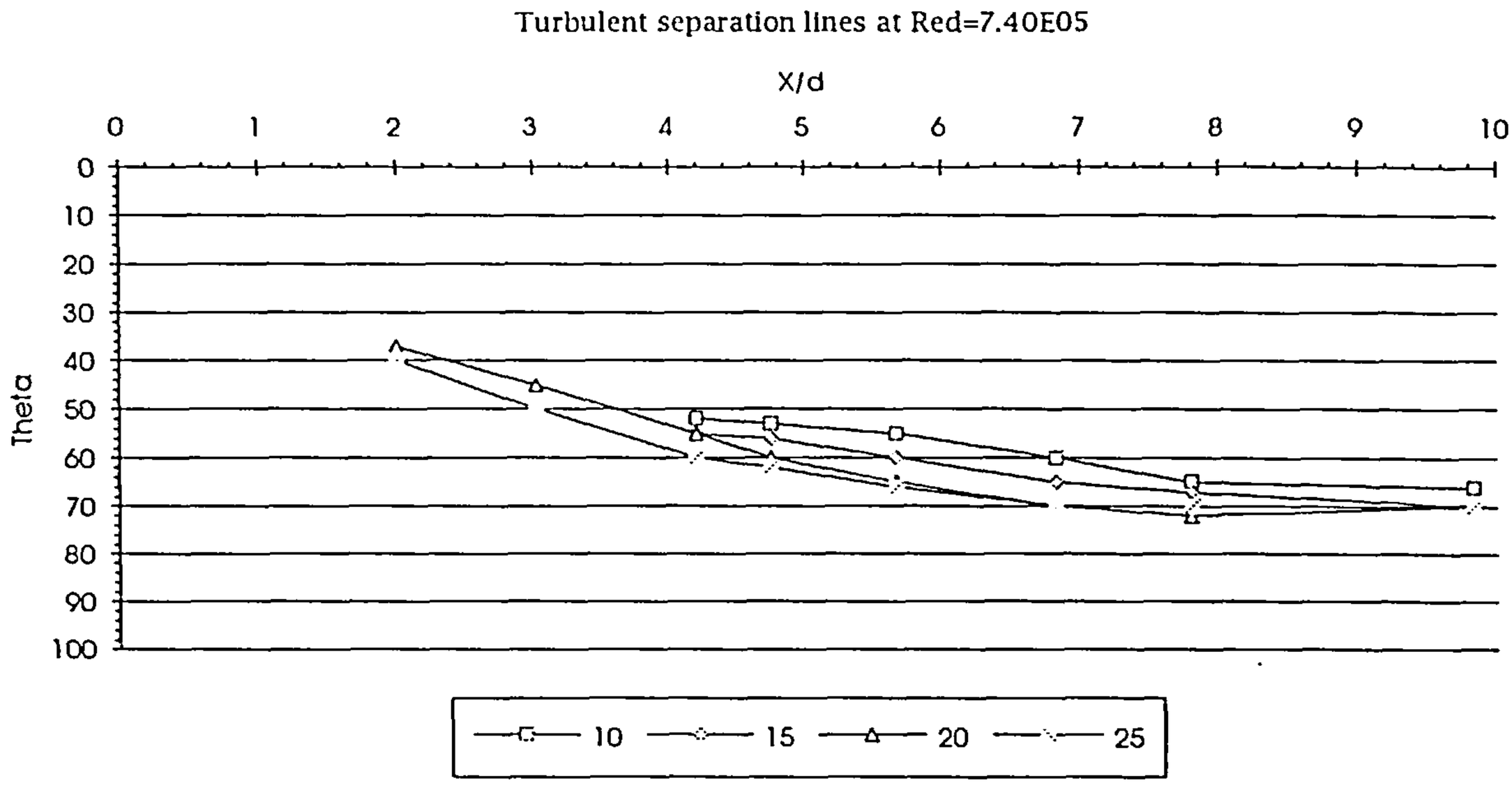

Figure 7.4.6.30

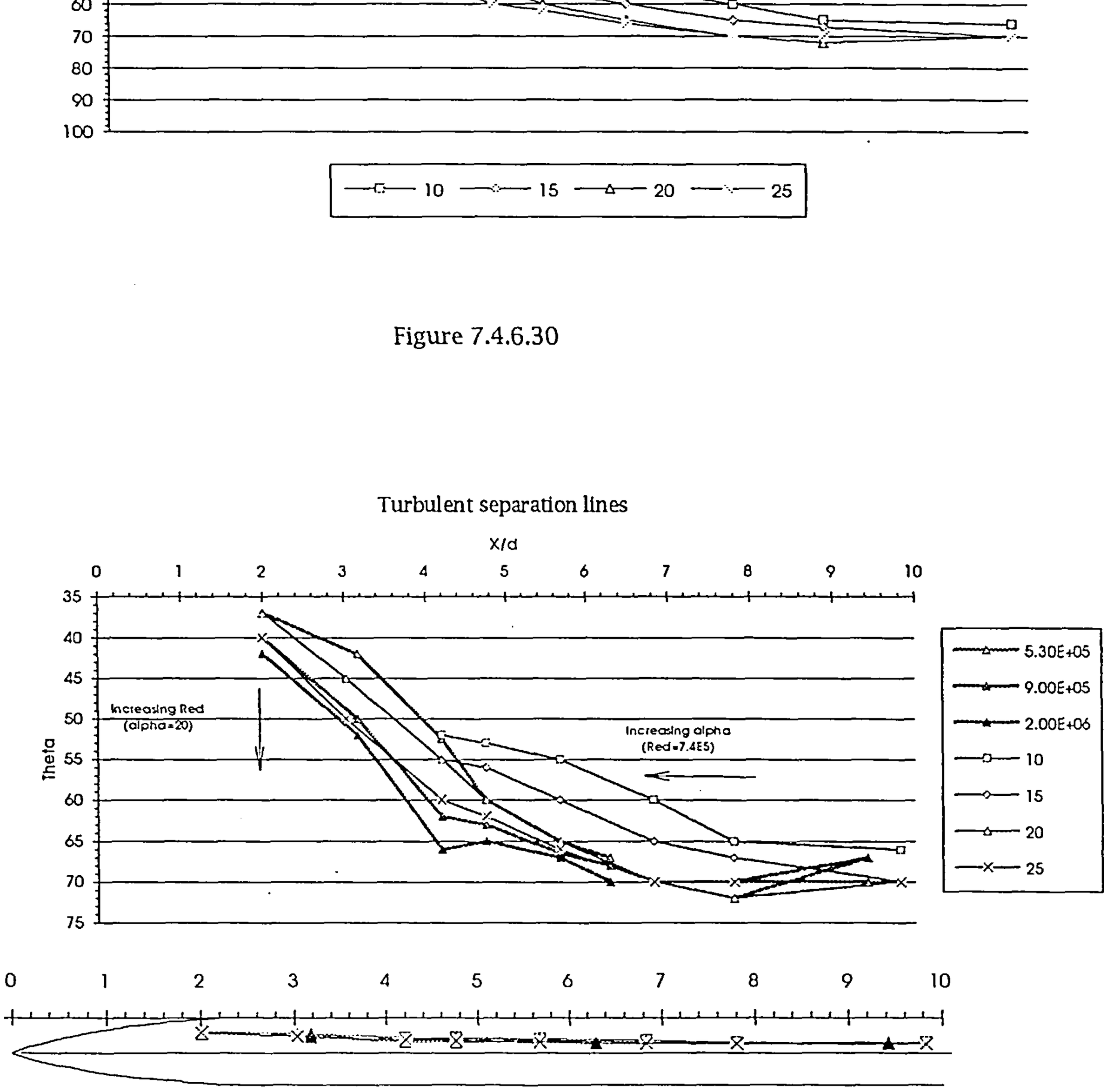

Figure 7.4.6.31

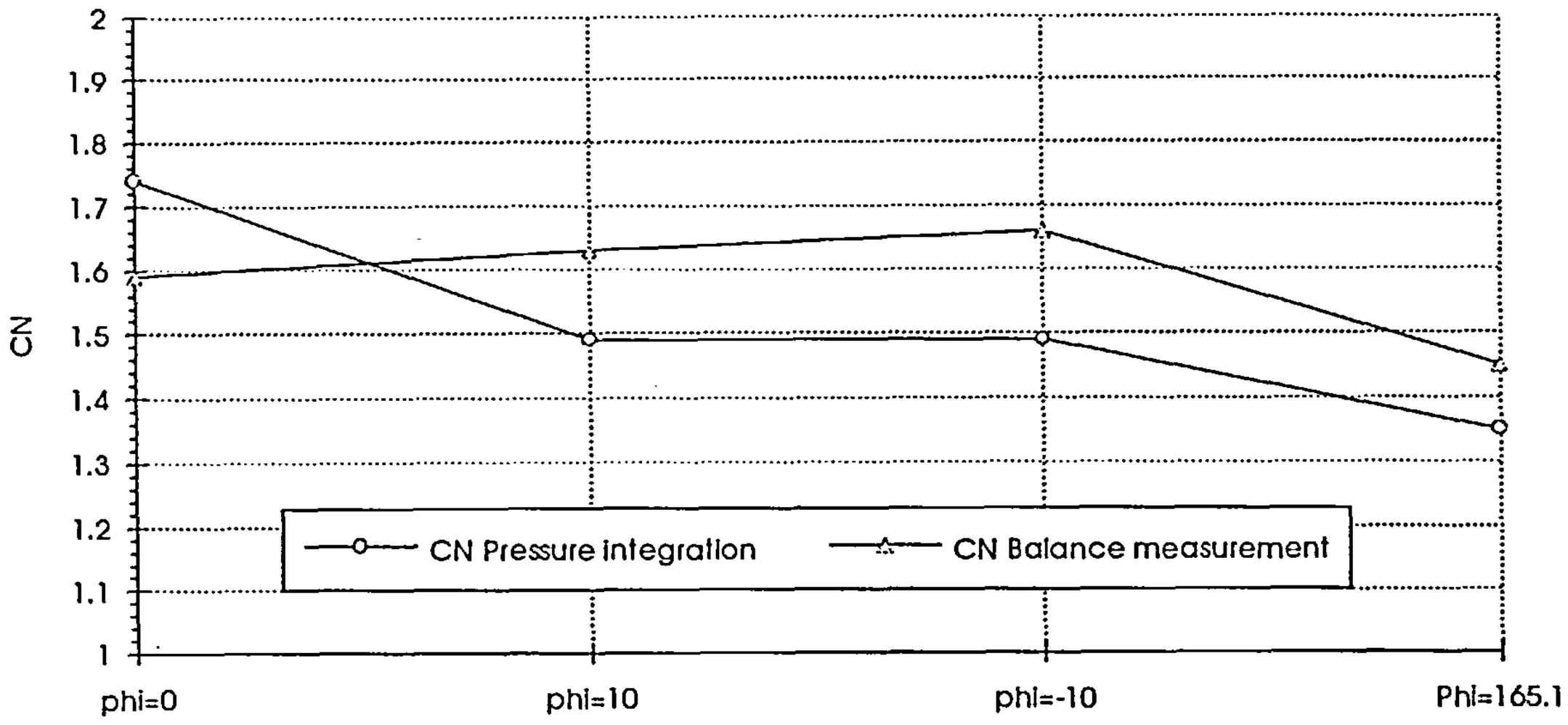

Figure 7.4.7.1

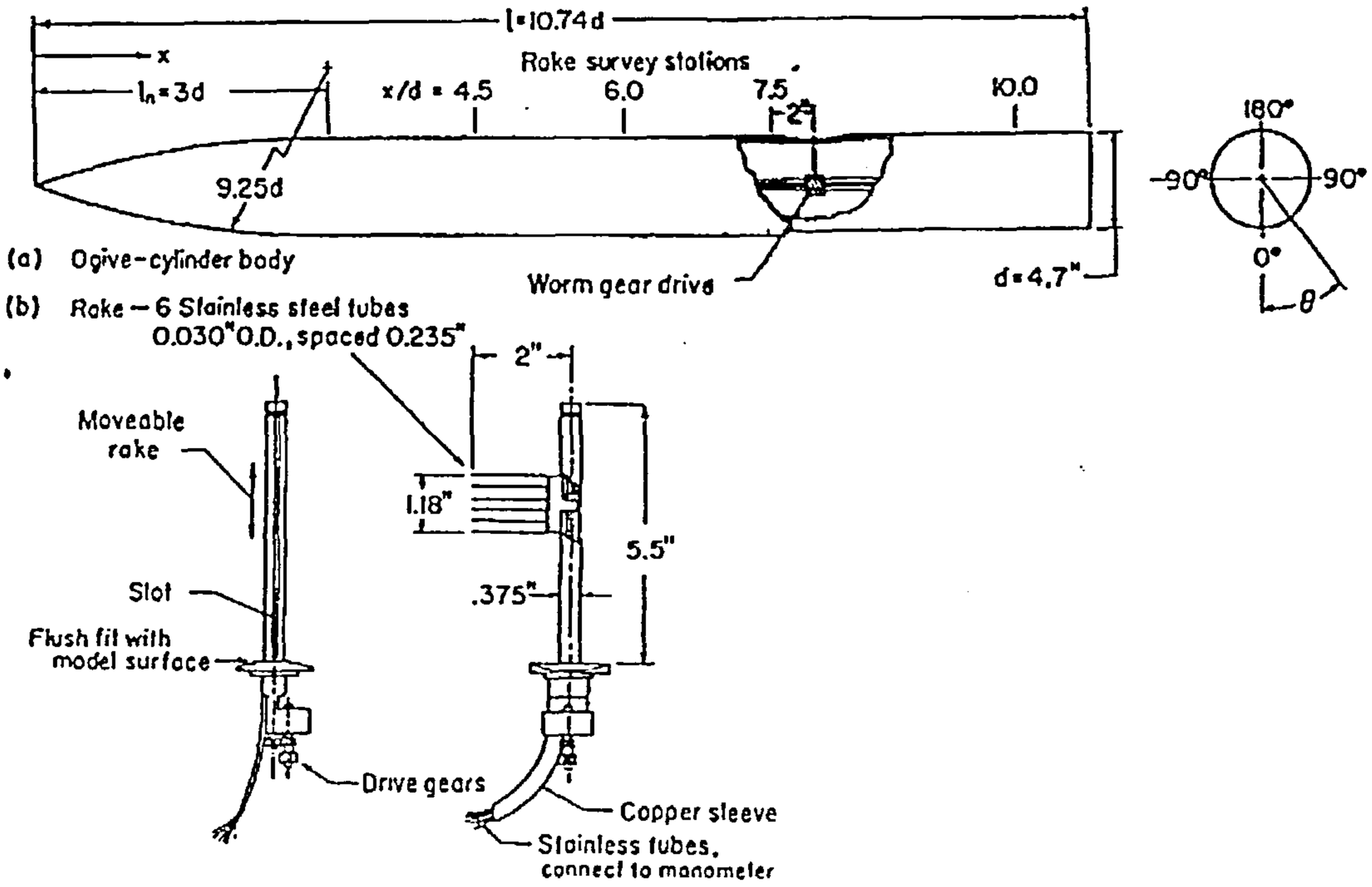

Figure 7.5.1.1
(After Tinling and Allen [32])

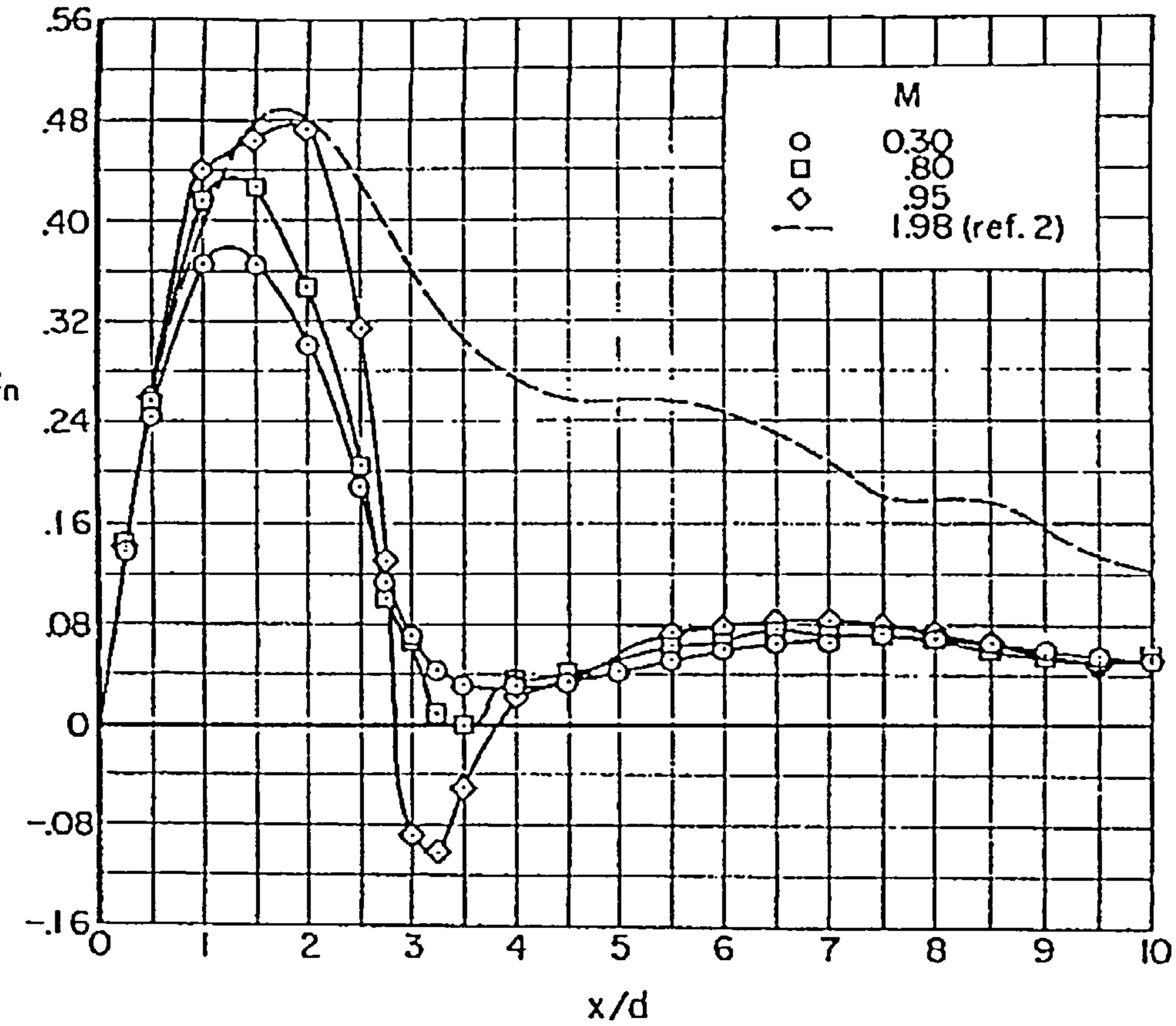

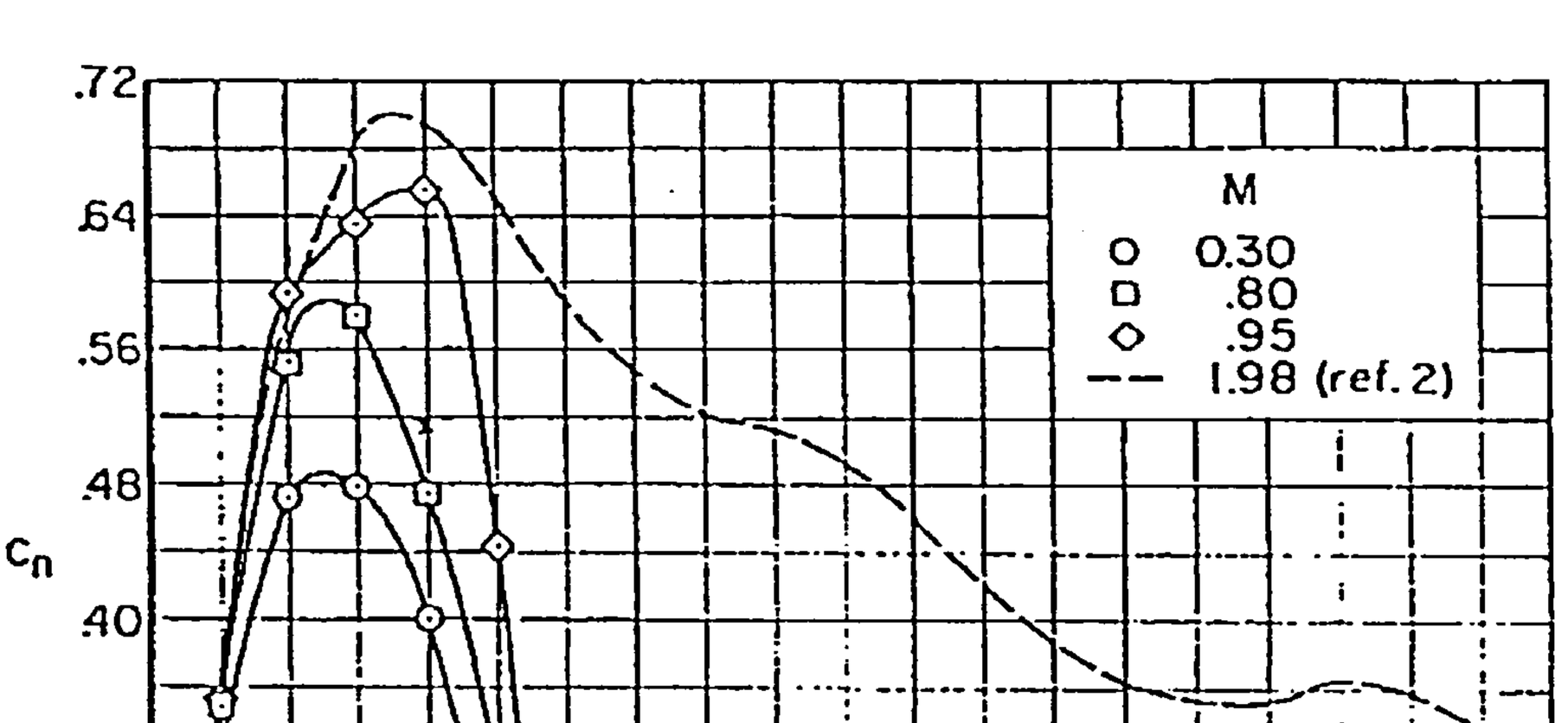

Figure 7.5.2.1

(After Tinling and Allen [32])

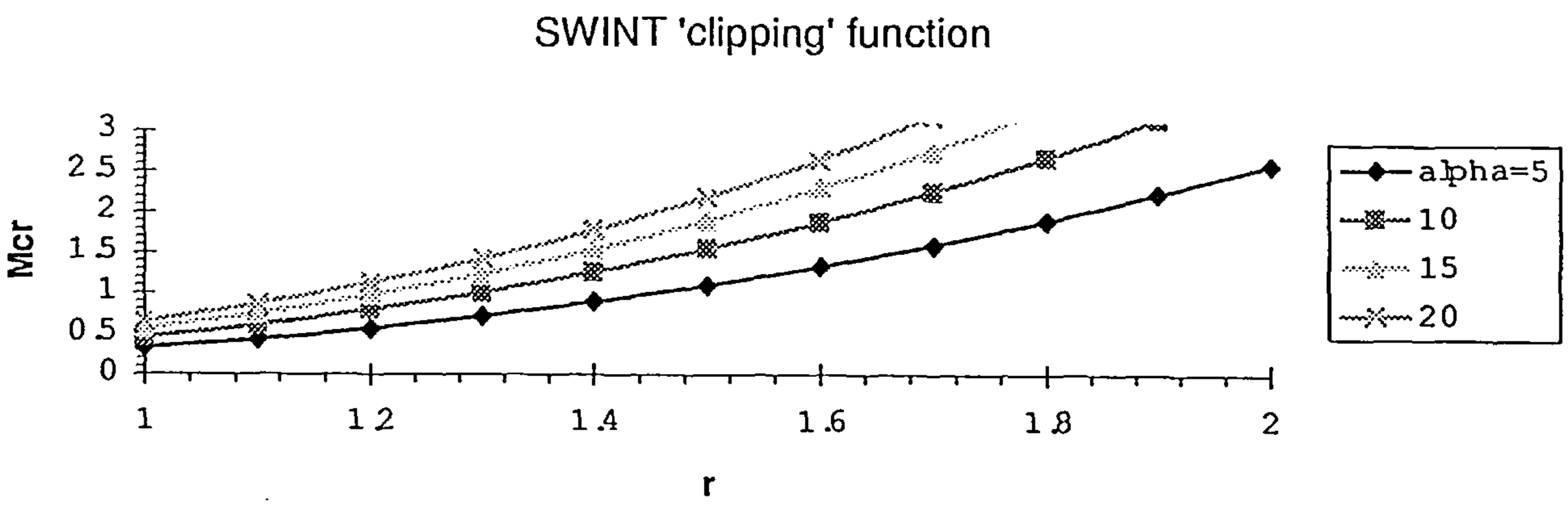

Figure 9.1.3.1

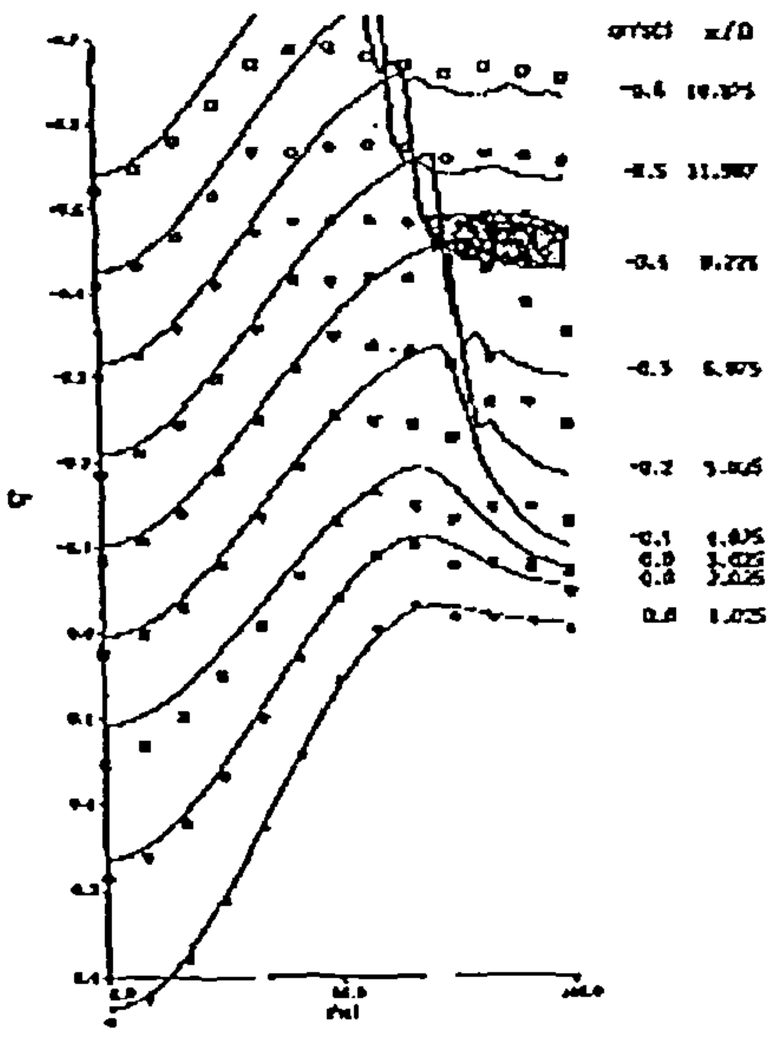

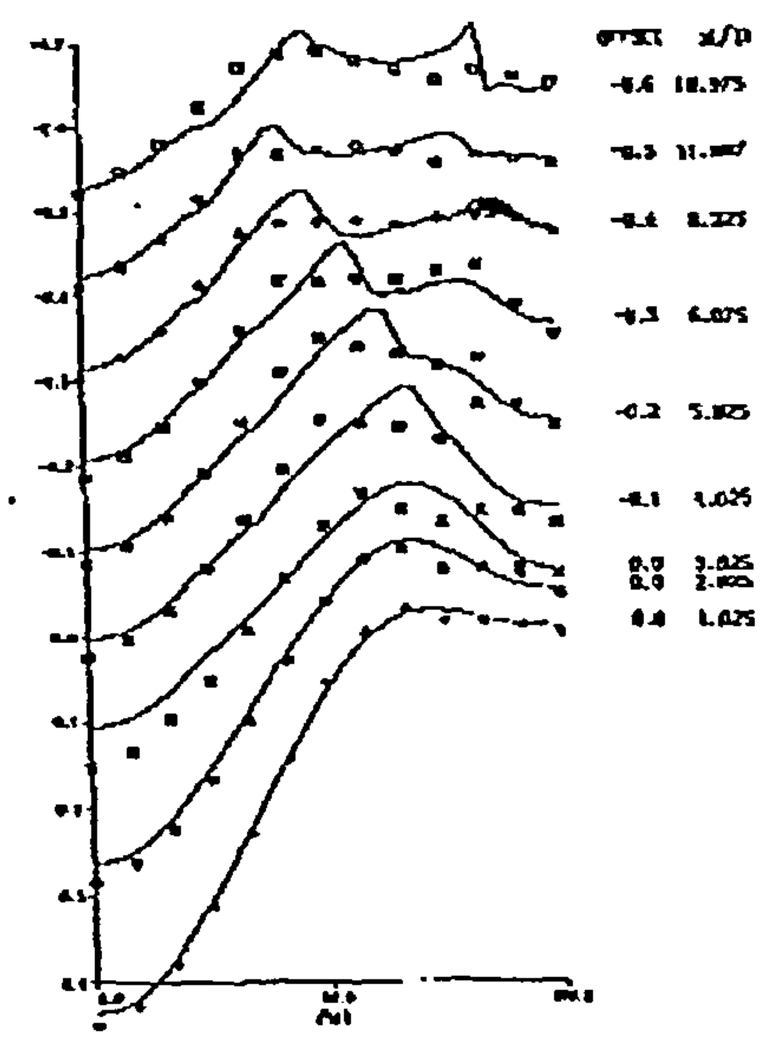

Figure 9.1.3.2 SWINT pressure distribution without clipping (left) and Figure 9.1.3.3 with clipping (right)

(After Jones et al [41])

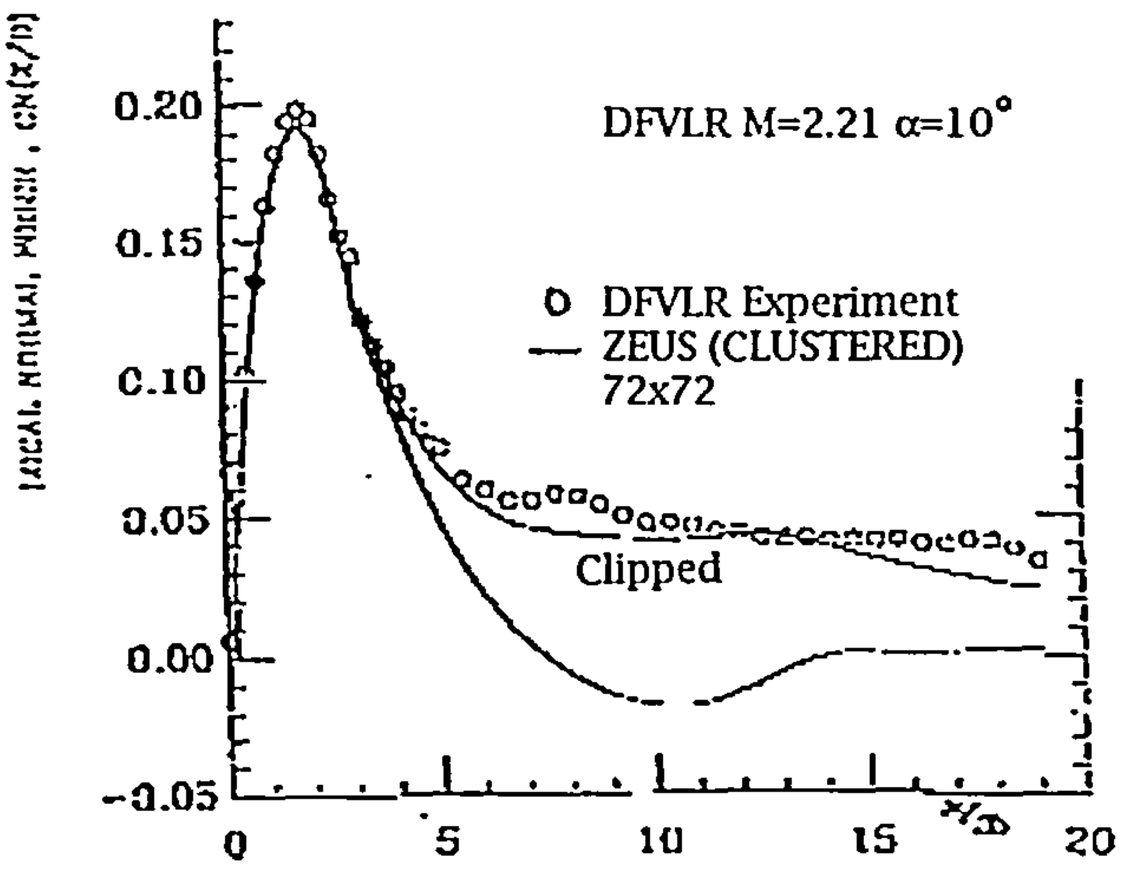

Figure 9.1.3.4 Local lift coefficient for DFVLR body. ZEUS with and without clipping.

(After Jones et al [41])

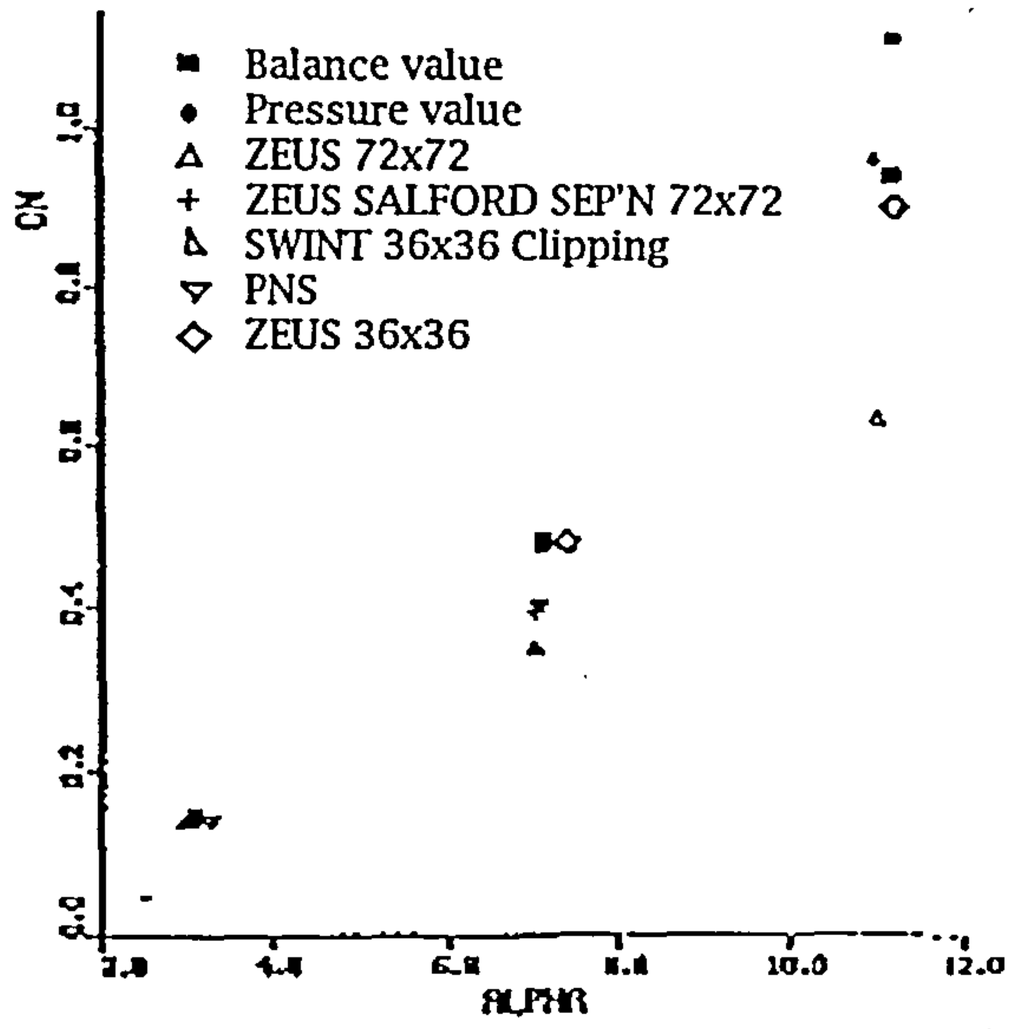

Figure 9.1.3.5 CN vs. α for M=2

(By Jones et al [41])

Figure 9.2.2.1 Zeta contours at z=4.0125, M=2.5, α=14

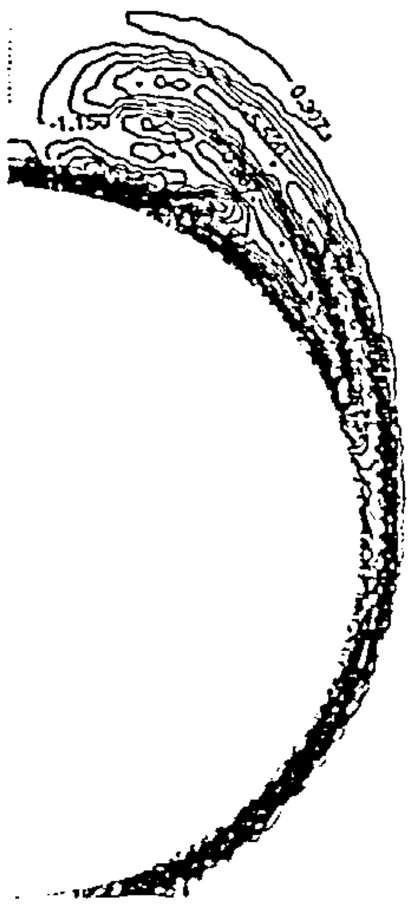

Figure 9.2.2.2 Eta contours at z=4.0125, M=2.5, α=14

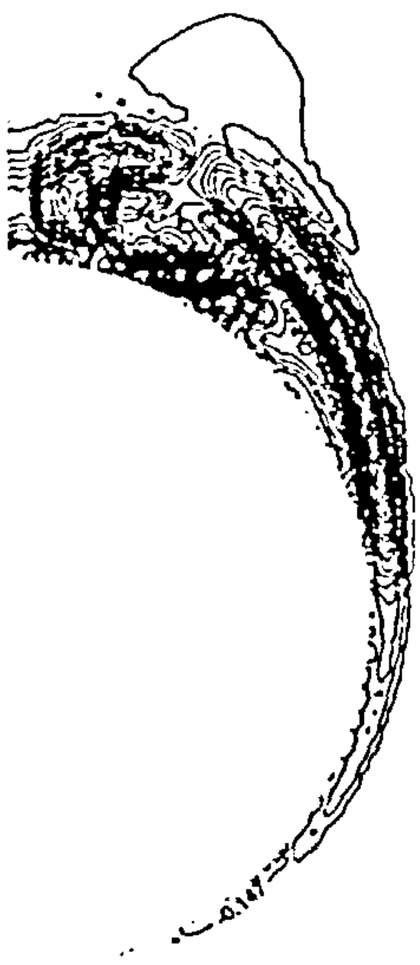

Figure 9.2.2.3 Xi contours at z=4.0125, M=2.5, α=14

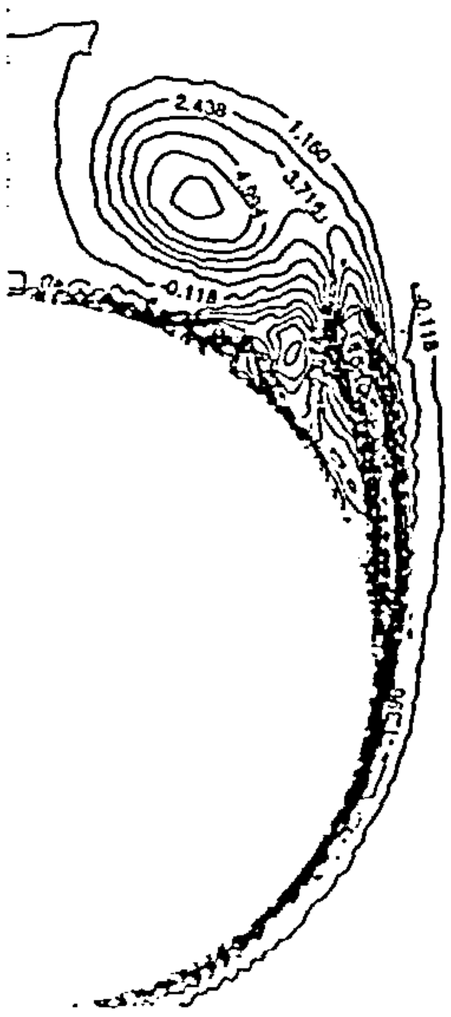

Figure 9.2.2.4 Zeta contours at z=5.7625, M=2.5, α=14

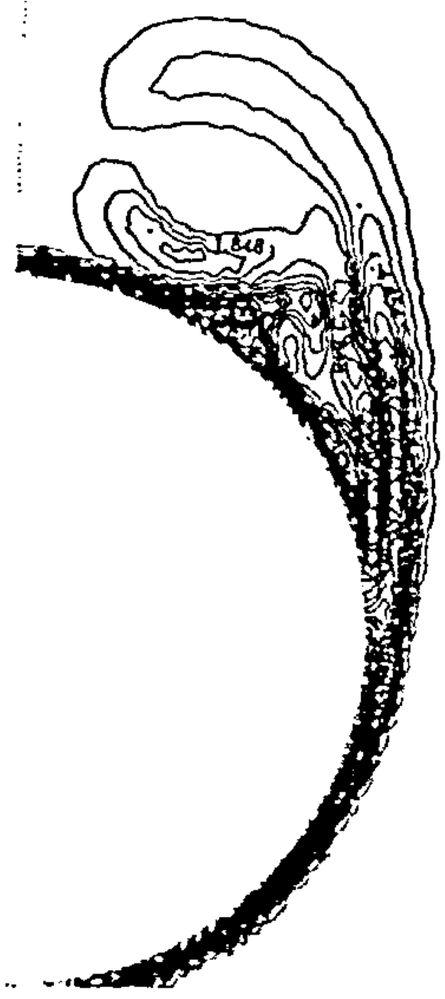

Figure 9.2.2.5 Eta contours at z=5.7625, M=2.5, α=14

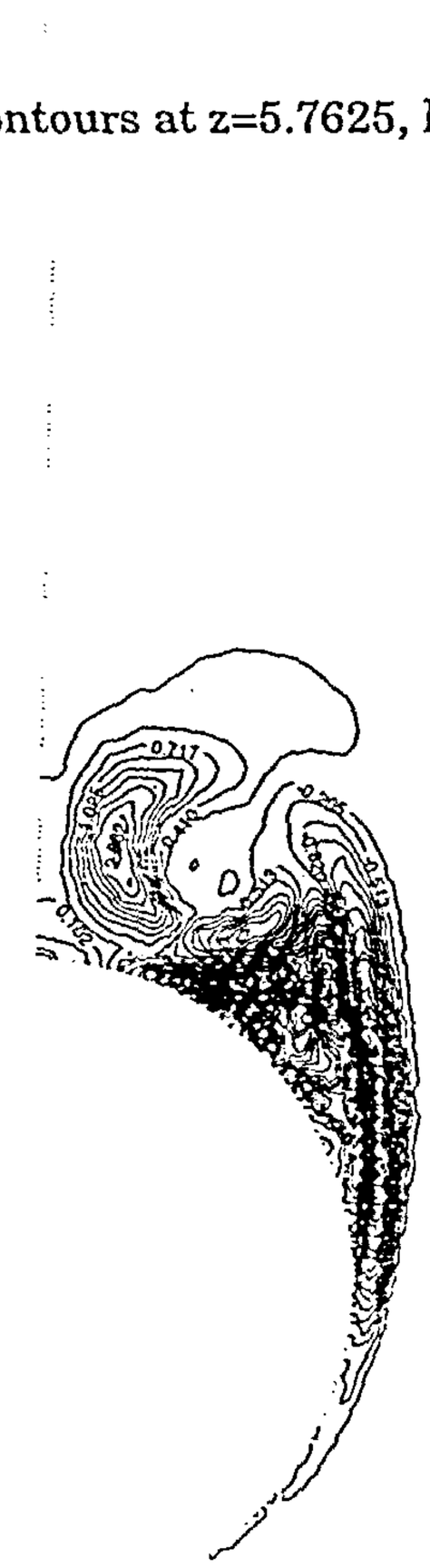

Figure 9.2.2.6 Xi contours at z=5.7625, M=2.5, α=14

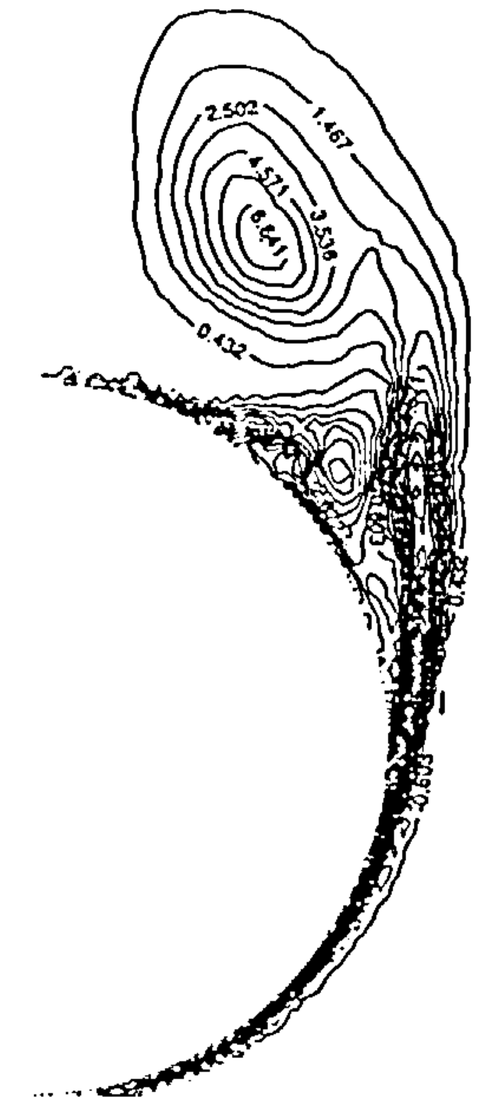

Figure 9.2.2.7 Zeta contours at z=7.2650, M=2.5, α=14

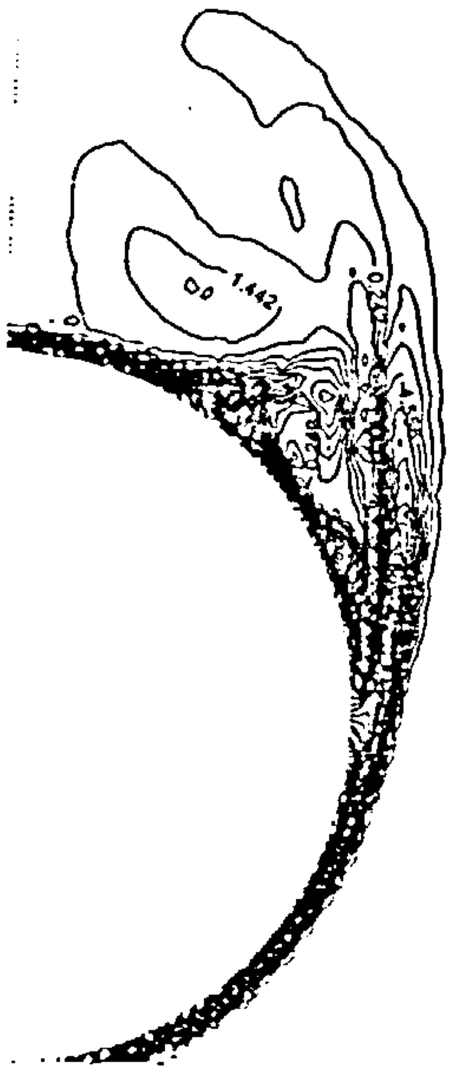

Figure 9.2.2.8 Eta contours at z=7.2650, M=2.5, α=14

Figure 9.2.2.9 Xi contours at z=7.2650, M=2.5, α=14

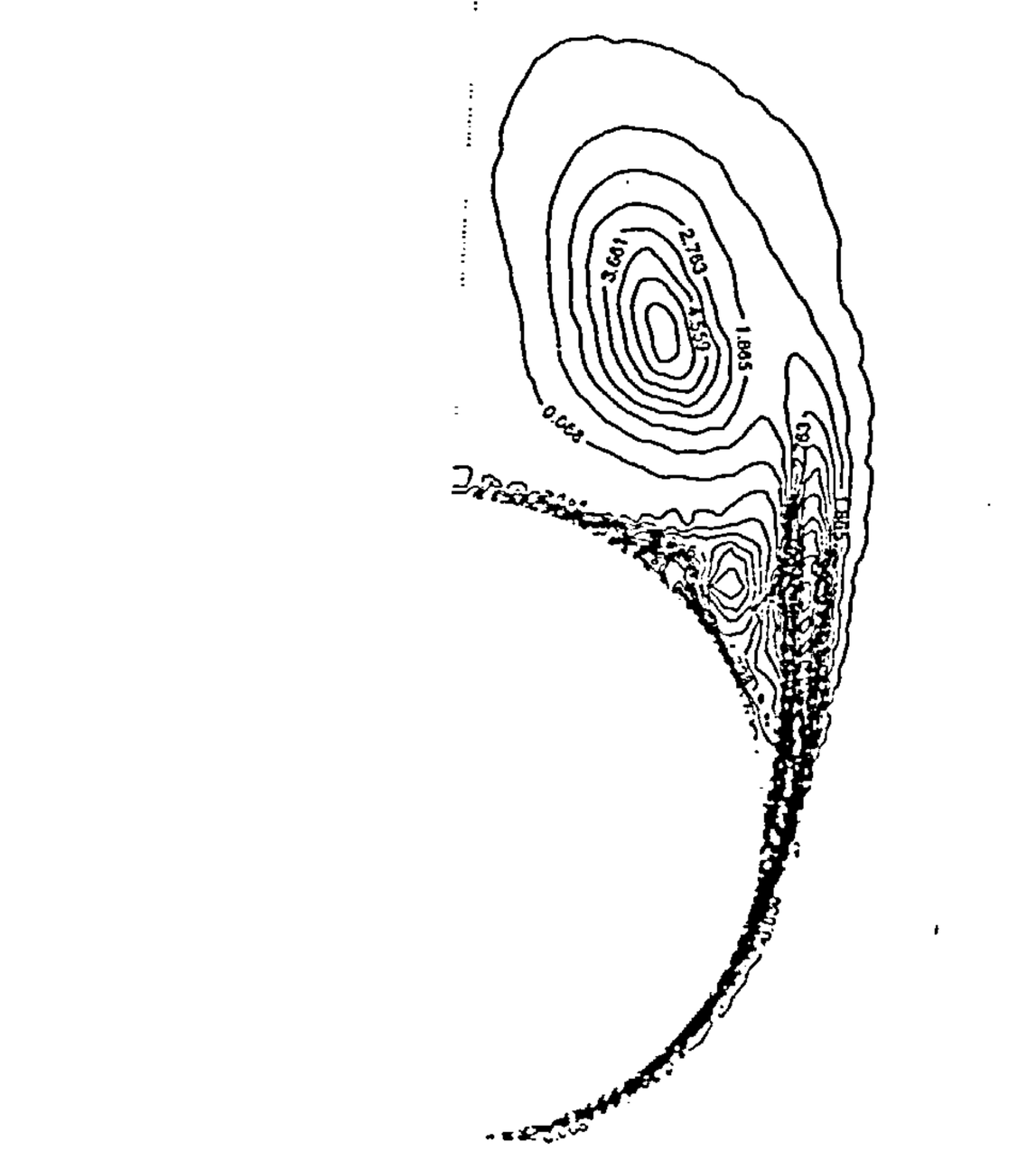

Figure 9.2.2.10 Zeta contours at z=8.5125, M=2.5, α=14

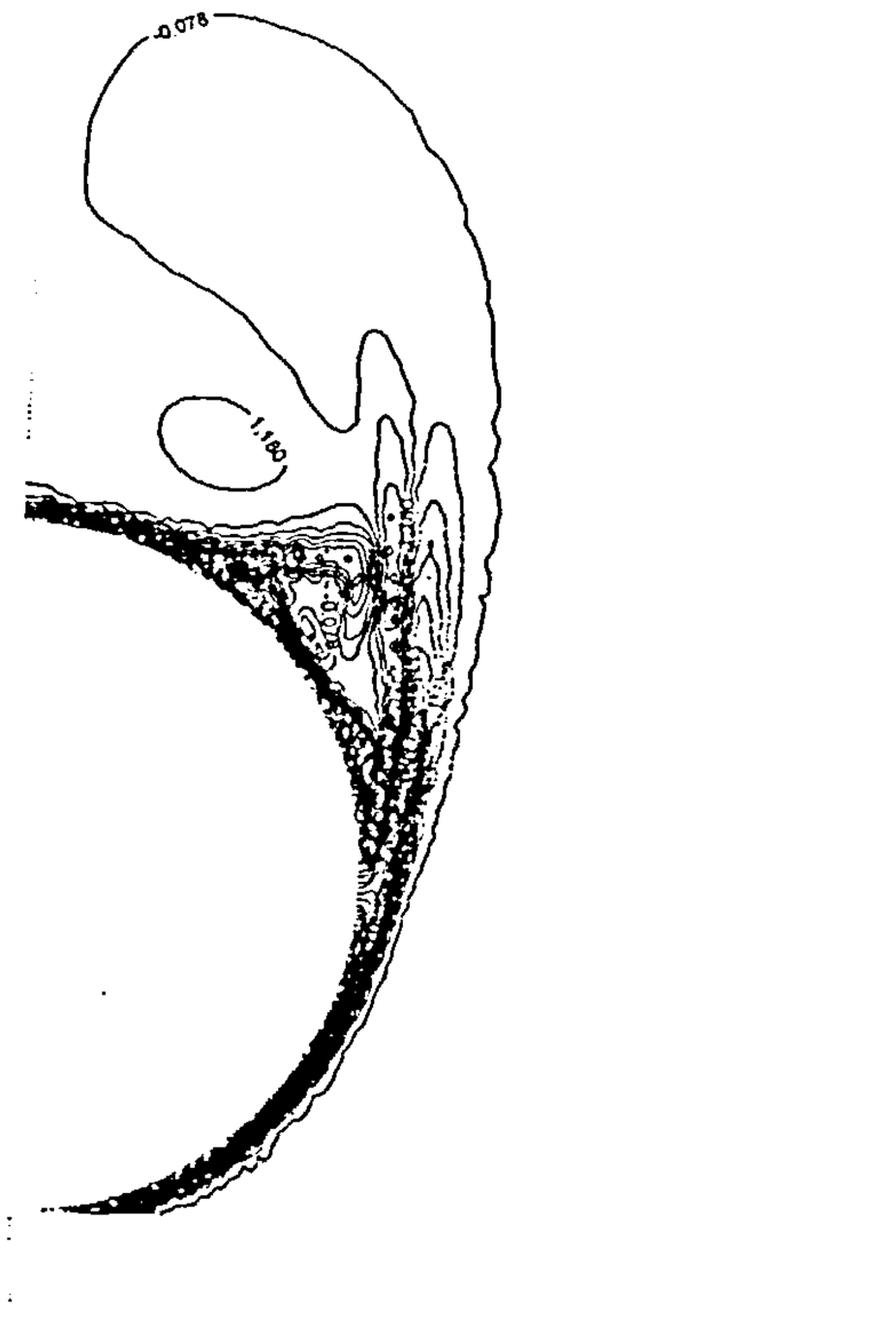

Figure 9.2.2.11 Eta contours at z=8.5125, M=2.5, α=14

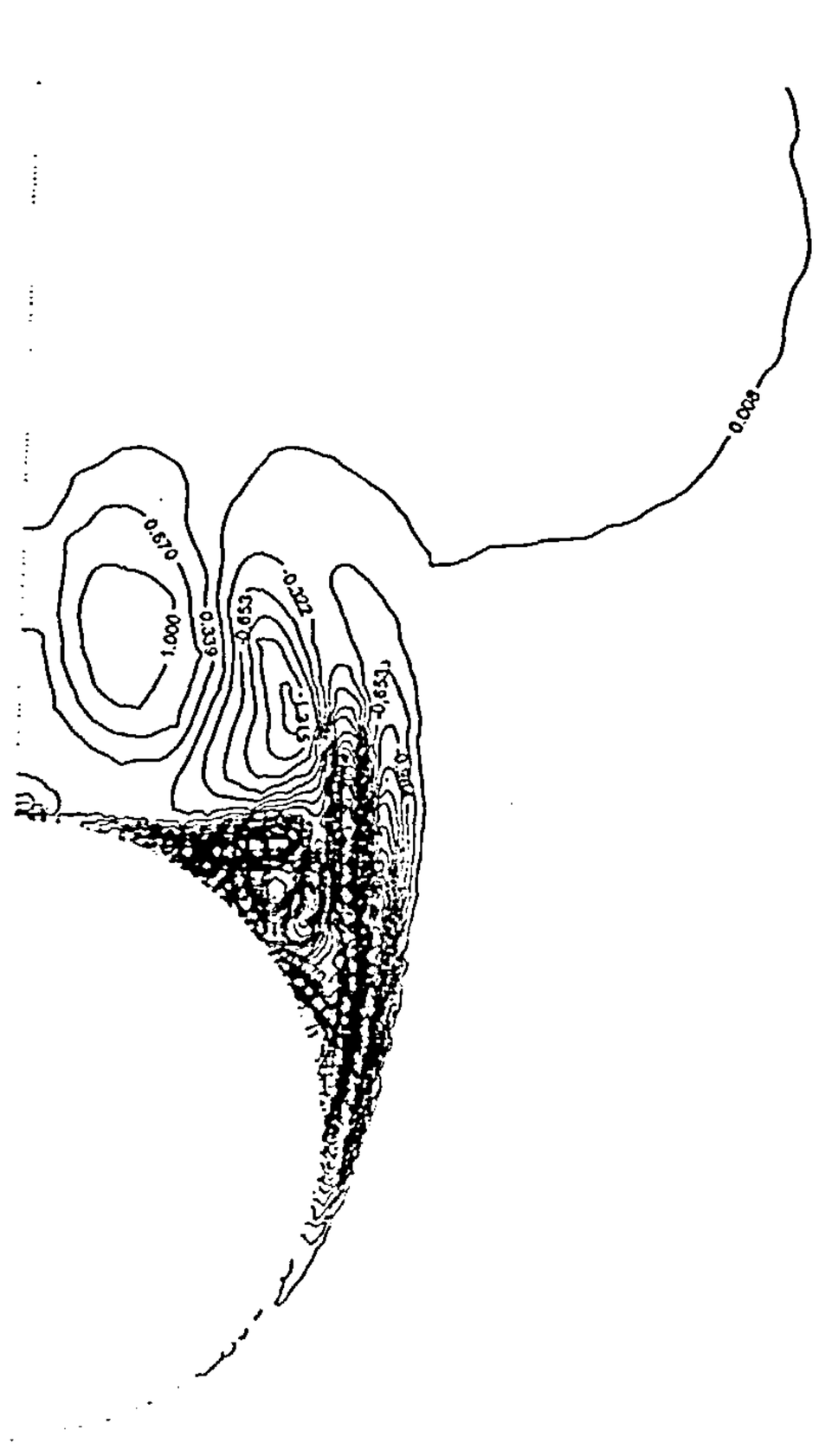

Figure 9.2.2.12 Xi contours at z=8.5125, M=2.5, α=14

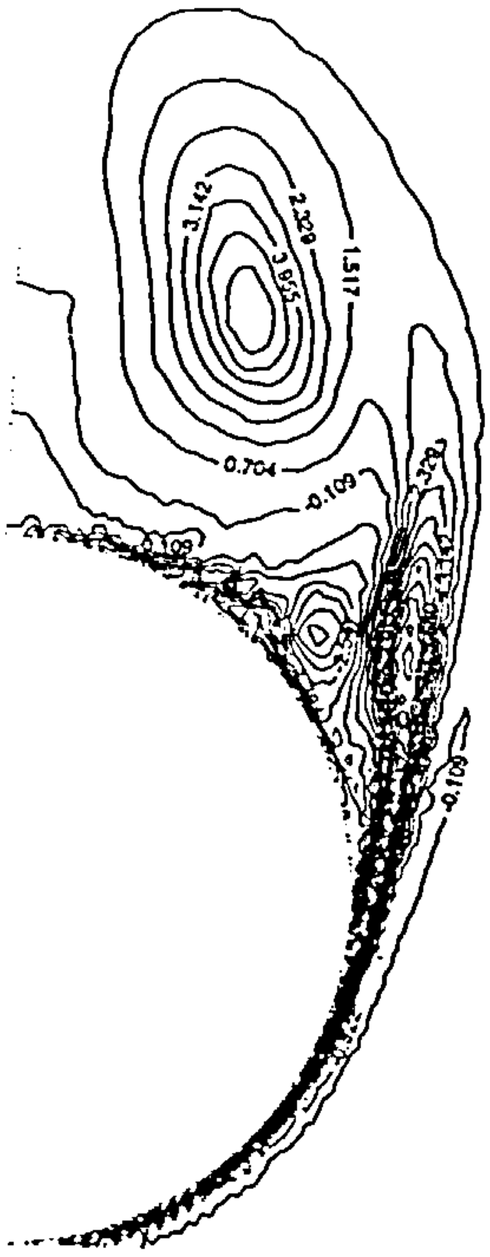

Figure 9.2.2.13 Zeta contours at z=9.7625, M=2.5, α=14

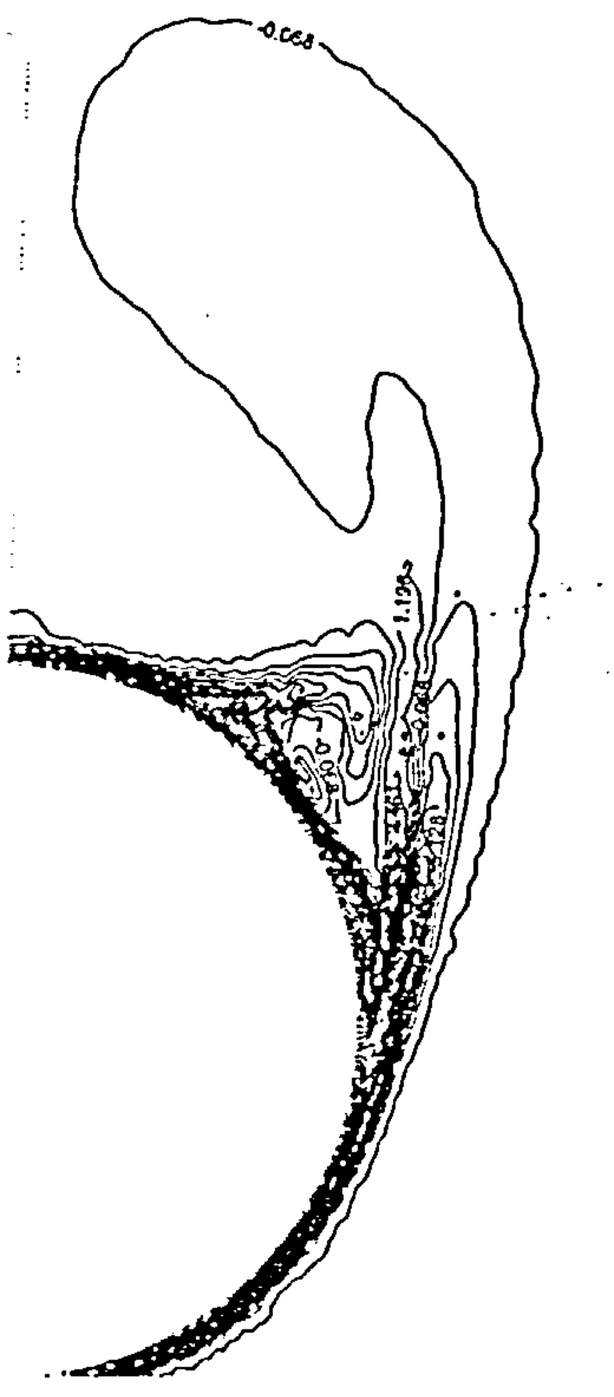

Figure 9.2.2.14 Eta contours at z=9.7625, M=2.5, α=14

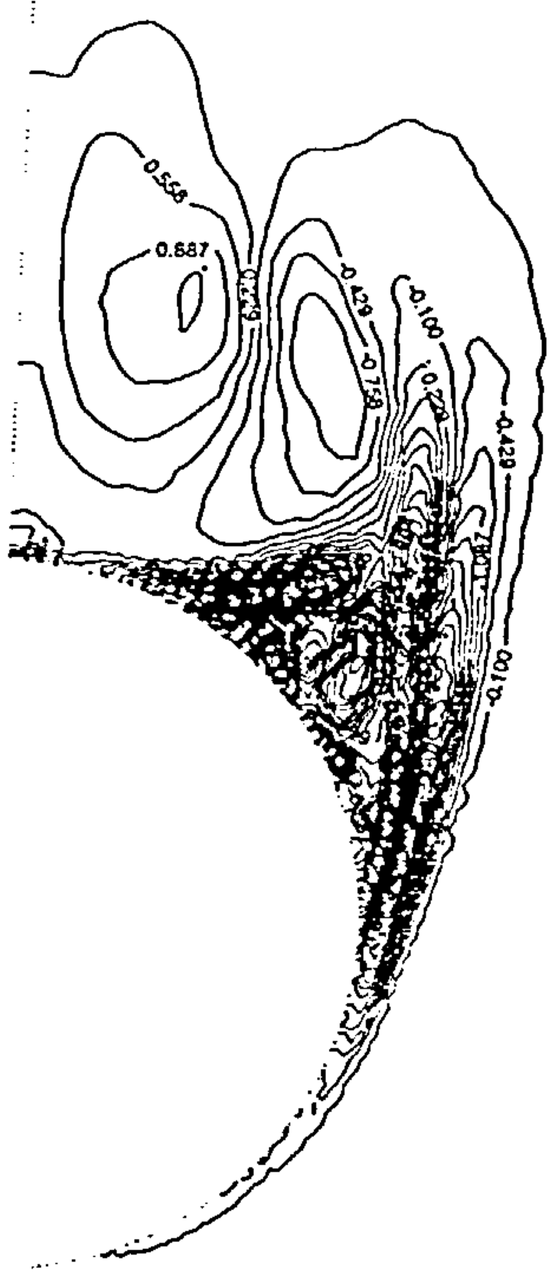

Figure 9.2.2.15 Xi contours at z=9.7625, M=2.5, α=14

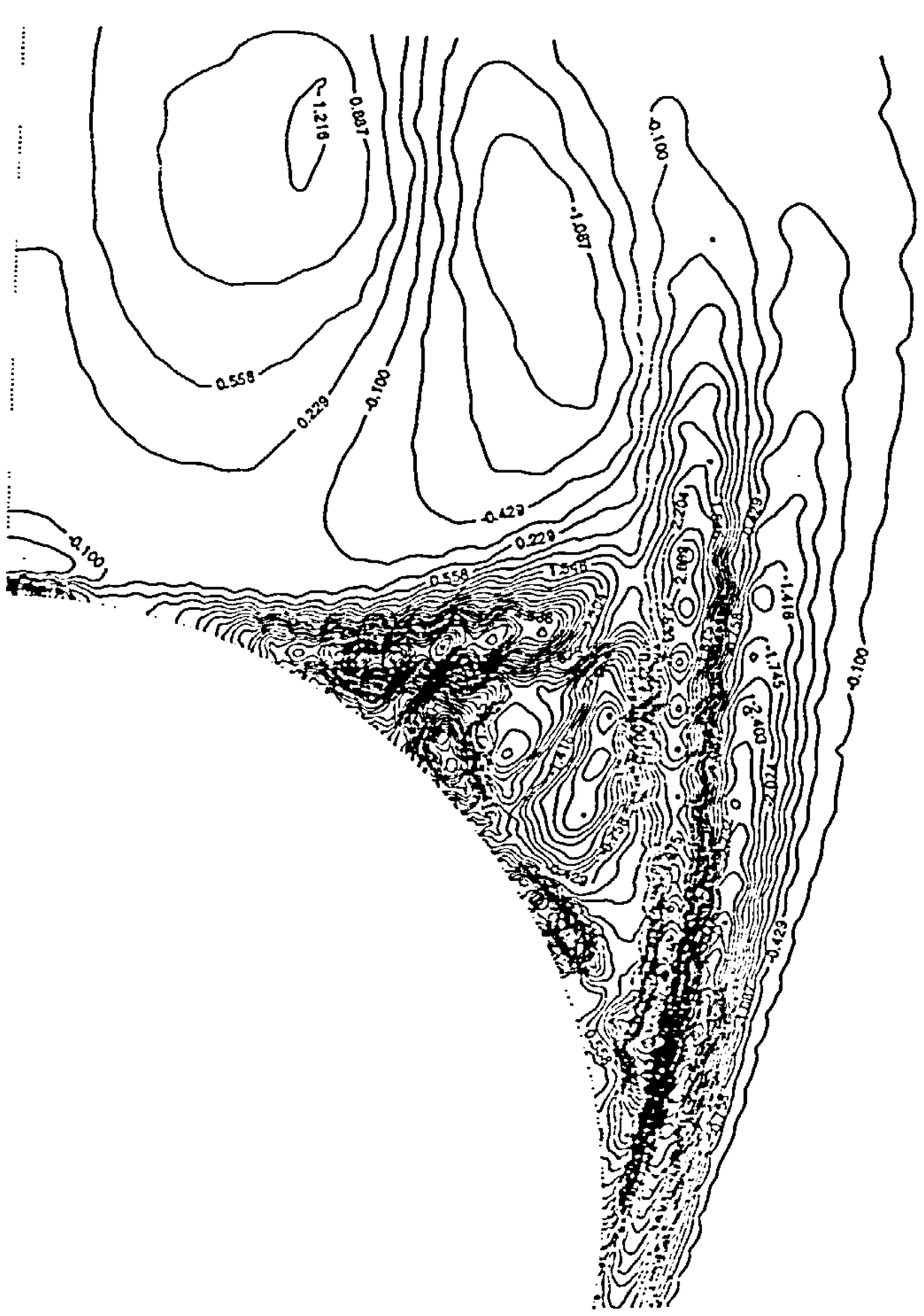

Figure 9.2.2.16 Eta contours at z=9.7625, M=2.5, α=14

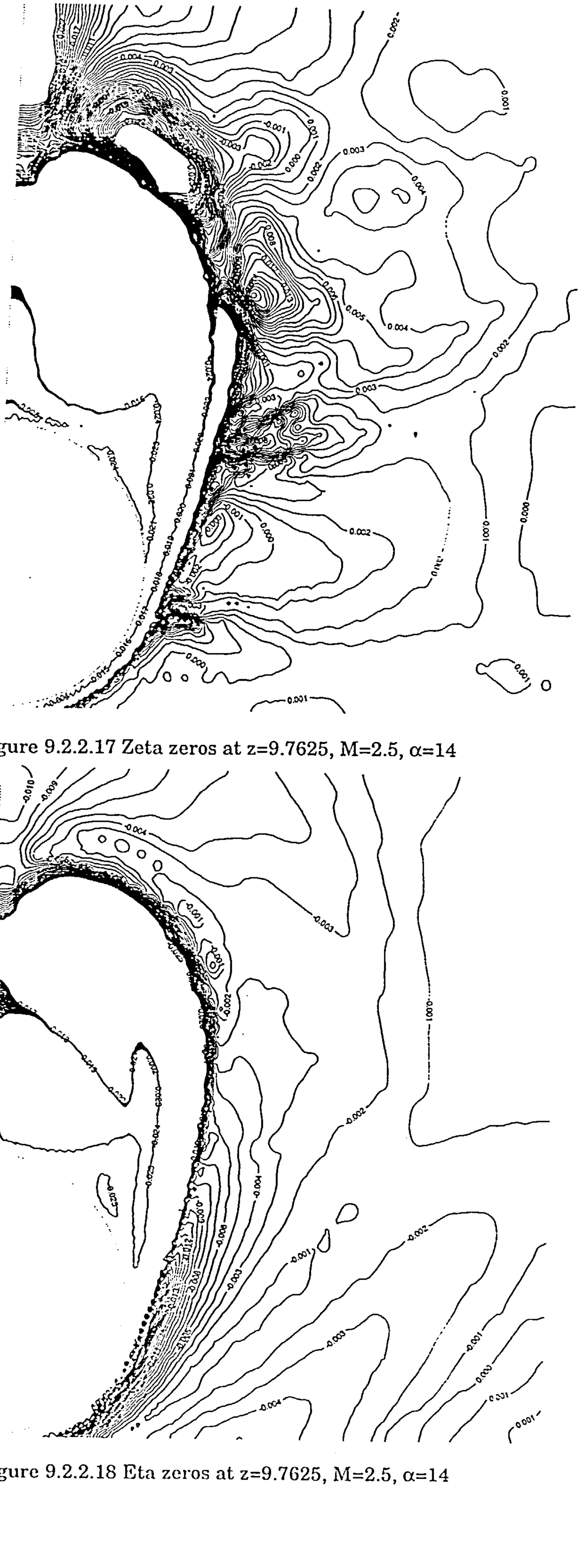

Figure 9.2.2.17 Zeta zeros at z=9.7625, M=2.5, α=14

Figure 9.2.2.18 Eta zeros at z=9.7625, M=2.5, α=14

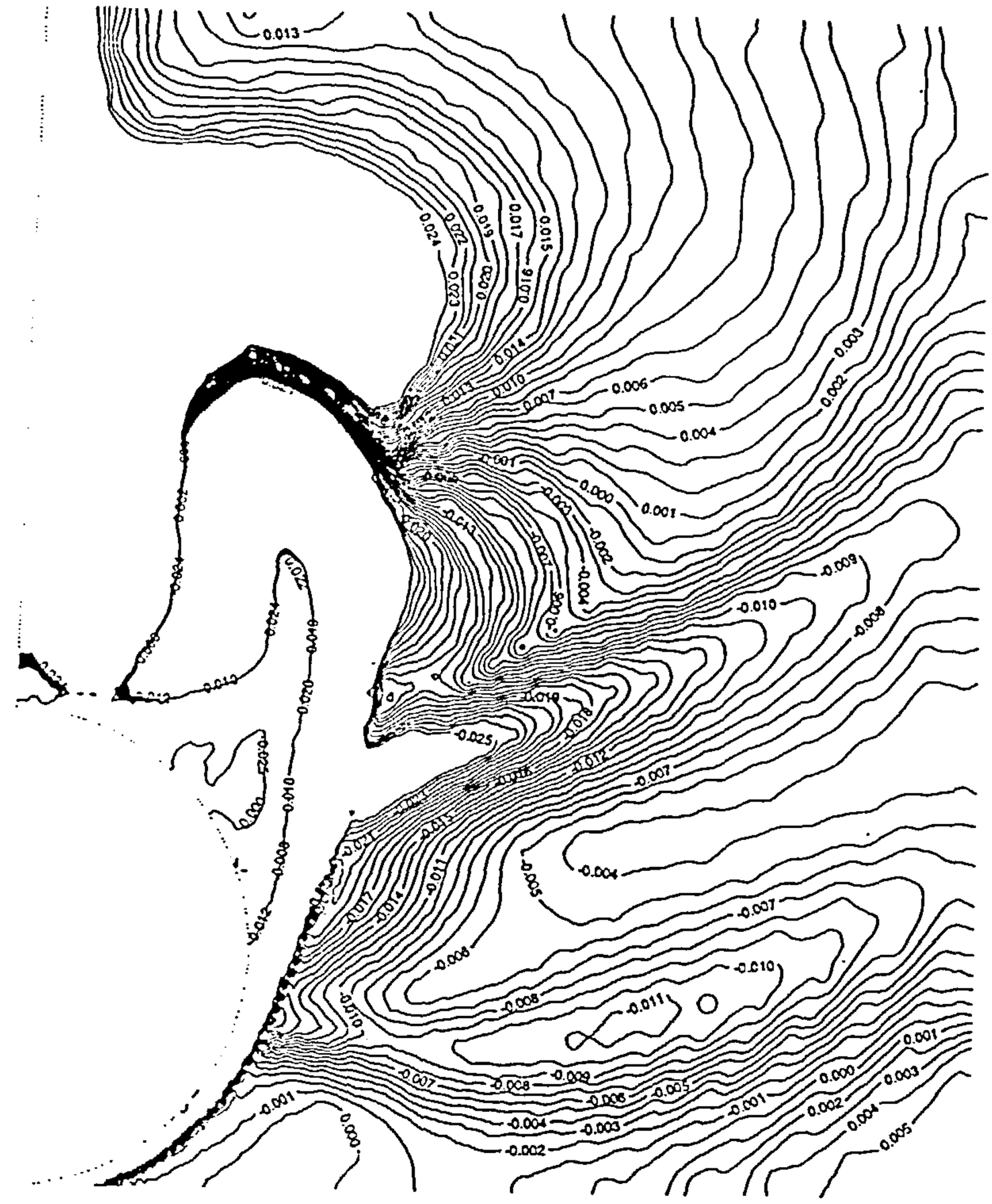

Figure 9.2.2.19 Xi zeros at z=9.7625, M=2.5, α=14

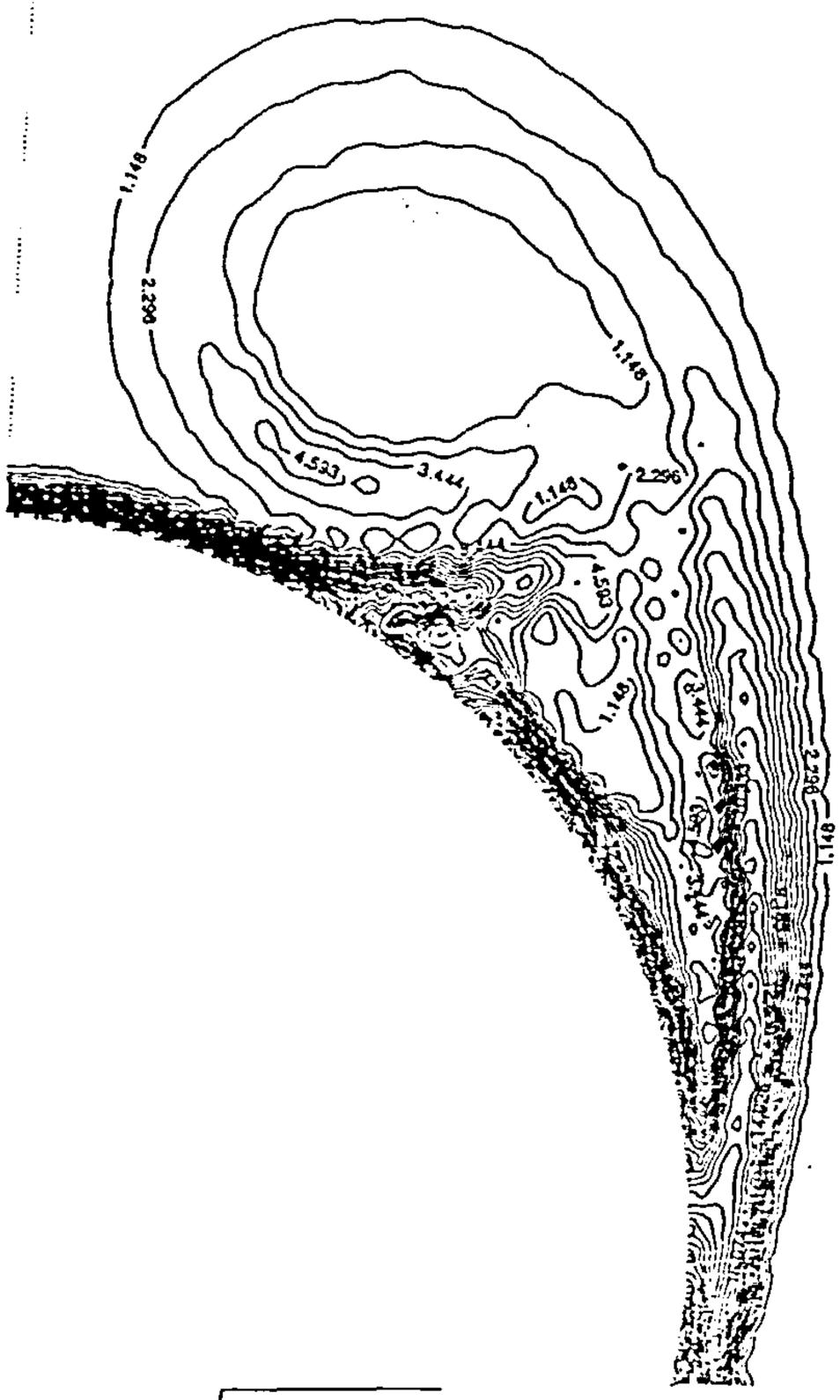

Figure 9.2.2.20 $\sqrt{\eta^2 + \xi^2}$ contours at z=5.76, M=2.5, α=14

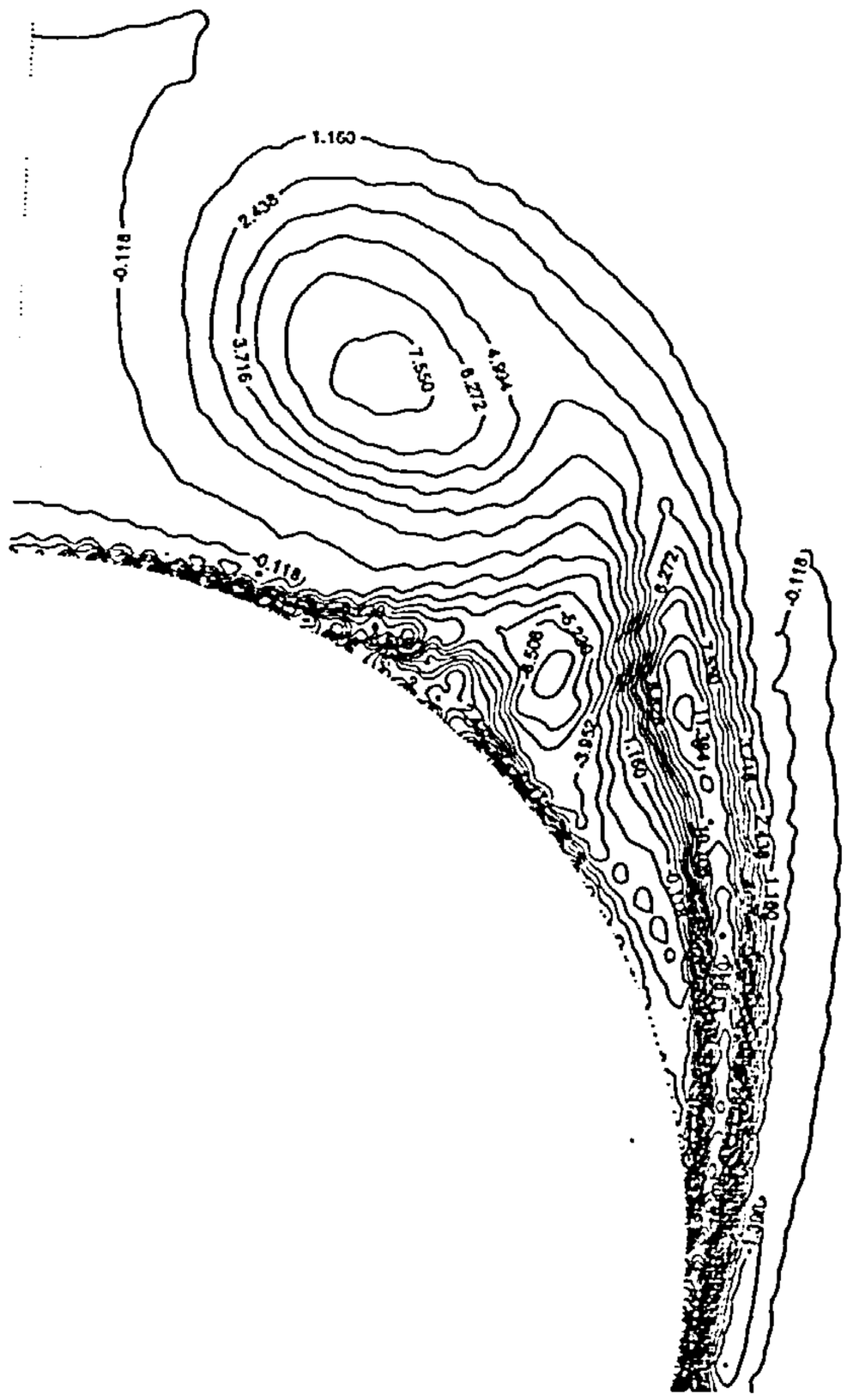

Figure 9.2.2.21 Zeta contours at z=5.76, M=2.5, α=14

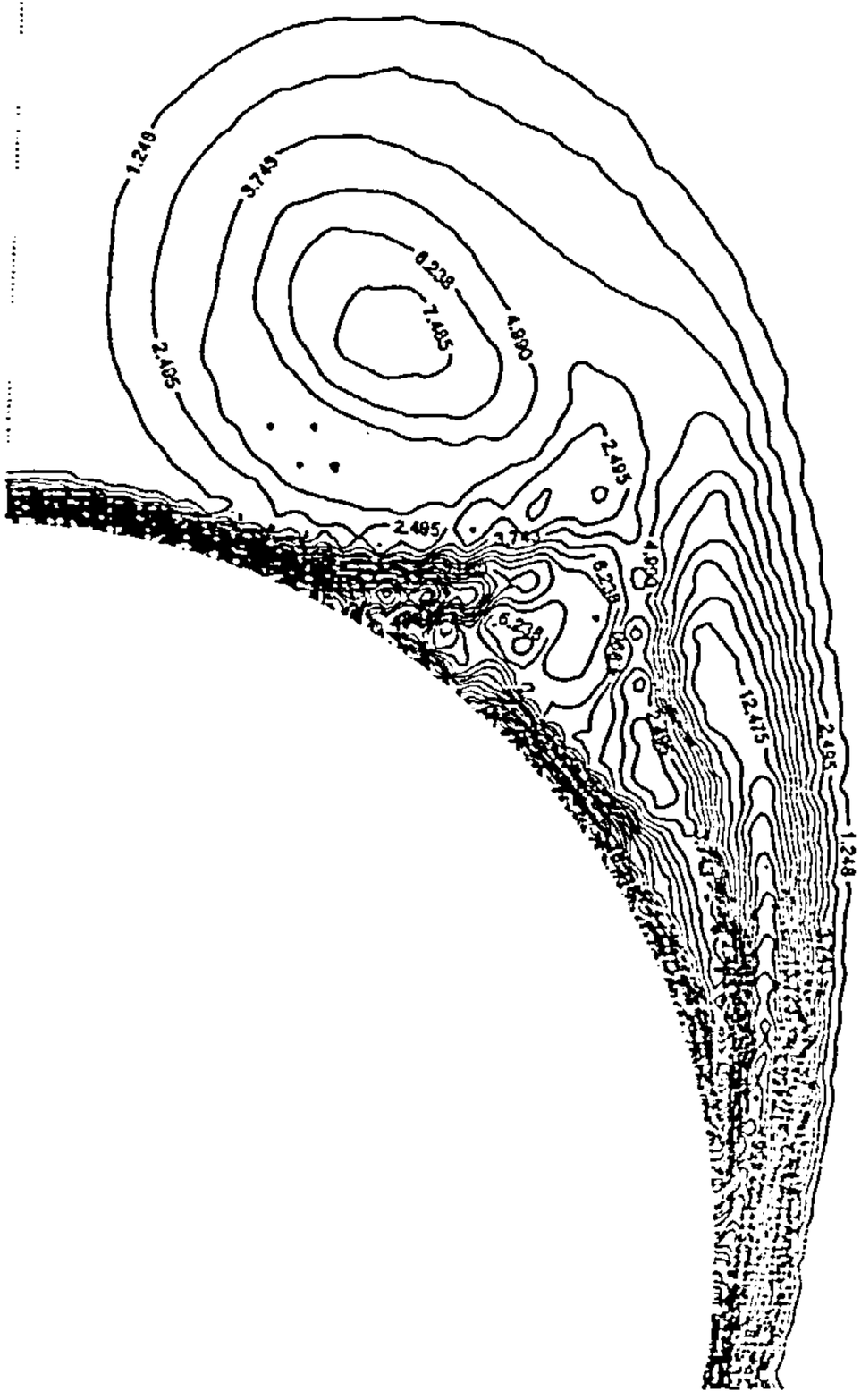

Figure 9.2.2.22 Total vorticity magnitude contours at z=5.76, M=2.5, α=14

Figure 9.2.2.23 non-Zeta magnitude as a % of total at z=4.0125, M=2.5, α=14

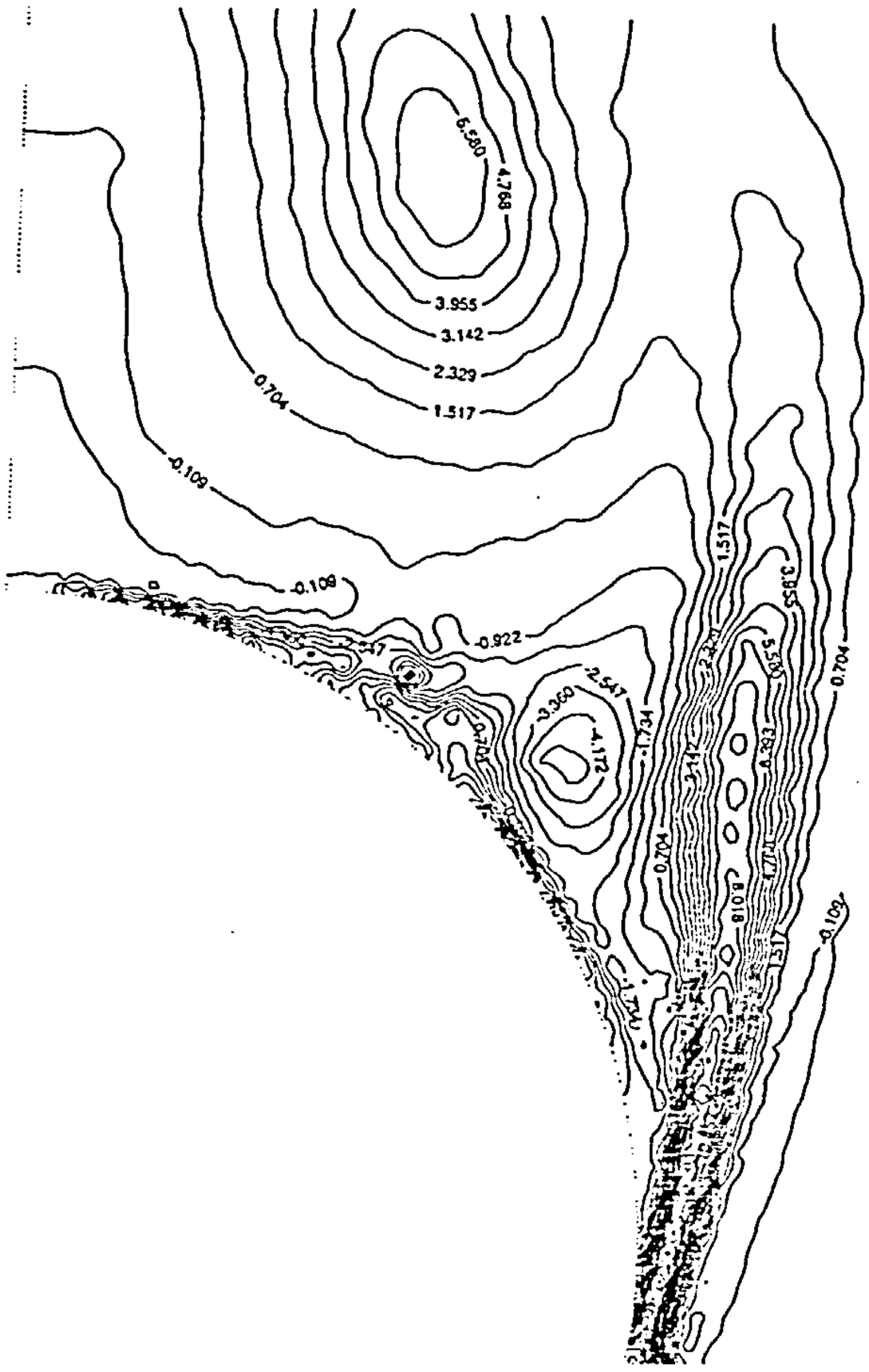

Figure 9.2.2.24 Zeta contours at z=9.7625, M=2.5, α=14

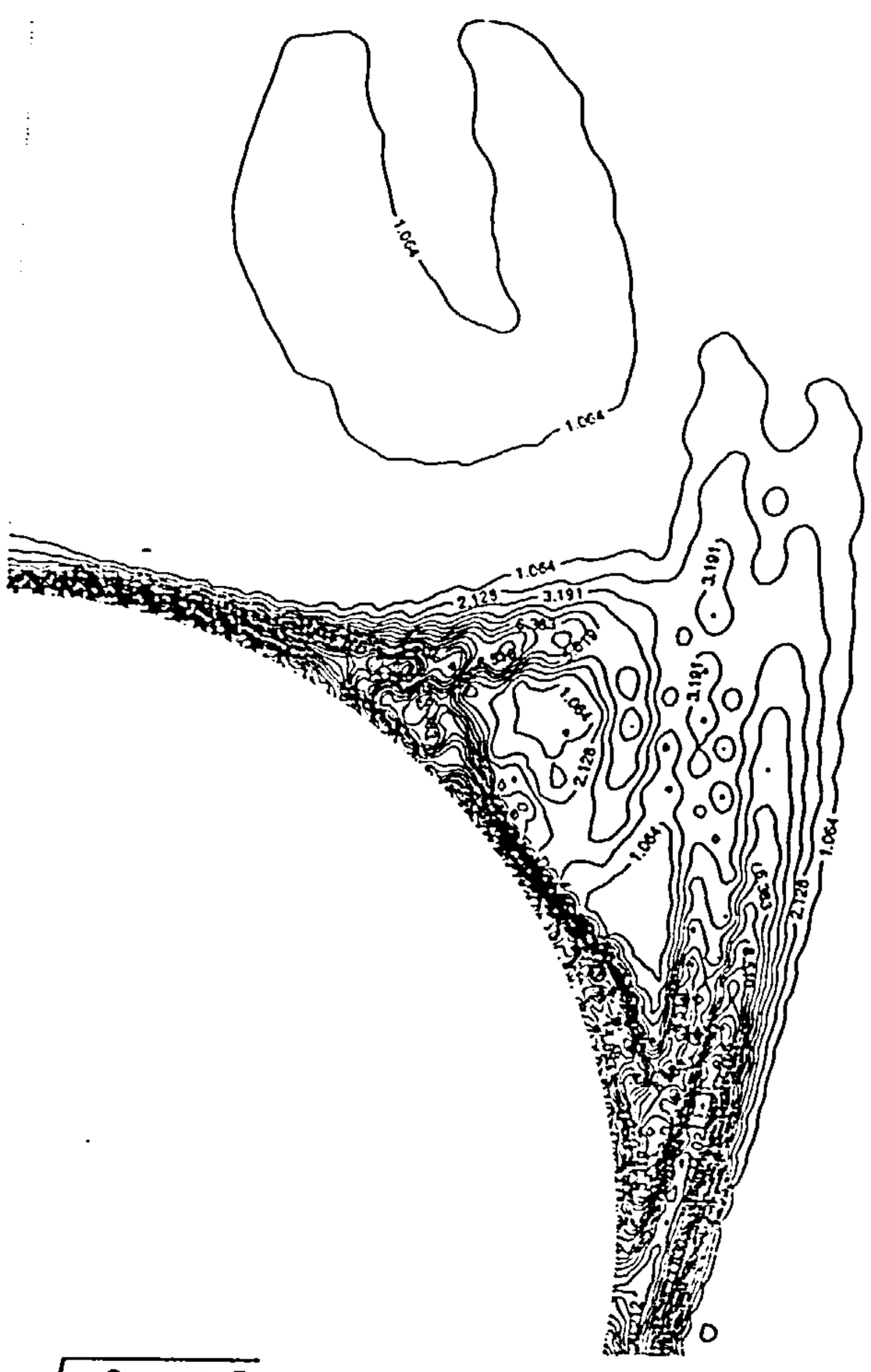

Figure 9.2.2.25 $\sqrt{\eta^2 + \xi^2}$ contours at z=9.7625, M=2.5, α=14

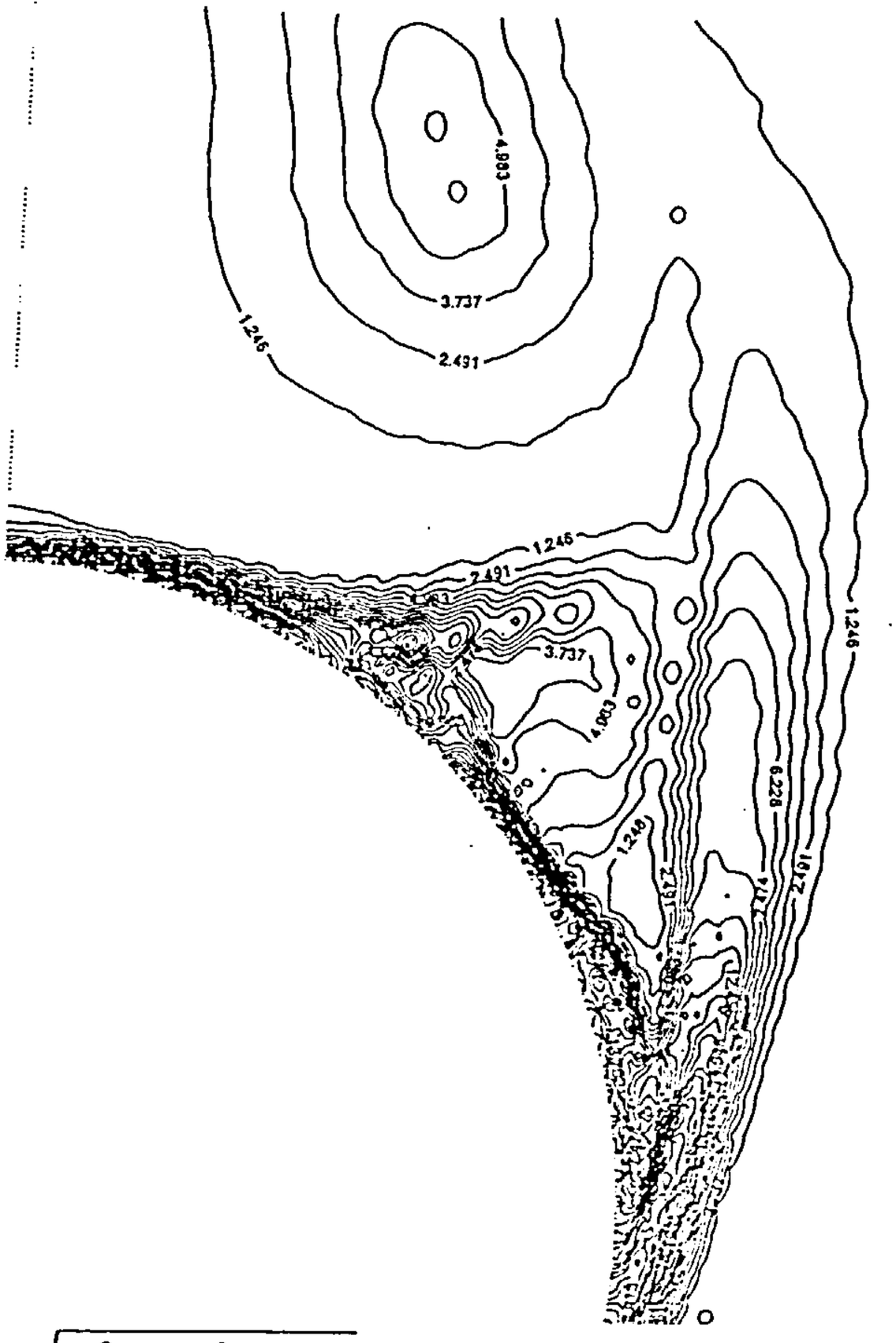

Figure 9.2.2.26 $\sqrt{\eta^2 + \xi^2 + \zeta^2}$ contours at z=9.7625, M=2.5, α=14

Figure 9.2.2.27 Non-Zeta vorticity magnitude as a % of total at z=9.7625, M=2.5, α=14

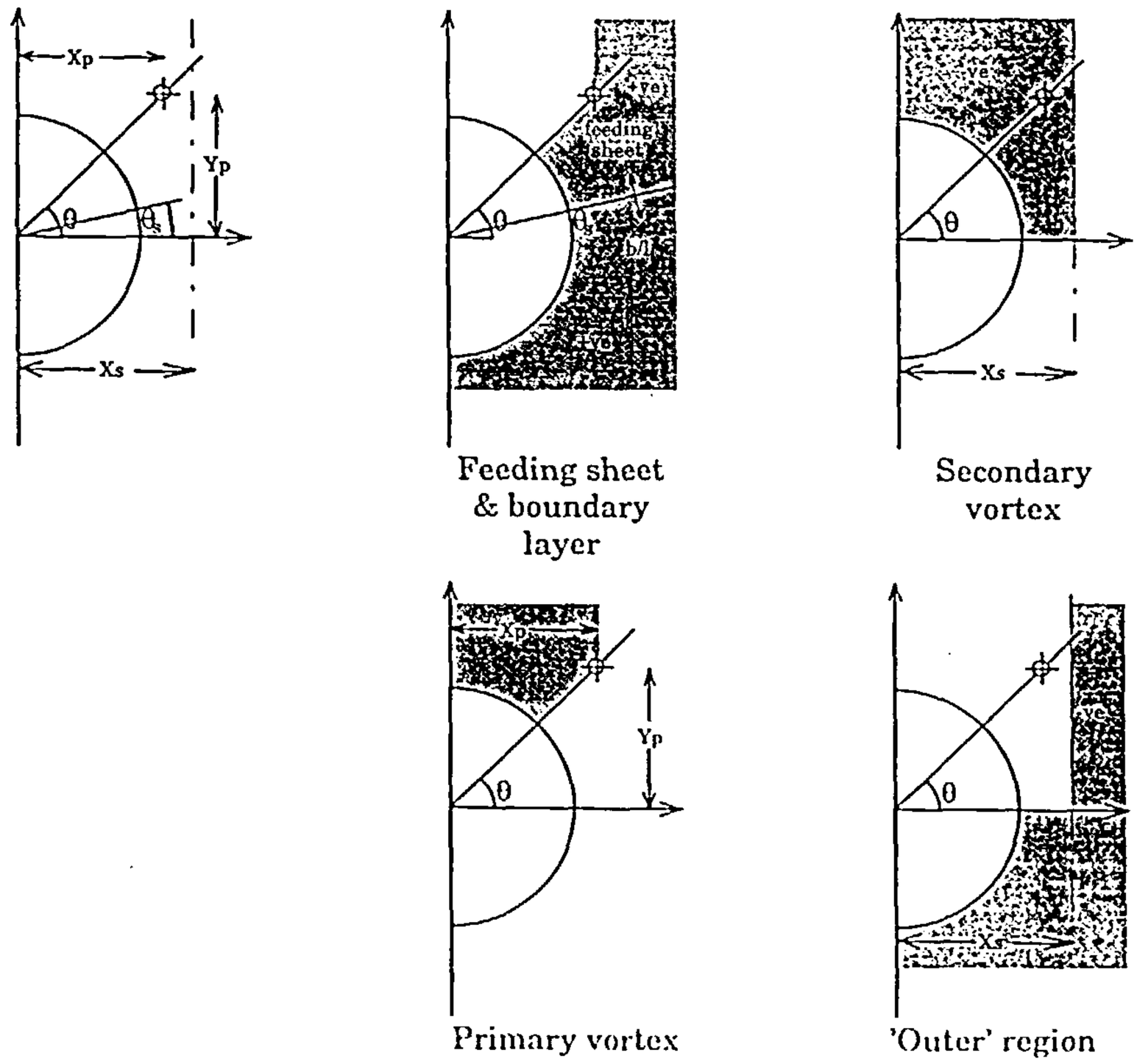

Feeding sheet & boundary layer

Secondary vortex

Figure 9.3.2.1 Regions of integration

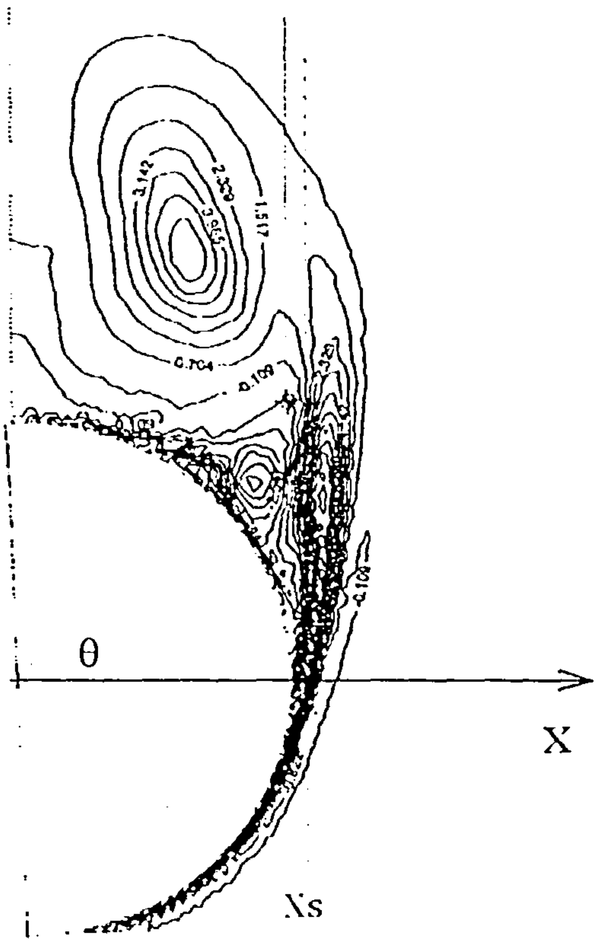

Figure 9.3.2.2 Determination of regions of integration

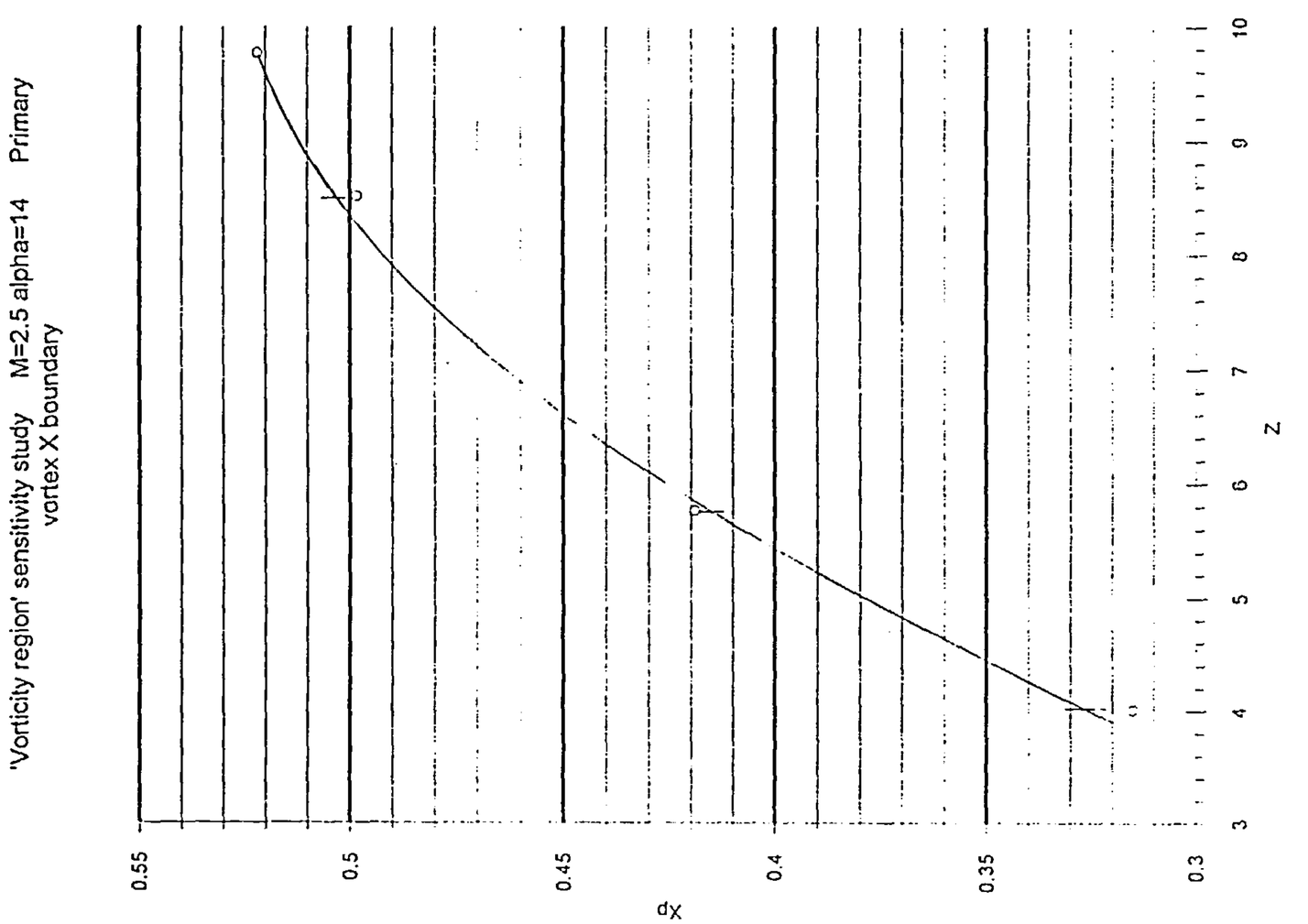

Figure 9.3.2.3

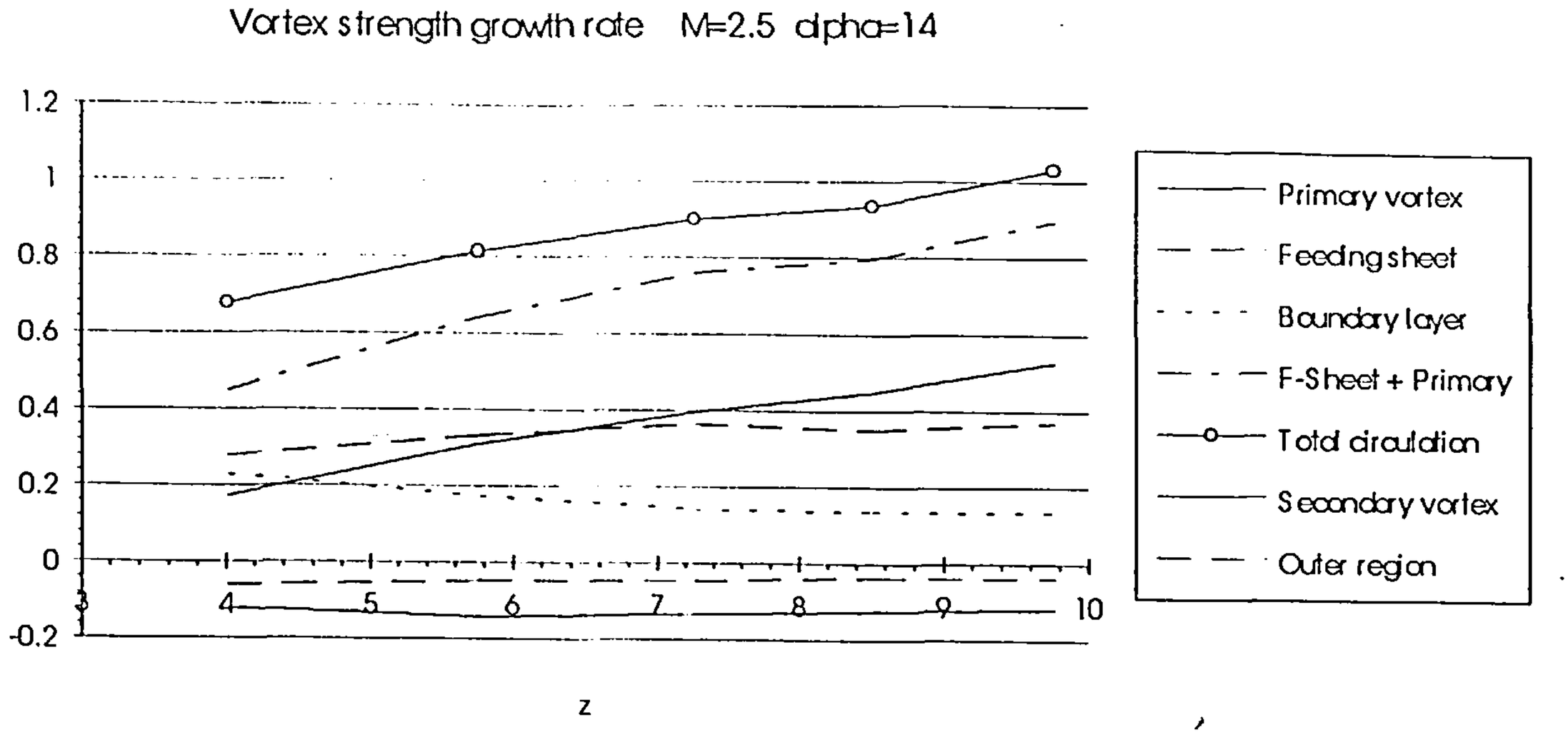

Figure 9.4.1.1

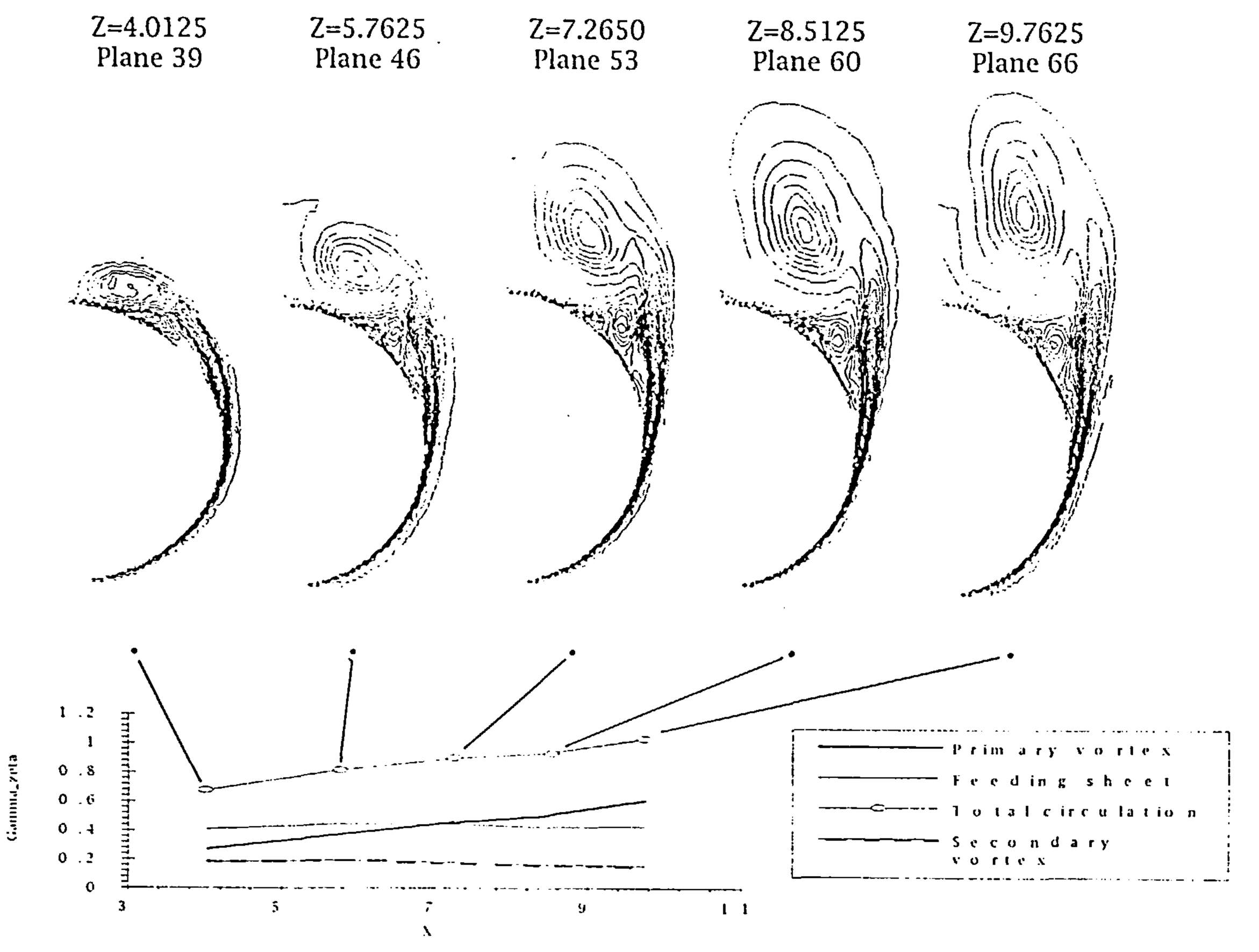

Figure 9.4.1.2

The development of the body vortex with progress downstream
ζ-component of vorticity contours from a P.N.S. solution at Mach 2.5 and alpha=14
Tangent-ogive cylinder body

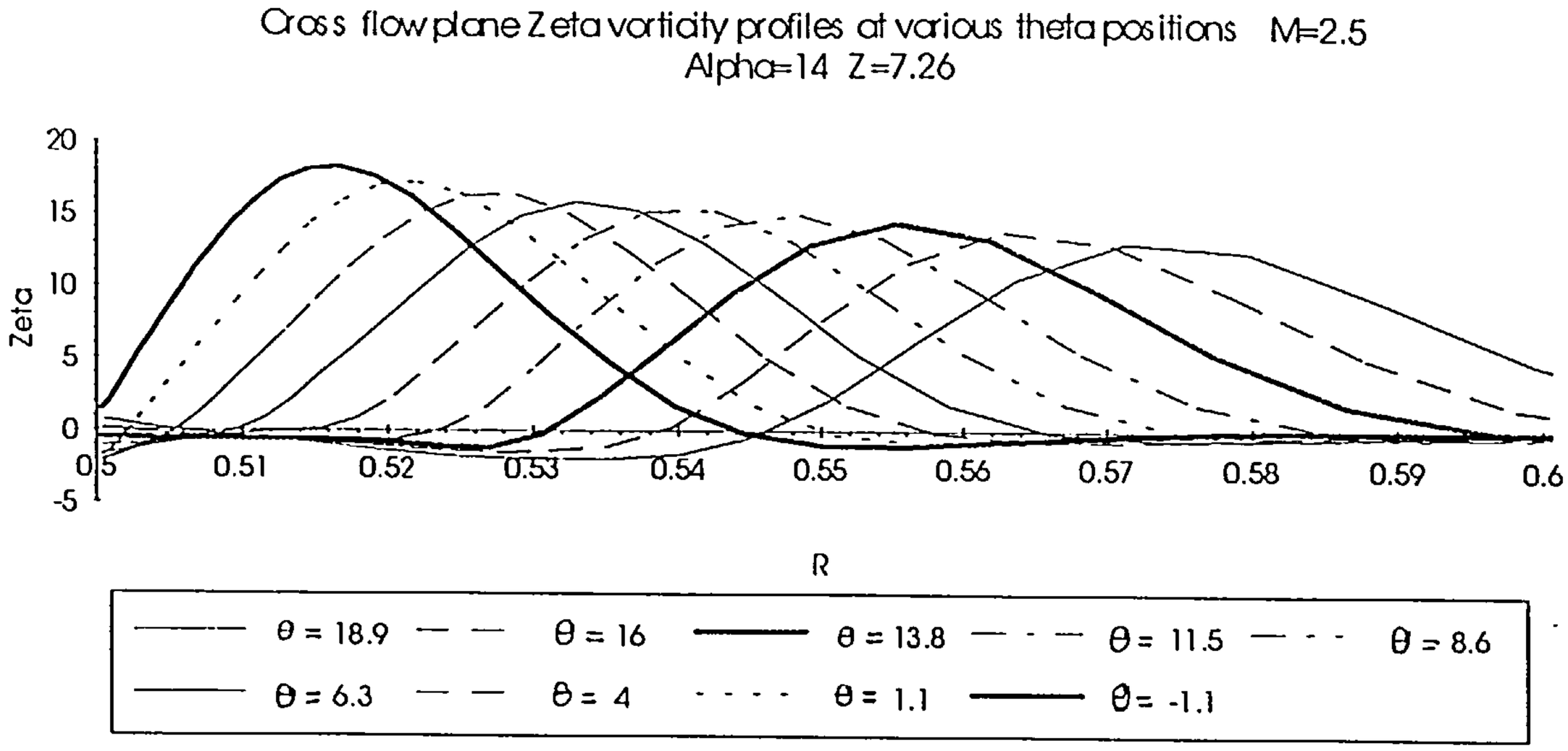

Figure 9.5.2.1

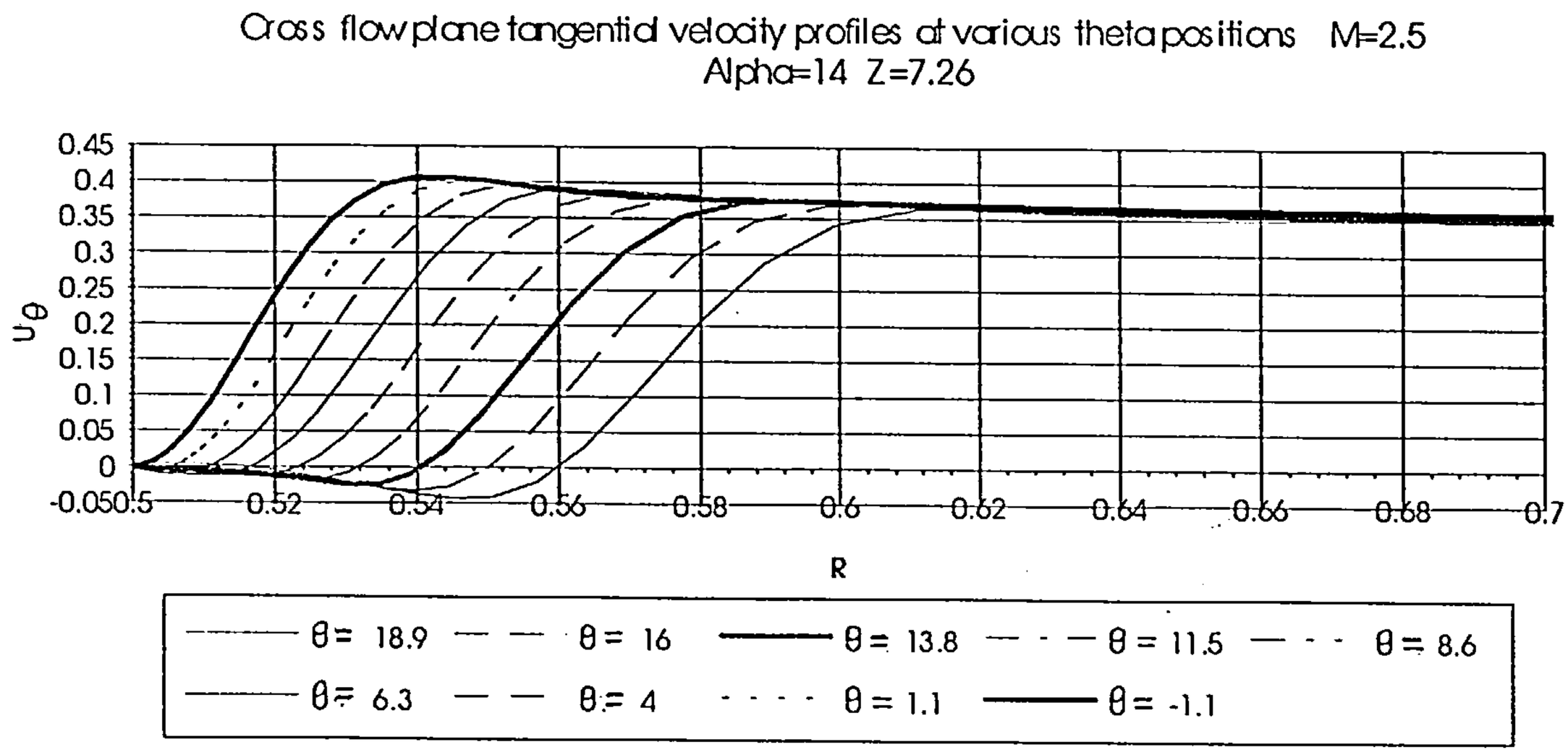

Figure 9.5.2.2

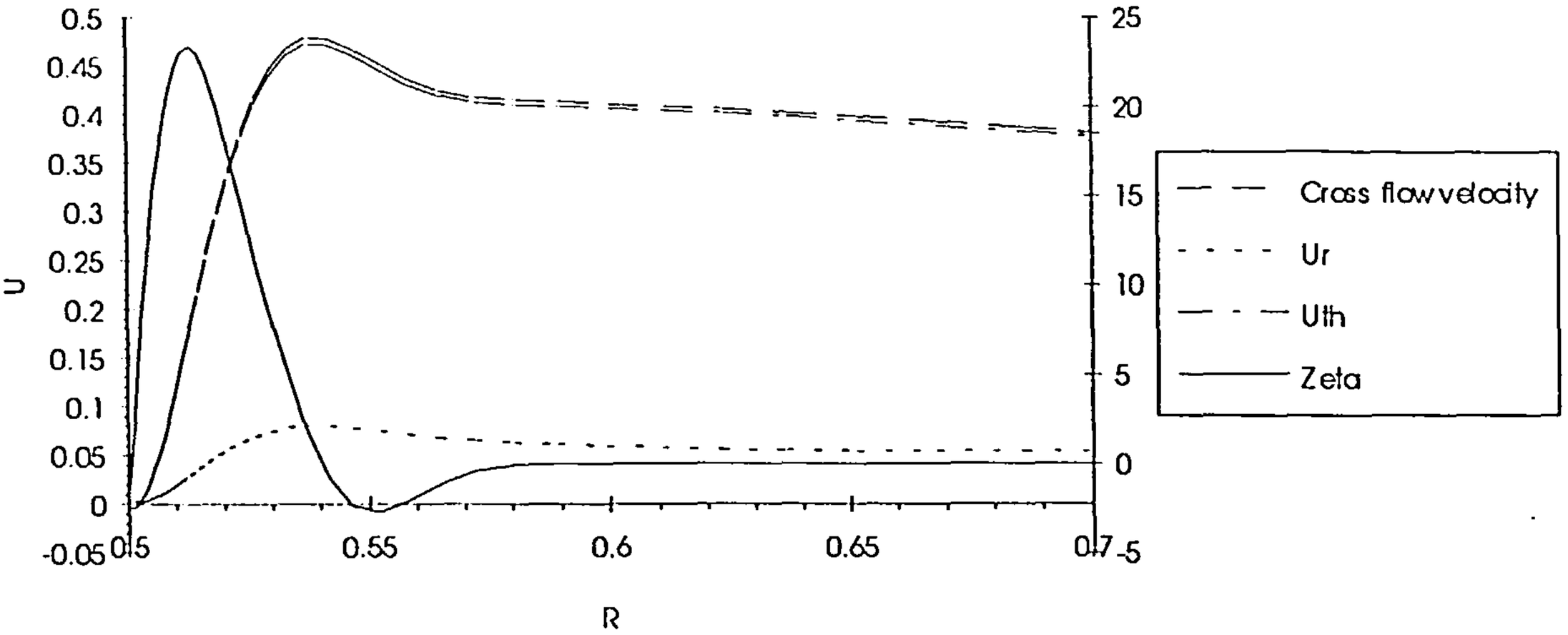

Figure 9.5.2.3

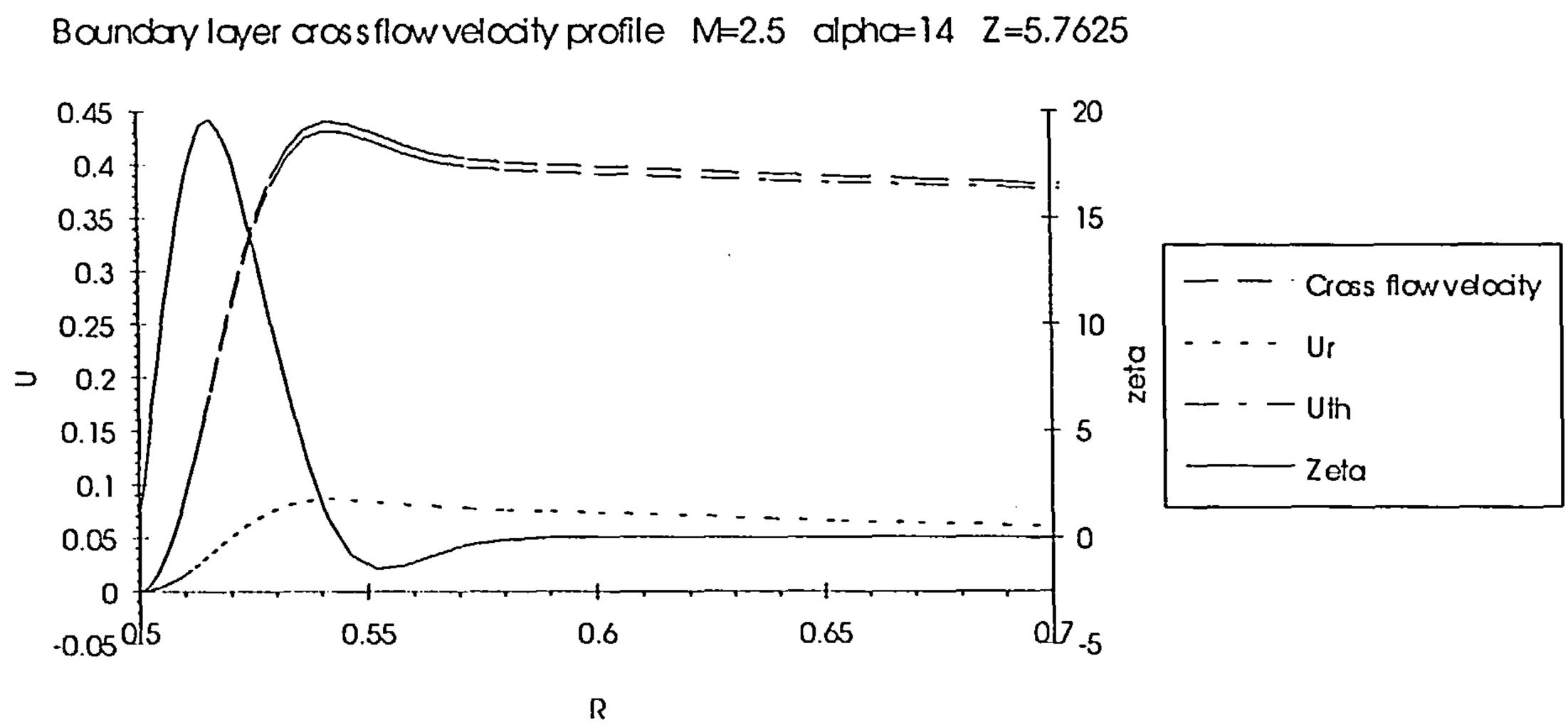

Figure 9.5.2.4

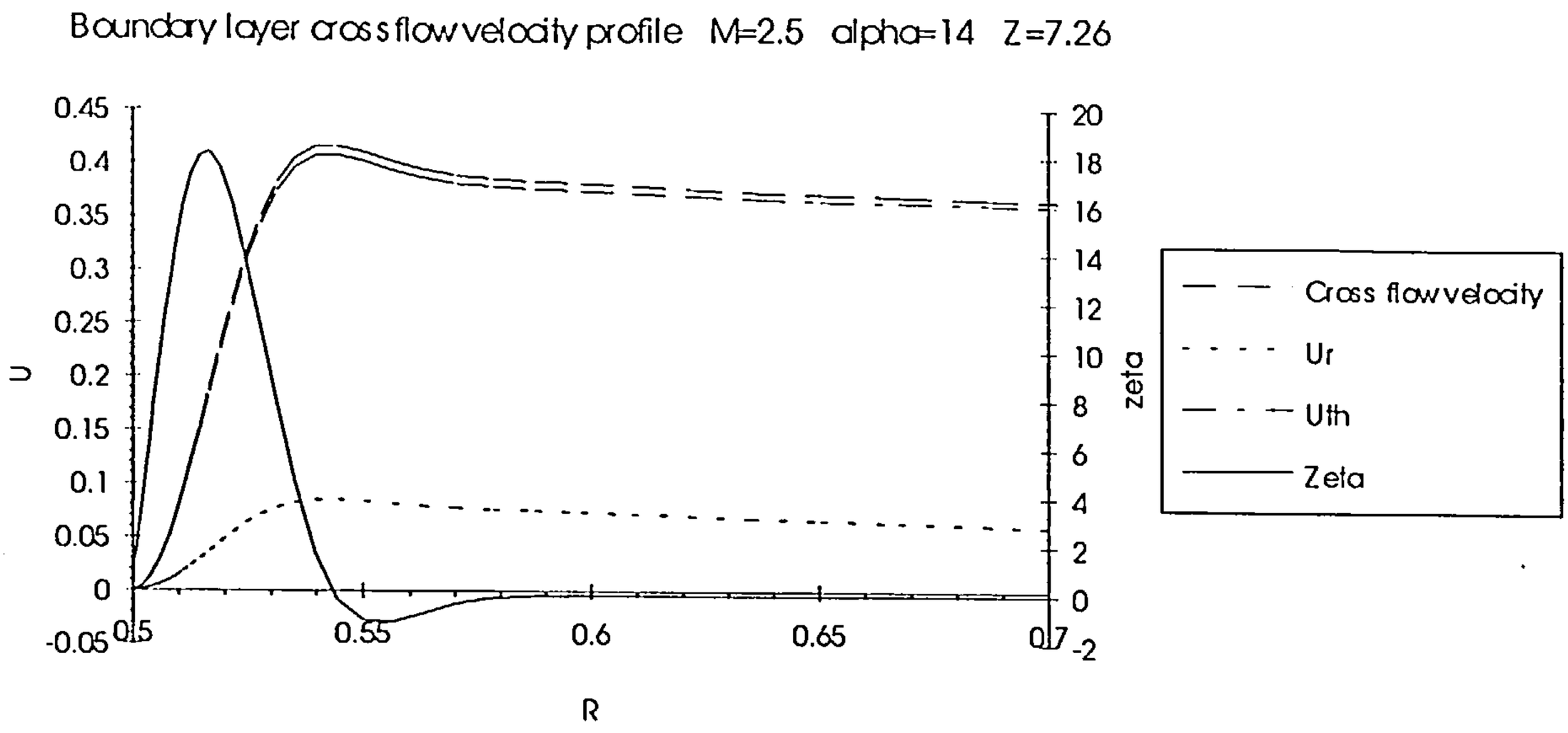

Figure 9.5.2.5

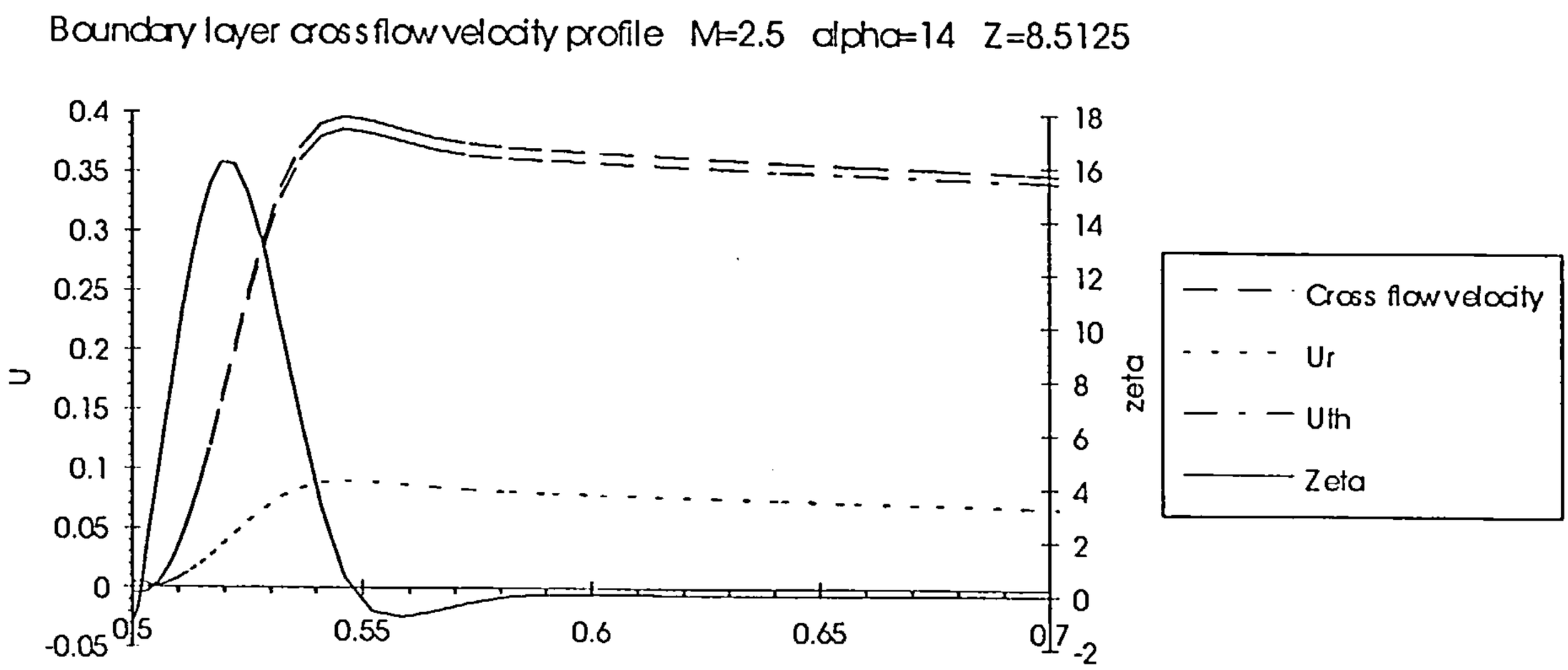

Figure 9.5.2.6

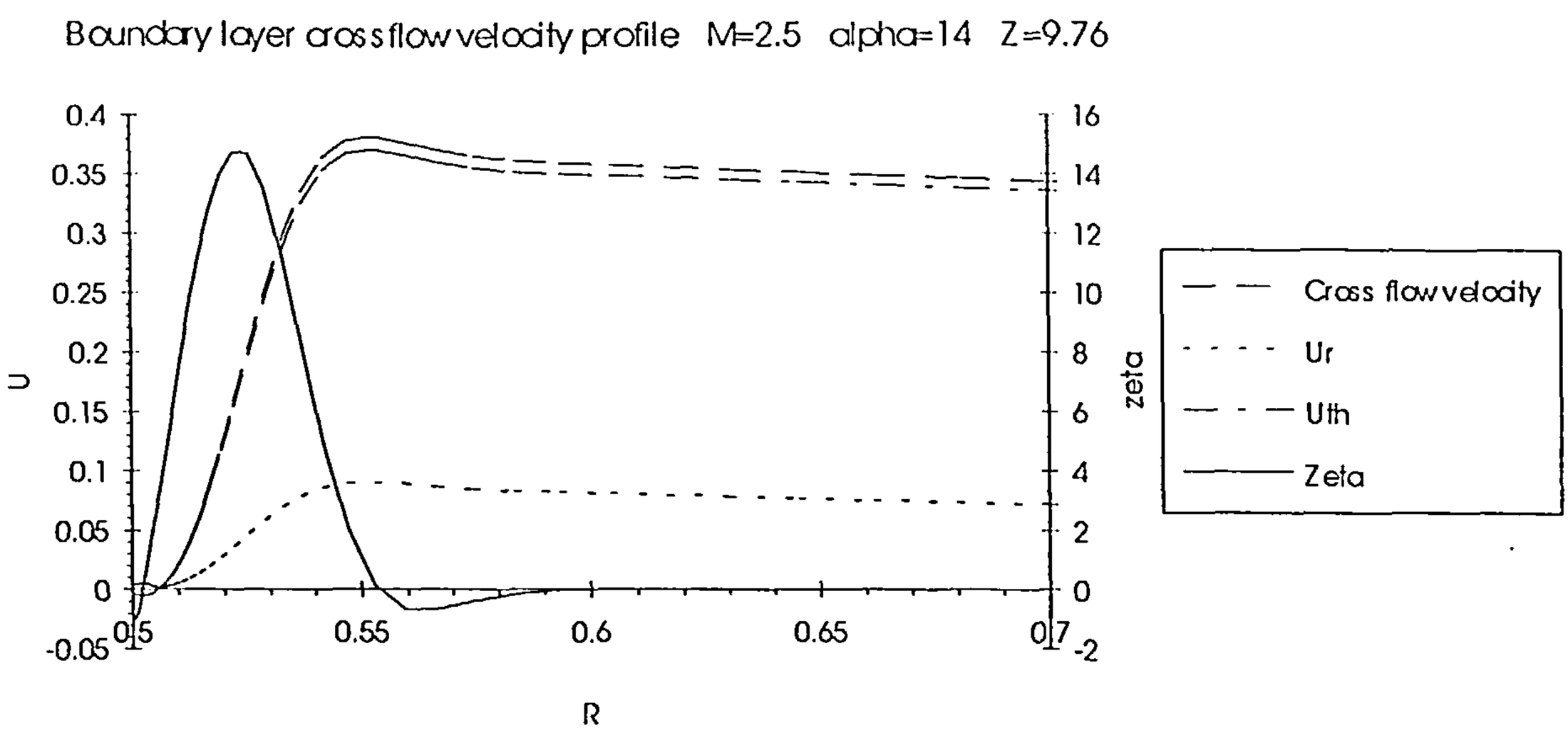

Figure 9.5.2.7

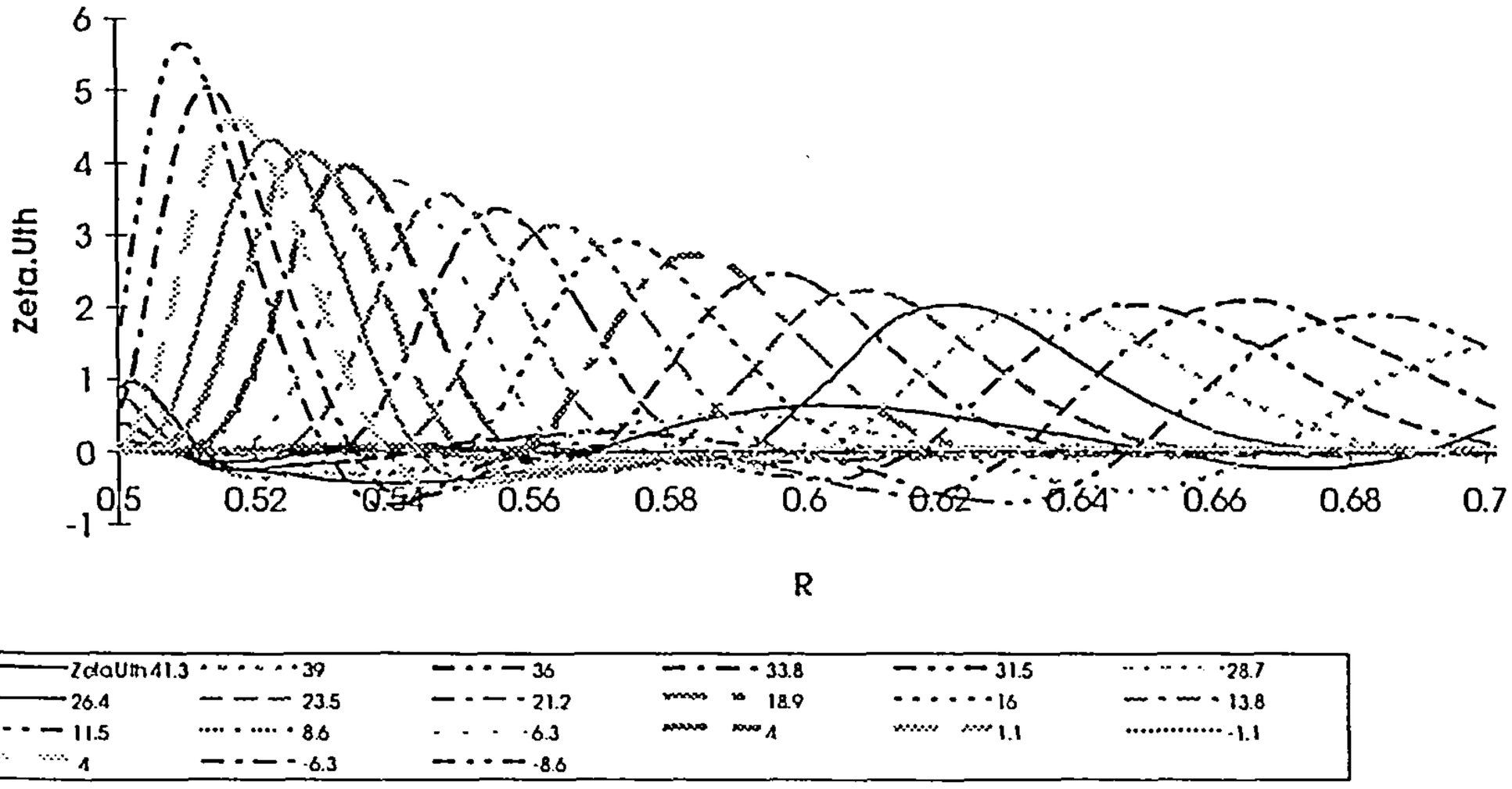

Figure 9.5.2.8

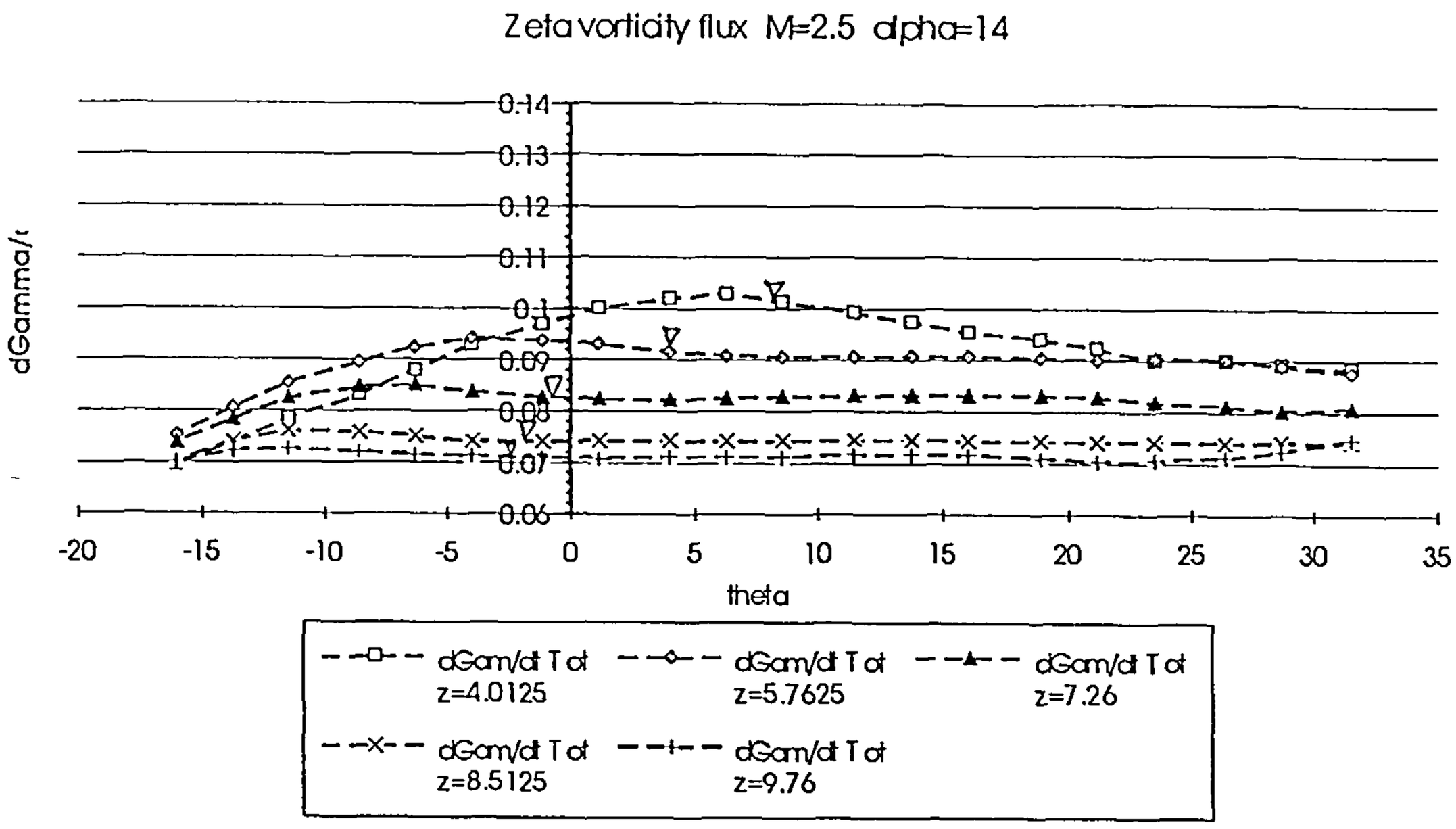

Figure 9.5.3.1

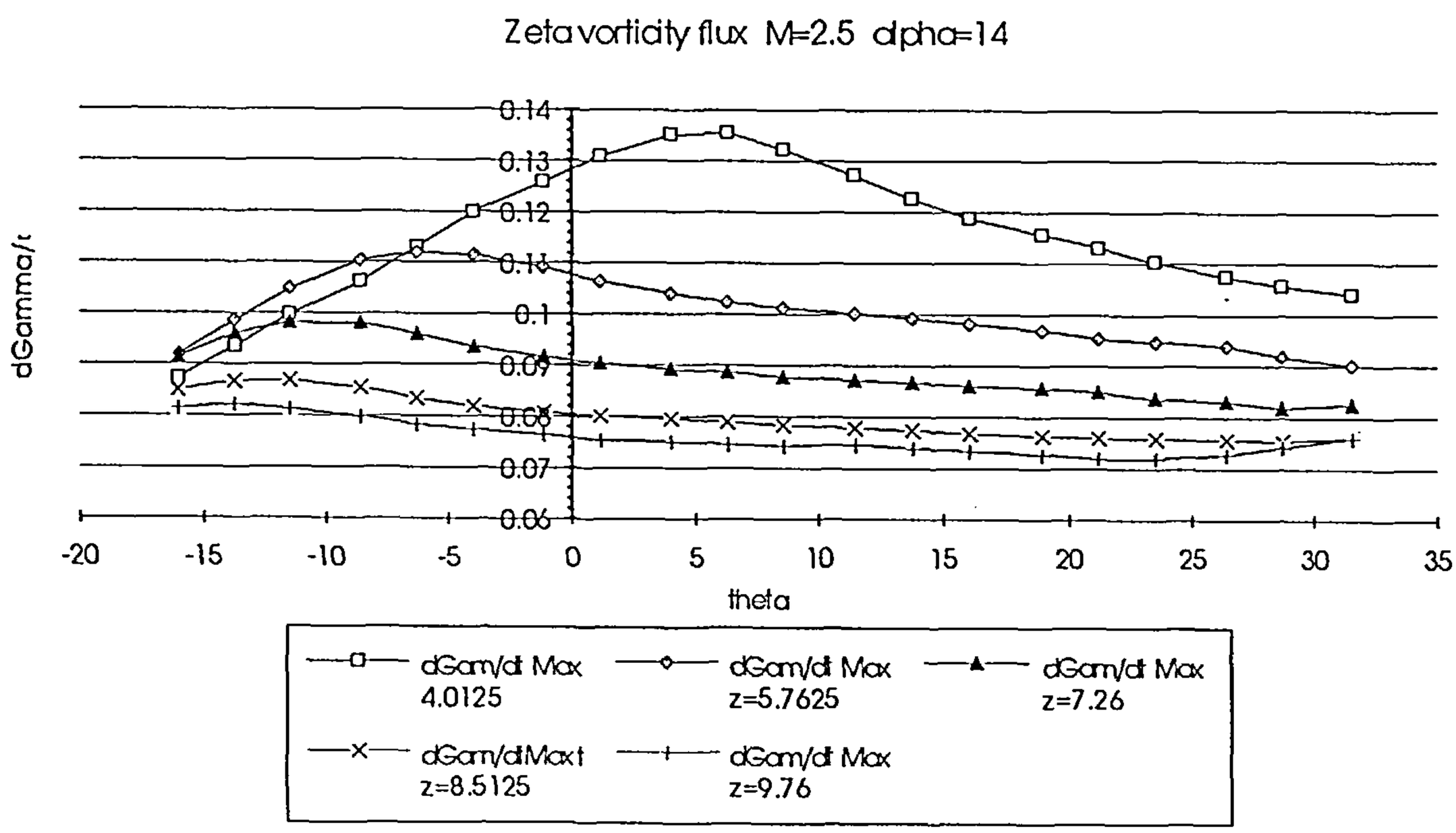

Figure 9.5.3.2

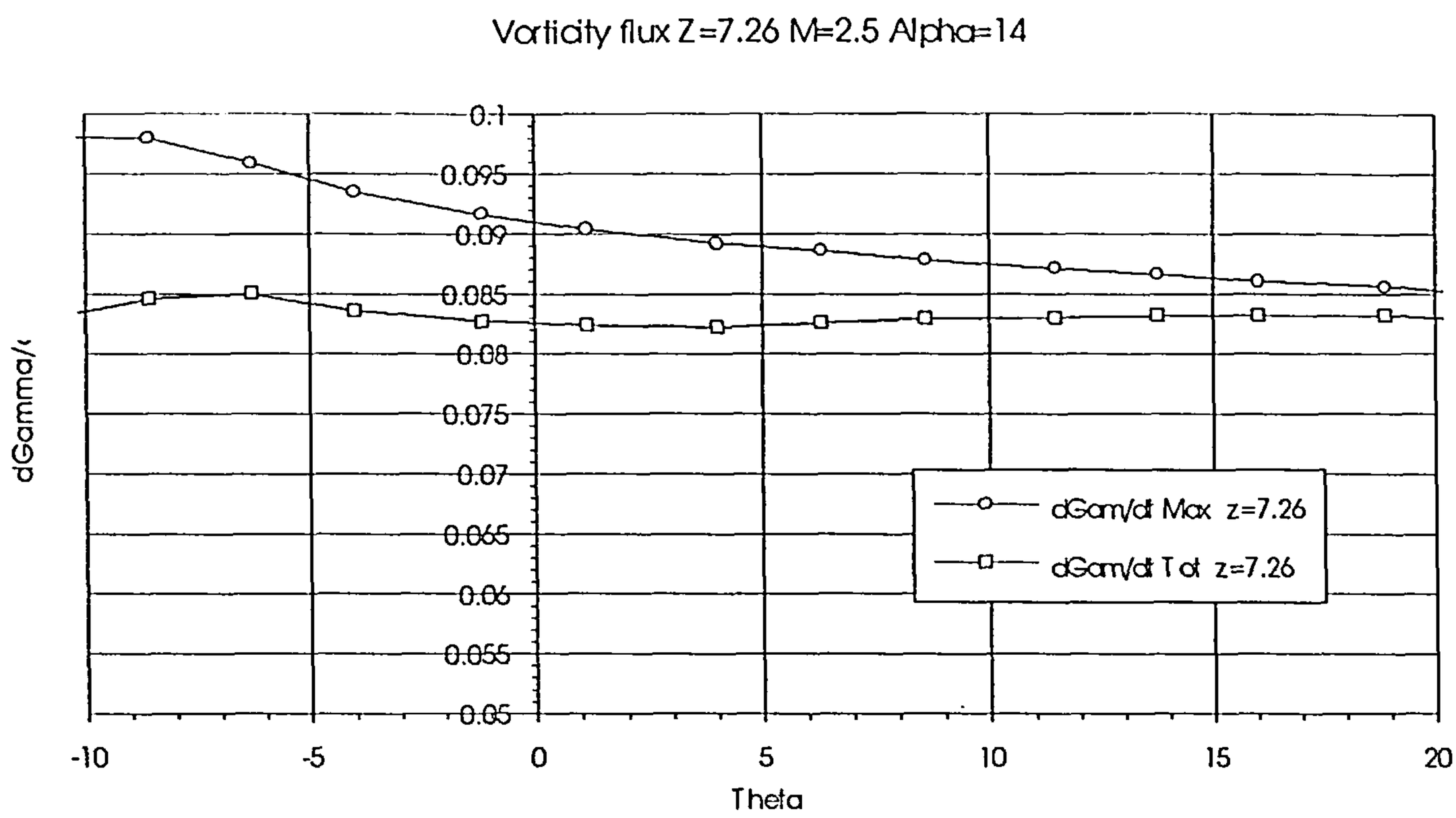

Figure 9.5.3.3

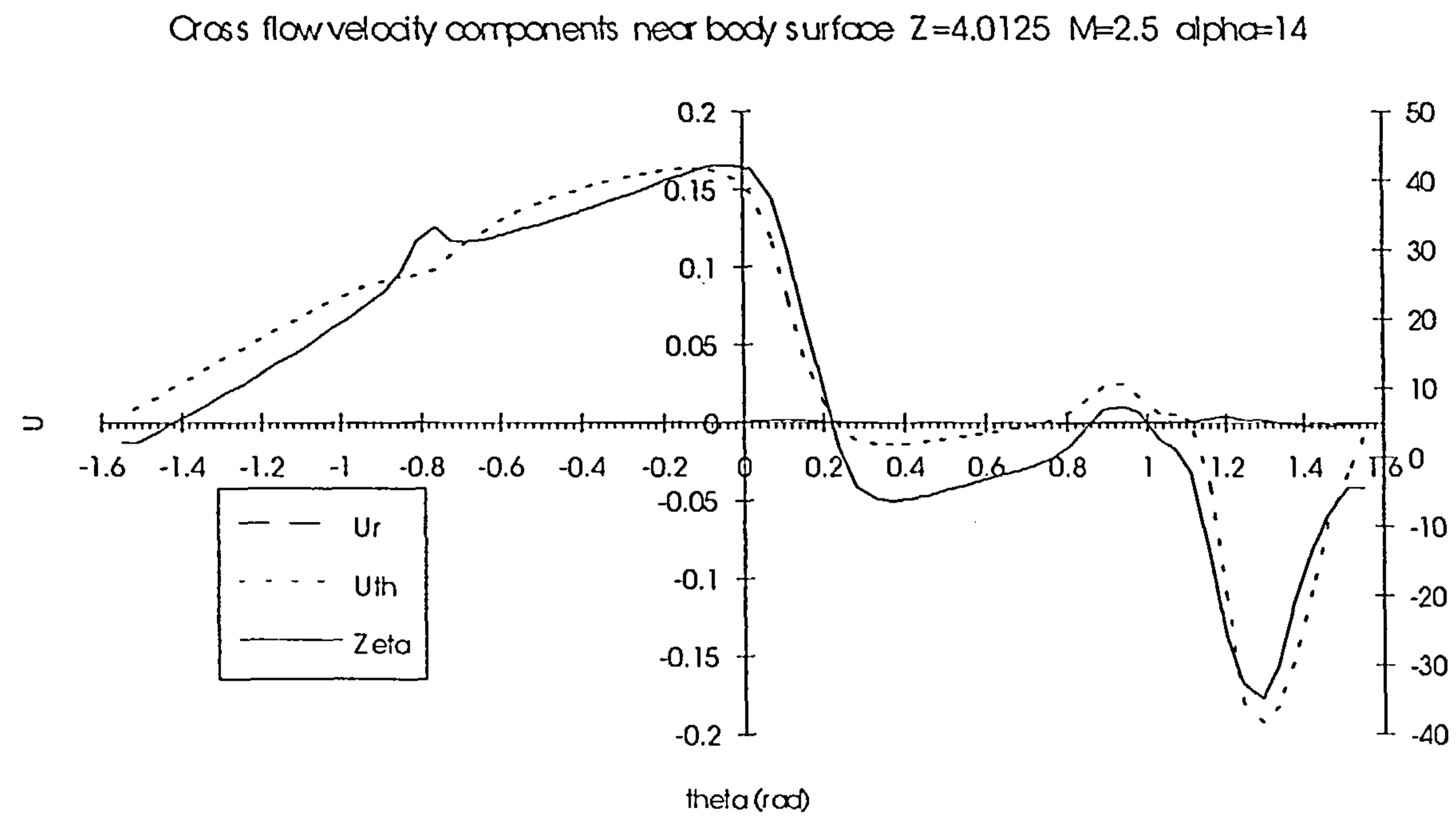

Figure 9.5.3.4

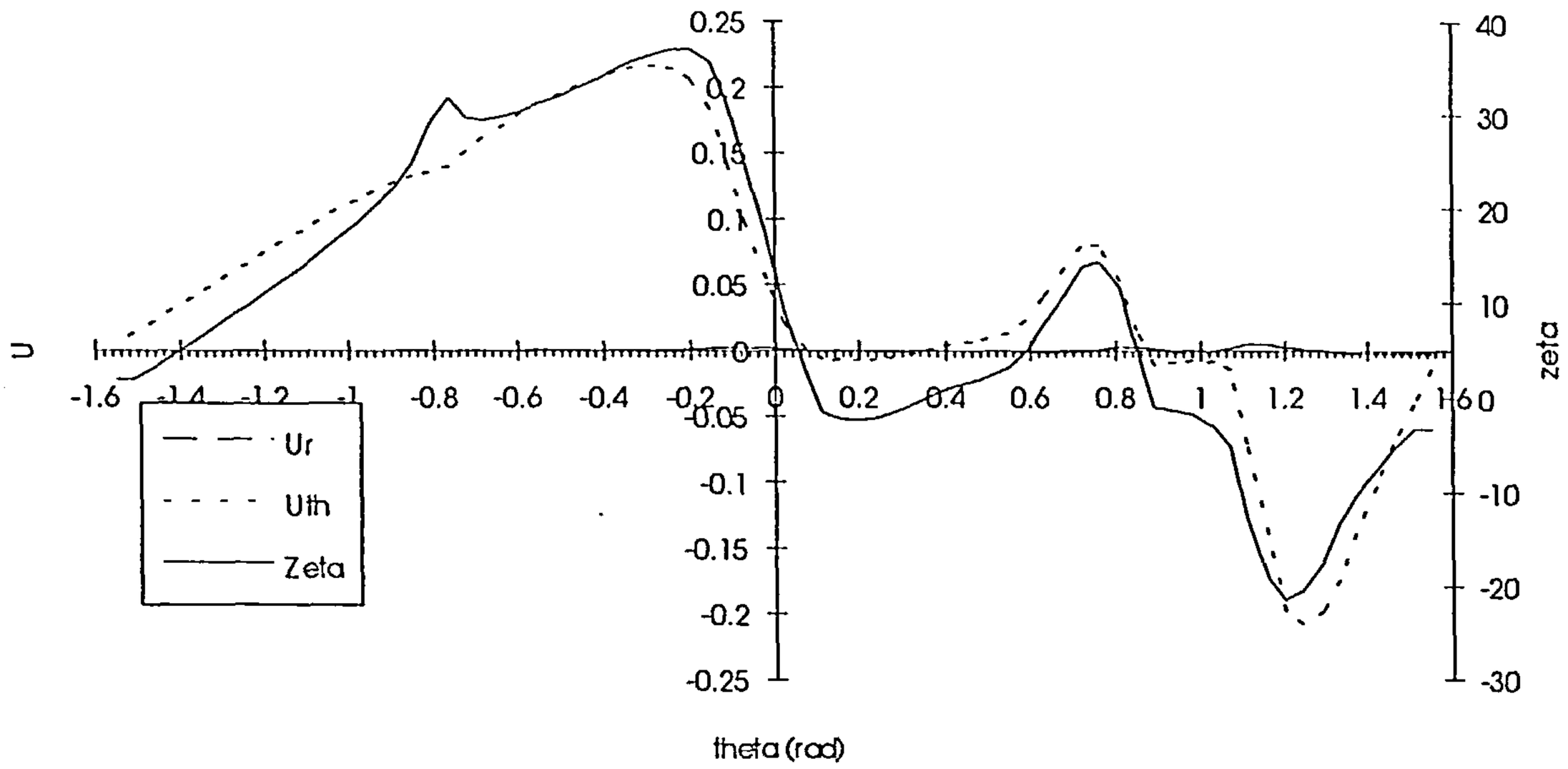

Figure 9.5.3.5

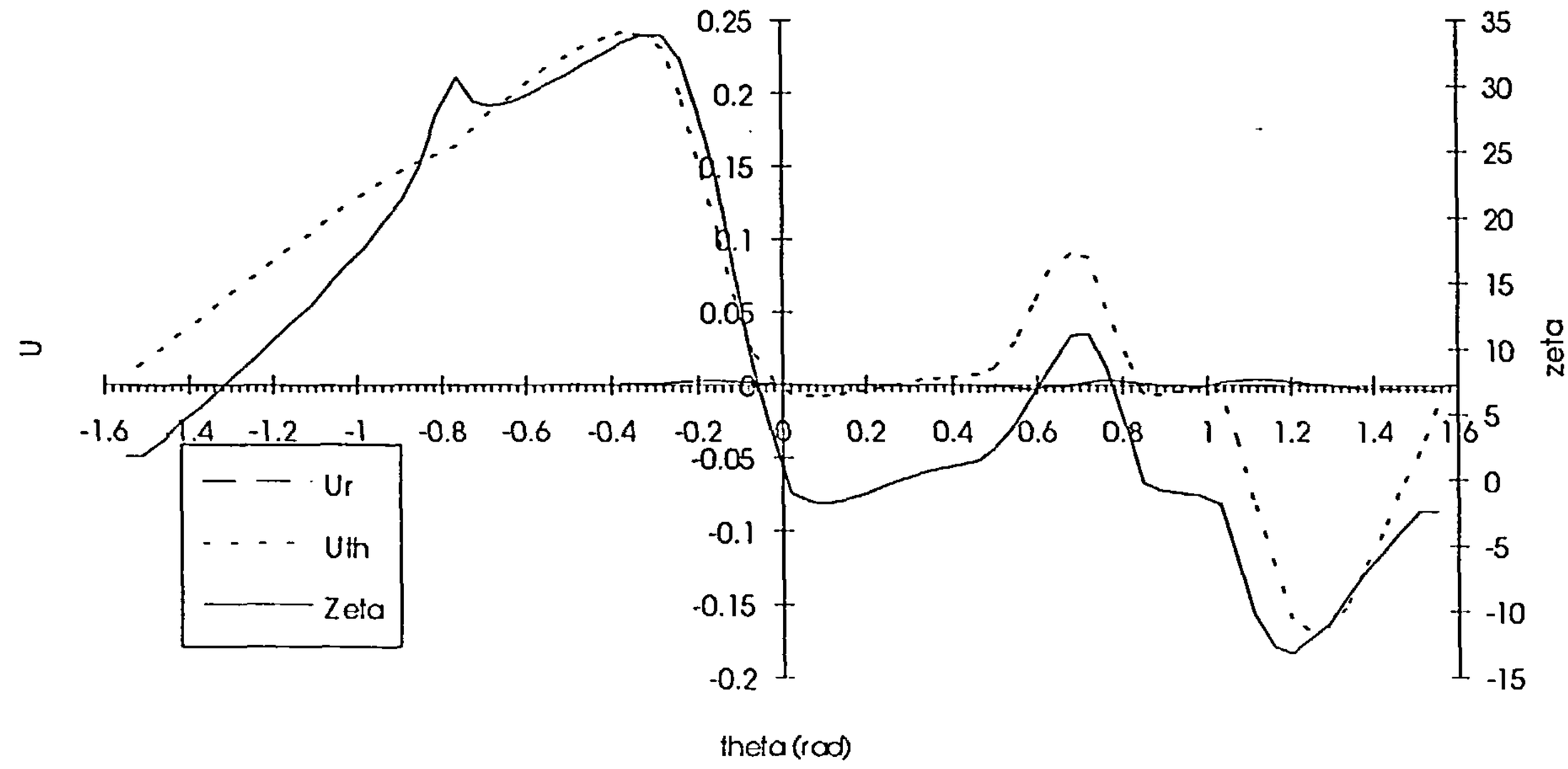

Figure 9.5.3.6

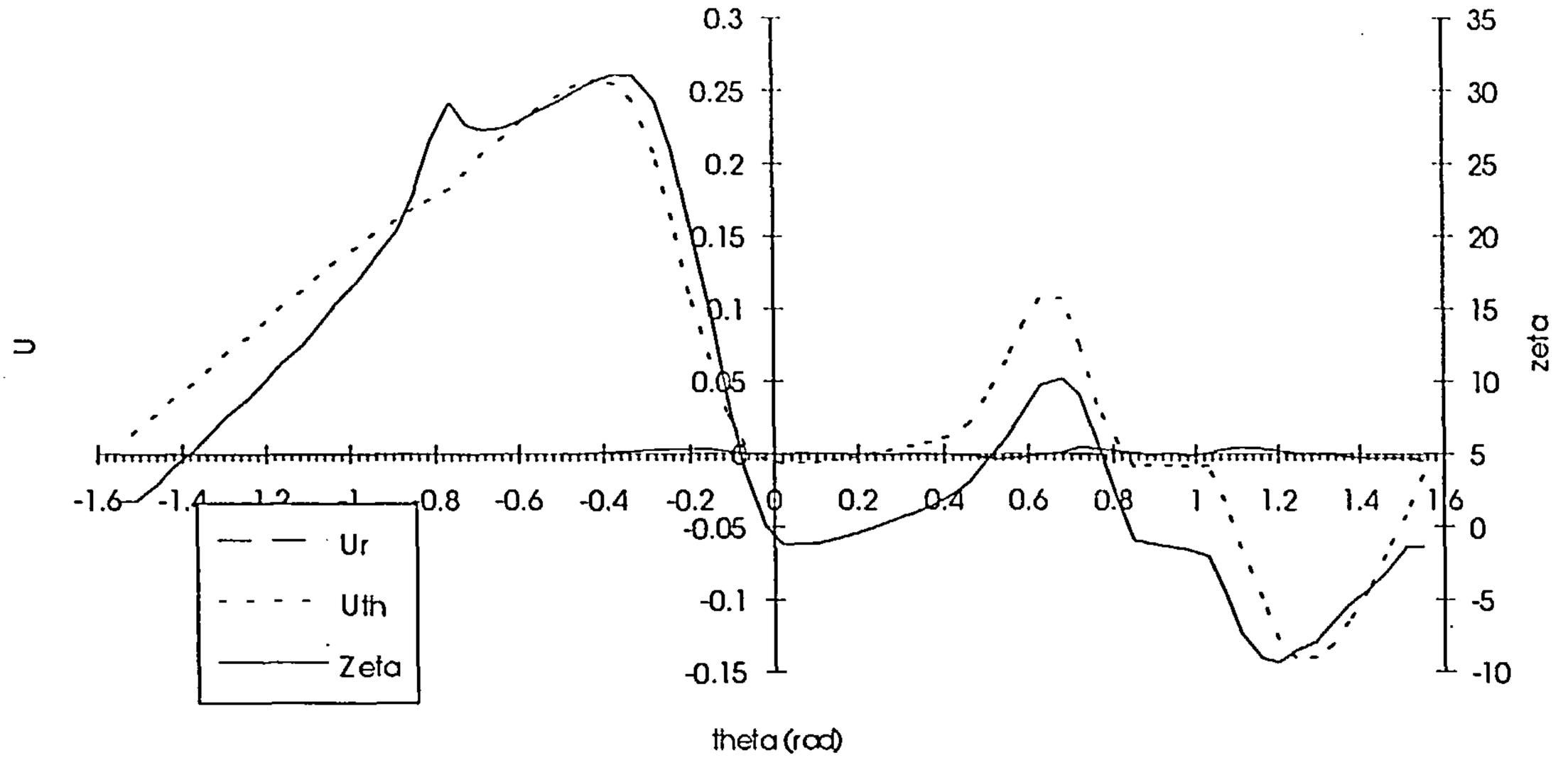

Figure 9.5.3.7

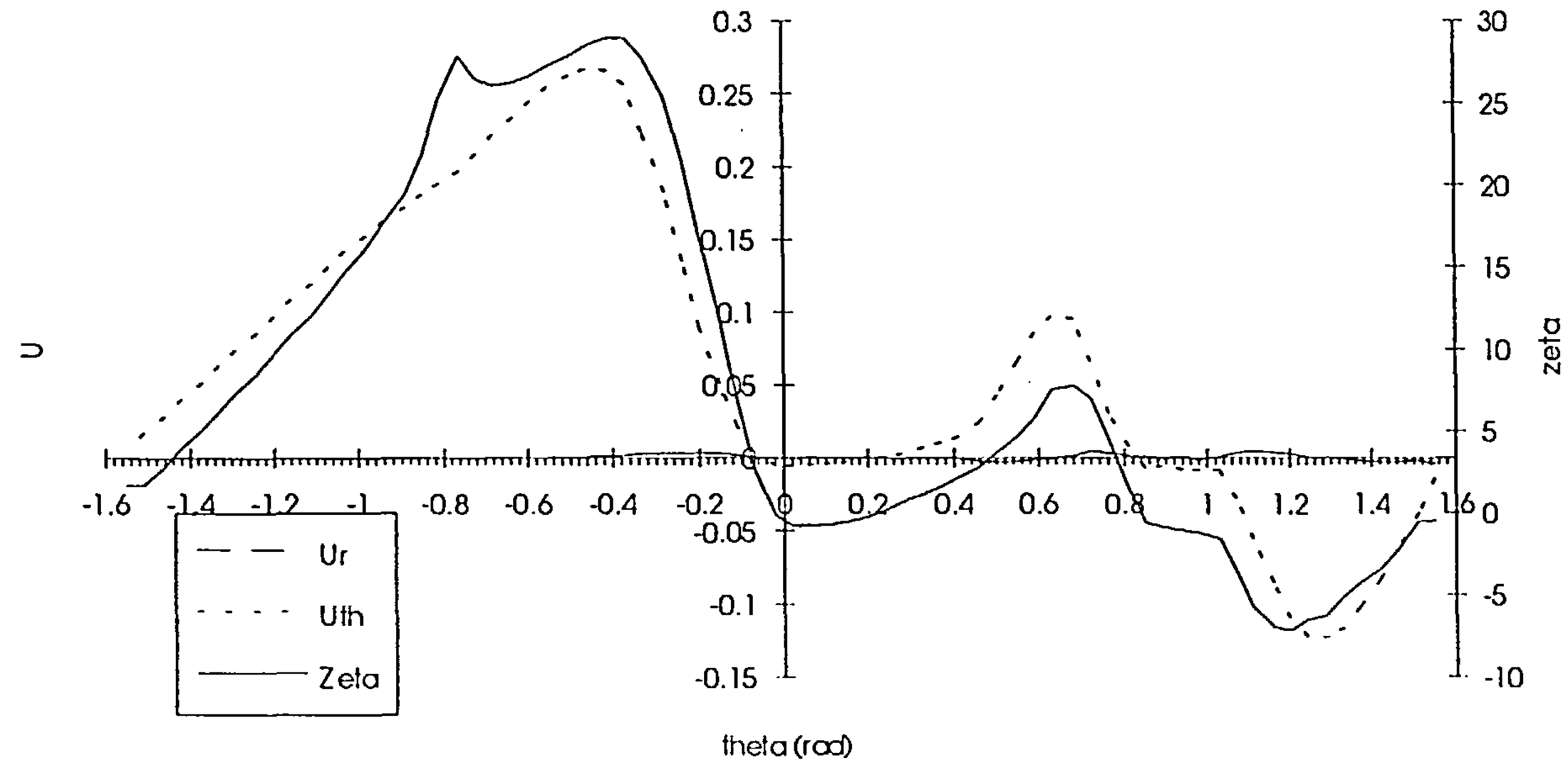

Figure 9.5.3.8

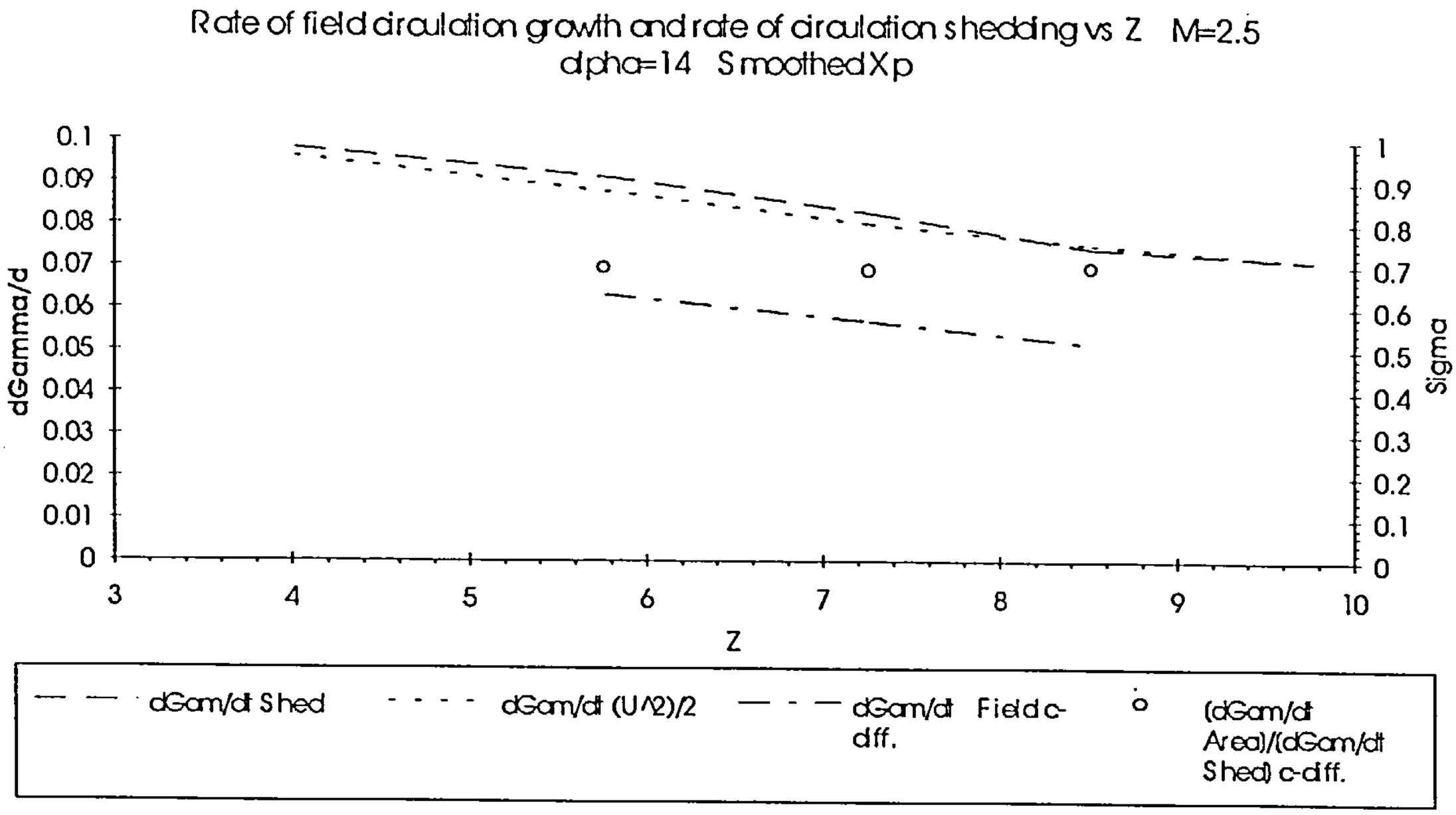

Figure 9.5.4.1

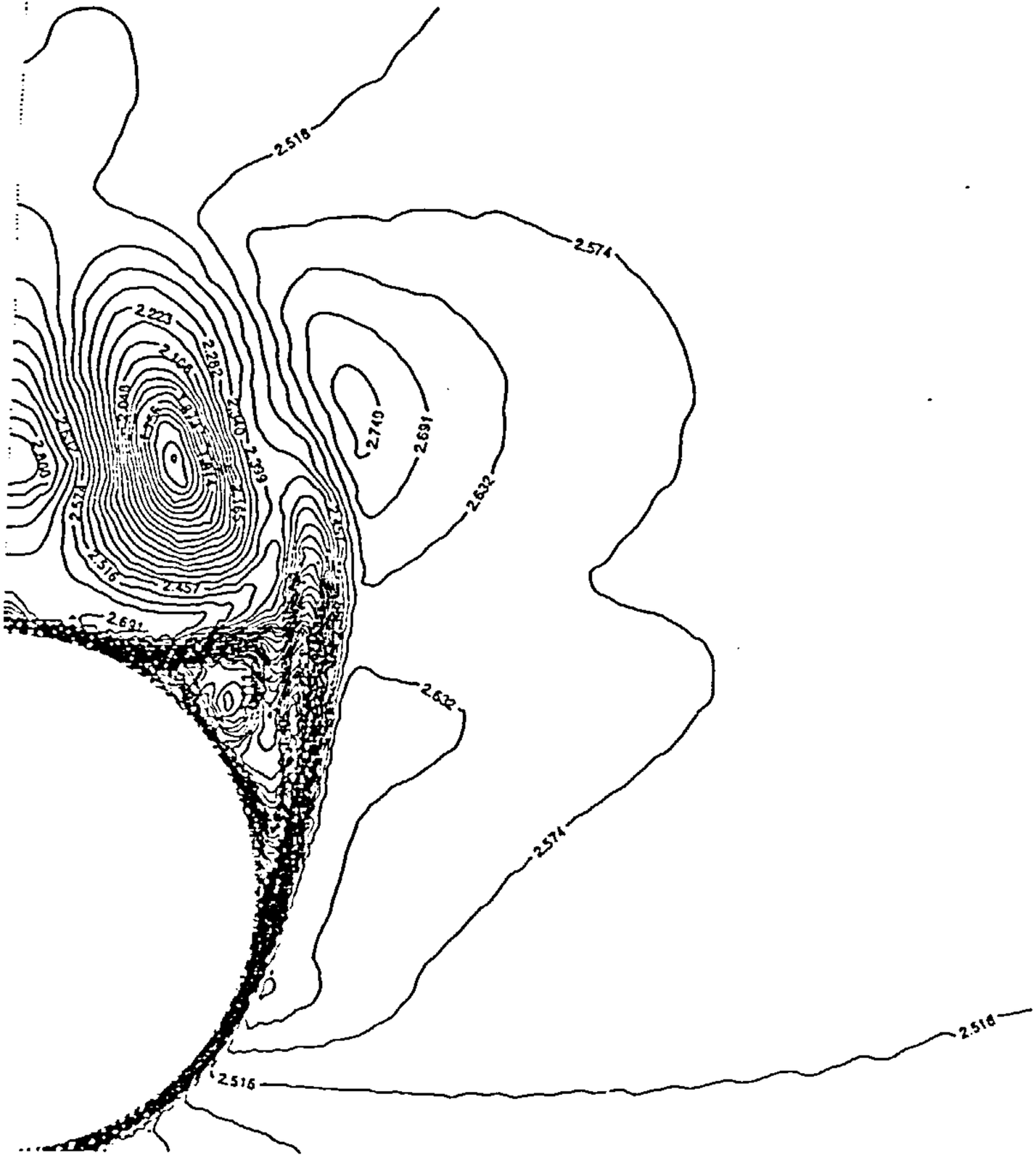

Figure 9.5.6.1 Mach number contours at z=9.7625, M=2.5, α=14

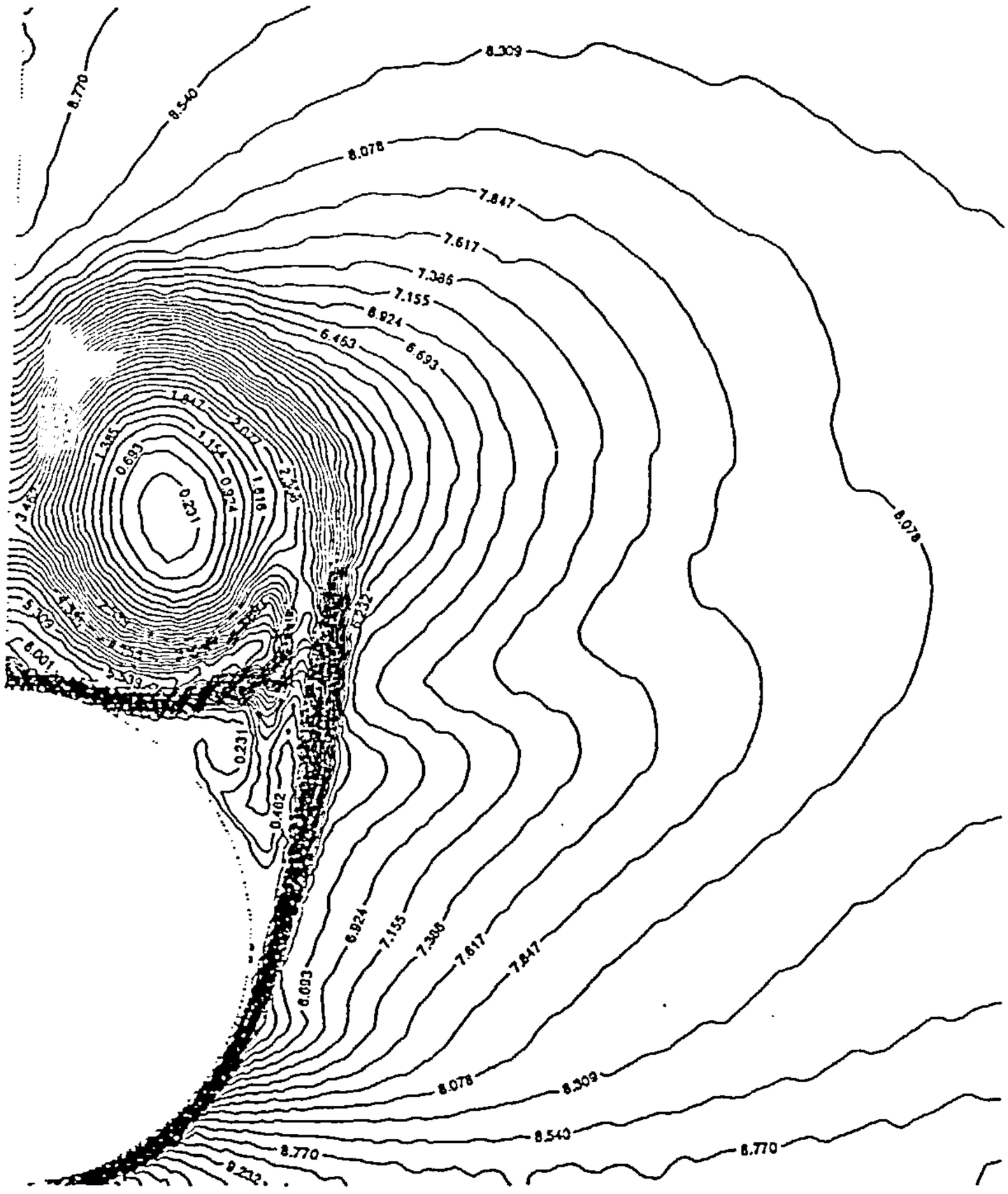

Figure 9.5.6.2 Total pressure contours at z=9.7625, M=2.5, α=14

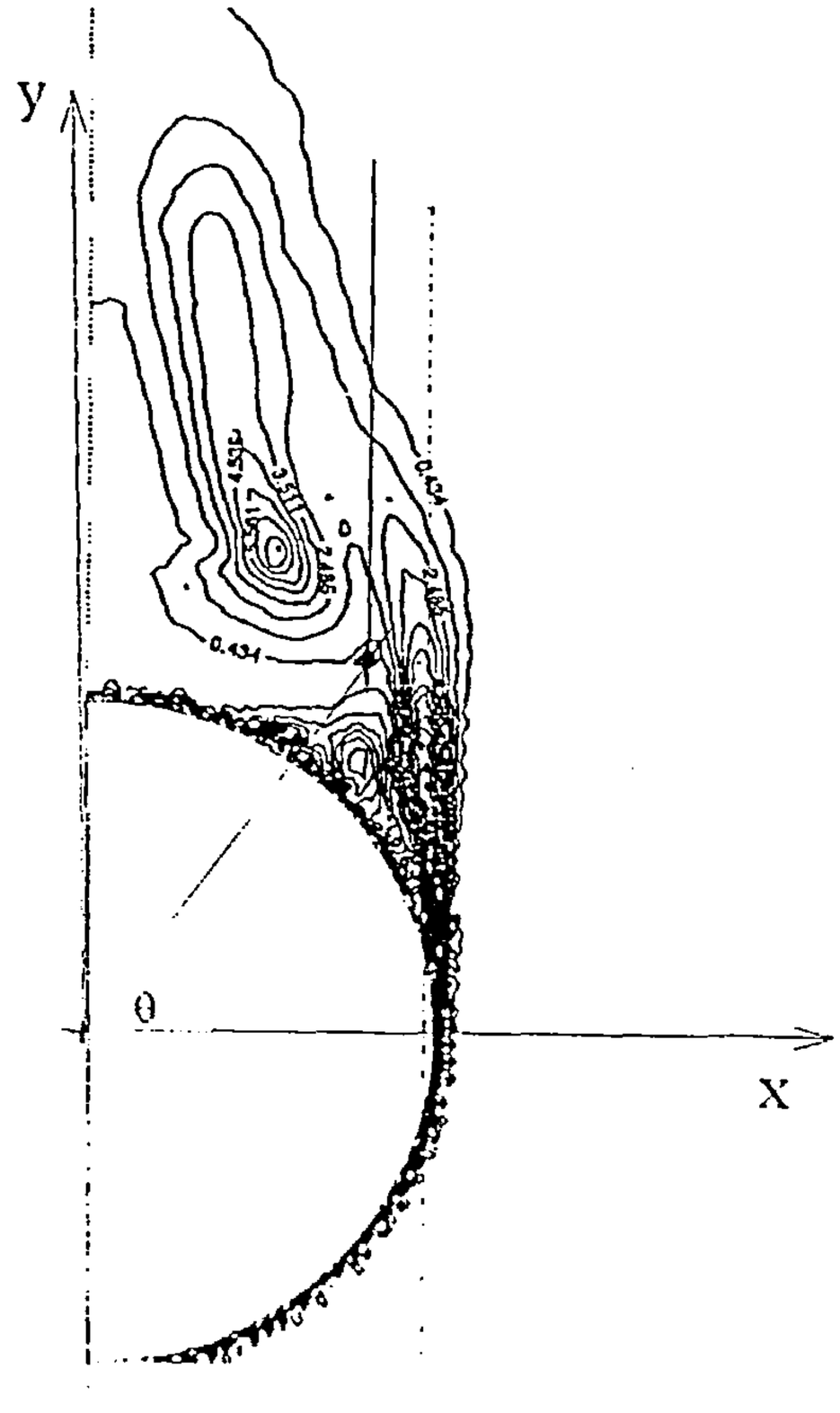

Figure 9.6.1.1 Determination of regions of integration

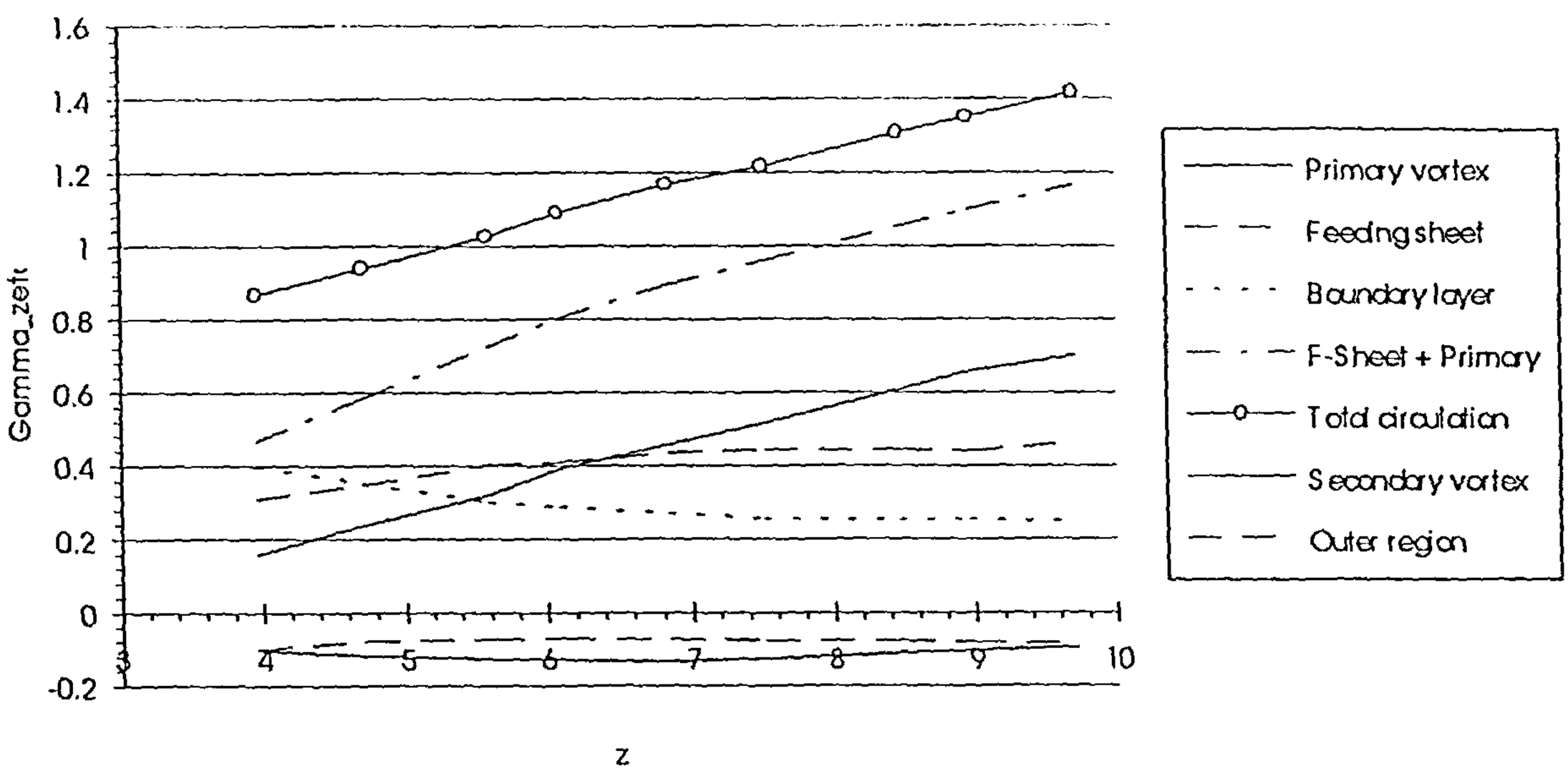

Figure 9.6.1.2

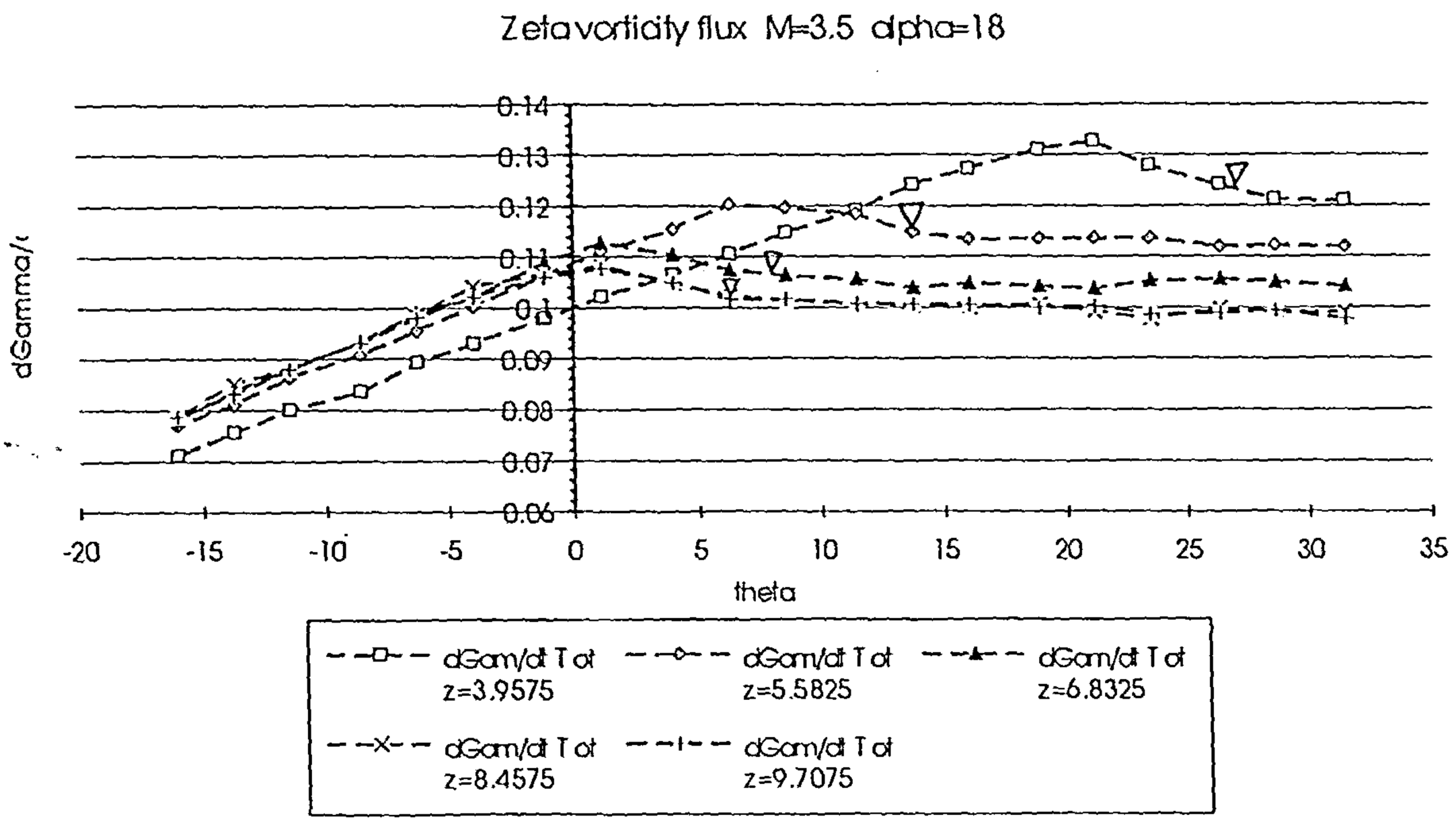

Figure 9.6.1.3

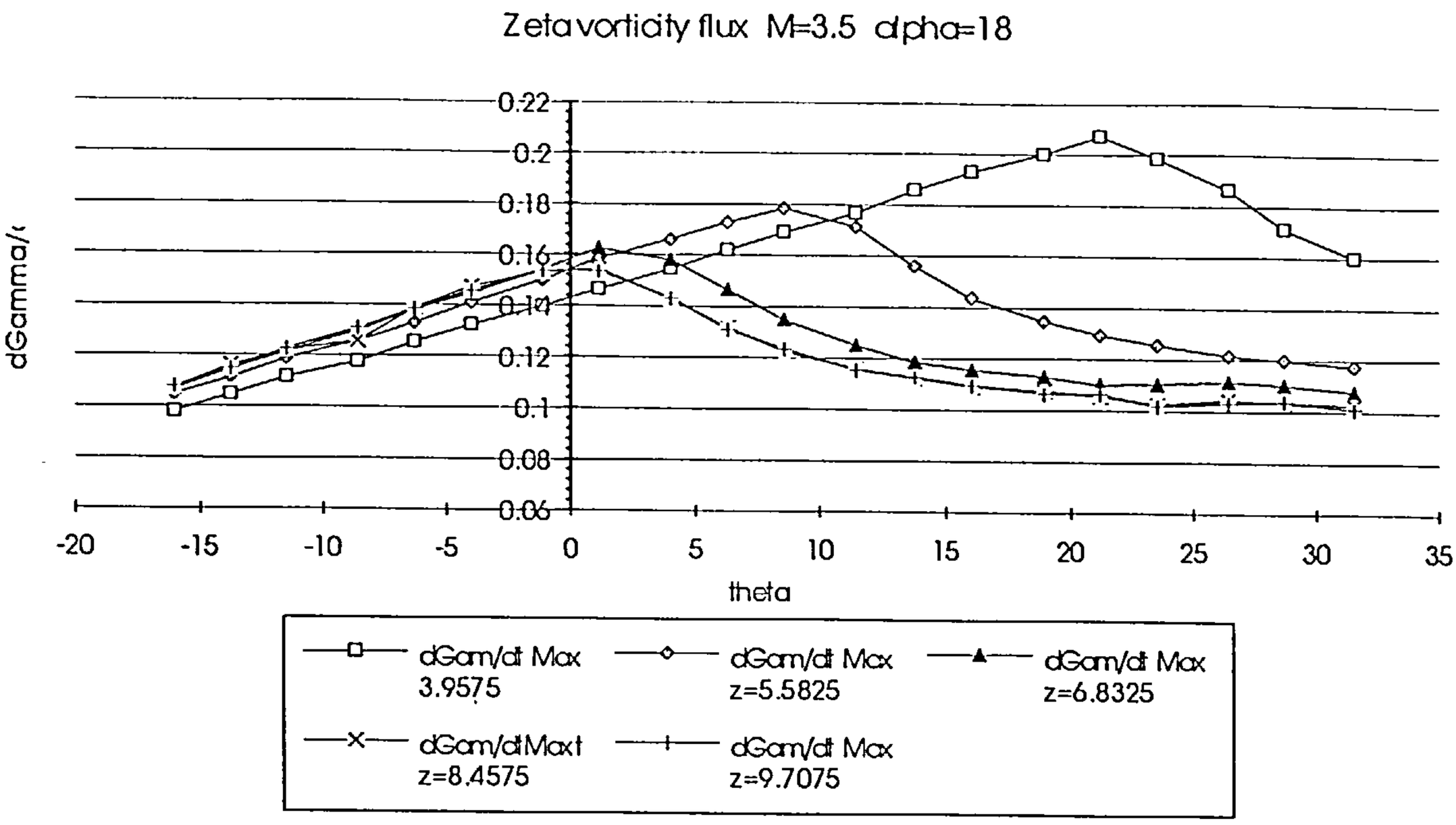

Figure 9.6.1.4

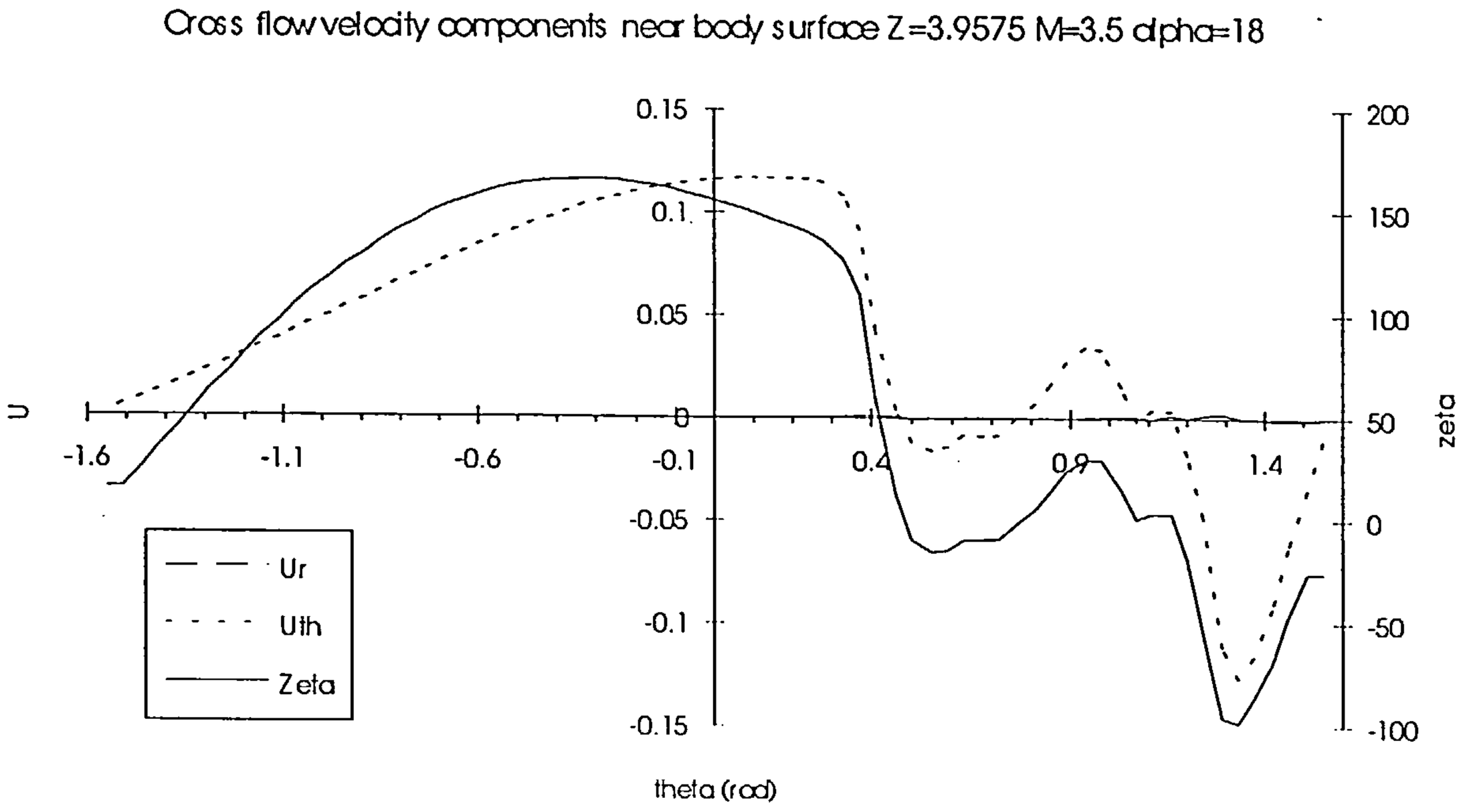

Figure 9.6.1.5

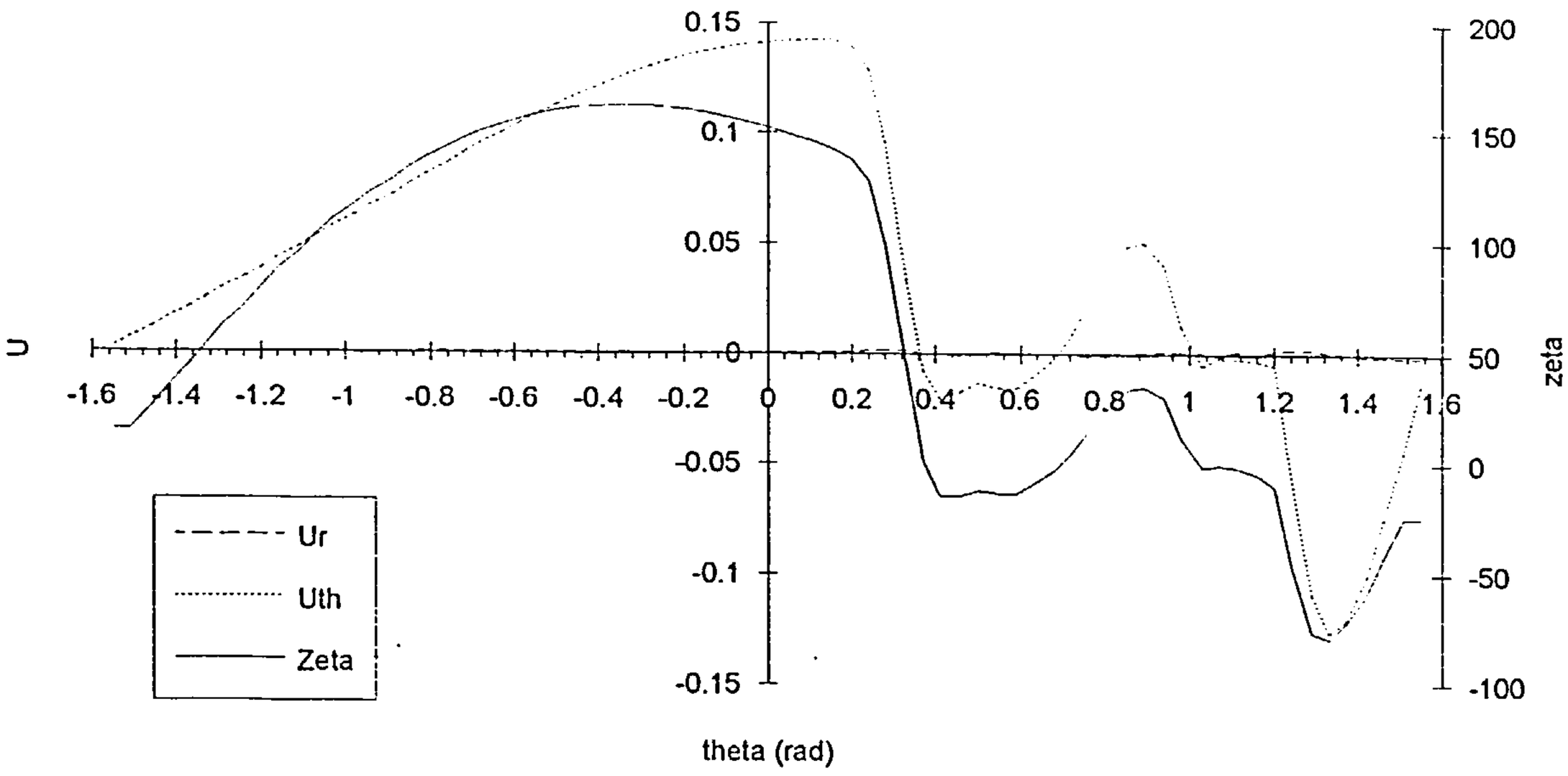

Figure 9.6.1.6

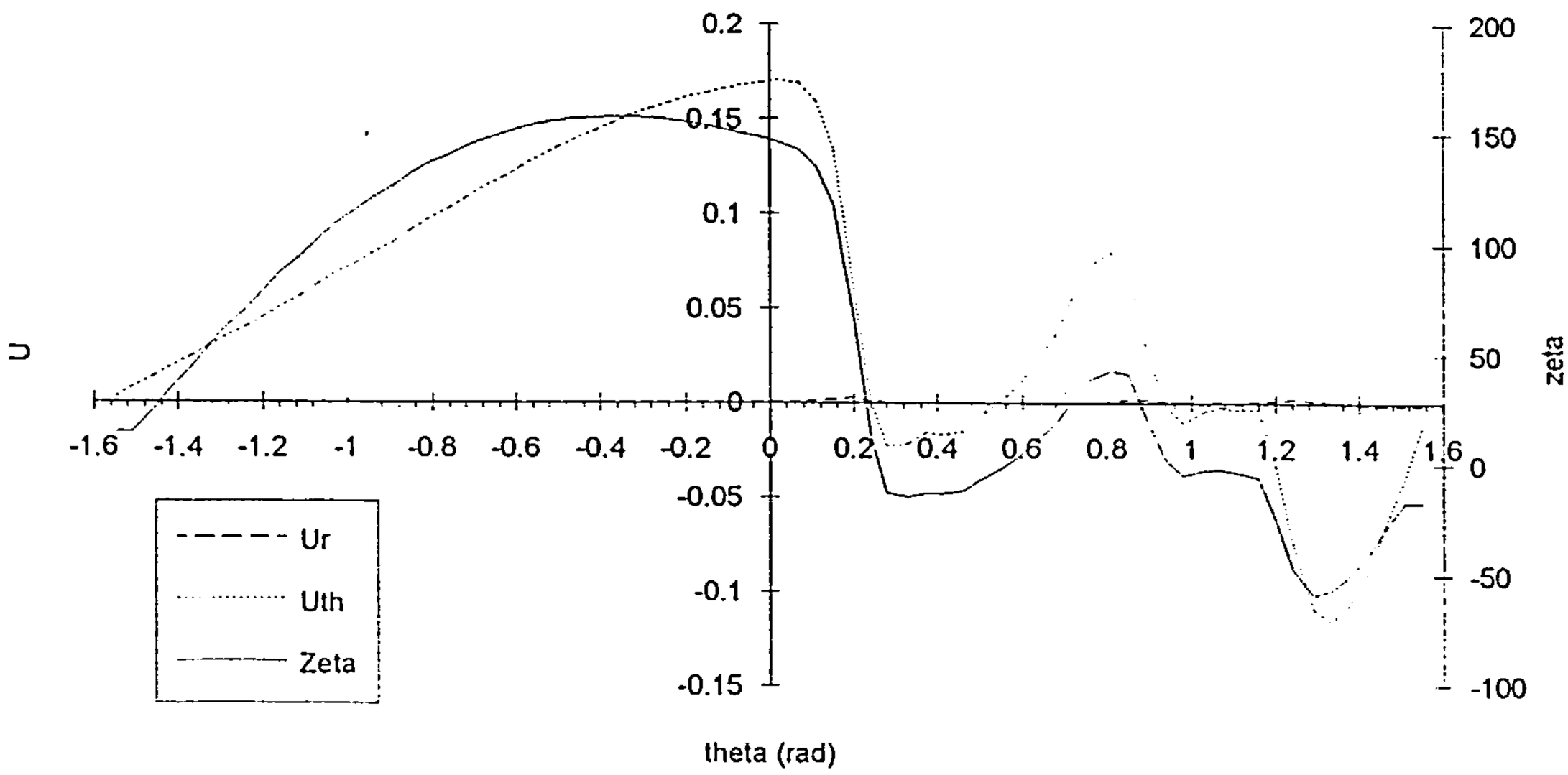

Figure 9.6.1.7

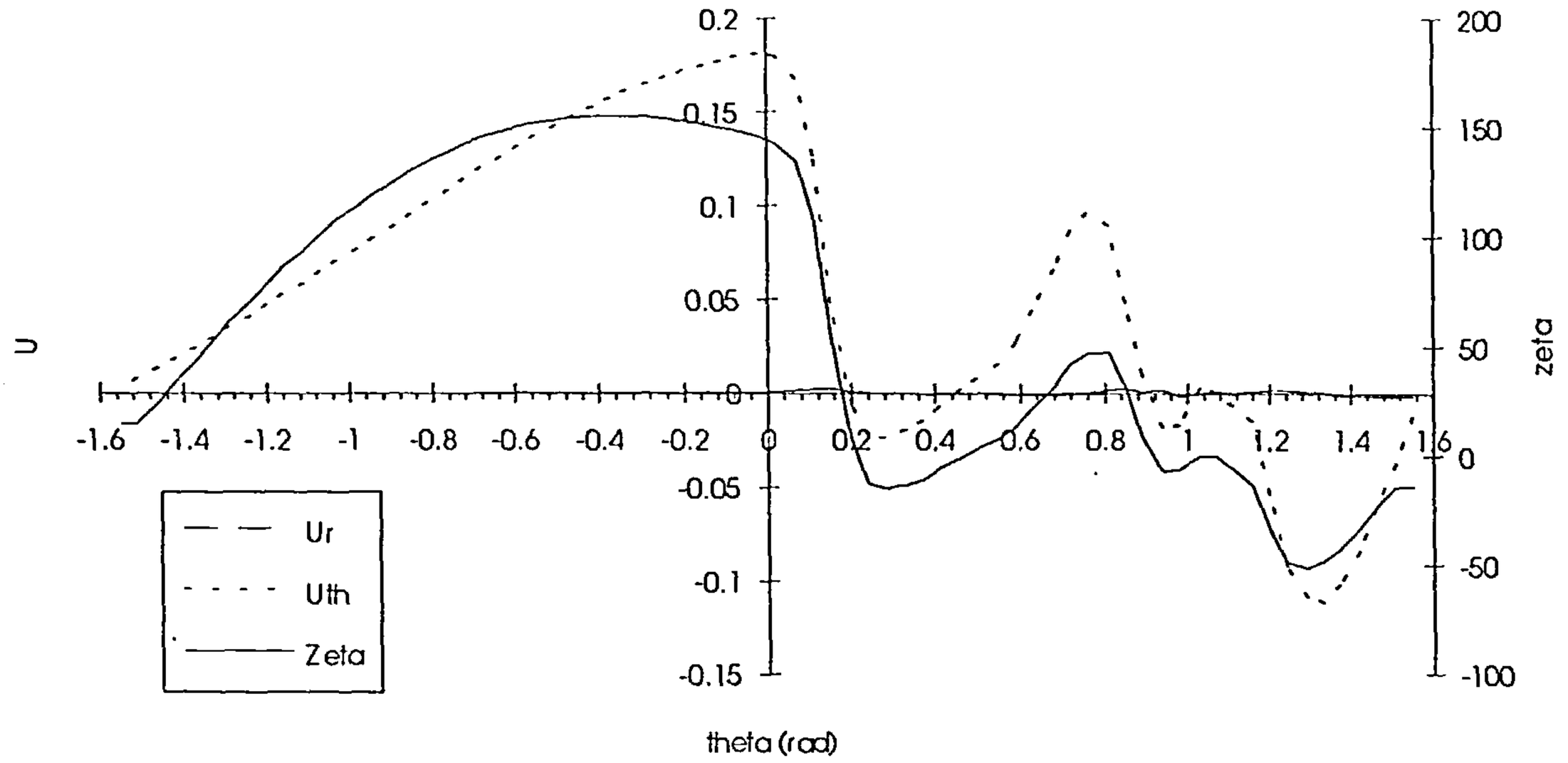

Figure 9.6.1.8

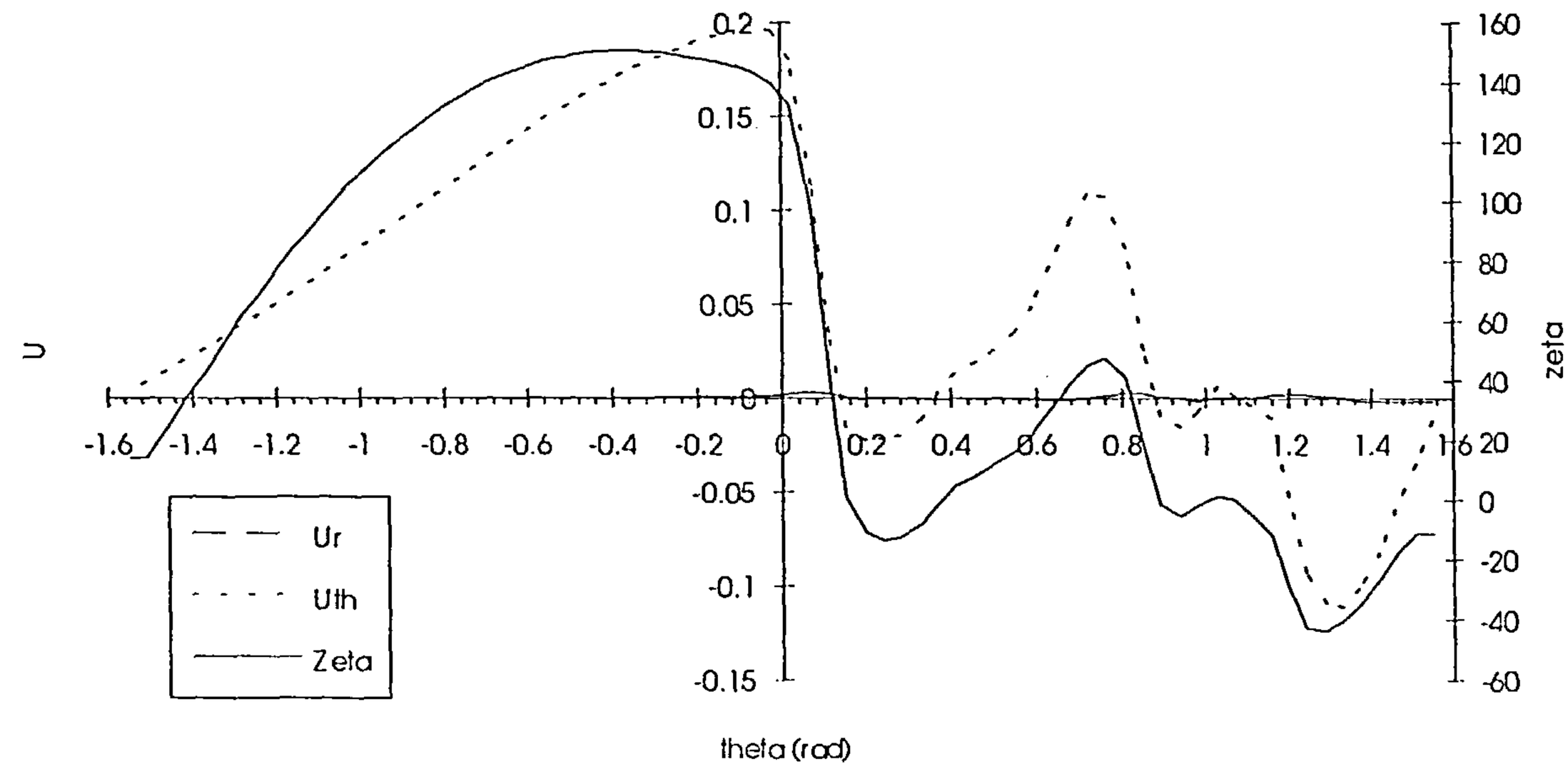

Figure 9.6.1.9

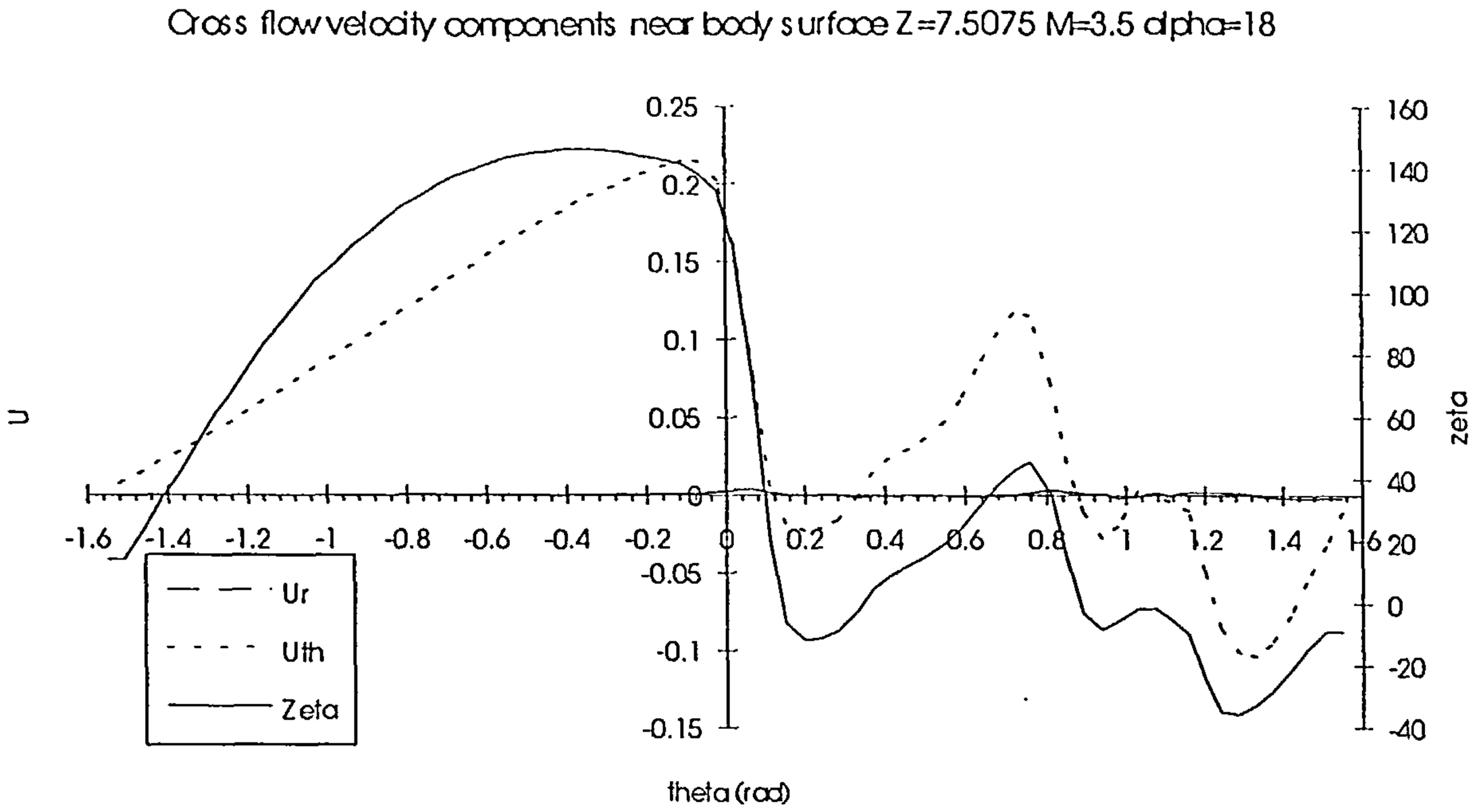

Figure 9.6.1.10

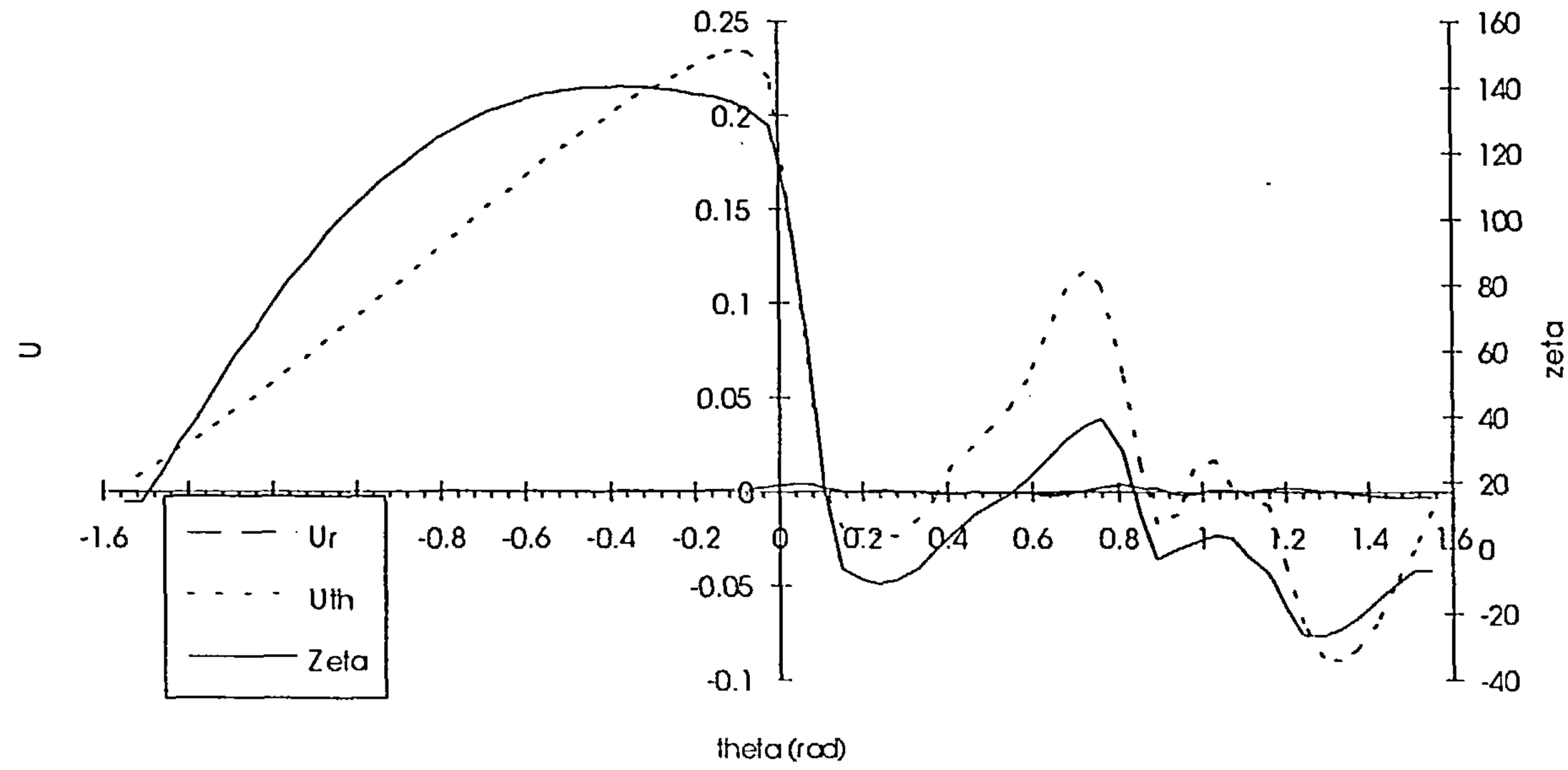

Figure 9.6.1.11

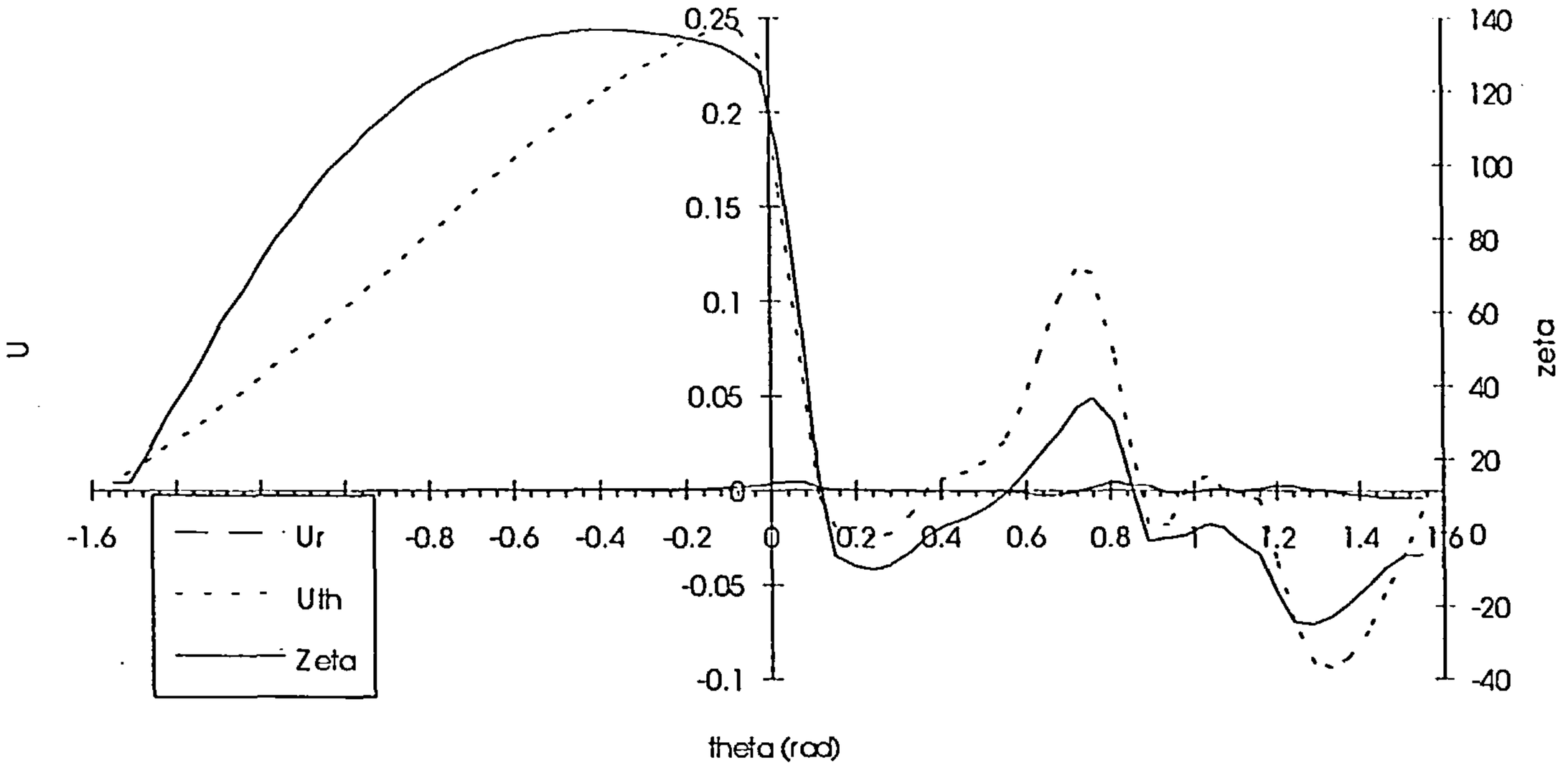

Figure 9.6.1.12

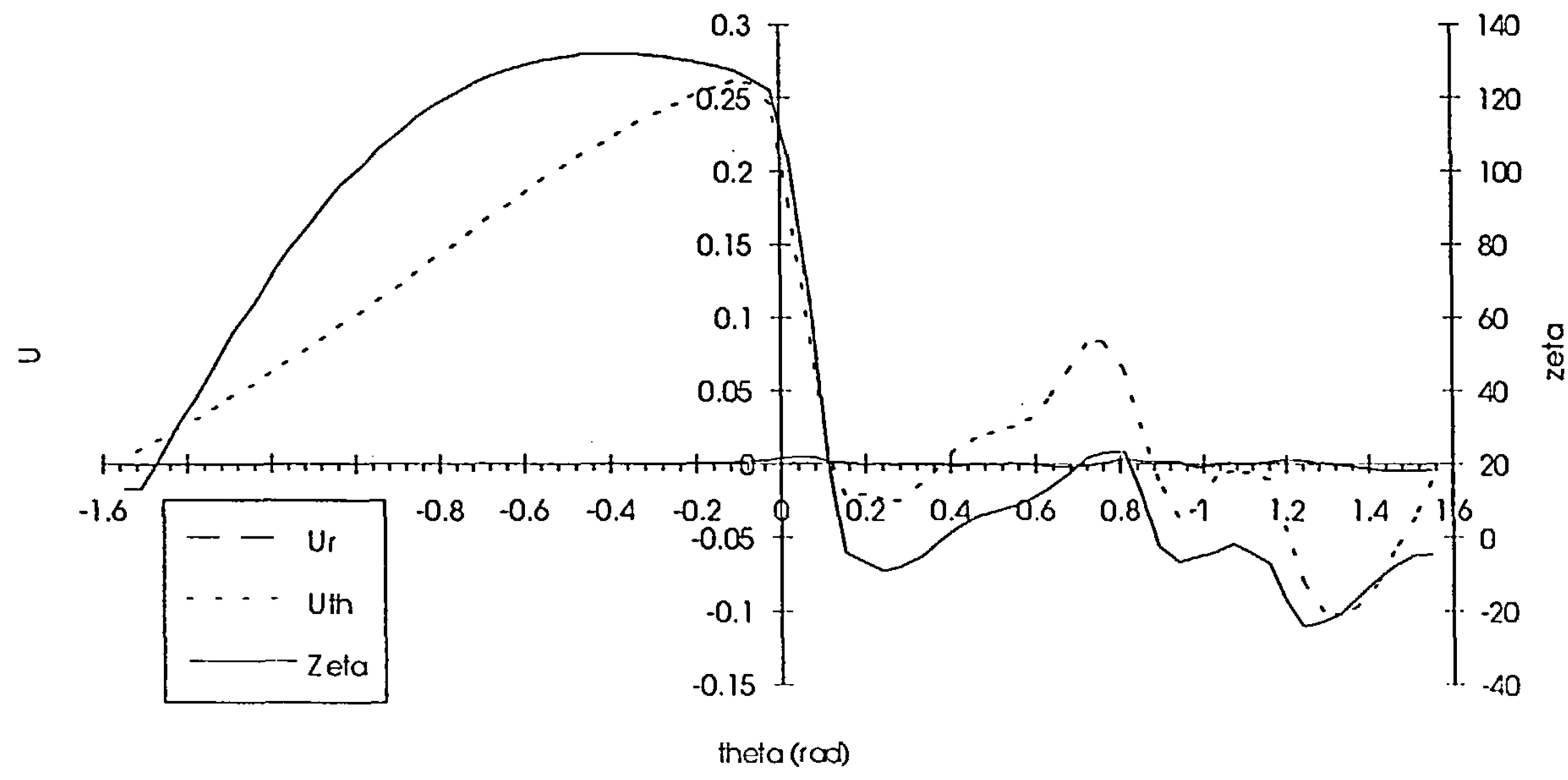

Figure 9.1.6.13

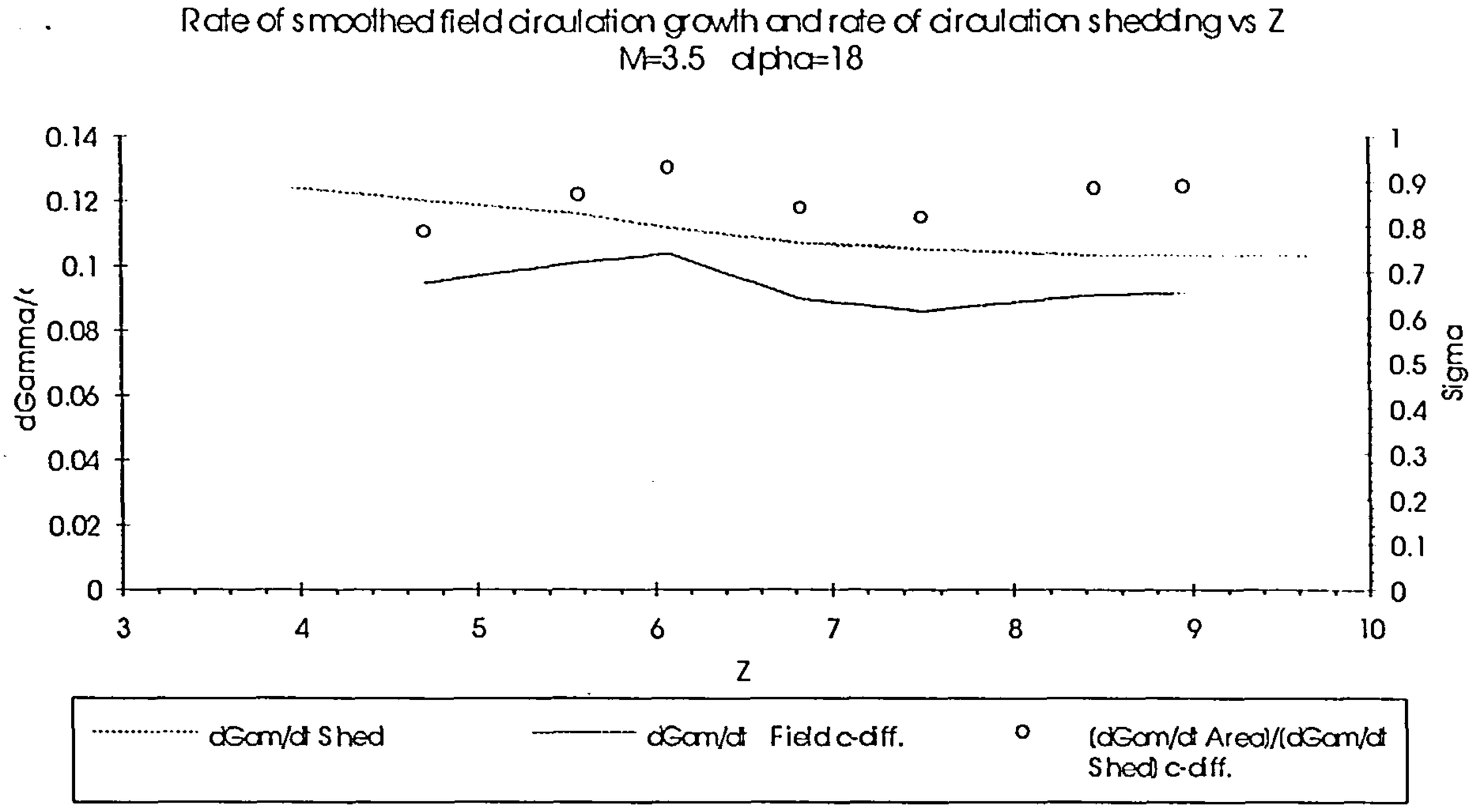

Figure 9.6.1.14

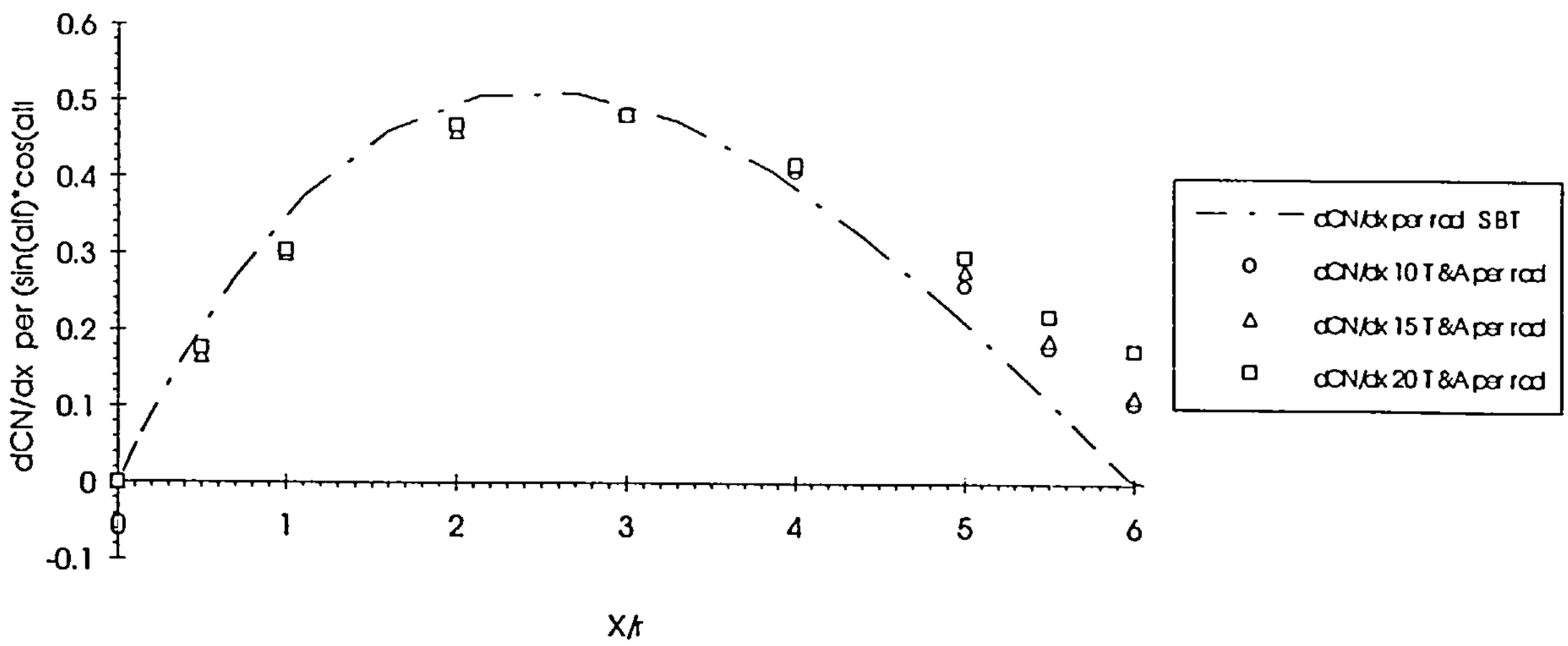

Figure 10.1.1.1

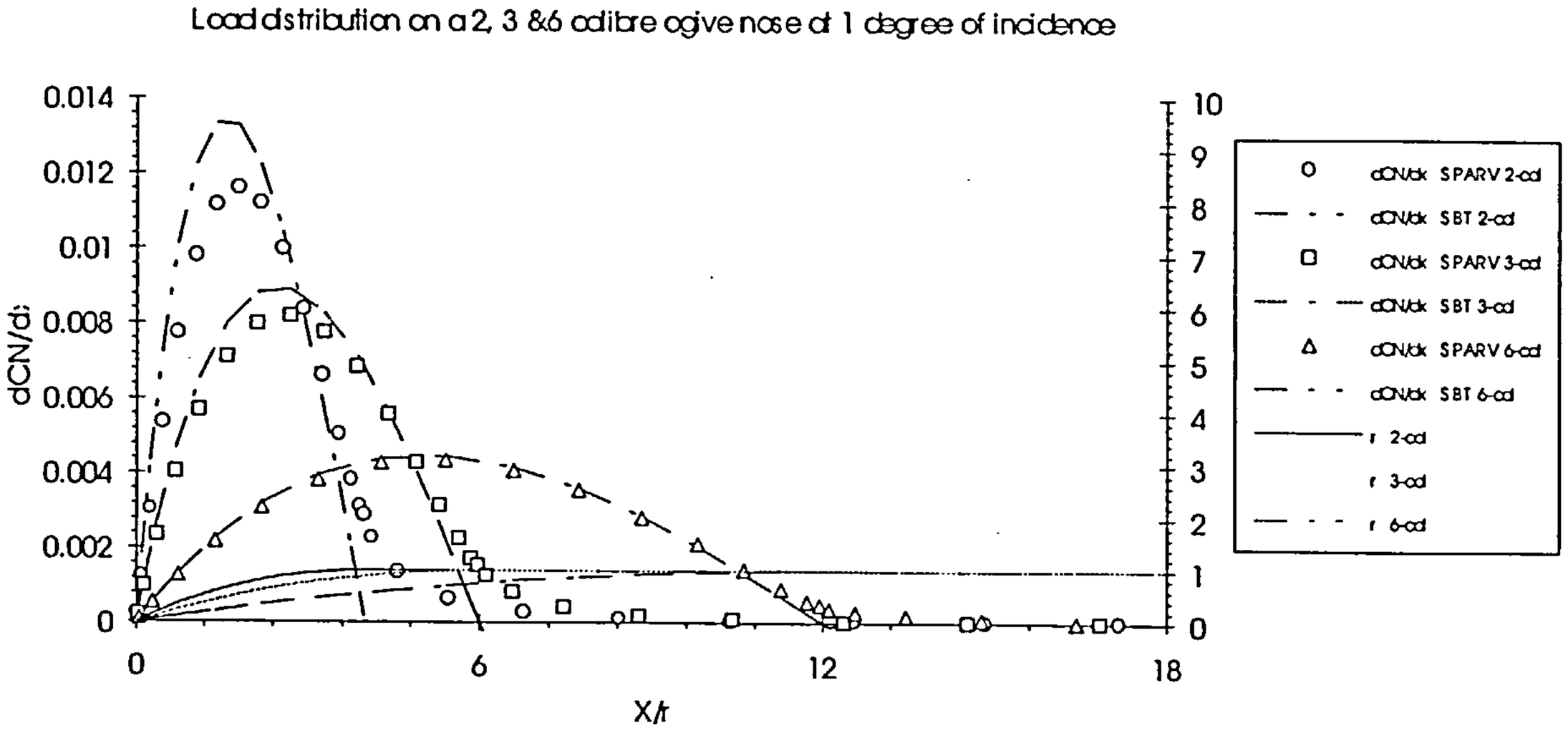

Figure 10.1.1.2

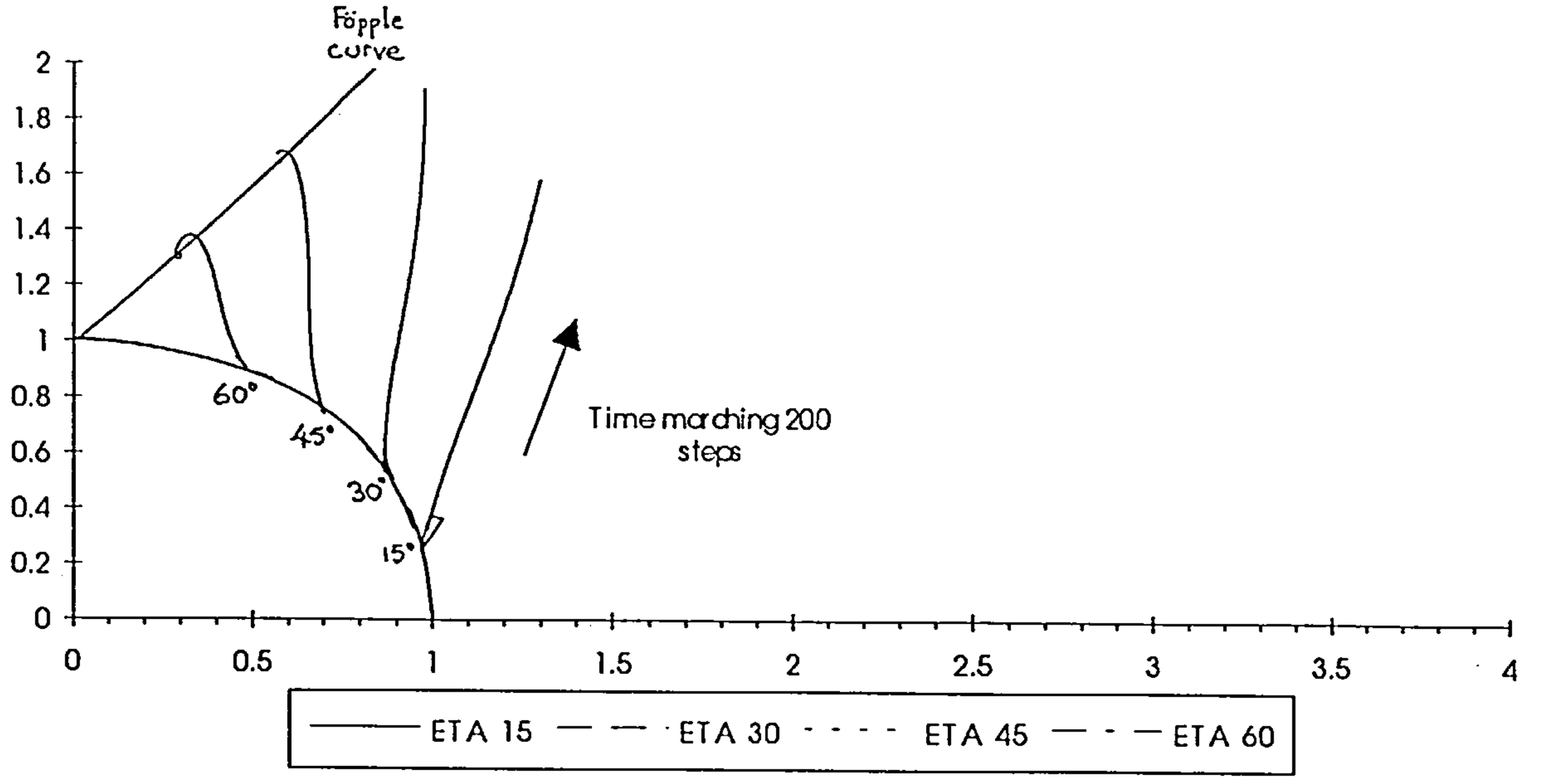

Figure 10.2.1.3

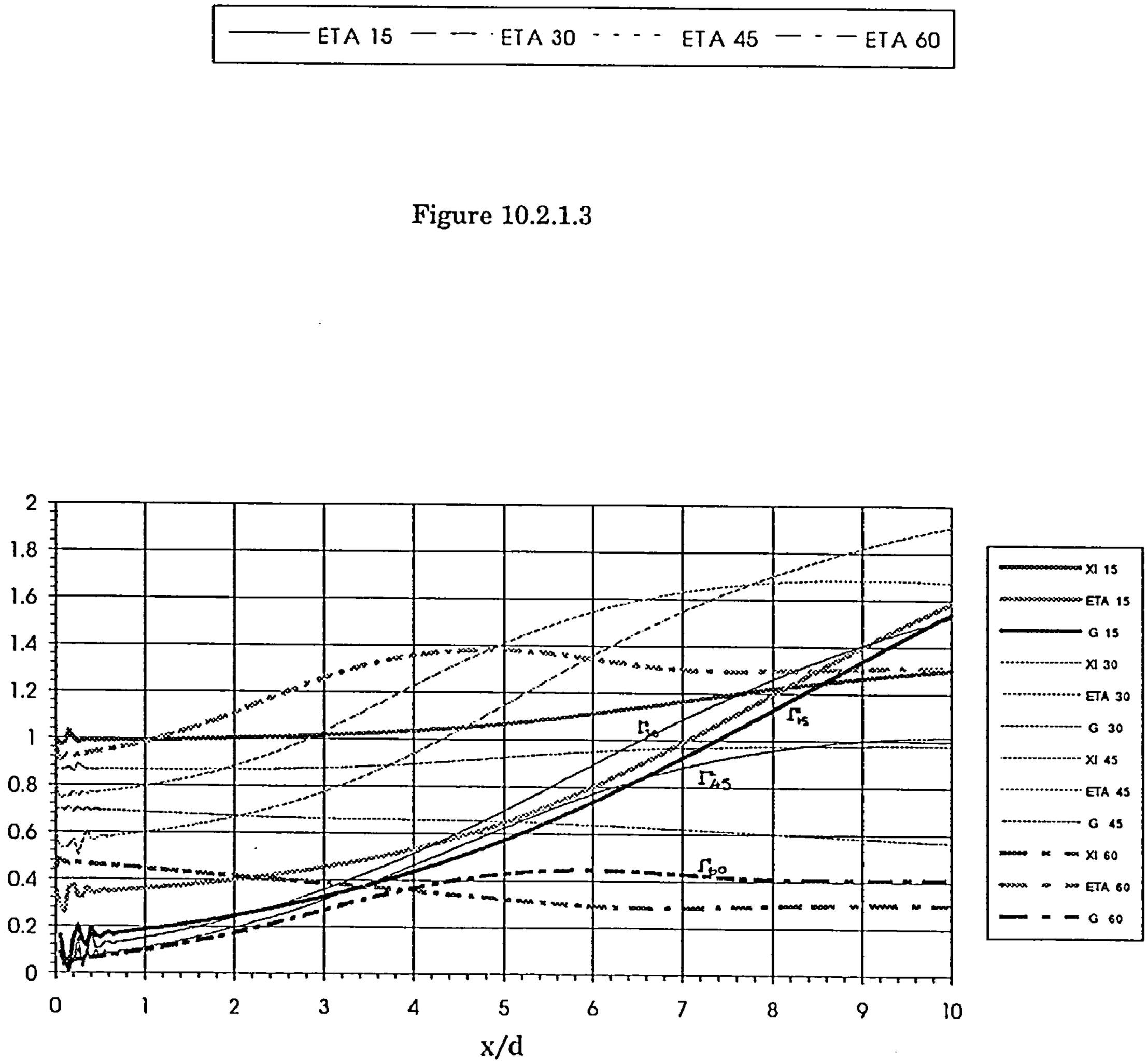

Figure 10.2.3.1

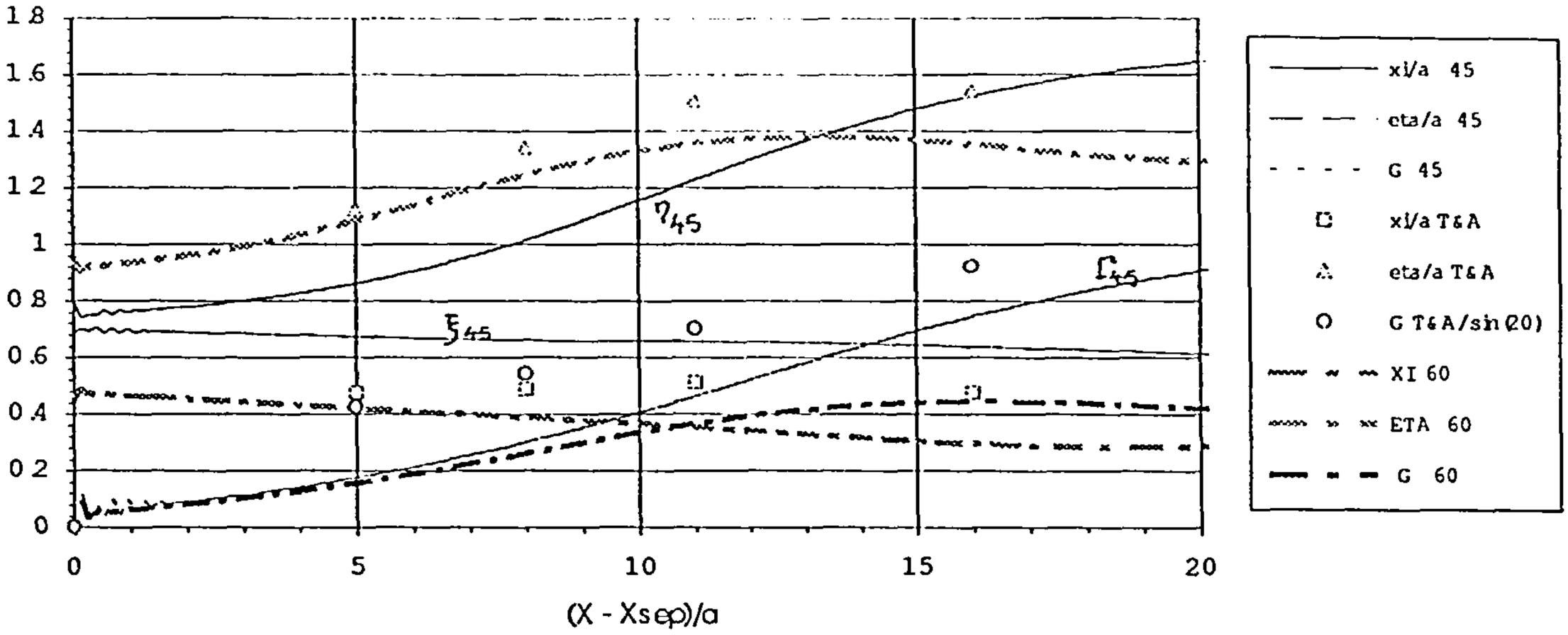

Figure 10.2.3.2

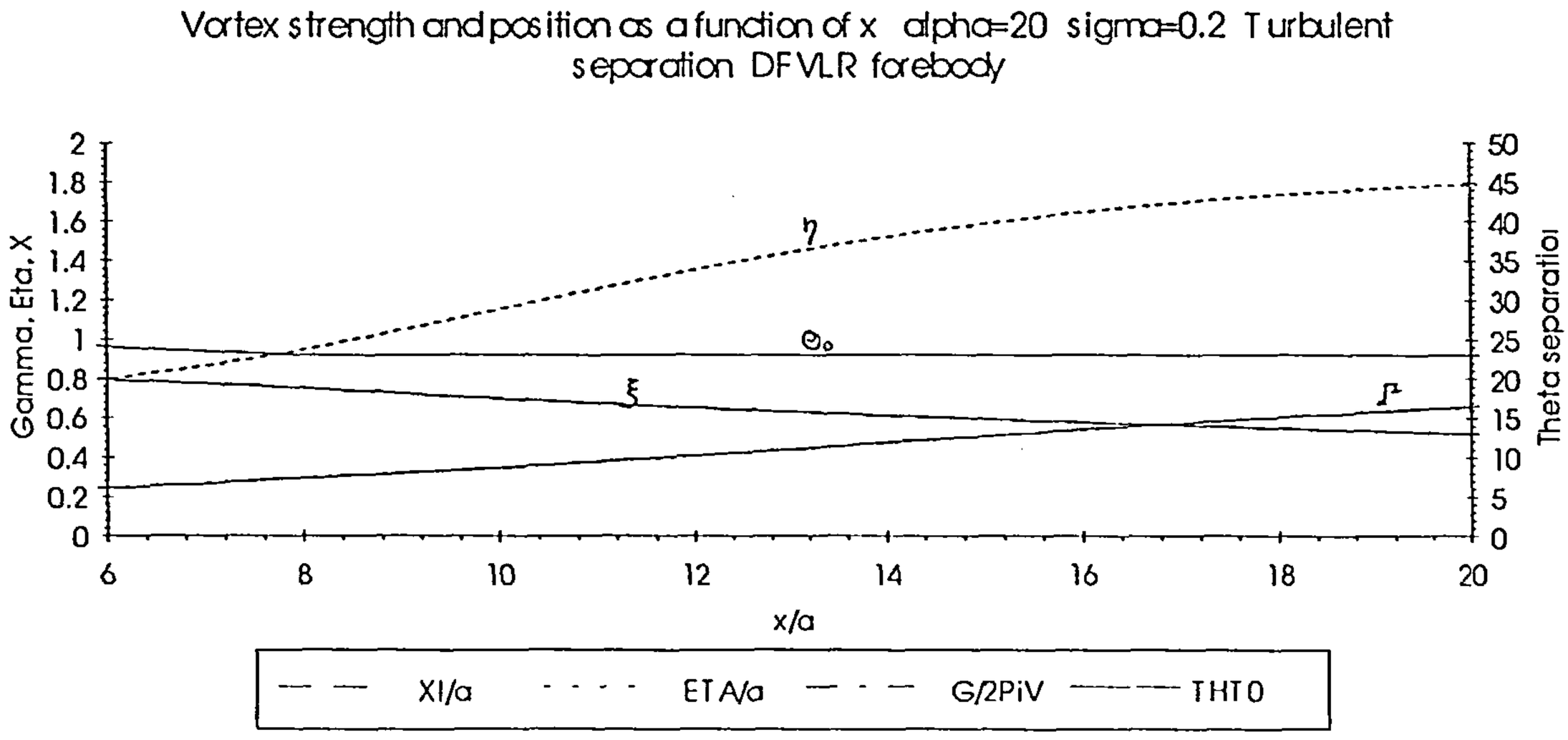

Figure 10.2.4.1

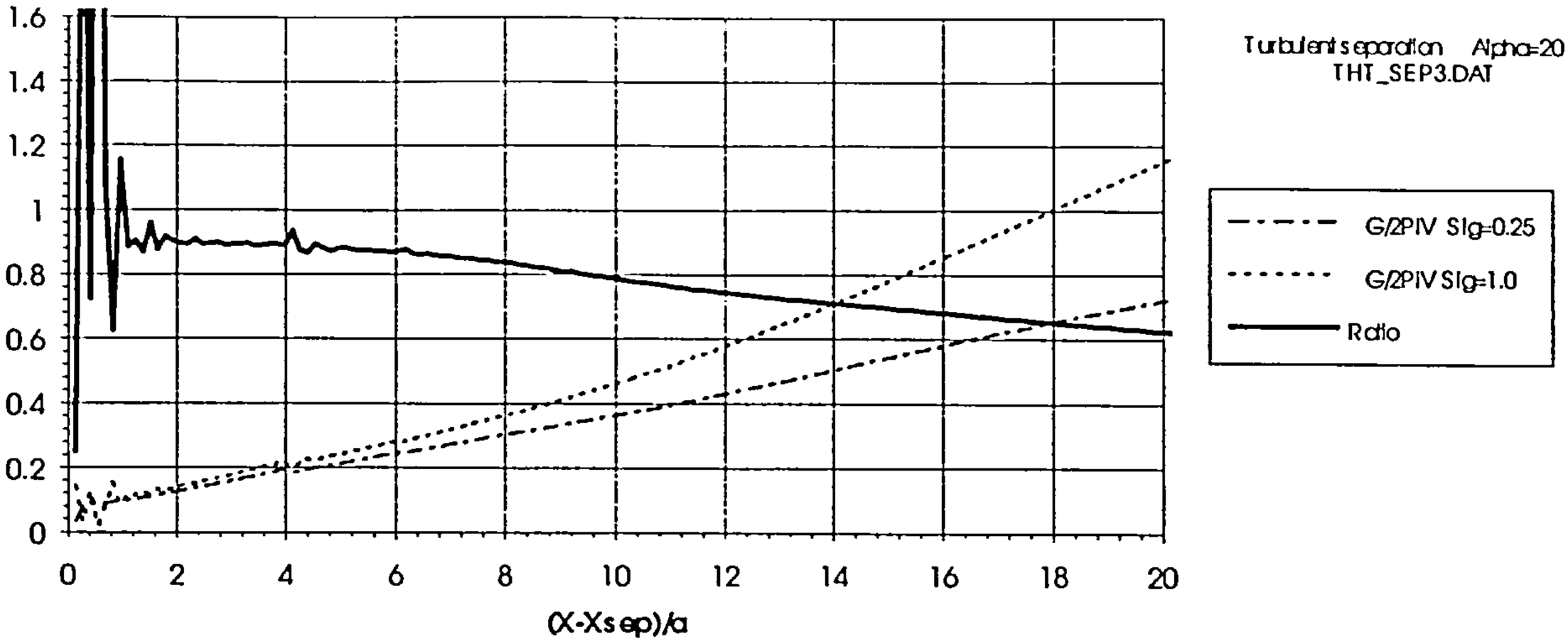

Figure 10.2.4.2

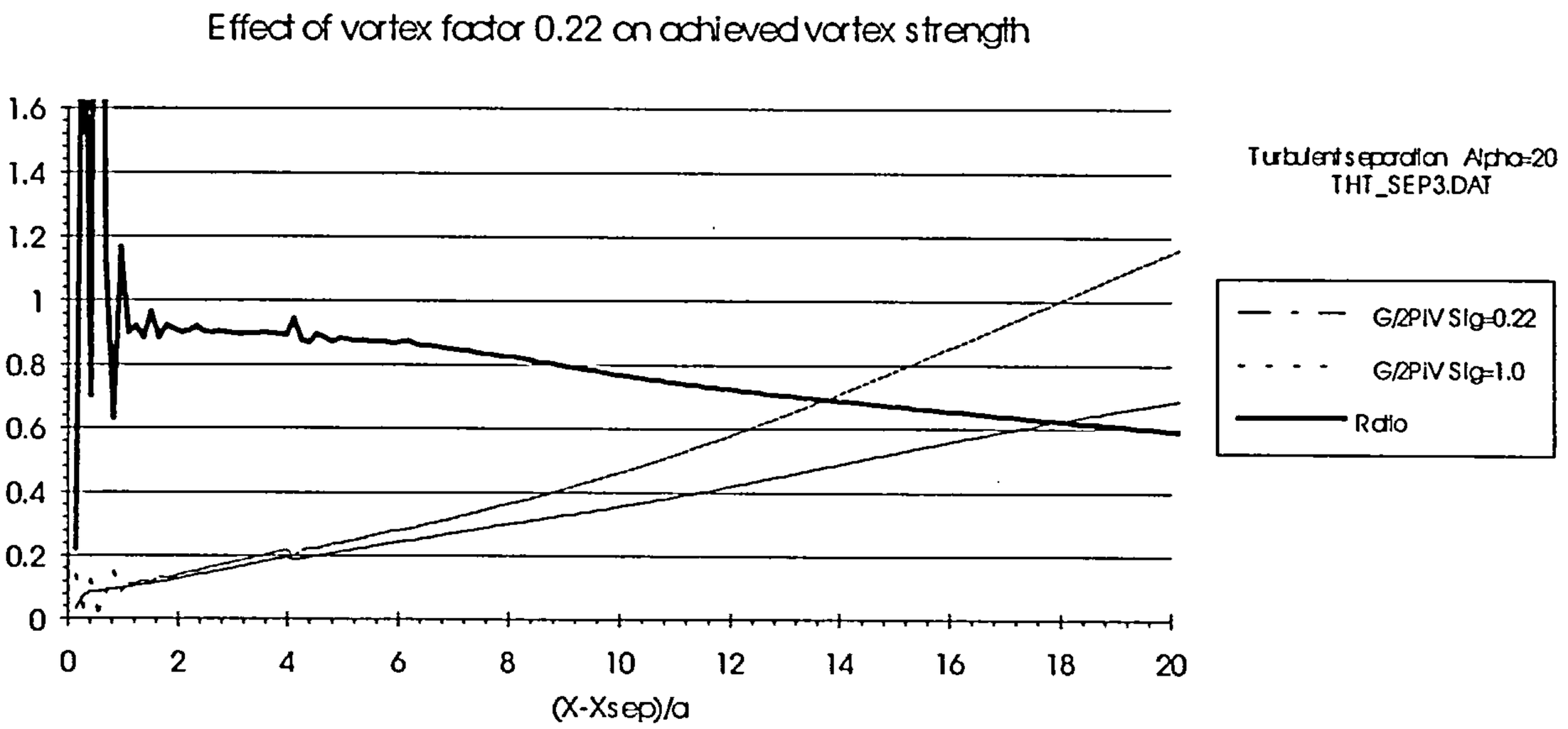

Figure 10.2.4.3

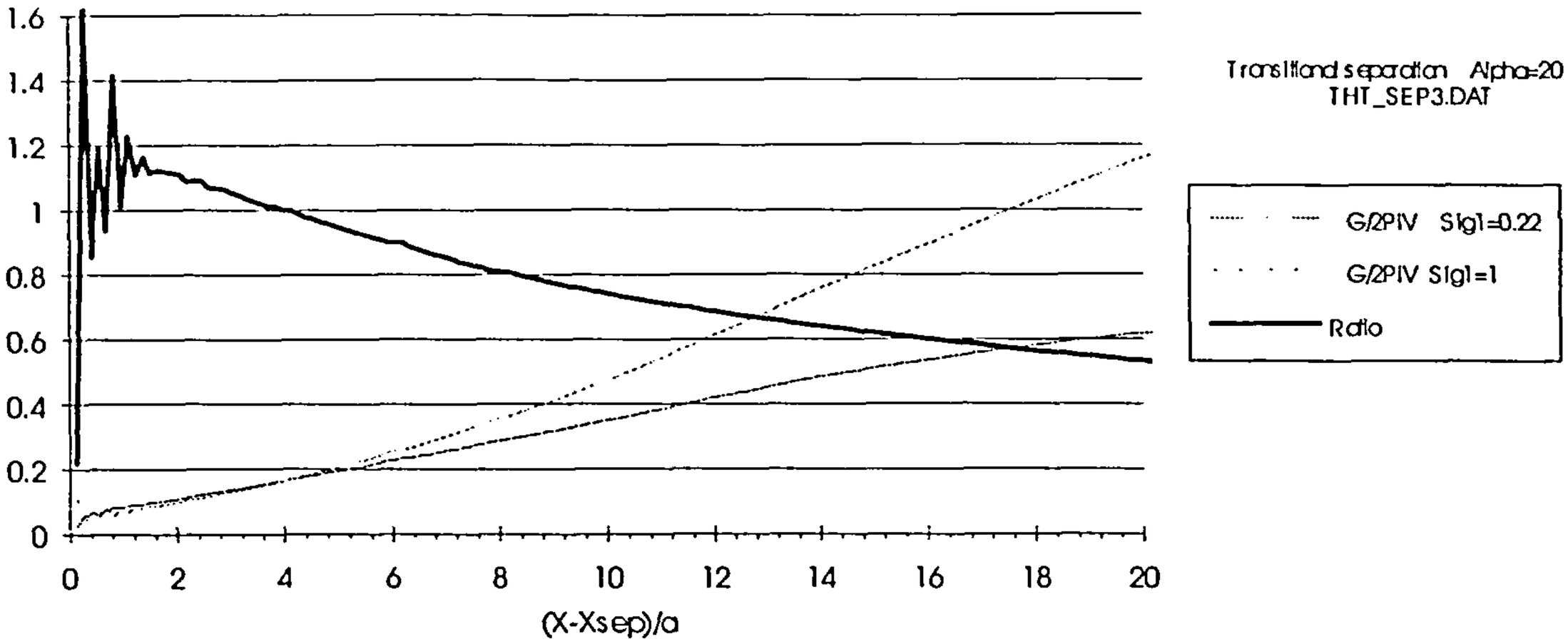

Figure 10.2.4.4

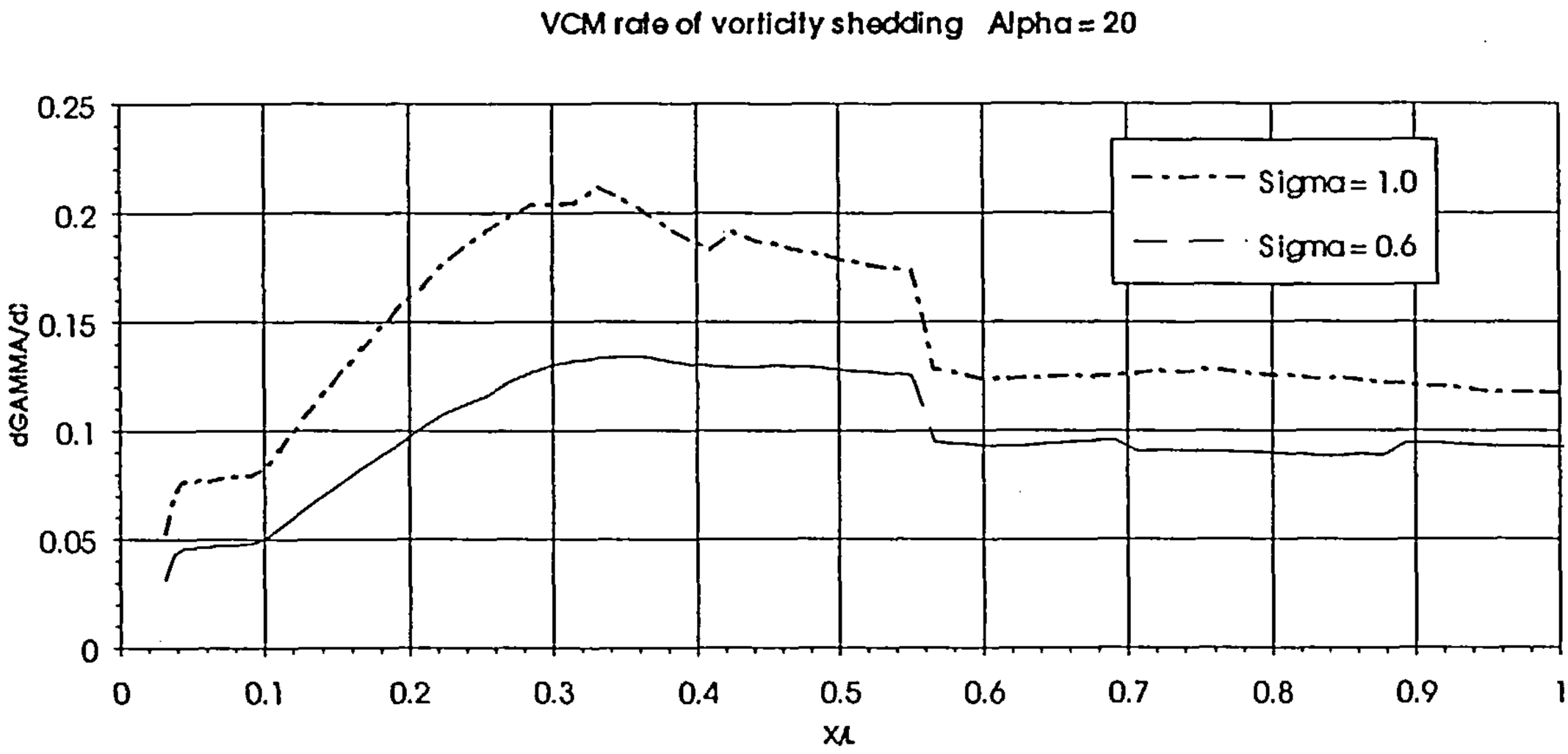

Figure 10.2.5.1

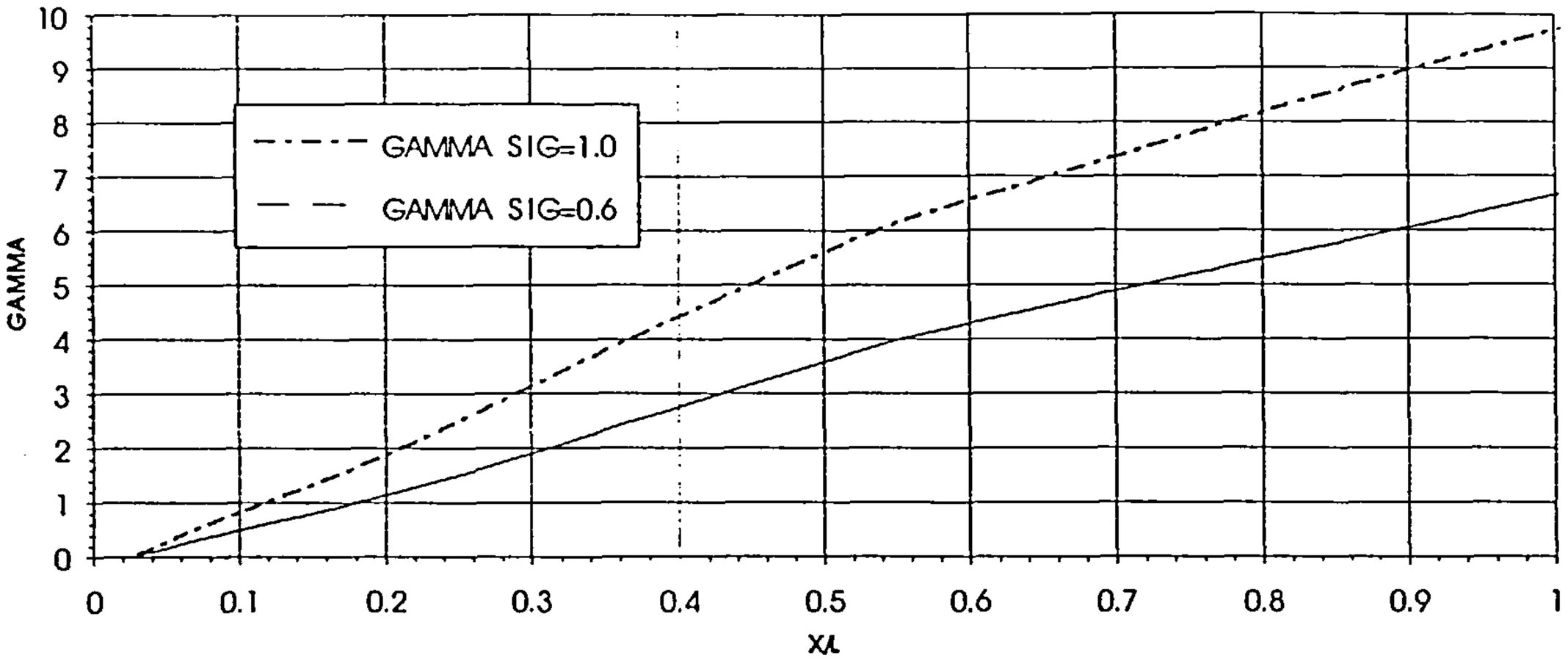

Figure 10.2.5.2

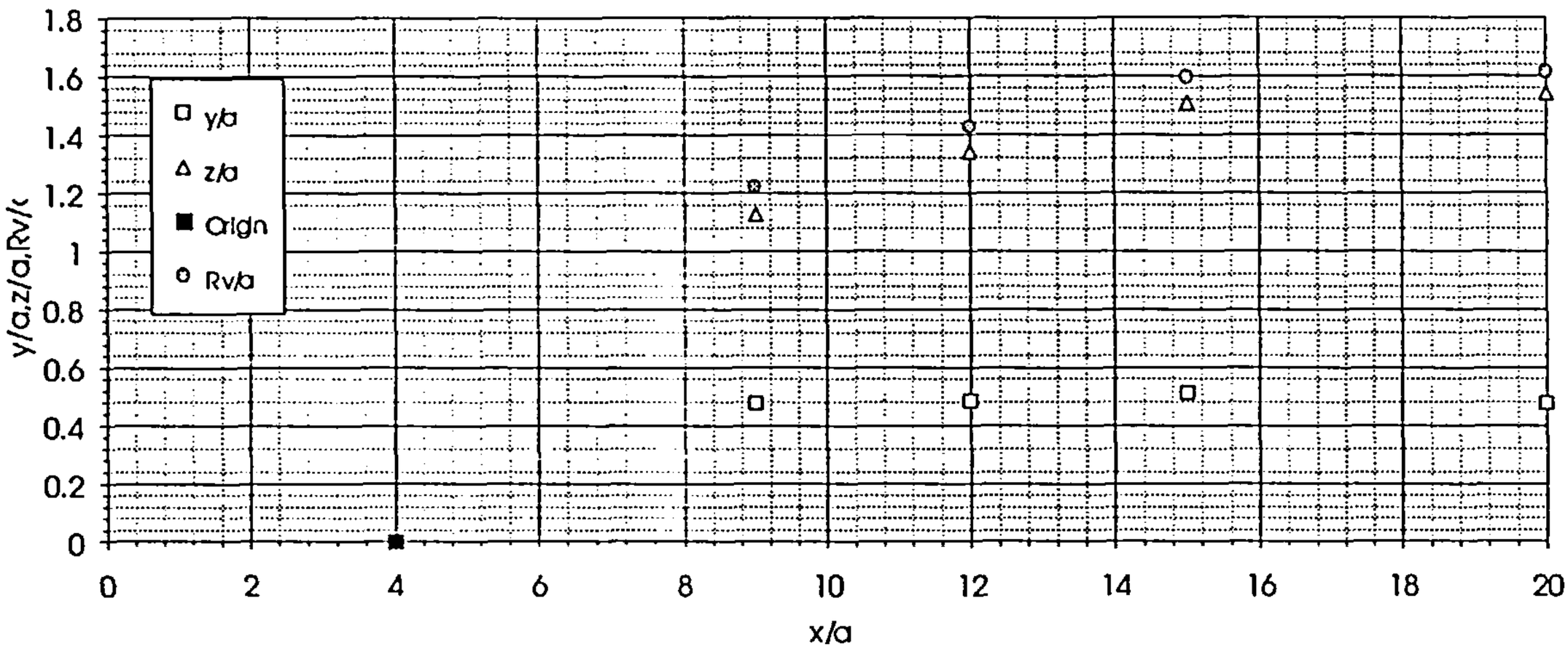

Figure 10.2.5.3

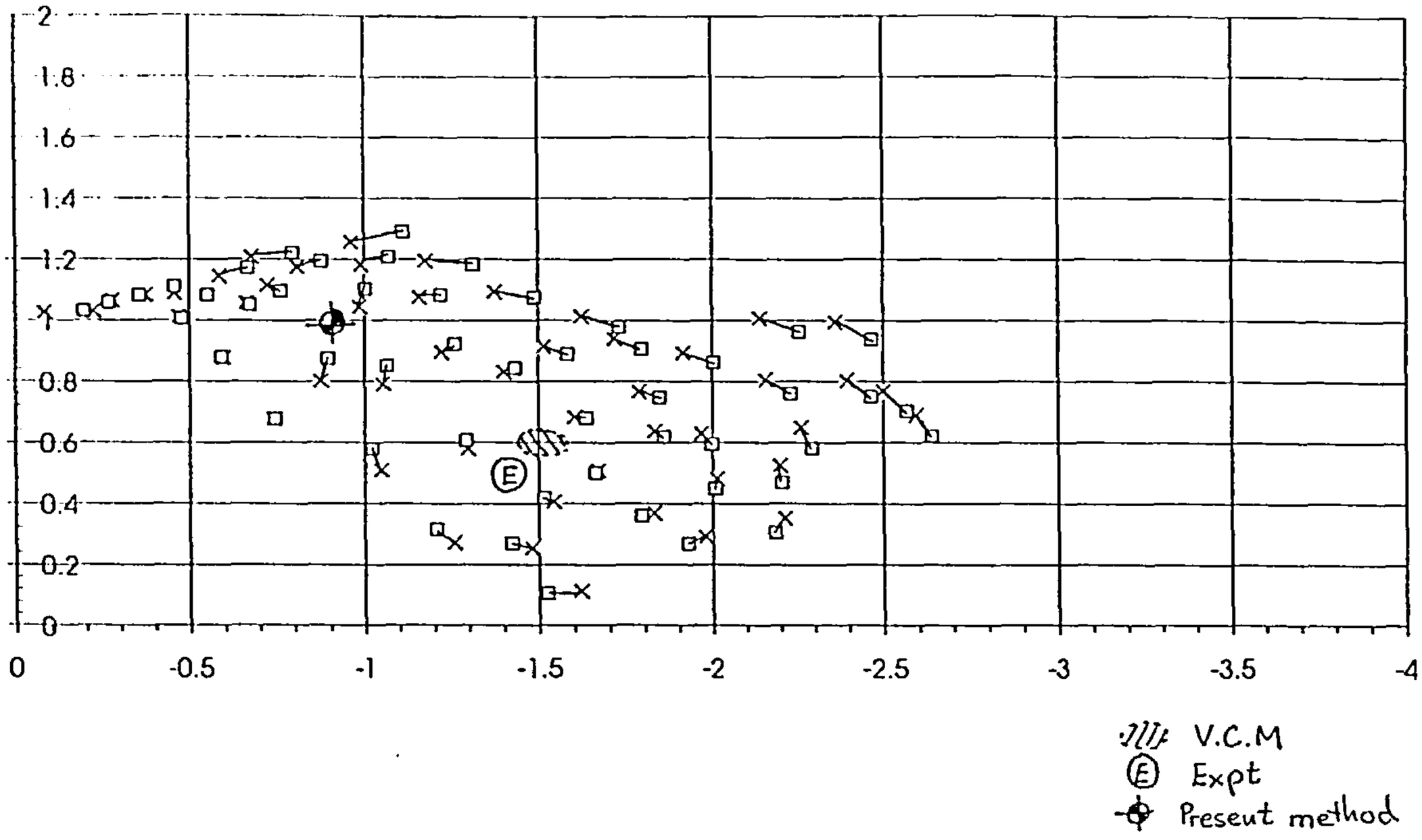

Figure 10.2.5.4 VCM σ=1.0 x/l=0.6131

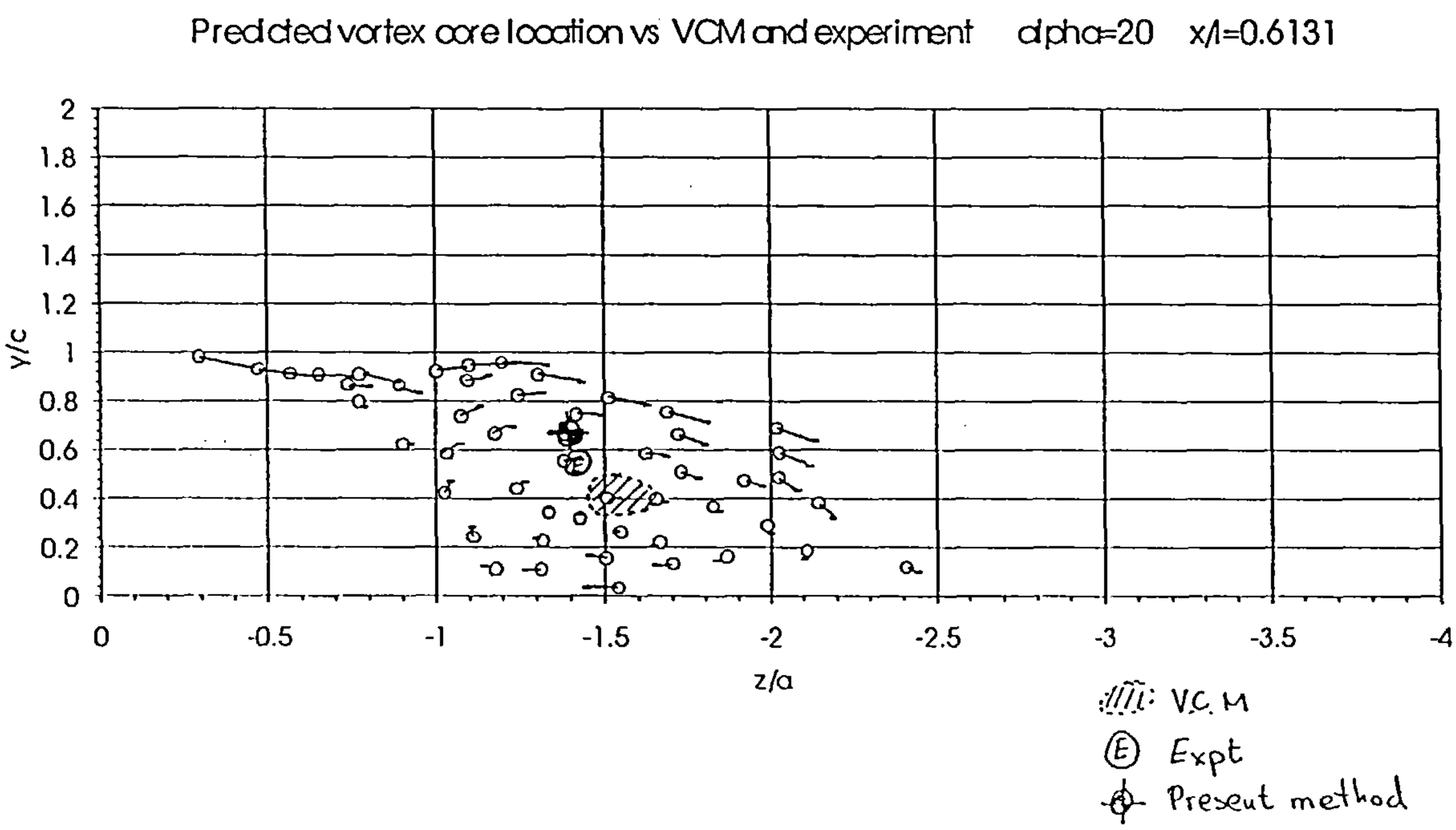

Figure 10.2.5.5 σ=0.6

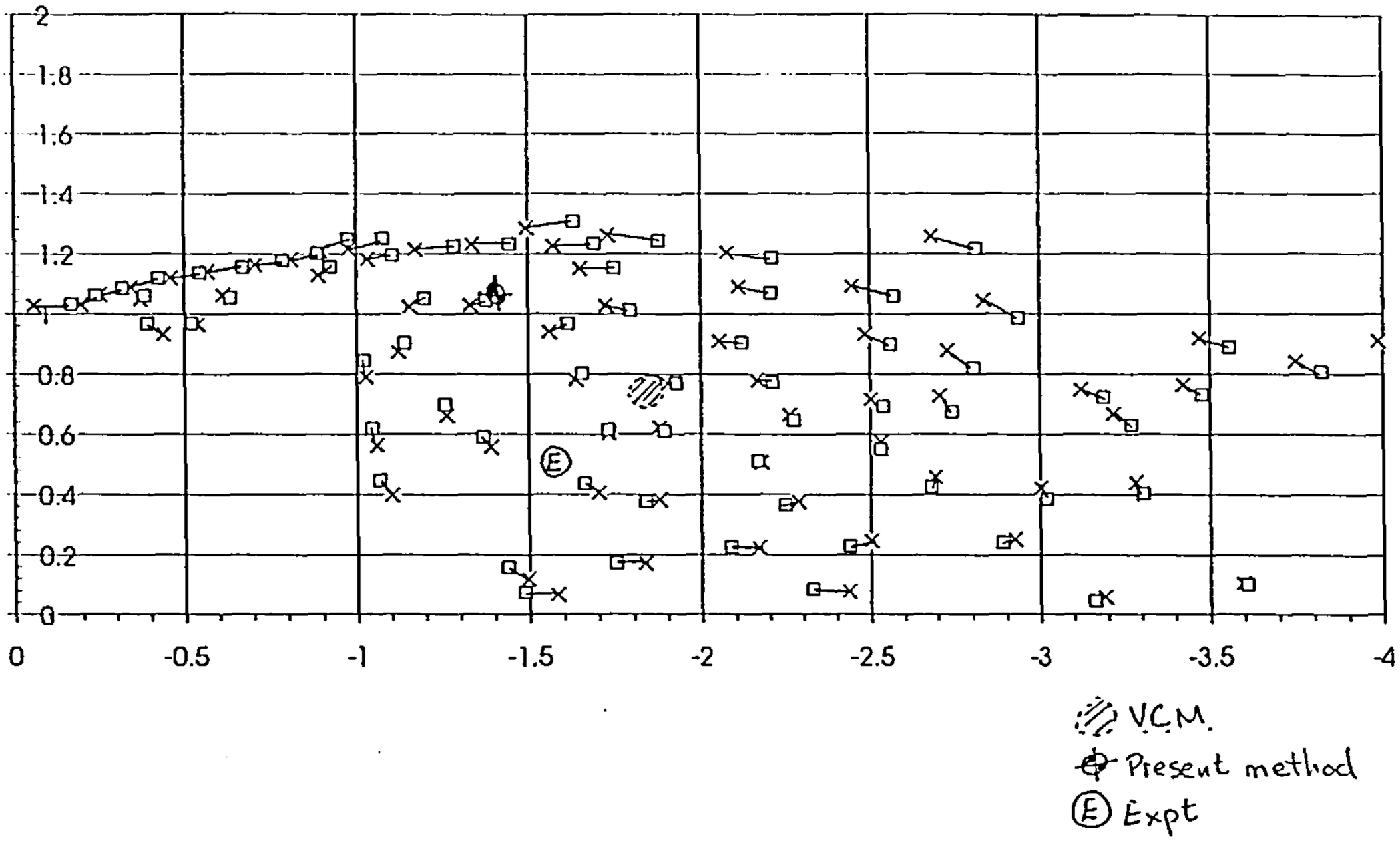

Figure 10.2.5.6 σ=1.0 x/l=0.9585

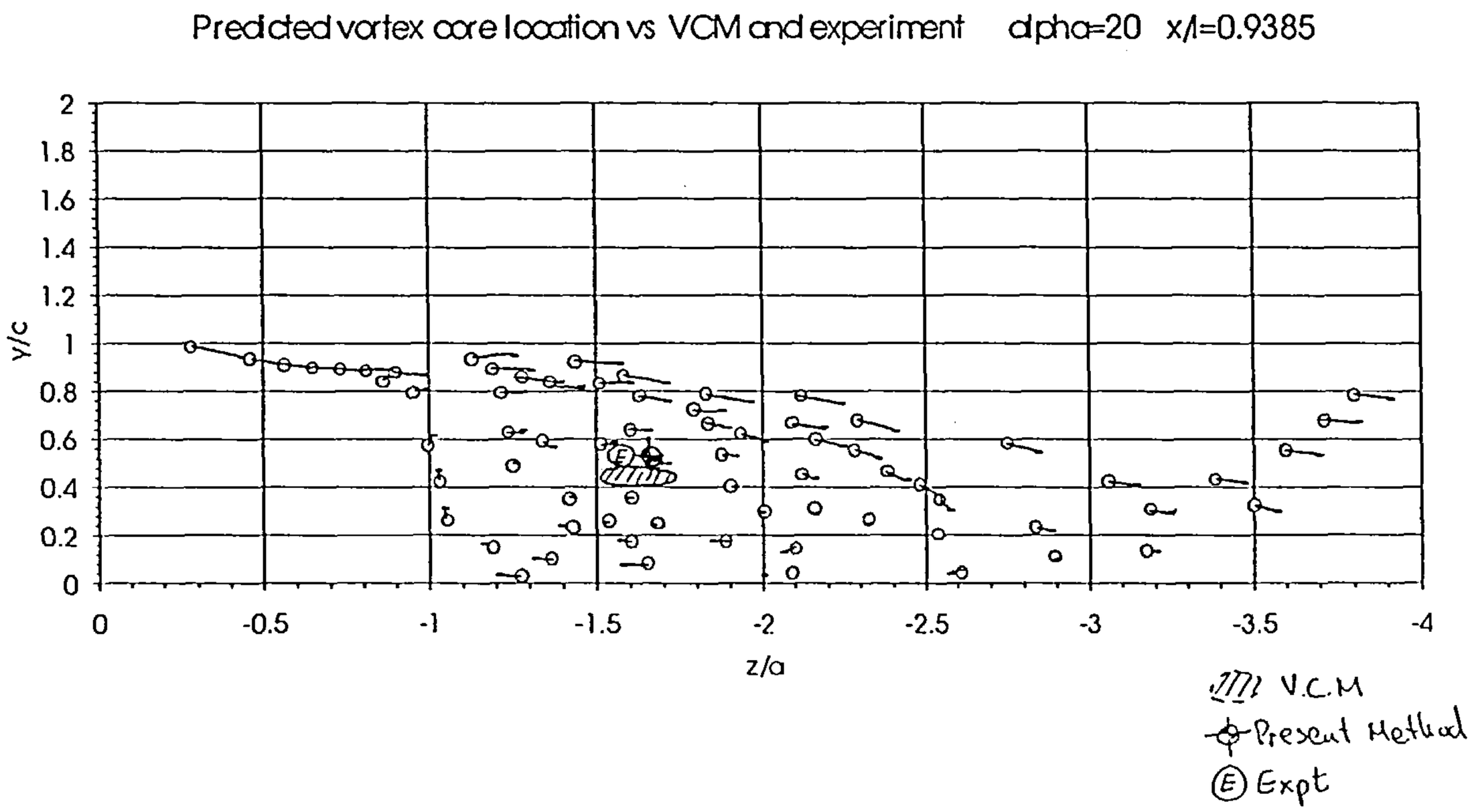

Figure 10.2.5.7 σ=0.6

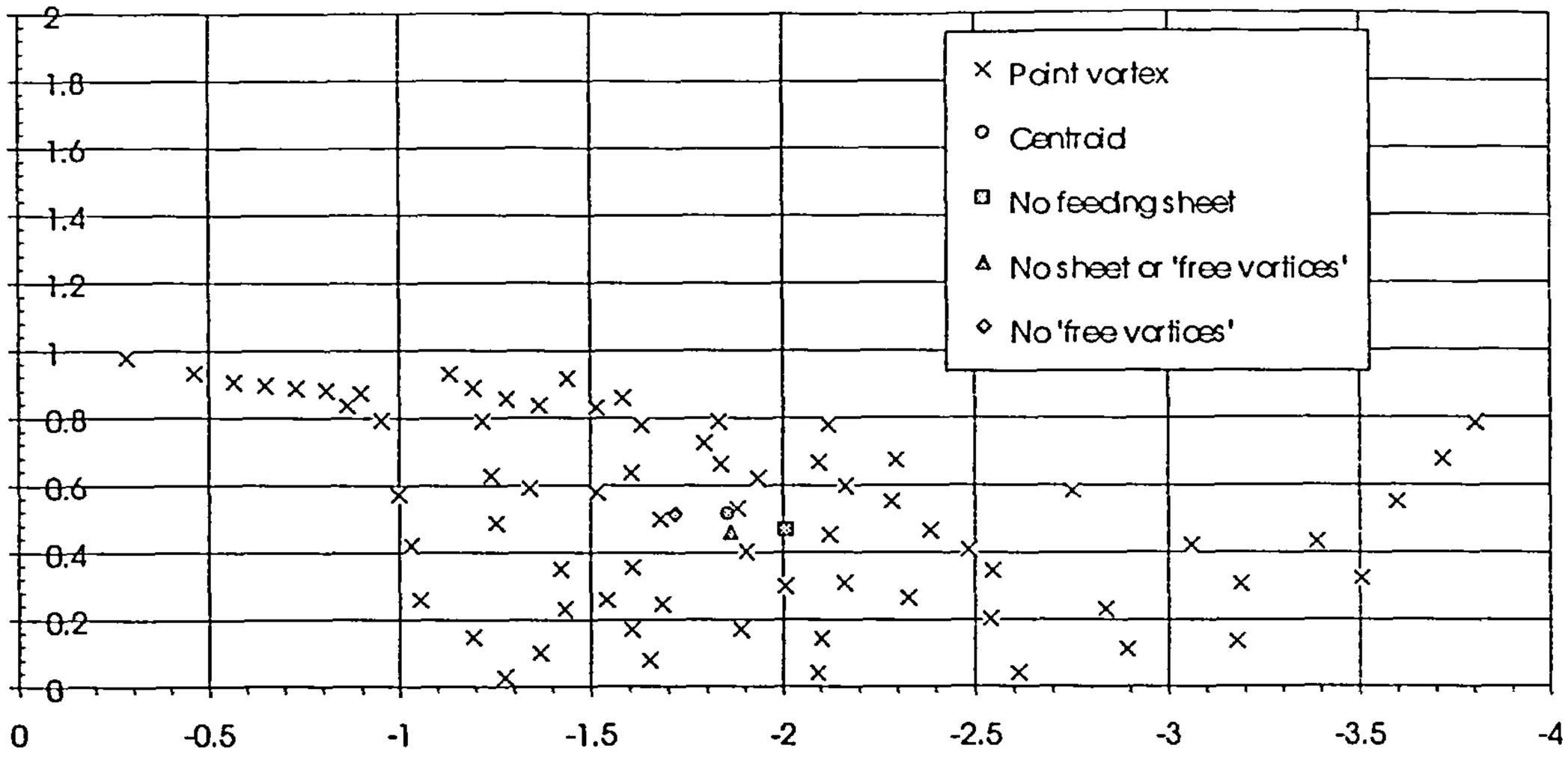

Figure 10.2.5.8

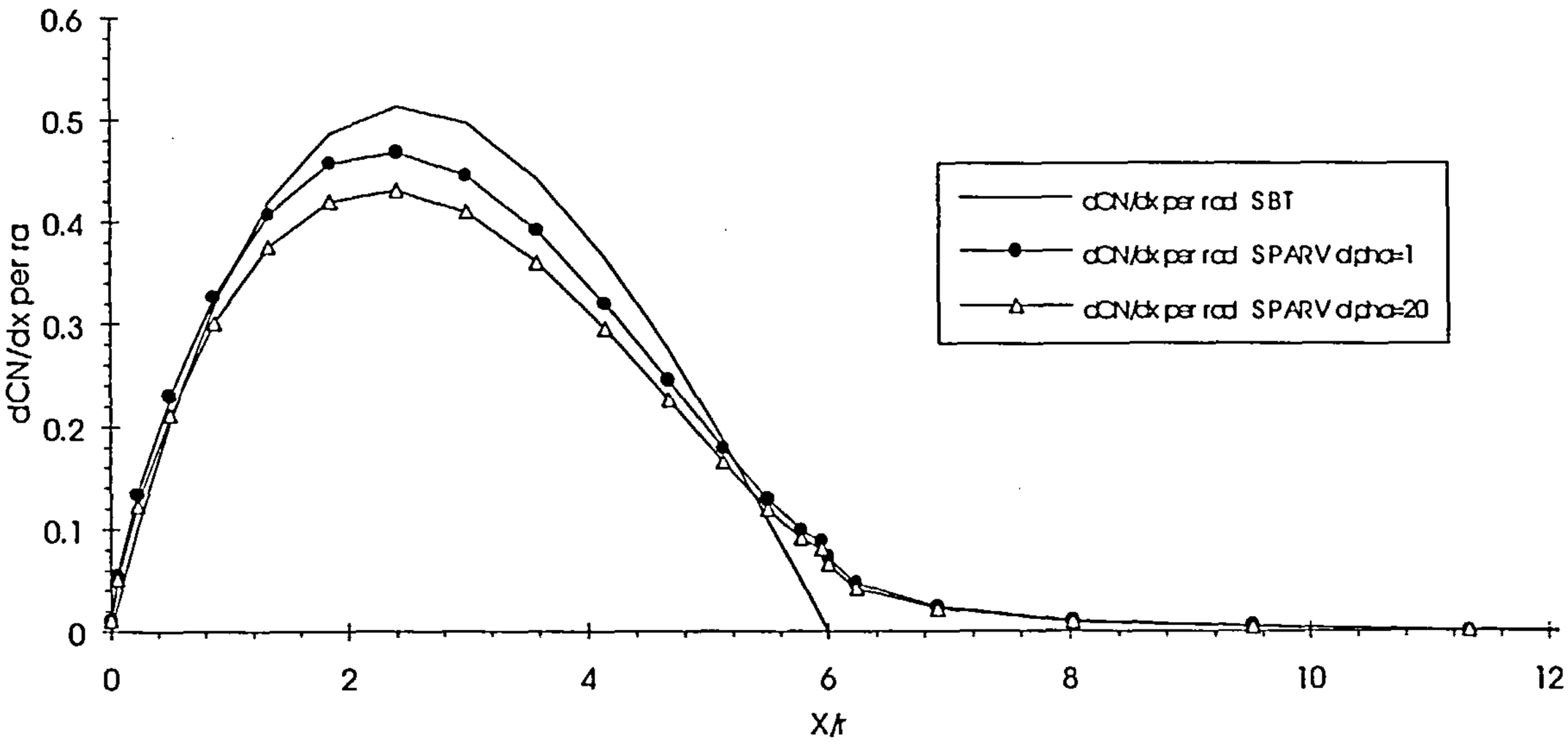

Figure 10.3.2.1

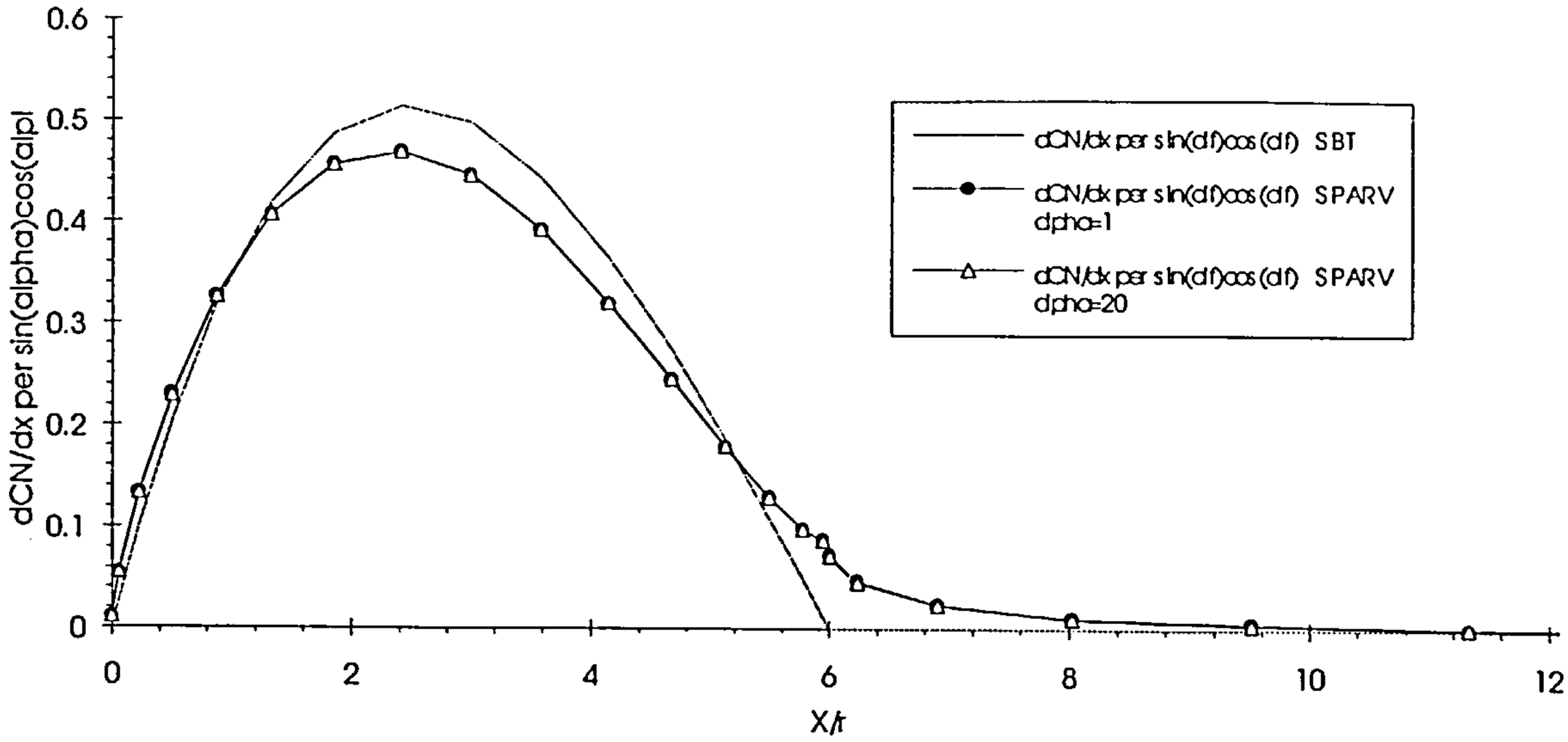

Figure 10.3.2.2

Load distribution on a 3 calibre ogive nose - 12 calibre cylinder - 3 calibre closure body using SPARV at alpha=1 degree

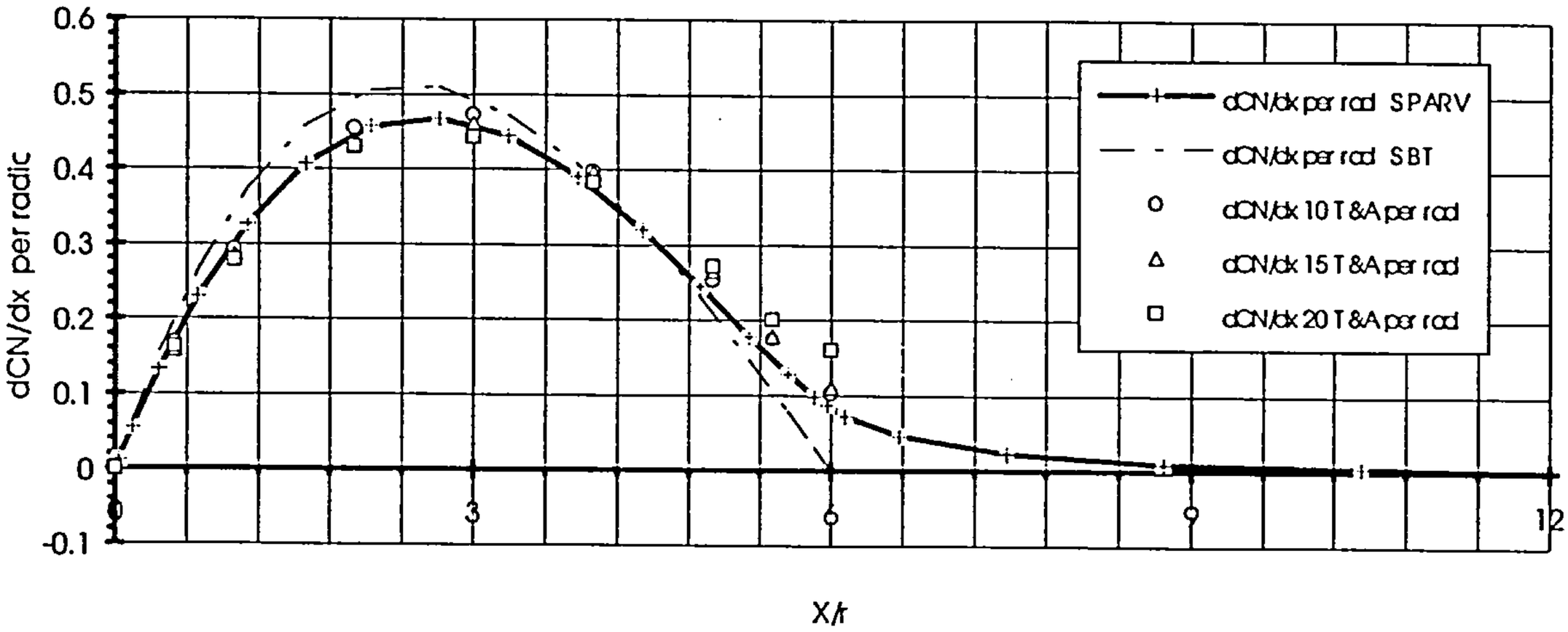

Figure 10.3.3.1

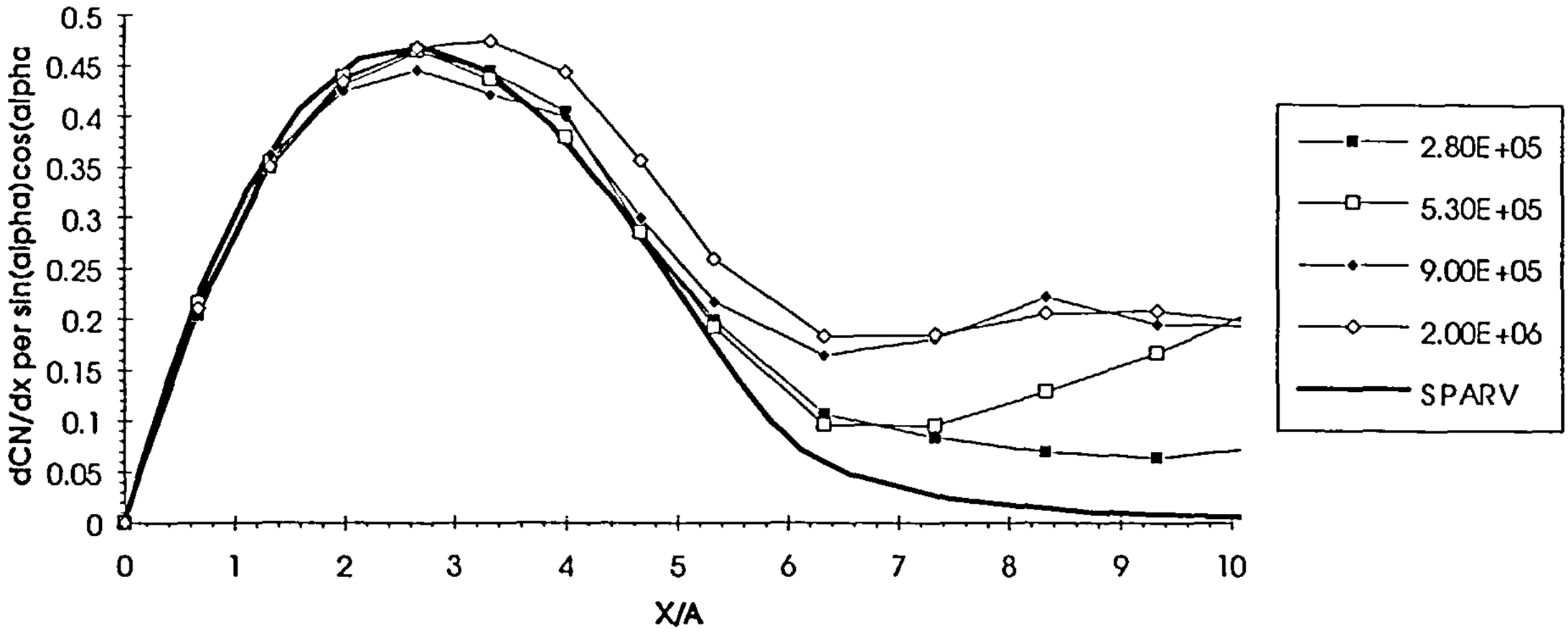

Figure 10.3.3.2

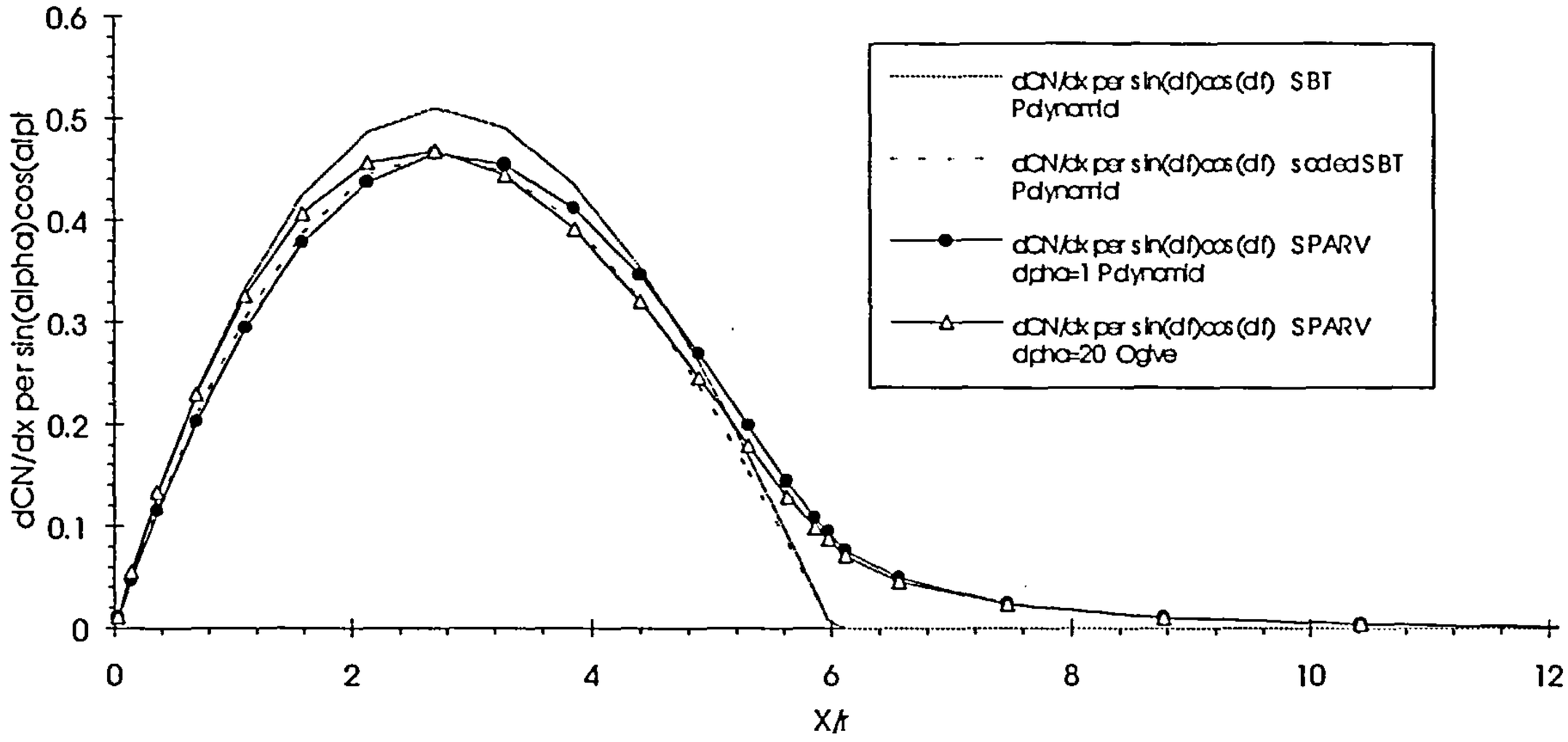

Figure 10.3.4.2

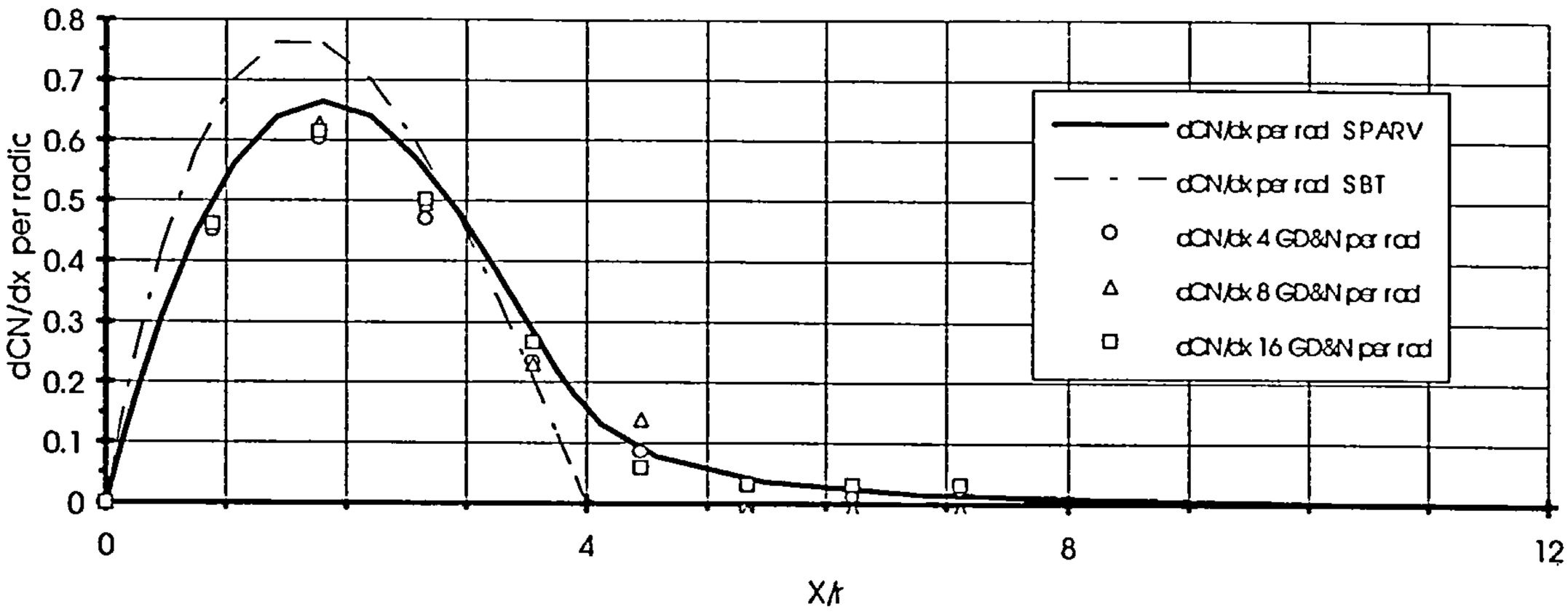

Figure 10.3.4.3

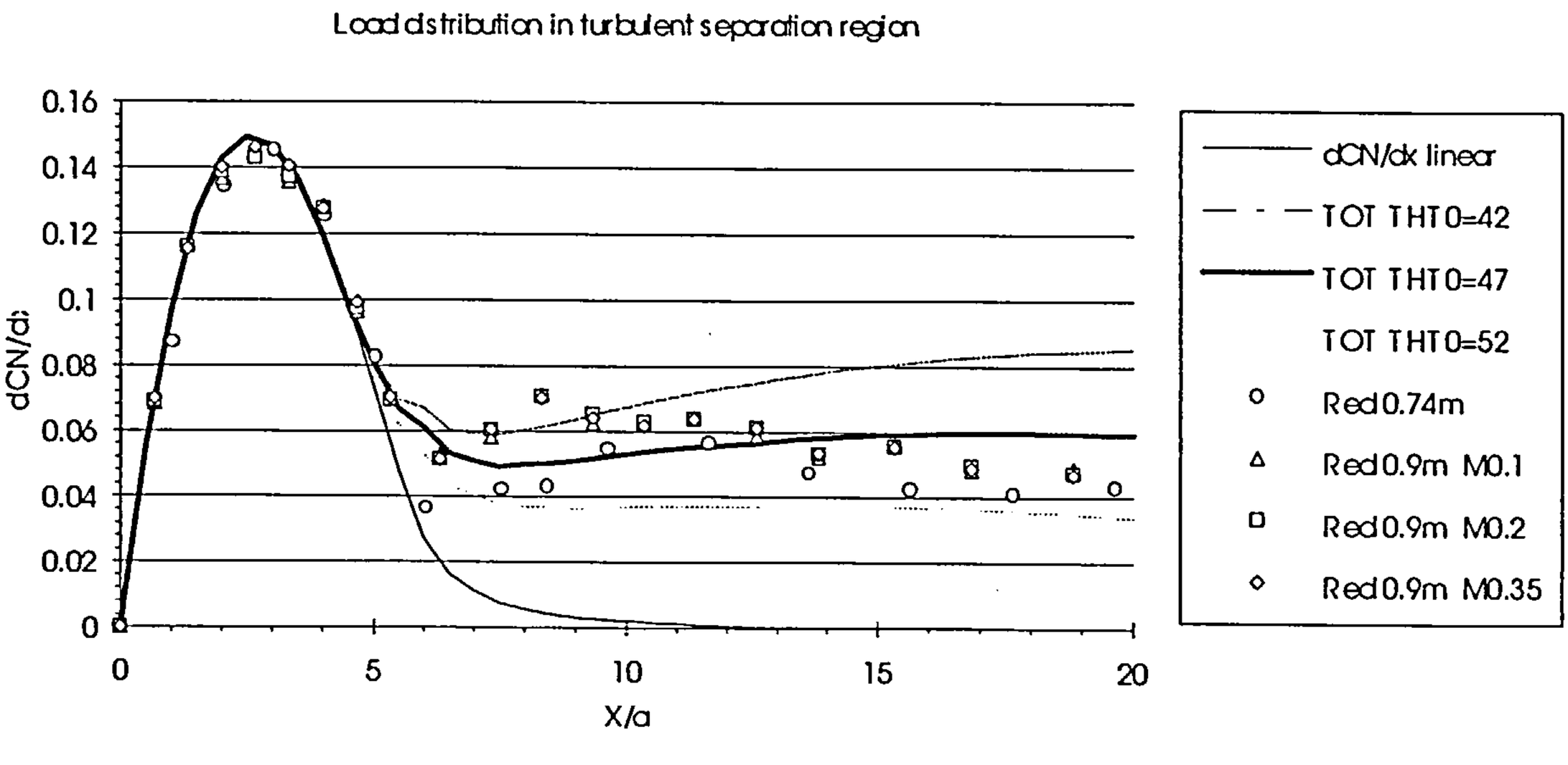

Figure 10.4.2.1

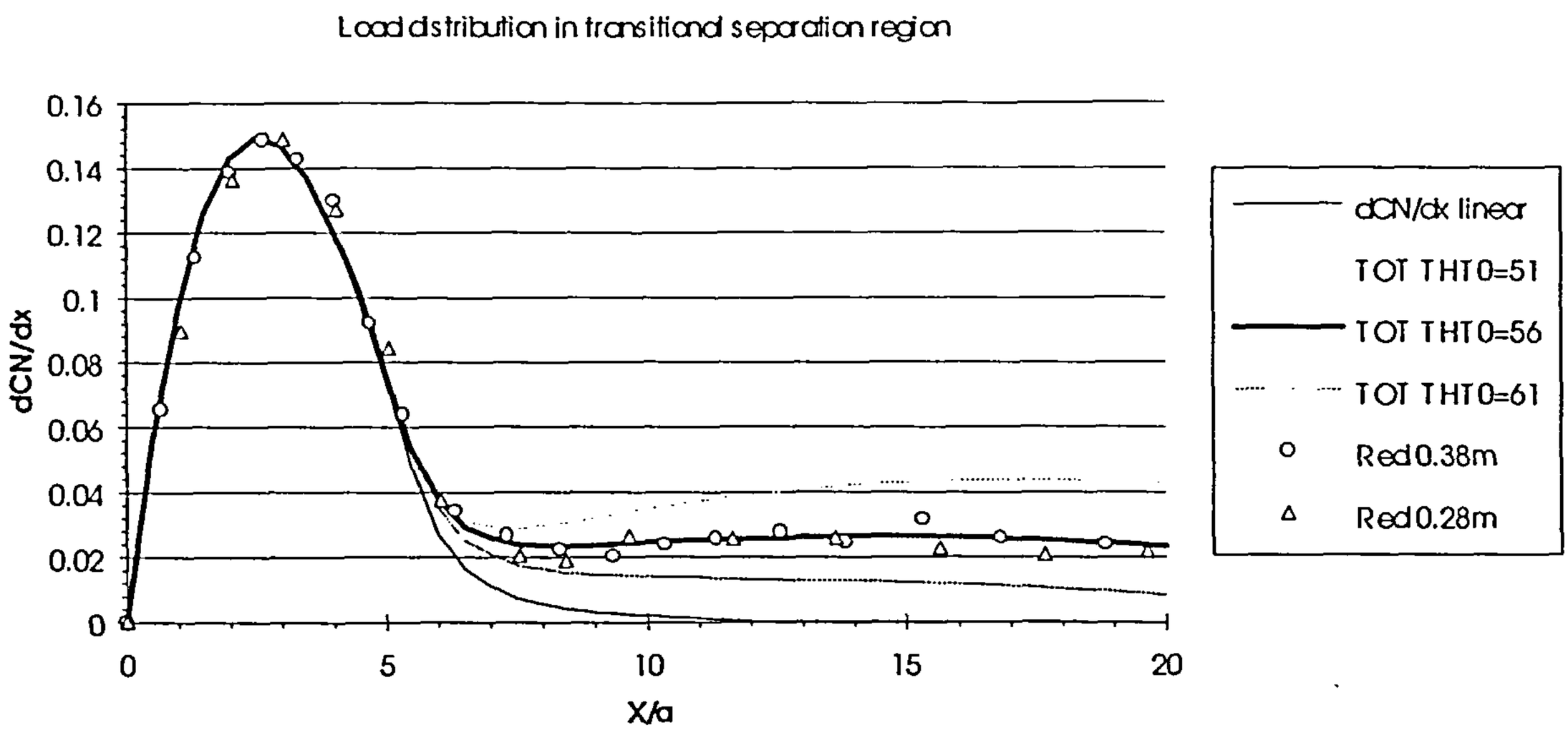

Figure 10.4.2.2

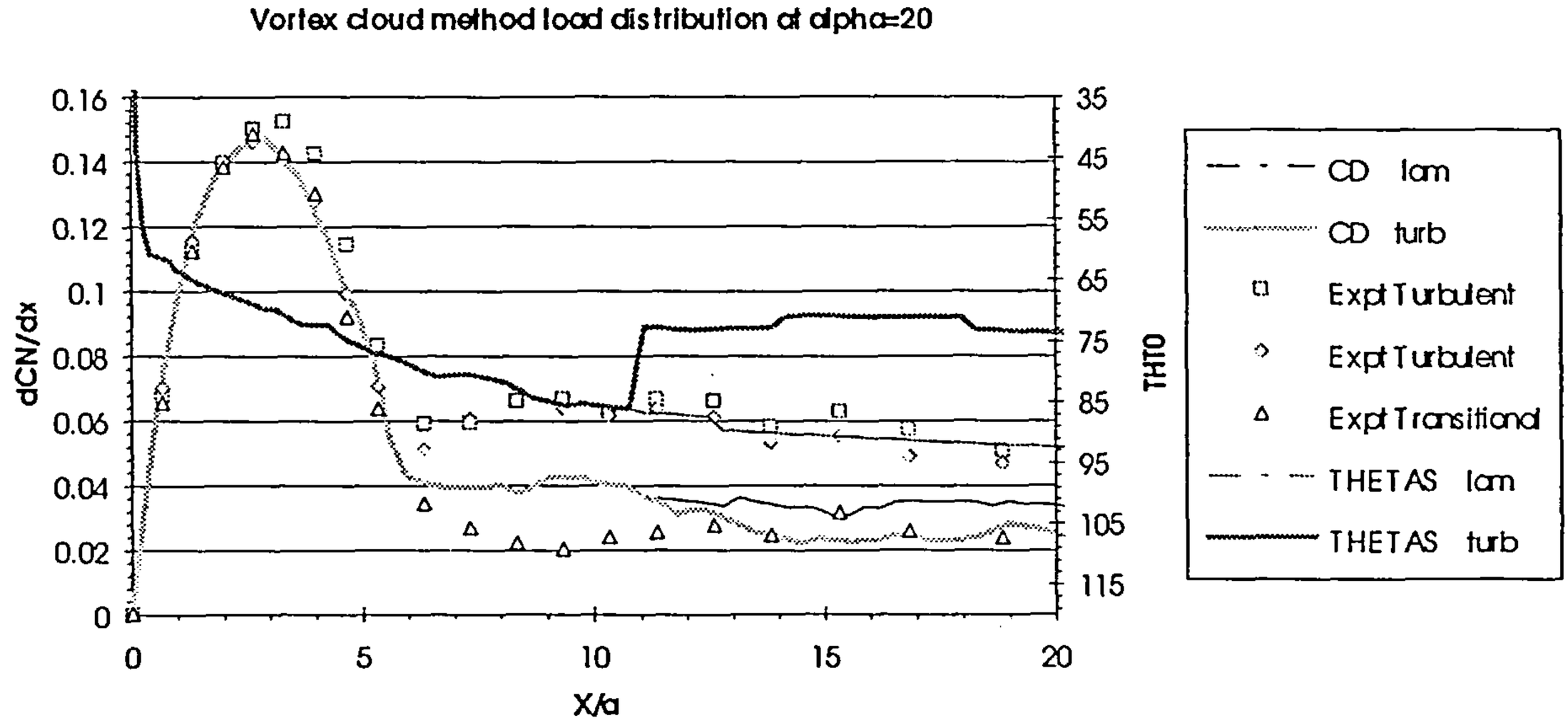

Figure 10.4.2.3

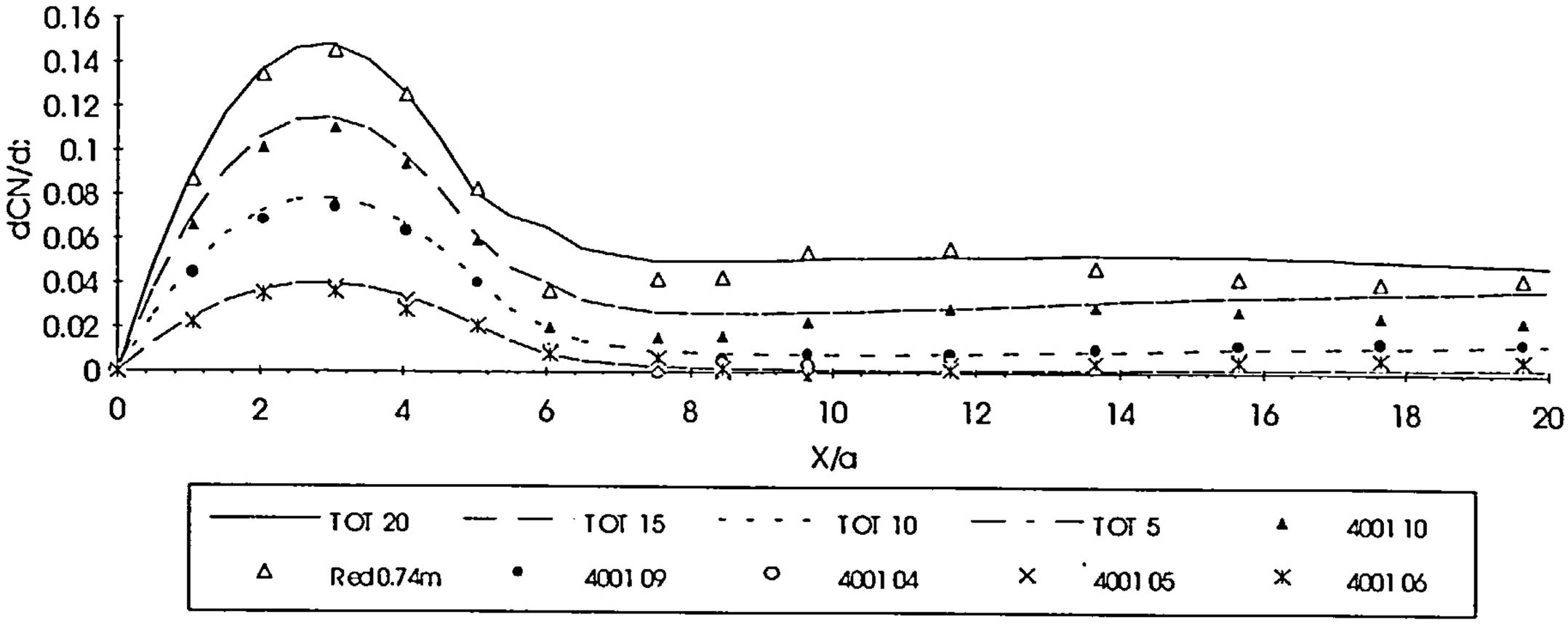

Figure 10.4.3.1

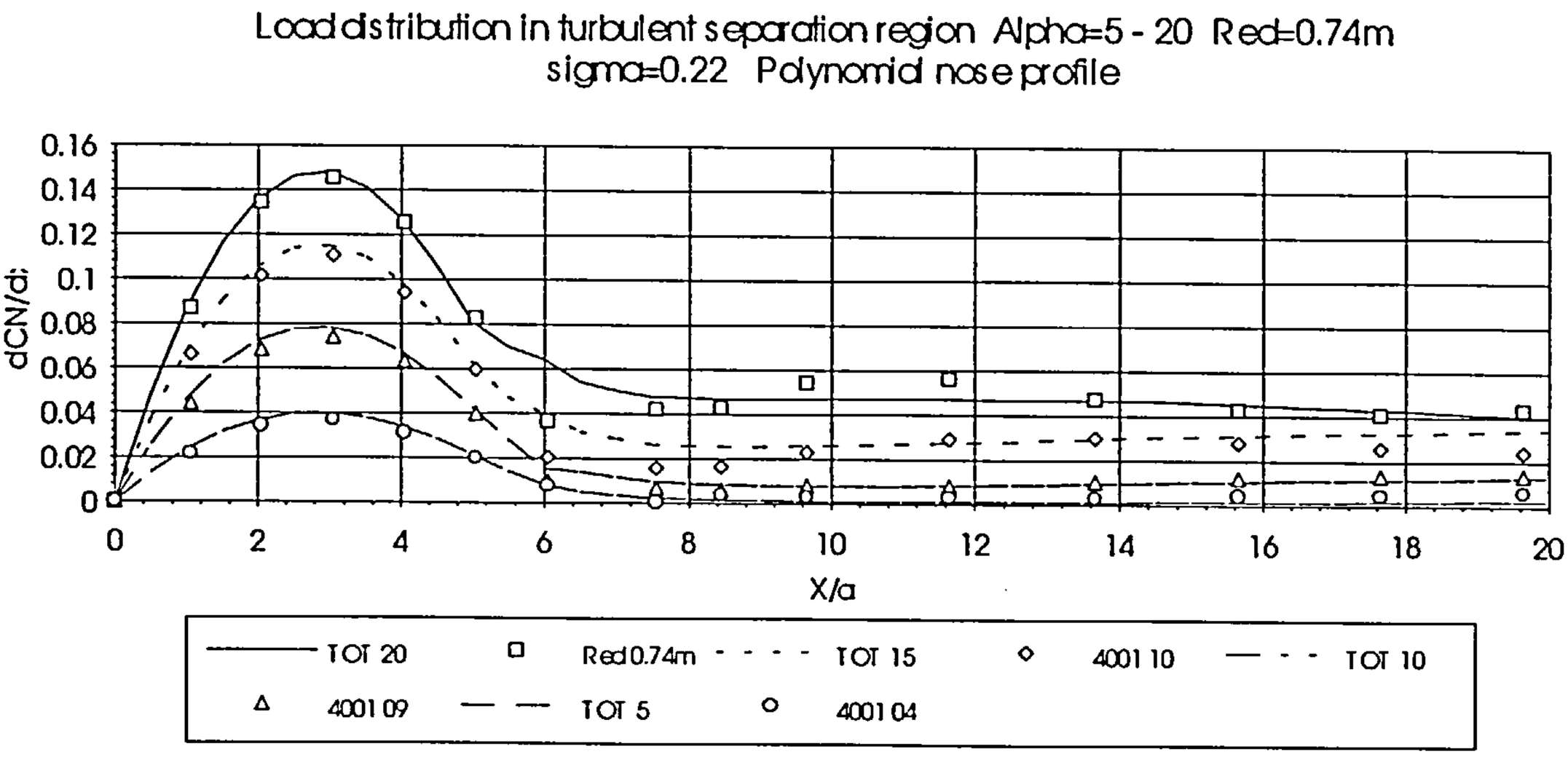

Figure 10.4.3.2

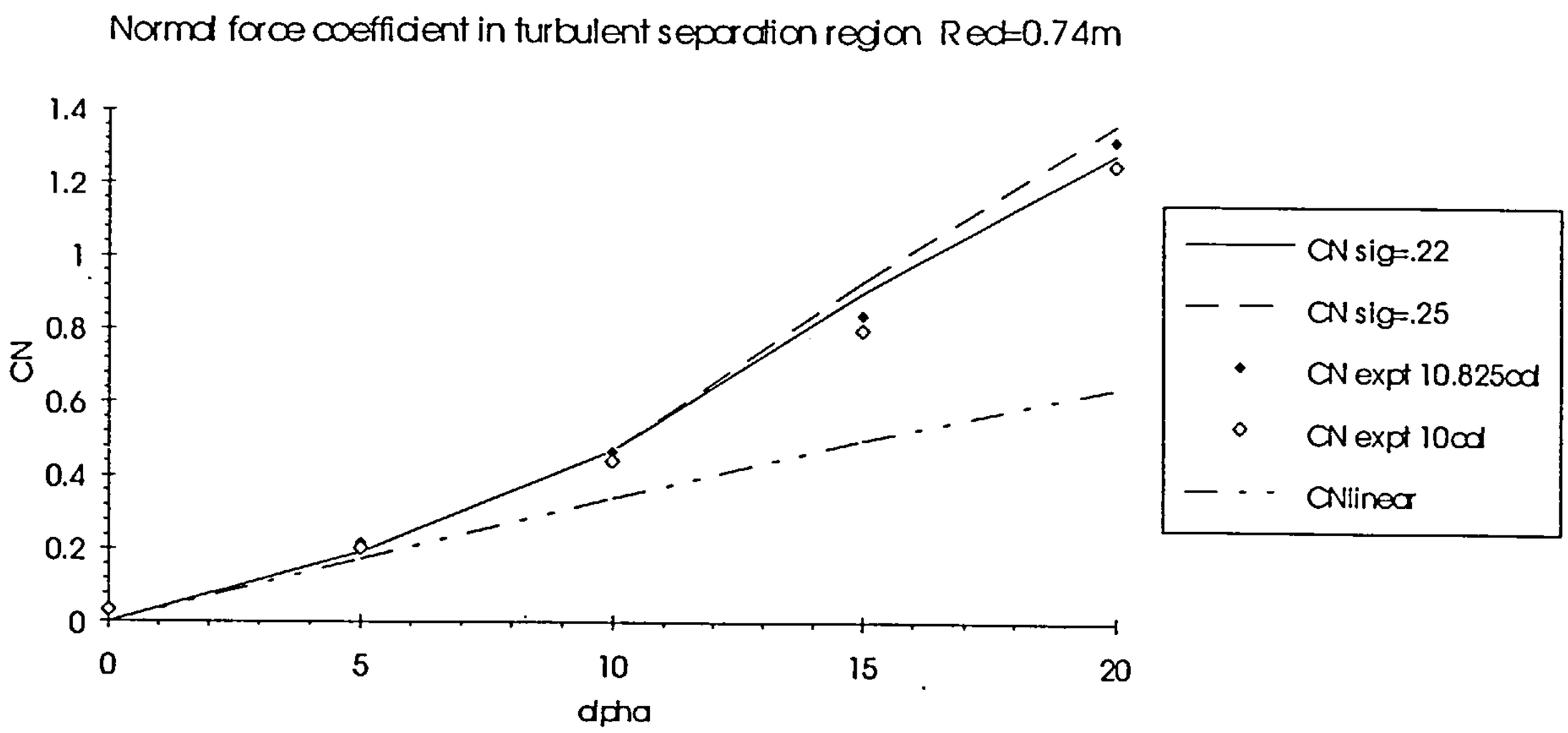

Figure 10.4.3.3

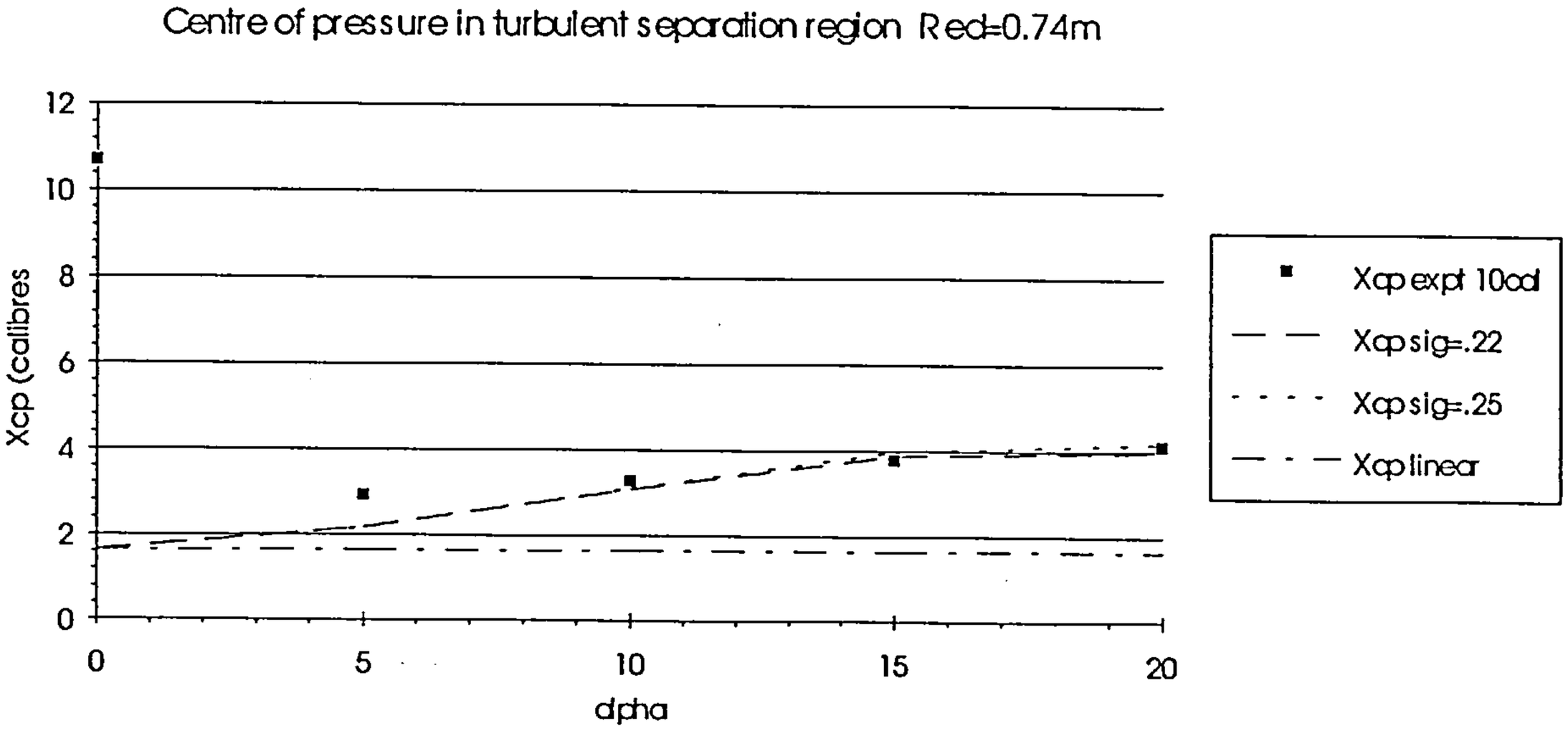

Figure 10.4.3.4

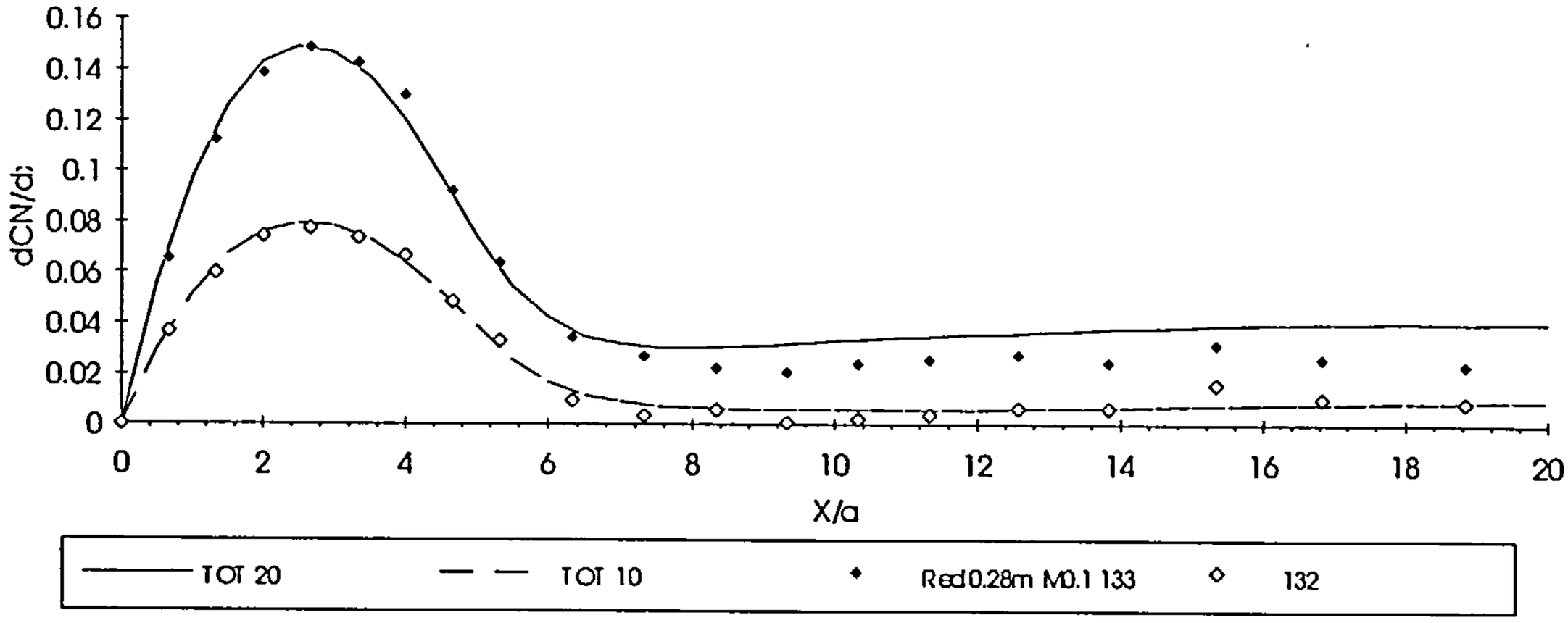

Figure 10.4.3.6a

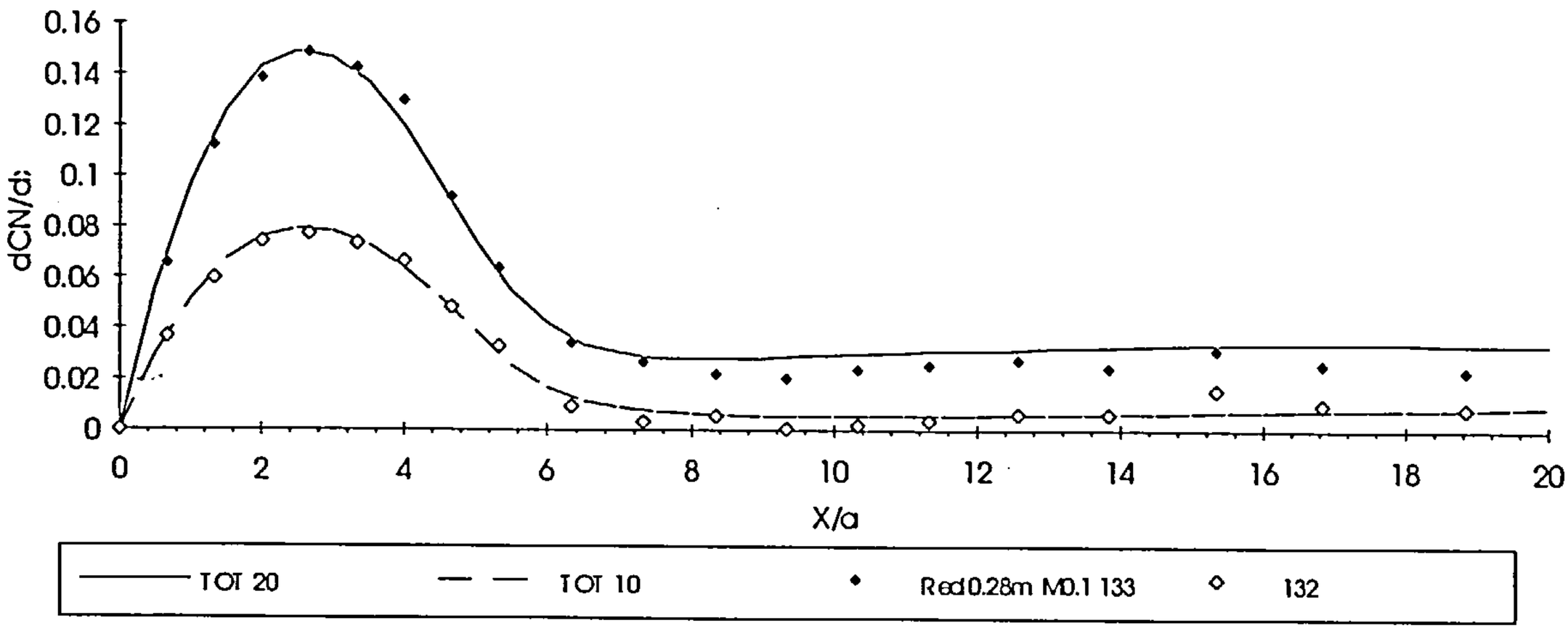

Figure 10.4.3.6b

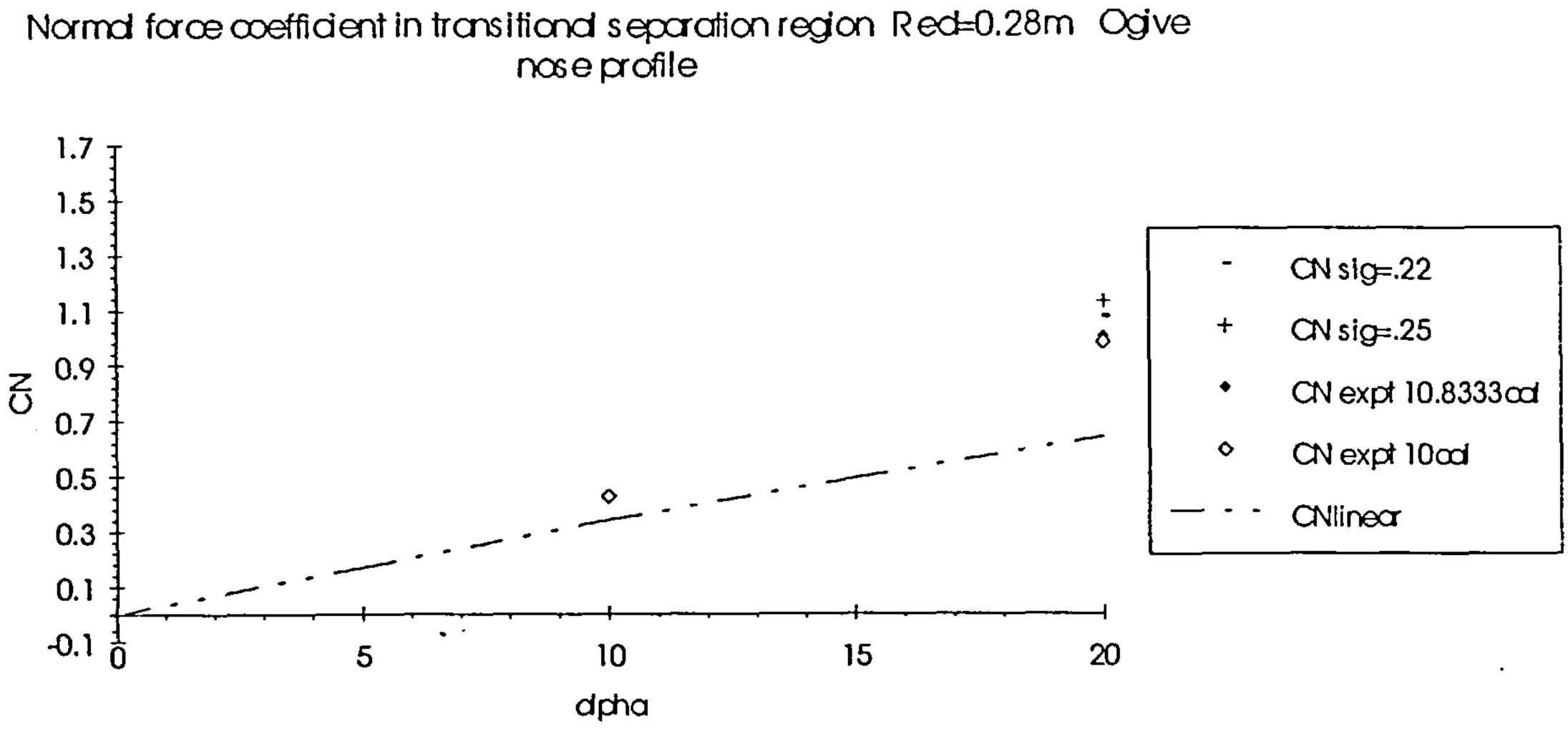

Figure 10.4.3.7

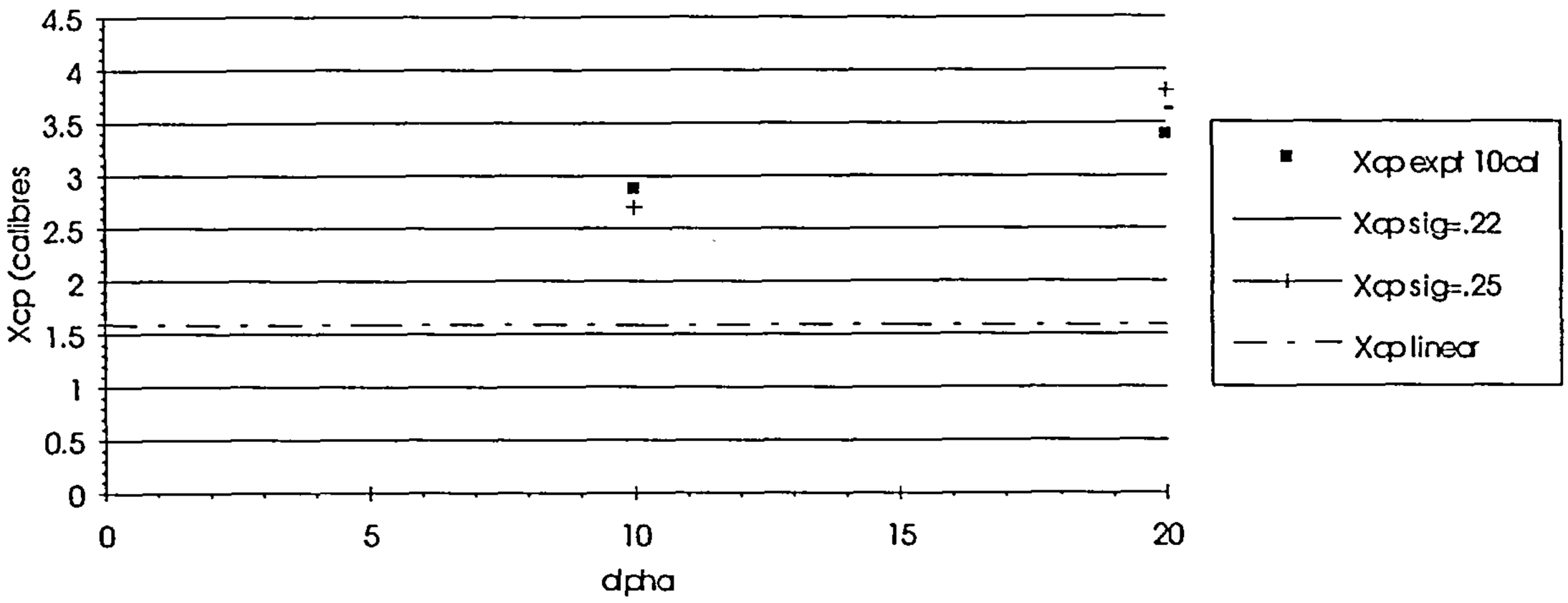

Figure 10.4.3.8

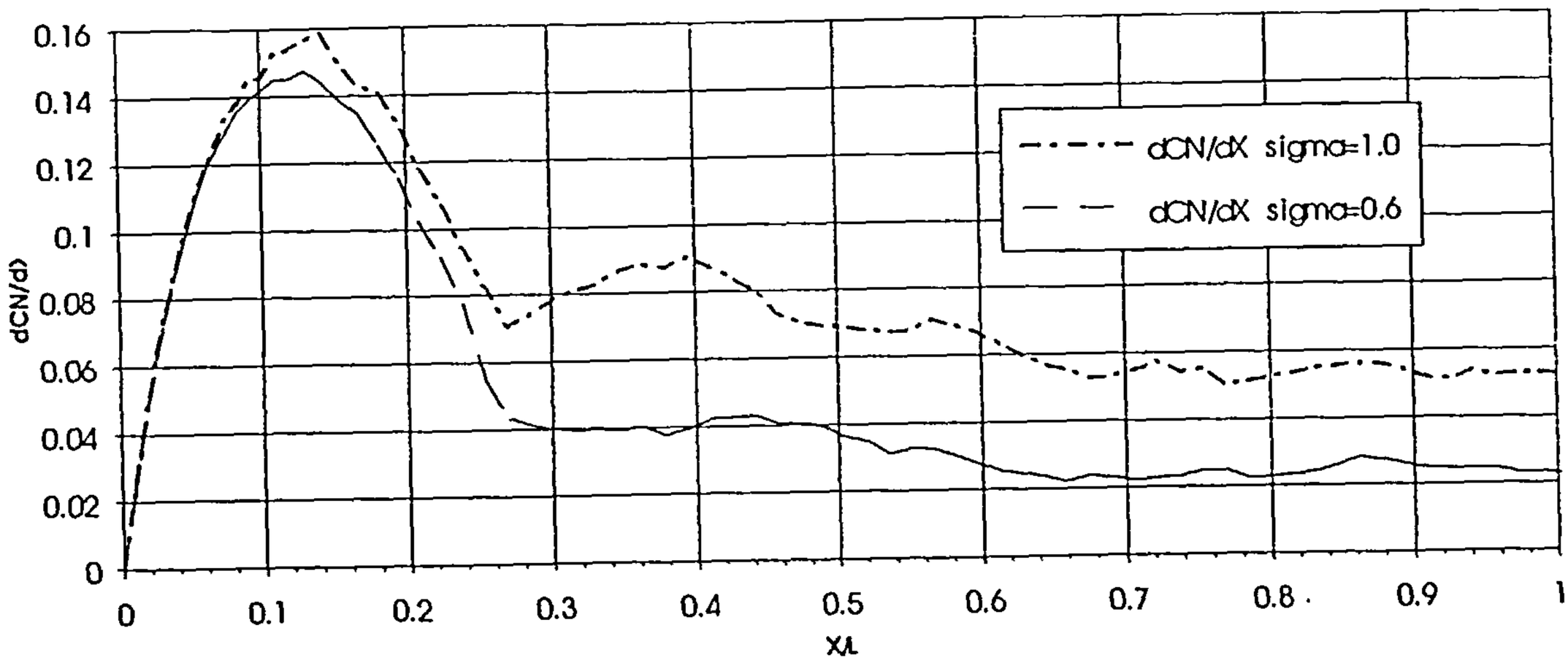

Figure 10.4.3.9

Load distribution in turbulent separation region Alpha=5 - 20
Red=0.74m sigma=0.2 Polynomial nose profile

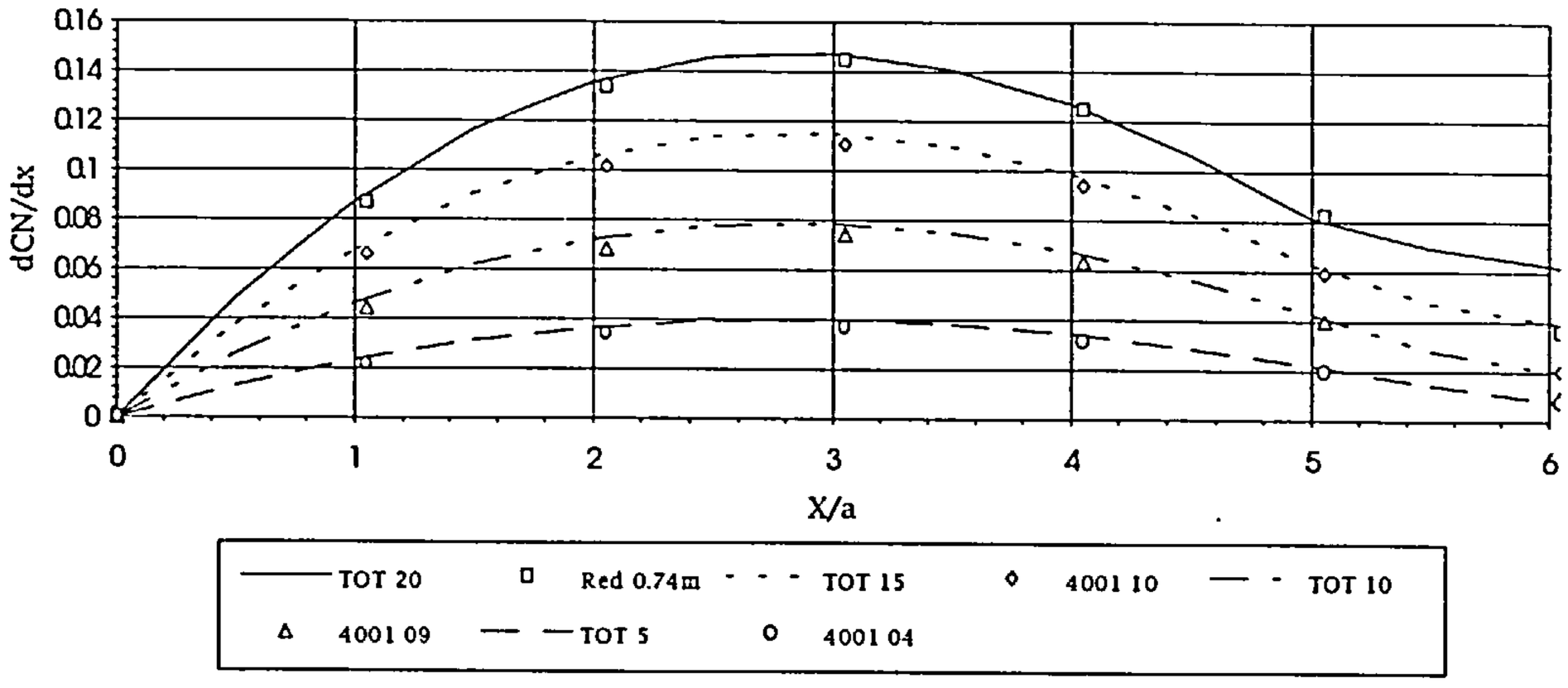

Figure 11.3.3.2

Load distribution in transitional separation region Alpha=5 -.20
Red=0.38m sigma=0.2 Polynomial nose profile

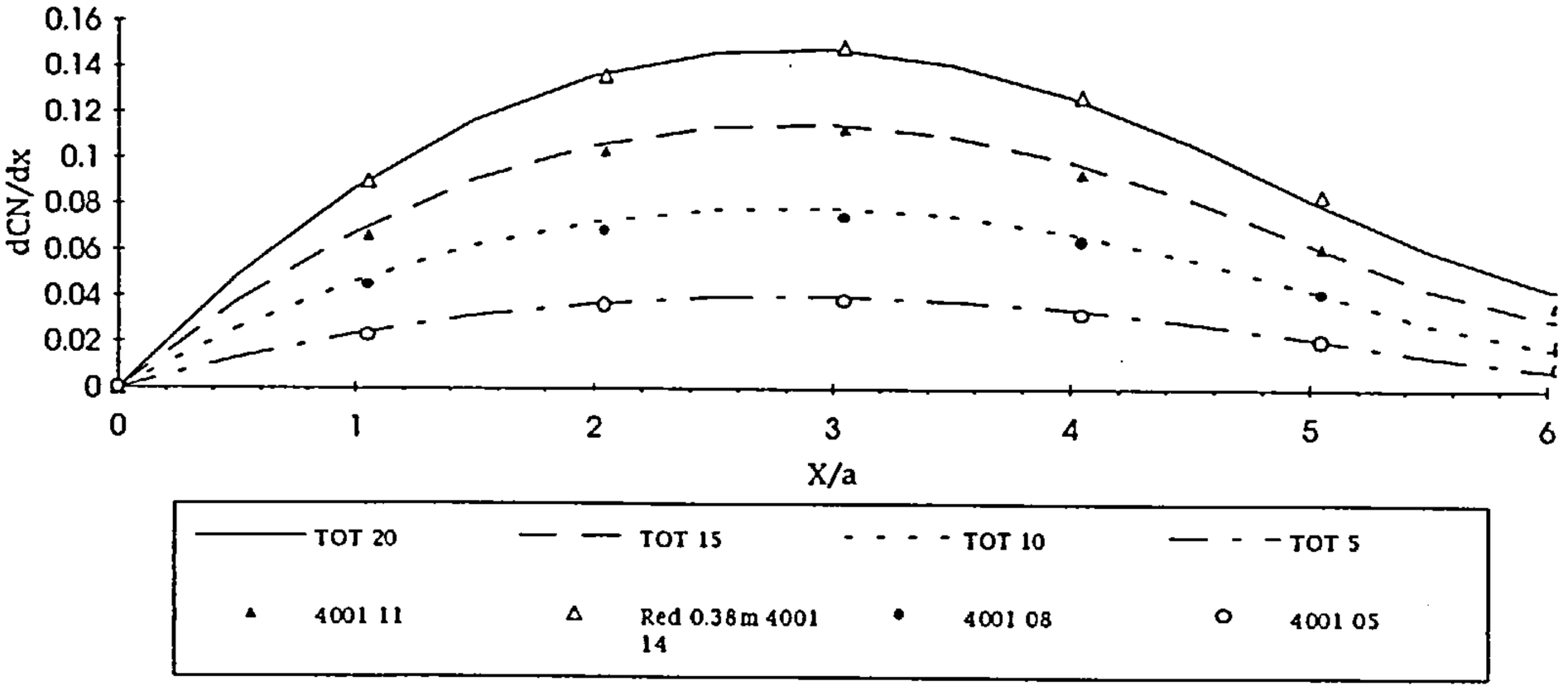

Figure 11.3.3.3

Load distribution in turbulent separation region Alpha=10 & 20
sigma=0.2 Ogive nose profile

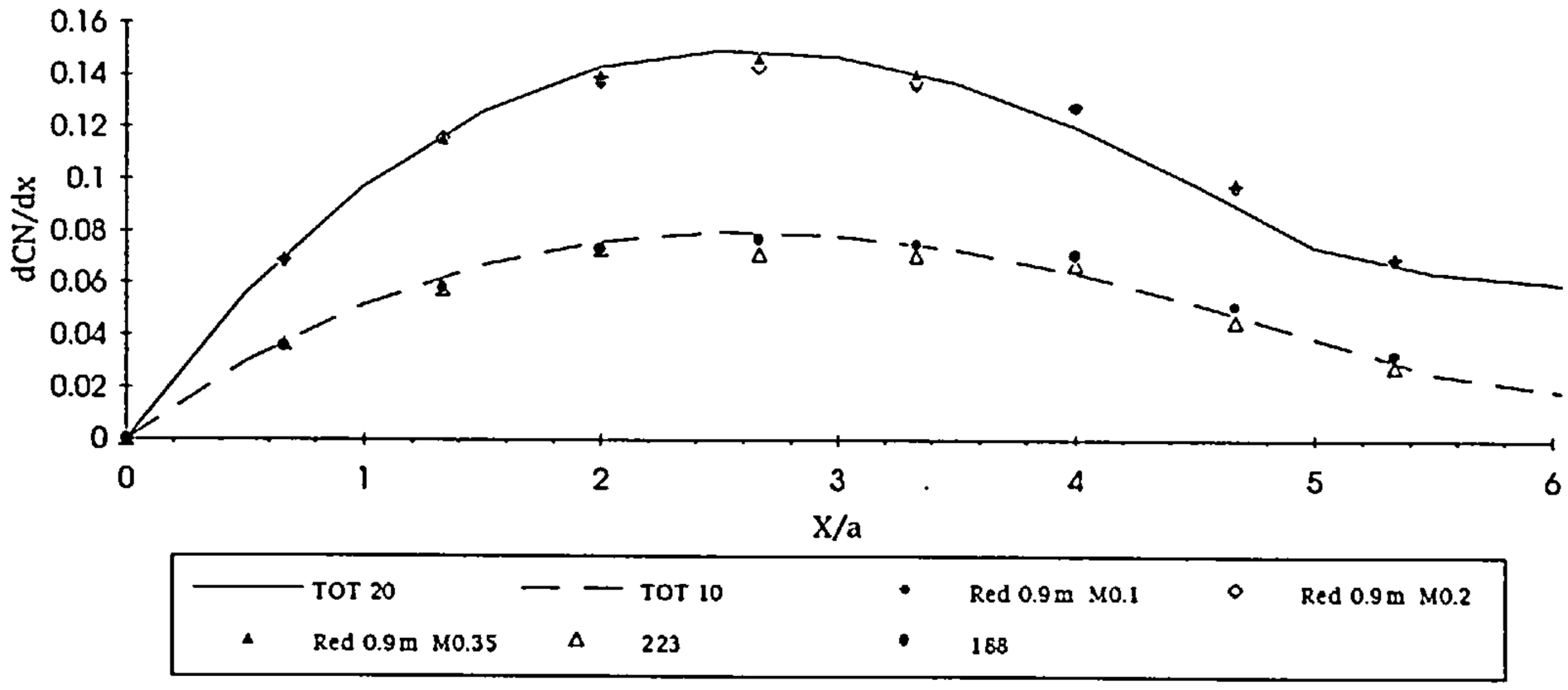

Figure 11.3.3.4

Load distribution in transitional separation region Alpha=10 & 20
sigma=0.2 Ogive nose profile

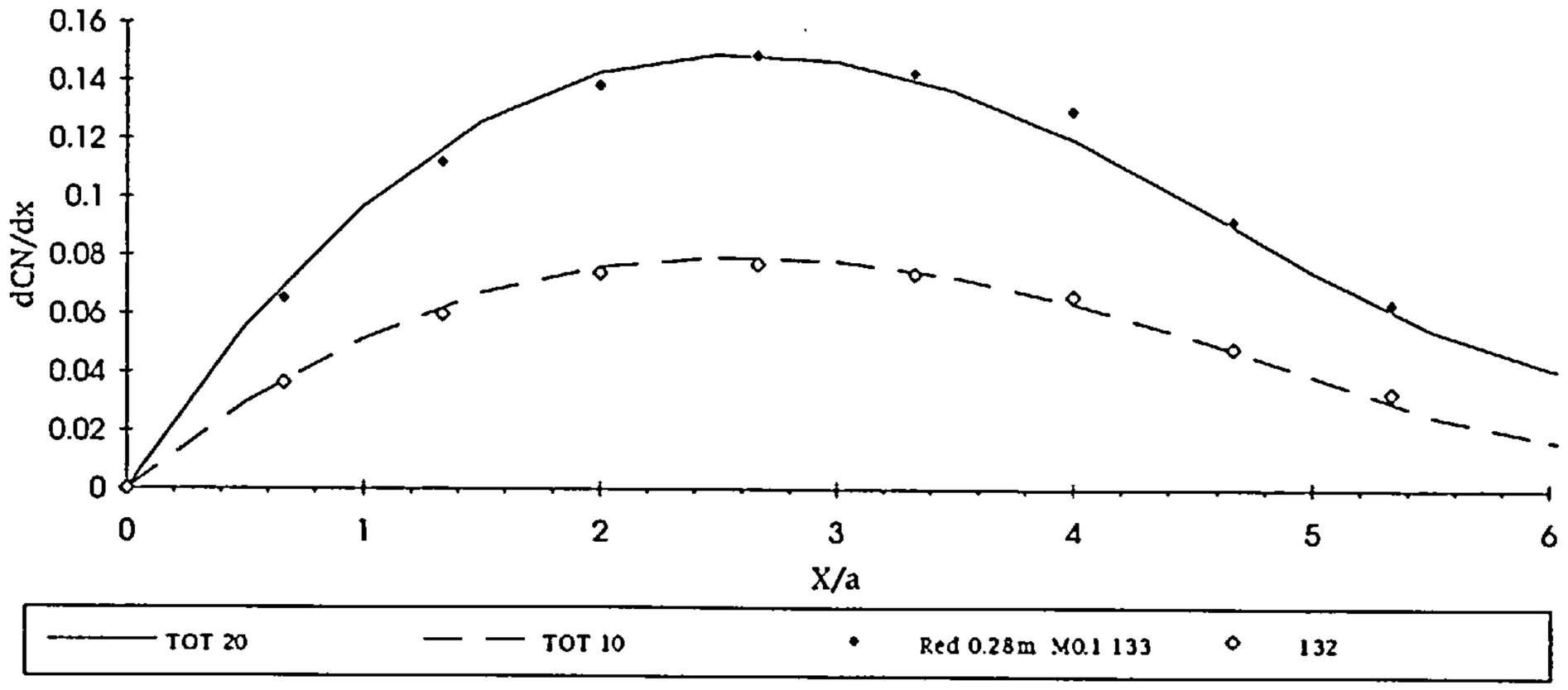

Figure 11.3.3.5

Load distribution in turbulent separation region Alpha=5 - 20
Red=0.74m sigma=0.2 Polynomial nose profile

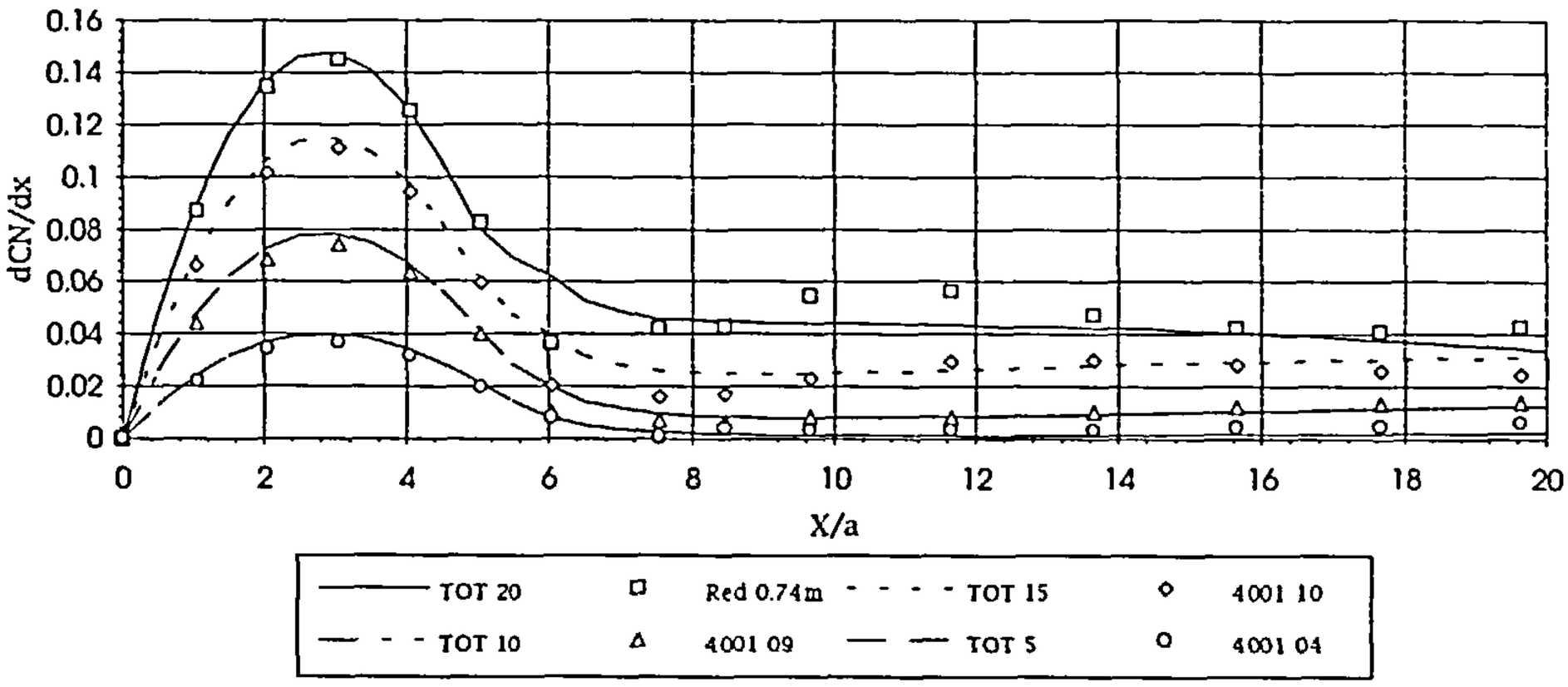

Figure 11.3.4.1

Load distribution in transitional separation region Alpha=5 - 20
Red=0.38m sigma=0.2 Polynomial nose profile

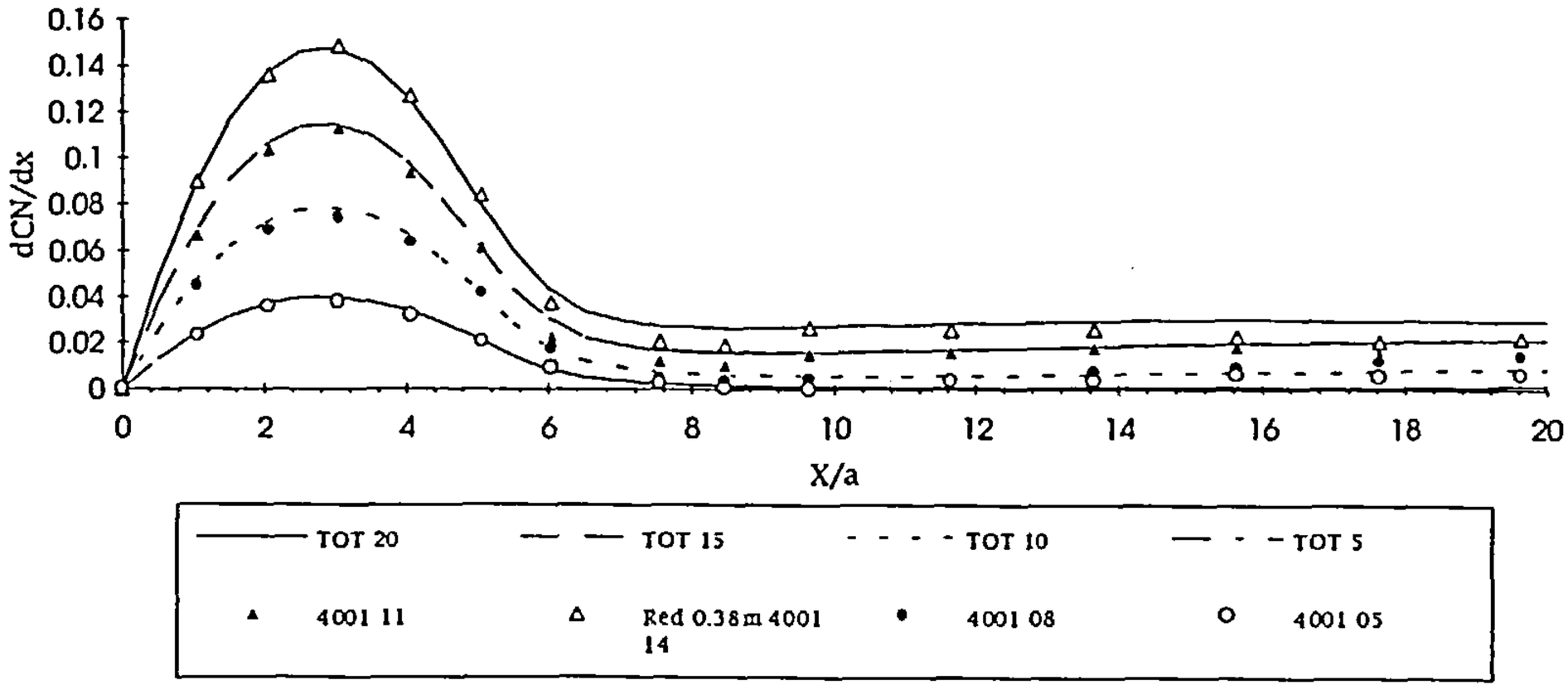

Figure 11.3.4.2

Load distribution in turbulent separation region Alpha=10 & 20
sigma=0.2 Ogive nose profile

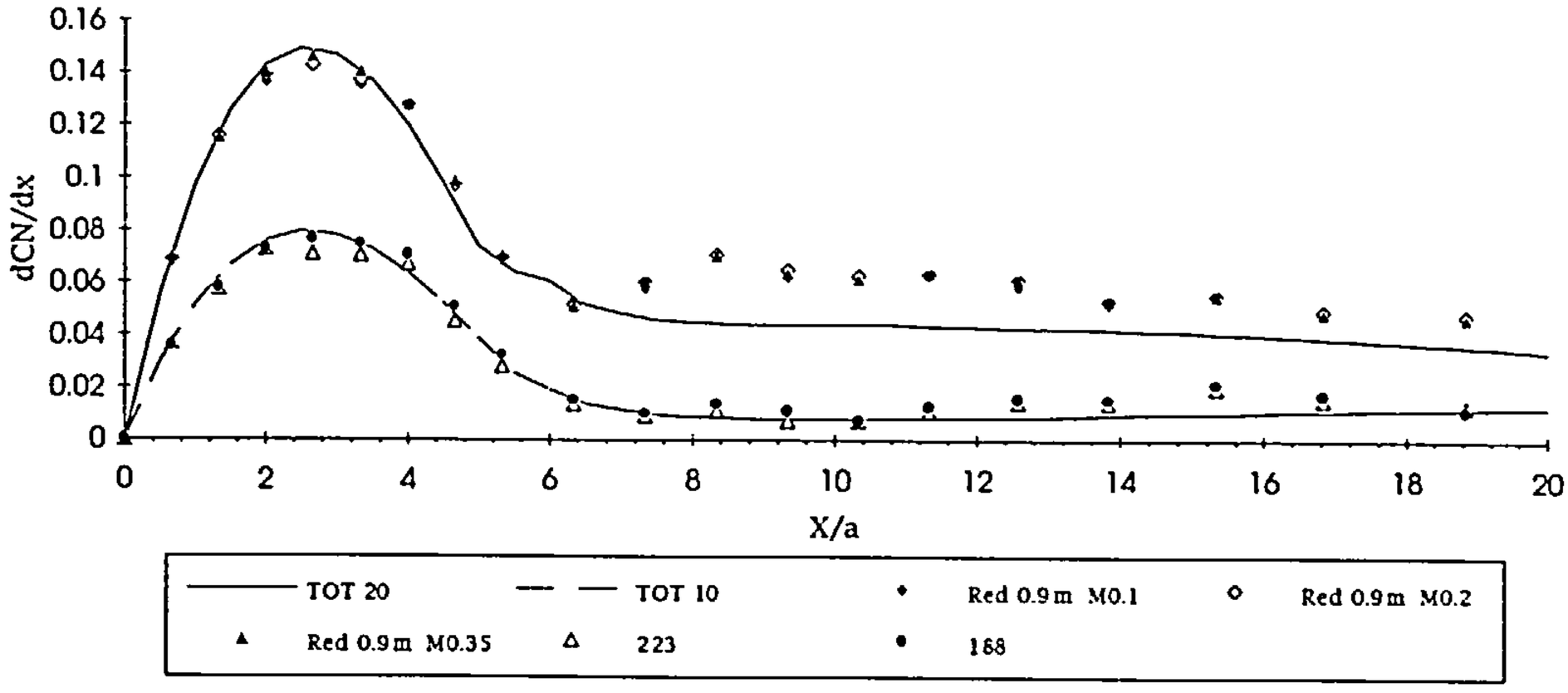

Figure 11.3.4.3

Load distribution in transitional separation region Alpha=10 & 20
sigma=0.2 Ogive nose profile

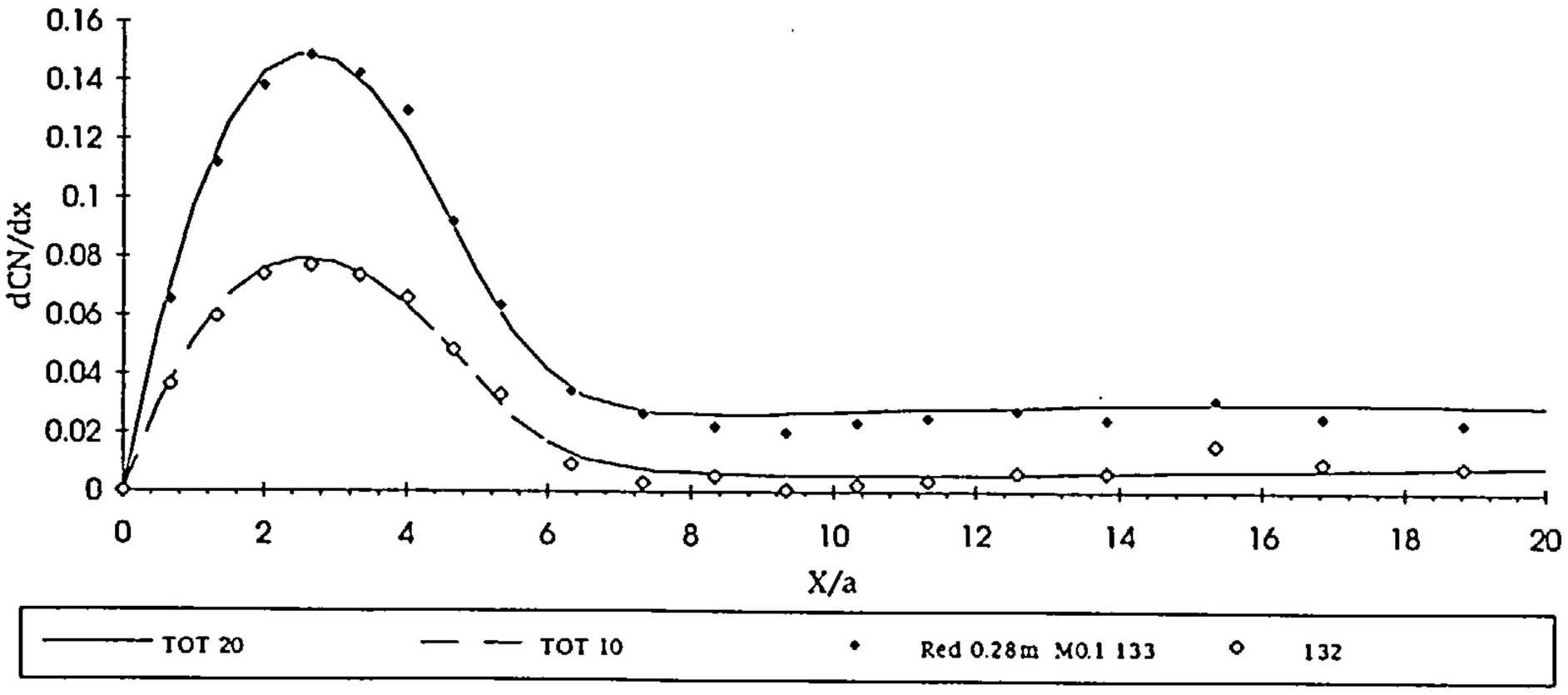

Figure 11.3.4.4

Normal force coefficient in turbulent separation region Red=0.74m

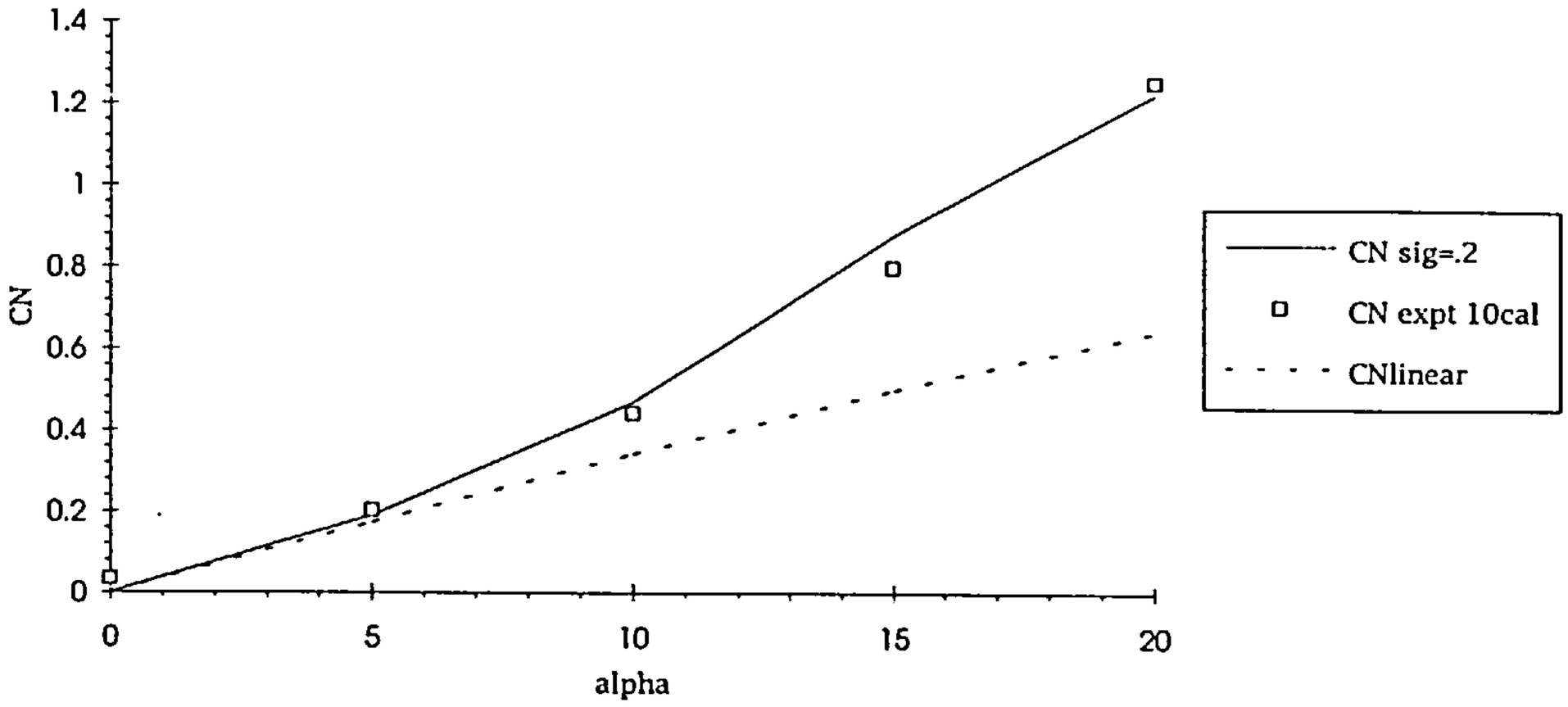

Figure 11.4.2.1

Pitching moment coefficient in turbulent separation region Red=0.74m

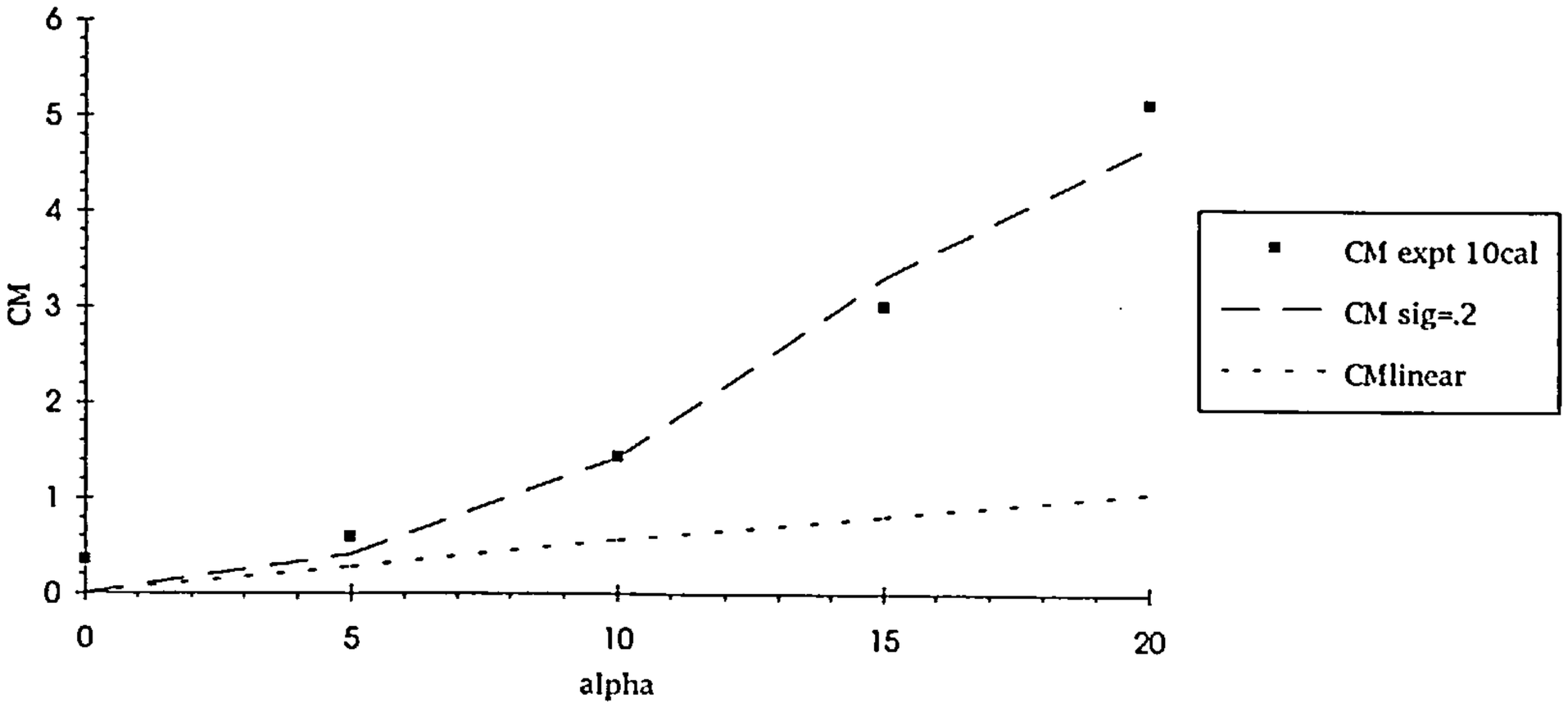

Figure 11.4.2.2

Centre of pressure in turbulent separation region Red=0.74m

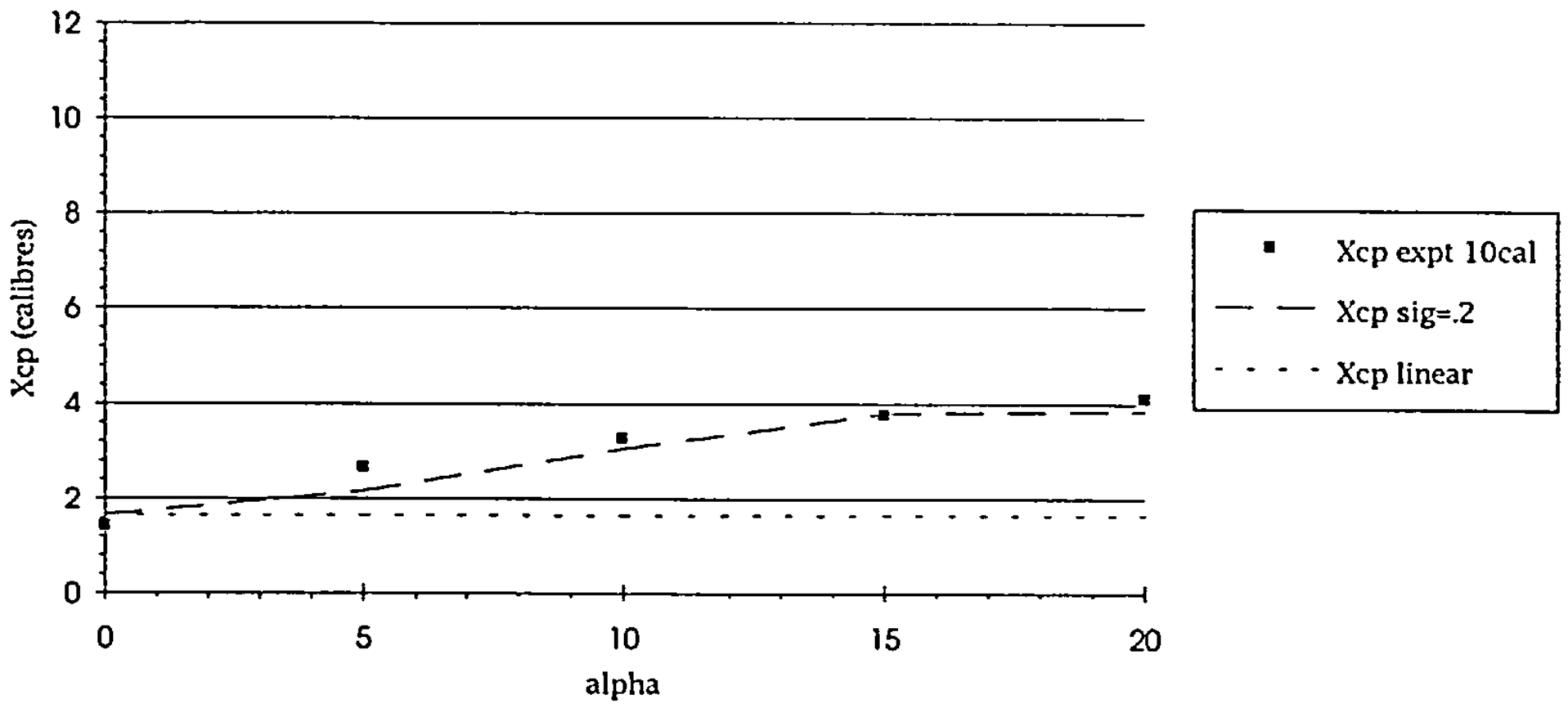

Figure 11.4.2.3

Normal force coefficient in transitional separation region Red=0.38m

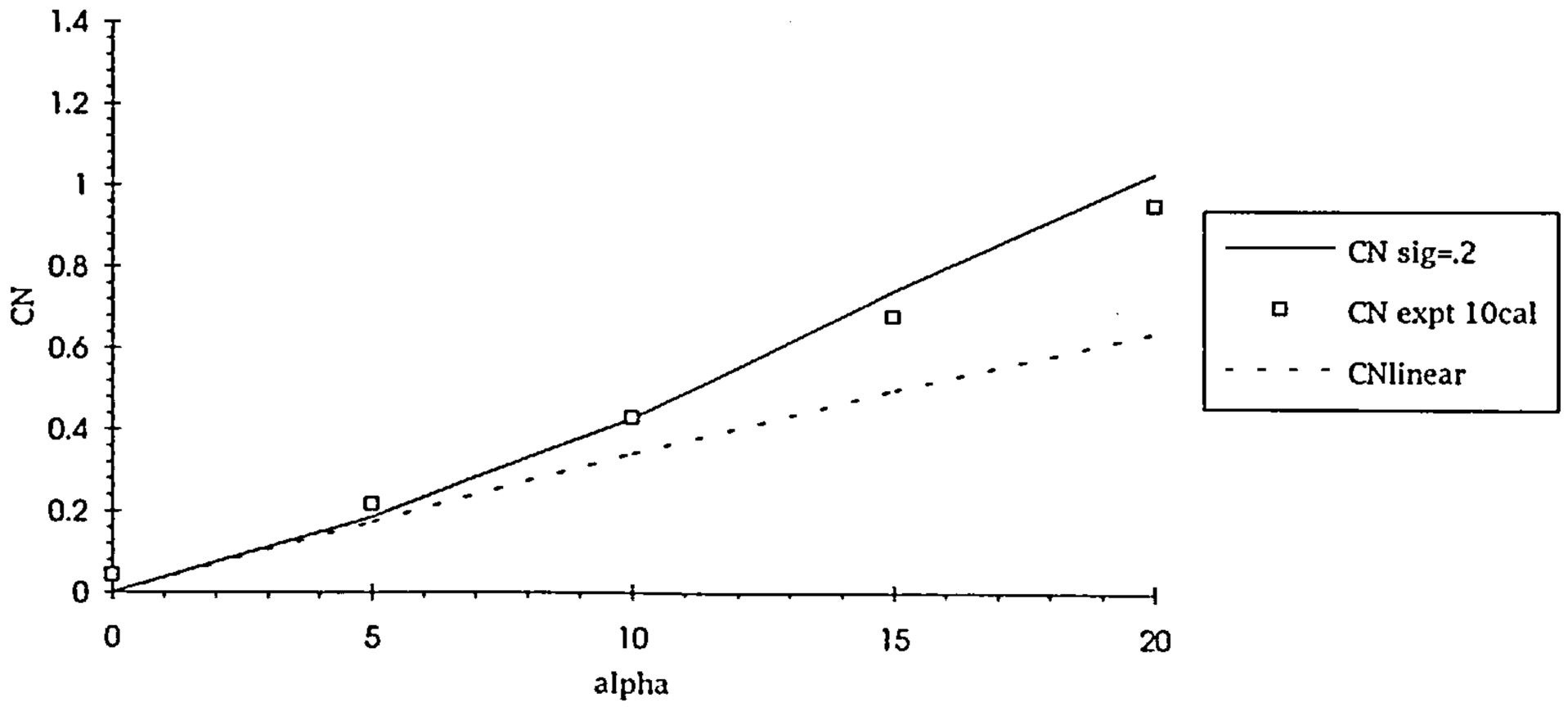

Figure 11.4.2.4

Pitching moment coefficient in transitional separation region Red=0.38m

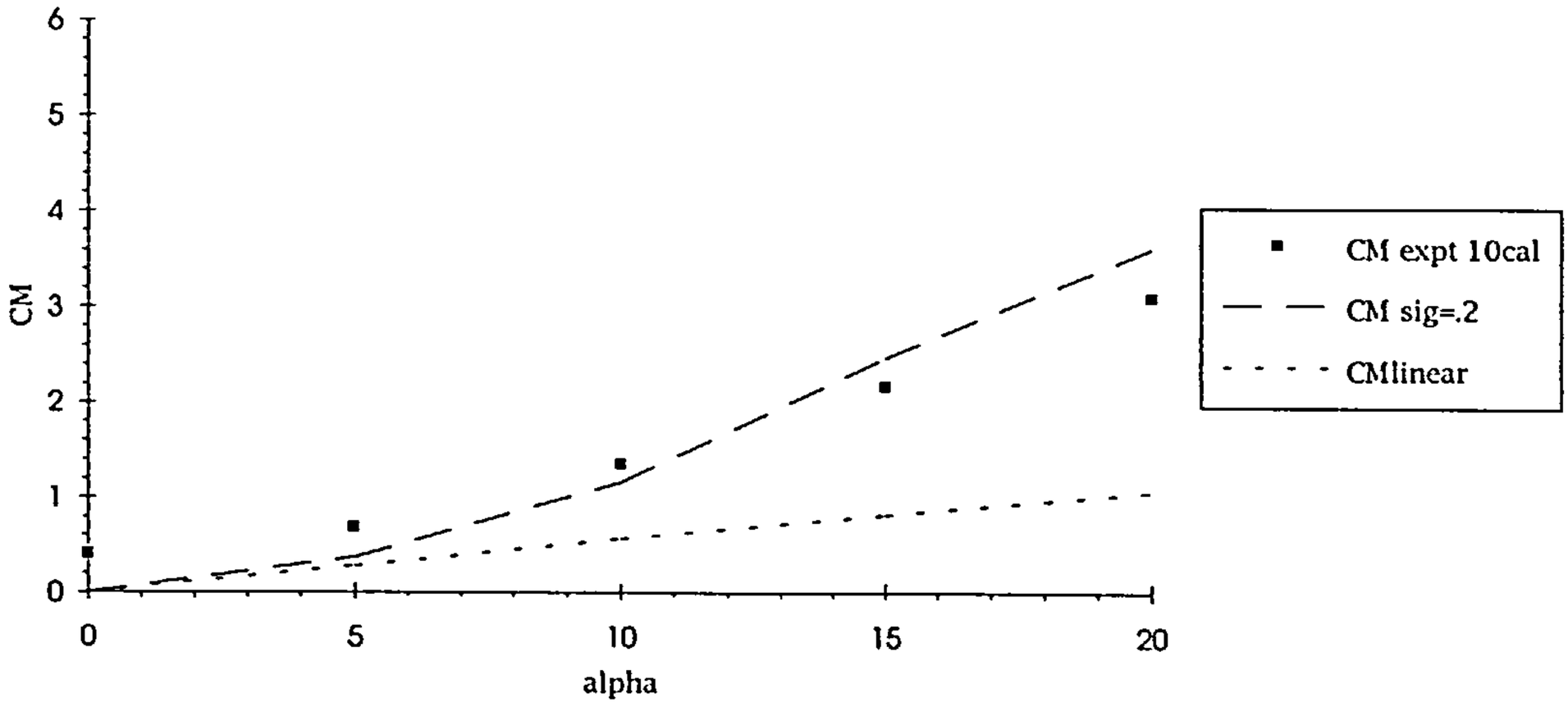

Figure 11.4.2.5

Centre of pressure in transitional separation region Red=0.38m

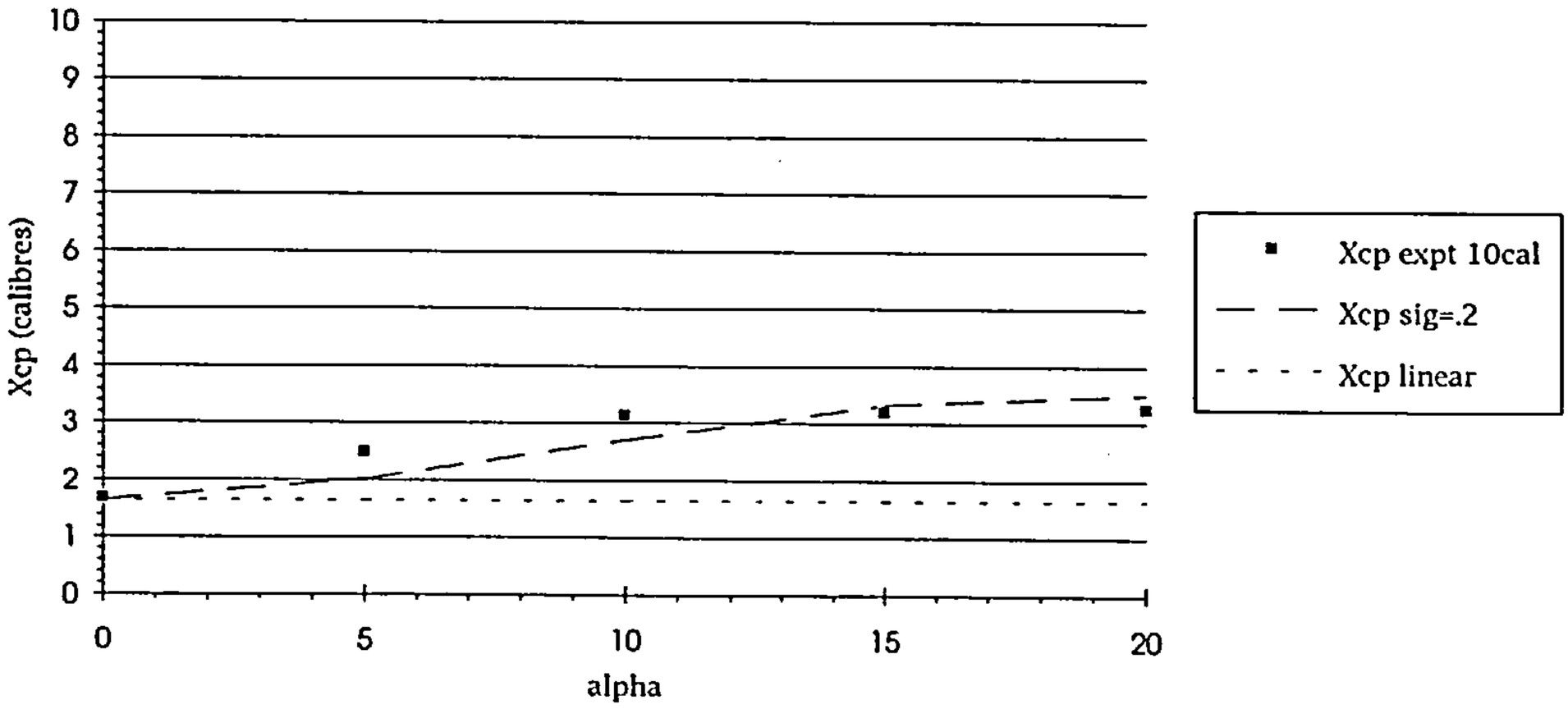

Figure 11.4.2.6

Normal force coefficient in turbulent separation region Red=0.9m Ogive nose profile

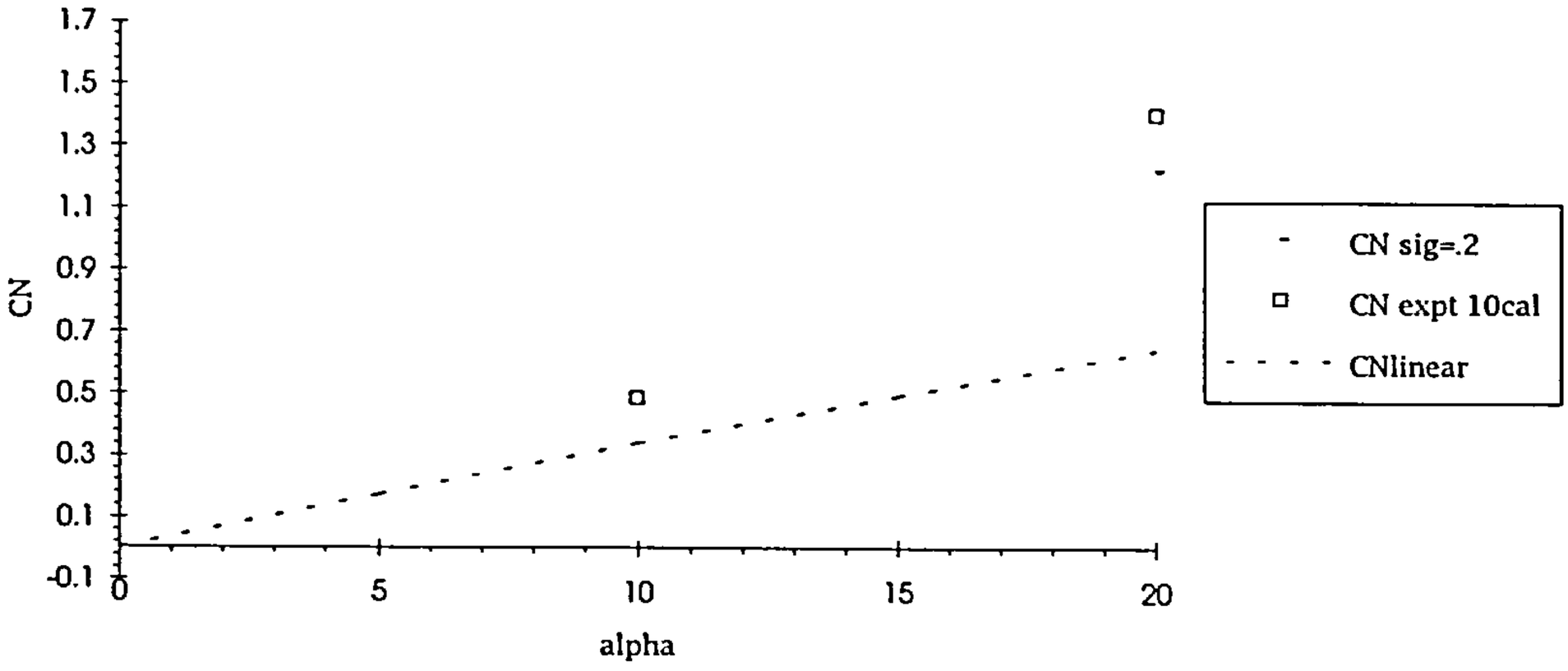

Figure 11.4.2.7

Pitching moment coefficient in turbulent separation region Red=0.9m Ogive nose profile

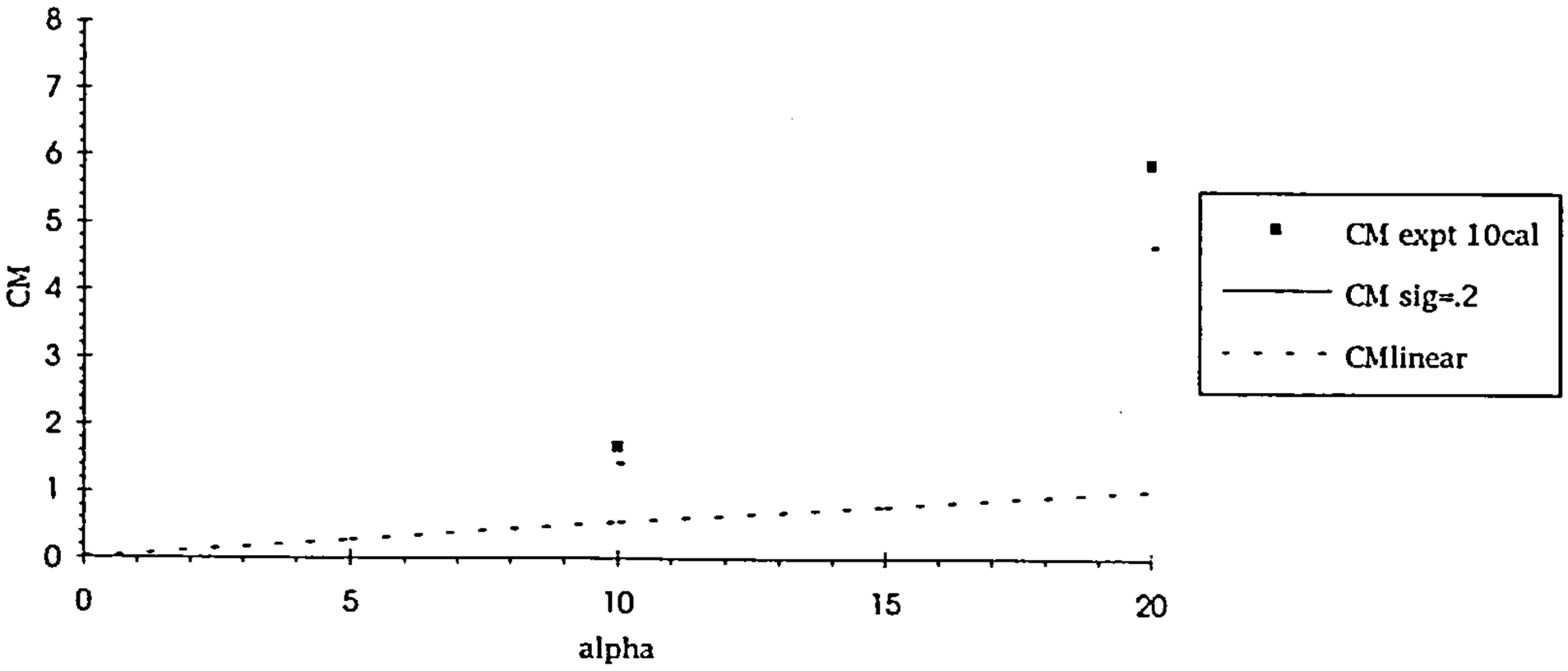

Figure 11.4.2.8

Centre of pressure in turbulent separation region Red=0.9m Ogive nose profile

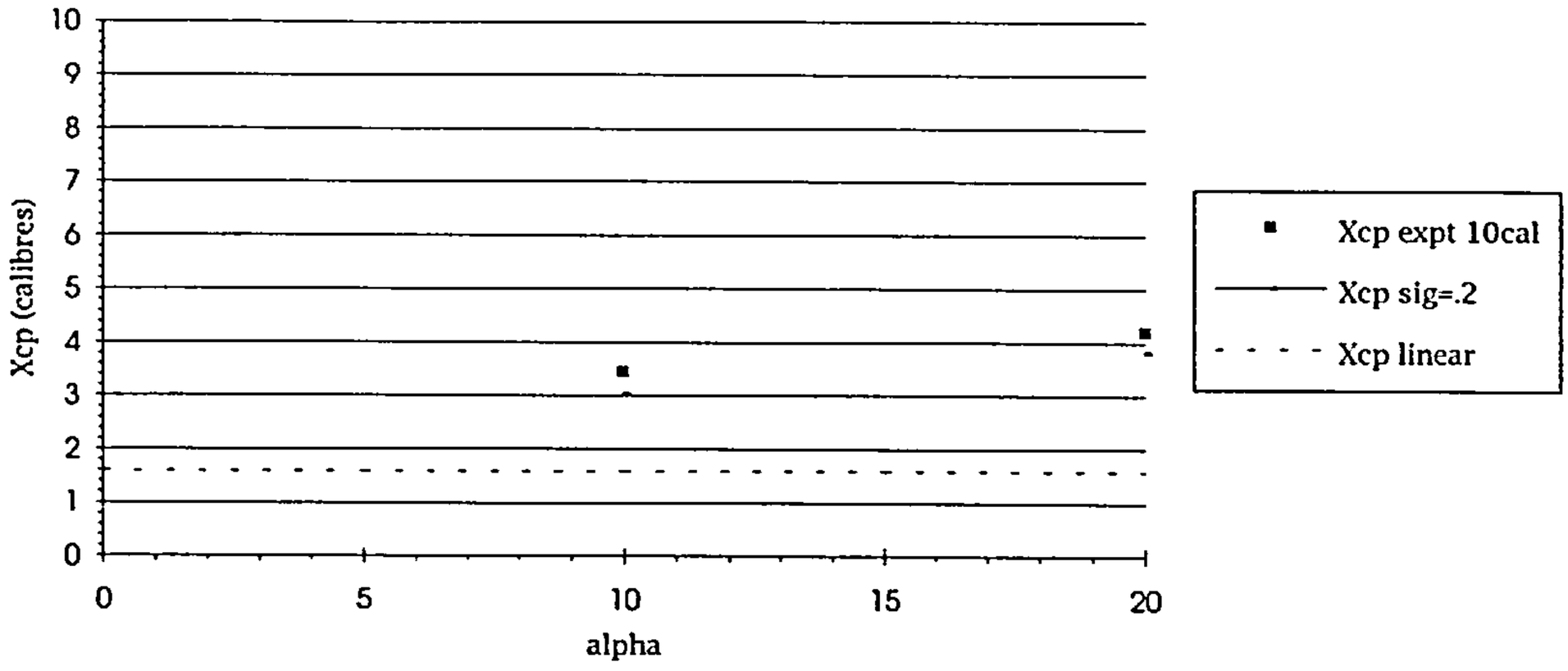

Figure 11.4.2.9

Normal force coefficient in transitional separation region Red=0.28m Ogive nose profile

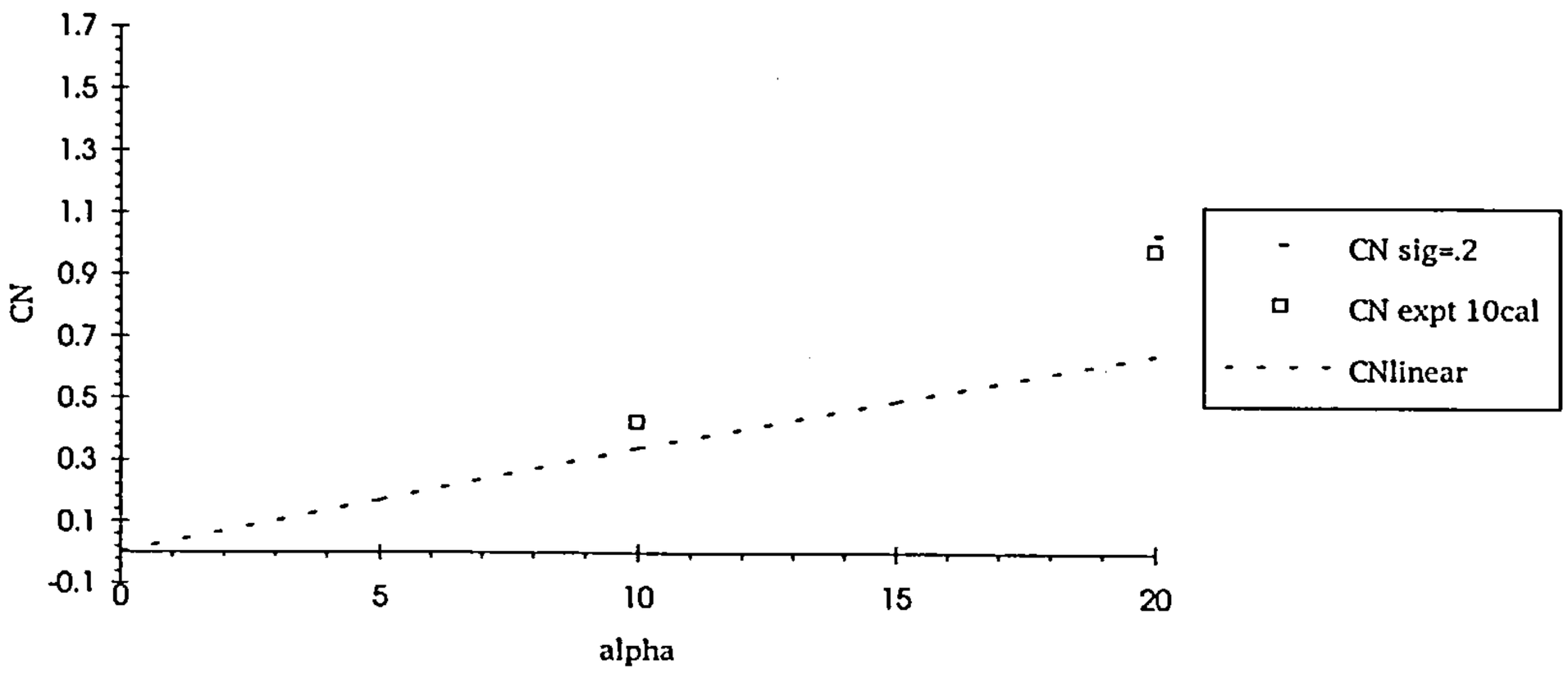

Figure 11.4.2.10

Pitching moment coefficient in transitional separation region Red=0.28m
Ogive nose profile

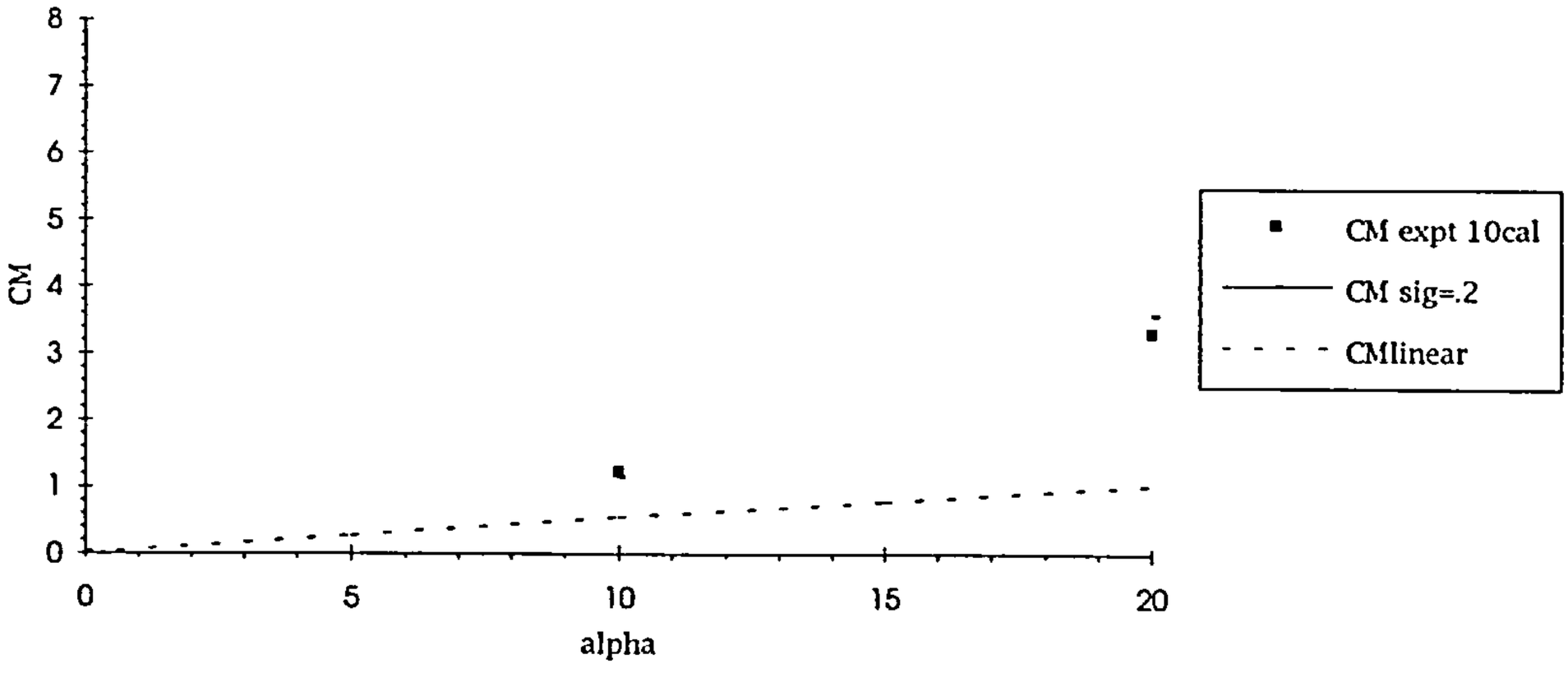

Figure 11.4.2.11

Centre of pressure in transitional separation region Red=0.28m Ogive nose profile

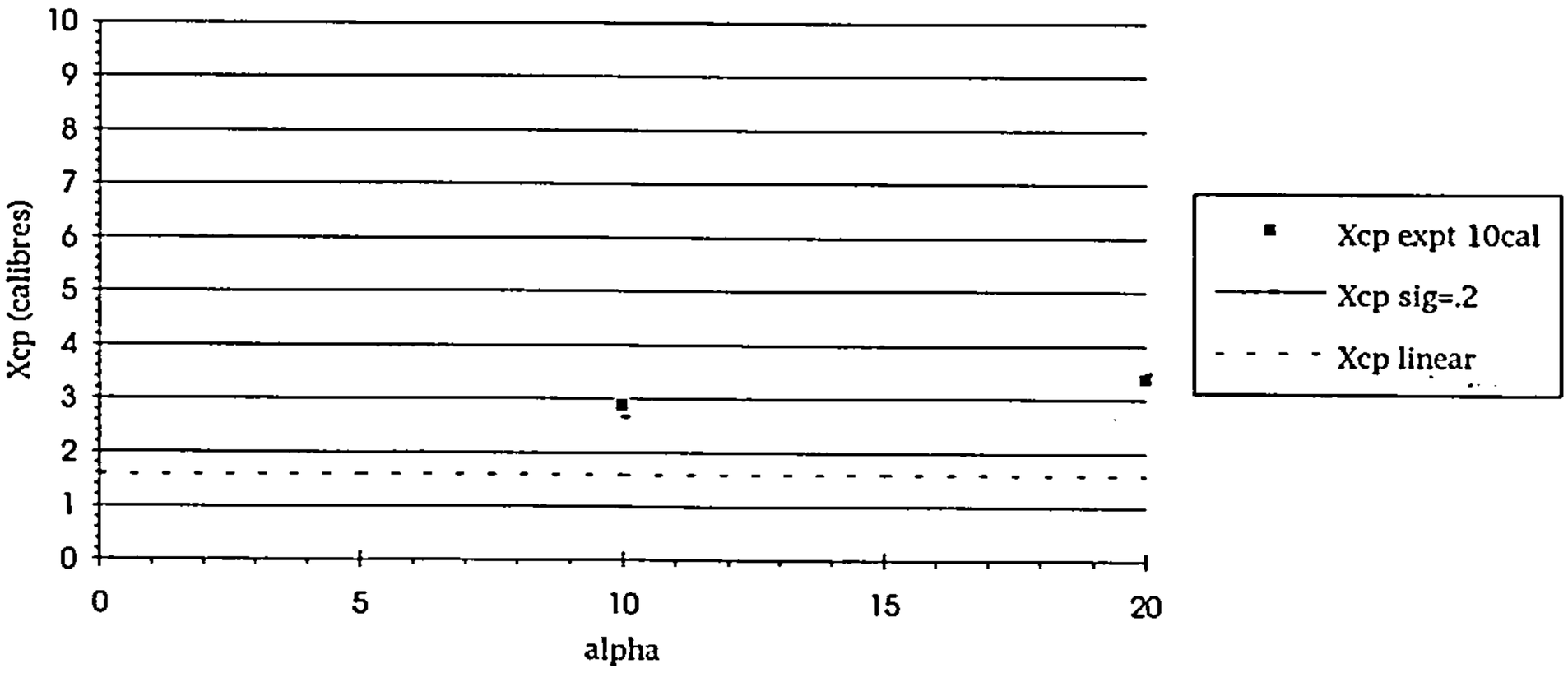

Figure 11.4.2.12

Predicted vortex core location vs VCM and experiment alpha=20
x/l=0.9385

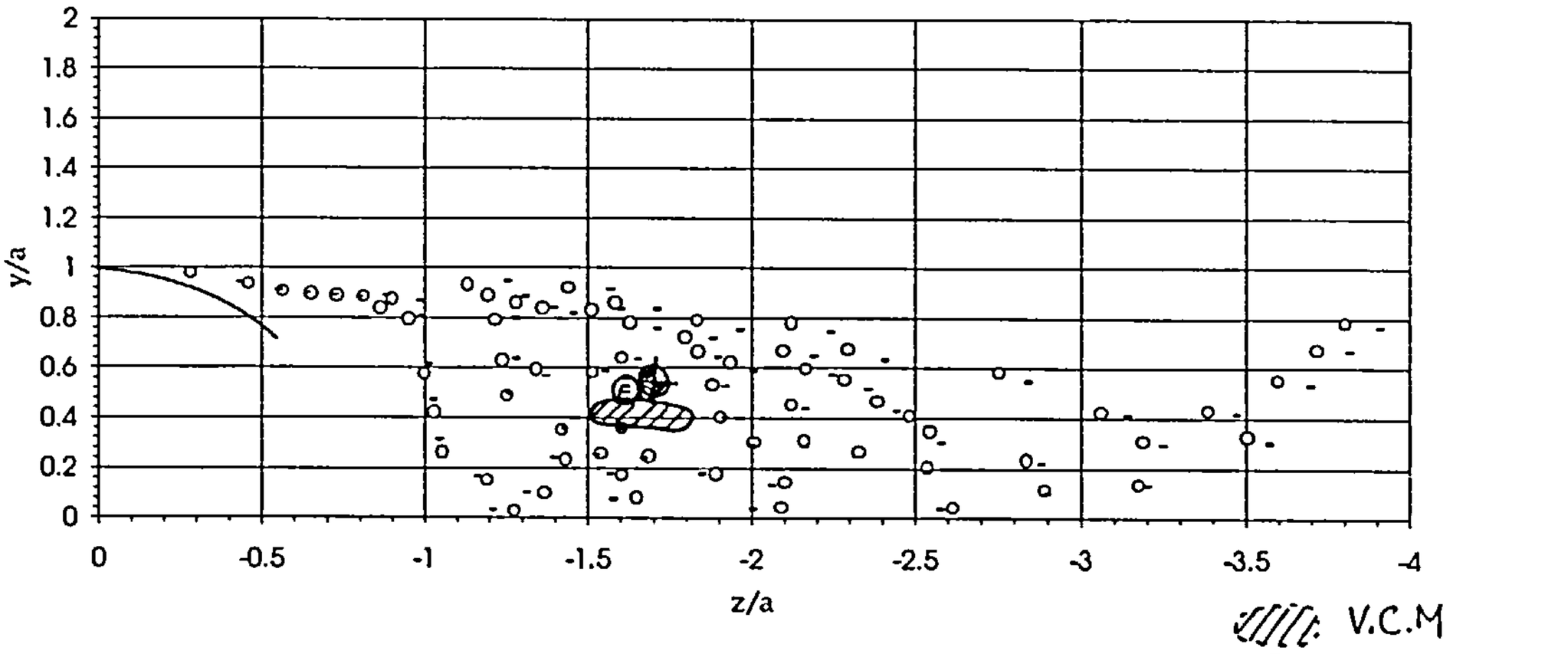

Figure 11.5.2.1

Predicted vortex core location vs VCM and experiment alpha=20
x/l=0.6131

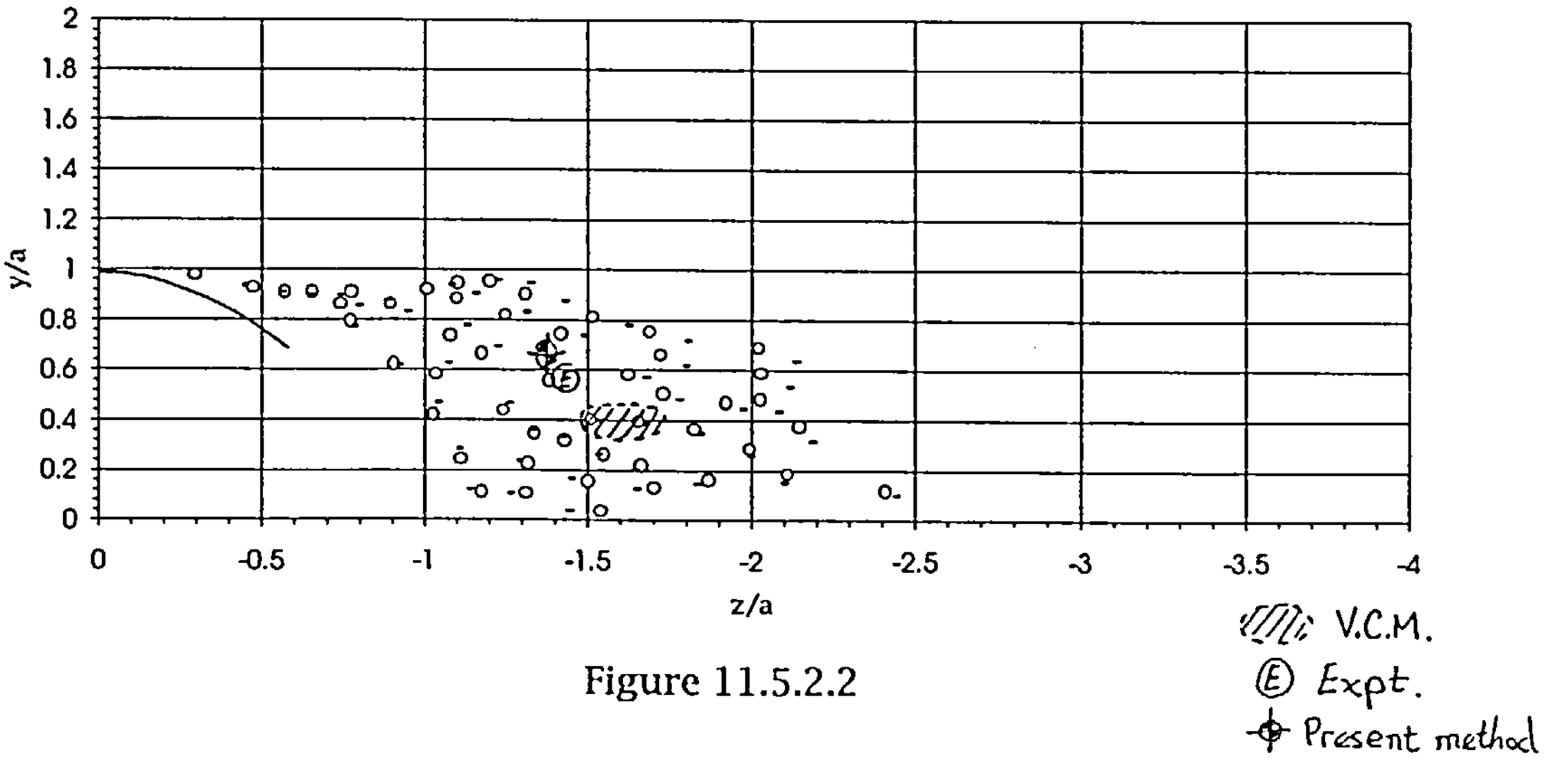

Figure 11.5.2.2

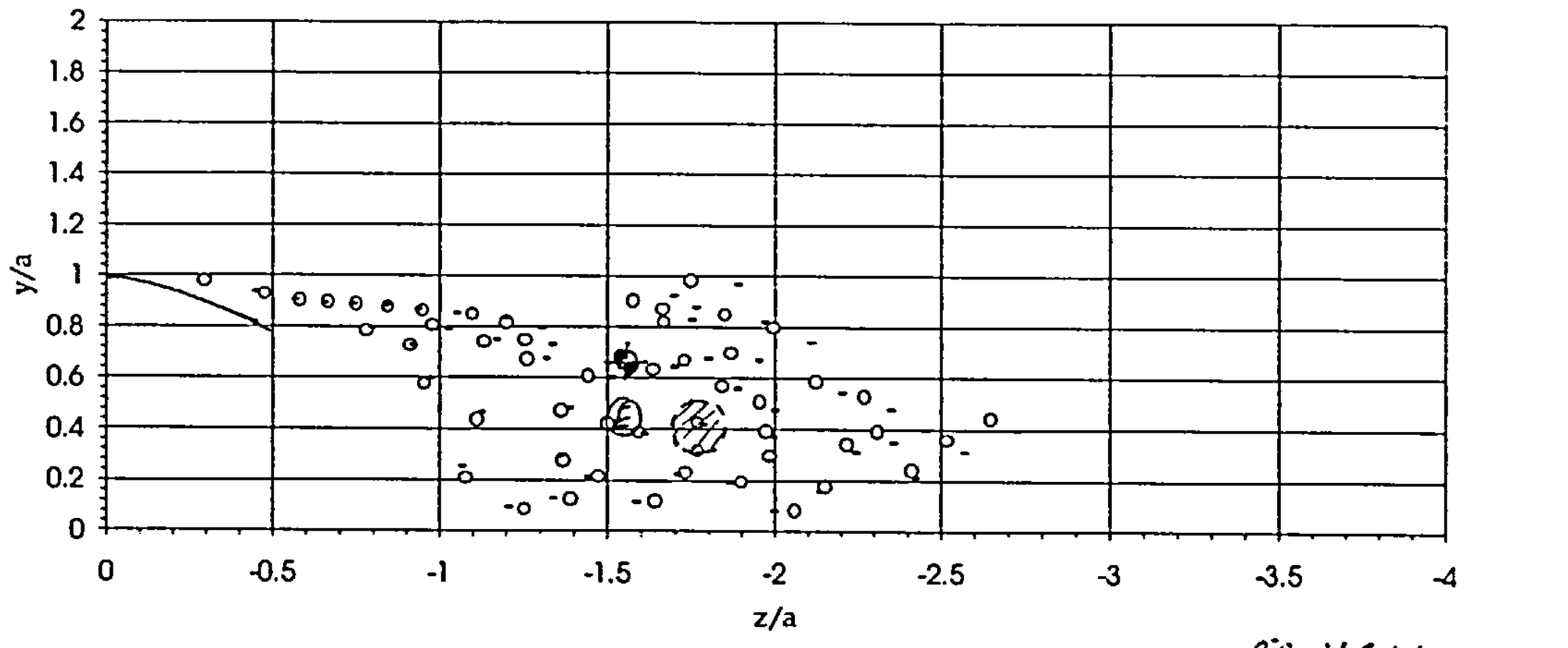

Figure 11.5.2.3

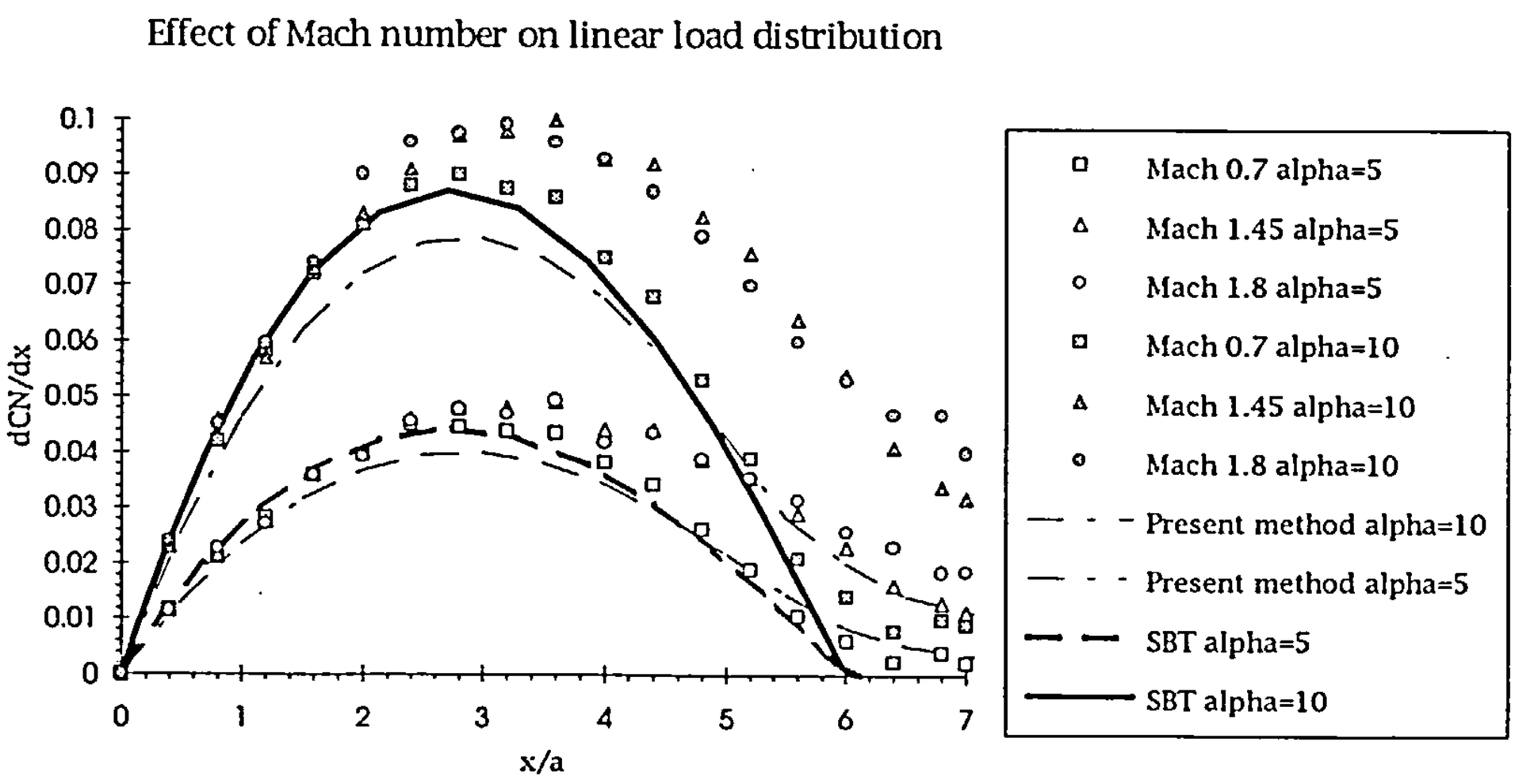

Figure 11.6.1.1

Effect of Mach number on load distribution

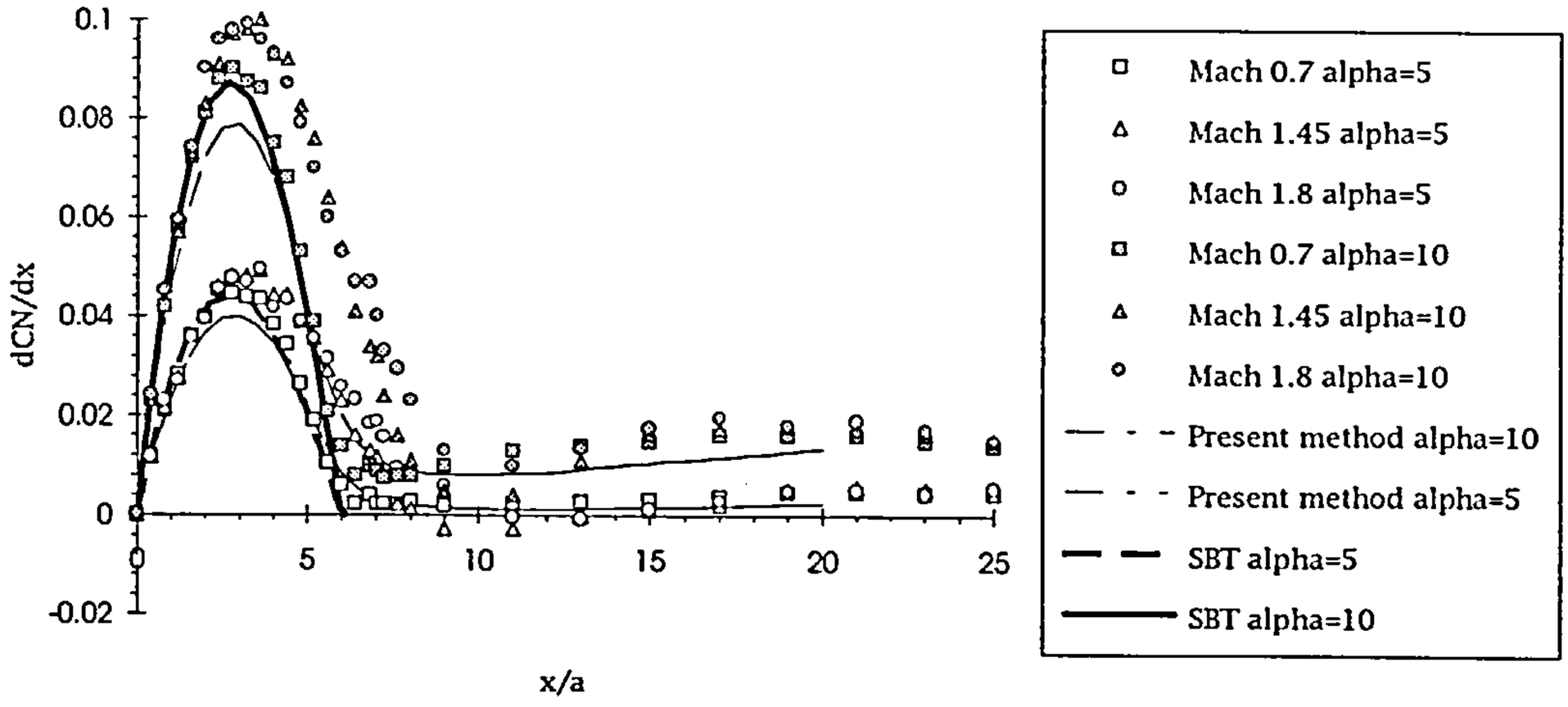

Figure 11.6.1.2

Geometry	C_p	$\frac{dC_N}{dx}$	C_N	ξ(x), η(x)	Γ(x)	Mach No. /R_N	Incidence	Reference	Availability
3 cal.ogive-7 cal. cylinder	✓	✓	✓	✓	✓	0.3 / 3.10^6, $0.44.10^6$ (/d)	5, 10, 15, 20, 24	**Tinling and Allen,** An investigation of the normal-force and vortex-wake characteristics of an ogive-cylinder body at subsonic speeds, NACA TN D-1297	✓
'slender curved body'	✓	✓	✓	✗	✗	0.89-1.12 /9-12.10^6 (/L)	4, 8, 12, 20	**Estabrooks, B.B.,** An analysis of the pressure distribution measured on a body of revolution at transonic speeds in the slotted test section of the Langley 8-foot transonic tunnel. NACA RM L52D21a	✓
'slender curved body' + slender nose with cylinder body	✓	✓	✓	✗	✗	0.6-1.2	4, 8, 12, 20	**Robinson, H.L.,** Pressures and associated aerodynamic and load characteristics for two bodies of revolution at transonic speeds. NACA RM L53L28a	✓
'slender curved body' + body wing		✓				0.6	4	**Loving, D.L. & Estabrooks, B.B.,** Transonic-wing investigation in the Langley 8-foot high-speed tunnel at a Mach number of 1.2 Analysis of pressure distribution of a wing-fuselage configuration having a wing of 45 sweepback, aspect ratio of 4, taper ratio 0.6 and NACA 65A006 airfoil section. NACA TIB 3344(12) NACA RM L51F07	✓
5.752 cal.ogive-15&7 cal. cylinder	✗	✗	✓	✗	✗	1.98	0-18	**Allen ,H.J. & Perkins E.W.,** A study of effects of viscosity on flow over slender inclined bodies of revolution. NACA R 1048	✓

ogive-boattail	×	✓	×	×	×	$0.58.10^6$ (/d)	-2, 0, 2, 3, 4, 5	**Christopher P.A.T., Hussain E. & Shaw C.T.** The subsonic aerodynamic characteristics of a body of revolution - A revised experiment CoA R 8408	✓
2 cal.ogive-4 cal. cylinder	✓	✓	×	×	×	$0.31.10^6$ (/d)	-2 ...10	**Llewelyn-Davies D.I T P.,** The experimental determination of the subsonic aerodynamic characteristics of an ogive-cylinder body including a comparison with theoretical estimates - volume 1 CoA R 8509	✓
Ogive-nose cylinder body								**Champigny P.** Pressure and force distributions on a 3D ogive nose and cylindrical body at high angles of attack ONERA Chatillon report GARTEur 01/AG04 Parts I-III 1983	ILL?
Ogive-nose cylinder body								**Hartmann K.** Pressure and force distributions on an ogive-nosed circular cylinder at high angles of attack in an incompressible airstream. DFVLR/AVA Gottingen Report IB 222-83 A05 (3 vols) 1983	ILL?
								Hartmann K. & Barth H. Druckverteilungsmessungen an einem rumpf und zwei flugel-rumpf-kombinationen zur untersuchung nichtlinaerer normalkraft- und momenton-charakteristiken. Forschungs-bericht aus der wehrtechnick B M Vg-FGWT 71-24: 1971	ILL?
								Roberts R.H Flow-field characteristics and aerodynamic loads on external stores near the fuselage and wing pylon positions of a swept-wing/ fuselage model at Mach numbers of 0.25 and 0.70 - Phase III AEDC TR-71-73 1971	ILL?

								Dillenius M.F.E.,Goodwin F.K. & Nielsen J.N. Prediction of supersonic store separation characteristics. Volume I - Theoretical methods and comparisons with experiment. AFFDL-TR-76-41 1976	ILL?
'slender curved body' -equation for R(x)	×	×	✓	×	×	0.4-1.53	0-20	**Allen H.J.** Estimation of the forces and moments acting on inclined bodies of revolution of high finess ratio. NACA RM A9I20 NACA TIB 2289	✓
5.75 cal ogive- nose 15 cal cylinder-body	✓	✓	✓	×	×	1.98	1, 2, 4, 6, 15	**Perkins E.W., & Kuehn D.M.** Comparison of the experimental and thoeretical distributions of lift on a slender inclined body of revolution at M = 2 NACA TN 3715 (Supersedes A53E01)	✓
3 cal ogive-nose 7 cal cylinder-body	✓	✓	✓	×	×	1.98	5, 10, 15, 20	**Perkins E.W., & Jorgensen L.H.** Comparison of the experimental and thoeretical normal-force distributions (including Reynolds number effects) on an ogive-cylinder body at Mach number 1.98 NACA TN 3716 (Supersedes A54H23)	✓

Table 7.3.3.1 Survey of accessible experimental data

Region	x/b	l_{region}	Γ	$\frac{V_1}{V_0}$	$\frac{V_2}{V_0}$	$\dot{\Gamma}$	$\frac{x_{mean}}{b}$	s
I	0.034 0.084	0.05	-.097	1.47 1.47	0.13 0.13	-1.125	0.059	0.06897
II	0.084 0.168	0.084	-0.136	1.47 1.42	0.13 0.18	-1.089	0.126	0.09986
III	0.168 0.252	0.084	-0.125	1.42 1.44	0.18 0.22	-1.053	0.21	0.09675
IV	0.252 0.336	0.084	-0.118	1.44 1.47	0.22 0.26	-1.115	0.294	0.0897

Table 7.3.7.4

Region	x/b	l_{region}	Γ	$\frac{V_1}{V_0}$	$\frac{V_2}{V_0}$	$\dot{\Gamma}$	$\frac{x_{mean}}{b}$	s
I	0.034 0.084	0.05	-0.107	1.47 1.47	0.13 0.13	-1.241	0.059	0.06897
II	0.084 0.168	0.084	-0.139	1.47 1.42	0.13 0.18	-1.114	0.126	0.09986
III	0.168 0.252	0.084	-0.128	1.42 1.44	0.18 0.22	-1.078	0.21	0.09675
IV	0.252 0.336	0.084	-0.116	1.44 1.47	0.22 0.26	-1.096	0.294	0.0897

Table 7.3.7.5

x/b	$\dot{\Gamma}$	$\frac{V_1}{V_0}$	$\frac{V_2}{V_0}$
0.034	-1.18	1.47	0.13
0.084	-1.20	1.47	0.13
0.168	-1.15	1.42	0.18
0.252	-1.11	1.44	0.22
0.336	-1.10	1.47	0.26
0.504		1.43	0.31

Table 7.3.7.5b

x/b	$\frac{V_1}{V_0}$	$\frac{V_2}{V_0}$	$\left(\frac{V_1}{V_0}\right)^*$	$\left(\frac{V_2}{V_0}\right)^*$	K	K^*
0.0			1.5			1.125
0.033			1.49	0.14		1.1
0.034	1.47	0.13			1.072	
0.084	1.47	0.13	1.47	0.17	1.072	1.066
0.168	1.42	0.18	1.42	0.18	0.992	0.992
0.252	1.44	0.22			1.013	
0.336	1.47	0.26			1.047	
0.504	1.43	0.31			0.974	

* Data interpolated by Fage & Johansen

Table 7.3.7.6

		Finite vortex street		Infinite vortex street	
	Measurement position	Karman	windtunnel	Karman	windtunnel
x/b	y/b	$\frac{\chi f}{V_0^2}$	$\frac{\chi f}{V_0^2}$	$\frac{\chi f}{V_0^2}$	$\frac{\chi f}{V_0^2}$
10	3.0	0.72	0.57	0.74	0.57
10	3.8	0.66	0.51	0.70	0.55

Table 7.3.7.7

x/b	$\dot{\Gamma}_{Area}$	$\dot{\Gamma}_{Contour}$	$\dot{\Gamma}_{Direct}$	$\dot{\Gamma}_{Approx}$
0				
0.033				
0.034			1.18	1.072
0.059	1.125	1.241		
0.084			1.2	1.072
0.126	1.089	1.114		
0.168			1.15	0.992
0.21	1.053	1.078		
0.252			1.11	1.013
0.294	1.115	1.096		
0.336			1.1	1.047
0.504				0.974

Table 7.3.7.8

No.	α	Reynolds	ϕ	Test no.
1	0	250000	0	4001 01
2	5			4001 06
3	10			4001 07
4	15			4001 12
5	20			4001 13
6	25			4001 18
7	30			4001 19
8	30			4001 97
9	35			4001 24
10	40			4001 25
11	44.4			4001 30
12	45			4002 01
13	50			4002 06
14	55			4002 07
15	60			4002 12
16	65			4002 13
17	70			4002 18
18	75			4002 19
19	80			4002 24
20	85			4002 27
21	90	250000	0	4002 28

Table 7.4.1.5 DFVLR test details at Reynolds number 0.25m

Test no.	Mach no.	Reynolds	ϕ	α
131	0.1	280000	0	0
132				10
133				20
134				30
135				35
136				40
137				45
139				50
140				55
141				60
142				65
143				70
144	0.1	280000	0	80

Table 7.4.2.2 ONERA test details at Reynolds number 0.28m

Mach	Reynolds	α	Test no.	ϕ
0.1	280000	10	132	0
		20	133	0
0.2	530000	10	148	0
		20	149	0
		20	255	10
		20	271	-10
		20	289	165
0.1	900000	20	209	0
0.2		10	223	0
0.2		20	224	0
0.35		20	164	0
0.2	2000000	10	188	0
		20	190	0
		30	191	0

Table 7.4.3.1 ONERA data

Reynolds	α	Test no.	ϕ
250000	5	4001 06	0
	10	07	
	15	12	
	20	13	
380000	5	05	
	10	08	
	15	11	
	20	14	
740000	5	04	
	10	09	
	15	10	
	20	15	
250000	20	31	30
740000		32	30
250000		37	60

740000		40	60
250000		47	90
740000		48	90
250000		50	120
740000		49	120
250000		59	150
740000		60	150
250000		61	180
740000		62	180
250000		71	210
740000		72	210
250000		73	240
740000		74	240
250000		83	270
740000		84	270
250000		85	300
740000		86	300
250000		94	330
740000		93	330

Table 7.4.3.2 DFVLR data